Journal of Engineering for Gas Turbines and Power

Published Quarterly by ASME

VOLUME 127 • NUMBER 3 • JULY 2005

TECHNICAL PAPERS

Fuels and Combustion Technology

Gas Turbines: Combustion and Fuels

Gas Turbines: Controls, Diagnostics & Instrumentation

Gas Turbines: Cycle Innovations

(Contents continued on inside back cover)

This journal is printed on acid-free paper, which exceeds the ANSI Z39.48-1992 specification for permanence of paper and library materials. ♾™
♲ 85% recycled content, including 10% post-consumer fibers.

Editor
LEE S. LANGSTON (2006)
Assistant to the Editor
LIZ LANGSTON
Associate Editors
Fuels and Combustion Technologies
K. M. BRYDEN (2008)
Internal Combustion Engines
J. C. COWART (2008)
M. S. WOOLDRIDGE (2008)
International Gas Turbine Institute
IGTI Review Chair
H. R. SIMMONS (2003)
A. J. STRAZISAR (2004)
K. C. HALL (2005)
Combustion and Fuels
P. MALTE (2006)
Structures and Dynamics
N. ARAKERE (2007)
M. MIGNOLET (2005)

PUBLICATIONS DIRECTORATE
Chair, **ARTHUR G. ERDMAN**

OFFICERS OF THE ASME
President, **RICHARD E. FEIGEL**
Executive Director,
VIRGIL R. CARTER
Treasurer,
T. PESTORIUS

PUBLISHING STAFF
Managing Director, Engineering
THOMAS G. LOUGHLIN
Director, Technical Publishing
PHILIP DI VIETRO
Production Coordinator
JUDITH SIERANT
Production Assistant
MARISOL ANDINO

Transactions of the ASME, Journal of Engineering for Gas Turbines and Power (ISSN 0742-4795) is published quarterly (Jan., April, July, Oct.) by The American Society of Mechanical Engineers, Three Park Avenue, New York, NY 10016. Periodicals postage paid at New York, NY and additional mailing offices. POSTMASTER: Send address changes to Transactions of the ASME, Journal of Engineering for Gas Turbines and Power, c/o THE AMERICAN SOCIETY OF MECHANICAL ENGINEERS, 22 Law Drive, Box 2300, Fairfield, NJ 07007-2300. **CHANGES OF ADDRESS** must be received at Society headquarters seven weeks before they are to be effective. Please send old label and new address. **STATEMENT from By-Laws.** The Society shall not be responsible for statements or opinions advanced in papers or ... printed in its publications (B7.1, par. 3).

COPYRIGHT © 2005 by the American Society of Mechanical Engineers. For authorization to photocopy material for internal or personal use under circumstances not falling within the fair use provisions of the Copyright Act, contact the Copyright Clearance Center (CCC), 222 Rosewood Drive, Danvers, MA 01923, Tel: 978-750-8400, www.copyright.com.

Canadian Goods & Services Tax Registration #126148048

Downloaded 03 Jun 2010 to 171.66.16.160. Redistribution subject to ASME license or copyright; see http://www.asme.org/terms/Terms_Use.cfm

(Contents continued)

Journal of Engineering for Gas Turbines and Power JULY 2005
Volume 127, Number 3

Gas Turbines: Heat Transfer

Gas Turbines: Industrial and Cogeneration

Gas Turbines: Manufacturing, Materials & Metallurgy

Gas Turbines: Structures and Dynamics

Gas Turbines: Microturbines and Small Turbomachinery

Internal Combustion Engines

(Contents continued on facing page)

Journal of Engineering for Gas Turbines and Power JULY 2005

Volume 127, Number 3

TECHNICAL BRIEF

The ASME Journal of Engineering for Gas Turbines and Power is abstracted and indexed in the following:

AESIS (Australia's Geoscience, Minerals, & Petroleum Database), Applied Science & Technology Index, Aquatic Sciences and Fisheries Abstracts, Civil Engineering Abstracts, Compendex (The electronic equivalent of Engineering Index), Computer & Information Systems Abstracts, Corrosion Abstracts, Current Contents, Engineered Materials Abstracts, Engineering Index, Enviroline (The electronic equivalent of Environment Abstracts), Environment Abstracts, Environmental Science and Pollution Management, Fluidex, INSPEC, Mechanical & Transportation Engineering Abstracts, Mechanical Engineering Abstracts, METADEX (The electronic equivalent of Metals Abstracts and Alloys Index), Pollution Abstracts, Referativnyi Zhurnal, Science Citation Index, SciSearch (The electronic equivalent of Science Citation Index), Shock and Vibration Digest

Fine Particulate Formation During Switchgrass/Coal Cofiring

Linda G. Blevins[1]
e-mail: lgblevi@sandia.gov

Thomas H. Cauley III

Combustion Research Facility,
P.O. Box 969, MS 9052,
Sandia National Laboratories,
Livermore, CA 94551-0969

Experiments to examine the effects of biomass/coal cofiring on fine particle formation were performed in the Sandia Multi-Fuel Combustor using fuels of pure coal, three combinations of switchgrass and coal, and pure switchgrass. For this work, fine particles with aerodynamic diameter between 10 nm and 1 μm were examined. A constant solid-fuel thermal input of 8 kW was maintained. The combustion products were cooled from 1200 to 420°C during passage through the 4.2 m long reactor to simulate the temperatures experienced in the convection pass of a boiler. Fine particle number densities, mass concentrations, and total integrated number and mass concentrations at the reactor exit were determined using a scanning mobility particle sizer. The fine particle number concentrations for cofiring were much higher than those achieved with dedicated coal combustion. However, the total integrated mass concentration of particles remained essentially constant for all levels of cofiring from 0% coal to 100% coal. The constant mass concentration is significant because pending environmental regulations are likely to be based on particle mass rather than particle size. [DOI: 10.1115/1.1804540]

1 Introduction

Cofiring of plant-derived biomass fuels in existing pulverized coal-fired power generation boilers has many advantages, including potential reductions of net CO_2, SO_2, and NO_x emissions [1,2]. While the effect of cofiring on these *gaseous* pollutant emissions has been widely studied [3–11], its effect on fine particulate emissions is not known. Here, fine particulates are defined as particles with aerodynamic diameters between 10 nm and 1 μm. This size range is sometimes referred to as the ultrafine fraction [12]. While recent studies have examined fine particle formation during cofiring of municipal solid waste (MSW) with coal [13–15], the effect of cofiring herbaceous fuels such as switchgrass with coal on fine particles has not been examined. Switchgrass is of interest because it is one of the dedicated energy crops being tested in several large scale demonstration projects [16–19]. The lack of research on fine particle formation during cofiring is a concern because of pending government fine particulate regulations [20–22]. Specifically, fine particles are a concern because they are less likely to be captured by electrostatic precipitators, cyclones, or baghouses than their larger counterparts [23–26].

To the authors' knowledge, only one study has addressed the effects of cofiring non-MSW biomass fuels on fine particulate matter emitted from a pulverized coal furnace [27]. In this previous study, fine particles were sampled from the stack of a 160 MW_e pulverized coal boiler cofired with 20% (thermal) straw. The authors found a fine particle mass concentration of 20–100 mg/m^3 (volume, m^3, is referenced to normal conditions of 20°C and 101 kPa). This mass concentration was higher than that achieved with dedicated coal combustion. Subsequent laboratory studies hinted that the increase in fine particle loading resulted from chlorination of vaporized alkali metals and/or sulfation reactions involving vaporized alkali metal species such as alkali chlorides and hydroxides and combustion-formed SO_2 [28–31]. Aerosol nucleation, coagulation, and growth by condensation follow as the alkali sulfate and chloride gases cool. The possibility of sulfation reactions is interesting because alkali metals (abundant in biomass but relatively scarce in coal) may synergistically combine with sulfur compounds (abundant in coal but scarce in biomass) to form a class of fine particles not present in significant amounts during coal or biomass combustion alone. Equilibrium calculations for typical combustion mixtures show that potassium sulfate (K_2SO_4) forms in the gas phase between 1100 and 1200°C and condenses below 1000°C, while condensed phase potassium chloride (KCl) forms below 800°C [7,32]. Sodium sulfate forms in the gas phase between 1000 and 1200°C, forms condensed particles below about 900°C, and solidifies below 400°C [28]. Other alkali containing particulates include silicates and aluminosilicates [28].

While the study mentioned earlier focused on straw/coal cofiring, to the authors' knowledge, fine particle formation during *switchgrass*/coal cofiring has never been studied experimentally. The purpose of this paper is to examine fine particle formation during switchgrass/coal cofiring. Experiments are used to examine the hypothesis that cofiring switchgrass with coal increases the number concentration of fine particles formed during combustion. While it is recognized that secondary fine particles can form from gaseous oxides of sulfur and nitrogen after they exit a boiler and enter the atmosphere [21,22], the present work focuses on primary fine particle formation within the combustion device only.

2 Experimental Methods

2.1 Reactor and Operating Conditions. Sandia's Multi-Fuel Combustor (MFC), shown schematically in Fig. 1, was used to simulate particle formation conditions in a boiler. The MFC is a down fired, electrically heated tubular reactor that is 4.2 m long and 15 cm in diameter. The interior of the MFC is made of silicon carbide and has seven independently heated 0.6 m long sections.

Unless otherwise noted, all volumetric rates of flow in this paper are referenced to standard conditions of 20°C and 101 kPa. A gas burner located at the top of the MFC was operated using 13.2 L/s±0.47 L/s (28.0 ft^3/min±1 ft^3/min) of combustion air and 1.0 L/s±0.047 L/s (2.15 ft^3/min±0.1 ft^3/min) of natural gas. The gas burner discharged a hot, vitiated air stream with about 9% O_2 at a temperature of about 1600°C into the MFC. Solid fuels were pneumatically injected into the vitiated air at the top of the MFC where the wall temperature was maintained at 1200°C. Combustion occurred in the top two MFC sections. The products were then cooled to 420°C using the average wall temperature profile shown in Fig. 1 to simulate the convection pass of a boiler. This temperature regime is of interest because it is where the synergistic alkali sulfation reactions and fume condensation occur [32]. Electric heaters in the top three sections maintained the wall temperatures within 10°C of the set points. To achieve maximum

---

[1] Author to whom correspondence should be addressed.

Contributed by the Fuels and Combustion Division of THE AMERICAN SOCIETY OF MECHANICAL ENGINEERS for publication in the ASME JOURNAL OF ENGINEERING FOR GAS TURBINES AND POWER. Manuscript received by the ICE Division, April 3, 2003; final revision received October 1, 2003. Associate Editor: S. Gollahalli.

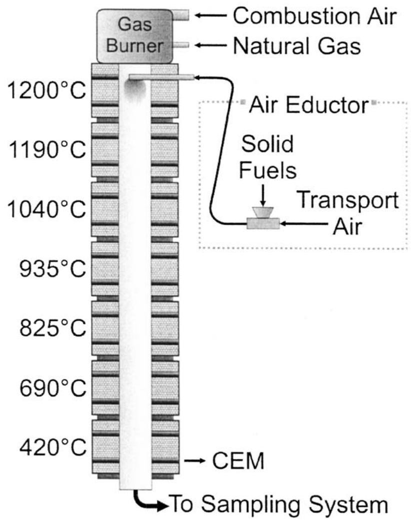

Fig. 1 Schematic of Sandia MFC showing wall temperatures used for the present experiments. The wall temperature gradient was selected to mimic the convection pass of a boiler. CEM =continuous emissions monitor.

cooling, the electric heaters in the bottom four sections were not active. Over the course of the experiments, wall temperatures in these bottom sections gradually increased by up to 100°C. The average temperature of each section during experimentation is shown in Fig. 1.

Delivery of cofired fuels in the MFC is achieved using two solid material screw feeders discharging into a common air eductor. The eductor (similar to an ejector pump) operates on the Bernoulli principle; a high-speed jet of transport air entrains the fuel as well as some ambient air. The eductor is the component shown schematically in the dashed box of Fig. 1. The ambient air entrainment rate was found by using transport N_2 in place of transport air and subsequently measuring the O_2 concentration downstream of the eductor. The air eductor used 2.12 L/s±0.083 L/s (4.5 ft^3/min±0.17 ft^3/min) of transport air and entrained 0.212 L/s ±0.023 L/s (0.45 ft^3/min±0.05 ft^3/min) of air, depending on the rates of solid fuel flow. The solid fuel feeders were calibrated using a receptacle, a stop watch, and a weighing scale.

The fuels used were Pittsburgh coal and switchgrass. Pittsburgh coal (sometimes called Pittsburgh number eight) is a high sulfur bituminous coal with an as-received higher heating value of 29.9 MJ/kg (12 900 Btu/lbm); the switchgrass used has an as-received higher heating value of 16.3 MJ/kg (7000 Btu/lbm). The higher heating value of the laboratory natural gas is 52.8 MJ/kg. Solid fuel ultimate, proximate, and ash analyses along with moisture are shown in Table 1. The sizes of the particles formed, whether they are condensable particles or the products of ash breakup, are expected to depend on the fuel size. The milled switchgrass was sieved to 1 mm. The coal was pulverized to a commercial grind (95% of mass in particles smaller than 150 μm diameter), which is typical of that used in boilers. In the commercial grind, ~42% by mass of particles have sizes smaller than 44 μm, ~35% of particles have diameters between 44 and 77 μm, ~22% of particles have diameters between 74 and 149 μm, ~1% have sizes between 149 and 300 μm, and ~0.2% have sizes between 300 and 600 μm.

To simulate the constant load of a power generator, the fuels were fed into the MFC at a constant solid-fuel thermal input of 8 kW based on the higher heating values provided earlier. The combined maximum heat release rate of the natural gas and solid fuels was 48 kW for all experiments. The amount of coal was varied between 0% thermal and 100% thermal in 25% intervals. The rates of solid fuel flow and the rates of K, Na, S, Cl, Si, Al, Ti, Fe, Ca, and Mg flow into the MFC are listed in Table 2. The total rate of reactant flow through the reactor varied from 1176 g/min for pure coal to 1190 g/min for pure switchgrass. Oxygen concentrations in the exhaust are also shown in the table. The oxygen concentration in the exhaust is not generally constant for a given total rate of heat release because the coal and switchgrass have different moisture concentrations, different carbon/hydrogen ratios, and different fuel-bound oxygen concentrations. The table demonstrates that, as switchgrass is added to coal, the rates of alkali metal, alkaline earth metal, and chlorine flow increase while the rates of flow of sulfur and refractory metals decrease. The rate of silicon input to the MFC remains essentially constant. These trends have implications for fine particle formation.

Reynolds numbers were computed for each of the seven reactor sections based on the MFC diameter (15 cm), average velocity, and gas properties evaluated at the local wall temperature. Reynolds number increased from 2400 to 3800 as the products traveled from inlet to exit, and resulting residence times were about 2 s. Combustion products were monitored with a continuous emissions monitor (CEM) during the course of experimentation to ensure that the CO_2 and O_2 concentrations exiting the MFC maintained reasonable agreement with C and O atom balances based on system inputs. Measured and predicted CO_2 and O_2 concentra-

Table 1 Fuel proximate, ultimate, ash, and heating value analyses, % dry basis, PC =Pittsburgh coal, SG=switchgrass. In ultimate analysis, oxygen is determined by difference.

Proximate			Ultimate			Ash		
	PC	SG		PC	SG		PC	SG
Fixed Carbon	49	14	C	72	49	SiO_2	41	63
Volatiles	40	82	H	5.0	4.6	Al_2O_3	21	0.98
Ash	11	4.6	O	6.8	41	TiO_2	0.89	0.21
			N	1.2	0.6	Fe_2O_3	29	1.3
Moisture	1.0	8.0	S	4.8	0.2	CaO	2.1	12
			Cl	0.0	0.03	MgO	0.78	3.7
						K_2O	1.7	6.2
						Na_2O	0.40	0.84
						SO_3	2.3	1.6
						P_2O_5	0.15	3.7

Higher heating value (MJ/kg, dry ash free)		
Natural gas	PC	SG
52.8	33.8	18.6

Table 2 Rates of mass flow of solid fuels and key elements, PC=Pittsburgh coal, SG =switchgrass

	% coal (thermal)				
	100	75	50	25	0
PC (g/min)	16.0	12.0	8.00	4.00	0.00
SG (g/min)	0.00	7.40	14.7	22.1	29.5
Exhaust O_2 (%v dry)	6.5±0.1	6.1±0.2	5.7±0.1	5.7±0.3	5.6±0.1
Ash (g/min)	1.7	1.6	1.5	1.4	1.3
PC ash (g/min)	1.70	1.3	0.87	0.44	0
SG ash (g/min)	0	0.31	0.62	0.94	1.3
K (mg/min)	24	34	44	54	64
Na (mg/min)	5.2	5.8	6.5	7.1	7.8
S (mg/min)	760	580	400	220	43
Cl (mg/min)	0	2	4	6	8
Si (mg/min)	334	342	350	359	367
Al (mg/min)	194	147	100	53.4	6.47
Ti (mg/min)	9.32	7.38	5.45	3.51	1.57
Fe (mg/min)	354	268	183	97.2	11.3
Ca (mg/min)	26.2	46.4	66.6	86.7	107
Mg (mg/min)	8.17	13.0	17.9	22.8	27.7

tions agreed within 10% and 20%, respectively. Approximate measured dry volumetric concentrations of CO_2 were 9%–10%, while O_2 concentrations were ≈6%.

2.2 Fine Particle Measurements. The sampling system shown in Fig. 2 is designed to reduce the amount of particle nucleation, the condensation of water and other species onto existing particles, and coagulation and agglomeration of existing particles in the sample probe and line [33]. Primary dilution is used to lower the concentrations of condensable species [34]. The primary dilution N_2 and the sampling system are maintained at or near 100°C to keep condensable species in the vapor phase. Secondary dilution further reduces condensable concentrations and reduces number concentrations to levels acceptable to the aerosol measurement instrument. The estimated temperature, velocity, and residence time in the sampling probe, shown in Fig. 3, are 450 K (average of 693 K process gas, 373 K dilution gas, and 300 K cooling jacket), 7 ms, and 65 ms, respectively. The product H_2O concentration at the sampling point is estimated to be about 15% by volume from mass balances. Primary dilution at 22:1 rapidly lowers the H_2O saturation ratio to a value below unity, assuring minimal H_2O condensation in the probe [35]. Condensation of other species is possible; sulfuric acid and heavy organics have vapor pressures of 1.3×10^{-3} Pa (10^{-5} Torr) and 1.3×10^{-10} Pa (10^{-12} Torr), respectively, at 25°C [36]. Estimation of saturation ratios for these compounds requires knowledge of their difficult-to-estimate concentrations in the combustion products, so it was not attempted. Representative coagulation rates can be estimated [35]: Assuming initial particle concentrations of 10^{10} particles/cm^3, monodisperse coagulation of particles between 0.1 and 1 μm within the probe in Fig. 3 results in less than a 20% increase in particle size and a 20%–40% decrease in number density within the probe [35]. Laminar flow was maintained and bends were kept to a minimum to reduce wall particle losses.

A 1–2 L/min sample was pulled from the 420°C MFC exit

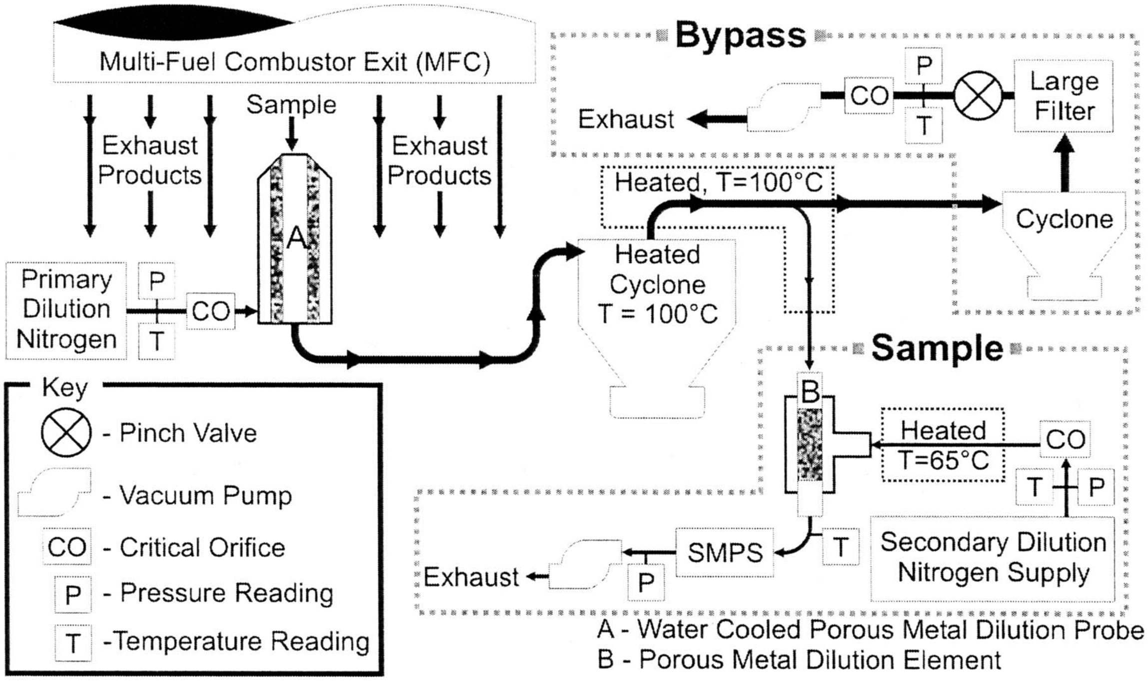

Fig. 2 Schematic of fine particle sampling system

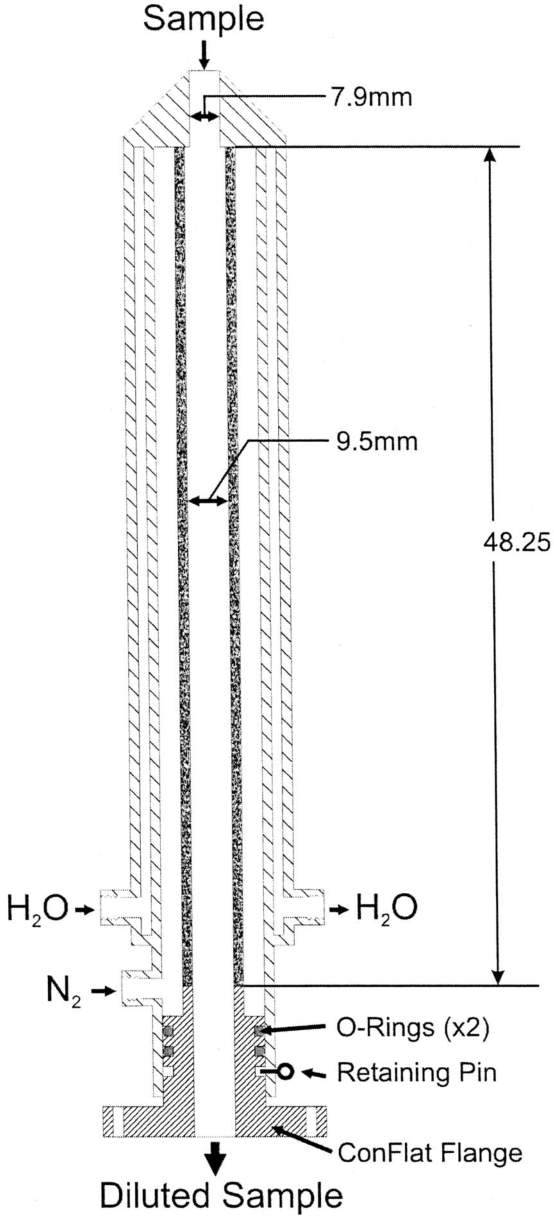

Fig. 3 Dilution probe used for fine particle sampling. The primary dilution ratio in the probe is 22:1.

plane into a water-cooled, 48 cm long, 0.95 cm inner diameter porous metal dilution probe (A in Fig. 2 and details in Fig. 3) supplied with a precisely controlled flow rate of clean, particle-free dilution N_2. Isokinetic sampling conditions were maintained, although they were not necessary for collection of the ultrafine, low-Stokes-number particles examined here. Nitrogen heated to about 100°C was added along the entire length of the probe to reduce the vapor pressure of the condensables and to minimize particle deposition on the probe walls. The primary dilution ratio in the probe was 22:1. Upon exiting the probe, the sample entered a 100°C cyclone for large particle removal.

A 0.02 L/min slip stream was removed and kept at 100°C as it entered the *sample* section, where it was diluted a second time in a porous metal element (B in Fig. 2) by clean, particle-free 65°C N_2. The secondary dilution ratio was 50:1. The 1 L/min diluted slip stream cooled to $25°\mathrm{C}\pm5°\mathrm{C}$ before entering a TSI Inc. scanning mobility particle sizer (SMPS).

The sample bypassing the SMPS was cleaned using a cyclone and filters before being metered and exhausted. To achieve stable dilution ratios, the rates of dilution N_2 and exhaust flow were maintained by critical flow orifices. These orifices were calibrated as a function of $P/\sqrt{T}$, where P and T are gas pressure and temperature, respectively, using an electronic bubble flow meter.

With primary and secondary dilution ratios of 22:1 and 50:1, respectively, the overall dilution ratio in the sample of interest was 1200:1. Measured size distributions were corrected using this dilution ratio to obtain undiluted distributions.

Particle size distributions as a function of aerodynamic diameter are measured using the SMPS. Aerodynamic diameter is defined as the diameter of a unit density sphere with the same settling velocity in air as the particle of interest. The SMPS consists of two instruments, a TSI 3081 differential mobility analyzer (DMA) and a TSI 3010-S condensation particle counter (CPC). The TSI Inc. aerosol instrument manager software continuously varies the DMA rod voltage and translates the CPC counts into a particle size distribution, taking into account a number of different correction factors (counting efficiency, charge efficiency, impactor type, etc). More information on the correction factors can be found elsewhere [37].

For these tests, a DMA voltage rise time of 165 s was used for three rates of air sheath flow, 2, 10, and 19 L/min. The voltage fall time was constant at 15 s. The 2 L/min flow provided the largest dynamic range, measuring particles between 90 nm and 1 μm. The 10 L/min flow allowed measurement of particles from 10 to 300 nm, and the 19 L/min flow allowed measurement of particles from 10 to 200 nm. Experiments with each flow rate were performed four times to determine uncertainties. Average values are reported with their respective uncertainties.

An experiment matrix of 15 trials, combining five coal thermal amounts (100%, 75%, 50%, 25%, and 0%) and three sheath flow rates (2, 10, and 19 L/min), was performed. To reduce systematic errors, the order of experiments was randomized. Type I uncertainties (statistical, Ref. [38]) were evaluated at 90% confidence in the mean using the Student's t distribution. For the majority of process values, type I uncertainty was low because of the large number of measurements taken. Type II uncertainties (nonstatistical, Ref. [38]) were estimated as the manufacturers' specifications of accuracy for each instrument.

The number and mass distribution functions are reported as $dN/d\log D_p$ and $dM/d\log D_p$, where N and M are the volumetric number concentration (#/cm^3) and volumetric mass concentration (μg/cm^3) of particles in a given size bin, respectively, D_p is the particle aerodynamic diameter (nm), and $d\log D_p$ is the constant logarithmic width of each size bin. Sixty-four divisions per decade of particle aerodynamic diameter are used for reporting the measurements; hence, the width for normalization is $d\log D_p=1/64$. Mass distributions are obtained from measured number distributions assuming a constant density of 1.2 g/cm^3. This density was selected as a conservative estimate of the density of fine particles formed by coal and/or biomass combustion. Typical biomass-formed substances such as alkali chlorides and alkali sulfates have densities between 2.0 and 2.7 g/cm^3, while coal char/ash has a density between 0.4 and 2.3 g/cm^3 [39]. The measured number distribution function and mass distribution functions are summed over all values of particle size and multiplied by $d\log D_p$ to obtain the total number density and mass concentrations, respectively.

3 Results

Figure 4 depicts the background number density distribution measured for the vitiated air from the natural gas burner with no solid fuels injected into the reactor. The number density of 10 nm particles is 4.0×10^7 particles/cm^3, and it decreases uniformly as particle size increases. Particles larger than 20 nm occur with diminishing concentrations below 10^4 particles/cm^3. The particles smaller than 20 nm possibly originate from MFC reactor wall deposits or from condensation aerosol formation in the sampling probe and/or sampling system.

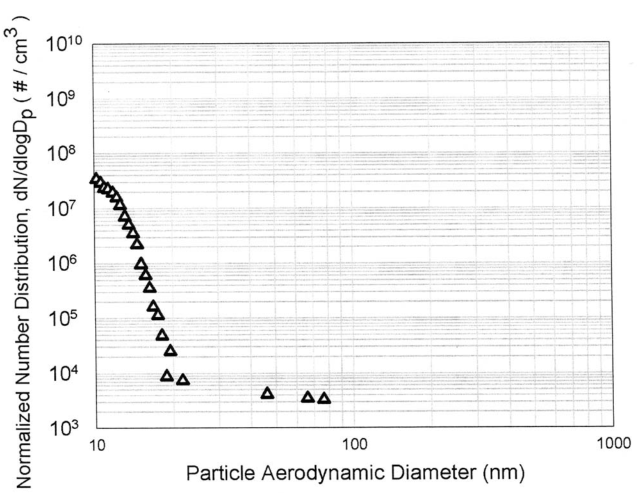

Fig. 4 Normalized number distribution for natural gas background

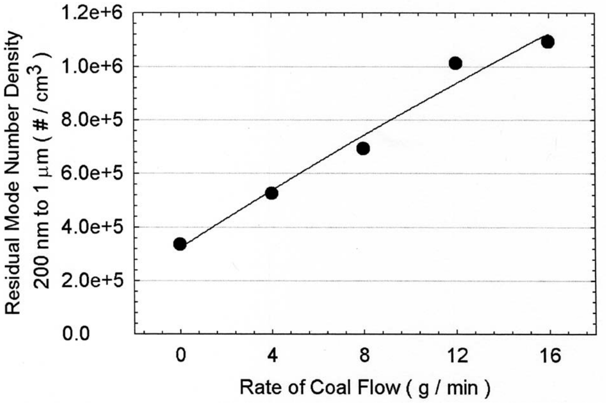

Fig. 6 Correlation of number density of particles between 200 nm and 1 μm with rate of coal addition to the reactor demonstrating that the particles in this size range originate from ash breakup

Measured number density distributions for 100%, 75%, 50%, 25%, and 0% coal are shown in Fig. 5. The 75% coal, 50% coal, and 25% coal conditions represent switchgrass/coal cofiring, while the 0% coal condition represents dedicated switchgrass combustion. Each curve is the average of 12 separate samples (four samples at each sheath flow rate) with the exception of 100% coal—one sample from 100% coal was discarded because of irregular fuel feeding. A few irregular feeding events are evident in Fig. 5; the large uncertainty intervals for the 50% coal trial near 100 nm represent the presence of two fuel feed spikes. Interestingly, for particles smaller than 13 nm, the distribution of coal-combustion-formed particles is similar to that from natural gas combustion (Fig. 4). Within experimental uncertainty, the number of particles per cubic centimeter is identical for coal and natural gas between 10 and 13 nm. The background number density associated with natural gas is not subtracted from the curves in Fig. 5 because the effects of the different fuels (natural gas, coal, biomass) are not generally expected to be linearly separable. For sizes above 13 nm, the coal makes more particles. As Fig. 5 depicts, the 100% coal particles have a bimodal distribution with a maximum of about 7.7×10^8 particles/cm^3 near 10 nm, a minimum of about 7.8×10^5 particles/cm^3 near 40 nm, and a smaller maximum of about 2.8×10^6 particles/cm^3 near 200 nm. The smaller sizes have relatively large uncertainties, which may result from the variability of condensation aerosol formation within either the sampling system or the MFC. The peak in particle size for 100% coal near 200 nm agrees with previous findings for coal combustion: Fine particles from pulverized coal combustion consist of a "condensable" mode and the beginning of the "residual" mode [24,40]. The condensable-mode particles originate from vaporization and condensation of volatile metals, while the residual mode particles originate from breakup of ash from the coal char. These two modes can be seen in Fig. 5 for 100% coal: The peak near 10 nm is the condensable mode, while the peak between 200 nm and 1 μm is the residual mode.

Another trend is apparent from Fig. 5. When switchgrass is burned with coal in any proportion or alone, the particle size distributions peak above 10^9 particles/cm^3 between diameters of 20 and 40 nm. The peak shifts towards larger diameters as the amount of biomass fuel increases. Hence, the peak number concentration for any of the biomass cases is two to three orders of magnitude larger than the peak particle number concentration for pure coal combustion. Addition of even a small amount of biomass to coal dramatically increases the particle loading between 10 and 100 nm.

The particle distribution for 100% switchgrass combustion exhibits only one maximum at about 40 nm in contrast to the two local maxima for 100% coal. Residual-mode particles from the switchgrass may not peak locally because the fuel has high volatile/low ash content and the metals appear in forms that are easily vaporized. The single mode of the biomass-generated fine particles may be either a broad condensable mode or it may be a combination of a condensable mode and a residual mode. The size of the particles formed during biomass cofiring and during dedicated biomass combustion suggests the presence of a high-concentration fume of condensable aerosols formed as the biomass combustion products cooled in the MFC.

For diameters greater than 150 nm, the particle number density from burning coal exceeds the particle number density for burning biomass with or without coal. Because the ash from each coal particle should produce three to five ash particles regardless of the coal particle's size [41], the number of residual particles formed from coal is expected to correlate with the amount of coal ash or coal added to the system. Figure 6 demonstrates that the number density of particles measured between 200 nm and 1 μm increases linearly as the rate of coal flow increases, which is consistent with the assumption that the coal-derived particles between 200 nm and 1 μm are residual-mode particles. In contrast, total number densities in Fig. 7 do not correlate linearly with the rate of coal mass flow (proportional to thermal percentage). The number of

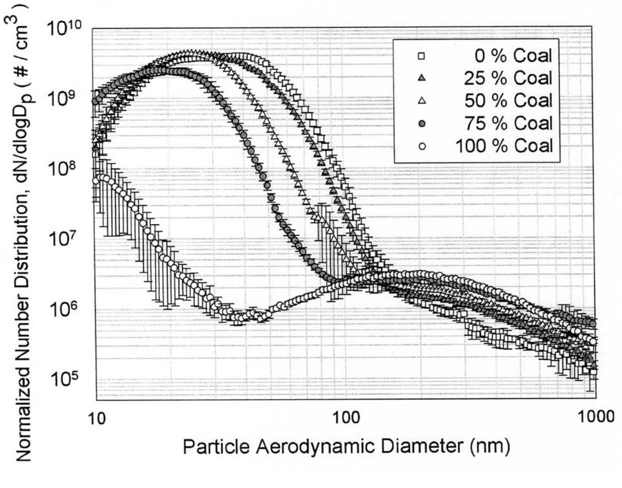

Fig. 5 Normalized number distribution for 0%, 25%, 50%, 75%, and 100% coal cofired with switchgrass. Type I uncertainty intervals are shown.

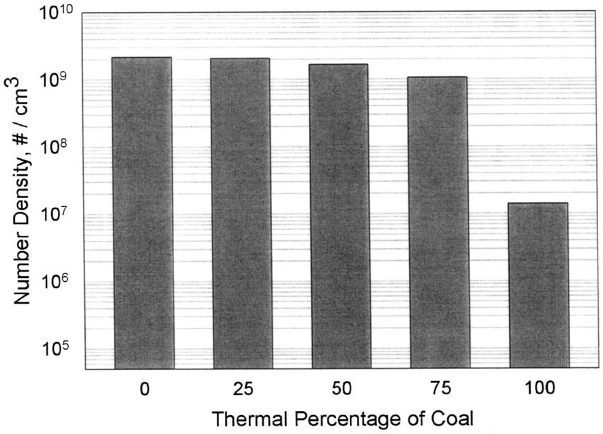

Fig. 7 Total number densities for particles between 10 nm and 1 μm in diameter for 0%, 25%, 50%, 75%, and 100% coal cofired with switchgrass

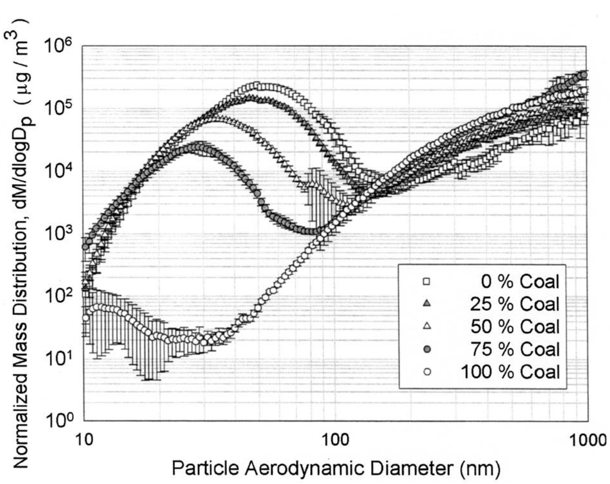

Fig. 8 Normalized mass distributions for 0%, 25%, 50%, 75%, and 100% coal cofired with switchgrass. Particle density is assumed to be 1.2 g/cm^3 density.

condensable particles is expected to depend on coal mass and on other variables such as temperature, local gas species, and metal speciation. The lack of correlation of the data from Fig. 5 with coal mass flow confirms that the measured particles between 10 nm and 1 μm contain a significant condensable-mode fraction.

Figure 7 shows the total measured number density of particles between 10 nm and 1 μm for all five fuel combinations derived from the distributions in Fig. 5. Addition of switchgrass in any amount increases the total number density by two orders of magnitude relative to coal. The increase in particle loading corresponds to increasing concentrations of Cl, Na, K, Mg, and Ca in the system. However, the particle loading does not increase linearly with the concentrations of these elements or with the rate of flow of switchgrass. This suggests that the species participating in the formation of the particles are present in excess for all of the switchgrass flows examined here. The fact that the increase is not linear with switchgrass amount may suggest that alkali sulfates are forming when the coal and biomass are present together. However, the fact that the particle loading is high for 100% switchgrass relative to cofiring hints that the fine particle formation observed here can be attributed to biomass alone. Examples of particles formed from the biomass combustion might be NaCl and/or KCl. A synergistic effect between coal and biomass is thus suggested but not proven.

Figure 8 shows a mass concentration distribution obtained combining the number distributions in Fig. 5 with an assumed particle density of 1.2 g/cm^3. The Fig. 8 concentrations cannot be compared in absolute value with the lower concentrations associated with particulate matter regulations (<100 μg/m^3) because regulations are developed based on stack emissions downstream of cleanup devices. While the absolute values on Fig. 8 must be interpreted cautiously because of the assumed density, the trends are revealing. The mass is concentrated primarily in particles larger than 100 nm for coal. The biomass confiring and pure biomass cases have local peaks between 30 and 50 nm. Interestingly, all of the distributions in Fig. 8 peak with a positive slope at 1 μm, indicating that a large portion of fine particle mass exists outside the measurable range of the SMPS.

Figure 9 shows integrated mass concentrations derived from the distributions in Fig. 8. The mass concentration is about 10^5 μg/m^3 for all fuel combinations. The concentration in Fig. 8 is analogous to that found upstream of a particle capture device in a practical combustion system. Figures 7 and 9 show that, although cofiring increases the number density of particles between 10 nm and 1 μm by two to three orders of magnitude, there is no significant change in the mass concentration. This finding is noteworthy because the gravimetrically determined mass concentrations of particles between 10 nm and 1 μm, a subset of those smaller than 2.5 μm that are likely to be regulated [20,21], should not change significantly when biomass is added to pulverized coal combustion.

Future efforts in this area should involve size-selective chemical sampling, a difficult challenge for small particles at low concentrations [42]. Current efforts in the present laboratory have focused on using thermal precipitation downstream of a differential mobility analyzer to deposit particles of known size onto substrates for subsequent electron microscopy. Particles with a diameter of 1 μm formed during 50% coal/50% biomass combustion have been identified using electron dispersive spectrometry to contain mostly sodium chloride. Some sulfur and potassium were also detected. However, challenges remain in being able to collect adequate particle concentrations to perform statistically significant and quantitative analyses. More research is needed to resolve these technical challenges.

4 Conclusions

Fine particle number densities from dedicated switchgrass combustion and from switchgrass/coal cofiring were two orders of magnitude higher than those from dedicated coal combustion in laboratory entrained flow reactor experiments. Fine particles

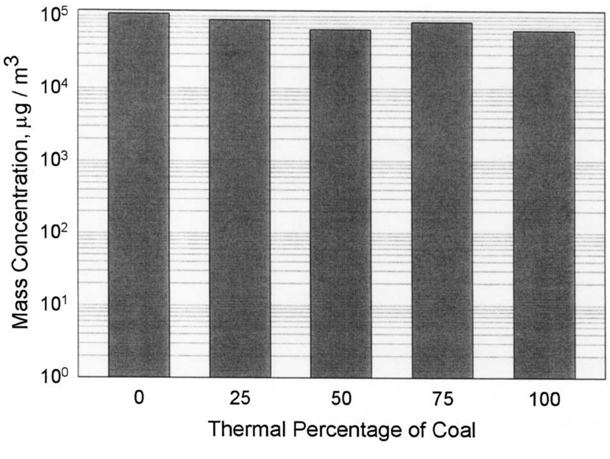

Fig. 9 Total mass concentrations between 10 nm and 1 μm in diameter for 0%, 25%, 50%, 75%, and 100% coal cofired with switchgrass

formed during coal combustion exhibited a condensable mode and a residual mode, in agreement with previous findings. Fine particles formed during switchgrass combustion exhibited only one broad particle size mode that may be attributable to either condensable particles or a combination of condensable and residual particles. Adding biomass to the coal significantly increased the number and mass of particles smaller than 100 nm, a trend which supports the existence of a strong condensable component in the particles formed from biomass combustion. A synergistic sulfate formation effect when coal and biomass are burned together is suggested, but further research is needed to isolate the effect. Although cofiring increases the total number density of ultrafine particulates by two orders of magnitude, it has no effect on the particle mass concentration. This is significant because regulations are likely to be composed on a mass basis rather than a number basis.

Acknowledgments

This paper is dedicated to the memory of Dr. Raymond Costello of the U.S. Department of Energy BioPower Program, who supported the work. Contributions of Gian Sclippa, Gilbert Hofacker, and Chris Shaddix are gratefully acknowledged. This paper was originally presented at the 2002 International Mechanical Engineering Congress and Exposition in New Orleans, Louisiana. Sandia is a multiprogram laboratory operated by Sandia Corporation, a Lockheed Martin Company, for the U.S. DOE under Contract No. DE-AC04-94-AL85000.

References

[1] Tillman, D. A., 2000, "Cofiring Benefits for Coal and Biomass," Biomass Bioenergy, **19**, pp. 363–364.

[2] Tillman, D. A., 2000, "Biomass Cofiring: The Technology; The Experience; The Combustion Consequences," Biomass Bioenergy, **19**, pp. 365–384.

[3] Dayton, D. C., 2002, "A Summary of NO_x Emissions Reduction From Biomass Cofiring," NREL/TP-510-32260, National Renewable Energy Laboratory, Golden, CO.

[4] Dayton, D. C., Belle-Oudry, D., and Nordin, A., 1999, "Effect of Coal Minerals on Chlorine and Alkali Metals Released During Biomass/Coal Cofiring," Energy Fuels, **13**, pp. 1203–1211.

[5] Robinson, A. L., Junker, H., Buckley, S. G., Sclippa, G., and Baxter, L. L., "Interactions Between Coal and Biomass When Cofiring," 1998, *Twenty-Seventh Symposium (International) on Combustion*, The Combustion Institute, Pittsburgh, p. 1351.

[6] Spliethoff, H., and Hein, K. R. G., 1998, "Effect of Co-Combustion of Biomass on Emissions in Pulverized Fuel Furnaces," Fuel Process. Technol., **54**, pp. 189–205.

[7] Hansen, P. F. B., Andersen, K. H., Wieck-Hansen, K., Overgaard, P., Rasmussen, I., Frandsen, F. J., Hansen, L. A., and Dam-Johansen, K., 1998, "Co-Firing Straw and Coal in a 150-MWe Utility Boiler: *In Situ* Measurements," Fuel Process. Technol., **54**, pp. 207–225.

[8] Pedersen, L. S., Morgan, D. J., Vandekamp, W. L., Christensen, J., Jespersen, P., and Damjohansen, K., 1997, "Effects on SO_x and NO_x Emissions by Co-Firing Straw and Pulverized Coal," Energy Fuels, **11**, pp. 439–446.

[9] Pedersen, L. S., Nielsen, H. P., Kiil, S., Hansen, L. A., Damjohanesn, K., Kildsig, F., Christensen, J., and Jespersen, P., 1996, "Full-Scale Co-Firing of Straw and Coal," Fuel, **75**, pp. 1584–1590.

[10] Abbas, T., Costen, P. G., and Lockwood, F. C., 1996, "Solid Fuel Utilization: From Coal to Biomass," *Twenty-Sixth Symposium (International) on Combustion*, The Combustion Institute, Pittsburgh, p. 3041.

[11] Vandekamp, W. L., and Morgan, D. J., 1996, "The Co-Firing of Pulverised Bituminous Coals With Straw, Waste Paper and Municipal Sewage Sludge," Combust. Sci. Technol., **121**, pp. 317–332.

[12] Oberdorster, G., 2001, "Pulmonary Effects of Inhaled Ultrafine Particles," Int. Arch. Occup. Environ. Health, **74**, pp. 1–8.

[13] Fernandez, A., Davis, S. B., Wendt, J. O. L., Cenni, R., Young, R. S., and Witten, M. L., 2001, "Public Health: Particulate Emission From Biomass Combustion," Nature (London), **409**, pp. 998–998.

[14] Seames, W. S., Fernandez, A., and Wendt, J. O. L., 2002, "A Study of Fine Particulate Emissions From Combustion of Treated Pulverized Municipal Sewage Sludge," Environ. Sci. Technol., **36**, pp. 2772–2776.

[15] Fernandez, A., Wendt, J. O. L., Cenni, R., Young, R. S., and Witten, M. L., 2002, "Resuspension of Coal and Coal/Municipal Sewage Sludge Combustion Generated Fine Particles for Inhalation Health Effects Studies," Sci. Total Environ., **287**, pp. 265–274.

[16] Amos, W., 2002, "Summary of Chariton Valley Switchgrass Co-Fire Testing at the Ottumwa Generating Station in Chillicothe, Iowa," NREL/TP-510-32424, National Renewable Energy Laboratory, Golden, CO.

[17] Mclaughlin, S. B., Ugarte, Dgdl, Garten, C. T., Lynd, L. R., Sanderson, M. A., Tolbert, V. R., and Wolf, D. D., 2002, "High-Value Renewable Energy From Prairie Grasses," Environ. Sci. Technol., **36**, pp. 2122–2129.

[18] Kzos, L. A., Downing, M. E., Wright, L. E., Cushman, J. H., McLaughlin, S. B., Tolbert, V. R., Tuskan, G. A., and Walsh, M. E., 2000, "Bioenergy Feedstock Development Program Status Report," ORNL/TM-2000/92, Oak Ridge National Laboratory, Oak Ridge, TN.

[19] Boylan, D., Bush, V., and Bransby, D. I., 2000, "Switchgrass Cofiring: Pilot Scale and Field Evaluation," Biomass Bioenergy, **19**, pp. 411–417.

[20] Sloss, L. L., and Smith, I. M., 2000, "PM10 and PM2.5: An International Perspective," Fuel Process. Technol., **65**, pp. 127–141.

[21] Tucker, W. G., 2000, "An Overview of PM2.5 Sources and Control Strategies," Fuel Process. Technol., **65**, pp. 379–392.

[22] Smith, I. M., and Sloss, L. L., 1998, "PM10/PM2.5—Emissions and Effects," IEA CCC/08, International Energy Agency Coal Research, London, UK.

[23] Senior, C. L., Helble, J. J., and Sarofim, A. F., 2000, "Emissions of Mercury, Trace Elements, and Fine Particles From Stationary Combustion Sources," Fuel Process. Technol., **65**, pp. 263–288.

[24] Lighty, J. S., Veranth, J. M., and Sarofim, A. F., 2000, "Combustion Aerosols: Factors Governing Their Size and Composition and Implications to Human Health," J. Air Waste Manage. Assoc., **50**, pp. 1565–1618.

[25] Ylatalo, S. I., and Hautanen, J., 1998, "Electrostatic Precipitator Penetration Function for Pulverized Coal Combustion," Aerosol Sci. Technol., **29**, pp. 17–30.

[26] Linak, W. P., and Wendt, J. O. L., 1994, "Trace-Metal Transformation Mechanisms During Coal Combustion," Fuel Process. Technol., **39**, pp. 173–198.

[27] Christensen, K. A., and Livbjerg, H., 1996, "A Field Study of Submicron Particles From the Combustion of Straw," Aerosol Sci. Technol., **25**, pp. 185–199.

[28] Wei, X. L., Lopez, C., Von Puttkamer, T., Schnell, U., Unterberger, S., and Hein, K. R. G., 2002, "Assessment of Chlorine-Alkali-Mineral Interactions During Co-Combustion of Coal and Straw," Energy Fuels, **16**, pp. 1095–1108.

[29] Christensen, K. A., and Livbjerg, H., 2000, "A Plug Flow Model for Chemical Reactions and Aerosol Nucleation and Growth in an Alkali-Containing Flue Gas," Aerosol Sci. Technol., **33**, pp. 470–489.

[30] Christensen, K. A., Stenholm, M., and Livbjerg, H., 1998, "The Formation of Submicron Aerosol Particles, HCl and SO_2 in Straw-Fired Boilers," J. Aerosol Sci., **29**, pp. 421–444.

[31] Iisa, K., Lu, Y., and Salmenoja, K., 1999, "Sulfation of Potassium Chloride at Combustion Conditions," Energy Fuels, **13**, pp. 1184–1190.

[32] Nielsen, H. P., Baxter, L. L., Sclippa, G., Morey, C., Frandsen, F. J., and Damjohansen, K., 2000, "Deposition of Potassium Salts on Heat Transfer Surfaces in Straw-Fired Boilers: A Pilot-Scale Study," Fuel, **79**, pp. 131–139.

[33] Sloss, L., 1998, "Sampling and Analysis of PM10/PM2.5," IEA CC/09, International Energy Agency Coal Research, London, UK.

[34] Biswas, P., 2001, "Measurement of High-Concentration and High-Temperature Aerosols," *Aerosol Measurement: Principles, Techniques, and Applications*, 2nd ed., P. A. Baron and K. Willeke, eds., Wiley-Interscience, New York, p. 903.

[35] Hinds, W. C., 2001, "Physical and Chemical Changes in the Particulate Phase," *Aerosol Measurement: Principles, Techniques, and Applications*, 2nd ed., P. A. Baron and K. Willeke, eds., Wiley-Interscience, New York, p. 83.

[36] Tobias, H., Beving, D., Ziemann, P., Sakurai, H., Zuk, M., McMurry, P., Zarling, D., Waytulonis, R., and Kittelson, D., 2001, "Chemical Analysis of Diesel Engine Nanoparticles Using a Nano-DMA/Thermal Desorption Particle Beam Mass Spectrometer," Environ. Sci. Technol., **35**, pp. 2233–2243.

[37] Anon., 2000, "Model 3080 Electrostatic Precipitator Manual," TSI, Inc., St. Paul, MN.

[38] Anon., 1997, "American National Standard for Expressing Uncertainty—U.S. Guide to the Expression of Uncertainty in Measurements," ANSI/NCSL Z540-2-1997, American National Standards Institute, National Conference of Standards Laboratories, Boulder, CO.

[39] Mitchell, R. E., Hurt, R. H., Baxter, L. L., and Hardesty, D. R., 1992, "Compilation of Sandia Coal Char Combustion Data and Kinetic Analyses," SAND92-8202, Sandia National Laboratories, Livermore, CA.

[40] Quann, R. J., and Sarofim, A. F., 1982, "Vaporization of Refractory Oxides During Pulverized Coal Combustion," *Nineteenth Symposium (International) on Combustion*, The Combustion Institute, Pittsburgh, PA, p. 1429.

[41] Sarofim, A., Howard, J., and Padia, A., 1977, "Physical Transformation of Mineral Matter in Pulverized Coal Under Simulated Combustion Conditions," Combust. Sci. Technol., **16**, pp. 187–204.

[42] Geller, M. D., Kim, S., Misra, C., Sioutas, C., Olson, B. A., and Marple, V. A., 2002, "A Methodology for Measuring Size-Dependent Chemical Composition of Ultrafine Particles," Aerosol Sci. Technol., **36**, pp. 748–762.

T. Shimada
Keihin Works,
NKK Corporation,
1-1 Minamiwatarida-cho,
Kawasaki-ku, Kawasaki 210-0855,
Japan

T. Akiyama

S. Fukushima

NKK Corporation,
1-1-2 Marunochi,
Chiyoda-ku,
Tokyo 100-8202, Japan

K. Mitsui
Photron Limited,
1-9-8 Shibuya,
Shibuya-ku,
Tokyo 150-0002, Japan

M. Jinno
Department of Applied Chemistry,
Graduate School of Engineering,
Nagoya University,
Nagoya 464-8603, Japan

K. Kitagawa

N. Arai

Research Center for Advanced Energy Conversion,
Nagoya University,
Furo-cho, Chikusa-ku,
Nagoya 464-8603, Japan

Ashwani K. Gupta
Department of Mechanical Engineering,
University of Maryland,
College Park, MD 20742
e-mail: akgupta@eng.umd.edu

Time-Resolved Temperature Profiling of Flames With Highly Preheated/Low Oxygen Concentration Air in an Industrial Size Furnace

A high-speed video camera was combined with a newly developed optical system to measure time resolved two-dimensional (2D) temperature distribution in flames. This diagnostics has been applied to measure the temperature distribution in an industrial size regenerative test furnace facility using highly preheated combustion air and heavy fuel oil. The 2D distributions of continuum emission from soot particles in these flames have been simultaneously measured at two discrete wave bands at 125 frames/sec. This allowed us to determine the temperature from each image on the basis of two-color 2D thermometry, in which the ratio of the 2D emission intensity distribution at various spatial position in the flame was converted into the respective 2D temperature distribution with much higher spatial resolution as compared to that obtainable with thermocouples. This diagnostic method was applied to both premixed and diffusion flames with highly preheated low oxygen concentration combustion air using heavy fuel oil. The results show that higher temperature regions exist continuously in the premixed flame as compared to the diffusion flame. This provided clear indication of higher NO emission from the premixed flame as compared to diffusion flames during the combustion of heavy fuel oil under high-temperature air combustion conditions. This observation is contrary to that obtained with normal temperature combustion air wherein diffusion flames result in higher NO_x *emission levels.* [DOI: 10.1115/1.1914801]

1 Introduction

Energy consumption in the industrial sector represents one of the major usages of energy. In the steel processing industrial sector the energy consumption required is very high and can be classified among the top energy consumers. Therefore, savings of energy in steel processing as well as other industrial furnaces is among the most important issues for energy conservation. The improvement of thermal efficiency of furnaces and power plants provide direct impact on decreased consumption of fossil fuel energy, which subsequently reduces emission of carbon dioxide to the atmosphere that is known to cause the greenhouse effect.

In an effort to increase the thermal efficiency with low emission of NO_x and noise, a new combustion technique, called high-temperature air combustion (also called HiTAC) has been studied [1–5]. This project has been supported by the New Energy Technology Development Organization (NEDO) of Japan under the national "High Performance Industrial Furnace Development Project." One of the authors of this paper (A.K.G.) was the international consultant to NEDO on this national project to provide his vision and leadership for successful project accomplishments with good collaborations between academia and industry. Field tests carried out using this project have successfully demonstrated fuel energy saving of about 30%, emissions reduction of about 25%, downsizing of the equipment by about 25% by this new and innovative method of combustion. In some cases significantly

---

Contributed by the Fuels and Combustion Division of THE AMERICAN SOCIETY OF MECHANICAL ENGINEERS for publication in the ASME JOURNAL OF ENGINEERING FOR GAS TURBINES AND POWER. Manuscript received by the F&C Division December 3, 2002; final revision received June 1, 2004. Associate Editor: S. R. Gollahalli.

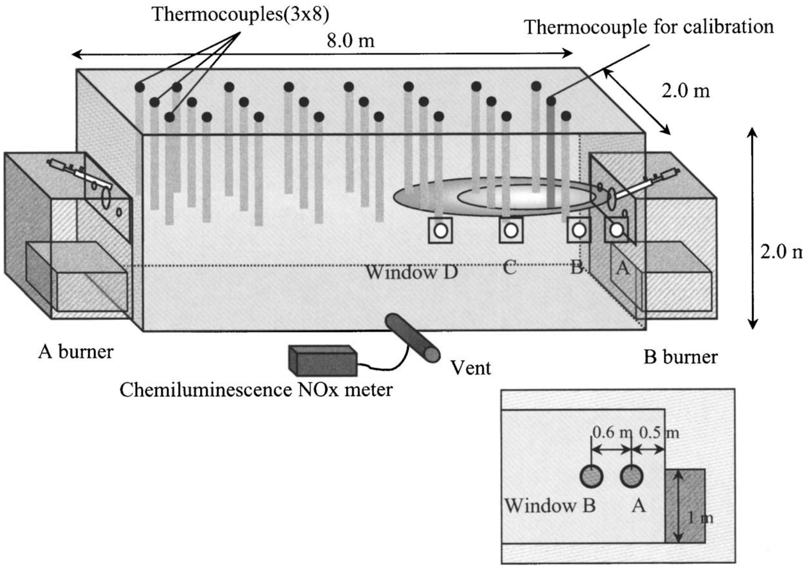

Fig. 1 A schematic diagram of the industrial size test furnace

more energy savings have been achieved [1]. Furthermore, the flammability limits are significantly improved with near isothermal combustion zone and significantly high heat flux from the combustion zone using high-temperature air combustion technology [1–5].

The combustion of fuels with highly preheated normal combustion air, using a regenerator in the form of a heat accumulator from the exhaust gases, increases the NO_x emission levels. In order to overcome this problem, the combustion air having very low oxygen concentration (few percent of oxygen in the combustion air) is used. Therefore, under high-temperature air combustion conditions, combustion occurs at very low oxygen concentration in the combustion air. In addition, the fuel jet velocity injected into the combustion air is very high. Under such conditions the NO_x emissions are very low as compared to normal combustion air despite very high temperature of the combustion air. The results obtained here have shown that NO_x emission is significantly different under the premixed and diffusion flame combustion conditions.

In our previous study [6–9], basic combustion characteristics were examined on an industrial size test furnace of high thermal efficiency using highly preheated and low oxygen concentration combustion air. Spectroscopically resolved profiles were obtained from the spontaneous emission of soot particles and from the radical species, such as OH, CH, C_2, and NO in luminous and nonluminous flames using a charge-coupled device (CCD) camera fitted with appropriate optical band-pass filters. Temperature profiles have also been obtained for premixed and diffusion flames formed with highly preheated and low oxygen concentration combustion air using two-color optical pyrometry method of gray body emission for the C_2 Swan band. The results revealed significant differences in the spatial distribution of radical species and temperatures. Localized zones of high temperature were found in the premixed flames that also resulted in higher levels of NO_x emission.

Our previous studies reported time-averaged (of the order of ten seconds) profiles. However, it is often very important to examine the temporal change in local temperature or its spatially resolved temperature distribution in flames. Thermal NO_x depends on instantaneous occurrence of high-temperature regions. In this study, a method to determine time-resolved profiles of flame temperature or soot surface temperature has been developed on the basis of narrow band two-color optical thermometry. The optical arrangement incorporates two narrow band-pass interference filters fitted to a high-speed metal oxide semiconductor (MOS) video camera. This provided observation of the two monochromatic flame images at two discrete wavelengths. The focus here is on the observed differences in time-resolved profiles of premixed and diffusion flames using heavy oil with special emphasis on the role of thermal field on NO_x emission.

2 Experiment

Test Furnace for Regenerative Combustion of Heavy oil. Figure 1 shows a schematic diagram of the industrial size regenerative test furnace facility. The figure also provides details on the observation windows A and B located on the B-side burner of the furnace. The furnace chamber was 8 m long, 2 m wide, and 2 m high and was installed with two regenerative burners (A and B) located on 2×2-m side walls of the furnace. The burner fired along the longitudinal direction (8-m-long section) of the furnace. High-temperature combustion air at low oxygen concentration was obtained using regenerative burners and this air was used for the combustion of heavy fuel oil. This furnace system was basically the same as that used in our previous study [4–6], except for the fuel injector fitted with an atomizer for the combustion of heavy fuel oil. Eight water-cooled pipes were located in the furnace floor at 1-m intervals that simulate the thermal load. These pipes therefore provided a measure of the heat output load and longitudinal distribution of heat flux in the furnace. As indicated in Fig. 1, an array of 0.5-mm wire diameter R-type thermocouples were suspended from the furnace ceiling to form a grid of 1-m size interval in the longitudinal direction, 0.75-m size in the horizontal direction, and 0.5-m size in the vertical direction of the furnace. Thus, the furnace had a total of 52 thermocouples as indicated in Fig. 1. The junction points of 22 thermocouples were located in the horizontal plane of the burner axis. These thermocouples provided information on the distribution of temperature on the flame axis in the furnace.

The pair of the regenerative burners were switched every 30 sec so that the flame was formed alternately between the two burners. The exhaust gases were passed through the honeycomb regenerator of aluminum/cordierite, which accumulated most of the exhaust heat prior to its discharge to the atmosphere. The oxygen concentration in the air could be reduced down to 2% by mixing the fresh air with the exhaust gases. During the following combustion period, the combustion air is preheated up to a maximum of 1550 K with the passage of air through the heated regenerator.

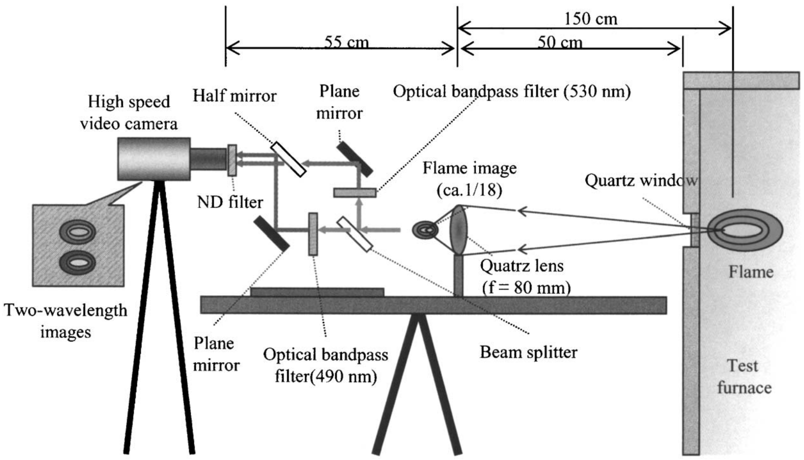

Fig. 2 A schematic diagram of the two wavelength high-speed video camera

With this air preheat temperature the highest attainable furnace temperature was 1623 K (measured 70 mm below the furnace ceiling at the furnace center). This thermocouple reading is referred to here as the average (characteristic) furnace temperature. This is reasonable as the temperature measured in the mid center region of the furnace with the two burners firing from the two opposite walls is a good indication of the characteristic mean thermal conditions in the furnace. It is recognized that the actual temperature at other spatial locations in the furnace may be considerably different than this mean value of the temperature.

Premixed and diffusion combustion conditions have been examined in order to determine the differences in the spatial distribution of flame temperature and NO_x emission. For the premixed combustion, the heavy fuel oil is mixed with the highly preheated combustion air in the central injector pipe located on the flame axis. However, for the diffusion combustion condition, the fuel is injected from the two nozzles located on the two opposite sides of the air injection nozzle so as to provide wider separation between fuel and air entering the furnace, see Fig. 1.

The test furnace is installed with four quartz windows (labeled as A, B, C, and D in the figure) in order to provide spectroscopic observation of the flame. In order to prevent the optical system from overheating by radiation from the flame, the windows have an iron screen coated with alumina/silica wool. The windows are normally closed with the above screens except for the relatively short measurement time.

Heavy Fuel oil and Operating Condition. The heavy fuel oil used is classified as the lighter one among heavy oils having an elemental composition (by wt. %) of 86.67 C, 13.19 H, 0.08 S, 0.01 N, and 0.05 water. The operating conditions of the test furnace for the premixed and diffusion combustion were as follows: flow rates of the heavy fuel oil and fresh air were 70.9 kg/h and 880 Nm^3/h, respectively. The other operating conditions were: thermal input load =920 kW, air preheats temperature =1383 K, equivalence ratio =0.842, oxygen concentration in air =3.5%, Reynolds number of air at the injection nozzle =51,000, and the resulting representative furnace temperature =1535 K (measured by the thermocouple located at center of the furnace).

NO_x Concentration. The NO_x concentration was measured with a chemiluminescence NO_x meter (Shimadzu NOA7000) by continuously sampling the exhaust gas from the ventilation duct located at mid point of the furnace (see Fig. 1).

Spectroscopic Two-dimensional Measurements. Figure 2

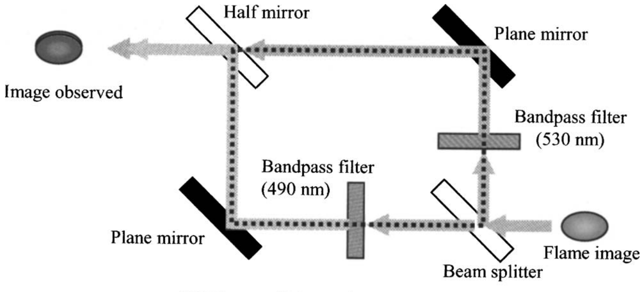

Without tilting of plane mirrors

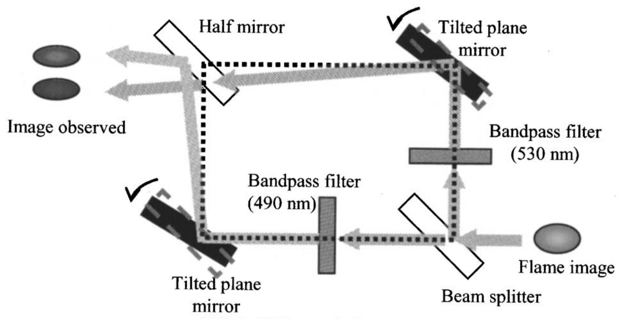

With tilting of plane mirrors

Fig. 3 Details of the optical system for separating the two wavelength images

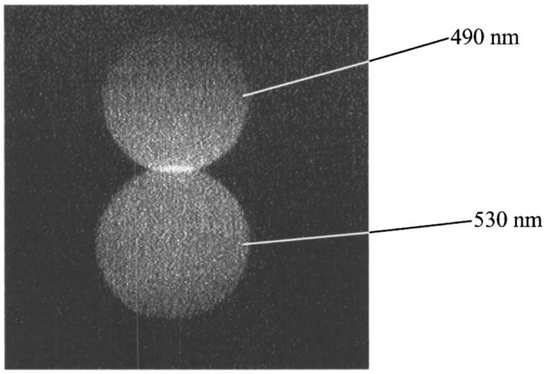

Fig. 4 Two wavelength images of background emission from furnace wall through window B

shows a schematic diagram of the measurement system developed for measuring time-resolved temperature profiles of flames. The system consists of synthetic quartz focusing lens (50 mm in diameter, $f=80$ mm), an optical system to separate the flame image into two images of different wavelengths, and a high-speed MOS video camera having 250 × 250 pixels that allowed a maximum sampling rate of 4500 frame/sec (Photron Ltd., Model FASTCAM Ultima 40K). The former two components are mounted on an optical bench and enclosed with a cover since the test furnace conditions were harsh and dirty. In a preliminary experiment, we tried to attach an intensifier to this camera to obtain enhanced sensitivity and higher temporal resolution. However, this was very difficult under harsh furnace conditions having strong radiation and electronic noise.

The flame image was focused on the detector with a magnification ratio of 1:18 (i.e., reduced size of image) by the lens. The high-speed MOS camera views the focused image through the chosen narrow band optical filter system. As shown in Fig. 2, the focused image enters the 50/50 beam splitter after which one beam passes through a 490.0 ± 28.0-nm optical band-pass filter while the other passes through a 530.88 ± 8.77-nm optical filter. The resulting monochromatic images are combined again into a single beam image using the half mirror after light is reflected from the plane mirrors. If the two images are superimposed completely, the high-speed MOS camera cannot discriminate them (see top sketch in Fig. 3). Tilting the plane mirrors counterclockwise, as shown in the bottom schematic of Fig. 3, allows one to separate the two images. Thus, the high-speed MOS video camera simultaneously monitors the two monochromatic images of the

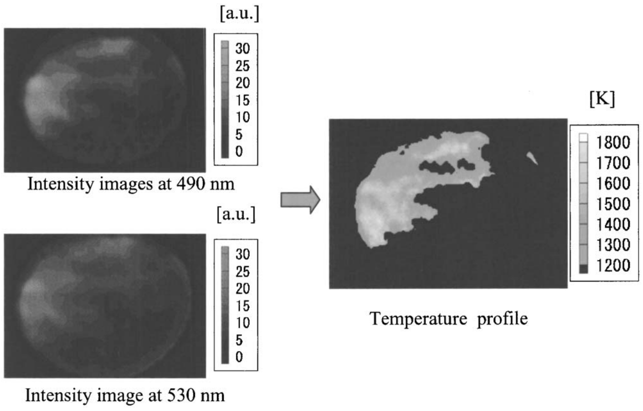

Fig. 5 Two wavelength images and temperature profile

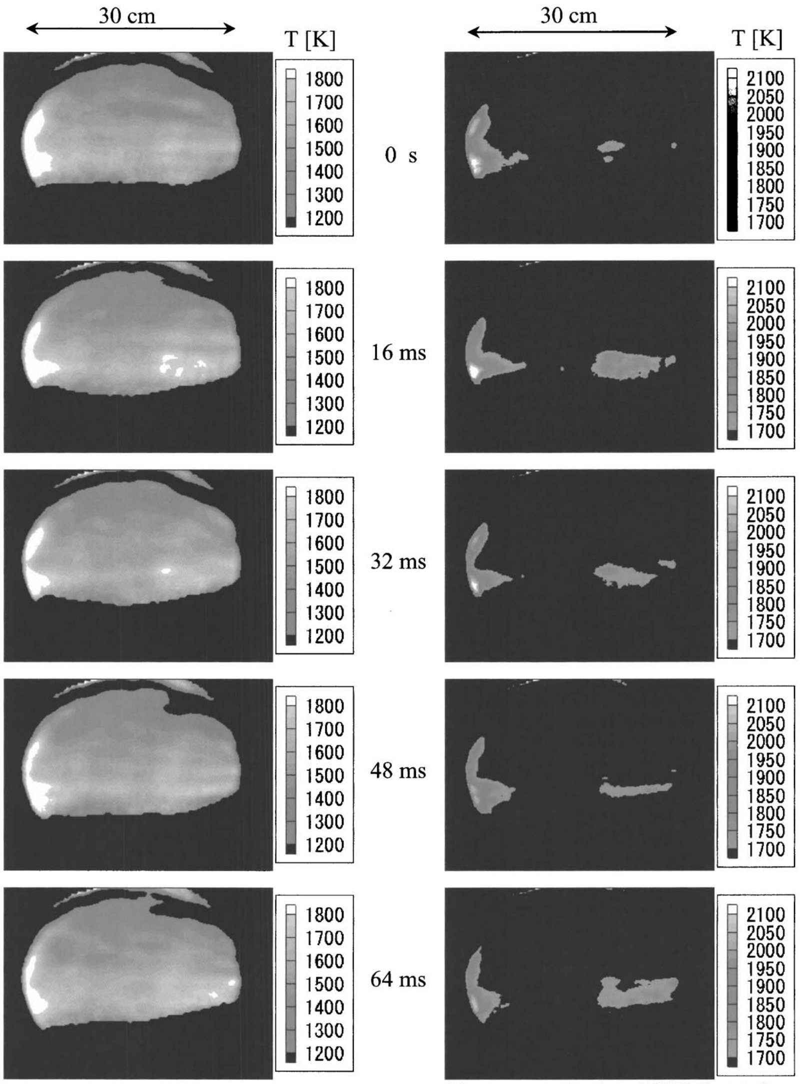

(Temperature region above 1700 K illustrated)

Fig. 6 Time-resolved temperature profiles of premixed flame through window A

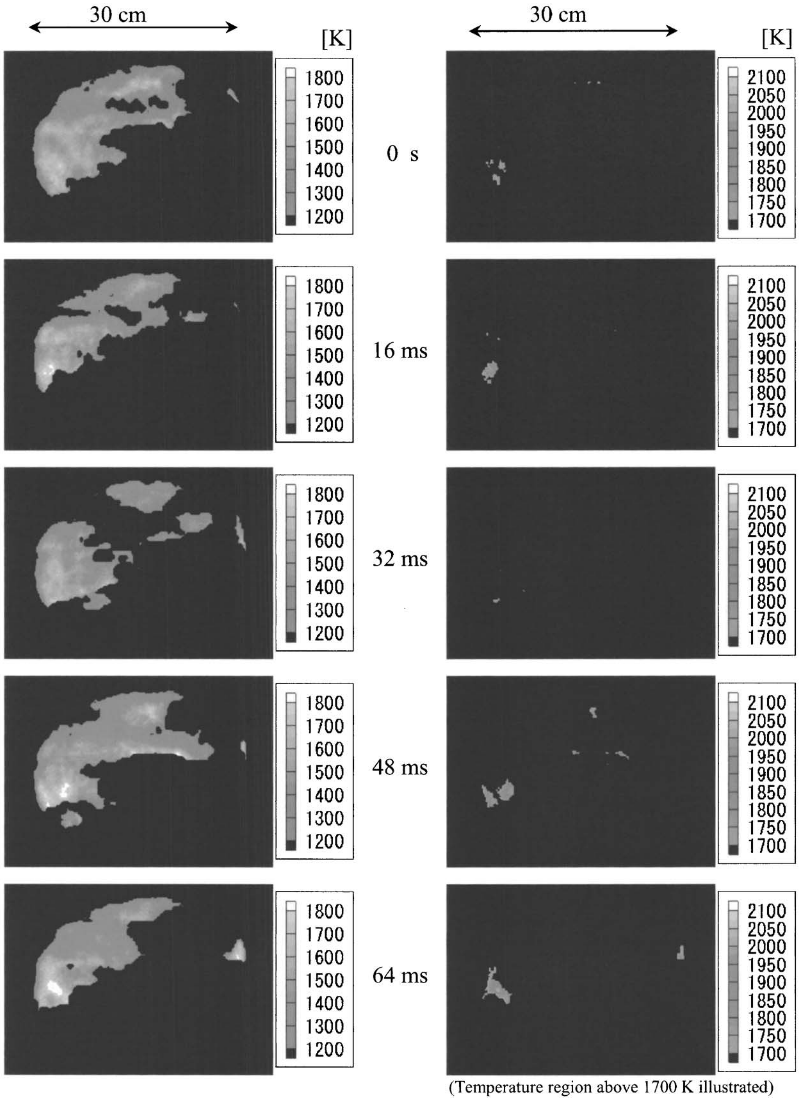

Fig. 7 Time-resolved temperature profiles of diffusion flame through window A

target flame in its field of view. It is also possible to use two separate high-speed CCD cameras fitted with a band-pass filter and this system will be better in terms of smaller loss of optical energy, albeit at a higher cost. However, a serious problem would be the difficulty to synchronize and follow up on the pixel-to-pixel discrepancy between the cameras.

A total of 8000 flame images were taken and stored in the memory bank 20 sec after the B burner was switched on. Data from 100 frames were post-processed. Similarly, out-of-focus images for the background were measured from the furnace wall, on the other side of the optical system, 20 sec after the B burner was switched off (i.e., after the flame was extinguished from the B burner during the alternate firing of the burners). This provided the background emission intensity from the furnace wall with the same optical system but with the flame turned off. The framing rate of the high-speed camera was set at 125 frames/sec with a gate period of 8 msec. As described above, if the measurement environment had less noise and also had less thermal radiation, then the intensifier could be used. In this case a much higher framing rate (40,500 frames/sec) and shorter gate period (0.025 msec) could be used. The frame information was stored in an interface memory bank and transferred to a computer after the run. The image data were post-processed in the laboratory using other computers to give temperature animations in pseudo-color. This diagnostics allowed one to successfully obtain temporal variation of temperatures (in the form of thermal video movies) at selected location in the furnace. This is the first time we have been able to obtain thermal video movies in a practical industrial furnace equipped with regenerative high performance burners.

Two-dimensional two-color thermometry, based on Planck's law, was applied to measure the distributions of flame temperatures in two dimensions. The two-dimensional (2D) spectral intensities of the continuum radiation from soot particles in a luminous flame were measured at two different wavelengths of 490.0(±28.0) nm and 530.88(±8.77) nm. The ratio is calibrated with the temperature measured from the thermocouple at a position corresponding to the high-speed MOS camera measurement. The signal intensity ratios at the pixel location were converted into two-dimensional temperature distribution. The errors due to the temperature dependence of the emissivity on the soot particles is almost negligible since the chosen wavelengths of narrow band-pass filters were very close to each other [10,11]. Therefore, the temperature obtained represents the surface temperature of soot. The optical diagnostic technique has also been calibrated against the temperature measured with a thermocouple.

A multi-channel CCD spectrometer (JASCO, Model MD-25T) was used to check the absence of molecular band spectra on the

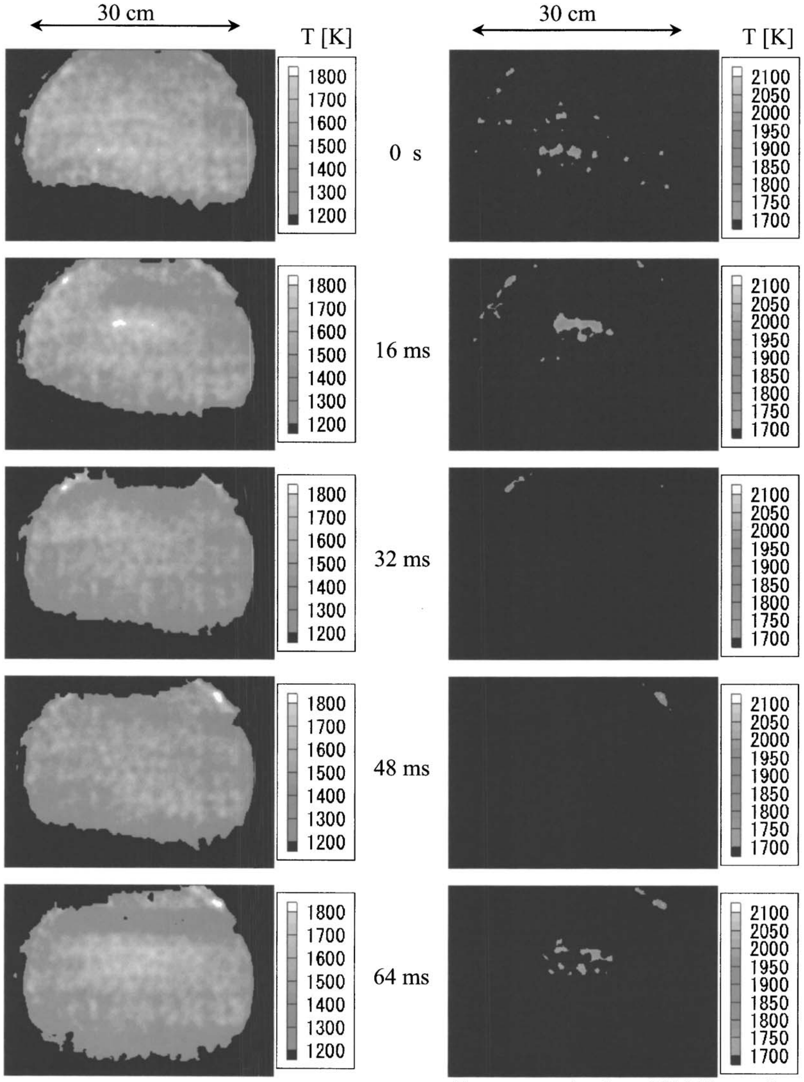

(Temperature region above 1700 K illustrated)

Fig. 8 Time-resolved temperature profiles of premixed flame through window B

continuum emission from soot particles, since the narrow band-pass 2D two-color thermometry can provide some errors from these sources. This procedure also allowed the selection of two wavelengths.

3 Results and Discussion

Transmittance Correction for the Simultaneous Two-Wavelength Images. Figures 4 and 5 show the single-shot images of background emission for the premixed flame from window B in the furnace wall (see Fig. 1), observed at two wavelengths of 490.0(±28.0) and 530.88(±8.77) nm. As seen from this figure, the transmittance and distributions through the two optical paths are different and not uniform. This is also reflected from the flame images. In particular, the transmittance is observed to decrease in the upper and lower edges of the two images. This is attributed due to the limited areas of the reflection mirrors to primarily cause this effect. The following correction was made in order to obtain the net intensity profiles of flame emission,

$$I_{\text{net}}(x,y) = \{I(x,y) - I_{\text{bg}}(x,y)\}/I_{\text{bg}}(x,y), \tag{1}$$

Where $I_{\text{net}}(x,y)$ refers to the net intensity distribution of the flame emission, $I(x,y)$ is the observed intensity, and $I_{\text{bg}}(x,y)$ is the background intensity distribution. The narrow band two-color thermometry procedure was applied to obtain the distribution of flame temperature, or more accurately the soot surface temperature. A single-shot temperature profile for the premixed flame is shown in the right column of Fig. 6. Here, a low-temperature threshold of 1200 K is applied for better viewing.

Time-Resolved Profiles of Flame Temperature. Figures 6 and 7 show the characteristic time-resolved profiles of the temperature (soot surfaces temperature with gray body assumption) measured through window A (i.e., at the upstream region of the flame) for the premixed and diffusion flame conditions, respectively. Figures 8 and 9 show temporally resolved profiles of temperature through window B for the premixed and diffusion flame conditions, respectively. The time of 0 sec correspond to the moment of 20 sec after the burner was switched on upon ignition, and the flame became instantaneously in steady-state condition due to the use of very high-temperature combustion air from the regenerator. In all the figures in the left column, the low-temperature threshold was set at 1200 K, similar to that set for the results shown in Fig. 6. However, in the right column, a higher temperature threshold of 1700 K was employed to show the higher temperature regions. Therefore, the temperature range for the results shown in Figs. 6–9 in the left column is from 1200 to 1800 K while that in the right column is from 1700 to 2100 K.

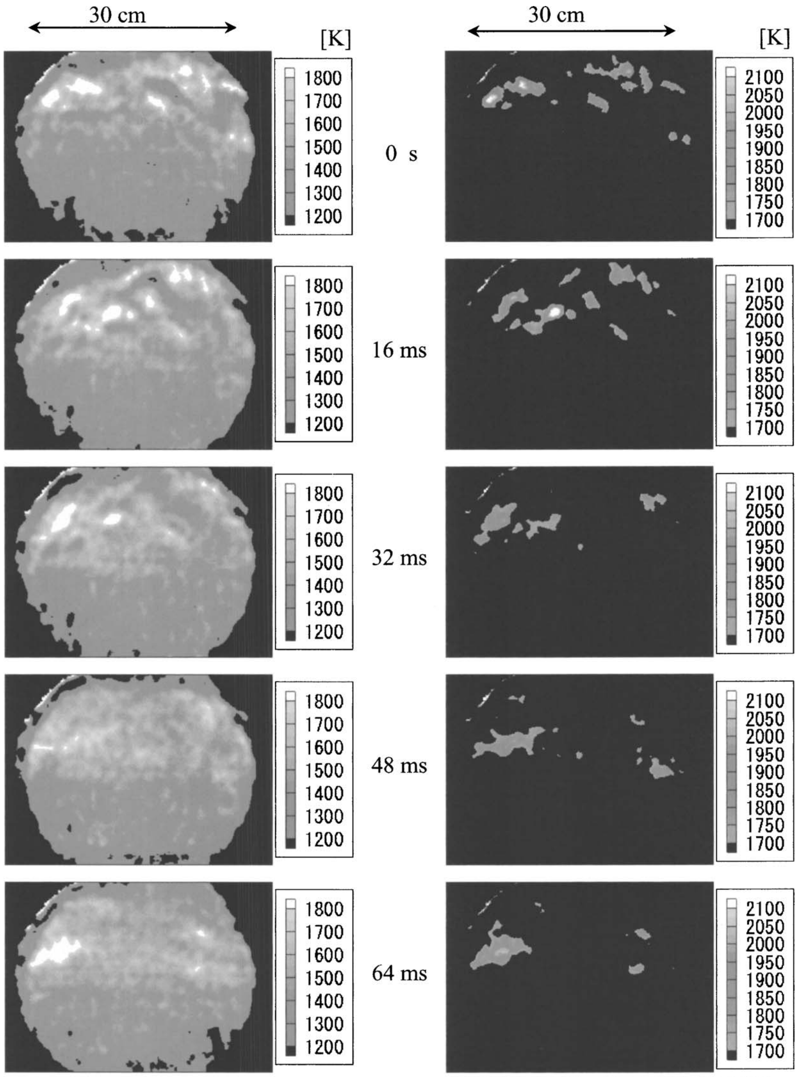

(Temperature region above 1700 K illustrated)

Fig. 9 Time-resolved temperature profiles of diffusion flame through window B

The temporal changes shown in Fig. 6 (right column) indicate that at upstream regions of the premixed flame, there are steady high-temperature regions on both the right and left sides along the central axis of the flame. In contrast for the diffusion flame (Fig. 7, right column), several high-temperature regions can be observed that temporally move in spatial position. These results are in agreement with those suggested in our previous work [8,12]. There is a high-temperature zone between windows A and B. Therefore, for the premixed case since the diffusive mixing process is not a controlling factor, the combustion starts earlier close to 60–90 cm downstream from the central injector exit. The high-temperature region in the right column is related to the ignition region. The temperature is lowered due to the processes of fuel vaporization and fuel decomposition at high temperatures, followed by the high-temperature region on the left side of window A.

In contrast for the diffusion flame, a finite amount of time duration is necessary for the fuel and air to mix prior to ignition. This ignition situation is clearly demonstrated in the upstream region for the results obtained from window A (see Fig. 7). The intense combustion takes place in the mid-stream region as viewed through window B (see Fig. 9). It should be noted that from these figures there are no steady high-temperature regions for the diffusion flame case as compared to the premixed flame case (compare results shown in Figs. 7 and 9 with Figs. 6 and 8). The small thermal regions are observed to be moving along the direction of the combusting flow. This difference is significant and directly responsible for the respective level of thermal NO_x production. Indeed the measured NO_x levels were found to be significantly lower for the diffusion flame case as compared to the premixed flame case. The NO_x concentrations using 3.5% O_2 concentration in the combustion air were measured in the exhaust stream of the furnace using a NO/NO_x chemiluminescent analyzer. The NO_x results were found to be 33 ppm for the diffusion flame and 125 ppm for the premixed flame (corrected to 11.0% O_2 in the gas). This is considerably low NO_x emission from a furnace with very high-temperature combustion air since the thermal NO_x levels increase exponentially with increase in air preheat temperature.

Analysis of Flame Temperature Fluctuation. Figures 10 and 11 show the profiles of average temperature and flame fluctuation in terms of standard deviation for the premixed and diffusion flame, respectively, obtained using 100 frames over time duration of 0.8 sec. For the premixed combustion, very high-temperature zones exist along the central axis of the flame at the upstream region (see the results in the right column of Fig. 10). The temperature information also indicates that the combustion volume of the premixed flame is smaller than that of the diffusion flame. As described above, the former is a result of the prompt ignition and

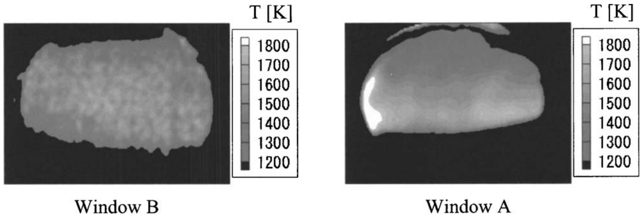

Average temperature profiles for premixed flame (n=100)

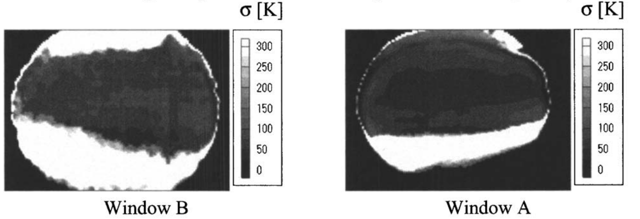

Standard deviation profiles for premixed flame (n=100)

Fig. 10 Profiles of average temperature and standard deviation of temperature for premixed flame

combustion of the premixed fuel-air mixture. In contrast, the mixing process is a rate-determining process for the diffusion combustion. Consequently, the flame volume is larger for the diffusion combustion case. These phenomena can also be observed from the temperature fluctuation data. The fluctuations are very small along the central axis of the premixed flame, where the mixing is not a dominant factor. At the outer regions of the premixed flame, the fluctuations become larger due to rapid mixing of premixed flame products with the surrounding fluid.

In contrast for the diffusion flame, the temperature fluctuations are larger at the upstream (window A) and mid upstream (the right side of window B) regions. This is mainly attributed to the intense mixing between the fuel and air, and some instability associated with flame ignition at the upstream region. It is to be noted that large temperature fluctuations are considered favorable for increased NO_x production at high temperatures. However, the mean temperatures in these regions of high-temperature fluctuations are much lower for the diffusion flame case. These large fluctuations for the diffusion flame case are, therefore, not responsible for the generation of high levels of thermal NO_x. In contrast for the premixed flame case the high temperatures are also associated with high-temperature fluctuations.

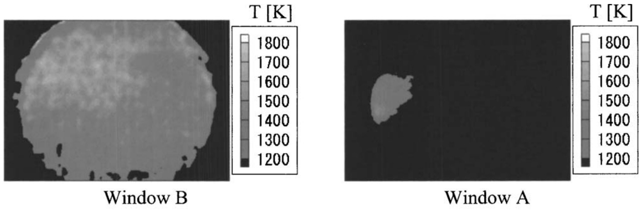

Average temperature profiles for diffusion flame (n=100)

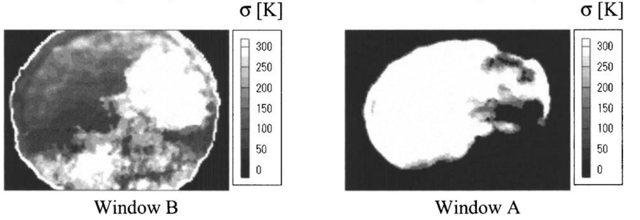

Standard deviation profiles for diffusion flame (n=100)

Fig. 11 Profiles of average temperature and standard deviation of temperature for diffusion flame

4 Conclusions

The followings conclusions can be made from this study:

(1) The industrial size test furnace having regenerative burners was assembled to examine the combustion behavior of heavy oil using high-temperature and low oxygen concentration combustion air. This furnace is primarily oriented towards steel processing.

(2) A high-speed MOS camera was used to measure the gray body emission of flame radiation at two different wavelengths. This system was successfully applied to measure the 2D time-resolved profiles of flame temperature in premixed and diffusion flames using high-temperature combustion air at low oxygen concentration.

(3) The diffusion flame is preferable from the viewpoint of low NO_x emission. This is in contrast to that known for the conventional flames (at normal oxygen concentration at low temperatures) in which lean premixed flames provide low NO_x emission. The source for the high NO_x production in premixed flame has been clearly demonstrated from the time-resolved profiles of flame temperature. High-temperature distribution was confined to a wider region for the premixed flame as compared to the diffusion flame case. These high-temperature regions in the premixed case are directly responsible for a higher value of thermal NO_x from the furnace.

(4) The temperature fluctuations were found to be larger in the upstream region of the diffusion flame (with low mean temperatures) while for the premixed case the high-temperature region was also found to coexist with high-temperature fluctuations. The large temperature fluctuations at low mean temperatures are not considered to be responsible for high NO_x emission since the absolute temperatures are not high enough for the formation of thermal NO_x.

Acknowledgments

This research was supported by NEDO and is greatly appreciated. One of the authors (A.K.G.) would also like to thank NSF, NASA, and NFK for their support of this research.

References

[1] Tsuji, H., Gupta, A. K., Hasegawa, T., Katsuki, K., Kishimoto, K., and Morita, M., 2003, *High Temperature Air Combustion—From Energy Conservation to Pollution Reduction*, CRC Press, Boca Raton, FL.

[2] NEDO Organization, 2000, "NEDO Project Reports, High Performance Industrial Furnace Development Project—High Temperature Air Combustion," Tokyo, Japan, March 21, p. 1.

[3] NKK Corporation, 1999, "NKK Technical Review No. 80, July 1999, New Energy and Industrial Technology Development," Tokyo, Japan, pp. 1–45.

[4] Ishiguro, T., Tsuge, S., Furuhata, T., Kitagawa, K., Arai, N., Hasegawa, T., Tanaka, R., and Gupta, A. K., 1999, *Proc. Twenty-Seventh Symposium (International) on Combustion*, The Combustion Institute, Pittsburgh, PA, pp. 3205–3213.

[5] Gupta, A. K., 2004, "Thermal Characteristics of Gaseous Fuel Flames using High Temperature Air," ASME J. Eng. Gas Turbines Power, **126**(1), pp. 9–19.

[6] Hino, Y., Sugiyama, S., Suzukawa, Y., Mori, I., Konishi, N., Ishiguro, T., Kitagawa, K., Arai, N., and Gupta, A. K., 2004, "2-Dimensional Spectroscopic Observation of Non-luminous Flames in an Regenerative Industrial Furnace using Coal Gas," ASME J. Eng. Gas Turbines Power, **126**(1), pp. 20–27.

[7] Shimada, T., Akiyama, T., Fukushima, S., Kitagawa, K., Arai, N., Ohkubo, Y., and Gupta, A. K., 2004, "Spectroscopic Observation of Heavy Oil Luminous Flames in an Industrial Regenerative Furnace," J. Propul. Power, **20**(5), pp. 919–926.

[8] Kitagawa, K., Konishi, N., Itoh, S., Terabyashi, T., Arai, N., Shimada, T., Akiyama, T., Fukushima, S., and Ohkubo, Y., 2002, "Iron and Steel Institute of Japan (ISIJ) International, Supplement," Vol. **42**, Tokyo, Japan, pp. 140–144.

[9] Kitagawa, K., Konishi, N., Arai, N., and Gupta, A. K., 2003, "Temporally Resolved 2-D Spectroscopic Study on the Effect of Highly Preheated and Low Oxygen Concentration Air on Combustion," ASME J. Eng. Gas Turbines Power, **125**, pp. 326–331.

[10] Tago, Y., Akimoto, F., Kitagawa, K., Arai, N., Hashimoto, M., and Churchill, S. W., 2001, "American Institute of Chemical Engineering (AIChE) Annual Meeting, Reno, NV," poster no. 228m.

[11] Gupta, A. K., and Lilley, D. G., 1985, *Flowfield Modeling and Diagnostics*, Abacus Press, Tunbridge Wells, UK.

[12] Hino, Y., Sugiyama, S., Suzukawa, Y., Mori, I., Konishi, N., Ishiguro, T., Kitagawa, K., Arai, N., and Gupta, A. K., 2004, "2-Dimensional Spectroscopic Observation of Non-luminous Flames in an Regenerative Industrial Furnace using Coal Gas," ASME J. Eng. Gas Turbines Power, **126**(1), pp. 20–27.

Yuichiro Tago
Department of Energy Engineering and Science,
Nagoya University,
Chikusa-ku, Nagoya 464-8603, Japan

Fumie Akimoto

Kuniyuki Kitagawa

Norio Arai[1]

Research Center for Advanced Energy
Conversion,
Nagoya University,
Chikusa-ku, Nagoya 464-8603, Japan

Stuart W. Churchill
Department of Chemical Engineering,
University of Pennsylvania,
311A Towne Building,
220 S. 33rd Street,
Philadelphia, PA 19104

Ashwani K. Gupta[2]
Department of Mechanical Engineering,
University of Maryland,
College Park, MD 20742
e-mail: akgupta@eng.umd.edu

Spectroscopic Measurements of High Emissivity Materials Using Two-Dimensional Two-Color Thermometry

Radiative heat transfer characteristics from the surface of a substance coated with a high-emissivity material have been examined from the measured two-dimensional (2D) temperature distribution using two-color thermometry principle. The technique utilized a charge coupled device camera and optical filters having either wide or narrow wavelength bandpass filters. The results obtained were compared to evaluate the accuracy of the temperature measurements. The 2D emissivity distributions were also derived from the measured 2D temperature distributions. The results indicate that the substrate coated with high-emissivity material exhibit high emission of radiation, resulting in effective cooling. The enhanced emissivity of materials also results in improved radiative heat transfer in heating furnaces and other high-temperature applications. The emissivity measured with the wide-bandpass filters increased with temperature. Atmospheric absorption, mainly due to humidity, made a negligible contribution to the total spectral intensity and to the temperature measurements. The small discrepancies are attributed to the dependence of emissivity on wavelength. Thus, the use of narrow-bandpass filters in thermometry is advantageous over the wide-bandpass ones. [DOI: 10.1115/1.1917889]

1 Introduction

It is well known that the energy flux emerging from the surface of a material is governed by the Stefan–Boltzmann law of radiative heat transfer and is proportional to the fourth power of the absolute temperature (i.e., T^4 dependency). Therefore, at high temperatures, the dominant mechanism of heat transfer is by radiation. This mechanism of heat transfer is often utilized to heat other materials because of the high emergent heat flux. In contrast, when heat is released as a radiative heat flux, the temperature of the surface of the material is reduced, thus preventing thermal degradation or oxidation of the material. The emissivity of the most heat-resistant materials (e.g., ZrO_2, Al_2O_3, and MgO) decreases with temperature at temperatures in excess of about 700 K. This tendency, as measured by Hashimoto et al. [1], is shown in Fig. 1. In our study, a high-emissivity the pigment, the B_4Si, is employed in the same way because it retains a high emissivity at high temperatures. The material used for the coating layer is a ceramic made from $BaO-SiO_2$ in which B_4Si particles are uniformly dispersed.

Samples coated with the high-emissivity materials are heated from the backside of the material using a liquefied petroleum gas (LPG)-air flame. The two-dimensional (2D) temperature distributions are determined by the two-color method [2] using a charged coupled device (CCD) camera fitted with an optical bandpass filter. This technology has usually been investigated using narrow-bandpass filters [3–5]. The 2D emissivity distributions are derived by measuring the intensity ratio of the images to that of a blackbody as estimated from the temperature distributions. With this method, appropriate optical bandpass filters should be selected in terms of different wavelengths and bandwidths. In this paper two kinds of filters, having narrow and wide bandpass widths, have been examined. The effect of these filters on the accuracy of measured temperature and emissivity distributions has been investigated.

2 Two-Color Thermometry With a Narrow-Bandpass Width

The theory of two-color thermometry is given in Refs. [4,6]. The Planck's law for the emittance $E_\lambda\{T\}$ from a blackbody having a temperature T at wavelength λ can be expressed as

$$E_\lambda\{T\} = \varepsilon_\lambda\{T\}\frac{2hc^2/\lambda^5}{\exp\{hc/\lambda kT\}-1} \tag{1}$$

where $\varepsilon_\lambda\{T\}$ is the emissivity.

For a blackbody the value of emissivity is unity. In the above expression, if $\exp\{hc/\lambda kT\} \gg 1$, then the Planck's law can be approximated by Wien's law, i.e.

$$E_\lambda\{T\} = \varepsilon_\lambda\{T\}\frac{2hc^2}{\lambda^5}\exp\{-hc/\lambda kT\} \tag{2}$$

In a practical experiment, the measured intensity $I_\lambda\{T\}$ is expressed as

---

[1] Deceased.

[2] To whom correspondence should be addressed.

Contributed by the Fuels and Combustion Division of THE AMERICAN SOCIETY OF MECHANICAL ENGINEERS for publication in the ASME JOURNAL OF ENGINEERING FOR GAS TURBINES AND POWER. Manuscript received December 20, 2002; final revision received August 10, 2004. Associate Editor: S. R. Gollahalli.

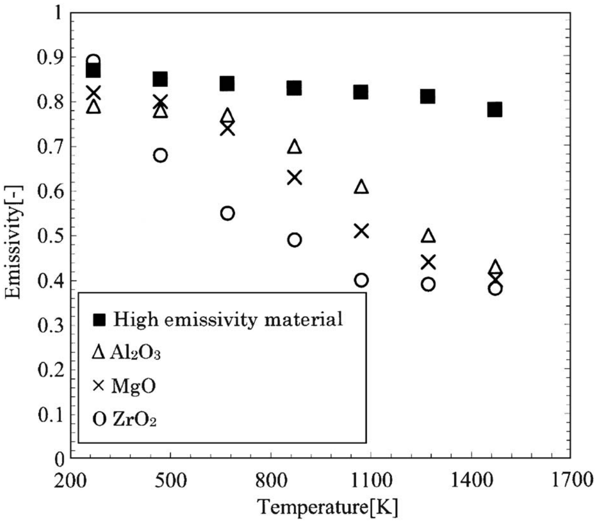

Fig. 1 Temperature dependency on emissivity for various materials

$$I_\lambda\{T\} = S_1\{\lambda\}\varepsilon_\lambda\{T\}\frac{2hc^2}{\lambda^5}\exp\left[-S_2\{\lambda,T\}\frac{hc}{\lambda kT}\right] \tag{3}$$

where $S_1\{\lambda\}$ and $S_2\{\lambda,T\}$ are constants for the specific experimental apparatus used. $S_1\{\lambda\}$ is a λ-dependent factor that takes into account the efficiency of the CCD camera, the transparency of the optical filters, and the reflectivity of the mirror. The constant $S_2\{\lambda,T\}$ is a function of both λ and T, due to the bandpass width of the optical filters.

The latter parameter is needed because the measured intensity is an integrated value with respect to λ within the bandpass width, and the intensity differs from that given by Planck's law at the central wavelength of the bandpass filter. This difference is expressed by dividing the ratio of integrated intensities at two central bandpass widths *R{Integrated}* by the ratio of monochromatic intensities at the two central wavelengths *R{Monochromatic}*. Thus, it can be expressed as

$$\frac{R\{Integrated\}}{R\{Monochromatic\}} = \left.\frac{\int I_{\lambda_1}d\lambda}{\int I_{\lambda_2}d\lambda}\right/\frac{I_{\lambda_1}}{I_{\lambda_2}} \tag{4}$$

In order to quantify the disagreement, the value of this ratio has been calculated. A drastic disagreement can be identified with the use of the wide-bandwidth filter at the lower temperatures. Under these conditions, the integrated intensity is about one-half of the theoretical value based on the Planck's law. Because Planck's law does not reconstruct the measured intensity, therefore the apparatus constant $S_2\{\lambda,T\}$ must be taken into account. In two-color thermometry, the ratio of intensities measured at two different wavelengths, $R\{T\}$ may be expressed as follows to obtain the surface temperature T. This is expressed as:

$$\begin{aligned} R\{T\} \equiv \frac{I_{\lambda_1}\{T\}}{I_{\lambda_2}\{T\}} &= \frac{S_1\{\lambda_1\}}{S_1\{\lambda_2\}}\frac{\varepsilon_{\lambda_1}\{T\}}{\varepsilon_{\lambda_2}\{T\}}\left(\frac{\lambda_2}{\lambda_1}\right)^5 \\ &\times\exp\left\{\frac{hc}{kT}\left(\frac{S_2\{\lambda_2,T\}}{\lambda_2}-\frac{S_2\{\lambda_1,T\}}{\lambda_1}\right)\right\} \end{aligned} \tag{5}$$

Because the indices $S_1\{\lambda_1\}/S_1\{\lambda_2\}$, $S_2\{\lambda_1,T\}$, and $S_2\{\lambda_2,T\}$ can be calibrated using a blackbody furnace, the temperature T can readily be estimated from the measured intensity ratio, $R\{T\}$, provided the emissivity does not have an appreciable dependence on wavelength, i.e., the emissivity at the two temperatures is the same, that is, ($\varepsilon_{\lambda_1}\{T\}=\varepsilon_{\lambda_2}\{T\}$).

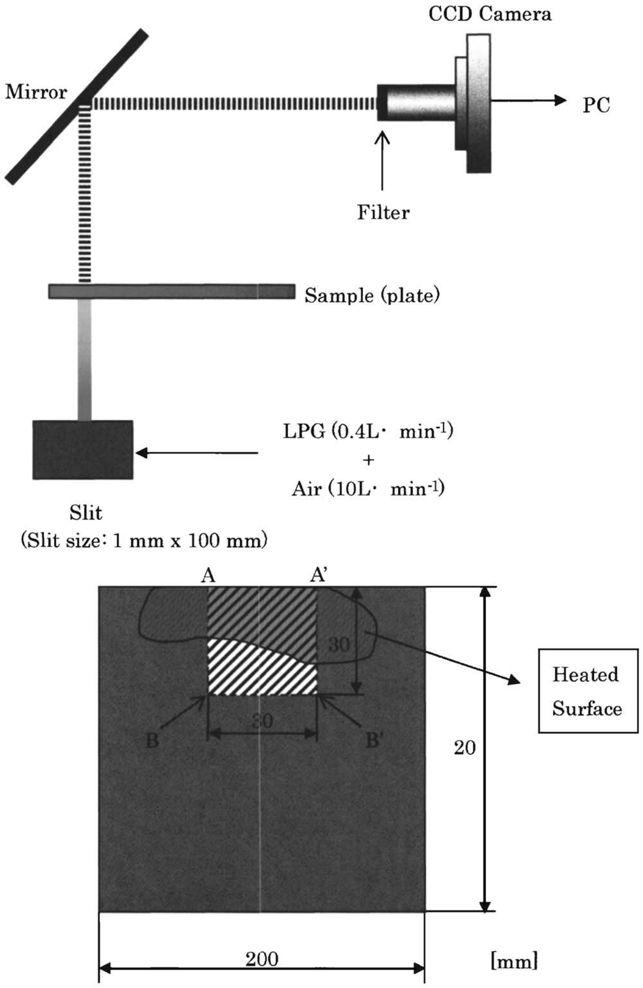

Fig. 2 Experimental apparatus (upper diagram) and sample plate (lower diagram)

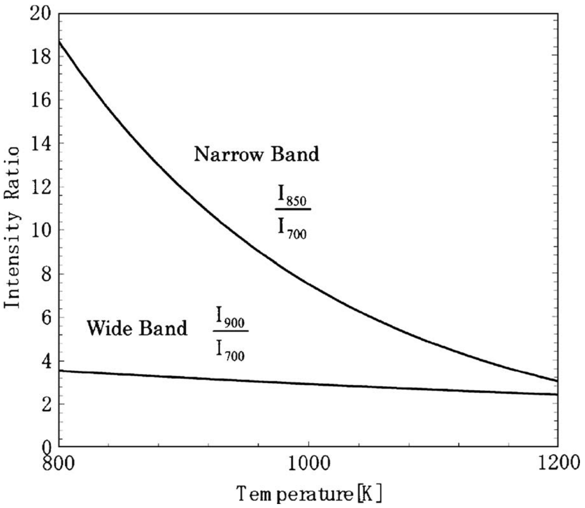

Fig. 3 Intensity ratio of blackbody furnaces with wideband and narrowband filters

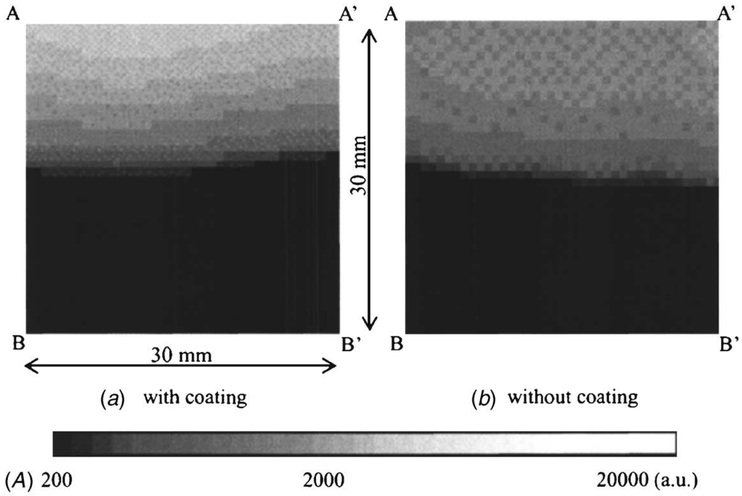

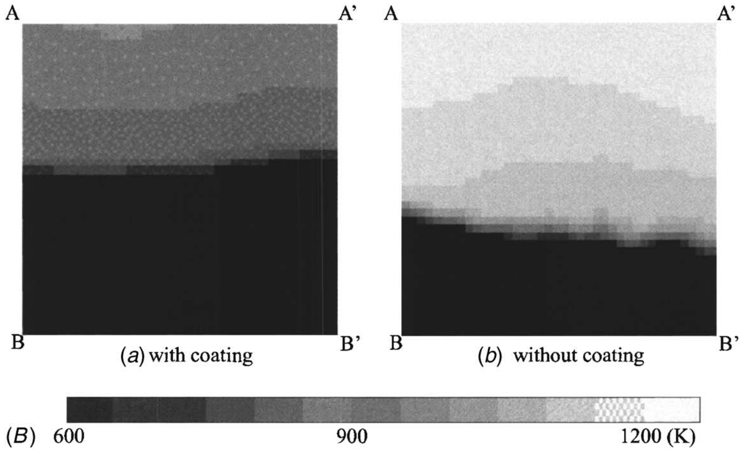

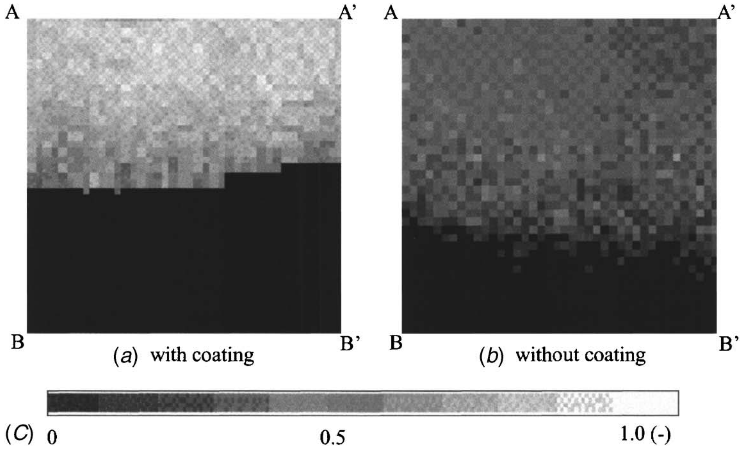

Fig. 4 **(*a*) Intensity distribution obtained with (left) and without (right) coating using wide-bandpass filters. (*b*) Temperature distribution obtained with (left) and without (right) coating using wide-bandpass filters. (*c*) Emissivity distribution obtained with (left) and without (right) coating using the wide-bandpass filters.**

3 Experiments

The experimental apparatus constructed for this experiment is shown schematically in Fig. 2. The area of the sample plate observed in this experiment, AA′BB′, is shown in the lower schematic of this figure. The backside of the sample plate was heated by a premixed flame formed with an LPG-air burner having a slit of 1 mm in width and 100 mm in length. The slit is located 3 mm from the edge of the sample. The flow rates of LPG and air were regulated at 0.4 and 10 ℓ min^{-1}, respectively. The equivalence ratio was kept constant at unity (i.e., stoichiometric mixture). The CCD camera fitted with the bandpass filters was used as the measurement system (see Fig. 2). Two wide-bandpass filters at wavelengths of 700 nm [full width at half maximum (FWHM): 220 nm] and 900 nm (FWHM 240 nm), and narrow-bandpass filters at 700 nm (FWHM 10 nm) and 850 nm (FWHM 10 nm) were selected, because it is necessary to avoid the atmospheric absorption bands. The heated surface of the sample plate was observed through the mirror in order to measure the emission

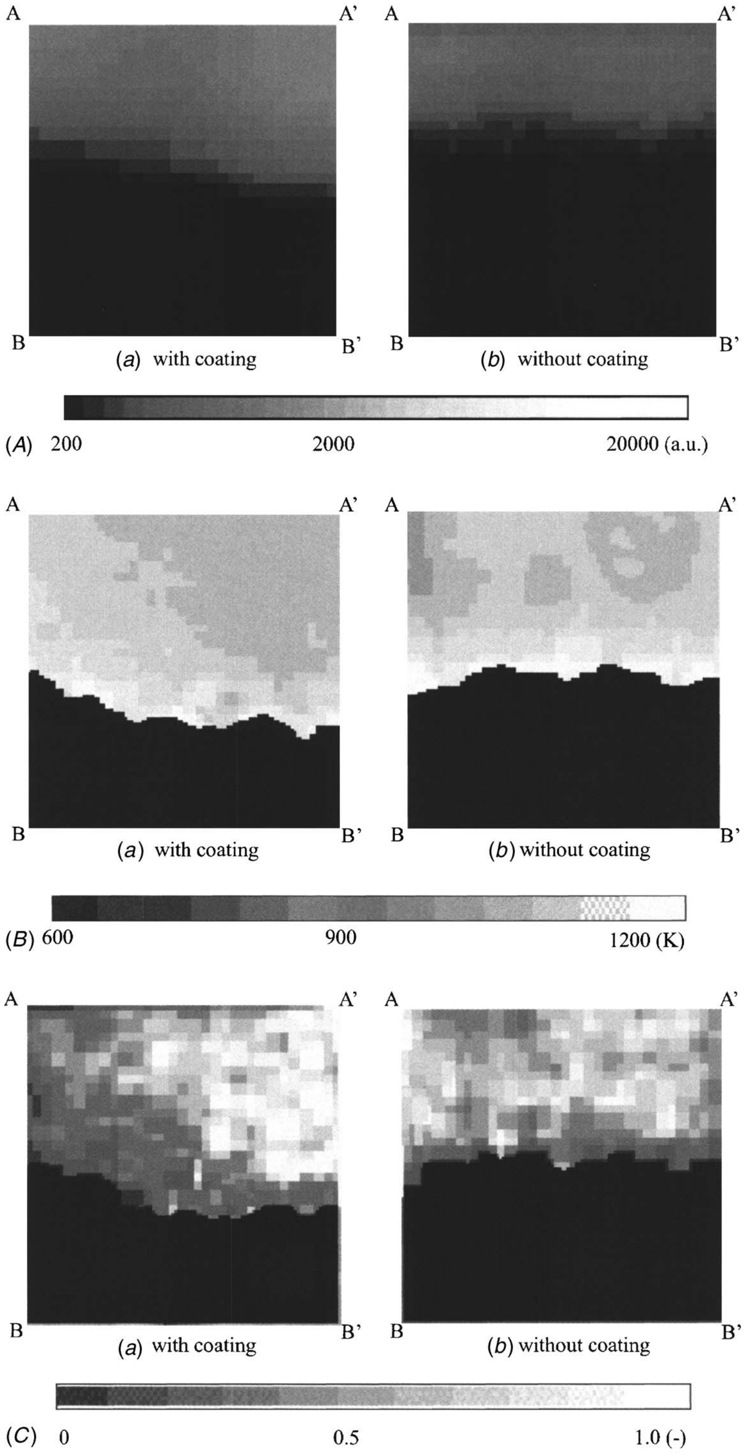

Fig. 5 (*a*) Intensity distribution obtained with (left) and without (right) coating using narrow-bandpass filters. (*b*) Temperature distribution obtained with (left) and without (right) coating using narrow-bandpass filters. (*c*) Emissivity distribution obtained with (left) and without (right) coating using narrow-bandpass filters.

image from the top. In this experiment, stainless plates (SUS304, having a size of 200 mm × 200 mm × 1 mm) coated with a high-emissivity material were used. An uncoated plate was examined for comparison. The structure of the high-emissivity material consists of B_4Si particles of about 80 μm in diameter dispersed in a layer of $BaO-SiO_2$ ceramic.

After the sample was heated sufficiently, 2D distributions of the intensity $I_{\lambda_1}\{x,y\}$, $I_{\lambda_2}\{x,y\}$ were measured with the above four filters. The 2D distribution of the ratio $R\{x,y\}(=I_{\lambda_1}\{x,y\}/I_{\lambda_2}\{x,y\}=R\{T\})$ was calculated. Then the 2D distribution of temperature $T\{x,y\}$ based on Eq. (5), was evaluated from comparison with the ratio of blackbody $R_b\{T\}$ produced by the blackbody furnace. Figure 3 shows the two-color ratio $R_b\{T\}$ for the blackbody furnace, measured with wideband and narrow-bandpass filters.

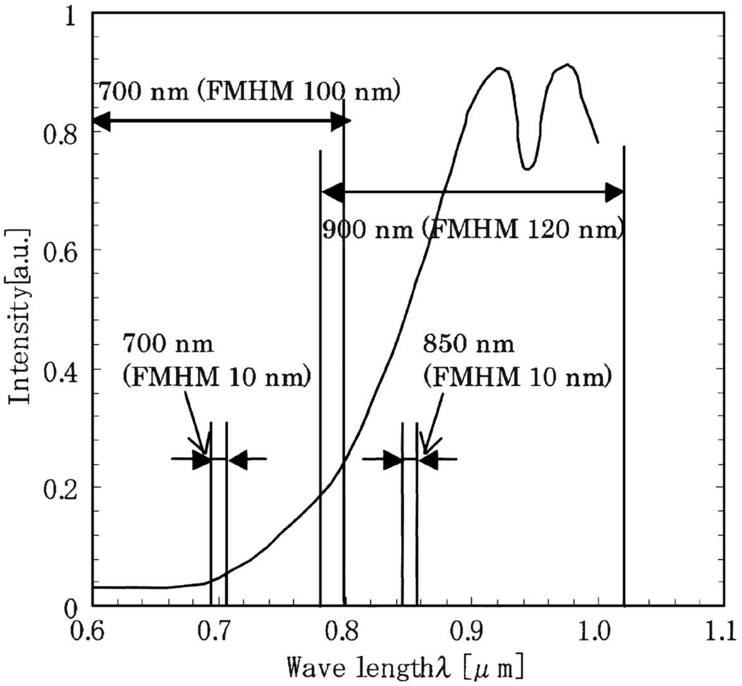

Fig. 6 Measured intensity spectra in the experimental range

Finally, the 2D distribution of the emissivity $\varepsilon\{x,y\}$ was estimated by comparing the measured 2D distribution of intensity $I_\lambda\{x,y\}$ and that of the blackbody $I_{b\lambda}\{T\}$.

4 Results and Discussion

After heating the sample until the intensity level reached an equilibrium value, the intensity distributions were measured using the CCD camera equipped with the appropriate optical filter. Then, the 2D distributions of temperature and emissivity were calculated from these measurements. The 2D distributions of spectral intensity, temperature, and emissivity for both with and without coating using the wide-bandpass filters, are shown in Figs. 4(*a*)–4(*c*) respectively, and those obtained with the narrow-bandpass filters, are shown in Figs. 5(*a*)–5(*c*) respectively. The intensity, temperature, and emissivity scale for each case is given below the figure. The 2D distribution of emissivity shown here was calculated from an intensity distribution at the wavelength of 700 nm, respectively. The measured areas of intensity correspond to AA′B′B in Fig. 2 (bottom diagram). In Figs. 4 and 5, the left diagram is for the surface coated with the high-emissivity material while the right diagram is without any coating. The former is seen to have a 40% higher intensity and a 200 K lower temperature than the latter. The emissivity of the surface without a coating extends up to 0.3 and that of the coated surface up to about 0.8. It is also seen from Figs. 4(*b*) and 5(*b*) that at high temperatures (above 1000 K) the surface temperature is lower for the coated material. This suggests that the coated surface release the heat input more efficiently, thereby suppressing the temperature rise. Figure 4(*c*) shows that the emissivity obtained with the wide-bandpass filters has a tendency to increase with increase in temperature. In contrast, the emissivity obtained with the narrow-bandpass filters has a tendency to decrease with temperature (compare Fig. 4(*c*) with Fig. 5(*c*)).

4.1 Atmospheric Absorption.

It is important to note that the wavelength ranges of the optical filters did not overlap with the strong atmospheric absorption bands. Nonetheless the effect of vapor around the instruments must be considered. The atmosphere absorption coefficient, calculated for a wavelength range from 600 to 1100 nm using the optical constant given by Kou et al. [7], is shown in Fig. 6 (see the curve in the figure). The results show that atmospheric absorption is more significant at the longer wavelengths. Therefore, it is to be expected that the intensity observed in the atmosphere is attenuated at longer wavelengths. The spectrum was measured with a multi-spectrometer (JASCO, MD-25T). As expected, an absorptive structure was found around 950 nm (see Fig. 6). This is mainly attributable to the humidity in air. Only this particular absorption band affects the intensity obtained with the wide-bandpass filter at the central wavelength of 900 nm. Also, this effect is expected to be very small, since the total intensity is reduced by only about 0.5% by this filter.

4.2 Another Way to Measure the Temperature.

Hashimoto et al. [1] measured the emissivity of basically the same material with a combination of thermocouples and a pyrometer. Their results, shown in Fig. 1, indicate that the emissivity decreases with increase in temperature. This result is in agreement with our result obtained with the narrow-bandpass filters.

As described above, atmospheric absorption results in a small decrease in the total intensity, but results in negligibly small errors in the temperature measurement. The errors in the emissivity obtained by the wide-bandpass two-color thermometry are mainly attributable to the dependence of the emissivity on wavelength. Thus, two-color thermometry using the narrow bandpass filters is advantageous as compared to that obtained using wide-bandwidth filters [4,8,9].

5 Conclusions

High emissivities can be obtained at high temperatures by coating the surface of a material with high-emissivity material. This provides improvement in radiative heat transfer and contributes to a higher efficiency for a furnace or related apparatus. The more effective heat release from the surface also prevents overheating and thermal damage of the materials. The use of narrow-bandpass filters is recommended in two-color thermometry. Small differences in results were found between our results using wide-bandpass filters and those obtained by Hashimoto et al. [1]. However, negligible differences were found using narrow-bandpass filters in place of the wide-bandpass filters.

Acknowledgment

The authors wish to thank Noritake Co., Ltd. for providing samples used in this study.

Nomenclature

c = velocity of light in vacuum ($\mathrm{m\ s^{-1}}$)
$E_\lambda\{T\}$ = emittance from a blackbody ($\mathrm{J\ m^{-3}\ s^{-1}}$)
h = the Planck constant (J s)
$I_{b\lambda}\{T\}$ = intensity of blackbody furnace (adu.)
$I_\lambda\{T\}$ = measured intensity (adu.)
$I_\lambda\{x,y\}$ = 2D distribution of measured intensity (adu.)
k = the Boltzmann constant ($\mathrm{J\ K^{-1}}$)
$R(Integrated)$ = ratio of integrated intensities within two band-pass widths
$R(Monochromatic)$ = ratio of monochromatic intensities at two central wavelengths
$R_b\{T\}$ = intensity ratio for two wavelengths of the blackbody furnace
$R\{T\}$ = intensity ratio for two wavelengths
$R\{x,y\}$ = 2D distribution of measured intensity ratio for two wavelengths
$S_1\{\lambda\}$ = apparatus constant
$S_2\{\lambda,T\}$ = apparatus constant
T = absolute temperature of surface (K)
$T\{x,y\}$ = 2D distribution of measured temperature (K)

Greek Symbols

$\varepsilon_\lambda\{T\}$ = surface emissivity
$\varepsilon\{x,y\}$ = 2D distribution of measured emissivity
λ = wavelength (m)

References

[1] Hashimoto, M., Kamata, Y., Shinoda, M., Kitagawa, K., Arai, N., and Iwata, M., 2003, "Development of High Emissivity Glass Ceramics and Spectroscopic and Numerical Evaluation of Performance," Therm. Sci. Eng., **11**(1), pp. 21–32 (in Japanese).

[2] Rybicki, G. B., and Lightman, A. P., 1979, *Radiative Processes in Astrophysics*, Wiley, New York.

[3] Yang, B., Liaw, P. K., Wang, H., Jiang, L., Huang, J. Y., Kuo, R. C., and Huang, J. G., 2001, "Thermographic Investigation of the Fatigue Behavior of Reactor Pressure Vessel Steels," Mater. Sci. Eng., A, **314**, pp. 131–139.

[4] Gupta, A. K., and Lilley, D. G., 1985, *Flowfield Modeling and Diagnostics*, Abacus, Tunbridge Wells, UK, p. 414.

[5] Huang, Y., Yan, Y., and Riley, G., 2000, "Vision-Based Measurement of Temperature Distribution in a 500-kW Model Furnace Using the Two-Colour Method," Measurement, **28**, pp. 175–183.

[6] Kurtz, J., Vulcan, T., and Steinberg, T. A., 1996, "Emission Spectra of Burning Iron in High-Pressure Oxygen," Combust. Flame, **104**, pp. 391–400.

[7] Kou, L., Labrie, D., and Chylek, P., 1993, "Refractive Indices of Water and Ice in the 0.65 to 2.5 micron range," Appl. Opt., **32**, pp. 3531–3540.

[8] Konishi, N., Kitagawa, K., Arai, N., and Gupta, A. K., 2002, "Two-Dimensional Spectroscopic Analysis of Spontaneous Emission From a Flame Using Highly Preheated Air Combustion," J. Propul. Power, **18**(1), pp. 199–204.

[9] Kitagawa, K., Konishi, N., Arai, N., and Gupta, A. K., 2002, "Temporally Resolved 2-D Spectroscopic Study on the Effect of Highly Preheated and Low Oxygen Concentration Air on Combustion," ASME J. Eng. Gas Turbines Power, **125**, pp. 326–331.

Online Combustor Stability Margin Assessment Using Dynamic Pressure Data

Tim Lieuwen
Assistant Professor
School of Aerospace Engineering,
Georgia Institute of Technology,
Atlanta, GA 30332-0150
e-mail: tim.lieuwen@aerospace.gatech.edu

This paper describes a strategy for determining a combustor's dynamic stability margin. Currently, when turbines are being commissioned or simply going through day to day operation, the operator does not know how the stability of the system is affected by changes to fuel splits or operating conditions unless, of course, pressure oscillations are actually present. We have developed a methodology for ascertaining the stability margin from dynamic pressure data that does not require external forcing and that works even when pressure oscillations have very low amplitudes. This method consists of signal processing and analysis that determines a real-time measure of combustor damping. When the calculated damping is positive, the combustor is stable. As the damping goes to zero, the combustor approaches its stability boundary. Changes in the stability margin of each of the combustor's stable modes due to tuning, aging, or environmental changes can then be monitored through an on-line analysis of the pressure signal. This paper outlines the basic approach used to quantify acoustic damping and demonstrates the technique on combustor test data. [DOI: 10.1115/1.1850493]

1 Introduction

In order for turbine operators and/or control systems to optimize overall system performance across the competing demands of emissions levels, power output, and engine life, maximum information about each component's health and performance is needed. One key issue that has emerged in dry, low NO_x (DLN) combustion systems is that of combustion instabilities—that is, self-excited, combustion-driven oscillations that generally occur at discrete frequencies associated with the combustor's natural acoustic modes [1,2]. Minimizing the amplitude of these oscillations is essential for maximizing hot section part life—however, tradeoffs between dynamics amplitude, emissions, and power output are routinely encountered [3].

The objective of this study is to describe a patent pending [4] methodology for determining the proximity of the combustor to instability; i.e., to monitor its dynamic stability margin. Currently, when turbines are being commissioned or simply going through day to day operation, the operator does not know how the stability of the system is affected by changes to fuel splits or operating conditions unless, of course, the system actually becomes unstable. This point is illustrated in Fig. 1, which plots combustor pressure amplitude data obtained from Georgia Tech's gas turbine combustor simulator. This figure shows that the combustor was unstable and stable at premixer velocities above and below, respectively, about 25.5 m/s.[1] Suppose now that this system is operated under a stable condition, say at a premixer velocity of 30 m/s. Although the turbine operator will know that the system is stable, they will not, in general, know how close the system is to instability. In addition, if the premixer velocity were decreased to 29 m/s, they would not know whether they have moved the system closer to or farther from the stability boundary. The objective of the work described here is to provide the turbine user with a quantitative description of how close the system is to its stability boundary, so that they can determine whether small changes in fuel splits, operating, or ambient conditions are likely to affect combustor dynamics.

Note that a similar objective of stability margin quantification was previously pursued by Johnson et al. [5]. Their technique required, however, external forcing of the combustor with a pulsing fuel injector and acoustic driver. As such, this technique may be useful in a lab setting but is probably not practical for a fielded system. In this study, we focus on the use of passive (i.e., no external forcing required) acoustic pressure measurements for this diagnostic. Similar analyses could also be carried out with other dynamic time series data, such as that obtained from optical, fuel/air ratio, temperature, or ion probes. Our motivation for using acoustic measurements follows from the simple fact that many fielded DLN combustors are already instrumented with pressure transducers, or at least equipped with access for such instrumentation, and, furthermore, are often continuously monitored. As such, implementing the techniques described here does not require new instrumentation but only modified data processing software.

2 Approach

The key objective of this work is to determine the rate at which acoustic oscillations are damped in a stable combustor. Under stable conditions, the overall pressure amplitude is determined by a competition between combustor damping processes and inherent background noise processes. In contrast, under unstable conditions, the oscillations are self-excited. As such, it can be anticipated that the overall level of acoustic damping, ζ, monotonically decreases to zero as the system moves from being strongly stable to the stability line, and actually becomes negative under unstable conditions. Our objective here is to quantify the combustor damping coefficient during stable conditions. Presumably, large and small values correspond to conditions that are far from and very close to the stability line, respectively.

Probably the most straightforward way to quantify damping levels is to introduce an external disturbance and monitor its rate of decay. As noted above, however, such a technique has a clear disadvantage of requiring additional hardware and is probably not feasible for day-to-day use in practical systems.

The approach taken here follows from the fact that inherent combustor noise is continuously exciting oscillations in the sys-

---

Contributed by the International Gas Turbine Institute (IGTI) of THE AMERICAN SOCIETY OF MECHANICAL ENGINEERS for publication in the ASME JOURNAL OF ENGINEERING FOR GAS TURBINES AND POWER. Paper presented at the International Gas Turbine and Aeroengine Congress and Exhibition, Vienna, Austria, June 13–17, 2004, Paper No. 2004-GT-53149. Manuscript received by IGTI, October 1, 2003; final revision, March 1, 2004. IGTI Review Chair: A. J. Strazisar.

[1] We recognize that there is some ambiguity in determining the bifurcation point at which oscillations transition from being damped to self-excited. Our use of the words "stable" and "unstable" are used here for descriptive purposes only and should not be taken as a precise characterization of the dynamical state of the system.

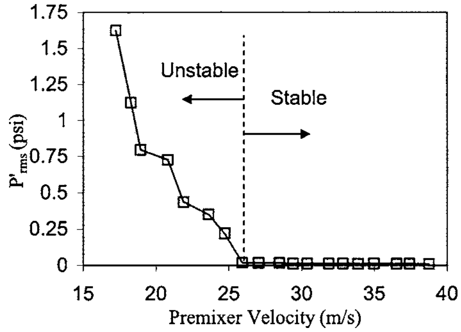

Fig. 1 Variation of dynamic pressure amplitude in combustor with premixer velocity

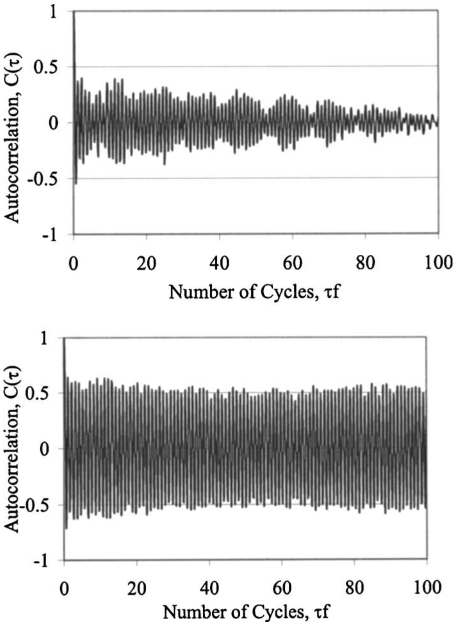

Fig. 2 Dependence of autocorrelation of raw acoustic pressure data measured under stable (top, $u=27$ m/s) and unstable (bottom, $u=21$ m/s) conditions

tem. These oscillations are dissipated at some rate that can be associated with a damping time scale, $\tau_{\mathrm{damp}} \propto 1/\zeta$. As such, oscillations excited at some time, $t=t_0$, will make a negligible contribution to the disturbance amplitude at times $t \gg t_0+\tau_{\mathrm{damp}}=t_2$. Therefore, oscillations at time t_2 will be poorly correlated with those at time, t_0. It therefore follows that the damping coefficient is directly related to the time interval, τ_{corr}, over which oscillations are correlated. Explicitly quantifying this relationship can be accomplished by mathematically modeling the oscillations.

The model we use follows the work of Zinn [6] and Culick [7], who have shown that acoustic oscillations in combustion chambers can be described as a superposition of nonlinearly interacting oscillators of the form

$$p'(t)=\xi(t)+\sum_{i=1}^{N} \eta_i(t) \tag{1}$$

$$\begin{aligned}&\frac{d^2\eta_i(t)}{dt^2}+2\tilde{\varsigma}_i\tilde{\omega}_i\frac{d\eta_i(t)}{dt}+\tilde{\omega}_i^2\eta_i(t)\\&=f_i\left(\eta_j(t),\frac{d\eta_j(t)}{dt},\ldots\right)+E_i(t). \quad i,j=1,2,\ldots,N\end{aligned} \tag{2}$$

The measured pressure, $p'(t)$, consists of the contributions of two sources: (1) the oscillations of N acoustic modes, η_1, $\eta_2,\ldots,\eta_N$, and (2) the "background noise" in the combustor, $\xi(t)$. The dynamics of the acoustic modes, η_i, are described by Eq. (2). The left-hand side of Eq. (2) describes harmonic oscillations of each mode at a frequency $\tilde{\omega}_i$. The function $f_i(\eta_j, d\eta_j/dt)$ describes linear and nonlinear "forcing" terms. The last term, $E_i(t)$, describes external forcing of the oscillator by noise.

Under stable conditions, the oscillations are generally of sufficiently low magnitude that nonlinear terms are negligible. In addition, if we lump the effects of the unsteady heat release into an effective damping and stiffness term, then the dynamics of each mode are described by the equation

$$\frac{d^2\eta_i(t)}{dt^2}+2\varsigma_i\omega_i\frac{d\eta_i(t)}{dt}+\omega_i^2\eta_i(t)=E_i(t) \tag{3}$$

Note that the "effective" damping, ζ, and frequency, ω_i, terms contain the unsteady heat release terms, which may, in reality, contain higher-order dynamics. Because the unsteady heat release terms are quite small, this is not likely to be a significant effect for the frequency term. It is probably more significant for the damping term, however, because combustors are often lightly damped, $\zeta \ll 1$. Including unsteady heat release effects in Eq. (3) requires the introduction of a highly uncertain heat release model, however. Moreover, as shown in the results section, Eq. (3) provides a useful model for interpreting data, although it certainly has limitations.

Equation (3) cannot be directly solved, because we do not know the temporal evolution of $E_i(t)$. For this reason, it is convenient to work with the autocorrelation of $\eta_i(t)$, defined as

$$C_i(\tau)=\frac{\int_0^T \eta_i(t)\,\eta_i(t+\tau)dt}{\int_0^T \eta_i^2(t)dt} \tag{4}$$

Taking the Fourier transform of Eq. (3), assuming that the power spectrum of the noise term, $E_i(t)$, is approximately constant over the oscillator bandwidth, and using the Wiener–Khinchin theorem [8], it can be shown that $C_i(\tau)$ equals

$$C_i(\tau)=e^{-\omega_i\varsigma_i\tau}(\cos(\omega_i\tau\sqrt{1-\varsigma_i^2})+\varsigma/\sqrt{1-\varsigma_i^2}\,\sin(\omega_i\tau\sqrt{1-\varsigma_i^2})) \tag{5}$$

Since ζ is quite small (e.g., it has values less than 0.1 for all data presented here), the second term in Eq. (5) is negligible compared to the first. As such, the autocorrelation oscillates at a frequency roughly equal to ω_i, and has an envelope that decays as $\exp(-\omega_i\zeta_i t)$. Therefore, Eq. (5) shows that the mode's damping coefficient can be directly related to the decay in the envelope of the autocorrelation. To illustrate, Fig. 2 plots two autocorrelations of the same data shown in Fig. 1 measured under stable and unstable conditions. Note that the amplitude of the autocorrelation steadily decays under stable conditions while it remains relatively constant under unstable conditions.

While the value of the damping coefficient could be directly fit to the envelope of the oscillatory $C_i(t)$, it is difficult to capture the instantaneous peak amplitude of each cycle without very high sampling frequencies. The envelope of the oscillatory autocorrelation can be calculated via its Hilbert transform, $H_i(t)$, which is defined as [9]

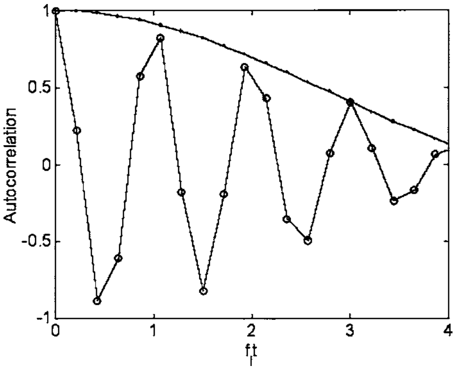

Fig. 3 Time dependence of the autocorrelation, $C_i(t)$, (○) and Hilbert transform of the autocorrelation (−). Raw data bandpass filtered about the 630 Hz mode with a fourth-orderButterworth filter, with a bandwidth set to 10% of the center frequency (u=33.9 m/s).

$$H_i(\tau)=\frac{1}{\pi}\int_{-\infty}^{\infty}\frac{C_i(t)}{\tau-t}dt \tag{6}$$

The Hilbert transform is useful because it can be used to determine the envelope of an oscillatory signal. For example, consider the signal, $G(t)=A(t)\sin \omega t$. It can be shown that $|G(t)+iH(G(t))|=A(t)$. To illustrate, Fig. 3 plots the time dependence of the autocorrelation and its Hilbert transform. The figure shows that the Hilbert transform faithfully captures the envelope of the oscillatory signal.

Once the envelope of the oscillatory signal has been determined, the damping coefficient can be estimated from the best fit of the equation $\exp(-\omega_i\zeta_i t)$. In our results, this was done by taking the natural logarithm of $H_i(t)$ and performing a least squares minimization procedure to determine ζ.

The above paragraphs have outlined a procedure for determining the stability margin from a time series. An important issue that must be addressed is how to determine the separate modal amplitudes, $\eta_i(t)$, from the measured pressure time series, $p(t)$. This can be done in a relatively straightforward fashion by simply bandpass filtering the data about each ω_i for $i=1$ to N modes. Determining the optimum filter width requires care, however. Clearly, the filter should be set narrow enough so that it only captures the energy from a single mode; i.e., the estimate of ζ_i should not be contaminated by energy from other modes. However, if the filter is set too narrow and/or with too sharp a cutoff, the autocorrelation may "ring" with characteristics that are dominated by the filter settings and not the data itself. To illustrate, Fig. 4 plots the typical measured dependence of the estimated ζ parameter upon the width, W, of a fourth-order Butterworth filter. The pass and stop band frequencies were set by dividing and multiplying, respectively, the center frequency by $1+W$. For very narrow filter widths, i.e., $W<0.03$, the damping estimate is nearly zero because the autocorrelation oscillates with little temporal decay. The damping estimate monotonically rises with W, and plateaus in the $W=10\%-20\%$ region. Presumably, the damping estimate would remain at this value for larger W if no other modes are present. However, further increases in W cause the damping factor to drop again, this time due to the filter picking up oscillations from other modes. The damping estimate in these cases is meaningless, however, as the autocorrelation envelope oscillates and no longer resembles the exponentially decaying equation that ζ is being estimated from. For all results shown here, a $W=0.1$ value was chosen.

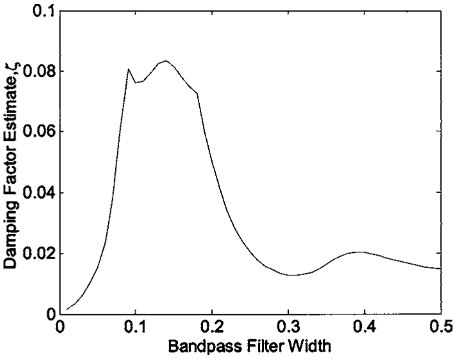

Fig. 4 Dependence of damping estimate, ζ, upon bandpass filter width (f_{center}=630 Hz, u=21.9 m/s; four cycles of data were used for an estimate)

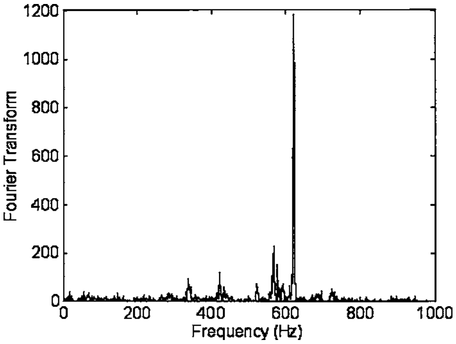

Fig. 5 Fourier transform of combustor pressure (u=25.9 m/s)

In closing this section, we summarize the key assumptions and limitations of the damping estimate analysis:

1. *Second-order oscillator*: The effects of unsteady heat release on driving/damping oscillations may introduce higher-order dynamics into the pressure oscillations.
2. *Spectrally flat background noise*: While combustor background noise processes are probably reasonably flat over the oscillator bandwidth, the scattering of narrow band sound waves from the flame generates additional background noise whose amplitude peaks at the natural mode frequency [10].
3. *No parametric disturbances*: We assume here that only external disturbances are present and do not account for the effects of disturbances in damping and frequency. Unfortunately, there is no rational method for incorporating them because their characteristics are not well understood (see also Refs. [11–13]).

3 Results

In this section, we present results obtained from the Georgia Tech gas turbine combustor simulator that has been described in detail elsewhere [14]. The specific dataset analyzed here has also been discussed extensively in Ref. [15]. A set of 18 test runs were chosen where the premixer velocity was varied between 17–39 m/s at a fixed flow rate and equivalence ratio (ϕ=0.89) by varying the degree of constriction of a backpressure valve. As such, the mean combustor pressure correspondingly varied from a low of 2 to a high of 5 atmospheres. As discussed elsewhere [14], instabilities in this combustor are excited at certain premixer velocities due to a coupling between the reactive mixture convective time and the chamber acoustics. These particular test runs were chosen because of the large variations in amplitude that occurred in two of the combustor modes and some variations in several others as well; as such, they serve as a useful demonstrator of the capabilities of the proposed method to simultaneously track the stability characteristics of several modes. A typical Fourier transform illus-

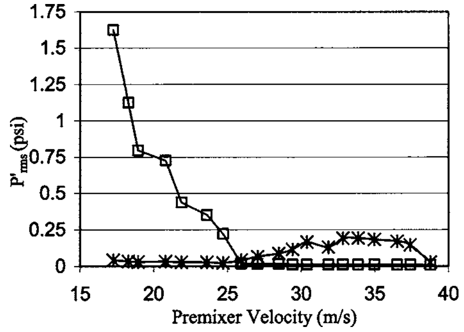

Fig. 6 Dependence of 430 (□) and 630 (*) Hz mode amplitude upon premixer velocity

trating these modes is shown in Fig. 5. The two dominant instabilities occur at 430 and 630 Hz. The dependence of their amplitude's upon premixer velocity is shown in Fig. 6. The larger peak amplitude of the 430 Hz mode is due to the higher mean combustor pressure at low velocities; i.e., they have comparable normalized disturbance amplitudes, p'/p_0.

Figure 7 and Fig. 8 plot the simultaneous dependence of the amplitude and damping coefficient of these modes. The damping coefficients were determined using the methods described above, and using a least squares minimization fit over four cycles of data. The use of four cycles is somewhat arbitrary, as other values can also be used with similar results within certain limits. We observed that best results were obtained by taking at least two cycles and no more than about ten cycles. With less than two cycles, not enough points are available to make an accurate damping estimate and the model does not fit the data very well (see "Concluding Remarks" for a further discussion). At longer time lags, the autocorrelation has values that are quite close to zero and oscillates slightly, rendering a fit at these low levels difficult.

Consider first Fig. 7, which plots the pressure amplitude and damping coefficient for the 430 Hz mode. Starting at the premixer velocity of 40 m/s, note the trend in the calculated damping coefficient with decreasing velocity. The estimated damping monotonically decreases, even while the actual pressure amplitude stays essentially zero. Clearly, this calculation suggests that the combustor stability margin is decreasing, a fact that is evident from an overall view of the pressure data.

A similar result is shown in Fig. 8 for the 630 Hz mode. The damping coefficient monotonically decreases as the premixer velocity increases from 15–25 m/s. In this case, the corresponding pressure amplitude actually decreases slightly in this velocity range, indicating that a wholly wrong conclusion about stability tendencies would have been obtained from an analysis of pressure magnitudes.

For completeness, Figs. 9–12 plot several results for other frequencies that at certain conditions could be observed as small peaks in the spectrum. For example, Fig. 9 plots a result for the 285 Hz mode. The amplitude of this mode remained quite small over the entire velocity range (note the units on the *y* axis), although it does appear that it may have achieved significant amplitudes at lower premixer velocities, where data was not taken.

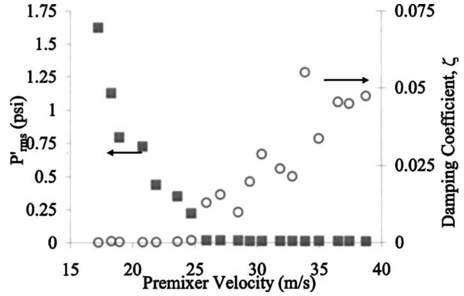

Fig. 7 Dependence of 430 Hz mode pressure amplitude (■) and damping coefficient (○) upon premixer velocity

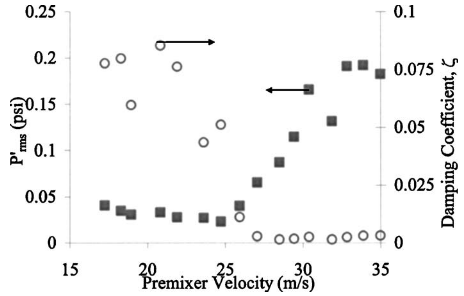

Fig. 8 Dependence of 630 Hz mode pressure amplitude (■) and damping coefficient (○) upon premixer velocity

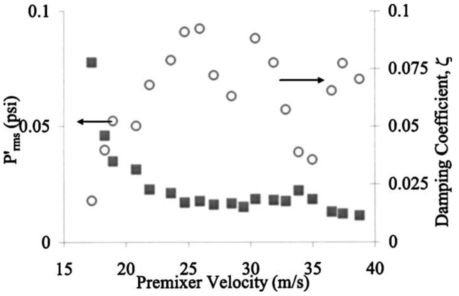

Fig. 9 Dependence of 285 Hz mode pressure amplitude (■) and damping coefficient (○) upon premixer velocity

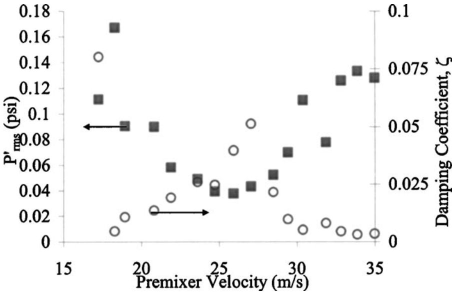

Fig. 10 Dependence of 730 Hz mode pressure amplitude (■) and damping coefficient (○) upon premixer velocity

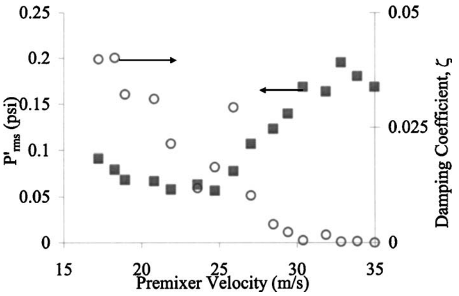

Fig. 11 Dependence of 570 Hz mode pressure amplitude (■) and damping coefficient (○) upon premixer velocity

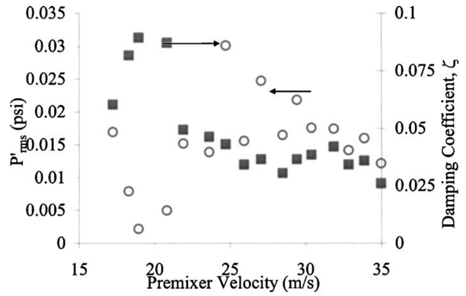

Fig. 12 Dependence of 132 Hz mode pressure amplitude (■) and damping coefficient (○) upon premixer velocity

4 Concluding Remarks

The results presented here clearly show that pressure data not only provide information about the amplitude of oscillations in an unstable combustor (as is currently done in fielded machines), but can also be used to track stability margin in cases where it is stable. While the results presented here were obtained from a single nozzle, lab scale combustor, efforts are underway to demonstrate this technique on fielded engines. To that end, an electric utility company has made available data obtained from each can of an instrumented, operational gas turbine. An analysis of these data shows similar results as those presented here. A key difference between the engine data and ours, however, is the presence of acoustic interactions between combustor cans. Because of these interactions, it is not clear how accurately subtle variations in the stability of one combustor can may be distinguished between those of adjoining ones. However, while there does appear to be some overall averaging of the stability margin between adjacent cans, can-to-can differences in stability are clearly observed in most cases.

It should be re-emphasized that a quantitative determination of the damping coefficient requires a mathematical model of the combustor oscillations. Clearly, improvements in the accuracy of the results could be obtained by utilizing a more accurate model (e.g., that includes the effects of heat release dynamics and parametric disturbances; see the last paragraph of the "Approach" section). For example, the model used here assumes that the autocorrelation envelope decays as $\exp(-\omega_i\zeta_i\tau)$, which agrees with the data in the $\sim 1 < f_i t < \sim 5$ time lag range; see Fig. 3. However, the dependence of $H_i(\tau)$ more closely exhibits an $\exp(-\omega_i\zeta_i\tau)^2$ dependence in the $f_i t < 1$ range. This poor fit of the model at low time delays necessarily introduces some dependence of the ζ estimate upon the length of the time series, a point noted in the "Approach" section.

Acknowledgment

This research was supported by the U.S. Department of Energy, Office of Fossil Energy, National Energy Technology Laboratory, under Contract No. 02-01-SR102 (Dr. Richard Wenglarz, technical monitor). Any opinions, findings, conclusions, or recommendations expressed herein are those of the authors and do not necessarily reflect the views of the DOE.

References

[1] Lee, J., and Santavicca, D., 2003, "Experimental Diagnostics for the Study of Combustion Instabilities in Lean, Premixed Combustors," J. Propul. Power, **19**, pp. 735–750.

[2] Richards, G., Straub, D., and Robey, E., 2003, "Passive Control of Combustion Dynamics in Stationary Gas Turbines," J. Propul. Power, **19**, pp. 795–810.

[3] Mongia, H., Held, T., Hsiao, G., and Pandalai, R., 2003, "Challenges and Progress in Controlling Dynamics in Gas Turbine Combustors," J. Propul. Power, **19**, pp. 822–829.

[4] Lieuwen, T., 2004, "Method for Monitoring Combustion Dynamics Stability Margin," Provisional Patent, filed Feb. 6.

[5] Johnson, C. E., Neumeier, Y., Lieuwen, T., and Zinn, B. T., 2000, "Experimental Determination of the Stability Margin of a Combustor Using Exhaust Flow and Fuel Injection Rate Modulations," *Proceedings of the Combustion Institute*, Vol. 28, pp. 757–764.

[6] Zinn, B. T., and Powell, E. A., 1970, "Nonlinear Combustion Instabilities in Liquid Propellant Rocket Engines," *Proceedings of the Combustion Institute*, Vol. 13, The Combustion Institute, Pittsburgh, PA.

[7] Culick, F. E. C., 1971, "Nonlinear Growth and Limiting Amplitude of Acoustic Oscillations in Combustion Chambers," Combust. Sci. Technol., **3**, pp. 1–16.

[8] Gardiner, C. W., 1997, *Handbook of Stochastic Methods*, Springer-Verlag, New York.

[9] Morse, P. M., and Feshbach, H., 1953, *Methods of Theoretical Physics*, Vol. 1, McGraw-Hill, New York.

[10] Lieuwen, T., Neumeier, Y., Rajaram, R., and Nair, S., 2003, "Measurements of Incoherent Acoustic Wave Scattering From Turbulent Premixed Flames," *Proceedings of the Combustion Institute*, Vol. 29, The Combustion Institute, Pittsburgh, PA., pp. 1809–1815.

[11] Lieuwen, T., and Banaszuk, A., 2002, "Background Noise Effects on Combustor Stability," ASME Paper No. GT-2002-30062.

[12] Burnley, V. S., 1996, "Nonlinear Combustion Instabilities and Stochastic Sources," Ph.D. thesis, California Institute of Technology.

[13] Clavin, P., Kim, J. S., and Williams, F. A., 1994, "Turbulence Induced Noise Effects on High-Frequency Combustion Instabilities," Combust. Sci. Technol., **96**, pp. 61–85.

[14] Lieuwen, T., Torres, H., Johnson, C., and Zinn, B. T., 2001, "A Mechanism for Combustion Instabilities in Premixed Gas Turbine Combustors," J. Eng. Gas Turbines Power, **123**, pp. 182–190.

[15] Lieuwen, T., 2002, "Experimental Investigation of Limit Cycle Oscillations in an Unstable Gas Turbine Combustor," J. Propul. Power, **18**, pp. 61–67.

A Critical Evaluation of NO_x Modeling in a Model Combustor

Lei-Yong Jiang[1]
e-mail: leiyong.jiang@nrc-cnrc.gc.ca

Ian Campbell

Gas Turbine Environmental Research Center,
Institute for Aerospace Research,
National Research Council Canada,
1200 Montreal Road, M-10,
Ottawa, Ontario, Canada, K1A 0R6

Reliable NO_x modeling depends on the accurate prediction of both velocity and temperature fields. The velocity and temperature fields of a propane diffusion flame combustor, with interior and exterior conjugate heat transfers, were first numerically studied. The results from three combustion models, together with the renormalization group (RNG) k-ε turbulence model and the discrete ordinates radiation model are discussed, and compared with comprehensive experimental measurements. The flow patterns and the recirculation zone length in the combustion chamber are excellently predicted, and the mean axial velocities are in fairly good agreement with the experimental data for all three combustion models. The mean temperature profiles are fairly well captured by the probability density function (PDF) and eddy dissipation (EDS) combustion models. However, the EDS-finite-rate combustion model fails to provide an acceptable temperature field. Based on the acceptable velocity and temperature fields, a number of NO modeling approaches were evaluated in a postprocessing mode. The partial-equilibrium approach of O and OH radical concentrations shows a significant effect on the thermal NO formation rate. In contrast, the prompt NO, the NO reburn mechanism and the third reaction of the extended Zeldovich mechanism have negligible effects on the overall NO formation in the present study. This study indicates that the semiempirical, postprocessing NO model can provide valuable NO simulations as long as the velocity and temperature fields are adequately predicted. [DOI: 10.1115/1.1850508]

Introduction

NO_x is a precursor for photochemical smog, contributes to acid rain and causes ozone depletion. As emission regulations become more stringent, it is vital to be able to model NO_x emissions in order to supplement or even to substitute expensive rig tests for the development of advanced combustion systems.

Much effort has been devoted to the understanding of nitrogen chemistry mechanisms in the last five decades. The current understanding of the mechanisms and rate parameters for the gas-phase reactions related to NO_x emission have been critically reviewed and evaluated by Miller and Bowman [1]. The NO_x formation issues under gas turbine combustion conditions have been excellently reviewed and discussed by Correa [2].

NO_x emission generated in model and practical combustors has been numerically studied by many researchers. The flow-field of a diffusion flame combustor, W251, was numerically studied by Volkov et al. [3] with a one-equation turbulence model and mixture fraction probability density function (PDF) combustion model. A NO_x flamelet model was used to predict NO_x emission in a postprocessing mode. Reasonable agreement was observed in comparison with the averaged measurements in the combustor exhaust. Price et al. [4] simulated the flow-field of a LM1600 gas turbine combustor during part load operation with the standard k-ε turbulence model, and the PDF and laminar flamelet combustion models. NO_x emission was also postprocessed. It was found that the predicted NO_x based on the flamelet model gave much closer agreement with the field data than the PDF model, due to accurate prediction of the oxygen radical concentration. With a flame generated manifold combustion model, Eggels [5] studied a premixed DLE gas turbine combustor, RB211. A postprocessing method was developed to solve differential equations for NO and N_2O. It was noticed that the nonperfect mixing of fuel and air had a strong effect on NO_x prediction. Cannon et al. [6] successfully applied large eddy simulation and a two-step assumed PDF combustion model to a premixed model combustor at practical engine operating conditions. The predicted NO_x emissions were compared with the measured values averaged over three sampling ports located 381 mm downstream of the injector. Good agreement was observed at equivalence ratio of 0.58 and 0.50. Kyne et al. [7] numerically studied a modern air-spray combustor with the PDF and flamelet combustion models, and the k-ε and Reynolds stress turbulence models. A new nonadiabatic PDF lookup table generator was developed to account for fuel spray evaporation process. The predicted temperature, major species and NO_x emission distributions were compared with the experimental measurements at five cross sections in the combustor. They pointed out that it was hard to pinpoint the reasons for the observed discrepancies without being able to compare the experimental and numerical velocity fields.

Due to a lack of confidence in predicting the velocity and temperature distributions in combustors, it is difficult to carry out a reliable evaluation of NO_x models applicable to practical combustors. It is well known that the NO_x formation rate is a highly nonlinear function of temperature and closely related to turbulence mixing process [1,2]. An accurate simulation of the velocity field provides a rational representation of the flow characteristics and turbulent mixing properties. These properties together with the chemical kinetics define the combustion processes and therefore the temperature distribution in the flow.

To provide a benchmark database for the evaluation and development of various physical models, a series of experiments were performed at National Research Council Canada (NRC). Measurements were made in a diffusion flame model combustor with advanced measurement techniques [8]. The comprehensive database included mean and fluctuating velocity components, mean temperature, radiation heat flux, as well as species and pollutant concentrations. The combustor geometry was relatively simple compared with practical combustion systems, but fundamentally similar and pertinent to the modeling of complex combustion systems.

The present work was divided into two phases. The velocity

---

[1] Corresponding author.

Contributed by the International Gas Turbine Institute (IGTI) of THE AMERICAN SOCIETY OF MECHANICAL ENGINEERS for publication in the ASME JOURNAL OF ENGINEERING FOR GAS TURBINES AND POWER. Paper presented at the International Gas Turbine and Aeroengine Congress and Exhibition, Vienna, Austria, June 13–17, 2004, Paper No. 2004-GT-53641. Manuscript received by IGTI, October 1, 2003; final revision, March 1, 2004. IGTI Review Chair: A. J. Strazisar.

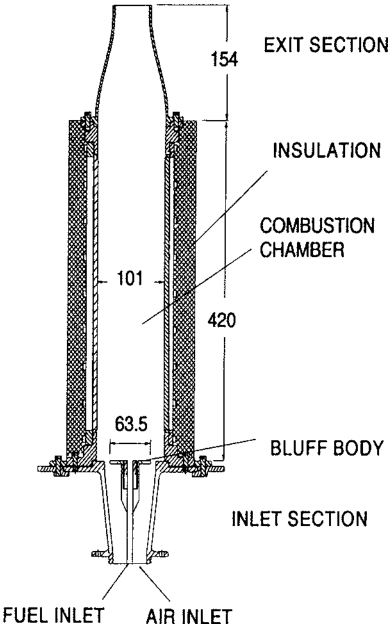

Fig. 1 The generic combustor

and temperature fields were first numerically studied and compared with the experimental data. Then, NO_x emission models were evaluated based on the accepted velocity and temperature field simulations. Unlike many combustor studies where the simulation was limited to the combustion chamber only, the computational domain in the present study covered the entire combustor flow-field from the fuel and air inlets to the nozzle exit. Moreover, the internal and external conjugate heat transfers from the combustion products to the flame holder body and insulation walls were also modeled.

Experimental Measurements

Figure 1 shows a schematic diagram of the model combustor, including the fuel and air entries, combustion chamber, disk flame-holder, and contracted exhaust section. Air entered the combustion chamber around a bluff body, while fuel was fed through the center of the disk flame-holder. The test rig was mounted on a three-axis traversing unit with a repeatability of ± 100 μm. The fuel used in the experiments was commercial grade propane, while air was delivered from a dry shop air supply. Both air and fuel flows were controlled by Sierra Side-Trak mass-flow controllers with 2% accuracy in full scale (fuel 100 l/min and air 2550 l/min).

To reduce the heat losses through walls, a 25.4-mm thick fiber blanket of Al_2O_3, was wrapped around the combustion chamber from the level of the disk flame-holder to the beginning of the exhaust section. Four narrow slots were cut into the blanket to allow appropriate physical and optical access to the chamber interior. Interchangeable sets of stainless steel and fused silica windows were used for physical probing using gas sampling probes, radiometers and thermocouples, and for optical probing using the laser Doppler anemometer (LDA). The viewing area of the windows measured 17 mm in width and 344 mm in length.

Measurements of velocity were made using both a 2- and 3-component LDA systems operating in the back scattering mode. In the lower section of the combustion chamber, limited optical access forced the use of a single fiberoptic head to measure axial and tangential velocities. In the upper section of the chamber, a complete three-component LDA system was used. Gas temperatures were acquired using an uncoated, 250-μm diameter, type "S" thermocouple mounted in a twin bore ceramic tube. Gas species measurements were made with a sampling probe connected to a Varian Model 3400 Gas Chromatograph. The major species measured were CO, CO_2, H_2, and C_3H_8. NO_x and NO were collected through the same probe but analyzed using a Scintrix NO_x analyzer.

Numerical Simulations

Axisymmetric, steady, turbulent, reacting flows were considered in the present study, and a commercial software package, Fluent, was used for the numerical simulations. The computation domain, selected physical models, boundary conditions, and solution methods are described in the following subsections.

Computational Domain. Since the flow-field was axisymmetric, 2D quadrilateral meshes were generated over the flow region, interior conjugate heat transfer region (the flame holder body within the inlet section) and exterior conjugate heat transfer region (the combustion chamber wall and the ceramic insulation around the combustion chamber). Fine grids were laid behind the flame-holder in the combustion chamber to resolve the recirculation region. Fine grids were also generated in the shear layers between the recirculation region and the fuel and air jets, as well as the gap between the flame-holder edge and the air inlet chamber wall. Coarse grids were used downstream of the combustion chamber and in the solid stainless steel and ceramic regions. A total number of 74,100 elements were used for most of the simulations. The skewness was less than 0.2 in the flow-field domain and the aspect ratio was less than 12 for 99.5% elements. Efforts were made to keep the wall parameter y^+ in the desired range (30 to 60). However, there were local low-velocity regions where the y^+ values were well below 30. A number of meshes were tested to ensure the mesh independence of the numerical solutions.

Turbulence and Combustion Modeling. The governing Favre-averaged conservation equations for mass, species, momentum and energy are not reproduced here. They can be readily found in many classic literatures, such as Ref. [9]. For closure of the above equations, the RNG k-ε turbulence model derived from a renormalization group theory [10] was used to model turbulence transfers in the reacting flow. This model has shown an excellent agreement between the numerical and experimental results for an isothermal flow over a backward facing step [11].

According to this model, the turbulent viscosity for high Reynolds number flows is expressed as

$$\mu_t = \rho C_\mu k^2/\varepsilon \tag{1}$$

where $C_\mu = 0.0845$, derived from the RNG theory. It is very close to the empirically determined value of 0.09 used in the standard k-ε model. The quantities of the turbulent kinetic energy, k, and dissipation rate, ε, are found from the following pair of equations:

$$\nabla \cdot (\rho \mathbf{v} k) = \nabla \cdot (\alpha_k \mu_{\mathrm{eff}} \nabla k) + G_k - \rho\varepsilon \tag{2}$$

$$\nabla \cdot (\rho \mathbf{v} \varepsilon) = \nabla \cdot (\alpha_\varepsilon \mu_{\mathrm{eff}} \nabla \varepsilon) + C_{1\varepsilon} \frac{\varepsilon}{k} G_k - C_{2\varepsilon}^* \frac{\rho \varepsilon^2}{k} \tag{3}$$

In the above equations, μ_{eff} is the effective viscosity, α_k and α_ε are the inverse Prandtl numbers, and $G_k = \mu_t S^2$ stands for the turbulence production with μ_t the turbulence viscosity and S the modulus of the mean rate-of-strain tensor, defined as $S \equiv \sqrt{2\mathbf{S}_{ij}\mathbf{S}_{ij}}$.

The main difference between the RNG and standard k-ε models is that the coefficient of the destruction term, $C_{2\varepsilon}^*$ in Eq. (3), is no longer a constant, but a function of flow mean strain rate and turbulence field (k and ε). It is defined by the following expression:

$$C_{2\varepsilon}^* \equiv C_{2\varepsilon} + \frac{C_\mu \eta^3 (1 - \eta/\eta_0)}{1 + \beta\eta^3} \tag{4}$$

where $\eta \equiv S\,k/\varepsilon$, $\eta_0 = 4.38$, $\beta = 0.012$. As a result, the RNG model is more responsive to the effects of flow strain rate and thus improves the accuracy for rapidly strained flows. The model constants, $C_{1\varepsilon}=1.42$ in Eq. (3) and $C_{2\varepsilon}=1.68$ in Eq. (4).

In addition, the RNG model provides an analytical formula to account for variations of turbulent Prandtl and Schmidt numbers in the flow for the energy and species equations [10,12],

$$\left[\frac{\alpha-1.3929}{\alpha_0-1.3929}\right]^{0.6321}\left[\frac{\alpha+2.3939}{\alpha_0+2.3929}\right]^{0.3679}=\frac{\mu_{\mathrm{mol}}}{\mu_{\mathrm{eff}}} \tag{5}$$

where μ_{mol} is the laminar viscosity, and $\alpha_0=1/\mathrm{Pr}_{\mathrm{mol}}$ or $1/\mathrm{Sc}_{\mathrm{mol}}$ (the inverse of the laminar Prandtl or Schmidt number). However, it should be mentioned that the inverse Prandtl numbers, $\alpha_k=\alpha_\varepsilon=\alpha$, in Eqs. (2) and (3) are determined by simply setting $\alpha_0=1$.

Three combustion models were used, including the eddy-dissipation (EDS), eddy-dissipation/finite-rate and probability density function (PDF) models. The EDS model is based on the work of Magnussen and Hjertager [13], which has been widely accepted in diffusion flame modeling [14]. For this model, a one-step global chemical reaction is assumed,

$$C_3H_8+5(O_2+3.76N_2)=3CO_2+4H_2O+5\times 3.76N_2 \tag{6}$$

and the reaction rate is governed by turbulent mixing, or the large-eddy mixing time scale, k/ε. The net rate of reaction of species "i" is given by the smaller of the two following expressions in kg/m^3 s,

$$R_i=\nu_i M_i A\rho\frac{\varepsilon}{k}\min\left[\frac{Y_{C_3H_8}}{\nu_{C_3H_8}M_{C_3H_8}},\frac{Y_{O_2}}{\nu_{O_2}M_{O_2}}\right] \tag{7}$$

$$R_i=\nu_i M_i AB\rho\frac{\varepsilon}{k}\frac{(Y_{CO_2}+Y_{H_2O})}{(\nu_{CO_2}M_{CO_2}+\nu_{H_2O}M_{H_2O})} \tag{8}$$

where Y is the mass fraction, ν stands for the stoichiometric coefficient, M represents the molecular weight, and the empirical constants, $A=4.0$ and $B=0.5$.

For the EDS-finite-rate model, an additional constraint to the propane-air combustion, a global chemical reaction rate from Westbrook and Dryer [15], was included,

$$R_{C_3H_8}=A\exp(-E/RT)[C_3H_8]^{0.1}[O_2]^{1.65}\quad(\mathrm{kmol/m^3\ s}) \tag{9}$$

where the pre-exponential factor, $A=4.836\times 10^9$ and the activation energy, $E=1.256\times 10^8$ J/kmol. The net reaction rate at each point in the flow-field is determined by the smallest one among the three expressions (7), (8), and (9).

The last combustion model is based on the mixture fraction approach with an assumption of fast chemistry [16]. It offers many advantages over the EDS and EDS-finite-rate models. It allows intermediate (radical) species prediction, dissociation effects, and more rigorous turbulence-chemistry coupling. The mixture fraction can be written in terms of atomic mass fraction as,

$$f=\frac{Z_i-Z_{i,\mathrm{ox}}}{Z_{i,\mathrm{fuel}}-Z_{i,\mathrm{ox}}} \tag{10}$$

where Z_i stands for the elemental mass fraction of element, "i," $Z_{i,\mathrm{ox}}$ and $Z_{i,\mathrm{fuel}}$ denote the elemental mass fraction of "i" at the oxidizer and fuel inlets, respectively. It is a common practice to assume that all species have the same diffusivity in turbulent flows. As a result, the mixture fraction becomes a conserved quantity, and the transport equations for the mean mixture fraction and its variance may be simplified as

$$\nabla\cdot(\rho\mathbf{v}\bar{f})=\nabla\cdot\left(\frac{\mu_t}{\sigma_t}\nabla\bar{f}\right) \tag{11}$$

and

$$\nabla\cdot(\rho\mathbf{v}\overline{f'^2})=\nabla\cdot\left(\frac{\mu_t}{\sigma_t}\nabla\overline{f'^2}\right)+C_g\mu_t(\nabla^2\bar{f})-C_d\rho\frac{\varepsilon}{k}\overline{f'^2} \tag{12}$$

where $f'=f-\bar{f}$, and the constants σ_t, C_g, and C_d take the values of 0.85, 2.86, and 2.0, respectively.

With the fast chemistry assumption, the chemical equilibrium calculation based on the minimization of Gibbs free energy can be used to determine the combustion system. For a defined combustion system, the instantaneous mole fractions of individual species, density and temperature at each point in the flow-field can be exclusively determined from the instantaneous mixture fraction in the adiabatic condition. When heat loss is concerned, as in the present study, the relationship may be generalized as

$$\phi_i=\phi_i(f,H) \tag{13}$$

where ϕ represents the instantaneous species mole fraction, density or temperature, and H is the instantaneous enthalpy.

The turbulence-chemistry interaction is accounted for by the β-function probability density function (PDF), $p(\bar{f},\overline{f'^2})$, which is determined solely by the mean and variance of mixture fraction [17]. The time-averaged values of species mole fractions and temperature are computed as

$$\overline{\phi_i}=\int_0^1 p(\bar{f},\overline{f'^2})\phi_i(f,H)df \tag{14}$$

Eighteen species were considered for the PDF model, including C_3H_8, CO_2, H_2O, O_2, N_2, CO, HO, H, O, H_2, C_3H_6, C_2H_6, C_2H_4, CH_4, CH_3, CH_2, CH, and C(s). The selection of these species was based on the basic chemical kinetics [18] and the requirements for emission modeling. To avoid complex equilibrium combustion processes in the rich flame region (it often does not represent the real combustion process), when the instantaneous equivalence ratio exceeded 1.75, the combustion reaction was considered extinguished and unburned fuel coexisted with reacted products.

NO_x Modeling. As NO_x occurs in trace quantities and has negligible effect on the flow-field, it is accordingly postprocessed [3–7]. Furthermore, for most flames, NO is predominant in NO_x emission, with oxidation to NO_2 in a postflame process that does not affect the total NO_x, and N_2O emission is less significant [2]. Therefore, a mass transport equation only for NO is solved for the NO_x emission study,

$$\nabla\cdot(\rho\mathbf{v}Y_{NO})=\nabla\cdot\left(\rho\frac{\mu_{\mathrm{eff}}}{\mathrm{Sc}_t}\nabla Y_{NO}\right)+S_{NO} \tag{15}$$

where Y_{NO} is the mean mass fraction of NO and Sc_t is the turbulent Schmidt number.

The source term, S_{NO}, in Eq. (15) is the sum of three NO formation and depletion rates, i.e., thermal NO, prompt NO and NO reburning. The thermal NO formation rate is determined by the extended Zeldovich mechanism,

$$\begin{gathered}O+N_2\Leftrightarrow N+NO\\ N+O_2\Leftrightarrow O+NO\\ N+OH\Leftrightarrow H+NO\end{gathered} \tag{16}$$

With the steady-state approximation for N and the partial equilibrium for H, suggested by Westenberg [19], the thermal NO can be obtained by the following equation in g mol/m^3 s,

$$\frac{d[NO]}{dt}=2K_1[O][N_2]\frac{\left(1-\dfrac{k_{-1}k_{-2}[NO]^2}{k_1[N_2]k_2[O_2]}\right)}{\left(1+\dfrac{k_{-1}[NO]}{k_2[O_2]+k_3[OH]}\right)} \tag{17}$$

where the reaction rates, $k_1=1.8\times 10^8 e^{-38,370/T}$, $k_{-1}=3.8\times 10^7 e^{-425/T}$, $k_2=1.8\times 10^4 Te^{-4680/T}$, $k_{-2}=3.81\times 10^3 Te^{-20,820/T}$, and $k_3=7.1\times 10^7 e^{-450/T}$, based on Hanson and Salimian's work [20].

To calculate the thermal NO formation rate with Eq. (17), the local values of temperature and species concentrations of O_2 and N_2 are obtained from the flow-field simulation. To find the O and OH concentrations, two approaches, equilibrium and partial equilibrium, are considered. For the equilibrium approach [19,21,22], the O concentration is estimated using the following expression in g mol/m^3,

$$[O]=3.97\times 10^5 T^{-1/2}[O_2]^{1/2}e^{-31{,}090/T} \tag{18}$$

in the case of the EDS combustion model. For the PDF combustion model case, the predicted local O concentration is used in the simulation. For the equilibrium approach, the effect of OH is neglected by simply setting $[OH]=0$ in Eq. (17).

For the partial equilibrium approach, Eq. (18) is replaced by the following expression [22,23],

$$[O]=36.64T^{1/2}[O_2]^{1/2}e^{-27{,}123/T} \tag{19}$$

and according to Baulch et al. [24] and Westbrook and Dryer [15], the OH concentration is estimated as,

$$[OH]=2.129\times 10^2 T^{-0.57}e^{-4595/T}[O]^{1/2}[H_2O]^{1/2} \tag{20}$$

The prompt NO is less significant in turbulent diffusion flames [2]. However, its formation involves a complex series of reactions and many possible intermediate species, with some uncertainties in the reaction mechanisms and rate parameters [1]. To avoid complex hydrocarbon combustion mechanisms, De Soete [25], based on the experimental data, derived a global empirical expression to estimate the prompt NO formation rate for C_2H_4–air flames. This approach was further developed to account for the effects of fuel type and fuel/air ratio for gaseous aliphatic alkane hydrocarbon fuels in a range of equivalence ratio from 0.6 to 1.6 [22,26,27]. The overall prompt NO rate is given by the following equation in g mol/m^3 s,

$$\frac{d[NO]}{dt}=fk_{pr}[O_2]^a[N_2][C_3H_8]e^{-E/RT} \tag{21}$$

where $f=4.75+0.0819n-23.2\phi+32\phi^2-12.2\phi^3$ with n the number of carbon atoms per molecule for the hydrocarbon fuel and ϕ the equivalence ratio, $k_{\text{pr}}=6.4\times 10^6$ and $E=72{,}500$ cal/g mol. The oxygen reaction order in Eq. (21) is estimated by the following expression:

$$a=\begin{cases} 1.0 & [X_{O_2}]\leqslant 4.1\times 10^{-3} \\ -3.95-0.9\ln[X_{O_2}] & 4.1\times 10^{-3}\leqslant [X_{O_2}]\leqslant 1.11\times 10^{-2} \\ -0.35-0.1\ln[X_{O_2}] & 1.11\times 10^{-2}<[X_{O_2}]<0.03 \\ 0 & [X_{O_2}]\geqslant 0.03 \end{cases} \tag{22}$$

where $[X_{O_2}]$ is the oxygen mole fraction.

The NO reduction is modeled by the following three reactions proposed by Bowman [21],

$$\begin{gathered} CH+NO\Leftrightarrow HCN+O \\ CH_2+NO\Leftrightarrow HCN+OH \\ CH_3+NO\Leftrightarrow HCN+H_2O \end{gathered} \tag{23}$$

The total NO depletion rate is given by

$$\frac{d[NO]}{dt}=-k_1[CH][NO]-k_2[CH_2][NO]-k_3[CH_3][NO] \tag{24}$$

in g mol/m^3 s, where $k_1=1\times 10^8$, $k_2=1.4\times 10^6 e^{-550/T}$ and $k_3=2\times 10^5$ for $1600\text{ K}\leqslant T\leqslant 2100\text{ K}$.

It should be noted that the above kinetic mechanisms and related parameters (Eqs. (17)–(24)) were derived from laboratories using either premixed laminar flames or shock-tube tests, and therefore the turbulent mixing effect on NO formation must be considered. Similar to the PDF combustion model, the turbulence-chemistry interaction is modeled by a β-function probability density function, $p(\bar{T},\overline{T'^2})$, in the present study. Assuming equal production and dissipation in the differential transport equation, the variance of temperature was calculated by the following expression:

$$\sigma^2=\frac{\mu_t k C_g}{\rho\varepsilon C_d}\left[\left(\frac{\partial\bar{T}}{\partial x}\right)^2+\left(\frac{\partial\bar{T}}{\partial y}\right)^2+\left(\frac{\partial\bar{T}}{\partial z}\right)^2\right] \tag{25}$$

where $C_g=2.86$ and $C_d=2.0$.

To account for the heat radiation between the gas mixture and combustion chamber walls, the discrete ordinates radiation model [28] was employed. The absorption coefficient of gaseous mixture was determined from the local species mass fractions in the mixture. At the wall boundaries, an enhanced wall boundary treatment was applied. In this approach, an enhanced two-layer model [29] was combined with enhanced wall functions [30], where the viscous region and the fully turbulent region were smoothly blended.

Polynomials were used to calculate the specific heat of species as a function of temperature. These polynomials were determined from the JANAF tables for the case of the PDF model; while in the case of the EDS and EDS-finite-rate models, the polynomials from Ref. [31] were used, where the chemical dissociation was considered. For other thermal properties such as molecular viscosity, thermal conductivity, diffusivity and absorption coefficient, the values at 900 K were used.

Boundary Conditions. The fuel mass flow rate was 16.2 g/s and the airflow rate was 550 g/s, and the corresponding equivalence ratio was 0.55. A turbulence intensity of 10% and hydraulic diameters (4× cross-section area/wetted perimeter) were used to estimate turbulence dissipation rate and kinetic energy at the fuel and air inlets. For both flows, the inlet temperature was 293 K.

The boundary temperatures were defined based on the experimental measurements or observations. A room temperature of 293 K was assigned to the inlet section walls, and the upstream edges of the combustion chamber and ceramic insulation walls. A linear temperature profile from 294 K to 405 K was specified along the axial outer boundary of the ceramic insulation. The temperature of the outer boundary of the exit nozzle was set to 823 K. The same temperature was assigned to the downstream edge of the combustion chamber wall since its heat resistance was much smaller than the ceramic insulation (the thermal conductivity is 25 W/m K for the stainless steel, while only 0.1 W/m K for the ceramic insulation). A linear temperature profile from 823 K to 405 K was assigned to the downstream edge of the insulation wall. The pressure at the combustor exit was set to the atmospheric value.

Solution Methods. A segregated solver with a second-order accurate scheme was used to resolve the flow-field. At convergence, the normalized residuals of flow variables were about or less than 10^{-5} in all test cases. The monitored axial velocities at two points in the shear layer downstream of the flame holder remained unchanged at least for the first four digits. A LINUX PC server with two Pentium 2.8-GH CPUs and 4-GB RAM was used to perform all simulations.

Results and Discussion

Velocity Distributions. The upper half of Fig. 2 shows the axial velocity contours and flow path-lines obtained with the PDF combustion model. The lower half of the figure presents the experimental data with the zero axial velocity lines specified. The contour plot provides a whole picture of comparison between the numerical and experimental results. The flow patterns in the combustion chamber are well captured by the numerical simulation. Two recirculation zones are formed behind the flame-holder although, in the experimental case, the central recirculation zone is not completely resolved and no flow path-lines are drawn due to

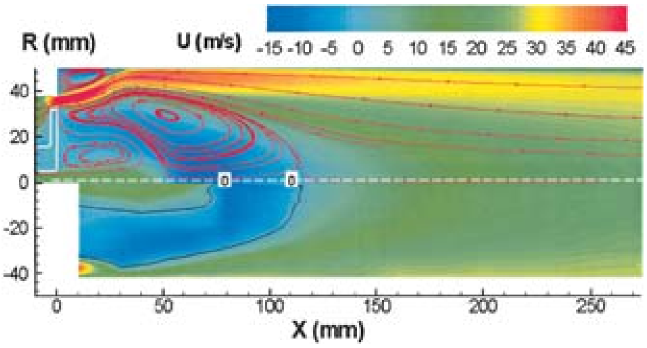

Fig. 2 Axial velocity contours and flow path lines

the limited data points. The central recirculation zone created by the fuel jet is completely confined within the annular recirculation zone created by the annular air jet. This implies that the transportation of fuel into the flow-field is realized only by the laminar and turbulent diffusion through the annular recirculation zone. As expected, another separated flow zone is observed at the upper left corner in the combustion chamber.

The axial velocity contours and flow path-lines for the EDS model are similar to those for the PDF model. It is also true for the case of the EDS-finite-rate combustion model, except that the annular recirculation zone is a little larger than the other two cases. The contour plots for the EDS and EDS-finite-rate models are not illustrated here due to the limited space.

Figure 3 presents the axial velocity profiles along the combustor centerline for the three combustion models and compared with the experimental results. The predicted trend and magnitude agree fairly well with the experimental data, particularly for the PDF model. From $x \approx 80$ mm, where the negative axial velocity is close to its peak value, up to $x = 360$ mm, the predicted axial velocities agree well with the experimental data for all three models. The maximum negative axial velocity is about -10 m/s. More remarkably, the reattachment point or the length of the recirculation region is excellently predicted (see both Figs. 2 and 3). The predicted reattachment point, where the axial velocity is zero in Fig. 3, is 104 mm, 106 mm, and 108 mm for the EDS, EDS-finite-rate, and PDF model, respectively. They are very close to the experimental value of 104 mm.

Discrepancies are observed at $x \approx 55$ mm. The predicted axial velocities are lower than the measured values, and the predicted velocity deficit region is wider than the experimental observation for all three models. These are consistent with the observation in Fig. 2, where the predicted central recirculation region is smaller than the measurements.

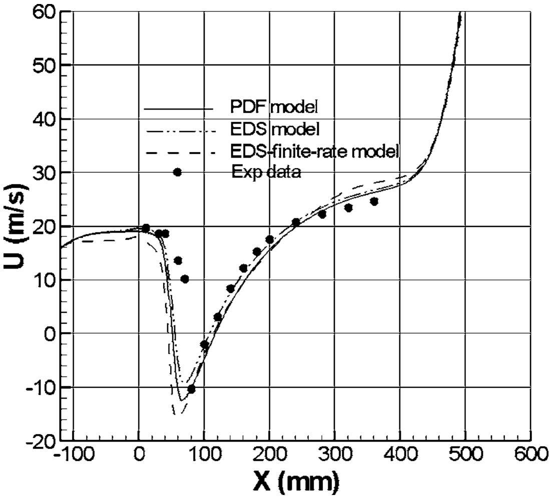

Fig. 3 Axial velocities along the combustor centerline

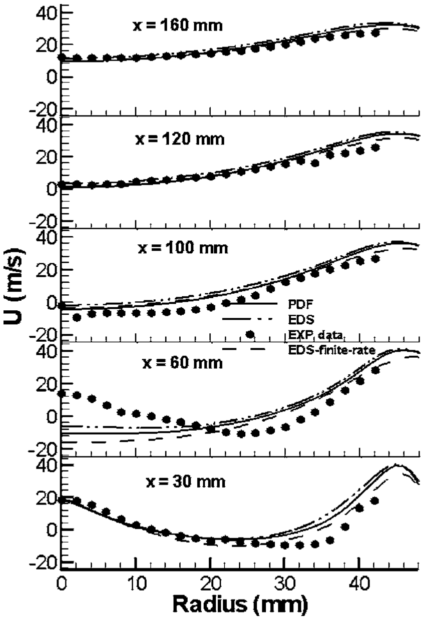

Fig. 4 Axial velocity profiles at cross sections $x = 30$ mm to 160 mm

Figures 4 and 5 give the detailed axial velocity profiles at cross sections from $x = 30$ mm to 360 mm. Again, the trend and magnitude are fairly well captured, except for the upstream section $x = 60$ mm. The axial velocity profiles downstream of the recirculation region ($x \geq 120$ mm) are in good agreement with the experimental data for all three models although the deviation up to 4 m/s can be found. Considerable discrepancies at sections $x = 30$ mm and 60 mm are attributed to the disagreement between the prediction and measurement around the central recirculation zone.

In general, three combustion models show similar performance. The fairly good agreements between the numerical results and experimental data suggest that the RNG turbulence model combined with the enhanced wall treatment is capable of predicting the flow separation and recirculation behind the axisymmetric bluff body, and the momentum mixing between the central wake and annular air for similar combustion systems.

Temperature Distributions. The predicted temperature contours from the PDF model are shown in the upper half in Fig. 6, and compared with the experimental results in the lower half. Owing to the limited physical access, the experimental data near the flame-holder are not available. As a whole picture, the predicted temperature distributions are fairly well correlated to the experimental data, except for the downstream portion within the annular recirculation zone. In this region, the predicted temperatures are higher than the measured values. This is due to the fact that the predicted central recirculation zone is smaller than the measurements as mentioned earlier. Fortunately, this small region has little effect on the NO prediction since the NO emission mainly occurs downstream of the recirculation region, as shown later.

Similar temperature distributions are observed for the EDS model results. However, the results from the EDS-finite-rate model are poor, substantially different from the other two models (not shown here due to the limited space). The high temperature region predicted by the EDS-finite-rate model is shifted about 125 mm upstream and the thermal wake region becomes shorter and narrower in comparison with the experimental results or other two cases. It should be mentioned that the EDS-finite-rate model re-

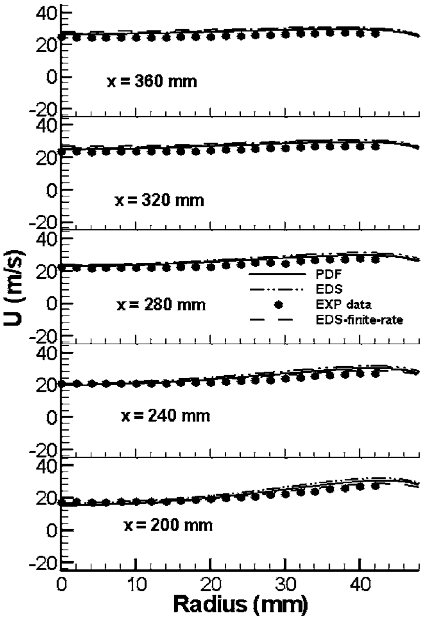

Fig. 5 Axial velocity profiles at cross sections $x=200$ mm to 360 mm

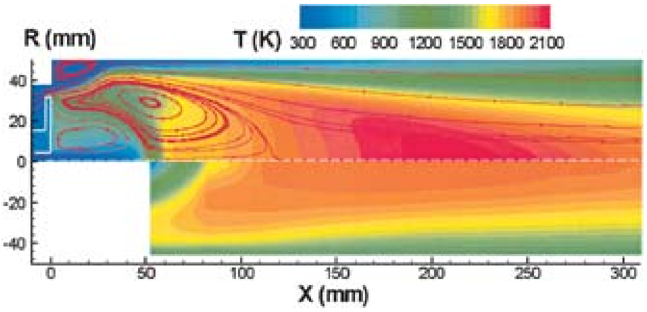

Fig. 6 Upstream temperature contours

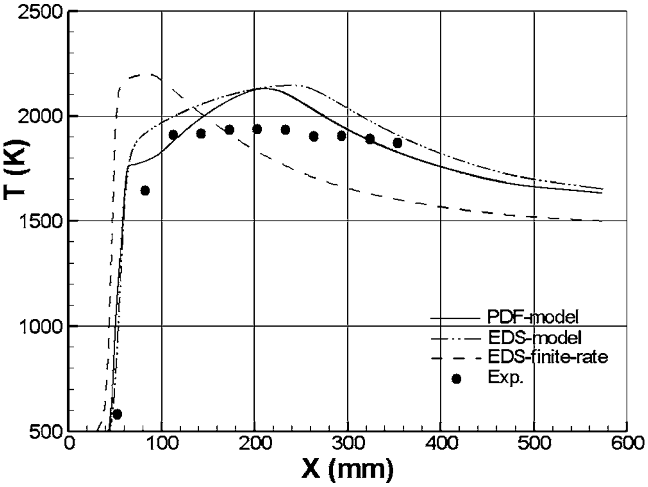

Fig. 7 Temperature along the combustor centerline

sults were confirmed by switching combustion model from the EDS to the EDS-finite-rate and iterating based on the converged EDS solution with the fuel mass fraction patched in the flow-field, and vice versa.

The detailed quantitative comparisons of temperature are given in Figs. 7–9. Figure 7 shows the predicted and measured temperature profiles along the centerline of the combustor. In the range of measurements (50 mm to 350 mm), the predicted temperatures for the PDF and EDS models agree fairly well with the experimental values although the predicted profiles show peaks in the middle portion, while the measurements tend to be flat. The maximum temperature along the centerline reaches about 2150 K for the EDS and PDF model, while the measured value is 1950 K. The PDF model illustrates the best agreement among the three models. Poor agreement is observed for the EDS-finite-rate model. The temperature is overpredicted in the upstream region and underpredicted in the downstream region.

Figures 8 and 9 show the temperature profiles at various cross sections from $x=52$ mm to 353 mm for the three combustion models. Again, the results obtained with the PDF and EDS models agree fairly well with the experimental results, except for the most upstream section and the region near the combustor wall. Poor agreement of the EDS-finite-rate model is also observed, particularly at two upstream sections.

From Figs. 6 to 9, it is found that the predicted temperatures from the EDS and PDF models are higher than the measured values in the center region from $x=140$ mm to 250 mm. The maximum difference is about 200 K. The reasons may be twofold. First, as mentioned earlier, the temperature was measured by a 0.25-mm thermocouple. Owing to the radiation and conduction losses from the thermocouple, the measurement error could exceed 100 K over regions where the gas temperature was high and the flow velocity was low [32]. The second reason may be that the predicted thermal spreading is somewhat less than the experimental observations. This leads to the temperature near the combustor wall underpredicted, as observed in Figs. 6 and 8–9.

Comparison of Figs. 8 and 9 with Figs. 4 and 5 indicates that the thermal mixing between the annular air and the wake flow behind the recirculation region is underpredicted although the momentum mixing is well captured. This suggests that different turbulent Prandtl and Schmidt numbers should be used to more accurately account for the thermal mixing.

Conjugate Heat Transfers. Figure 10 shows the temperature contours in the inlet section and near the flame-holder. The temperature gradually increases towards downstream and reaches about 650 K at the downstream surface of the flame-holder, which

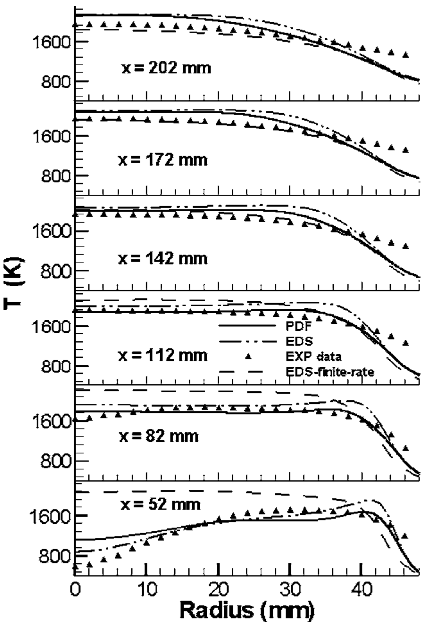

Fig. 8 Temperature profiles at cross sections $x=52$ mm to 202 mm

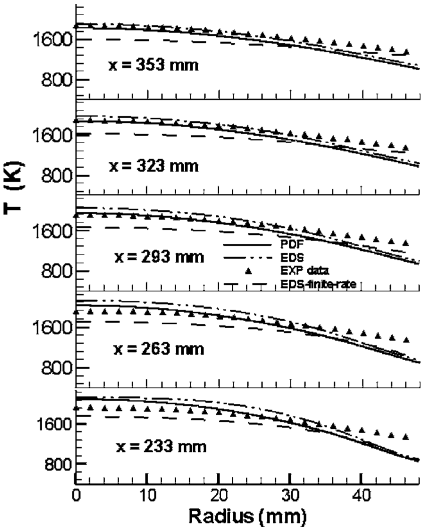

Fig. 9 Temperature profiles at cross sections $x=233$ mm to 353 mm

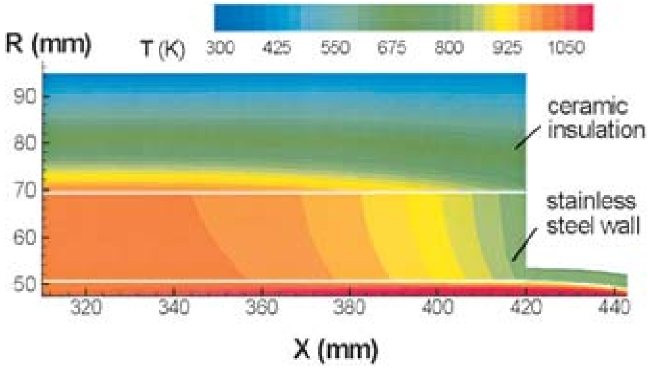

Fig. 11 Temperature contours near the insulation wall

indicates that the flame-holder did not get very hot during operation. This is qualitatively consistent with the experimental observation, i.e., no deformation of the thin flame-holder was found after all measurements. Figure 10 also shows that the flame starts at the middle of the disk edge and spreads around the recirculation envelope, where the recirculated mixture of hot gases and fuel mixes with the fresh air and burns. This agrees with the experimental fact that a carbon deposit was found at the middle of the disk edge, which indicated where the combustion began.

Figure 11 illustrates the exterior conjugate heat transfer between the combustion products and the combustion chamber wall and ceramic insulation. Steep temperature gradients in the ceramic insulation are observed owing to its very low heat conductivity. Large temperature gradients also occur near the downstream edge of the stainless steel wall due to the large temperature difference between the combustion products and the environment.

NO Modeling. As mentioned earlier, a reliable evaluation of NO models depends on the correct prediction of both velocity and temperature fields. In this study, both the velocity and temperature fields are fairly well predicted by the RNG turbulence model, combined with the discrete ordinates radiation model, and the PDF and EDS combustion models. This provides a suitable base for the evaluation of NO models. Since the EDS-finite-rate combustion model fails to provide an acceptable temperature field, it is not considered in the evaluation.

The sensitivity of various NO model options to the overall NO formation was investigated. Figure 12 presents the results obtained with the PDF combustion model at the cross section, $x=300$ mm, where the NO concentration is high.

In Fig. 12, the full model profile indicated by the green line represents the NO simulation considering the thermal, prompt and reburn NO mechanisms, the partial-equilibrium O and OH approach, as well as the turbulence effect. Also plotted are curves that evaluate various NO model options. It is found that the contribution by the prompt NO, denoted by the dashed red line, is negligibly small. This is attributed to a number of reasons. First, the prompt NO, in general, is insignificant in turbine diffusion flame combustors [2]. In the present case, the gaseous fuel with a relatively low fuel/air equivalence ratio of 0.55 and long residence time in the combustor, the prompt NO rate tends to be even lower. Second, it mainly occurs within the recirculation region since this region is fuel rich and close to the flame zone [1]. As shown in Fig. 2, the air enters the recirculation region through laminar and turbulent diffusion only because the fuel jet is completed confined within the recirculation region. Consequently, the O_2 mole fraction within this region is very small (<0.001) and then the prompt NO rate calculated with Eq. (21) is low. Third, the prompt NO definition used here should be clarified. As mentioned by Bachmaier et al. [26], Fenimore (1971) divided the NO formation into two parts: one due to the Zeldovich mechanism assuming O radi-

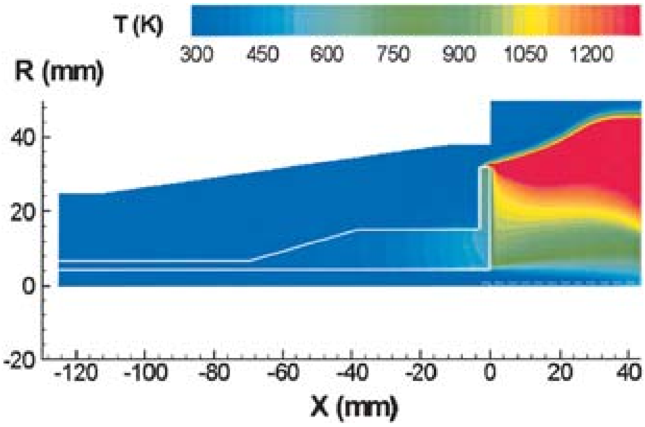

Fig. 10 Temperature contours near the flame holder

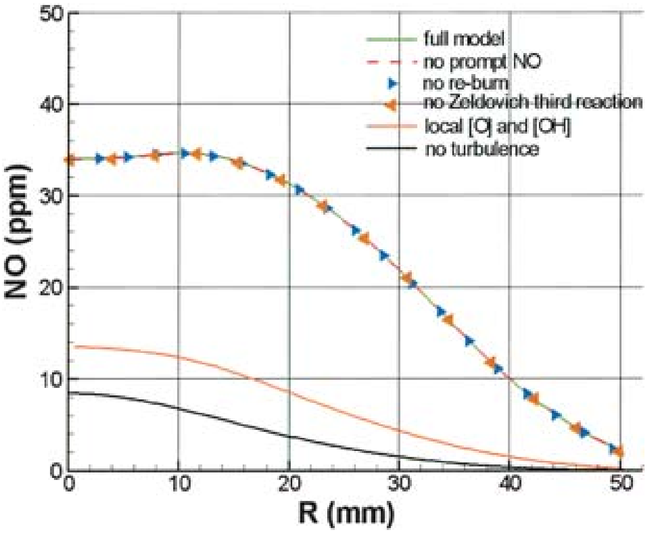

Fig. 12 No profiles at $x=300$ mm, PDF combustion model

cals in equilibrium, and the rest including the Zeldovich mechanism due to the non-equilibrium effect of O radicals and the prompt NO mechanism as well. However, in the present study, the NO formation due to the nonequilibrium effect of O radicals is excluded from the prompt NO calculation. Finally, the equivalence ratio of 0.55 is slightly below the lower limit of Eq. (21), and the extrapolation may have caused some error.

Figure 12 also shows that the NO reburn mechanism (right triangles) has negligible effect on the overall NO generation. This may be attributed to the low concentrations of CH_i and NO for the present operating conditions. Consequently, the reduction of NO through the three reactions in Eq. (23) is negligible. This is consistent with the observation by Ishii et al. [33], where the effects of various NO model options on the NO prediction in a gas-fired regenerative furnace were studied.

Furthermore, Fig. 12 also indicates that the third reaction of the extended Zeldovich mechanism (Eq. (16)), denoted by left triangles, has negligible effect on the overall NO formation. By examining the order of magnitude, the effect of OH on the overall thermal NO formation is found to be minor in general. For the gaseous fuel and relatively low equivalence ratio, the peak temperature is relatively low and the OH concentration is very small. Consequently, the effect of OH on the predicted thermal NO rate (Eq. (17)) can be neglected. This is also consistent with Ishii's observation [33].

The importance of using the partial-equilibrium approach for O and OH radicals to calculate the thermal NO formation rate has been recognized by many researchers [1,4,7,33]. As shown in Fig. 12, the NO formation obtained with the local O and OH concentrations predicted by the PDF model is significantly lower than that from the full model. This agrees with Ishii's observation [33], where the predicted average values were compared with the experimental data at the devices exits.

The remarkable effect of the flow turbulence on the NO formation rate is also included in Fig. 12. The computed results using the mean flow parameters, denoted by the black line, are much lower than the other cases. This supports the earlier statement that the NO modeling is closely related to the flow characteristics and turbulent mixing properties.

Similar results were also observed for the EDS combustion model case, except for the effect of the reburn mechanism since the local species concentrations of CH, C_2H, and C_3H were not available in the simulations with the EDS combustion model.

Figure 13 compares the predicted NO contours from the EDS combustion model (top) and the experimental data (bottom). The numerical results were obtained with the thermal and prompt NO mechanisms, the partial-equilibrium O and OH approach, as well as the turbulence effect. The values are in reasonable agreement with the experimental results. The predicted maximum NO is 55.0 ppm, which is very close to the experimental value of 54.2 ppm. There are discrepancies between the numerical and experimental results. The predicted NO region is a little wider and shifted about 70 mm downstream in comparison with the measurements. A similar NO contour plot is observed for the PDF combustion model case, however, the predicted NO magnitudes are lower than those for the EDS model case.

Figure 14 presents the detailed quantitative comparisons between the numerical and experimental results. The NO profiles at cross sections, $x = 51$ mm to 290 mm are drawn for both the EDS and PDF combustion models. All numerical results were obtained with the thermal and prompt NO, the partial-equilibrium O and OH, and the turbulence effect. The reburn mechanism was also included in the PDF combustion model case. At downstream sections, the trend and magnitude are fairly correlated with the measurements, particularly for the EDS model results. At upstream sections, large deviations are obvious due to the downstream shift of the NO region, as shown in Fig. 13. This may suggest that the NO formation mechanisms and related parameters obtained from laboratories should be modified to properly account for the time delay of NO formation in practical combustors.

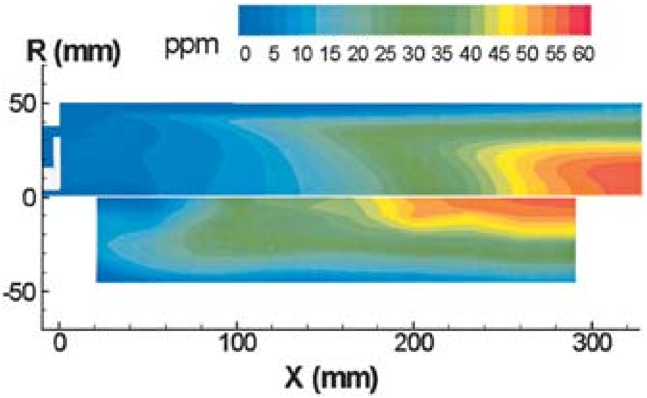

Fig. 13 Comparison between measured and predicted NO for EDS combustion model

There are considerable differences between the EDS and PDF combustion model results. This is mainly attributed to the minor differences in the temperature fields. As shown in Figs. 8 and 9, the predicted temperature profiles with the PDF model are slightly lower than those from the EDS model, except for the first section. Although these temperature differences are small, for example, the difference in the maximum temperature is only 27 K, they can cause substantial discrepancies in the predicted NO magnitudes. As pointed out by Correa [2], the thermal NO formation is very sensitive to the temperature change, and a temperature perturbation of 90 K can double the thermal NO formation rate at temperature around 2200 K. The NO prediction results from the PDF will be further studied by reconsidering the species selection.

Considering the difficulties involved for accurate NO prediction and the fact that the maximum NO emission is less than 60 ppm in the present case, the current results are very encouraging. This indicates that the semiempirical, postprocessing, NO model can provide reasonable results for practical combustion systems as long as the temperature and velocity fields are adequately predicted.

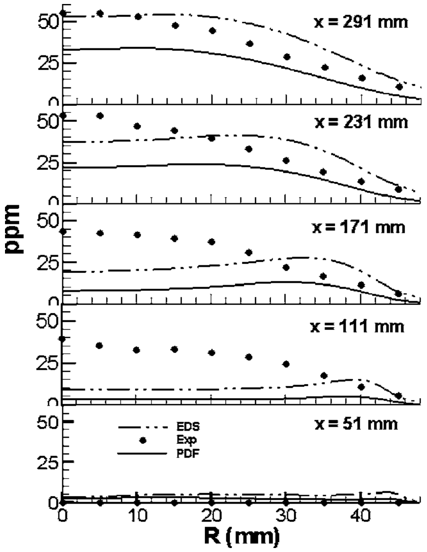

Fig. 14 NO profiles at $x = 51$ mm to 291 mm

Conclusions

A propane diffusion flame combustor with the interior and exterior conjugate heat transfers was numerically studied with three combustion models, i.e., the EDS model, the EDS-finite-rate model and the PDF model. Also used were the RNG $k-\varepsilon$ turbulence model, the discrete ordinates radiation model and various NO models. The results were compared with the comprehensive experimental measurements.

The detailed flow patterns and mean velocity profiles are well captured by all three combustion models. More importantly, the recirculation length is excellently predicted. For the temperature field, the results obtained from the PDF and EDS models agree fairly well with the experimental results. However, the EDS-finite-rate model fails to provide an acceptable temperature field.

The proper predictions of velocity and temperature fields provide a reliable base to evaluate the NO emission models. For the present conditions, the prompt NO, the NO reburn mechanism and the third reaction of the extended Zeldovich mechanism do not add to the overall NO formation. On the contrary, the nonequilibrium O and OH approach and the flow turbulence have significant effects on the NO formation. The NO values predicted by the semiempirical NO model and the EDS or PDF combustion model are promising in comparison with the experimental results. The downstream shift of the predicted NO region should be further studied and modifications to the current NO models might be necessary.

Acknowledgment

The authors are grateful to Dr. Keith Depooter for his valuable comments and suggestions during the preparation of this paper.

References

[1] Miller, J. A., and Bowman, C. T., 1989, "Mechanism and Modeling of Nitrogen Chemistry in Combustion," Prog. Energy Combust. Sci., **15**, pp. 287–338.

[2] Correa, S. M., 1992, "A Review of NO_x Formation Under Gas-Turbine Combustion Conditions," Combust. Sci. Technol., **87**, pp. 329–362.

[3] Volkov, D. V., Belokin, A. A., Lyubimov, D. A., Zakharov, V. M., and Opdyke, Jr., G., 2001, "Flamelet Model of NO_x in a Diffusion Flame Combustor," Trans. ASME: J. Eng. Gas Turbines Power, **123**, pp. 774–778.

[4] Price, G. R., Botros, K. K., and Goldin, G. M., 2001, "CFD Predictions and Field Measurements of NO_x Emissions From LM1600 Gas Turbine During Part Load Operation," ASME Paper No. GT-2000-350.

[5] Eggels, R. L. G. M., 2001, "Modeling of NO_x Formation of a Premixed DLE Gas Turbine Combustor," ASME Paper No. GT-2001-0069.

[6] Cannon, S. M., Zuo, B., and Smith, C. E., 2003, "LES Prediction of Combustor Emissions From a Practical Industrial Fuel Injector," ASME Paper No. GT-2003-38200.

[7] Kyne, A. G., Pourkashanian, M., Wilson, C. W., and Williams, A., 2002, "Validation of a Flamelet Approach to Modeling 3-D Turbulent Combustion Within an Airspray Combustor," ASME Paper No. GT-2002-30096.

[8] Campbell, I., "A Comprehensive Experimental Study of a Generic Combustor," to be published.

[9] Poinsot, T., and Veynante, D., 2001, "Theoretical and Numerical Combustion," R. T. Edwards, Inc., Philadelphia, PA.

[10] Yakhot, V., and Orszag, S. A., 1986, "Re-Normalization Group Analysis of Turbulence: I. Basic Theory," J. Sci. Comput., **1**(1), pp. 1–51.

[11] Yakhot, V., Orszag, S. A., Thangam, S., Gatski, T. B., and Speziale, G. G., 1992, "Development of Turbulence Models for Shear Flows by a Double Expansion Technique," Phys. Fluids A, **4**(7), pp. 1510–1520.

[12] Choudhury, D., 1993, "Introduction to the Renormalization Group Method and Turbulence Modeling," Fluent Inc. TM-107.

[13] Magnussen, B. F., and Hjertager, B. H., 1976, "On Mathematical Models of Turbulent Combustion With Special Emphasis on Soot Formation and Combustion," *Proceedings of the 16th Symposium on Combustion* (International), pp. 719–729.

[14] Bilger, R. W., 1989, "Turbulent Diffusion Flames," Annu. Rev. Fluid Mech., **21**, 101, pp. 101–135.

[15] Westbrook, C. K., and Dryer, F. L., 1984, "Chemical Kinetic Modeling of Hydrocarbon Combustion," Prog. Energy Combust. Sci., **10**, pp. 1–57.

[16] Sivathanu, Y. R., and Faeth, G. M., 1990, "Generalized State Relationships for Scalar Properties in Non-Premixed Hydrocarbon/Air Flames," Combust. Flame, **82**, pp. 211–230.

[17] Kuo, K. K. Y., 1986, *Principles of Combustion*, John Wiley and Sons, New York.

[18] Glassman, I., 1987, *Combustion*, Academic Press, San Diego, CA.

[19] Westenberg, A. A., 1971, "Kinetics of NO and CO in Lean, Premixed Hydrocarbon-Air Flames," Combust. Sci. Technol., **4**, pp. 59–64.

[20] Hanson, R. K., and Salimian, S., 1984, "Survey of Rate Constants in the N/H/O System," *Combustion Chemistry*, W. C. Gardiner, ed., Springer, New York.

[21] Bowman, C. T., 1991, "Chemistry of Gaseous Pollutant Formation and Destruction," *Fossil Fuel Combustion*, W. Bartok, and A. F. Sarofim, eds., John Wiley & Sons, New York.

[22] Fluent Inc., 2003, "Fluent 6.1 Documentation."

[23] Warnatz, J., "NO_x Formation in High Temperature Processes," University of Stuttgart, Germany.

[24] Baulch, D. L., Cobos, C. J., Cox, R. A., Esser, C., Frank, P., Just, Th., Kerr, J. A., Pilling, M. J., Troe, J., Walker, R. W., and Warnatz, J., 1992, "Evaluated Kinetic Data for Combustion Modeling," J. Phys. Chem. Ref. Data, **21**(3), pp. 411–734.

[25] De Soete, G. G., 1975, "Overall Reaction Rates of NO and N_2 Formation From Fuel Nitrogen," Proceedings of 15th Symposium (International) on Combustion, pp. 1093–1102.

[26] Bachmaier, F., Eberius, K. H., and Just, T. H., 1973, "The Formation of Nitric Oxide and the Detection of HCN in Premixed Hydrocarbon-Air Flames at 1 Atmosphere," Combust. Sci. Technol., **7**, pp. 77–84.

[27] Dupont, V., Pourkashanian, M., Williams, A., and Woolley, R., 1993, "The Reduction of NO_x Formation in Natural Gas Burner Flames," Fuel, **72**, No. 4, pp. 497–503.

[28] Raithby, G. D., and Chui, E. H., 1990, "A Finite-Volume Method for Predicting a Radiant Heat Transfer in Enclosures With Participating Media," J. Heat Transfer, **112**, pp. 415–423.

[29] Jongen, T., 1992, "Simulation and Modeling of Turbulent Incompressible Flows," Ph.D. thesis, EPF Lausanne, Lausanne, Switzerland.

[30] Kader, B., 1993, "Temperature and Concentration Profiles in Fully Turbulent Boundary Layers," Int. J. Heat Mass Transfer, **24**(9), pp. 1541–1544.

[31] Rose, J. W., and Cooper, J. R., 1977, *Technical Data on Fuel*, John Wiley & Sons, New York.

[32] Sislian, J. P., Jiang, L. Y., and Cusworth, R. A., 1988, "Laser Doppler Velocimetry Investigation of the Turbulence Structure of Axisymmetric Diffusion Flames," Prog. Energy Combust. Sci., **14**(2), pp. 99–146.

[33] Ishii, T., Zhang, C., and Sugiyama, S., 2000, "Effects of NO Models on the Prediction of NO Formation in a Regenerative Furnace," J. Energy Resourc. Technol., **122**, pp. 224–228.

Laser-Based Investigations of Periodic Combustion Instabilities in a Gas Turbine Model Combustor

R. Giezendanner

P. Weigand

X. R. Duan

W. Meier

U. Meier

M. Aigner

DLR, Institute of Combustion Technology,
Pfaffenwaldring 38-40,
70569 Stuttgart, Germany

B. Lehmann

DLR, Institute of Propulsion Technology,
Cologne, Germany

The driving mechanism of pulsations in gas turbine combustors depends on a complex interaction between flow field, chemistry, heat release, and acoustics. Experimental data on all these factors are therefore required to obtain insight into the coupling mechanisms during a pulsation period. In order to develop a comprehensive experimental database to support a phenomenological understanding and to provide validation data for numerical simulation, a standard burner for optical investigations was established that exhibits strong self-excited oscillations. The burner was a swirl-stabilized nonpremixed model combustor designed for gas turbine applications and operated using methane as fuel at atmospheric pressure. It was mounted in a combustion chamber, which provides almost unobstructed optical access. The periodic combustion instabilities were studied by a variety of phase-resolved laser-based diagnostic techniques, locked to the frequency of the dominant pressure oscillation. Measurement techniques used were LDV for velocity measurements, planar laser-induced fluorescence for imaging of CH and OH radicals, and laser Raman scattering for the determination of the major species concentrations, temperature, and mixture fraction. The phase-resolved measurements revealed significant variations of all measured quantities in the vicinity of the nozzle exit, which trailed off quickly with increasing distance. A strong correlation of the heat release rate and axial velocity at the nozzle was observed, while the mean mixture fraction as well as the temperature in the periphery of the flame is phase shifted with respect to axial velocity oscillations. A qualitative interpretation of the experimental observations is given, which will help to form a better understanding of the interaction between flow field, mixing, heat release, and temperature in pulsating reacting flows, particularly when accompanied by corresponding CFD simulations that are currently underway. [DOI: 10.1115/1.1850498]

Introduction

The control of combustion instabilities has become a major issue in the design of rocket motors [1], jet engines [2], and industrial gas turbines [3]. Lean premixed combustors, which allow a substantial reduction of pollutant emissions of gas turbines, are particularly susceptible to thermoacoustic oscillations. These instabilities affect the operating range, reliability, and lifetime of an engine and impose additional design requirements.

Thermoacoustic instabilities in turbulent combustion are the result of a complex interaction between flow field, acoustics, chemical kinetics, nonstationary heat release, and pressure fluctuations. The situation is especially complex for swirl flames relevant for gas turbine combustors. Although the mechanisms responsible for amplification, self-sustenance, or damping of combustion-driven acoustic oscillations are far from being fully understood, successful control of instabilities has been demonstrated using both passive [4] and active methods [5–7]. Various modeling approaches have been reported in the literature as well [8–10]. Passive control has the advantage of easy implementation, but is specific for an individual configuration. Active control is based on the modification of the flame transfer function [11] and therefore requires knowledge of the burner response to perturbations. With few exceptions, little data is available on the response of a swirl flow to active modulation of flame parameters [12].

A systematic development of strategies for both active and passive control mechanisms can profit from a better understanding of the mechanisms that govern the generation of combustion instabilities, as well as their response to modulation of the flame transfer function. Comprehensive measurements of a multitude of observables in a standardized burner, which cover more than a single feature like acoustic characterization or flow field, can help to gain a deeper insight into the dynamics of combustion instabilities.

The purpose of this study was therefore to compile an extensive experimental database on a combustor with practical relevance. These data characterize the relevant properties responsible for the formation of periodic instabilities. Among those are the flow field, heat release, pressure pulsation, temperature, and gas composition. The data obtained may serve as a basis for the validation of numerical models, but at the same time also for a phenomenological understanding of the causality of events that lead to the formation of combustion oscillations. The multitude of different observations in a standard burner results in a much clearer picture of the interactions between different phenomena that drive combustion instabilities compared to a single measurement. Both approaches—numerical simulation and phenomenological interpretation—lead to the ultimate goal to derive design tools for combustors that allow a stable operation over a wide range of operating conditions. The experimental methods used in this study to obtain these experimental data include laser-based techniques like Laser-Doppler velocimetry (LDV), Raman scattering, and planar laser-induced fluorescence (PLIF) for phase-resolved measurements of flow field, gas composition, temperature, and heat release, respectively. The optical techniques were accompanied by

---

Contributed by the International Gas Turbine Institute (IGTI) of THE AMERICAN SOCIETY OF MECHANICAL ENGINEERS for publication in the ASME JOURNAL OF ENGINEERING FOR GAS TURBINES AND POWER. Paper presented at the International Gas Turbine and Aeroengine Congress and Exhibition, Vienna, Austria, June 13–17, 2004, Paper No. 2004-GT-53366. Manuscript received by IGTI, October 1, 2003; final revision, March 1, 2004. IGTI Review Chair: A. J. Strazisar.

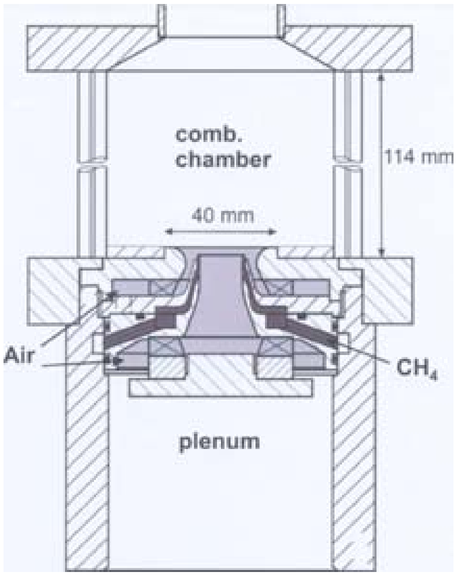

Fig. 1 Schematic view of combustor

acoustic measurements for the identification of the instability regions of the burner, as well as to generate a phase-coupled trigger signal for the lasers and detection system from the plenum, and to determine the phase shift between the acoustic waves in the plenum and the combustor.

Experimental

Combustor. A schematic view of the combustor selected as a standard system for optical investigations is shown in Fig. 1. The burner is a modified version of a gas turbine combustor with air blast nozzle for liquid fuels [13]. Gaseous fuel is injected from an annular slot between two corotating airflows. The slot has a width of 0.5 mm and is separated along its circumference into 72 sections with an area of 0.5×0.5 mm^2 by cross pieces extending 5 mm deep into the slot; this design suppresses any swirl in the fuel flow before entering the combustion chamber. The inner air nozzle has a diameter of 15 mm; the outer annular air nozzle has 17 and 25 mm inner and outer diameter, respectively. The outer nozzle extends into a contour with a 40 mm outer diameter. The inner air and the fuel nozzle are recessed upstream with respect to the exit of the outer air nozzle by 4.5 mm. Both partial airflows are fed from a common plenum chamber with air at room temperature. Details of the nozzle, as well as results of flow field measurements, have been reported by Lehmann [14].

The combustion chamber has a square 85×85 mm^2 cross section with a length of 114 mm, ending through a contoured transition in a circular exhaust with a 40 mm inner diameter. The four sidewalls of the chamber consist of quartz plates with a thickness of 1.7 mm, which are held in place by four steel rods. This design allows almost unobstructed optical access from all sides. A Brüel&Kjaer 4938 microphone is installed in the plenum to follow the pressure fluctuation; in addition, its pulse-shaped output is used as a trigger source for the diagnostic setup. The microphone is flush mounted on the side wall of the plenum chamber. A FFT analyzer is used to monitor and to record the frequency characteristic and the temporal variation of the fluctuating pressure.

A second microphone probe in one of the rods holding the windows allowed recording the acoustic signal in the combustor. It was mainly used to measure the phase shift between the acoustic waves in the combustor and the plenum. Its signal was less suitable as a trigger source for the optical measurement system, because it was affected by random combustion noise to a larger extent compared to the plenum signal.

The burner was operated at an atmospheric pressure with methane as fuel. The pressure drop across the nozzle was not measured. Mass flows for fuel and air were 0.18 and 3.76 g/s, respectively, corresponding to an equivalence ratio of $\Phi=0.75$ at a thermal power of 10 kW. Fuel and air mass flows were kept constant using electronic mass flow controllers (Tylan FC-2925V for air, Brooks 2851 for CH$_4$); these controllers depend on a large pressure drop, which, in combination with a several meters long elastic supply tube to the plenum, damped efficiently any pressure fluctuations from the supply lines. Because of their long response time of >100 ms, no additional oscillations could be induced by the controllers themselves. A swirl number of 0.55 was calculated from the measured velocity components at this operating point. Under these conditions, the flame exhibits a strong acoustic oscillation at 290 Hz.

Diagnostic Techniques. Details of the velocity measurements have been reported in Ref. [14]. A DISA/DANTEC LDV system was used in combination with an Ar$^+$ laser for the measurement of the axial (u) and radial (v) velocity component. At each location in the flame, 10 000–15 000 individual measurements were performed, while the pressure signal was recorded simultaneously. This allowed assignment of each velocity measurement to a phase angle of the acoustic oscillation in a postprocessing step.

The experimental arrangement for phase-resolved planar LIF measurements of OH, formaldehyde, and CH is described in [15]. OH radicals can exist over a large region of space and indicate the presence of hot products of combustion as well as the flame front. Formaldehyde is formed in low-temperature combustion processes (cool flame chemistry) and reflects fuel-rich regions of moderate temperatures. Although these two species can contribute to the visualization of flame structures and mixing properties, measurements of H$_2$CO will not be considered here; the focus will be on PLIF imaging of the CH radical. Its time-averaged concentration distributions can—with some restrictions—be regarded as a qualitative measure for heat release rates [16]; therefore, the change of CH concentrations over a phase of the acoustic oscillation provides valuable information about the interaction of pulsation pressure and heat release, which is a key building block for the understanding of thermoacoustic flame effects.

LIF signals are affected by quenching, which reduces the fraction of radicals that emit the excitation energy by radiation, instead of nonradiative collisional deactivation. Quenching rates depend on the temperature and chemical environment and are therefore difficult to quantify. However, in the case of OH, it has been shown that in nonpremixed methane/air flames, even under unfavorable circumstances, the relative error caused by ignoring the variation in quenching rates leads to an error of 20% or less for the measured relative OH densities [17]. This is because OH exists in detectable quantities only in a small range of temperatures and mixture fractions. The same argument holds for CH, although less information on quenching is available for this radical.

Time-resolved, i.e., single-pulse images of CH radical distributions are characterized by small turbulent structures with large spatial and temporal fluctuations. They have the shape of strongly wrinkled, thin strings or sometimes closed loops, which can be expected if a laser sheet cuts through a very thin flame front forming the surface of a corrugated volume. Examples of single-pulse CH images can be found in [15]. Averaging up to 500 images was therefore necessary to isolate phase angle-dependent structural variations from the stochastic fluctuations resulting from turbulence.

Laser Raman scattering was used for the pointwise simultaneous measurements of the concentrations of all major species $(O_2, N_2, CH_4, H_2, CO, CO_2, H_2O)$. A pulsed flash lamp pumped dye laser at a wavelength of 489 nm was used to induce Raman scattering. Its pulse output energy was about 3 J in a pulse length of ≈ 3 μs. The spatial resolution, which is given by the diameter of the focused laser beam and the geometry of the detection sys-

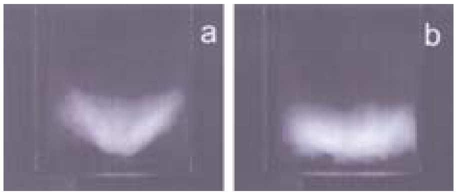

Fig. 2 Photographs of steady (*a*) and oscillating flame

tem, was 0.6×0.6 mm. Quantitative number densities were derived from measured Raman signals by calibration measurements for each individual compound. Instantaneous values for mixture fractions could be derived from the set of species concentrations, and the temperature information was obtained from the total number density using the ideal gas law [18]. The measurement uncertainty for the mean values is typically 3%–4% for the temperature and mixture fraction, the single-pulse uncertainties are 4%–5%.

Results

The two photographs of the flame shown in Fig. 2 correspond to a "quiet" operating point, i.e., a condition with no dominant acoustic oscillation, and a state with a strong self-excited oscillation at a frequency of about 290 Hz. The visible appearance of the flame changes significantly when it enters the oscillating mode; the flame appears to be localized closer to the burner faceplate. This is in agreement with the results of the CH PLIF and Raman measurements, as will be discussed later. The occurrence and intensity of this oscillation depends strongly on the equivalence ratio; the 290 Hz oscillation is found in the region between $\Phi=0.7$ and 0.8. The acoustic response of the system surely plays a key role for the sustenance and amplification of a periodic instability; however, this observation suggests that the origin of this effect is not purely of an acoustic nature. Furthermore, the instability is not a Helmholtz-type oscillation, because the frequency shows little response to variation of the combustion chamber or plenum geometry.

The following results will be presented as phase-averaged measurements of velocity, concentrations, and temperatures. The phase angles referred to in this section are defined such that 0 deg corresponds to minimum pressure in the plenum. It was found that the pressure in the plenum lagged behind the combustor pressure with a frequency-dependent phase difference; for the 290 Hz oscillations investigated here, the delay was about 50 deg. This value is consistent with the different transit times for a sound wave from the nozzle to the positions of the microphone probes in the combustor and the plenum, respectively.

Figure 3 shows two PLIF images of OH with a phase angle difference of 180 deg. The size of the images is 85×62 mm^2, i.e., they cover the entire width of the combustion chamber. The lower edge of the light sheet ends about 2 mm above the burner faceplate. The lower intensity on the left side of both images results from a slight absorption of the laser light across the flame. The black horizontal lines mark a distance of 5 mm above the nozzle, where temperature profiles have been calculated from Raman measurements (see below). It can be seen that considerable differences between average distributions at different phase angles can be found in a region near the burner axis up to 15–20 mm above the nozzle, as well as very close to the faceplate, while at larger distances downstream, the phase-dependent fluctuations trail off. Figure 4 shows CH LIF distributions in a close-up of the area where significant phase-dependent effects were found in the OH images. Under lean conditions, OH concentrations remain high as long as the temperature is high.

The fact that OH is found at large distances from the burner therefore suggests that high temperatures prevail at a larger distance. This qualitative result is in agreement with temperature data from Raman measurements. Conversely, CH is found only in regions where heat release takes place, and is removed quickly when reactants are consumed. The CH images therefore show that the heat release zones are limited to a region up to 25 mm above the burner and 35 mm radial distance. The shape and size of this region changes with phase angle. Since CH distributions are a qualitative measure for local heat release rates, integration of the CH LIF intensities over an image yields a relative total average heat release rate at each phase angle.

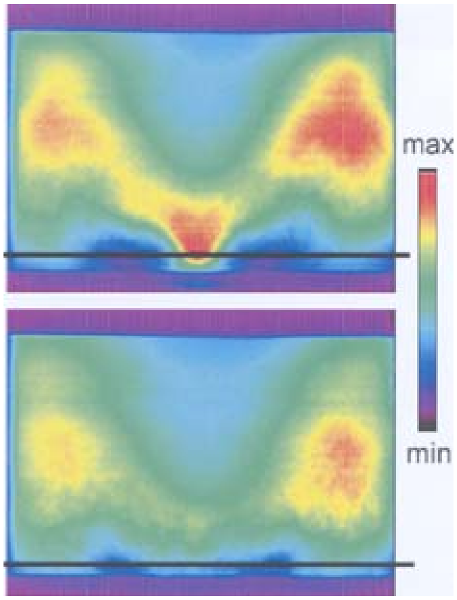

Fig. 3 OH LIF images for two phase angles with 180 deg phase angle separation

Radial profiles of the average axial and radial velocity components u and v at a distance of 1 mm from the burner are shown in Fig. 5. Two of the curves—for 90 deg and 270 deg—refer to the same phase angles as in Fig. 4. It can be seen that just like for OH and CH, the largest changes of the axial velocity u with phase angle are found near the burner axis. A strong inner recirculation

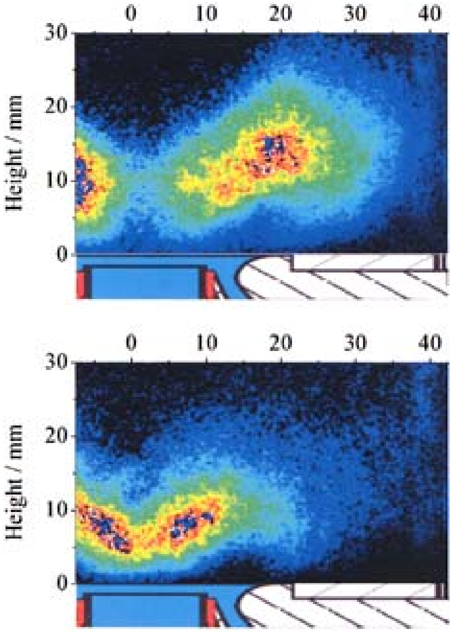

Fig. 4 CH LIF distributions at $\alpha=90$ deg (top) and 270 deg

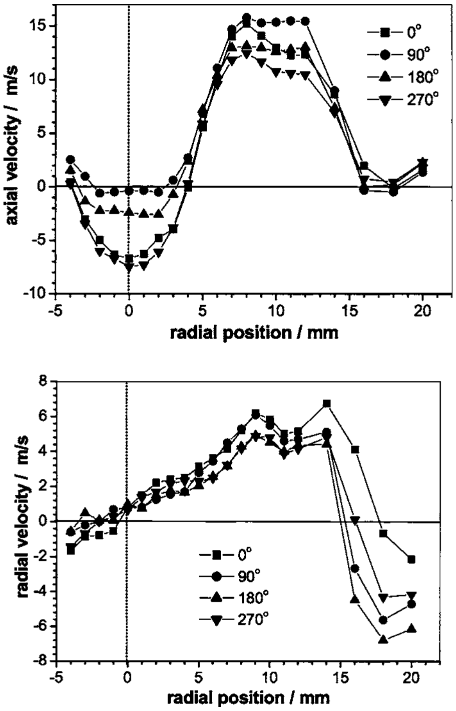

Fig. 5 Axial (top) and radial (bottom) velocity profiles for four phase angles at 1 mm distance from the burner

zone is observed, with upstream velocities varying between 0 and 8 m/s depending on the phase angle. In contrast, at radial distances $r<12$ mm, the profiles of the radial velocity v show little change over a period of the oscillation. The negative values at $r>15$ mm indicate the presence of an outer recirculation zone. The highest axial velocities are found between the inner and outer recirculation zones at radial positions between 5 and 15 mm, where fuel and air from the nozzle flow into the chamber.

While velocity profiles could be measured as close as 1 mm to the burner, the smallest axial distance for the Raman measurements was 5 mm from the nozzle exit. Figure 6 shows radial profiles of the temperature at this location. Again, a large variation with the phase angle can be noticed near the burner axis. The lowest temperatures are found in a region around $r=15$ mm, between the inner and the outer recirculation zone, where cold air is injected and mixes with hot combustion products. The shape of the temperature profile is in good qualitative agreement with the OH images at the same axial distance (Fig. 3), where the highest concentrations are found on the axis and a minimum in the mixing region. The high temperatures and OH concentrations on the burner axis, in connection with the large negative axial velocity component close to the nozzle at phase angles around $\alpha=270$ deg, indicate that the inner recirculating flow transports hot combustion products upstream close to and even into the inner nozzle during this phase of the acoustic cycle.

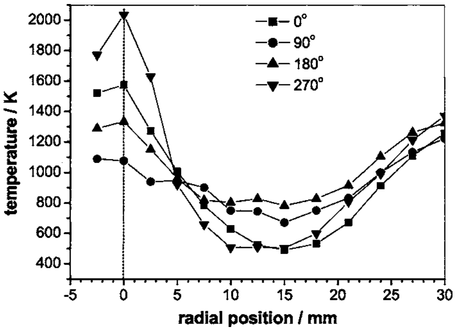

Fig. 6 Radial temperature profiles for four phase angles at 5 mm distance from the burner

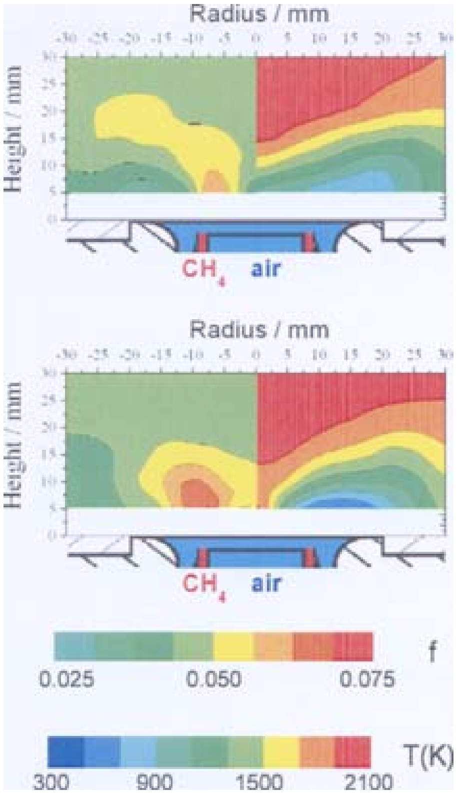

Fig. 7 Mixture fraction *f* (left) and temperature (right) at 90 deg (top) and 270 deg (bottom) phase angle

The simultaneous measurement of multiple species concentrations allows the calculation of local mixture fractions, which play an important role on ignition and flame propagation properties. As an example mixture fraction distributions (left) and temperatures (right) are shown in Fig. 7 for the 90 deg and 270 deg phase angle, respectively. A stoichiometric mixture corresponds to a mixture fraction of 0.055 for this flame. It is interesting to note that a region with a near stoichiometric condition, which is localized near the fuel nozzle exit at $\alpha=270$ deg, spreads outward to the region of high heat release rates at $\alpha=90$ deg.

Discussion

When the observations of different measured quantities and their evolution over a period of the acoustic oscillation are combined, some conclusions can be drawn about effects and causal links that drive the instability. In the following, we will attempt to give a qualitative explanation of the mechanisms that link acoustic, thermodynamic, and aerodynamic effects to sustain a periodic instability in this particular burner configuration.

As mentioned before, at $\alpha\approx270$ deg, there is a noticeable penetration of hot burnt gases into the inner nozzle, leading to mixing and preheating of air near the axis. At this point, high mixture fractions, i.e. CH_4 concentrations, are observed near the fuel nozzle. After this, the negative axial velocity component becomes smaller; the inlet flow carries fuel-enriched gas toward the flame zone. Half a period later, at $\alpha\approx90$ deg, the u component near the axis is at its maximum, and the fuel has been transported to the flame region, where near-stoichiometric mixtures are found now, as shown on the top of Fig. 7. For a typical flow velocity of about 10 m/s, the flow needs about 1.5 ms to be transported from the nozzle to the flame region at a distance of about 15 mm. This time

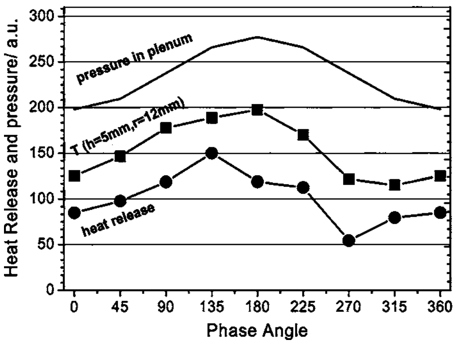

Fig. 8 Phase angle dependence of pressure, temperature, and integral heat release

for half a period is in good agreement with the observed acoustic frequency of 290 Hz. After this time, the temperature at the lower part of the flame region has increased by more than 200 deg, compared to $\alpha=270$ deg. Hot combustion products that were transported from the outer recirculation zone toward the flame region, as indicated by the negative v component of the velocity, have contributed to this heating. These developments are summarized in Fig. 8. The stoichiometry and temperature are therefore favorable for increasing reaction rates, resulting in an intensified heat release, which varies in phase with temperature at $h=5$ mm and $r\approx 12.5$ mm. The observation of a variation of heat release as a consequence of fluctuating mixture fraction has also been reported by Lieuwen et al. [19]. The fact that the burner is nonpremixed may therefore be essential for the occurrence of this particular instability. The increased heat release is followed by a thermal expansion, leading to a pressure rise in the combustor, which could be detected by the microphone (see Fig. 8). This pressure increase is associated with higher axial velocities, compared to the tangential velocity component, and therefore a lower swirl number. Since the intensity of the inner recirculation depends on swirl, this sequence of events tend to counteract the initial situation, which is characterized by an intense inner recirculation zone and high mixture fractions only near the fuel nozzle exit. This means that the driving mechanism for an enhanced heat release becomes weaker. However, a lower heat release rate decreases thermal expansion and thus increases the swirl number, therefore reestablishing the initial condition of a strong inner recirculation. Therefore, the feedback loop is closed, and another cycle of the instability can start.

Conclusions

A combustor with features relevant for gas turbine applications has been defined as a standard object for investigations of thermoacoustic instabilities. Multiple acoustic and laser-based measurement techniques have been applied to provide a comprehensive database that characterizes the variety of phenomena associated with a self-excited periodic instability. It has been demonstrated that a combined study of flow field, heat release and acoustics forms the basis of a much better understanding of the causal links that couple aerodynamic, thermodynamic, and acoustic phenomena, resulting in a periodic instability. More important, such observations can assist in validating future numerical models, which are expected to assess the potential for combustion instabilities already during the design phase of a combustor, independent of a particular configuration.

Acknowledgment

This work has been supported in part by the AG TURBO association, Grant No. 0327060B, by the German Bundesministerium für Wirtschaft und Technologie (BMWi).

The authors thank W. Stricker for helpful discussions and B. Noll for contributions obtained from numerical simulations.

References

[1] Fabignon, Y., Dupays, J., Avalon, G., Vuillot, F., Lupoglazoff, N., Casalis, G., and Prévost, M., 2003, "Instabilities and Pressure Oscillations in Solid Rocket Motors," Aerosp. Sci. Technol., **7**, pp. 191–200.

[2] Konrad, W., Brehm, N., Kameier, F., Freeman, C., and Day, I. J., 1998, "Combustion Instability Investigations on the BR710 Jet Engine (96-TA-36)," ASME J. Eng. Gas Turbines Power, **120**, pp. 34–40.

[3] Hobson, D. E., Fackrell, J. E., and Hewitt, G., 2000, "Combustion Instabilities in Industrial Gas Turbines—Measurements on Operating Plant and Thermoacoustic Modeling," ASME J. Eng. Gas Turbines Power, **122**, pp. 420–428.

[4] Steele, R. C., Cowell, L. H., Cannon, S. M., and Smith, C. E., 2000, "Passive Control of Combustion Instability in Lean Premixed Combustors," ASME J. Eng. Gas Turbines Power, **122**, pp. 412–419.

[5] Paschereit, C. O., Gutmark, E., and Weisenstein, W., 1998, "Structure and Control of Thermoacoustic Instabilities in a Gas-Turbine Combustor," Combust. Sci. Technol., **138**, pp. 213–232.

[6] Cohen, J. M., Stufflebeam, J. H., and Proscia, W., 2001, "The Effect of Fuel/Air Mixing on Actuation Authority in an Active Combustion Instability Control System," ASME J. Eng. Gas Turbines Power, **123**, pp. 537–542.

[7] Campos-Delgado, D. U., Zhou, K., Allgood, D., and Acharya, S., 2003, "Active Control of Combustion Instabilities Using Model-Based Controllers," Combust. Sci. Technol., **175**, pp. 27–53.

[8] Dowling, A. P., and Hubbard, S., 2000, "Instability in Lean Premixed Combustors," Proc. Inst. Mech. Eng., **214**, pp. 317–332.

[9] Brookes, S. J., Cant, R. S., Dupere, I. D. J., and Dowling, A. P., 2001, "Computational Modeling of Self-Excited Combustion Instabilities," ASME J. Eng. Gas Turbines Power, **123**, pp. 322–326.

[10] Pankiewitz, C., and Sattelmayer, T., 2003, "Time Domain Simulation of Combustion Instabilities in Annular Combustors," ASME J. Eng. Gas Turbines Power, **125**, pp. 677–685.

[11] Krebs, W., Flohr, P., Prade, B., and Hoffmann, S., 2002, "Thermoacoustic Stability Chart for High Intensity Gas Turbine Combustion Systems," Combust. Sci. Technol., **174**, pp. 99–128.

[12] Bernier, D., Ducruix, S., Lacas, F., and Candel, S., 2003, "Transfer Function Measurements in a Model Combustor: Application to Adaptive Instability Control," Combust. Sci. Technol., **175**, pp. 993–1013.

[13] Cao, M., Eickhoff, H., Joos, F., and Simon, B., 1987, "Influence of Operating Conditions on the Atomisation and Distribution of Fuel by Air Blast Atomizers," ASME Propulsion and Energetics Panel 70th Symposium, Crete, AGARD Conference Proceedings 422, p. 8.1.

[14] Lehmann, B., and Mante, J., 1999, "Experiments on the Flow Characteristics Behind Swirl Nozzles in Atmospheric Combustion Chambers," *Fourteenth Int. Symposium on Airbreathing Engines*, September 5–10, Florence, Italy, Paper AIAA-99-IS-221.

[15] Giezendanner, R., Keck, O., Weigand, P., Meier, W., Meier, U., Stricker, W., and Aigner, M., 2003, "Periodic Combustion Instabilities in a Swirl Burner Studied by Phase-Locked Planar Laser-Induced Fluorescence," Combust. Sci. Technol., **175**, pp. 721–741.

[16] Najm, H. N., Paul, P. H., Mueller, C. J., and Wyckoff, P. S., 1998, "On the Adequacy of Certain Experimental Observables as Measurements of Flame Burning Rate," Combust. Flame, **113**, pp. 312–332.

[17] Barlow, R. S., and Collignon, A., 1991, "Linear LIF Measurements of OH in Nonpremixed Methane–Air Flames: When are Quenching Corrections Unnecessary," 29th Aerospace Sciences Meeting, Reno/Nevada, January 7–10, American Institute of Aeronautics and Astronautics, AIAA Paper 91-0179.

[18] Keck, O., Meier, W., Stricker, W., and Aigner, M., 2002, "Establishment of a Confined Swirling Natural Gas/Air Flame as a Standard Flame: Temperature and Species Distributions From Laser Raman Measurements," Combust. Sci. Technol., **174**, pp. 73–107.

[19] Lieuwen, T., Neumeier, Y., and Zinn, B. T., 1998, "The Role of Unmixedness and Chemical Kinetics in Driving Combustion Instabilities in Lean Premixed Combustors," Combust. Sci. Technol., **135**, pp. 193–211.

Evaluation of an Enhanced Bank of Kalman Filters for In-Flight Aircraft Engine Sensor Fault Diagnostics

Takahisa Kobayashi
QSS Group, Inc.,
21000 Brookpark Road,
Cleveland, OH 44135

Donald L. Simon
U.S. Army Research Laboratory,
NASA Glenn Research Center,
MS-77-1, 21000 Brookpark Road,
Cleveland, OH 44135

In this paper, an approach for in-flight fault detection and isolation (FDI) of aircraft engine sensors based on a bank of Kalman filters is developed. This approach utilizes multiple Kalman filters, each of which is designed based on a specific fault hypothesis. When the propulsion system experiences a fault, only one Kalman filter with the correct hypothesis is able to maintain the nominal estimation performance. Based on this knowledge, the isolation of faults is achieved. Since the propulsion system may experience component and actuator faults as well, a sensor FDI system must be robust in terms of avoiding misclassifications of any anomalies. The proposed approach utilizes a bank of (m+1) Kalman filters where m is the number of sensors being monitored. One Kalman filter is used for the detection of component and actuator faults while each of the other m filters detects a fault in a specific sensor. With this setup, the overall robustness of the sensor FDI system to anomalies is enhanced. Moreover, numerous component fault events can be accounted for by the FDI system. The sensor FDI system is applied to a nonlinear simulation of a commercial aircraft gas turbine engine, and its performance is evaluated at multiple power settings at a cruise operating point using various fault scenarios. [DOI: 10.1115/1.1850505]

Introduction

In-flight sensor fault detection and isolation (FDI) is critical to maintaining reliable engine operation during flight. The propulsion system is operated at demanded conditions by the aircraft engine control system which computes control commands based on sensor measurements. Any undetected sensor faults, therefore, may cause the control system to drive the engine into an undesirable operating condition. If a sensor fails, it is crucial to detect and isolate the fault as soon as possible so that such scenarios can be avoided. A sensor FDI system which is capable of doing so with high reliability is indispensable for flight safety enhancement. A challenging issue in developing reliable sensor FDI systems is to make them robust to other faults, besides sensor faults, that can occur during flight. Engine component performance can degrade gradually due to usage, and abruptly due to fault events such as foreign or domestic object damage. Likewise, errors can exist between the commanded and actual actuator positions. Such anomalies result in shifts in sensed engine variables from their nominal values. Therefore, a sensor FDI system which is developed without accounting for possible component or actuator faults may result in false alarms, missed detections, or misclassifications when such faults do occur.

An approach to in-flight sensor FDI for aircraft propulsion system was addressed by Merrill et al. [1] through the utilization of a bank of Kalman filters. In this approach, each Kalman filter is designed based on a specific hypothesis (such as the failure of a specific sensor). When a single sensor fails, only the one Kalman filter with the correct fault hypothesis can maintain low residual values, indicating that the specific sensor has failed. This work was later extended by Kobayashi et al. [2] to account for not only sensor faults, but also actuator and component faults. This approach exhibited improved robustness of the FDI system; however, the number of component fault events that could be accounted for by the FDI system was limited to the number of available sensors. In spite of such limitations, the previous research [2] revealed potential areas for further improvement of an FDI system. In this paper, lessons learned from the earlier work are incorporated to enhance the bank of Kalman filters for an in-flight sensor FDI application. The objectives of sensor FDI are as follows:

1. Avoid missed detections: When a single sensor is faulty, it must be correctly detected and isolated.
2. Avoid false alarms: Nonfault-related factors that exist in the real environment, such as sensor noise and modeling uncertainty, should not be diagnosed as a sensor fault.
3. Avoid misclassifications: Component or actuator faults should not be misclassified as a sensor fault.

In this paper, a sensor FDI system is developed and applied to a nonlinear simulation of a commercial aircraft gas turbine engine. The FDI system performance is evaluated at multiple power settings at a cruise operating point using various fault scenarios.

Development of Robust Sensor Fault Detection and Isolation System

The problem approach to sensor FDI is similar to that of Ref. [2]. A depiction of the propulsion system with the sensor FDI system is shown in Fig. 1. During flight, the sensors, actuators, and engine components are susceptible to failure. The sensor and actuator faults dealt with in this paper are "soft" failures. Soft failures are defined as inconsistencies between true and measured sensor values (or true and commanded actuator position) that are relatively small in magnitude and thus difficult to detect, whereas "hard" failures are large in magnitude and thus more readily detectable. Soft failures can take different forms such as a fixed scale factor, a fixed bias, a drift, or intermittent spikes. Among these, only the fixed bias is considered in this paper for FDI evaluation purposes, although the proposed FDI approach is applicable

---

Contributed by the International Gas Turbine Institute (IGTI) of THE AMERICAN SOCIETY OF MECHANICAL ENGINEERS for publication in the ASME JOURNAL OF ENGINEERING FOR GAS TURBINES AND POWER. Paper presented at the International Gas Turbine and Aeroengine Congress and Exhibition, Vienna, Austria, June 13–17, 2004, Paper No. 2004-GT-53640. Manuscript received by IGTI, October 1, 2003; final revision, March 1, 2004. IGTI Review Chair: A. J. Strazisar.

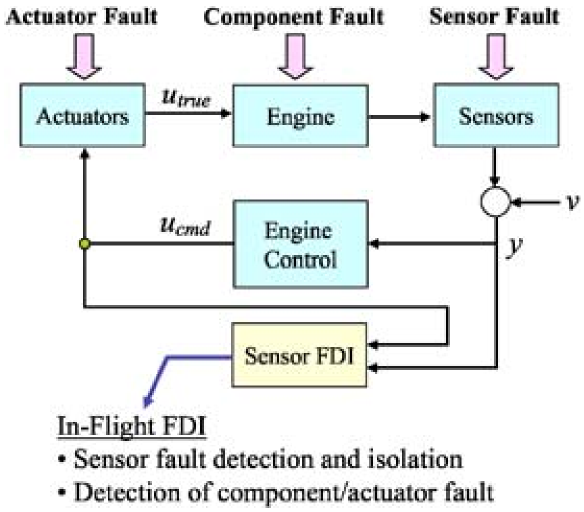

Fig. 1 Propulsion system with sensor fault detection and isolation system

to other soft failure types as well. Engine component faults are modeled in the simulation environment by abruptly shifting the health parameters which indicate component performance deviations from a reference base point.

The FDI system uses two sets of input signals: sensor measurements and control commands. Those sensors used by the control system are also used by the FDI system for monitoring purposes. Given these two sets of input signals, the FDI system seeks to detect and isolate any faulty sensors. The approach to sensor FDI is based on the utilization of a bank of Kalman filters, where each filter is designed with a unique hypothesis to monitor a specific sensor. In addition to sensors, components and actuators may also fail during flight. Therefore, it is necessary to make the FDI system robust to these faults so that misclassifications of component and actuator faults as sensor faults do not occur. This issue is addressed by designing one additional Kalman filter which assumes that components and actuators may be faulty. When the propulsion system experiences a sensor fault or component/actuator faults, only the one Kalman filter with the correct hypothesis is able to maintain accurate estimation performance. Consequently, the detection and isolation of sensor faults or the detection of component/actuator faults can be achieved. As can be seen in Fig. 1, the outputs of the FDI system are not integrated with the control system in the present work. The integration of these systems for fault accommodation purposes will be pursued in future work. In the following sections, the design approach for the FDI system is discussed in detail.

Kalman Filter Design for Sensor Fault Detection. The Kalman filter design approach is based on the linear model representation of a plant. The linearized engine model under consideration is represented by the following state space equations:

$$\begin{aligned} \dot{x} &= A(x-x_{\mathrm{ss}})+L(h-h_{\mathrm{ref}})+B(u_{\mathrm{cmd}}-u_{\mathrm{ss}})+Bb \\ y-y_{\mathrm{ss}} &= C(x-x_{\mathrm{ss}})+M(h-h_{\mathrm{ref}})+D(u_{\mathrm{cmd}}-u_{\mathrm{ss}})+Db+v \end{aligned} \tag{1}$$

where the vectors x, h, u_{cmd} represent state variables, health parameters, and control commands, respectively. The subscript "ss" indicates the steady-state point (or the base point at which the model was linearized). The vector h_{ref} represents a reference health condition. The sensor measurement vector, y, is corrupted by sensor noise v. The vector b represents the bias in the actuation system; it is zero when there is no actuator bias. The health parameter and bias vectors are unknown inputs to the system that affect engine operation. The matrices A, B, C, D, L, and M have appropriate dimensions.

For sensor fault detection, m Kalman filters are designed where m is the number of sensors being monitored. Each Kalman filter estimates the state vector using a unique set of $(m-1)$ sensors. The sensor which is not used by a particular filter is assumed to be the potentially faulty one (fault hypothesis) and thus monitored by that filter. For instance, the ith filter uses the sensor subset y^i that excludes the ith sensor, where i is an integer from 1 to m. When the ith sensor is faulty, all Kalman filters use faulty information except for the ith filter. Consequently, the ith filter is able to accurately estimate the state vector from fault-free sensor measurements, whereas the estimates of the remaining filters are distorted by the faulty sensor measurement. The Kalman filter equation that monitors the ith sensor is given as follows:

$$\begin{aligned} \dot{\hat{x}} &= A(\hat{x}-x_{\mathrm{ss}})+B(u_{\mathrm{cmd}}-u_{\mathrm{ss}})+K^i(y^i-\hat{y}^i) \\ \hat{y}^i-y^i_{\mathrm{ss}} &= C^i(\hat{x}-x_{\mathrm{ss}})+D^i(u_{\mathrm{cmd}}-u_{\mathrm{ss}}) \end{aligned} \tag{2}$$

where $\hat{x}$ and $\hat{y}^i$ are the estimates of the state vector and the ith sensor-subset vector, respectively. The matrices C^i and D^i are a subset of C and D, respectively, with the ith row deleted, and K^i is a Kalman gain matrix corresponding to the matrix pair (A, C^i). In order for the Kalman filter to converge, the matrix pair (A, C^i) must be observable.

The accuracy of the estimated state variables is indicated by a weighted sum of squared residuals (WSSR) which is computed as follows:

$$\mathrm{WSSR}^i=(y^i-\hat{y}^i)^T(\Sigma^i)^{-1}(y^i-\hat{y}^i) \tag{3}$$

where

$$\Sigma^i=\mathrm{diag}[\sigma^i]^2.$$

The vector σ^i represents the standard deviation of the ith sensor-subset. The square matrix Σ^i normalizes the residual vector $(y^i-\hat{y}^i)$. The value of the fault indicator signal, WSSR, increases if the sensor subset used by a Kalman filter contains a faulty measurement. In order to detect an anomaly in the sensor set, the fault indicator signals are compared against pre-established detection thresholds. If all fault indicator signals except one exceed the threshold, it indicates that the Kalman filter whose fault indicator signal did not exceed the threshold is the one with the correct fault hypothesis. Consequently, this filter is isolated, and the sensor excluded by this filter is identified as the faulty one.

It should be noted that the Kalman filter in Eq. (2) does not account for the influence of health parameters or actuator biases that appear in Eq. (1). Therefore, any deviations of these parameters from the design point can cause an increase in the values of the fault indicator signals. Depending on their magnitude, such deviations may induce a fault misclassification scenario where all fault indicator signals except one exceed the detection threshold. To avoid such scenarios, additional features that account for health parameter and actuator bias deviations must be built into the FDI system. For the health parameters, two possible deviation types need to be considered: (1) gradual degradation due to aging, and (2) abrupt degradation due to component faults. An approach to deal with the gradual degradation was discussed in Ref. [2]. That is, estimate all health parameters once per a number of flights using ground-based trend monitoring techniques [3–5], update the reference health condition (h_{ref}) and the linear engine model in Eq. (1), and then update the Kalman filter. As long as this updated reference health condition remains close enough to the actual condition (which continues to degrade with time), the interference of the gradual degradation on the Kalman filters designed through Eq. (2) will remain small. Abrupt degradation ($\Delta h=h-h_{\mathrm{ref}}$ in Eq. (1)) due to component faults or actuator bias needs to be handled by other means. The approach taken in this paper is to design another Kalman filter which assumes that components and/or actuators may be faulty. If this filter is able to maintain low residual values in the case of component and/or actuator faults, misclassifications of these faults as a sensor fault may be avoided. The design of this additional Kalman filter is discussed in the following section.

Kalman Filter Design for Component and Actuator Fault Detection. Ideally, a Kalman filter which is capable of accurately estimating all health parameters is desirable. Such a filter would be able to maintain accurate sensor estimation (and thus low residuals) even in the presence of component faults. However, the number of health parameters that can be estimated is limited to the number of available sensors [6]. Aircraft engines have a limited number of sensors which is, in general, less than the number of health parameters. Therefore, estimating all health parameters is not realistic. An alternative approach, which can meet the aforementioned objective while using a limited number of sensors, is to estimate a subset of health parameters. In Ref. [2], it was observed that the Kalman filter, designed with a subset of health parameters, could retain accurate estimation of sensor outputs when applied to a ‘‘degraded’’ engine simulation. The accuracy of the estimated health parameters, however, was poor as the Kalman filter attributed the steady-state mismatch caused by health degradation to the subset of health parameters being estimated. Therefore, the estimated health parameters no longer indicate the actual health condition, but instead, they are ‘‘tuning’’ parameters that the Kalman filter can use to generate accurate sensor estimates. This concept of ‘‘tuning’’ is applied to the design of a Kalman filter in this section. The idea is to use tuning parameters (a subset of health parameters) with which the Kalman filter can maintain good sensor estimation performance no matter what combination of health parameters is shifted from their reference point. The Kalman filter equation that incorporates the tuning parameters is given as follows:

$$\begin{aligned} \dot{\hat{x}}_{\text{aug}} &= \begin{bmatrix} A & L_d \\ 0 & 0 \end{bmatrix} (\hat{x}_{\text{aug}} - \bar{x}_{\text{ss}}) + \begin{bmatrix} B \\ 0 \end{bmatrix} (u_{\text{cmd}} - u_{\text{ss}}) + K(y - \hat{y}) \\ \hat{y} - y_{\text{ss}} &= [C \;\; M_d](\hat{x}_{\text{aug}} - \bar{x}_{\text{ss}}) + D(u_{\text{cmd}} - u_{\text{ss}}) \end{aligned} \tag{4}$$

where

$$\hat{x}_{\text{aug}} = \begin{bmatrix} \hat{x} \\ d \end{bmatrix}, \quad \bar{x}_{\text{ss}} = \begin{bmatrix} x_{\text{ss}} \\ 0 \end{bmatrix}$$

The vector d contains the tuning parameters. The matrices L_d and M_d are selected columns of L and M, respectively, and their columns correspond to the tuning parameters. As discussed earlier, all health parameters gradually deviate from the healthy baseline. This deviation is called ‘‘baseline degradation’’ (h_{ref} in Eq. (1)) and can be tracked by ground-based trend monitoring techniques once per a number of flights. As the gradual degradation progresses, all Kalman filters need to be updated (It is desirable to update both state-space matrices and steady-state points. If this is not achievable, then at least the steady-state points must be updated, while maintaining the state-space matrices obtained at the healthy baseline condition.) based on the estimated baseline degradation so that the Kalman filters will operate within the linear range of a degraded engine. The tuning parameters are the deviation values from this updated reference point.

Similar to the Kalman filters designed for sensor fault detection, the accuracy of the estimated sensor measurements is indicated by a weighted sum of squared residuals (WSSR) which is computed as follows:

$$\text{WSSR} = (y - \hat{y})^T (\Sigma)^{-1} (y - \hat{y}) \tag{5}$$

where

$$\Sigma = \text{diag}[\sigma]^2$$

The vector σ represents the standard deviation of the sensor set. It should be noted that this filter uses all sensors of the given sensor suite. The assumption of this filter is that all sensors are healthy and that components are potentially faulty (fault hypothesis).

The fault indicator signal of this filter must meet two requirements: (1) it must remain small in the case of component faults and (2) it must increase in the case of a sensor fault. These two conditions are required to indicate whether the fault hypothesis of this filter is correct or incorrect. It was found that this WSSR could meet the first condition, but not the second one. In the case of a sensor fault, the WSSR could remain small depending on which sensor is faulty. After some investigation, it was found that, whenever the WSSR remains small in the presence of a faulty sensor, the sensor fault is attributed to the engine internal condition: the tuning parameters. In other words, the Kalman filter tries to ‘‘explain’’ a sensor fault by shifting the tuning parameters. If it is successful in doing so, the value of WSSR remains small.

To address this shortcoming, another fault indicator signal is used. This signal, a weighted sum of squared tuners (WSST), is computed as follows:

$$\text{WSST} = W_d (d^T d) \tag{6}$$

where W_d is a designer selected weighting factor. Regardless of the fault type, the value of WSST increases when a fault occurs. However, the following two conditions were observed: (1) the increase in WSST is generally small in the component fault case, and (2) the increase in WSST becomes excessively large whenever this Kalman filter maintains a low WSSR value in the presence of a faulty sensor. Based on these observations, the two fault indicator signals (WSSR and WSST) are used in combination to indicate whether the fault hypothesis of this filter is correct or incorrect. If both signals remain below their detection thresholds, the fault hypothesis is correct, i.e., component faults may exist but all sensors are healthy. If at least one of them exceeds the detection threshold, the fault hypothesis is incorrect, and thus a sensor fault is believed to exist. Through this approach, sensor and component faults can be distinguished. It should be noted that as the magnitude of a component fault increases, the value of WSST increases and eventually exceeds the detection threshold. By the time this happens, it is expected that each fault indicator signal generated for sensor fault detection would already have exceeded its threshold so that misclassifications of component faults as a sensor fault will be avoided.

So far, only the component fault case has been discussed in this section. Actuator faults can be handled by either augmenting the tuning parameter vector in Eq. (4) with the actuator bias term in Eq. (1) or designing single Kalman filters for each of the actuators as was done in Ref. [2]. However, a different approach is taken in this paper. When an actuator is biased, it causes a measurement shift in multiple sensors, similar to the component fault case. The Kalman filter designed with tuning parameters can handle such multiple measurement shifts and, therefore, is considered to have some robustness to actuator faults as well, i.e., the two fault indicator signals will remain small when actuators are faulty. Therefore, the Kalman filter with tuning parameters is used to detect both component and actuator faults. If this filter is not robust to actuator faults, then the designer must take one of the aforementioned approaches to meet design objectives.

It should be noted that, when the Kalman filter with tuning parameters is isolated from the rest of the filters, the specific component(s) and/or actuator(s) which are faulty are not identified. For further diagnosis of the component and actuator faults, another set of Kalman filters, each designed for a specific fault event (such as foreign object damage, domestic object damage, fuel system failure, etc.), may be used. Since it is already known that a fault exists, a detection threshold is not needed. Instead, by ranking the likelihood of plausible faults based on the Kalman filter estimation accuracy, the possibility of misclassifications may be reduced. This process was demonstrated by Volponi et al. [7], and a high success rate was exhibited.

Overall Sensor FDI Architecture. The overall architecture of the sensor FDI system is shown in Fig. 2. The FDI system is composed of a bank of $(m+1)$ Kalman filters where m is the

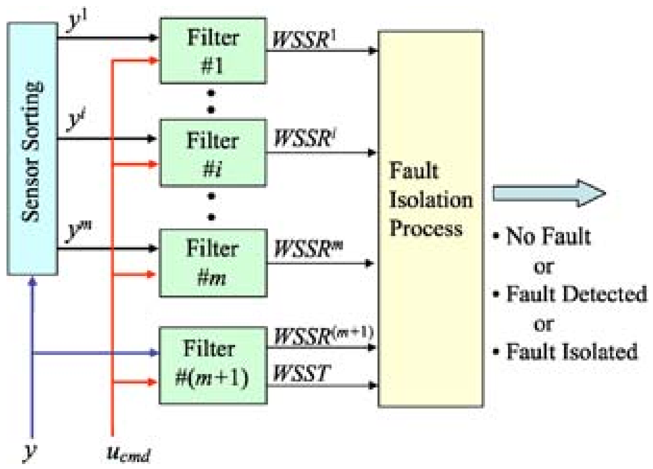

Fig. 2 Architecture of the sensor FDI system

number of sensors being monitored. Kalman filters 1 through m are used to detect sensor faults while the $(m+1)$st Kalman filter is used for the detection of component/actuator faults. With this bank of Kalman filters, the following assumptions are made:

1. Only one sensor may fail at a time.
2. Multiple components and actuators may fail at a time.
3. Only one of the above two types of failures may occur at a time.

In the fault isolation process, the fault indicator signal generated by each Kalman filter is compared against a predefined detection threshold. If a fault indicator signal exceeds the threshold, it indicates that the corresponding Kalman filter is using an incorrect fault hypothesis. The Kalman filter #$(m+1)$ generates two fault indicator signals, and at least one of them must exceed the threshold to indicate that its fault hypothesis is incorrect.

Table 1 summarizes the fault isolation process. There are eight possible scenarios, as enumerated in Table 1, that the fault isolation process may encounter. When sensors, actuators, and components are all nominal, all fault indicator signals will remain below their thresholds, indicating that no fault exists in the system (scenario 1). When a fault occurs, the value of each fault indicator signal except for the one with the correct hypothesis will increase. The increased amount will vary for each fault indicator signal as each filter has a different response or sensitivity to a particular fault. Depending on the type and severity of the fault, some fault indicator signals may exceed their thresholds while others may remain below. If at least one fault indicator signal exceeds its threshold, the fault isolation process declares that a fault was detected. However, the isolation of a fault can not be achieved as long as at least two Kalman filters do not have a threshold violation. Scenarios 2–5 represent these cases where a fault can be detected but not isolated. When a threshold violation occurs for all Kalman filters except one, then this single Kalman filter is isolated from the rest, and the fault hypothesis used by this filter reveals the identity of the fault. Thus, the isolation of a sensor fault is achieved in scenario 6, and the detection of a component and/or actuator fault is achieved in scenario 7. Finally, as discussed earlier, when a threshold violation occurs for all Kalman filters, the fault isolation process declares that a large component and/or actuator fault has occurred (scenario 8).

Table 2 State, health, actuator, and sensor variables

State Variables	XNL, XNH, TMHS23, TMHS3, TMHSBL TMHSBC, TMHS41, TMHS42, TMHS5
Health Parameters	FAN efficiency, FAN flow capacity BST efficiency, BST flow capacity HPC efficiency, HPC flow capacity HPT efficiency, HPT flow capacity LPT efficiency, LPT flow capacity
Actuators	WF36, VBV, VSV
Sensors	XN12, XN25, P25, T25, PS3, T3, T49

Application of FDI Methodology to an Aircraft Engine Simulation

In this section, the FDI design methodology is applied to an aircraft engine simulation. A description of the engine simulation is given first. From the engine simulation, piecewise linear models are generated along the steady-state power setting line at a cruise condition. Based on these linear models, the piecewise Kalman filter model is developed in order to cover multiple power settings.

Engine Model. The engine model used in this paper is a nonlinear simulation of an advanced high-bypass turbofan engine. This engine is constructed as a Component Level Model (CLM), which assembles the following five major components of an aircraft engine: Fan (FAN), Booster (BST), High-Pressure Compressor (HPC), High-Pressure Turbine (HPT), and Low-Pressure Turbine (LPT). The health parameters, which represent the component performance deterioration, are adjustments to efficiency and flow capacity scalars of the above five components. The current version of the simulation does not have health parameters for the combustor. The engine state variables, health parameters, actuation variables, and sensor measurements are shown in Table 2.

The outputs of the seven sensors in Table 2 are fed into the digital engine control unit. At the cruise operating condition evaluated in this study, the power lever angle (PLA) value is con-

Table 1 Summary of fault isolation process

		$WSSR^{(m+1)}$ and $WSST$ for Kalman Filter #$(m+1)$ (Component and/or Actuator Fault Hypothesis Filter)	
		Both remain below threshold	Either one or both exceed threshold
$WSSR^i$ for Kalman Filters #1~#m (Sensor Fault Hypothesis Filers)	All WSSRs remain below threshold	1) No fault exists	2) Detection of fault (no isolation)
	At least one WSSR exceeds threshold and at least two WSSRs remain below threshold	3) Detection of fault (no isolation)	4) Detection of fault (no isolation)
	All but one WSSR exceed threshold	5) Detection of fault (no isolation)	6) Detection and isolation of sensor fault
	All WSSRs exceed threshold	7) Detection of component and/or actuator fault	8) Detection of large component and/or actuator fault

Table 3 Sensor noise standard deviation in % of the trim values at maximum power

Sensor	σ
XN12	0.25
XN25	0.25
P25	0.50
T25	0.75
PS3	0.50
T3	0.75
T49	0.75

verted to the desired corrected low-pressure spool speed (an indicator of thrust). The control system adjusts three actuation variables to cause the corrected measured low-pressure spool speed value to match the commanded value. PLA varies from 38 to 72 deg.

The standard deviations of the sensor noise used in this paper are shown in Table 3. The values are given in percent of the steady-state values at the maximum power setting (PLA=72).

Piecewise Kalman Filter Model. At the selected cruise condition, piecewise linear engine models are generated along the steady-state power setting line where PLA varies from 38 to 72 deg. A linear engine model is composed of trim values and state space matrices. For each of these linear models, a Kalman gain is computed. Then, the piecewise Kalman filter model is developed by linking the piecewise linear models and the corresponding Kalman gains. The architecture of the piecewise Kalman filter model is shown in Fig. 3.

The piecewise Kalman filter model is composed of the steady-state (base-point) model, state-space matrices, and Kalman gains. The steady-state model captures nonlinear engine characteristics along the power setting line, while the state-space matrices (dynamic model) capture off-nominal engine behavior due to perturbations from the steady-state line. These three elements of the Kalman filter model are saved in table lookup form. For a given set of two input signals (u_{cmd}, y), the steady-state values, the state-space matrices, and a Kalman gain constitute the Kalman filter equation, by which the state variables and sensor outputs are estimated. As PLA moves from one point to another, those elements saved in the lookup table are interpolated linearly based on a scheduling parameter. In the current model, the estimated low-pressure spool speed (XN12) is used as the scheduling parameter. It should be noted that the scheduling parameter can be a function of multiple parameters as in Refs. [1,8]. More detailed discussion regarding the piecewise linear state variable model can be found in Refs. [8,9].

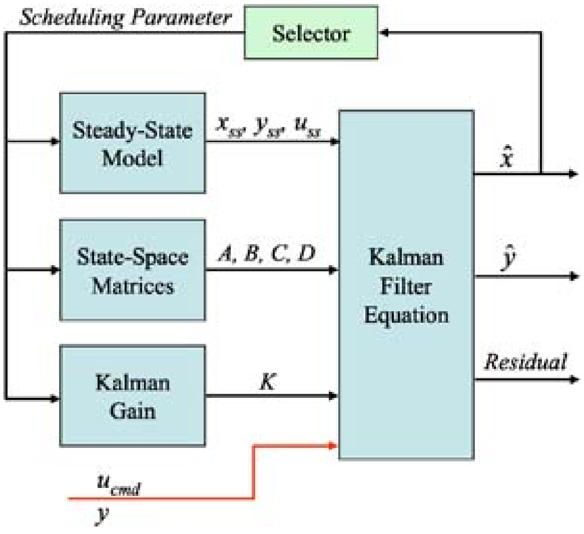

Fig. 3 Architecture of piecewise Kalman filter model

By using the architecture of Fig. 3, a piecewise Kalman filter model is built for each fault hypothesis (Eqs. (2) and (4)), and a bank of Kalman filters is formed as shown in Fig. 2. The FDI system is now able to cover the full PLA range at a fixed ambient condition of the selected cruise point. In order to expand the range of ambient conditions over which the FDI system can operate, the parameters of the Kalman filters must be corrected based on inlet condition, however, this additional step is not pursued in this paper.

Selection of Tuning Parameters. The selection of the tuning parameters for designing the $(m+1)$st Kalman filter is critical in order to achieve overall sensor FDI performance at an acceptable level. It is desirable to have some optimal selection methods; however, the tuning parameters used in this paper were selected by trial and error. The selected tuning parameters are: FAN flow capacity, BST flow capacity, HPC efficiency, HPC flow capacity, HPT flow capacity, and LPT flow capacity. With these tuning parameters, the Kalman filter is able to accurately estimate sensor outputs even if all 10 health parameters are shifted from a reference point. Again, it should be remembered that the tuning parameters do not indicate the actual health condition although they are selected from the health parameters.

Modifications to the FDI System. During the preliminary evaluation of the FDI system, it was found that the Kalman filter design approach for the fault detection of the XN25 and T25 sensors had to be modified. When either of these sensors is biased, the control system generates a large off-nominal variable stator vane (VSV) command. As discussed earlier, piecewise linear models are generated along the steady-state power setting line. Any control input deviation from this steady-state line is the delta input to the linear models. Under normal fault-free engine operation, any control input deltas remain relatively small, and therefore the linear models are valid to describe the off-nominal engine behavior. However, when one of the aforementioned two sensors is biased, the engine operates at a condition where the steady-state VSV command is significantly shifted from its nominal value. This large shift, used as an input to linear model, exceeds the linear range and gives the appearance that VSV is biased. The assumption of the bank of Kalman filters for sensor FDI is that at most one sensor is faulty while the others, including the actuators, remain at their nominal condition. Therefore, with the large shift in the VSV command input, the Kalman filters designed for monitoring XN25 and T25 are not able to accurately estimate state variables and sensor outputs, and consequently a large fault indicator signal is generated. In the meantime, the Kalman filter designed with tuning parameters is able to generate low fault indicator signals since this filter can handle the shifts in multiple parameters. Thus, without modifications, the FDI system will misclassify XN25 or T25 sensor faults as the component/actuator fault case.

To address this problem, the Kalman filters for the XN25 and T25 sensors are designed based on the augmented state vector which is composed of the state vector and the VSV bias term. This approach, which was used in Ref. [2], allows the Kalman filters to estimate a bias in VSV. When a large off-nominal steady-state VSV value is commanded, the Kalman filters attribute this large input to the estimated VSV bias. With this modification, the effect of a large command input that corrupts the estimation of these Kalman filters is reduced, and therefore the sensor outputs are accurately estimated. The problem of a large off-nominal shift in the VSV command is specific to the control system used in the current study. If a different control design is employed, this problem may not be encountered; instead, new challenges may appear.

Table 4 Minimum positive bias isolated by the sensor FDI system (% of steady-state value at maximum power)

	PLA=50	PLA=60	PLA=68
XN12	1.6	1.9	2.1
XN25	4.7	4.0	3.4
P25	2.9	3.5	5.0
T25	2.1	2.0	2.0
PS3	3.2	5.1	6.7
T3	2.8	3.5	4.1
T49	2.3	2.9	3.2

Performance Evaluation of the Sensor FDI System

In this section, the FDI system is evaluated at three PLA settings: 50, 60, and 68 deg. As discussed earlier, the three objectives of sensor FDI are to avoid (1) missed detections, (2) false alarms, and (3) misclassifications. The evaluation is based on each of these objective categories. Additionally, the robustness of the FDI system is evaluated.

Evaluation 1: Missed Detections. When a single sensor is faulty, it must be correctly detected and isolated. If this objective is not achieved, it is considered that the FDI system missed the detection of the sensor fault. To assess the missed detection rate generated by the FDI system, it is desirable to have design specifications which define the bias magnitude at which sensors transition from "nominal" to "faulty" operation. Since such information is not available in this study, the minimum sensor bias that the proposed FDI system can isolate is determined for each of the sensors. If design specifications are available, the FDI system, or specifically the detection thresholds, may be adjusted to meet a desired performance level.

Table 4 shows the minimum positive bias in each sensor that could be isolated by the FDI system at the three power settings considered. The numbers are given in percent of the steady-state values at the maximum power setting (PLA=72). All sensor biases of these magnitudes were isolated correctly. The magnitude of the minimum isolated bias varies with sensor type and also with power setting. This variation in the magnitude depends on how easily the "correct" Kalman filter can be isolated from the rest of the filters. For most of the test cases, the fault indicator signal which exceeded the threshold last (the correct one must remain below the threshold) is the one corresponding to the Kalman filter with tuning parameters. Therefore, overall sensor isolation performance of the FDI system depends not only on the sensor suite but also the selection of tuning parameters. The worst case, or the largest minimum bias value that could be isolated, is the 6.7% PS3 sensor bias. If the isolation of smaller magnitude faults is desired, the detection thresholds must be set lower. However, this adjustment may result in increased false alarms and misclassifications.

When PLA is moved beyond the value of 68 deg, it becomes very difficult to isolate XN25 sensor bias. As mentioned, bias in this sensor causes a large off-nominal shift in the steady-state VSV command input. Similarly, the off-nominal steady-state shift in the WF36 command input increases as PLA increases. When PLA exceeds 68, this off-nominal WF36 shift becomes too large for the linear model to handle. As a result, XN25 sensor bias is diagnosed as a component/actuator fault by the FDI system. This problem may be solved by augmenting the state vector with a WF36 bias term as was done for the VSV input. However, this further step has not been taken in this work.

Evaluation 2: False Alarms. When the FDI system is applied to a real engine, nonfault-related factors which exist in the real environment, such as sensor noise and modeling uncertainty, should not be diagnosed as a sensor fault. If this happens, the FDI system will have generated a false alarm. Since the Kalman filter design approach accounts for these nonfault-related factors to some degree, the estimator should handle them well as long as they do not deviate significantly from their assumed values.

Table 5 Nonfault-related factors tolerated by the FDI system

	PLA=50	PLA=60	PLA=68
Noise Factor	9%	11%	13%
Model Mismatch	0.7%	0.4%	0.3%

In the previous evaluation step, the FDI system was applied to the nonlinear engine simulation at three different power settings. When there was no sensor bias, no false alarm was generated. This means that the Kalman filters are able to handle the given sensor noise (Table 3) and the model mismatch that exists between the nonlinear engine simulation and its linear representation. In this section, the robustness of the FDI system to sensor noise and modeling uncertainty is evaluated by varying the magnitude of these factors.

At the steady-state condition of the three power settings used in the previous section, either the sensor noise level or the model uncertainty level is increased. By increasing these factors, the FDI system may eventually generate a false alarm (only one fault indicator signal remaining below the detection threshold). In this study, however, the level of sensor noise and model uncertainty is increased up to the initial point of fault detection where the threshold is just exceeded by at least one fault indicator signal. If the FDI system can tolerate a large magnitude increase in these factors, it is considered that the likelihood of generating false alarms is very small.

In the simulation, the sensor noise is increased by multiplying the standard deviation (Table 3) by a scale factor. Model uncertainty is introduced by shifting all 10 health parameters of the nonlinear engine simulation by the same amount from the healthy baseline. Since the FDI system was designed based on a "healthy" engine, the outputs of the "degraded" nonlinear engine simulation deviate from the design point of the FDI system. Table 5 shows the level of sensor noise scale factor and model uncertainty (steady-state model mismatch) that the FDI system can tolerate, i.e., all fault indicator signals remain below the threshold. The noise scale factor was increased by 1% increments while the steady-state model mismatch was increased by 0.1% increments to obtain these results. When the level of either one of these two factors is increased, the other was kept at the nominal design condition.

As the noise scale factor was increased, the values of all WSSR signals increased even though the Kalman filters could maintain good estimation accuracy of sensor outputs. This increase is due to the fact that the normalization factor (Σ in Eqs. (3) and (5)) used to generate WSSR is based on the assumed noise intensity. Noise that exists in the real environment is never certain. Therefore, the detection threshold has been selected to account for the uncertainty in noise statistics. The FDI system can tolerate, at worst, a 9% (at PLA=50) noise increase. If this value is considered too small, then the detection threshold must be increased accordingly.

Similarly, the fault indicator signals increase as the level of steady-state model mismatch is increased. Model mismatch causes a shift in all sensor measurements from the reference point, as if small biases were injected into all sensors. Since the Kalman filter assumes that the sensor outputs are corrupted only by white noise, it is not able to maintain good estimation accuracy when model mismatch is present. The variation in fault indicator signals due to model mismatch must be accounted for in threshold selection. The FDI system can tolerate, at worst, a 0.3% (at PLA=68) shift in all

Table 6 Component and actuator fault scenarios for the FDI performance evaluation

		Delta Range	# of Cases
Single Component Fault	FAN	[1%, 4%]	50
	BST	[1%, 4%]	50
	HPC	[1%, 4%]	50
	HPT	[1%, 3%]	100
	LPT	[1%, 3%]	100
Multiple Component Fault	FAN BST	[2%, 4%] [1%, 3%]	100
	BST HPC	[2%, 4%] [1%, 3%]	100
	FAN BST HPC	[2%, 4%] [1%, 3%] [0.5%, 2%]	100
	HPT LPT	[1%, 3%] [1%, 3%]	200
Single and Multiple Actuator Fault	WF36 VBV VSV	5% 5% 5%	150

health parameters. Again, if this value is considered too small, then the detection threshold must be increased accordingly.

Evaluation 3: Misclassifications. A misclassification is an event where the FDI system correctly detects a fault that exists in the engine but classifies it as the wrong fault. For example, when an anomaly other than a sensor fault occurs in the aircraft engine, the sensor FDI system should not classify it as a sensor fault. If it does, it is considered that the FDI system misclassified the fault. Such anomalies can occur to engine components during flight due to fault events such as foreign or domestic object damage. Anomalies can also exist in actuators due to mechanical or electrical failure in the actuation systems. In order to avoid misclassification, the FDI system contains one additional Kalman filter designed with tuning parameters as discussed earlier. When components or actuators are faulty, the two fault indicator signals (WSSR and WSST) of this filter should not exceed the threshold. If this can be achieved, the FDI system will not misclassify component or actuator faults as a sensor fault. In this section, the FDI system is evaluated as to whether it can avoid misclassifications of component and actuator faults.

Table 6 shows the component/actuator fault scenarios used to evaluate the FDI system at the three power settings (PLA=50, 60, 68). For each engine component, both efficiency and flow capacity are shifted randomly within the range shown in the table. This range is considered to encompass any reasonable failure scenarios. All component shifts are made in the negative direction, except for HPT and LPT flow capacities which are shifted in both positive and negative directions. The actuator bias is also varied randomly in both positive and negative directions within the specified range. The actuator bias range is shown in percent of full-scale values.

For the 3000 test cases evaluated (the 1000 fault scenarios shown in Table 6 at each of the three power settings), no misclassifications were encountered. This demonstrates the significant robustness of the FDI system to component and actuator faults. This robustness is largely due to the Kalman filter with tuning parameters. If this filter is not included, the FDI system is more likely to misclassify faults. To verify this claim, the FDI system was "standardized" by removing the Kalman filter with tuning parameters and then re-evaluated. For the 1000 fault scenarios at each of the three power settings, the number of component/actuator fault cases that this "standard" FDI system misclassified as a sensor fault were as follows: 97 (PLA=50), 113 (PLA=60), and 108 (PLA=68).

Table 7 Minimum positive bias isolated by the sensor FDI system in the presence of 0.3% baseline degradation mismatch

	PLA=50	PLA=60	PLA=68
XN12	1.7	2.1	2.3
XN25	4.3	3.8	Misclassification
P25	3.0	3.7	4.9
T25	2.2	2.1	2.0
PS3	2.8	4.5	6.0
T3	3.1	3.9	4.5
T49	1.9	2.4	2.7

During the evaluation of the "robust" FDI system (the Kalman filter with tuning parameters included), it was noted that, in some of the fault scenarios, a threshold violation occurred for all Kalman filters. If this happens, the FDI system indicates that a large component/actuator fault may have occurred (see Table 1).

Evaluation 4: Robust Sensor Fault Isolation. All engine components gradually degrade with time due to usage. As discussed earlier, the baseline degradation (shift in all health parameters from the healthy baseline) can be tracked by ground-based trend monitoring systems, and the estimated baseline degradation can be used to update the FDI system for in-flight fault diagnostics. It is unlikely that the estimated baseline degradation will match perfectly with the actual condition. In order to assess the influence of baseline mismatch on the sensor fault isolation performance, the FDI system is evaluated in the presence of the error in the estimated baseline degradation.

In this test case, the estimated baseline is set to the healthy baseline condition (i.e., a trend monitoring system concluding that the engine is healthy), and consequently the design of the FDI system is based on a healthy engine. This FDI system is then applied to the nonlinear engine simulation with small baseline degradation. A 0.3% shift is injected to all 10 health parameters. With this magnitude, the FDI system indicates that no fault exists in the system at the three power settings (see Table 5). In the presence of this baseline degradation mismatch, a bias is injected into each sensor. Table 7 shows the minimum positive bias isolated by the FDI system. Again, the numbers are given in percent of the steady-state values at the maximum power setting (PLA=72).

All sensor biases were isolated correctly, except for one case where the XN25 sensor is biased at a PLA setting of 68 deg. As discussed before, the isolation of the XN25 sensor is very difficult at high power settings because of the large off-nominal shift in the VSV and WF36 command inputs. As a result, the XN25 sensor bias is misclassified as a component/actuator fault. Since it is known that the XN25 sensor bias causes large shifts in multiple parameters (one sensor and two actuator commands), some intelligence must be built in to the FDI system to account for this knowledge. In the rest of the scenarios, the FDI system exhibits good performance. For some sensors, smaller bias can be isolated compared to the results shown in Table 4. The worst case, or the largest minimum bias value that could be isolated, is the 6.0% PS3 sensor bias. It is especially encouraging that the FDI system did not attribute a fault in one sensor to a different sensor which, if it had occurred, would have created a very challenging environment for further accommodation steps.

Discussion

In-depth evaluation is a critical part in the development of an in-flight FDI system. The multiple objectives that the FDI system must handle often conflict with each other. Consequently, enhancing one aspect of the FDI performance does not necessarily result in the enhancement of overall performance. For instance, the minimum sensor bias magnitudes that the FDI system can isolate may be reduced by setting detection thresholds at a lower value. This modification, however, may result in increased false alarms and misclassifications. Through extensive evaluation, the FDI system can be matured to a point where its overall performance is satisfactory. To reach such a mature point, the sensor FDI system developed in this paper needs further evaluation and enhancement. Some of the issues that must be addressed in future work are discussed below.

First, the ambient conditions over which the FDI system can operate must be expanded. In the real environment, the ambient condition continually changes even in the cruise phase. As discussed earlier, this expansion can be accomplished by correcting the parameters of the Kalman filters based on inlet pressure and temperature measurements. In this "corrected" dimension, the FDI system must be evaluated for its diagnostic performance, sensitivity to ambient condition changes, and sensitivity to inlet sensor faults.

The evaluation results presented in this paper were obtained at fixed PLA values or fixed target low-pressure spool speeds (a fixed PLA value does not necessarily mean a fixed steady-state condition when faults are present in the system). Since the PLA movement is expected to be small in the cruise phase of a commercial aircraft, the FDI system was developed to be robust enough to handle small PLA movements, i.e., false alarms are not generated during minor transients. When the FDI system operates under relatively large PLA movements, however, some of the sensor estimates lag behind the actual measurements, causing an increase in the fault indicator signals. Eventually, the fixed detection thresholds are exceeded, and false alarms are generated. To account for relatively large PLA movements, adaptive detection thresholds which vary with transient conditions need to be introduced, as done in Ref. [1]. Then, the FDI system needs to be evaluated for its diagnostic capability during PLA transients.

Conclusion

An approach based on a bank of Kalman filters was investigated for the development of an aircraft engine sensor fault detection and isolation (FDI) system. This approach utilizes multiple Kalman filters, each of which is designed based on a specific fault hypothesis. When the propulsion system experiences a fault, only one Kalman filter with the correct hypothesis can maintain the nominal estimation performance. Based on this knowledge, the isolation of faults is conducted. The sensor FDI system developed in this paper utilizes a bank of $(m+1)$ Kalman filters where m is the number of sensors being monitored. The additional Kalman filter is used to detect component and actuator faults. With this setup, the isolation of sensor faults or the detection of component/actuator faults can be achieved.

The sensor FDI system was applied to a nonlinear simulation of a commercial aircraft gas turbine engine, and its performance was evaluated at multiple power settings at a cruise operating point. After an extensive evaluation, the following three conclusions can be made: (1) the FDI system can correctly isolate a faulty sensor, (2) the FDI system can tolerate variations in sensor noise and model uncertainty, and (3) the FDI system is robust to component and actuator faults in terms of avoiding misclassifications. Some difficulties in isolating faults in two sensors due to the influence of the engine control system were noted. Further study is needed in the area of integration with control systems for performance improvement of the FDI system.

Acknowledgments

This research was funded by the NASA Aviation Safety and Security Program as a task under the Propulsion System Safety Technologies Element.

Nomenclature

BST = booster
FAN = fan
FDI = fault detection and isolation
HPC = high-pressure compressor
HPT = high-pressure turbine
LPT = low-pressure turbine
P25 = HPC inlet pressure
PLA = power lever angle
PS3 = combustor inlet static pressure
T25 = HPC inlet temperature
T3 = combustor inlet temperature
T49 = LPT inlet temperature
TMHS23 = BST metal temperature
TMHS3 = HPC metal temperature
TMHS41 = HPT nozzle metal temperature
TMHS42 = HPT metal temperature
TMHS5 = LPT metal temperature
TMHSBC = combustor case metal temperature
TMHSBL = combustor liner metal temperature
VBV = variable bleed valve
VSV = variable stator vane
WF36 = fuel flow
XN12 = low-pressure spool speed, measured
XN25 = high-pressure spool speed, measured
XNH = high-pressure spool speed, state variable
XNL = low-pressure spool speed, state variable

References

[1] Merrill, W. C., DeLaat, J. C., and Bruton, W. M., 1988, "Advanced Detection, Isolation, and Accommodation of Sensor Failures-Real-Time Evaluation," J. Guid. Control Dyn., **11**(6), pp. 517–526.
[2] Kobayashi, T., and Simon, D. L., 2003, "Application of a Bank of Kalman Filters for Aircraft Engine Fault Diagnostics," ASME Paper GT2003-38550.
[3] Volponi, A. J., 1994, "Sensor Error Compensation in Engine Performance Diagnostics," ASME Paper 94-GT-58.
[4] Doel, D. L., 2003, "Interpretation of Weighted-Least-Squares Gas Path Analysis Results," J. Eng. Gas Turbines Power, **125**, pp. 624–633.
[5] Kobayashi, T., and Simon D. L., 2001, "A Hybrid Neural Network-Genetic Algorithm Technique for Aircraft Engine Performance Diagnostics," Paper AIAA-2001-3763.
[6] España, M. D., 1993, "On the Estimation Algorithm for Adaptive Performance Optimization of Turbofan Engines," Paper AIAA-93-1823.
[7] Volponi, A. J., DePold, H., Ganguli, R., and Chen, D., 2000, "The Use of Kalman Filter and Neural Network Methodologies in Gas Turbine Performance Diagnostics: A Comparative Study," ASME Paper 2000-GT-547.
[8] Kerr, L. J., Nemec, T. S., and Gallops, G. W., 1991, "Real-Time Estimation of Gas Turbine Engine Damage Using a Control Based Kalman Filter Algorithm," ASME Paper 91-GT-216.
[9] Brotherton, T., Volponi, A., Luppold, R., and Simon, D. L., 2003, "eSTORM: Enhanced Self Tuning On-Board Real-Time Engine Model," *Proceedings of the 2003 IEEE Aerospace Conference*, Big Sky, MT.

Theodosios Korakianitis
James Watt Professor
of Mechanical Engineering,
University of Glasgow,
Glasgow G12 8QQ, UK
e-mail: t.Alexander@mech.gla.ac.uk

N. E. Vlachopoulos
Panafon SA,
Athens, Greece

D. Zou
Department of Physical Therapy,
Washington University,
St Louis, MO 63130

Models for the Prediction of Transients in Closed Regenerative Gas Turbine Cycles With Centrifugal Impellers

This paper presents transient-flow component models for the prediction of the transient response of gas turbine cycles. The application is to predict the transient response of a small solar-powered regenerative gas-turbine engine with centrifugal impellers. The component sizes are similar to those under consideration for the solar-powered Space Station, but the models can easily be generalized for other applications with axial or mixed-flow turbomachinery. New component models for the prediction of the propagation of arbitrary transients in centrifugal impellers are developed. These are coupled with component models for the heat exchangers, receiver and radiator. The models are based on transient applications of the principles of conservation of mass, energy, and momentum. System transients driven by sinusoidal and double-step inputs in receiver salt temperature are presented and discussed. The new turbomachinery models and their coupling to the heat-exchanger models simulates disturbance-propagation in the components both upstream and downstream from the point of generation. This permits the study of the physical mechanisms of generation and propagation of higher-frequency contents in the response of the cycle. [DOI: 10.1115/1.1806450]

Introduction

The steady-flow performance of various gas-turbine engines can be predicted to any desirable degree of model complexity, depending on available information. Models for the prediction of transient incompressible fluid flow through simple stationary passages are relatively easy to develop, because of the constant density assumption, and are readily available [1]. Similarly, models for the prediction of transient compressible fluid flow through simple stationary passages are relatively easy to develop by predicting with characteristics the time of propagation of transients. Transient-flow models for axial and centrifugal compressor and turbine passages, where the passages are rotating and work is added to or extracted from the flow, are harder to develop. The time currently required for computational fluid dynamics (CFD) transient computations through the components of a complex gas-turbine power plant makes them unsuitable for predicting the transient response of gas-turbine components and power plants through speed, load, and mass transients.

Non-CFD models suitable for predicting the transient performance of compressors and turbines fall into three main categories. The first category predicts the transient performance by obtaining equations resembling transfer functions in control theory, using phenomenological analyses of component behavior (for example, Kuhlberg et al. [2]; Kalnitsky and Kwatny [3]). In the second category the unsteady conservation equations (mass, momentum, and energy) are written in a lumped-parameter approach (or alternatively finite volumes are considered along a mid-streamline) through one or more components. Many of the models in the second category use some assumption to minimize the effects of compressibility, or the effects of mass storage or mass depletion inside the component through the transient. For example, the system of equations is solved assuming either incompressible fluid, or no storage of mass in the component volumes through the transient, or another assumption that simplifies the transient for one or more of the flow properties (for example, Adams et al. [4]; Corbett and Elder [5]; Macdougal and Elder [6]). In the third category assumptions are made for the delay of transport of perturbations from component inlet to outlet, based on mechanical analogs (for example, Ray and Bowman [7]; Fink, Cumpsty and Greitzer [8]). All three categories may incorporate routines for predicting relations between inlet and outlet properties from the component performance maps.

In a previous paper (Korakianitis, Hochstein, and Zou [9]) we presented models of the second category (using the unsteady form of the conservation laws) for the prediction of the propagation of arbitrary transients through regenerative-gas-turbine cycle components. The three-point lumped-parameter models for the turbomachinery components resulted in what is called a stiff system of algebraic and differential equations. Numerical stability considerations and multiple iteration passes through the turbomachinery components imposed very restrictive upper and lower time-step limits in the integration. They also imposed limits on the amplitude of the disturbances for which the system model could be run. Therefore the allowable time step was very small, so that both the total time of transient flow studied and the frequency of fluctuations were unrealistically fast. The purpose of this paper is as follows: to present a new set of improved models for the propagation of transients through centrifugal impellers; to couple them to the other transient component models to form the regenerative gas-turbine cycle; and to present typical time-dependent results with realistic transients that can be run in reasonable times (accomplished because the new transient centrifugal turbomachinery models run significantly faster than the previous ones). The new models can also handle much larger disturbance amplitudes. As an application, the models are used to predict the transients of a regenerative gas-turbine engine that is approximately suitable for providing power to the Space Station.

Cycle Configuration

The important inputs to predict the transient performance of gas turbines are the type and size of engine components, details of

---

Contributed by the International Gas Turbine Institute and presented at the 39th International Gas Turbine and Aeroengine Congress and Exposition, The Hague, The Netherlands, June 13–16, 1994. Manuscript received November 1, 1993; final revision received February 1, 1994. Paper No. 94-GT-342. Associate Editor: E. M. Greitzer.

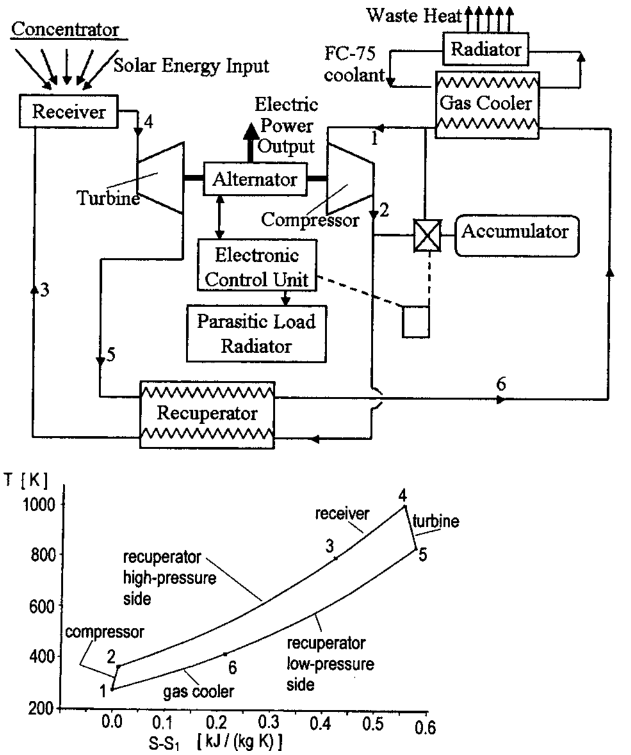

Fig. 1 Component schematic and temperature-entropy diagram for the regenerative Brayton cycle. (The value of S_1 is arbitrary).

their geometric construction, working fluid, and inputs driving the transient. Our previous turbomachinery models considered flow properties at the inlet, middle, and outlet of the impeller (requiring only a cursory description of the centrifugal geometry). The present centrifugal component models are finite-difference models through the impeller passage requiring several nodes within the passage of the component and a more-elaborate description of the impeller geometry, as explained in the next section.

Simplified component and approximate temperature-entropy diagrams for the solar-powered closed regenerative Brayton-cycle engine suitable to provide electrical power to the Space Station are shown in Fig. 1. Component arrangements and dimensional information are included in the earlier paper (Korakianitis, Hochstein, and Zou [9]). Approximate dimensions and other information for the system are included in many NASA and NASA-contractor reports such as the two reports by Rocketdyne [10,11]. Select information used in this paper is included in the Appendix.

Power for the Space Station can be provided in part by a photovoltaic module, and in part by two regenerative Brayton cycles similar to the one illustrated in Fig. 1, each providing approximately 30 kW. The working fluid is a mixture of helium and xenon (He-Xe) gases, modeled as a perfect gas with constant $c_p = 520.4$ J/(kg·K) and $c_v = 312.2$ J/(kg·K). At the design point the compressor and turbine pressure ratios are just below 2:1 (the turbine pressure ratio is a little lower than the compressor pressure ratio due to pressure losses), and the mass-flow rate is approximately 0.8 kg/s. The compressor and turbine are small radial impellers. Solar energy is collected by the concentrator, focused onto the phase-change eutectic salt (LiF-CaF$_2$) in the receiver, and transferred to the working fluid. Energy is rejected from the cycle through the gas cooler. The gas cooler, in what is called the coolant loop, uses a liquid mixture of 75% $C_2H_3F_3O$ and 25% H_2O (called FC −75) to reject energy via the radiator to space. The centrifugal compressor, radial turbine, and alternator rotate as a single unit at a (approximately) constant speed of 32 000 rpm (minimum 30 000 rpm, maximum 36 000 rpm). The system rotates in space in and out of the shadow of the earth with a period of approximately 90 minus, implying transients for the receiver and cooler. The receiver phase-change salt is used to provide energy at an almost-constant temperature to the cycle. In the following system transients are driven with 0.5%, 5.0%, and 15.0% sinusoidal or double-step variations in the receiver salt temperature T_{sl} specifying either constant-speed/variable alternator work, or allowing variable-speed/prescribed alternator power. In operating practice, these and other system transients are handled by changing the mass-flow rate of the working fluid through the components (by adding and subtracting working fluid in the accumulator), and/or by shedding some of the electrical power output in the parasitic-load radiator.

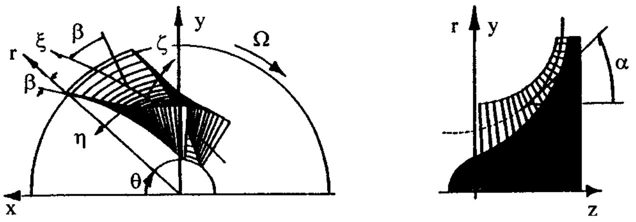

Fig. 2 Rotating-passage geometry for centrifugal impellers

The new centrifugal-component transient performance models can handle larger disturbance amplitudes, as well as the expected 90-min orbital period in reasonable CPU and run times. Although the following models are applied to the system illustrated in Fig. 1, the principles are general and they can be used in different gas-turbine engines with different components.

Turbomachinery Models

The flow through general centrifugal turbomachinery passages (see Fig. 2) is assumed compressible, adiabatic, viscous (or inviscid), unsteady, one-dimensional (along ξ) with area change $A(\xi)$. The flow is considered along the rotating curvilinear frame of reference (ξ,η,ζ) in the middle of the blade passage.

The governing equations are derived from the time-dependent form of the conservation of mass, momentum, and energy applied to a simple control volume shown in Fig. 3:

$$\left\{\begin{array}{c} dm^i/dt-(\dot{m}^i_{in}-\dot{m}^i_{ot}) \\ d(I^i_\xi)/dt-(\dot{I}^i_{\xi,in}-\dot{I}^i_{\xi,ot}) \\ d(m^i e^i_0)/dt-(\dot{m}^i_{in}h^i_{0,in}-\dot{m}^i_{ot}h^i_{0,ot}) \end{array}\right\} = \left\{\begin{array}{c} 0 \\ \sum (F^i_{\xi,inv}+F^i_{\xi,vis}) \\ \delta W^{i\leftarrow}_{is}+\delta W^{i\leftarrow}_{fr} \end{array}\right\} \qquad (1)$$

Introducing the one-dimensional variations of the properties along ξ as shown in Fig. 3, the governing equations are obtained in a conservative form in the rotating frame of reference. The resulting partial differential equations nondimensionalized with the total properties at the inlet, the inlet flow area, and the passage length, are:

$$\frac{\partial \mathbf{q}}{\partial t}+\frac{\partial \mathbf{F}}{\partial \xi}=\mathbf{b} \qquad (2)$$

where

$$\mathbf{q}=\left\{\begin{array}{c} \rho A \\ \rho A w \\ \rho A e_R \end{array}\right\}$$

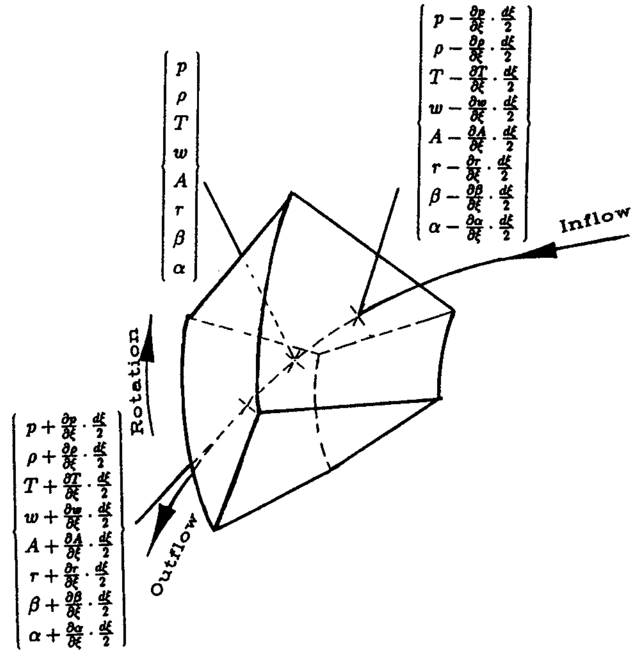

Fig. 3 Control-volume model with 1-D variations for the centrifugal impeller passages

$$\mathbf{F}=\left\{\begin{array}{c}\rho A w\\ A(\rho w^2+p)\\ Aw(\rho e_R+p)\end{array}\right\}$$

$$\mathbf{b}=\left\{\begin{array}{c}0\\ p\,\dfrac{dA}{d\xi}+\rho A\left[\sin\beta\,\dfrac{d\Omega r}{dt}+\Omega^2 r\sin\alpha\cos\beta\right]+f_{\mathrm{fr},\xi}A_{\mathrm{fr},\xi}\\ -\rho A(\Omega r-w\sin\beta)(d\Omega r/dt)-f_{\mathrm{fr},\eta}A_{\mathrm{fr},\eta}\Omega r\end{array}\right\}$$

In the momentum term of vector **b** one can identify from left to right the area gradient effects, the Coriolis acceleration effects, the centrifugal force effects, and the wall friction effects, for all faces of the element. In the energy term of vector **b** one can identify from left to right the Coriolis acceleration effects, and the wall friction effects in the tip region. (These are zero for shrouded impellers.) The viscous forces between the walls and the fluid have been included in the form of frictional forces per unit length. Those forces can be approximated using a friction coefficient approach and a corresponding Reynolds number. In Eqs. (2), w represents the relative flow velocity along the mean streamline direction (ξ), and e_R is the so-called rotating total energy per unit mass (the equivalent of total energy for a stationary frame of reference) defined by:

$$e_R=\frac{T}{\gamma-1}+\frac{w^2-(\Omega r)^2}{2} \tag{3}$$

so that the state equation for the gas takes the form:

$$p=\rho\cdot(\gamma-1)\cdot\left(e_R-\frac{w^2-(\Omega r)^2}{2}\right) \tag{4}$$

This model requires the specification of flow angles [near the operating point these are assumed to be equal to the blade angles $\beta(\xi)$ along the mean streamline], passage turning angles from axial to radial direction ($\alpha(\xi)$), and radii ($r(\xi)$). The above set of governing equations is valid for the whole range of turbomachinery components, from axial to mixed-flow to radial, and can be used to model viscous and inviscid compressor and turbine passages. These models are more realistic than the simple actuator disk model used in our previous study, and obviate the need to use compressor and turbine performance maps.

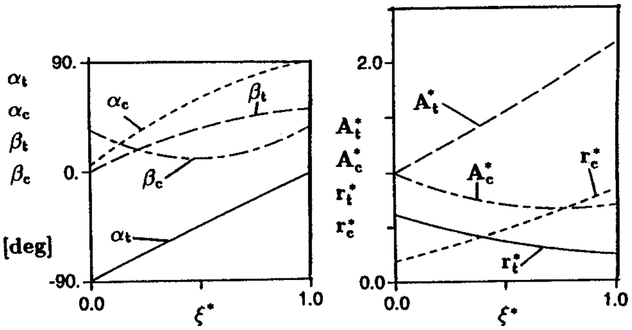

Fig. 4 Compressor and turbine impeller geometries expressed in nondimensional parameter form. Key turbomachinery dimensions are included in the Appendix.

An eigenvalue/eigenvector analysis of the spatial operator of the above equations indicates that they are hyperbolic in nature. Any finite difference or finite volume scheme appropriate for hyperbolic equations can be used. For the results shown in this paper a new finite-difference scheme has been used. This new scheme is based on the theory of characteristics, and uses the right-eigenvector matrix as a basic operator. The governing equations are projected in a disturbance propagation space (characteristic space) and upwinded. The solution vector is then reconstructed by algebraic manipulations. This new scheme has been validated by comparisons with one- and two-dimensional steady and unsteady-flow cases, and it provides faster and more-accurate solutions than other similar schemes. The working implementation of the new scheme used in this paper is explicit, first-order accurate in time, and second-order accurate in the spatial direction (ξ). As in most explicit hyperbolic algorithms the time and space differences must satisfy the CFL criterion, $dt/dx<\mathrm{CFL}$, where CFL is usually smaller than unity. The CFL numbers used in this paper were in the range $0.2<\mathrm{CFL}<0.8$.

The compressor and the turbine were discretized in 20 elements each. The distributions of $r(\xi)$ and $A(\xi)$ were derived from parabolic distributions passing from the middle, inlet, and outlet compressor and turbine dimensions shown in the Appendix. The $\alpha(\xi)$ and $\beta(\xi)$ distributions were derived from the typical distributions for centrifugal components published by Krain and Hoffmann [12]. These distributions are shown in nondimensionalized form in Fig. 4.

The calculation of the instantaneous work is based on the transient control-volume adiabatic bulk-flow energy equation:

$$\delta W_{me}^{i\leftarrow}=d(m^i e_0^i)/dt-(\dot m_{\mathrm{in}}^i h_{0,\mathrm{in}}^i-\dot m_{\mathrm{ot}}^i h_{0,\mathrm{ot}}^i) \tag{5}$$

This equation is applied for each control volume at each time instant. The instantaneous work output for the whole passage is evaluated by summing over the corresponding number of the control volumes:

$$W_{\mathrm{me}}^{\leftarrow}=\sum\,\delta W_{\mathrm{me}}^{i\leftarrow} \tag{6}$$

The above equations give a positive number for a compressor (work addition to the working fluid) and a negative number for a turbine (work extraction from the working fluid).

Heat Exchanger and Radiator Models

These models are similar to those presented in the previous study (Korakianitis, Hochstein and Zou [9]). However, their coupling with the turbomachinery and inertia models to create the overall system model is different. Some critical details for the heat exchanger and radiator models are presented below for completeness.

The steady-state performance of heat exchangers (receiver, regenerator and gas cooler) is evaluated using the design-point effectiveness of the unit and the method of the number of heat transfer units (N_{tu}, Kays and London [13]). The values of ϵ, ratios of specific-heat-capacity rates, and N_{tu} for design-point operation of the receiver, recuperator and gas cooler are given in the Appendix.

In the receiver the salt temperature T_{sl} remains approximately constant during normal operation. However, in the following we are using variations in salt temperature to study system transients. Transients in sink temperature, or a combination of such transients could also be used. The pressure drops in the heat-exchanger passages are modeled as a function of working-fluid properties, flow arrangement, and heat transfer characteristics using models presented in Kays and London [13]. Similarly, the pressure drops in other system ducts are modeled as a function of the local properties in the ducts.

For transient performance the counter-flow and cross-counter-flow heat exchangers are modeled by dividing the control volume into sections along the flow direction, with three elements in each section for fluids *a* and *b* and the wall *w*, as illustrated in Figs. 3 and 4 of the earlier paper (Korakianitis, Hochstein and Zou [9]). Fluid *b* may be flowing in the counter-flow or cross-counter-flow direction with respect to fluid *a*. Steady-flow and transient pressure drops in the receiver and other duct-type passages are modeled as described in the heat exchangers. The recuperator, receiver, and gas cooler are divided into eight elements, while the radiator is divided into ten elements (for each fluid each wall section).

Coupling of the Models

Given the geometry of the components, the state of the system (cycle condition) at any time *t* is prescribed by the combination of $\{T,p,\dot{m}\}$ at all points along the flow path. In the heat-exchanger and radiator models one prescribes the flow conditions at the inlet, and the models return the flow conditions along the flow path in the component, and at the outlet. The turbomachinery models for subsonic flow require two boundary conditions at the inlet, and one boundary condition at the outlet of the component. In the turbine T_{04}, p_{04}, and p_5 are used. In the compressor T_{01}, $\dot{m}_1$, and p_2 are used.

All calculations start from an initial guess for steady-flow conditions, or from previously calculated steady-flow conditions. In order to obtain an initial steady-flow condition, the system is run to convergence (with no driving excitation). The models are called successively for each time step, starting from the turbine, along the direction of working-fluid flow. After each iteration around the closed cycle the conditions are updated, and the process is repeated until a steady-flow condition is achieved (the flow properties at all points do not change with time). Because the initial guess is fictitious (it does not satisfy the governing equations), all intermediate solutions until the steady-flow condition is reached are not realistic states of the cycle. The final steady-flow condition gives the correct distribution of flow properties along the flow path, and the correct total working-fluid mass in the cycle. In the sample transients shown in the following, these initial calculations in search of the initial steady-flow condition occur from $t=0$ to approximately $t=15\,000$ s, and they are not shown in the time traces. When searching for the steady-flow condition, faster convergence is obtained by starting from an initial guess for the state of the system that is reasonably close to the steady-flow solution. Key parameters of the cycle at the steady-state operating point have the values shown in Table 1. The following figures show the time-evolution of various parameters (nondimensionalized with their values at the beginning of the transients, shown in Table 1).

Table 1 Values at the beginning of transients

Variable	Value	Variable	Value
T_{sk}	186.0 K	T_5	837.2 K
T_{sl}	1042.0 K	p_5	189.8 kPa
T_1	275.2 K	T_6	415.5 K
p_1	185.7 kPa	p_6	187.4 kPa
T_2	363.3 K	$\dot{m}$	0.845 kg/s
p_2	351.6 kPa	Ω	3351 rad/s (32,000 rpm)
T_3	794.0 K		
p_3	349.2 kPa	$\dot{W}_t$	76.9 kW
T_4	1007.7 K	$\dot{W}_c$	31.9 kW
p_4	337.9 kPa	$\dot{W}_s$	45.0 kW

Cycle transients can be driven in a variety of ways, such as variations in salt temperature T_{sl}; variations in sink temperature T_{sk}; loss of coolant pumps; loss of some of the radiator panels; and others. Because of the large thermal inertia of the radiator, variations in T_{sk} have small effects on the overall cycle. In the following we show constant-speed/variable-work and variable-speed/prescribed-work transients. These are driven by sinusoidal excitations in T_{sl} of approximately orbital period (90 min), and by double-step excitations in T_{sl}.

For constant-speed transients the inertia of the rotating unit is not needed in the models. For variable-speed operation the dynamic equation of the unit is used to evaluate the instantaneous acceleration:

$$\frac{d}{dt}\left(\frac{J\Omega^2}{2}\right)=\dot{W}_s-\dot{W}_{al}=\dot{W}_t-\dot{W}_c-\dot{W}_{fr}-\dot{W}_{al}\Rightarrow$$
$$\dot{\Omega}=\frac{\dot{W}_t-\dot{W}_c-\dot{W}_{fr}-\dot{W}_{al}}{J\Omega} \tag{7}$$

where for the compressor-alternator-turbine rotating unit $J=23.39\times10^{-6}\ \mathrm{kg\cdot m^2}$. The instantaneous acceleration $\dot{\Omega}$ is integrated in time to give the rotational speed of the unit at the next time instant. The variable-speed model requires that one prescribes the time-variation of alternator work, which can be arbitrary. In the variable-speed sample cases shown below the alternator work was specified as invariant with time, and equal to the alternator work of the steady-flow condition at the beginning of the transient.

Our previous model (Korakianitis, Hochstein and Zou [9]) required iterations at each time step to maintain the correct total working-fluid mass in the cycle. It also imposed very small time-step limits because of the restrictions in the old transient turbomachinery models. The present transient-system model is about six orders of magnitude faster than the previous transient one. Two factors contribute to this dramatic reduction in computational time. The first is that the present turbomachinery models are far more stable, and permit much larger time steps. The second is that the new model does not require an iteration for the working-fluid mass, because it maintains by default the correct mass throughout the time integrations. This is achieved automatically due to the upstream-downstream linking of flow properties in the turbomachinery models. The above was verified by monitoring the working-fluid mass in the cycle throughout the following transients.

Discussion of Sample Transients

Sample transients starting from an initial steady-flow condition have been excited by sinusoidal variations in T_{sl} of period 90 min (approximately orbital period); and double-step variations in T_{sl}. In the latter T_{sl} is increased by a certain amount at a given time instant, and later T_{sl} is decreased to its original value, so that the final steady-flow condition is identical to the initial one. In the transient figures turbine values are shown as solid lines, compre-

Table 2 Legend for the lines used in the transient figures

Variable	Value
	turbine
	compressor
	shaft

sor transients are shown as longer dashed lines, and the resultant shaft transients are shown as shorter dashed lines (Table 2)

Figure 5 illustrates the results of the first sample case. This is a constant-speed/variable-work system response to a 15% sinusoidal transient in T_{sl} for six periods, starting at $t=20\,000$ s from the steady-state condition. The responses are all periodic, after the initial three or so periods, at the driving period. After the initial disturbance in T_{sl} there is an initial time lag from T_{sl} to T_4 due to the thermal inertia of the receiver. Then there is a second smaller time lag from T_4 to T_5 as the disturbance travels through the turbine. Similarly, there are consecutive time lags from component to component as the disturbance propagates in the flow path. Changes in $\{T_4,p_4,\dot{m}_4\}$ are followed by changes in $\{T_5,p_5,\dot{m}_5\}$ a short time later. This disturbance then propagates in the low-pressure side of the recuperator (6-1), and at the same time they affect the high-pressure side of the recuperator, so that disturbances are initiated at $\{T_2,p_2,\dot{m}_2\}$ and $\{T_3,p_3,\dot{m}_3\}$. These become new, secondary sources of disturbance, starting at points 2 and 3, and affecting the cycle both upstream and downstream. Meanwhile the initial disturbance that had reached point 1, after a short delay passes through the compressor (point 2), and reaches the high-pressure side of the recuperator. This disturbance in $\{T_2,p_2,\dot{m}_2\}$ becomes a tertiary source of disturbance that affects the properties at points 3, 5, and 6. Such disturbances are initiated and propagate through the components repeatedly throughout any system transient, resulting in smaller, higher-frequency disturbances affecting every system transient.

As indicated by the insert in the temperature response of Fig. 5, there is a time lag between the responses at compressor and turbine outlet. The turbine responds first, while the thermal disturbance travels through the rest of the components and reaches the compressor outlet approximately 100 s later. Expansion disturbances travel faster, at the local fluid velocity minus the local acoustic velocity through the components. Compression disturbances travel even faster, at the local fluid velocity plus the local acoustic velocity through the components. The temperature disturbances are much slower than the pressure disturbances due to the large thermal inertia of the heat exchangers.

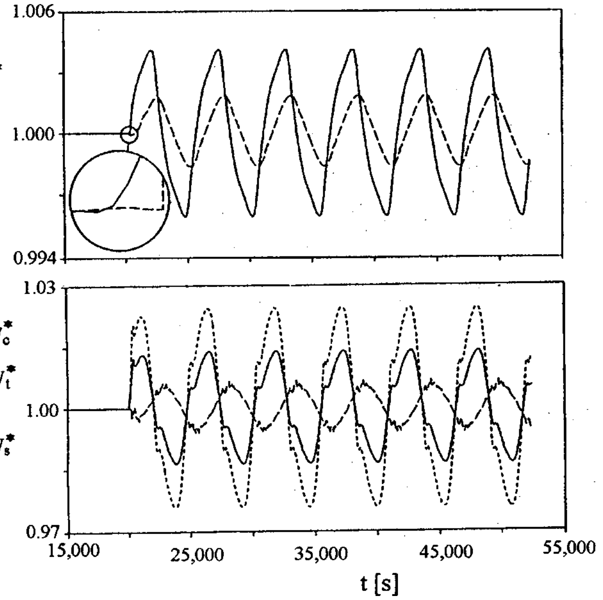

Fig. 5 First sample case. System response with constant-speed/variable-work model to 15% sinusoidal variation in T_{sl}. Table 2 identifies the different line types used in the figure.

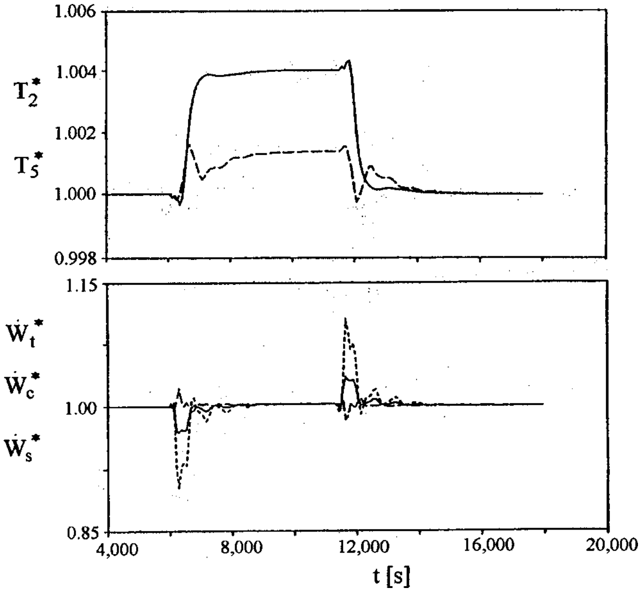

Fig. 6 Second sample case. System response with constant-speed/variable-work model to 15% double-step variation in T_{sl}. Table 2 identifies the different line types used in the figure.

Although all the responses in $\{T,p,\dot{m}\}$ shown in Fig. 5 are periodic after the initial three or so periods, and the period is the same as the sinusoidal driving period in T_{sl}, they contain higher-frequency contents of much smaller amplitudes than the fundamental. The higher-frequency contents are generated by the primary, secondary, tertiary, and so on disturbances in flow properties, generated and traveling as explained above.

The shaft work $\dot{W}_s$ shown in Fig. 5 is the turbine work $\dot{W}_t$ minus the compressor work $\dot{W}_c$. The temperature delays due to the thermal inertia in the heat exchangers generate periodic variations in $\dot{W}_t$ and $\dot{W}_c$ that are almost out of phase, thus generating large periodic variations in $\dot{W}_s$. The exact relation between the phases in compressor and turbine work is a function of the size of the cycle components, and it depends on the characteristics of the driving excitation. (For example in the variable-speed sample cases shown below the compressor and turbine work are almost in phase).

Figure 6 illustrates the results of the second sample case. This is a constant-speed/variable-work system response to a 15% double-step transient in T_{sl}, starting at t=6000 s from the steady-state condition. The 90-min interval between the two steps corresponds to 5400 s. Approximately 4000 s after the first step (at t≈10 000 s) the system approaches a new steady state. Approximately 4000 s after the end of the second step (at t≈15 400 s), the system approaches the initial steady state. The initial high-amplitude responses in flow properties immediately after the steps are followed by smaller-amplitude variations caused by the secondary and tertiary disturbance-propagation effects (explained in the first sample case). Since the amplitude of the driving disturbances in T_{sl} in the first and second sample cases are the same, the corresponding amplitudes of responses in flow properties in the two cases are about the same. In the first sample case the time derivatives of the driving disturbance were smooth, but in the second sample case they are very large. This introduces higher-amplitude higher-frequency contents in the exciting disturbance and in the

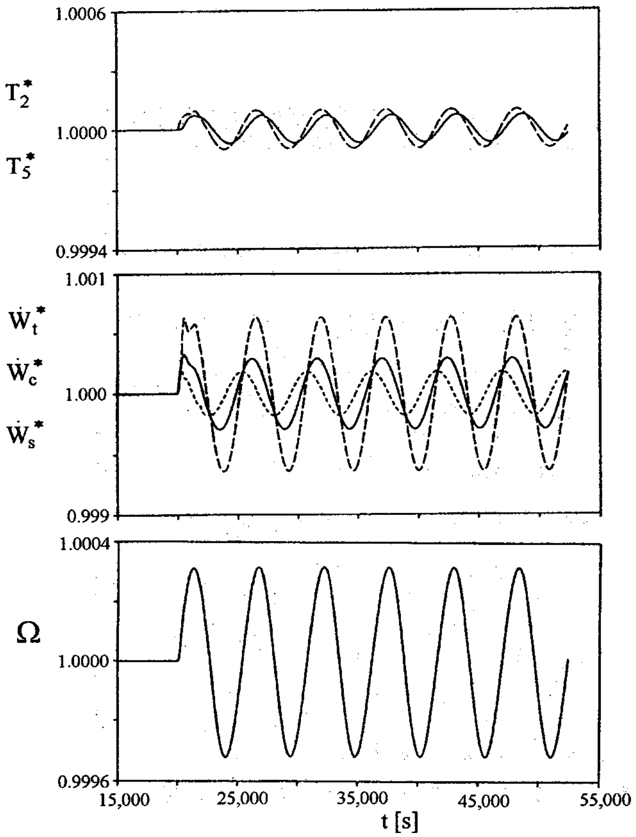

Fig. 7 Third sample case. System response with variable-speed/constant-alternator-work model to 0.5% sinusoidal variation in T_{sl}. Table 2 identifies the different line types used in the figure.

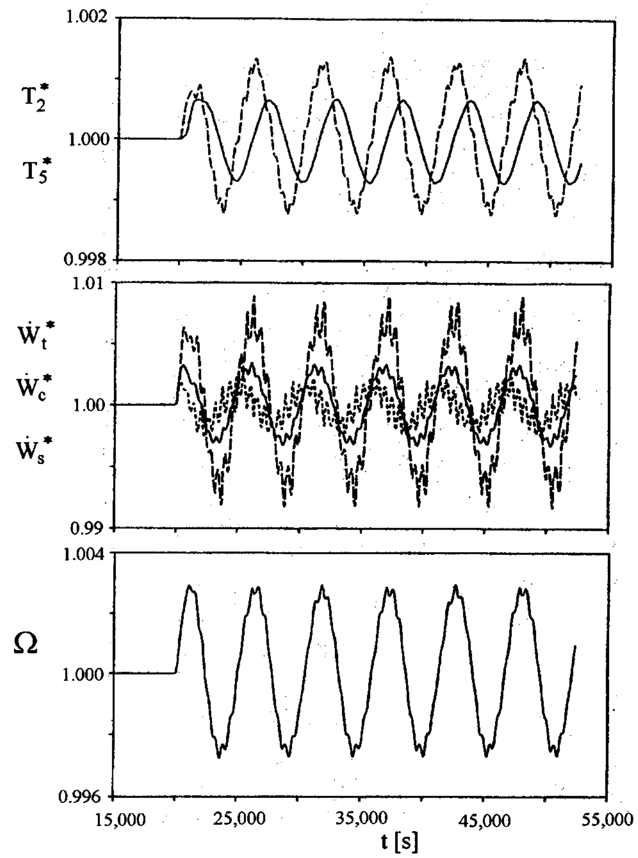

Fig. 8 Fourth sample case. System response with variable-speed/constant-alternator-work model to 5% sinusoidal variation in T_{sl}. Table 2 identifies the different line types used in the figure.

system response. This has two effects. First, it enlarges the response due to expansion and compression waves. Second, it enlarges the response due to the secondary and tertiary disturbance amplitudes. The overall effect of the higher-amplitude higher-frequency contents is shown in the pressure and work responses in Fig. 6.

The turbine is the component immediately after the excitation in T_{sl}, but the high-pressure side of the recuperator is between the compressor outlet and the excitation in T_{sl}. Therefore in all constant-speed/variable-work cases the response in T_5 has a higher amplitude than the response in T_2.

In the variable-speed cases the changes in shaft speed are additional sources of disturbances, upstream and downstream for the compressor and the turbine responses. This creates high-frequency contents in the responses of the variable-speed cases in addition to the primary, secondary, and tertiary effects explained in the sinusoidal cases.

Figure 7 illustrates the results of the third sample case. This is a variable-speed/constant-alternator-work system response to a 0.5% sinusoidal transient in T_{sl}, for six periods starting at $t = 20\,000$ s from the steady-state condition. In this case the driving excitation has a small amplitude, the secondary and tertiary effects are much smaller, and the higher-frequency contents are not as evident as in the first two sample cases. The exception to this observation is at the beginning of the first excitation period, for two reasons. The dominant reason is that in the steady-flow condition the shaft speed has no time derivatives, while the beginning of the transient introduces a finite change in the time-derivatives in the shaft speed. This introduces initial large secondary and tertiary disturbance effects, as explained in the above paragraph. A lesser reason is the effect of the same changes in time derivatives in flow properties at the beginning of the transient. In this case the response in shaft speed is almost sinusoidal, and the higher-frequency contents in shaft speed are not visible. The almost-sinusoidal changes in shaft speed are such that they put the sinusoidal variations in compressor work almost in phase with the sinusoidal variations in turbine work, so that the resultant sinusoidal variation in shaft work is small.

Figure 8 illustrates the results of the fourth sample case. This is a variable-speed/constant-alternator-work system response to a 5% sinusoidal transient in T_{sl}, for six periods starting at $t = 20\,000$ s from the steady-state condition. The amplitude of the driving excitation is an order of magnitude larger than that of the third case. The larger amplitude of the excitation makes the effects of shaft speed changes, as well as the primary, secondary, and tertiary effects of disturbance propagation much more pronounced than in the third case. The result is a significant high-frequency fluctuation in all flow properties, but the fundamental harmonic of the responses is still sinusoidal and at the period of the driving excitation in T_{sl}. Unlike the third case, the variations in shaft speed show the high-frequency effects of disturbance propagation. Similarly to the third case, the fundamental-harmonic changes in shaft speed are such that they put the fundamental-harmonic variations in compressor work almost in phase with the fundamental-harmonic variations in turbine work. The resultant variation in shaft work contains high-frequency contents, but the fundamental-harmonic variation is still small.

Figure 9 illustrates the results of the fifth sample case. This is a variable-speed/constant-alternator-work system response to a 5% double-step transient in T_{sl}, starting at $t = 20\,000$ s from the steady-state condition. In contrast to the second case, the 90-min orbital period was not sufficient for the system to reach a new steady state after each step. This delay in reaching a steady state is

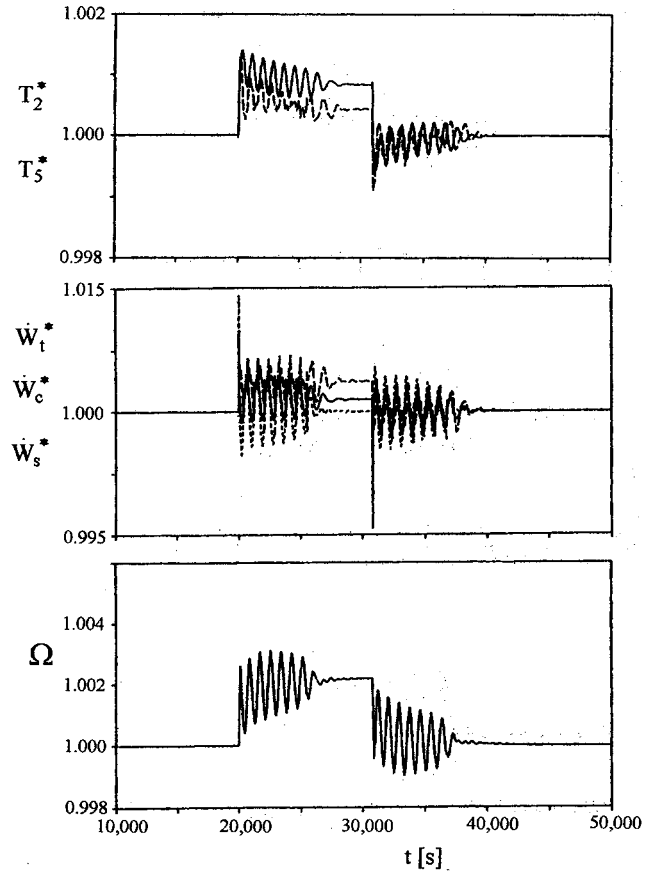

Fig. 9 Fifth sample case. System response with variable-speed/constant-alternator-work model to 5% double-step variation in T_{sl}. Table 2 identifies the different line types used in the figure.

due to the changes in shaft speed. The time interval between the two steps was increased to 180 min, or 10 800 s. Approximately 10 000 s after the first step (at $t \approx 30\,000$ s) the system approaches a new steady state. The second step occurs at $t = 30\,800$ s. Approximately 10 000 s after the end of the second step (at $t \approx 40\,800$ s) the system approaches the initial steady state. The initial high-amplitude responses in flow properties immediately after the steps are followed by decaying amplitude variations. These are caused by the corresponding variations in shaft speed required to achieve constant alternator work. Secondary and tertiary disturbance-propagation effects of smaller amplitude are evident throughout the transient. Similarly to the third and fourth cases, the changes in shaft speed are such that they put the variations in compressor work almost in phase with the variations in turbine work. The resultant variation in shaft work contains high-frequency contents, but the overall variation is small.

Figure 10 shows a comparison of a variable-speed/constant-alternator-work to a constant-speed/variable-work case. The former is identical to case four. The latter is a system response to a 5% sinusoidal transient in T_{sl}, for six periods starting at $t = 20\,000$ s from the steady-state condition. (These two cases are driven by the same excitation.) The variations in compressor work for the constant-speed case are almost out of phase with the variations in compressor work for the variable-speed case, and the amplitudes are of the same order. The variations in turbine work for the constant-speed case are almost in phase with the variations in turbine work for the variable-speed case, but the amplitudes differ by a factor of 5. As a result, the fundamental amplitude of the variations in shaft work are much smaller in the variable-speed case than those in the constant-speed case, by an order of magnitude. The response of the variable-speed case has significantly higher-frequency contents than the constant-speed case. This is due to the additional disturbance effects due to the changes in shaft speed, as explained above.

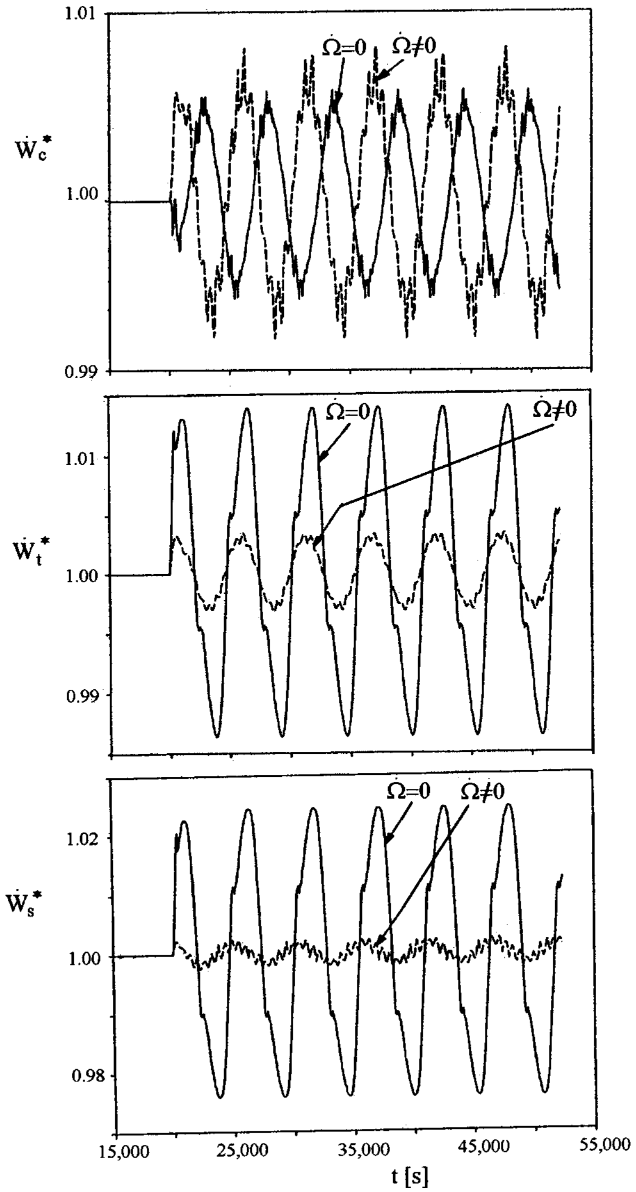

Fig. 10 A comparison of constant-speed/variable-work model with variable-speed/constant-alternator-work model to 5% sinusoidal variation in T_{sl}

Conclusions

New steady-state and transient models suitable for predicting the behavior of centrifugal (and mixed-flow and axial) turbomachinery components have been developed. These are coupled to steady-state and transient models suitable for predicting the performance of heat exchangers and radiators. The component models are based on the transient form of conservation of mass, energy and momentum within each component. These component models have been coupled to simulate a closed-cycle regenerative gas-turbine cycle, whose components are similar to those under consideration for the powering unit of the Space Station. Various system transients have been studied. For illustration, transients driven by step and sinusoidal variations in eutectic salt temperature (variations in energy input to the cycle), and under constant and varying shaft speed, have been included. In gas-turbine cycles with heat exchangers the long thermal-response times of the heat exchangers dominates the turbomachinery response.

The numerical models for the transient turbomachinery are inherently stable, permitting fast computations for large-amplitude disturbances for the individual components and for the overall cycle. They also permit a physically correct coupling with the transient models for the heat exchangers and the radiator. This predicts correctly the upstream and downstream propagation of disturbances from the point where they were introduced. The coupling of the disturbances in the low-pressure and high-pressure streams of the recuperator is a source of secondary and tertiary disturbance generation, which introduces low-amplitude high-frequency content in the overall system response. The higher-frequency content is more pronounced in cases of higher derivatives in the time evolution of the excitation. Variations in shaft speed are an additional source of disturbances. These add higher-frequency content in the overall cycle response, and affect both the phases and the amplitudes of the flow properties at every point in the cycle. As a result the relative phase of the compressor and turbine work is affected by the size of the components in the cycle, and by the relationship between shaft speed and alternator work. Variations in the overall cycle work may be enhanced or damped, depending on these relative phases and amplitudes. In the constant-speed cases shown in this paper the compressor and turbine work were almost out of phase, giving relatively large variations in overall cycle work. In the variable-speed cases shown in this paper the compressor and turbine work were almost in phase, giving smaller variations in overall cycle work.

Appendix: Description of Components

(Note that the components of the Space Station were under development at the time of writing.) The following information was used to produce the results shown in this study. The receiver has 82 tubes of Haynes 188 steel of outlet diameter 22.2 mm and active tube length 2.5 m. At design-point receiver operation $\epsilon=0.8730$, $N_{tu}=2.0635$, and $C_{\min}/C_{\max}=0.0000$. The recuperator is a pure counterflow plate-fin unit of length 0.37 m, width 0.32 m, and height 0.49 m. The high-pressure side has 62 sandwiches of fins, with 630 (0.15 mm thick) CRES 304L fins per m, with height 3.2 mm. The low-pressure side has 63 sandwiches of fins, with 630 (0.15 mm thick) CRES 304L fins per m, with height 3.9 mm. At design-point recuperator operation $\epsilon=0.9404$, $N_{tu}=15.7763$, and $C_{\min}/C_{\max}=1.0000$. The gas cooler is an eight-pass cross-counterflow plate-fin heat exchanger. The fin sandwiches are rectangular offset, 2.3 mm high. The gas side has 470 (0.15 mm thick) CRES 304L fins per m, with height 2.3 mm. The liquid side has 790 (0.15 mm thick) CRES 304L fins per m, with height 1.9 mm. At design-point gas-cooler operation $\epsilon=0.9430$, $N_{tu}=6.4501$, and $C_{\min}/C_{\max}=0.7428$. The radiator has 8 aluminum 2.3 m×8.0 m panels. Key turbomachinery parameters are shown in Table 3.

Table 3

Variable	Value
V_c	60×10^{-6} m^3
$r_{c,\mathrm{tp}}$	0.065 m
$r_{c,m}$	0.037 m
$A_{c,\mathrm{in}}$	3.60×10^{-3} m^2
$A_{c,m}$	3.05×10^{-3} m^2
$A_{c,\mathrm{ot}}$	2.50×10^{-3} m^2
V_t	100×10^{-6} m^3
$r_{t,\mathrm{tp}}$	0.095 m
$r_{t,m}$	0.053 m
$A_{t,\mathrm{in}}$	4.00×10^{-3} m^2
$A_{t,m}$	5.06×10^{-3} m^2
$A_{t,\mathrm{ot}}$	5.65×10^{-3} m^2

Nomenclature

A = Area
c = specific heat capacity
C = heat capacity rate $C\equiv\dot{m}c_p$
D = diameter of a component
e_R = rotating total energy per unit mass
f = force per unit mass
h = heat-transfer coefficient
I = linear momentum
J = rotating-unit inertia
k = heat conductivity of the wall
L = length of a component
m = mass
N_{tu} = number of heat transfer units
p = pressure
Q = energy transferred as heat
r = radius
R = (universal gas constant)/(molecular weight)
t = time
T = temperature
U = absolute flow velocity
V = volume
W, $\dot{W}$ = work, power
w = relative velocity in the ξ direction
x, y, z = Cartesian stationary coordinate system
α = passage angle from axial direction (Fig. 2)
β = blade angle from meridional direction (Fig. 2)
ϵ = heat-exchanger effectiveness
σ = (emissivity)×(Stefan-Boltzmann constant)
r, θ, ζ = cylindrical stationary coordinate system
ξ, η, ζ = rotating coordinate system in the impeller
Ω = angular velocity

Subscripts

0 = total property
1, 2, . . . ,6 = thermodynamic-cycle points
a, b = working fluids in heat exchangers
al = input to alternator shaft
c = compressor
cv = control volume
cd = cold fluid
fr = friction
ht = hot fluid
i = element counter in difference equations
in = into component
m = mean
me = mechanical
max = maximum
min = minimum
ot = out of component
p = at constant pressure (c_p)
r = radiation
s = shaft power to alternator
sk = sink (temperature)
sl = eutectic salt (temperature)
t = turbine
tp = impeller tip
v = at constant volume (c_v)
w = wall
x, y = Cartesian directions

Superscripts

n = counter in time-difference equations
′-″ = primary and secondary coolant loops
* = nondimensional quantity

References

[1] Moody, F. J., 1990, *Introduction to Unsteady Thermofluid Mechanics*, Wiley, New York.

[2] Kuhlberg, J. F., Sheppard, D. E., King, E. O., and Baker, J. R., 1969, ‘‘The Dynamic Simulation of Turbine Engine Compressors,’’ AIAA Paper No. 69-486.

[3] Kalnitsky, K. C., and Kwatny, H. G., 1981, ‘‘A First Principles Model for Steam Turbine Control Analysis,’’ ASME J. Dyn. Syst., Meas., Control, **103**, pp. 61–68.

[4] Adams, J., Clark, D. R., Louis, J. R., and Spanbauer, J. P., 1965, ‘‘Mathematical Modeling of Once-Through Boiler Dynamics,’’ Trans. IEEE, Power Apparatus Syst., **84**, pp. 146–156.

[5] Corbett, A. G., and Elder, R. L., 1974, ‘‘Stability of an Axial Flow Compressor With Steady Inlet Conditions,’’ J. Mech. Eng. Sci., **16**, pp. 377–385.

[6] Macdougal, I., and Elder, R. L., 1983, ‘‘Simulation of Centrifugal Compressor Transient Performance for Process Plant Applications,’’ ASME J. Eng. Power, **105**, pp. 885–890.

[7] Ray, A., and Bowman, H. F., 1976, ‘‘A Nonlinear Dynamic Model of a Once-Through Subcritical Steam Generator,’’ ASME J. Dyn. Syst., Meas., Control, **98**, pp. 332–339.

[8] Fink, D. A., Cumpsty, N. A., and Greitzer, E. M., 1992, ‘‘Surge Dynamics in a Free-Spool Centrifugal Compressor System,’’ ASME J. Turbomach., **114**, pp. 321–332.

[9] Korakianitis, T., Hochstein, J. I., and Zou, D., 1993, ‘‘Prediction of the Transient Thermodynamic Response of a Closed-Cycle Regenerative Gas Turbine,’’ ASME J. of Turbomach. (in press), ASME Paper No. 93-GT-136.

[10] Rocketdyne, 1986, ‘‘Space Station Work Package WP-04 Power System Preliminary Analysis and Design Document,’’ Rocketdyne RI/RD85-320-2, December.

[11] Rocketdyne, 1989, ‘‘Allied-Signal Interim Design Review for the CBC/PGS for the NASA Space Station Freedom,’’ Rocketdyne Report No. 41-9311, November.

[12] Krain, H., and Hoffmann, W., 1989, ‘‘Centrifugal Impeller Geometry and its Influence on Secondary Flows,’’ in AGARD Conference Proceedings CP-469 ‘‘Secondary Flows in Turbomachines.’’

[13] Kays, W. M., and London, A. L., 1984, *Compact Heat Exchangers*, McGraw-Hill, New York.

Adapting the Micro-Gas Turbine Operation to Variable Thermal and Electrical Requirements

Fabio Bozza
Maria Cristina Cameretti
Raffaele Tuccillo

Dipartimento di Ingegneria Meccanica per
l'Energetica (D.I.M.E.),
Università di Napoli Federico II,
Via Claudio 21,
80125 Napoli, Italy

This paper examines the possibilities for a micro-gas turbine operation under a wide range of thermal and mechanical load requirements. The authors focus the attention on a partially recuperated thermal cycle based on a by-pass option towards the heat recovery boiler, in order to adapt the gas turbine operation to increasing needs of thermal output. In addition, a variable speed operation is considered as a more reliable method for decreasing the mechanical output without producing an excess in efficiency decay. The actual possibilities of the above-named regulation tools are examined by an integrated procedure which involves, besides an accurate thermodynamic preliminary analysis, the component matching study and the CFD based simulation of the combustion chamber. [DOI: 10.1115/1.1806839]

Introduction

The increasing interest in the micro-gas turbine utilization for cogenerating applications [1–9] solicits the researchers to define the most effective systems for ensuring its satisfactory operation within a wide range of operating conditions. As it is well established, the competitiveness of this machine is mainly based on the possibility of both adopting a great variety of gaseous and liquid fuels and meeting several requirements in terms of thermal to power output ratios.

On the other hand, the most up-to-dated technical trends indicate that an efficient baseline configuration of the micro-gas turbine must mandatorily make use of recuperated cycles [5,8], in order to compensate the lower firing temperature and pressure ratio levels, compared with those of large-scale gas turbines.

The simultaneous presence of the recuperating heat exchanger and of the heat recovery boiler suggests an interesting way for complying with several requirements of electrical and thermal output from the plant. In other words, an appropriate sharing of the exhaust gas flows either to the recuperator or directly to the boiler may lead to a "partially recuperated" cycle with different rates of available heat in the gas turbine exhausts.

The purpose of the present work is, first, to verify the effectiveness of this idea by an energetic point of view, by examining the extent of the range of thermal and electrical requirements which can be fulfilled by this method and the related energy saving indices. Next, the authors will deal with the most challenging problem of checking the practical adaptability of the single plant components to each modified operating conditions.

Really, a turbine off-design condition is induced by the modified firing temperature level and, similarly, the compressor itself can be involved in stall or choking limits. This aspect will be verified through an authors' methodology which includes the compressor and turbine matching in the cycle analysis [10,11], the latter referring both to conventional and to low LHV fuels obtained by bio-mass [2] or solid waste gasification [6].

Finally, particular care will be addressed to the study of combustor off-design conditions. The proposed regulation method produces significant changes in the air inlet temperature and in the fuel-to-air ratio, both parameters affecting the actual flammability limits and combustion development. This aspect will be examined through a CFD analysis [12–16] whose main inputs are provided by the above described cycle calculation. The combustor simulation, also including the pollutant prediction, will therefore provide the ultimate information about the practical application of the proposed regulation method for the micro-GT based cogenerating plant.

Micro-Gas Turbine Features

Although the typical micro-gas turbine applications cover a wide range of mechanical output [1–9], the example discussed in this paper refers to a MGT of the 100 kW class, whose specifications are given in Table 1. As it is well known from the recent technical literature, a recuperated cycle is necessary to meet the requirements of an acceptable thermal efficiency, due to the reduced values of the main cycle parameters, i.e., the pressure ratio and the turbine inlet temperature. The first one is chiefly related to the actual possibilities of radial turbomachines which are often derived from the turbocharger technology [1], while the second one ensures a reliable operation without adopting a turbine blade cooling system.

In addition, the attractiveness of these devices is strongly dependent on the possibility of burning different fuels, like those obtained by either bio-mass [2] or solid waste [6] gasification as an alternate choice to the classical natural gas employment. The fuel characteristics considered in the following are given in Table 2, where the symbols BIOM(o) and BIOM(a) designate bio-mass fuels obtained by oxygen and air based gasification processes, respectively. The solid waste (SW) fuel is obtained from an oxygen based pyrolisis [6] and the resulting composition is fairly similar to that of the BIOM(o) fuel. In both cases a relevant hydrogen content is present and the consequent adiabatic flame temperature, T_{0f}, is higher than in the natural gas case. On the contrary, the BIOM(a) fuel is characterized by a dramatic percentage of inert species which explain both the low LHV level and the high value of the fuel/air stoichiometric ratio.

Finally, the interest in the MGT is increased by the possibility of exploiting the residual thermal energy in the exhausts [9]. Like in all co-generating applications, a good plant flexibility is considered to be a base tool for satisfying different thermal to mechanical load ratios. The authors' proposal is based upon the option represented in Fig. 1, which displays the baseline MGT layout with the possibility of splitting the exhaust mass flow either to the recuperator or directly to the heat recovery boiler inlet, according to the by-pass ratio:

Contributed by the International Gas Turbine Institute (IGTI) of THE AMERICAN SOCIETY OF MECHANICAL ENGINEERS for publication in the ASME JOURNAL OF ENGINEERING FOR GAS TURBINES AND POWER. Paper presented at the International Gas Turbine and Aeroengine Congress and Exhibition, Atlanta, GA, June 16–19, 2003, Paper No. 2003-GT-38652. Manuscript received by IGTI, October 2002, final revision, March 2003. Associate Editor: H. R. Simmons.

Table 1 Base features of the micro-gas turbine (MGT)

	Micro-GT specifications
Mechanical arrangement	Single shaft
Pressure ratio	3.9
Turbine inlet temperature	1223 K
Rated mechanical output/speed	110 kW/64000 rpm
Compressor	1 Radial flow compressor
Turbines	1 radial flow turbine

Table 2 Natural gas and gaseous fuels from bio-mass and solid waste gasification composition and properties

Fuel composition (%, molar)	Natural gas (NG)	BIOM(o)	BIOM(a)	SW
CH_4	**92.00**	**18.00**	**9.00**	**7.00**
C_2H_6	3.70	2.00	⋯	7.00
C_3H_8	1.00	2.00	⋯	7.00
C_4H_{10}	0.25	2.00	⋯	⋯
N_2	2.90	8.00	56.00	⋯
H_2	⋯	**25.00**	**9.00**	**18.00**
CO	⋯	33.00	12.00	61.00
CO_2	0.15	10.00	20.00	⋯
H_2O	⋯	⋯	⋯	⋯
Mol. mass, g/mol	17.34	21.92	28.51	23.76
LHV (kJ/kg)	47 182	19198	2798	21697
h_{0f} (kJ/kg)	−4266.9	−3720.1	−1649.5	−2923.9
f_{st}	0.0620	0.1680	1.257	0.1530
T_{of} (K)	2220	2231	1571	2300

$$X_b = 1 - \frac{\dot{m}_{g,R}}{\dot{m}_g} \qquad (1)$$

where $X_b=0$ leads to a fully recuperated cycle, while $X_b>0$ increases the amount of thermal output for district or industrial heating. In the latter case, the fuel mass flow rate, $\dot{m}_f$, must be obviously raised to maintain the same level of $T.I.T.$

A preliminary thermodynamic analysis will put into evidence the expected performance parameters of the co-generating plant but the following sections will also employ a more deepened methodology aiming to check the actual operating conditions of the several components which are induced by the different options outlined before, namely the following:

- The adoption of different fuels produces changes in the mass flow rate through the turbine, so that the matching conditions of the rotating devices are altered.
- Similarly, part load conditions must be investigated, together with the activation of the recuperator by-pass option. In addition, a more interesting perspective is offered by the employment of a variable-frequency electric generator [7] which could allow an extension of the range of both thermal and mechanical requirements which can be satisfied. In this case, the gear-box in Fig. 1 could be replaced by a direct-drive connection.
- Combustor off-design conditions are induced both by the changes in the fuel supplied and by the actual recuperator effectiveness in all cases with $X_b>0$. These are characterized by a decrease in the air temperature at combustor inlet and therefore the combustion effectiveness must be investigated, together with the variations in both flammability limits and self-ignition conditions.

Methods for Gas Turbine Plant Analysis

The plant and component analysis is carried out through a number of steps of increasing deepening, namely the following.

Thermal Cycle Analysis. The study of the thermodynamic processes that take place through the several plant components in accordance with the layout in Fig. 1 relies on an accurate model based on the following

- Evaluation of the thermochemical equilibrium of the species involved in the several processes and originating from the combustion of the different fuels in Table 1. Gas composition and thermodynamic properties are calculated by accessing the JANAF tables [17].
- Recuperator efficiency and related pressure losses are computed as a function of the actual gas flow rate through this device. This last parameter is moreover affected by power output, fuel composition, and by-pass ratio. A typical efficiency profile is displayed in Fig. 2 as a function of the gas/air flow rate ratio [8]. The laminar gas flow regime through the several passages is responsible for the effectiveness decrease when the nondimensional flow rate increases [4,8]. Nevertheless, for a very reduced flow rate an opposite behavior is expected [8] as a consequence of relevant off design operation of the device. Figure 2 also reports the operating points expected at rated power output and zero by-pass, for both natural gas and the low LHV biomass fuel. A linear variation of pressure losses is also specified as a function of the nondimensional gas flow rate.

A reliable preliminary prediction of the gas turbine performance is therefore allowed, in order to estimate the potential of several solutions in terms of the fuel adopted or of the by-pass option

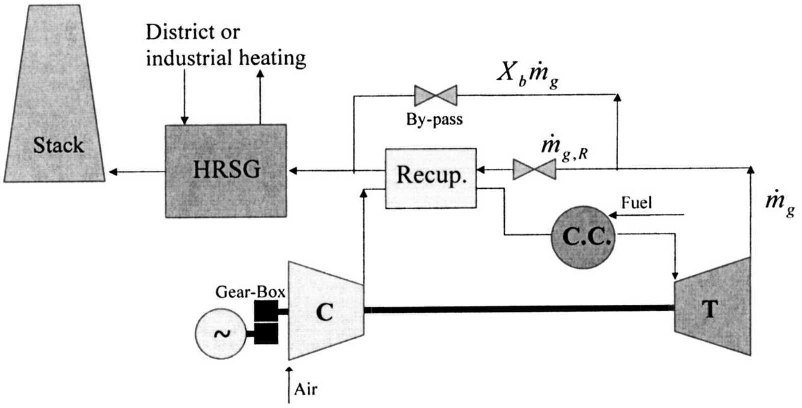

Fig. 1 Schematics of micro-gas turbine integrated with devices for recuperated cycle and heat recovery

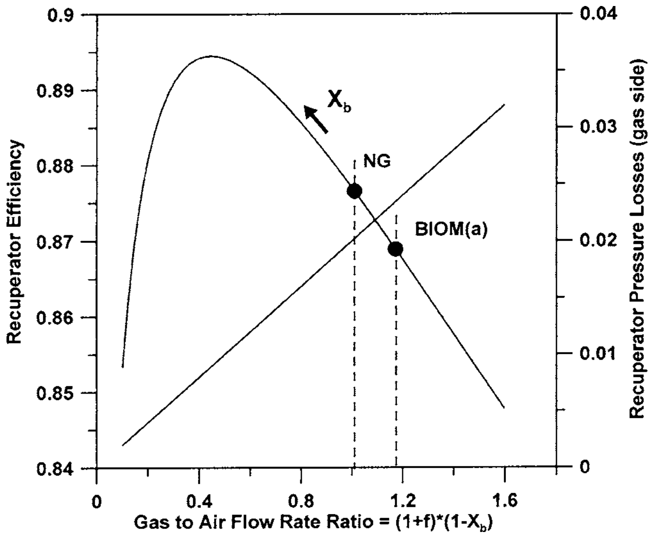

Fig. 2 Effect of nondimensional flow rate on recuperator effectiveness and pressure losses

activation. Such profiles are also employed within the component matching procedure, and a different effectiveness and pressure loss can be evaluated at each load level of the MGT.

Thermo-Kinetic NO Model. The kinetic equations which describe the mechanism of thermal NO formation [11,18,19] are solved in the residence time domain by updating both local temperatures and species concentrations through chemical equilibrium calculations. In this way, the method [19], which is included in the thermodynamic analysis, is sensitive to a number of key parameters, like

- the overall residence time of the reactants and products through the combustion chamber;
- the time and mass flow rate sharing in the combustor regions (i.e., primary, secondary and dilution zones); and
- the steam concentration (if any) in the oxidant or the amount of water or steam injected into the primary zone.

The comparison with experiments has demonstrated that the model leads to an effective prediction of actual emission data, provided that a good calibration of the above parameters is performed [11]. To this purpose a CFD based analysis, as the one discussed in the following, may represent a reliable identification tool.

Component Matching Analysis. This approach is of particular interest when dealing with off design conditions induced by either thermal or mechanical load variations. Moreover, the component operation is affected by changes in the type of fuel injected or in the by-pass ratio. Thus the matching analysis allows a more realistic estimation of actual variations which can be expected in plant performances and emissions. In addition, this step provides more accurate inputs to the detailed fluid-dynamic analysis of the combustion chamber, as described at the following step.

A typical matching procedure among the rotating and stationary components leads to the estimation of the whole operating domain of the plant [11,16,20]. The latter is determined under the hypothesis of the application of a variable speed load [6,9]. The off-design computation proceeds with a direct access to the radial flow turbine and compressor maps (Figs. 3 and 4). The recuperator characteristics in Fig. 2 are also accessed at each load level. The operating domain (Figs. 4–6) is bounded by both turbomachinery limitations (i.e., compressor stall or choking, turbine choking, etc.) and by functional considerations (maximum allowable turbine inlet temperature, shaft speed, power output, etc.).

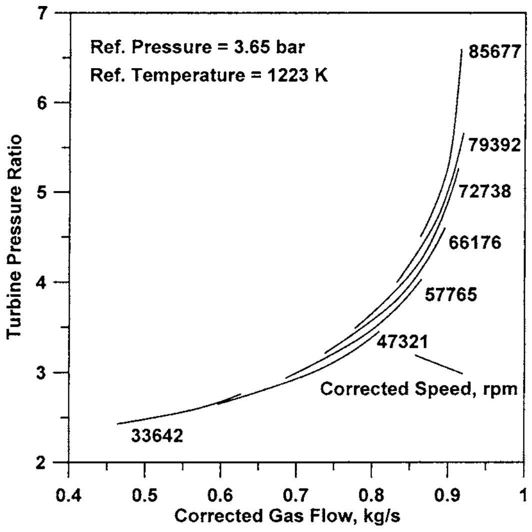

Fig. 3 Characteristics of the radial turbine of the MGT

The level of by-pass ratio can also change the extent of the operating domain, as shown in Fig. 5. More remarkable modifications are expected in the case of low-LHV fuel injection, as a consequence of the increased mass flow through the turbine. Each point inside such domains satisfies the closure conditions of the matching problem (i.e., the discharge pressure must be equal to the ambient pressure increased by the pressure losses through the heat recovery devices end the stack) and therefore represents a possible operating condition for the plant. The design point location is also marked in Fig. 5.

The iso-contours of each parameter defining the thermal cycle can be finally drawn inside the matching domain. As an example, Fig. 6 shows the levels of the pressure loss inside the HRSG derived from the recuperator characteristics in Fig. 2. The latter is mainly a function of the exhaust flow rate, basically dependent on the turbine speed, as expected.

CFD Analysis of the Combustion Chamber. The simulation of the reacting flows employs the widely known *KIVA3V* code [21,22] which has been expressly adapted by the authors to this purpose [10,11,16]. A full combustion simulation is developed, including the flow through the liner, for a better evaluation of both

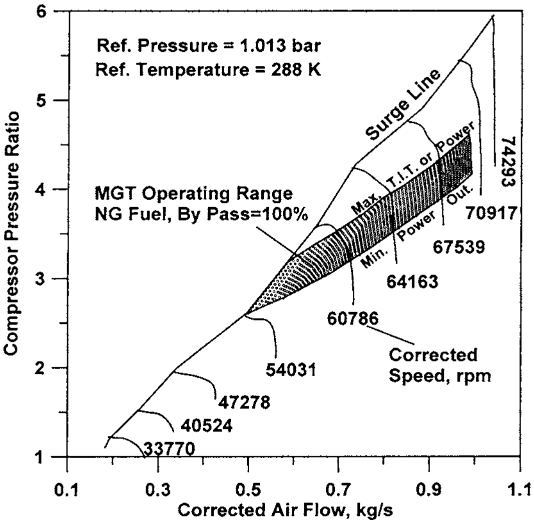

Fig. 4 MGT operating range superimposed on the compressor characteristics

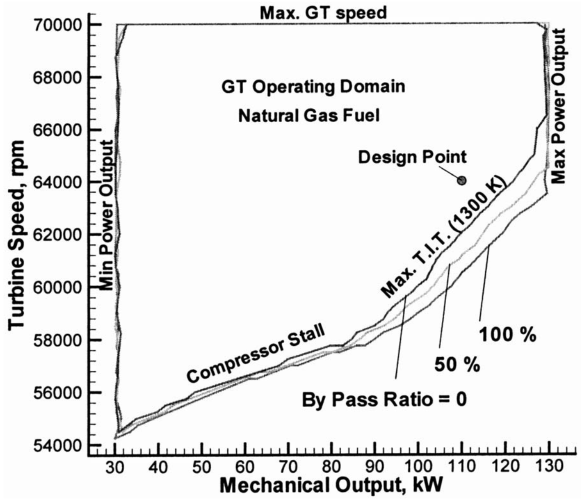

Fig. 5 Typical MGT operating domains at various by-pass levels

the air flow rate splitting between the several combustor regions and the flow conditions through secondary and dilution holes [23].

As a first application of the CFD simulation to a MGT combustion chamber, the authors have selected an annular combustor geometry which was already tested in previous works [11,16]. The adaptation to the new gas turbine size was made by scaling the original combustor in both span-wise and azimuthal directions and by maintaining the chamber length. The first choice ensures almost the same velocity levels as in the original combustor (which equips an aero-derivative gas turbine of the 20 MW class) while the latter allows preservation of the same order of magnitude for the residence times.

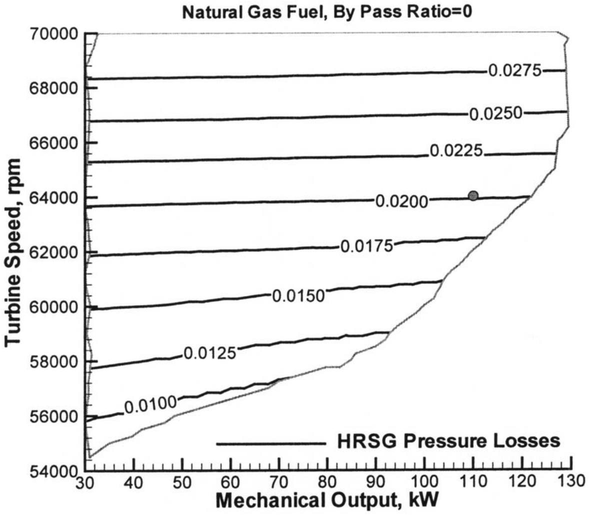

Fig. 6 Iso-contours of HRSG pressure losses inside the MGT operating domain

The resulting scaled height and average diameter are of about 4 and 10 cm and these values correctly fit the typical compressor and turbine sizes for this application. The authors' choice must be intended, however, as a first attempt to simulate the combustion in a MGT chamber by following their previous experiences. An appropriate definition of the actual combustor geometry should at least consider a comparison between the annular and the tubular type. For example, the latter configuration could be more correct for connecting the flows from the recuperator, while the first one could allow a direct linking to the compressor diffuser on the combustor entry side and to the turbine vanes on the opposite one.

A schematic view of the burner and liner arrangement and of the secondary and dilution port location is given in Fig. 7, together with some details of the 60 000 vertex grid [16,24]. A 12 deg three-dimensional sector was considered, according to the periodical arrangement of both 30 inlet air swirlers and 30 fuel injectors with 30 deg full cone-shaped jets.

Both boundary and initial conditions are assigned in accordance with the gas turbine simulation results.

- Total pressure and temperature of the combustor intake flows result from the component matching analysis; the inlet axial velocity is calculated to meet the actual amount of air flow rate entering the combustor, which is automatically split into the primary air and the secondary and dilution air flows through the liner.
- Static pressure at combustor exit is determined by evaluating the outlet velocity level and a total pressure loss (3% of the total inlet pressure) through the combustion chamber.
- A swirled intake air flow into the primary zone, with a constant flow angle of 60 deg is assumed.

The code performs the solution of the unsteady Navier–Stokes system of equations with an arbitrary Lagrangian–Eulerian method [21,22]. Viscous flow effects and the fuel–air mixing and turbulent chemistry rates as well are approached with a classical two-equation (κ-ε) model.

Regarding the chemical reaction rates, a global two-step methane oxidation mechanism was introduced [25,26]:

$$1)\ CH_4+\tfrac{3}{2}O_2\rightarrow CO+2H_2O$$

$$R_{f1}=10^{15.220}\exp(-20{,}643/T)[CH_4]^{1.460}[O_2]^{0.5217}$$

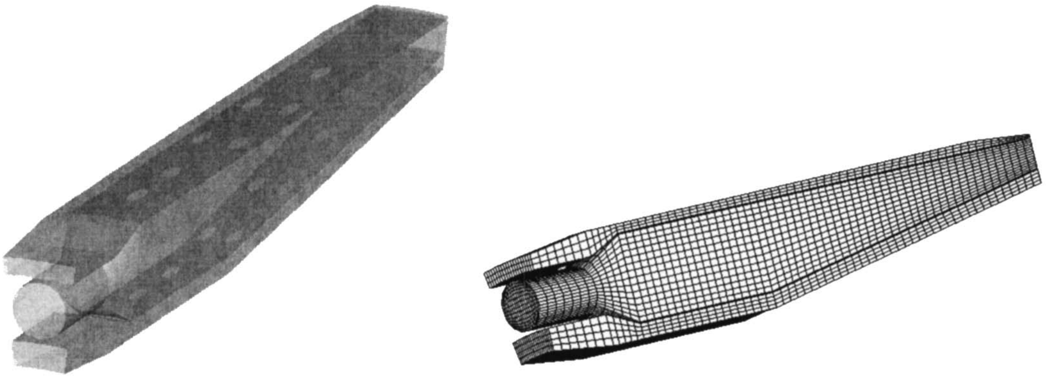

Fig. 7 Computational mesh and schematic view of the 3D sector of the MGT combustor

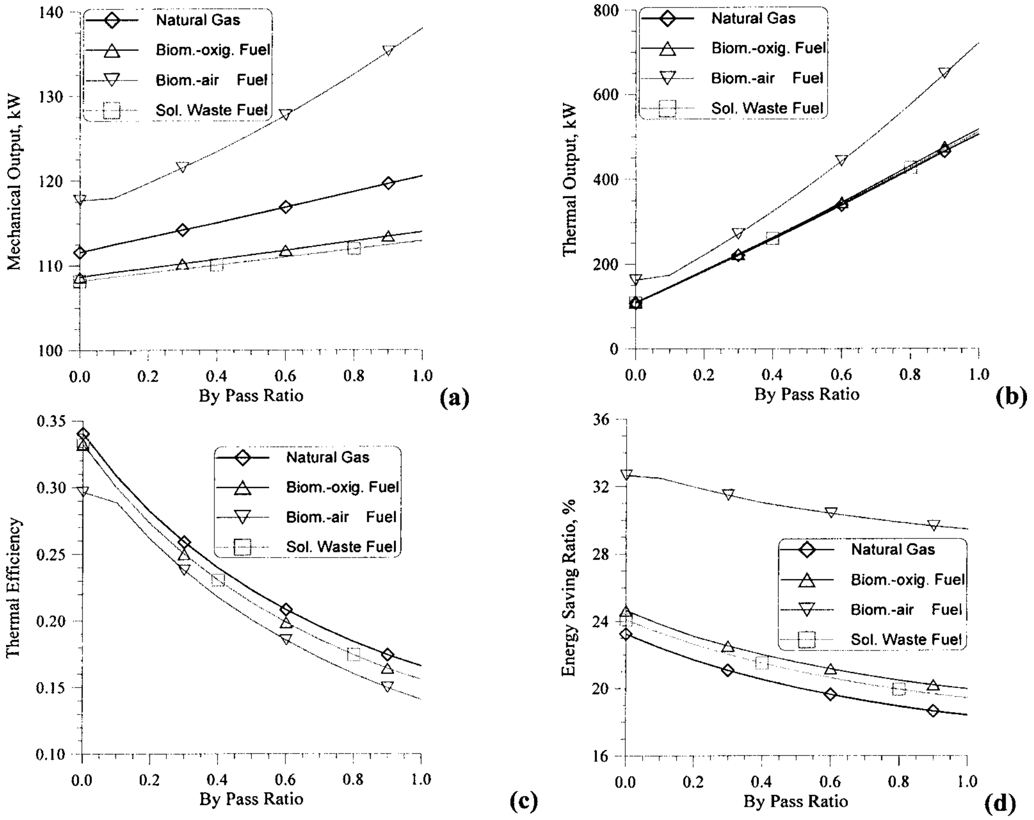

Fig. 8 Performance data of the MGT versus the by-pass ratio

$$R_{b1}=0 \tag{2}$$

$$2)\ CO+\tfrac{1}{2}O_2\leftrightarrow CO_2$$

$$R_{f2}=10^{14.902}\exp(-11\,613/T)[CO]^{1.6904}[O_2]^{1.570}$$

$$R_{b2}=10^{14.349}\exp(-62\,281/T)[CO_2]^{1.0}$$

The first equation is also employed for higher-order hydrocarbon oxidation, while the second one is also assumed for the carbon monoxide combustion in the BIOM and SW fuels.

The hydrogen oxidation in the bio-mass or solid-waste derived fuel is approached by a single step reaction of the type

$$H_2+\tfrac{1}{2}O_2\rightarrow H_2O$$

$$R_f=10^{11.740}\exp(-7500/T)[H_2][O_2] \tag{3}$$

$$R_b=0$$

The actual reaction rates are calculated as

$$\omega_r=\min(\omega_{k,r}\ \omega_{t,r}) \tag{4}$$

where $\omega_{k,r}$ is the rate associated with the kinetically controlled mechanisms in Eqs. (2) and (3) and $\omega_{t,r}$ is the turbulent mixing-controlled rate of the Magnussen and Hjertager model [27].

The set of chemical kinetics equations is completed by those of the extended Zel'dovich mechanism [18] for the prediction of thermal nitric monoxide formation. The equations are simultaneously solved in each computational cell by an algorithm that determines the formation rate of the species involved in the process [11].

Two empirical correlations for the auto-ignition delay time of methane are used in some of the test cases presented. The first one has been generated by Spadaccini et al. [28,29] and the auto-ignition delay is calculated as

$$\tau=2.21\times10^{-14}\exp(22\,659/T)[O_2]^{-1.05}[CH_4]^{0.33} \tag{5}$$

The validity is limited to temperatures of 1300 K and above. So the correlation by Li and Williams [29,30], for the low temperatures defined as less than 1300 K, is also introduced:

$$\tau=(2.6\times10^{-15}[O_2]^{-4/3}[CH_4]^{1/3})/T^{0.92}\exp(-13\,180/T) \tag{6}$$

Although the above equations identify the auto-ignition threshold, in this first application they are assumed to be able to establish a flammability criterion since they incorporate information about the local fuel to air equivalence ratio. The values of τ are, in fact, sensitive to the oxidant and fuel concentrations. Either an excess in fuel contents or an oxygen lack would increase the delay times and the mixture ignition could not take place within the computational cell.

The delay time concept is transformed into a spatially delayed ignition by comparing the τ values with those, τ', necessary for the mixture to reach each computational cell, say,

$$\tau'=\frac{\sigma}{V'} \tag{7}$$

where σ is the distance between the injector location and the cell and V' is the average velocity along the same direction. The ignition occurs wherever the $\tau'>\tau$ condition is fulfilled.

Computational Results

The preliminary thermodynamic analysis aims at an assessment of the potential of the MGT to provide acceptable performance parameters mainly in co-generating application.

The results of the thermal cycle simulation are shown in Figs. 8–10 and refer to a firing temperature of 1223 K with an air mass flow rate of 0.8 kg/s, leading to a rated mechanical output for natural gas fuelling of nearly 110 kW. An electrical efficiency of 0.91 will ensure an electrical output of 100 kW.

The analysis is extended to all fuels in Table 2 and it examines the effect of the X_b parameter on the energetic performances of

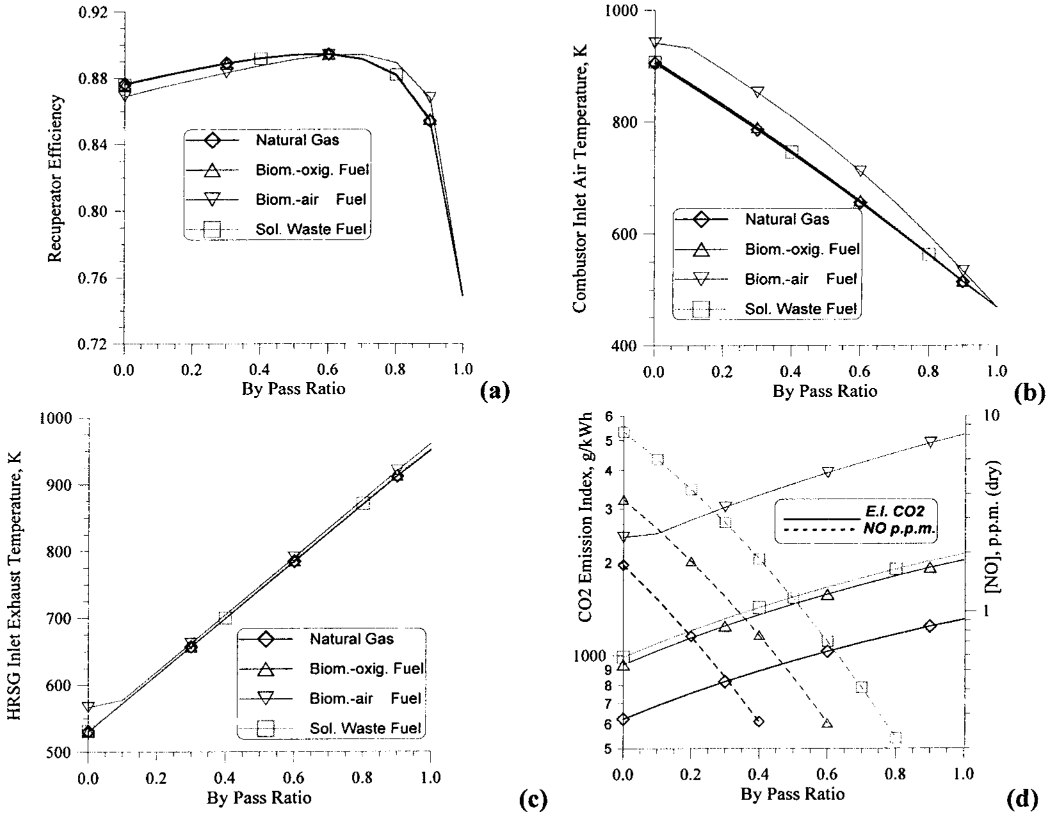

Fig. 9 Cycle parameters and emission data of the MGT

the MGT. It must be pointed out that the cycle analysis neglects the energy requirements for bio-mass or solid-waste treatment, so that an eventual performance increase related to these fuels must be intended as a possible compensation of the increased investment and energy costs.

On the other hand, the results account for the variation in fuel flow rates which are needed in accordance with their different calorific values. The net mechanical outputs in Fig. 8(*a*) include both this effect and the compression work for supplying the fuel at the required injection pressure (5.5 bar). The higher fuel rates, especially in the BIOM(*a*) case, suggest a mechanical and thermal output increase (Figs. 8(*a*) and 8(*b*)) which must be confirmed by a more accurate analysis based on the component matching. On the contrary, the efficiency decrease in the low LHV fuel cases can be explained by the larger amount of thermal energy which is needed by the combustion products to reach the assigned firing temperature.

Regarding the influence of the X_b parameter, the thermal output increase and the efficiency decrease are expected results, while the mechanical output trend can be explained by the reduced pressure losses through the recuperator with the higher values of the by-pass ratio. The increase in exhaust mass flow rate also plays a role in this sense. The most interesting indication refers to the energy saving ratio which is estimated by comparing the actual energy consumption to the one resulting from reference values of the overall plant efficiency (at generator terminals) and boiler efficiency of 0.38 and 0.9, respectively. This performance parameter (Fig. 8(*c*)) increases with the lower LHV fuels, which involve higher mass flows to the HRSG, and preserves an acceptable level over a wide X_b range, also in the less favorable case of natural gas fuelling.

The more detailed results in Fig. 9 give reason of the performance data trend in Fig. 8 and they also put into evidence some problems related to either the employment of different fuels or the assumption of too high values of the by-pass ratio:

- The higher the X_b values, the lower is the air temperature at combustion inlet (Fig. 9(*b*)) and therefore the ignition conditions can be significantly penalized. This situation must be investigated by the *CFD* based combustor analysis.
- Similarly a MGT operation based on the X_b variation involves the possibility of severe gas temperatures at the HRSG inlet (Fig. 9(*c*)) and therefore the materials of both recuperator and heat recovery heat exchanger should comply with this situation.
- The CO_2 emission index in Fig. 9(*d*) presents unfavorable levels in the cases of both bio-mass and solid-waste derived fuels, even in the case of a fully recuperated thermal cycle ($X_b=0$). These values become fairly unacceptable when X_b increases. The NO levels, estimated for a residence time of 25 ms and a primary fuel to air equivalence ratio of 0.55, are rather negligible in all cases.

Finally, the results in Figs. 8 and 9 refer to a heat recovery addressed to the production of a low pressure saturated steam ($ps=1$ bar). Increasing this parameter makes it more difficult for the exhaust gas temperature profile through the HRSG to match the pinch-point condition (10 K), especially for low X_b values. Consequently, a higher stack temperature can be observed (Fig. 10(*a*)) and this results in a reduced possibility of energy saving (Fig. 10(*b*)).

The latter figure evidences that the choice of higher X_b values should be more appropriate in accordance with increased steam pressures and it could represent a good compromise between the cycle efficiency decay and the preservation of an acceptable energy saving level. In this sense, more favorable indications can be expected from the employment of the BIOM and SW fuels as demonstrated by the results in Fig. 8(*d*).

Component Matching Analysis. This computational issue is addressed to verify the preliminary results of the thermodynamic

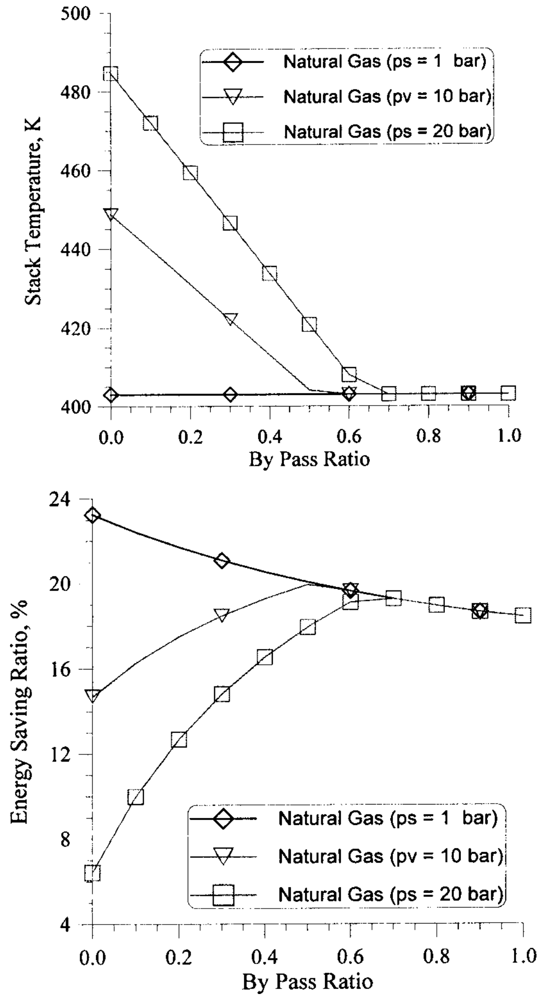

Fig. 10 Influence of the steam pressure on stack temperature and energy saving ratio

analysis by including the estimation of the flow capacities of the rotating components (Figs. 3 and 4). Therefore the main cycle parameters are not predetermined but they result from the actual matching conditions. Table 3 therefore puts into evidence that the same level of mechanical output is accomplished with different firing temperatures, mainly according to the fuel characteristics. Consequently, the exhaust temperatures at the recuperator and HRSG inlet are rather different from those predicted by the previous analysis.

An encouraging indication is given by the pressure ratio, which remains fairly unaltered, because of the favorable slope of the radial turbine curves in Fig. 4. Thus, choked flow conditions do not take place even in the most critical case of the BIOM(a) fuel and the compressor operation is preserved from stall inception.

Once the performance at the rated mechanical output has been assessed, the matching analysis proceeds with the investigation of the possibilities offered by the MGT to provide different levels of mechanical and thermal output at part-load operation. Figure 11 displays the iso-contours of the main performance parameters obtained for various by-pass ratios, in the case of natural gas fueling. In particular Fig. 11(a) highlights that the variable speed operation allows us to maintain higher thermal efficiency and energy saving levels at part-load with respect to the constant speed case. Really, the constant speed operating line in this figure suggests a steep decay in both efficiency and energy saving ratio when the mechanical output reduces; thus any operating line with a positive slope in the same plane would produce more favorable effects, so confirming the indications that can be found in current literature [7,9].

Different regulation strategies can therefore be issued depending on the actual characteristics of the variable-frequency electric generator, and the design point efficiency levels could be approximately preserved up to about the 60% of the rated output. Figure 11(b) allows estimation of both thermal output and exhaust gas temperature available at the HRSG inlet. The performance iso-contours patterns are of course greatly influenced by the by-pass ratio chosen. As examples, Figs. 11(c) and 11(d) show the same parameters resulting from a 50% by-pass ratio. Both thermal efficiency and energy savings are reduced with respect to the previous case but, at the same time, a much higher thermal output at an increased temperature is now available. In this second case, following an optimal speed-load line, it is also possible to maintain an approximately constant exhaust temperature at part-load. The above situation is confirmed at the highest by pass ratio of 100%, even if a considerable reduction of both thermal efficiency and energy saving is induced (Figs. 11(e) and 11(f)). In conclusion, the proposed control method of the MGT, based on a variable-frequency electric generator and on the employment of recuperator by-pass valves, seems to substantially improve the cogenerating MGT capabilities of efficiently complying with different requirements of electrical and thermal outputs.

Similar considerations could hold when different fuels are employed (Fig. 12). In this case, as expected, a more evident variation of the MGT operating domain is found, especially for the BIOM(a) fuel and for the higher by-pass ratio (Fig. 12(c)). Both the employment of this low LHV fuel and the absence of a recuperated cycle are in fact responsible for the maximum increase of mass of fuel injected, which produces an advanced compressor stall, as shown in the figure. This can also limit the part-load variable-speed operation of the whole plant.

CFD Analysis of the Combustor. The results in this section aim at a substantial confirmation of those based on a simply thermodynamic approach, by analyzing the flow and properties distribution throughout the combustion chamber.

The main issue is related to the comparison between the combustion of natural gas and of the fuels derived from bio-mass or solid waste gasification. It must be reminded that the same combustor geometry is assumed in all cases and this corresponds to a check of its adaptation potential to different operating conditions. A second key matter concerns the combustion analysis for different X_b values, thus for variable air inlet temperatures.

In both cases, an important role is played by the ignition delay model in Eqs. (5) and (6), which can be helpful to provide indications about the combustion development and completion under dramatically changed conditions.

Regarding to the primary fuel/air equivalence ratio, the CFD analysis proceeds fairly in accordance with the preliminary indications provided by the thermodynamic calculations. Really, the corresponding value for natural gas, $X_b=0$, operation is close to 0.55, so suggesting a typical lean combustion development.

The numerical time-dependent integration proceeds through computational cycles whose time step results both from the cell grid size (the average side of the hexahedral elements is 0.15 cm) and from the application of numerical stability criteria. The average time step was of 9.3×10^{-6} s, and it decreased to 4.2×10^{-6} s in the BIOM(a) case, due to the generally higher velocity levels related to the greater fuel mass addition.

The convergence histories, in terms of mean exit temperatures, are displayed in Fig. 13, and a first comparison is allowed between the behavior with different fuels (Fig. 13(a)) or under increasing values of the X_b parameter (Fig. 13(b)). In both cases, the final temperatures meet the values predicted by the thermodynamic analysis but a first detection of problems related with the ignition delay time is allowed in Fig. 13(b).

Really, the results in Fig. 13(a) are obtained for $X_b=0$ (see

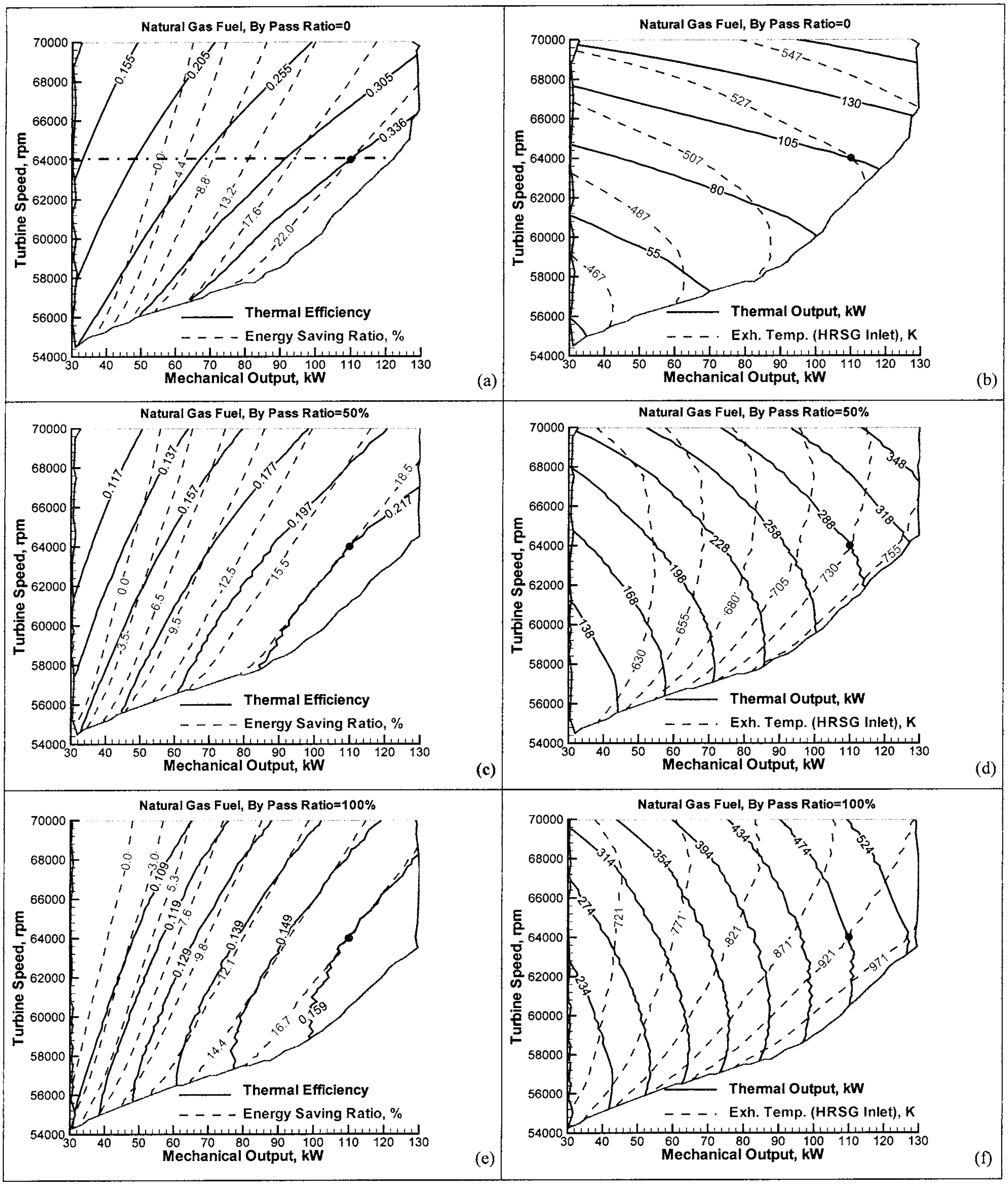

Fig. 11 Operating domains and performance curves of the MGT for different by-pass ratios

Table 3) and therefore the inlet temperatures are sufficiently high to practically overcome self-ignition problems. The response delay in the BIOM(*a*) case may be simply attributed to the reduced time steps, as indicated. When the by-pass ratio is increased for the same power output of 110 kW (Fig. 13(*b*)), the effect of the inlet air temperature becomes remarkable and the response characteristics of the combustion system are strongly affected even in terms of the development of the time-dependent numerical process.

Figures 14–21 allow discussion of detailed flow and properties distributions. The results refer to the converged solution (i.e., at the last iteration step in Fig. 13).

As a first indication on the behavior of different fuels, the temperature distributions in Fig. 15 remain rather similar in the case of natural gas fueling and of a medium LHV fuel like that derived from solid wastes. The indication about the thermal NO formation (Fig. 16) conflict with those provided by the thermo-kinetic model adopted within the thermodynamic analysis. This is due to the

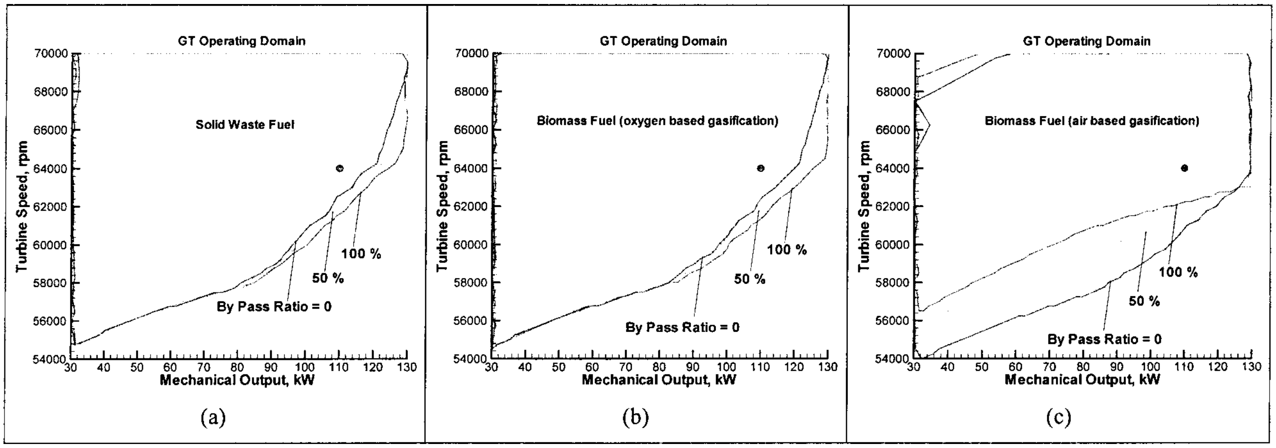

Fig. 12 Operating domains of the MGT fuelled with BIOM or SW fuels

different temperature peaks and residence times which result either from the CFD or from the simplified model. Figure 15 clearly indicates, as a matter of fact, that the extension of the maximum temperature region and the related level itself are slightly reduced in the SW case, probably due to the different local equivalence ratios. The NO level at combustor exit is, however, negligible as expected.

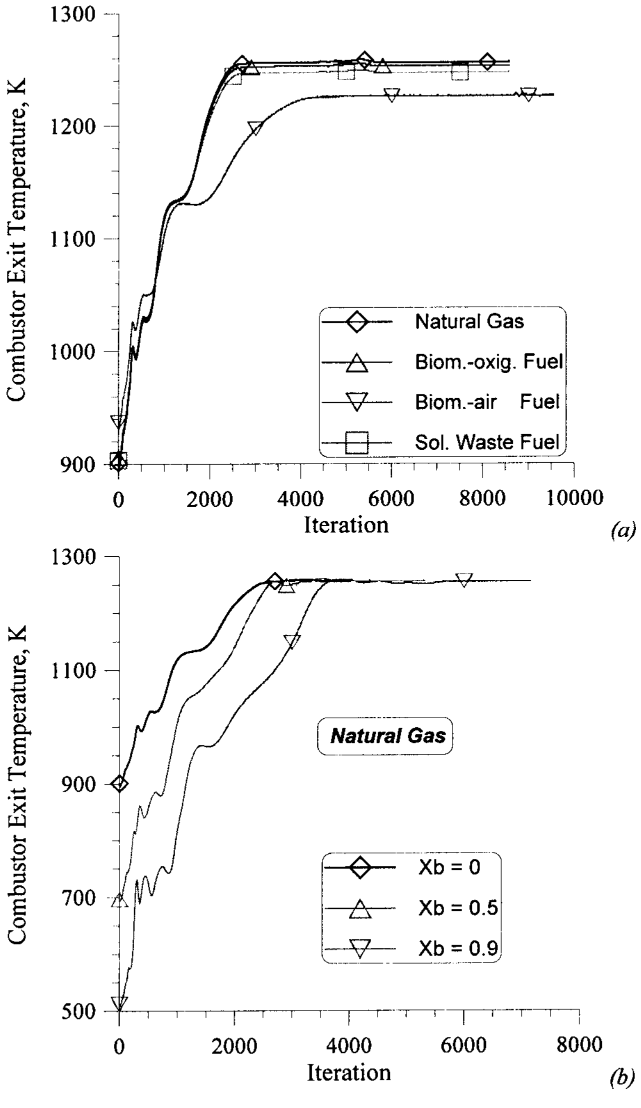

Fig. 13 Convergence histories of the CFD combustion analyses (combustor inlet conditions at rated power output)

A more impressive comparison is the one concerning the situations originating from the different air temperature levels induced by the X_b variations.

The location of the temperature peaks (Fig. 17), and therefore of the pre-mixed flames, is substantially forward-shifted when X_b increases, as a spatial effect of the augmented ignition delay times. The effect is also highlighted by the fuel distributions in Fig. 18, which demonstrate that the natural gas consumption throughout the combustor is much slower when the maximum by-pass ratios are chosen.

The main consequences can be observed in Figs. 19–21. The flame shift towards the combustor exit produces a less uniform temperature distribution in the combustor outlet plane (Fig. 19) so that increased thermal stresses can be induced for the turbine stator vanes. While the NO concentrations are below significant levels (Fig. 20), the CO concentration progressively increases with the X_b parameter (Fig. 21), due to the delayed ignition which avoids the completion of the two-step mechanisms in a larger combustor region.

Thus the CFD analysis of the combustion process can provide the definite response about the actual possibilities for the MGT combustor to operate with different fuels or under varying inlet temperature levels.

Conclusion

The authors attempted in this paper to provide a comprehensive overview of the plant and component performance of a micro-gas turbine under different load and fueling conditions.

Several tools have been adopted for this analysis, in order to first assess the potential of the MGT based cogenerating plant by a thermodynamic approach and then refining the off-design prediction in order to emphasize the better results which can be achieved when introducing a variable speed regulation.

The plant flexibility is strongly augmented both by adopting different fuels and with the possibilities of adapting the thermal and mechanical output to different requirements. The preliminary appealing indications resulting from the thermodynamic and matching analysis have been verified by a CFD simulation of a scaled combustion chamber. This study has put into evidence that a satisfactory adaptation to different conditions can be foreseen but the ultimate combustor geometry should be severely checked

Table 3 Results of the matching analysis of the MGT (rated mechanical output of 110 kW, $X_b=0$)

Fuel	$\dot{m}_a$ (kg/s)	$\dot{m}_f$ (kg/s)	T_{cc} (K)	p_{cc} (bar)	$T.I.T.$ (K)	T_g (K)	T_{HRSG} (K)	P (kW)	Q (kW)	η	R (%)	$EICO_2$ (g/kWh)	[NO] p.p.m., dry
Natural gas	0.8076	0.0069	913.4	3.86	1239.6	943.3	526.5	109.0	104.9	0.335	21.8	632.3	1.90
SW	0.8072	0.0151	927.6	3.88	1255.9	956.3	528.7	109.6	107.1	0.334	23.8	984.0	10.45
BIOM(o)	0.8073	0.0172	930.8	3.88	1256.9	957.2	528.9	110.3	107.8	0.334	24.3	929.1	4.81
BIOM(a)	0.8072	0.1424	915.1	3.88	1213.0	930.5	573.7	109.6	169.3	0.275	30.7	2611.8	0.0015

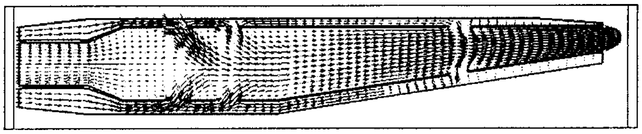

Fig. 14 Flow field in the combustor mid-plane

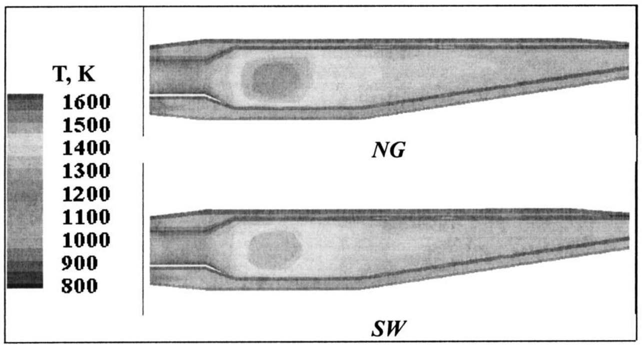

Fig. 15 Temperature distribution in the combustor periodic meridional plane

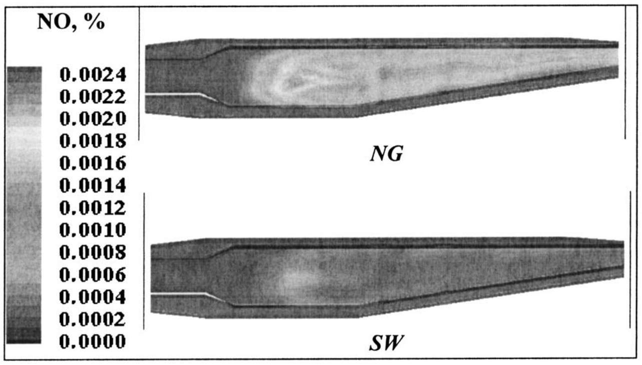

Fig. 16 Thermal NO distribution in the periodic meridional plane

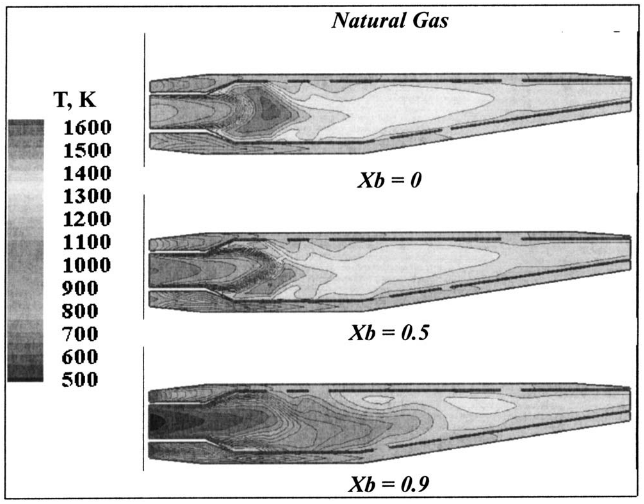

Fig. 17 Temperature distribution in the combustor mid-plane

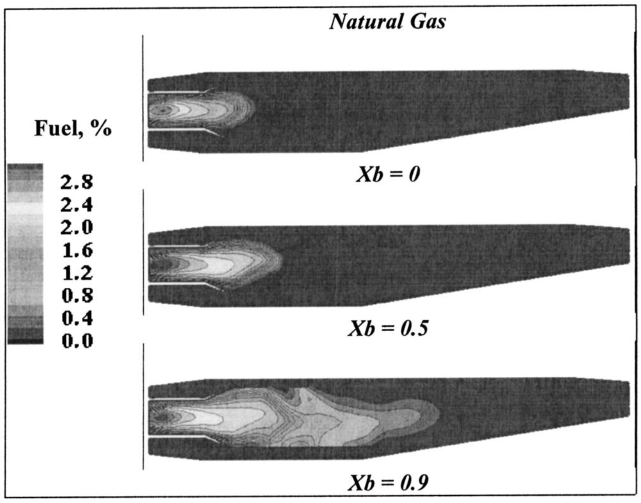

Fig. 18 Fuel distribution in the combustor mid-plane

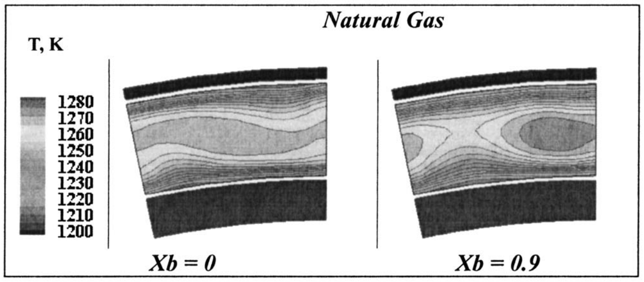

Fig. 19 Temperature distribution in the combustor exit plane

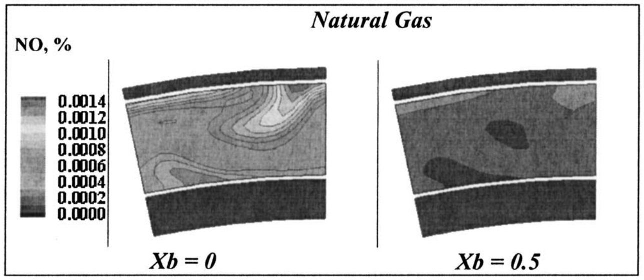

Fig. 20 Thermal NO distribution in the combustor exit plane

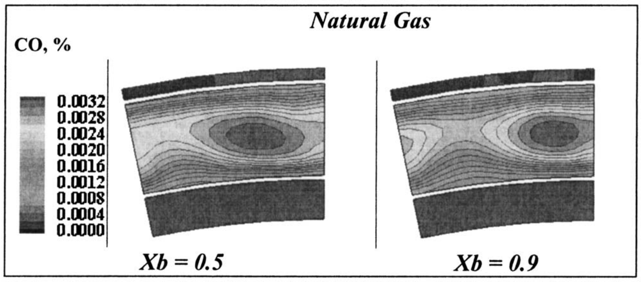

Fig. 21 CO distribution in the combustor exit plane

in order to determine the actual operating range which is allowed for an efficient operation, so suggesting the main direction for the future authors' work.

Acknowledgments

The paper refers to an Italian National Research Project (PRIN-MIUR 2002) concerning the dynamics of energy conversion systems. The Ansaldo Ricerche S.p.A. is acknowledged for suggesting provisional data of the MGT cycle parameters.

Nomenclature

BIOM = bio-mass derived fuel
$EICO_2$, $EINO$ = CO_2, NO emission indices
f_{st} = Fuel/air stoichiometric ratio
h_{0f} = enthalpy of formation
k_f, k_b = reaction rate constants
LHV = lower heating value
$\dot{m}$ = mass flow rate
NG = natural gas
P = mechanical power
Q = thermal output
p = pressure
ps = steam pressure
p.p.m. = concentration in parts per million
$R\%$ = energy saving ratio
R_f, R_b = reaction rates
t = time
SW = solid-waste derived fuel
T, $T.I.T.$ = temperature, turbine inlet temperature
X_b = by-pass ratio
x = mass fraction

Subscripts

a = air
cc = combustion chamber inlet
f = fuel
k = kinetic
g = exhaust gas
ox = oxidant
R = recuperator
t = turbulent

Greek

ε = turbulent dissipation rate
η = plant thermal efficiency
κ = turbulent kinetic energy
σ = injector distance
τ = ignition delay time
φ = equivalence ratio
ω = net reaction rate

References

[1] Rodgers, C., 2000, "25-5 kWe MicroturbineDesign Aspects," ASME Paper No. 2000-GT-0626.
[2] Buhre, B. J. P., and Andries, J., 2000, "Biomass-Based, Small-Scale, Distributed Generation of Electricity and Heat Using Integrated Gas Turbine-Fuel Cell Systems," ASME Paper No. 2000-GT-0022.
[3] Ohkubo, Y., et al., 2001, "Development of Dry Low-NOx Combustor for 300 kW Class Gas Turbine Applied to Co-Generation System," ASME Paper No. 2001-GT-0083.
[4] Lagerström, G., M.Sc, and Xie, Max, 2002, "High Performance & Cost Effective Recuperator for Micro-Gas Turbines," ASME Paper No. GT-2002-30402.
[5] Takase, K., Furukawa, H., and Nakano, K., 2002, "A Preliminary Study of An Inter-Cooled and Recuperative Microgasturbine Below 300 kW," ASME Paper No. GT-2002-30403.
[6] Fantozzi, F., Di Maria, F., and Desideri, U., 2002, "Integrated Micro-Turbine and Rotary-Kiln Pyrolysis System as a Waste to Energy Solution for a Small Town in Central Italy—Cost Positioning and Global Warming Assessment," ASME Paper No. GT-2002-30652.
[7] Kimijima, S., and Kasagi, N., 2002, "Performance Evaluation of Gas Turbine-Fuel Cell Hybrid Micro Generation System," ASME Paper No. GT-2002-3011.
[8] Proeschel, R. A., 2002, "Proe 90™ Recuperator for Micro-Turbine Applications," ASME Paper No. GT-2002-30406.
[9] Campanari, S., Boncompagni, L., and Macchi, E., 2002, "Microturbines and Trigeneration: Optimization Strategies and Multiple Engine Configuration Effect," ASME Paper No. GT-2002-30417.
[10] Bozza, F., Cameretti, M. C., and Tuccillo, R., 2001, "Performance Prediction and Combustion Modelling of Low-CO2 Emission Gas Turbines," ASME Paper No. 2001-GT-0066.
[11] Bozza, F., Cameretti, M. C., Marro, A., and Tuccillo, R., 2000, "Performance and Emission Analysis of a Variable Load Operated Gas Turbine," *Advanced Energy Systems*, Vol. 40, pp. 400–415.
[12] Tolpadi, A. K., Prakash, C., Hura, H., and Mongia, H. C., 1998, "Advanced Combustion Code: Overall Description Prediction of a Jet Diffusion Flame and Combustor Flowfields," ASME Paper No. 98-GT-229.
[13] Malecki, R. E., et al., 2001, "Application of an Advanced CFD-Based Analysis System to the PW6000 Combustor to Optimize Exit Temperature Distribution. Part A," ASME Paper No. 2001-GT-0062.
[14] Sivaramakrishna, G., et al., 2001, "CFD Modeling of the Aero Gas Turbine Combustor," ASME Paper No. 2001-GT-0063.
[15] Eggels, R. L. G. M., and Brown, C. T., 2001, "Comparison of Numerical and Experimental Results of a Premixed DLE Gas Turbine Combustor," ASME Paper No. 2001-GT-0065.
[16] Bozza F., Cameretti, M. C., and Tuccillo R., 2002, "The Employment of Hydrogenated Fuels From Natural Gas Reforming: Gas Turbine and Combustion Analysis," ASME Paper No. GT-2002-30414.
[17] Mc Bride, B. J., and Gordon, S., 1994, "Computer Program for Calculation of Complex Equilibrium Composition and Applications," NASA RP 1311, Parts I and II.
[18] Zel'dovich, Y. B., Sadovnikov, P. Y., and Frank-Kamenetskik, D. A., 1947, "Oxidation of Nitrogen in Combustion," Academy of Science of SR, Institute of Chemical Physics, Moscow-Leningrad.
[19] Bozza, F., Fontana, G., and Tuccillo, R., 1994, "Performance and Emission Levels in Gas Turbine Power Plants," ASME J. Eng. Gas Turbines Power, **116**, pp. 53–62.
[20] Bozza, F., Senatore, A., and Tuccillo, R., 1996, "Thermal Cycle Analysis and Components Aero-Design for Gas Turbine Concept in Low-Range Cogenerating Systems," ASME J. Eng. Gas Turbines Power, **118**, pp. 792–802.
[21] Hirt, C. W., Amsden, A. A., and Cook, J. L., 1974, "An Arbitrary Lagrangian-Eulerian Computing Method for All Flow Speed," J. Comput. Phys., **14**, pp. 227–253.
[22] Amsden, A. A., 1997, "KIVA-III v: Block Structure KIVA Program Engine With Vertical or Canted Valves," LA—Los Angeles 13313–MS, Los Alamos.
[23] McGuirk, J. J., and Spencer, A., 2000, "Coupled and Uncoupled CFD Prediction of the Characteristics of Jets From Combustor Air Admission Ports," ASME Paper No. 2000-GT-0125.
[24] Price, G. R., Botros, K. K., and Goldin, G. M., 2000, "CFD Predictions and Field Meausurements From LM1600 Gas Turbine During Part Load Operation," ASME Paper No. 2000-GT-350.
[25] Nicol, G. D., Malte, P. C., Hamer, A. J., Roby, R. J., and Steele, R. C., 1998, "A Five-Step Global Methane Oxidation—NO Formation Mechanism for Lean Premixed Gas Turbine Combustione," ASME Paper No. 98-GT-185.
[26] Miller, J. A., and Bowman, C. T., 1989, Prog. Energy Combust. Sci., **15**, p. 287.
[27] Magnussen, B. F., and Hjertager, B. H., 1977, "On Mathematical Modeling of Turbulent Combustion With Special Emphasis on Soot Formation," 16th Symposium on Combustion, The Combustion Institute, Pittsburgh, PA.
[28] Spadaccini, L. J., and TeVelde, L. J., 1982, "Autoignition Characteristics of Aircraft Type Fuels," Combust. Flame, **46**, pp. 283–300.
[29] Roy, C. J., Moran, A. J., and Thomas, G. O., 2001, "Autoignition Characteristics of Gaseous Fuels at Representative Gas Turbine Conditions," ASME Paper No. 2001-GT-0051.
[30] Li, S. C., and Williams, F. A., 2000, "Reaction Mechanism for Methane Ignition," ASME Paper No. 2000-GT-145.

Theodosios Korakianitis
James Watt Professor
of Mechanical Engineering,
University of Glasgow,
Glasgow G12 8QQ, Scotland UK
e-mail: t.alexander@mech.gla.ac.uk

T. Sadoi
Engine Design Division,
Mitsubishi Motors Corporation,
Kyoto, Japan

Turbocharger-Design Effects on Gasoline-Engine Performance

Specification of a turbocharger for a given engine involves matching the turbocharger performance characteristics with those of the piston engine. Theoretical considerations of matching turbocharger pressure ratio and mass flow with engine mass flow and power permits designers to approach a series of potential turbochargers suitable for the engine. Ultimately, the final choice among several candidate turbochargers is made by tests. In this paper two types of steady-flow experiments are used to match three different turbochargers to an automotive turbocharged-intercooled gasoline engine. The first set of tests measures the steady-flow performance of the compressors and turbines of the three turbochargers. The second set of tests measures the steady-flow design-point and off-design-point engine performance with each turbocharger. The test results show the design-point and off-design-point performance of the overall thermodynamic cycle, and this is used to identify which turbocharger is suitable for different types of engine duties.

[DOI: 10.1115/1.1808428]

Introduction

Whether they operate on the two-stroke or four-stroke thermodynamic cycle, whether they are naturally aspirated or turbocharged and intercooled, whether they are fueled by gasoline, diesel, or other fuels, piston engines can operate over a wide portion of their minimum-to-maximum speed and power range. The engine's fuel map (Fig. 1) shows thermal efficiency contours on a power-speed or torque-speed map while identifying minimum and maximum speed, minimum and maximum power, bearing and turbocharger limits, and other limits of operation. Different measures of the engine's performance (efficiency, or torque, or power) may be optimized, for instance with injection and valve timing, manifold tuning, etc., in a smaller range of speeds and powers, whose location on the speed-power engine map is dictated by the engine duty. The drop-off in performance away from this optimum range is not as high as the corresponding one in turbomachines. Turbomachine performance is highly dependent on the gas angles at entry to and exit from all (blading and other) flow passages, and therefore exhibit high performance over a narrower range of operation. Typically, the operating shaft speed of turbomachines is an order of magnitude higher than that of piston engines, so that turbomachines are much smaller than piston engines for comparable mass-flow rates.

The brake power output $\dot{W}_{ot}$ delivered by gasoline and diesel engines is limited by the mass-flow rate of air $\dot{m}_a$ that can go through the engine in its operating cycle. This mass-flow rate of air is proportional to $\rho_{a,i}$, the density of the charge as it is admitted to the piston-engine cylinder (Heywood, 1988 [1])

$$\dot{m}_a = \dot{m}_f(A/F) \tag{1}$$

$$\dot{W}_{ot} = \eta_{th}[\dot{m}_a(F/A)]LHVF \tag{2}$$

$$\dot{m}_a = \eta_v \rho_{a,i} V_d \frac{N}{n_c} \tag{3}$$

$$bmep = \frac{\dot{W}_{ot}}{V_d(N/n_c)} \tag{4}$$

where (F/A) is the fuel-air ratio at the operating condition. For naturally aspirated engines the volumetric efficiency is about 0.85, and for turbocharged engines it is between 0.95 and 1.1, depending on engine technology. (For two-stroke engines V_d is the swept volume of the scavenge pump.)

In diesel engines at a given engine speed, load is controlled by changing the amount of fuel (F) admitted to the cylinder. This is done less efficiently in gasoline engines, where at a given engine speed load is controlled mainly by throttling the flow at the intake manifold, thus reducing the pressure and density of air admitted to the cylinder. Fuel-injected gasoline engines can also change fuel timing and amount of fuel injected, while direct-injection (in the cylinder) gasoline engines can improve volumetric efficiency over (intake manifold) port-injected engines, where fuel vapor takes some volume from the incoming air.

In naturally aspirated engines $\rho_{a,i}$ is determined by the temperature and pressure of air as it enters the cylinder. This density is increased with compressors (often followed by intercoolers) in various supercharging and turbocharging schemes. In supercharging the compressor is mechanically driven by the engine. In turbocharging the compressor is driven via an exhaust gas turbine. The basic idea of turbocharging was introduced by R. Diesel in Germany in 1896 (just 18 years after the first successful Otto-cycle engine). At the beginning of this century D. Clark (England, 1901), and A. Rateau and L. Renault (France) developed supercharging devices. The idea of a turbocharger for a diesel engine was patented by A. Buchi (Switzerland, 1905). Gasoline-engine turbochargers were first developed by Rateau in 1917. Initially, turbocharged engines were used for racing cars only. Around 1954 GM developed the first turbocharged gasoline engines for passenger cars.

The drivers of superchargers are directly (mechanically) coupled to engine speed, and their compressors respond fast to engine speed and mass-flow changes. The drivers of turbochargers (the turbine) are indirectly (aero-thermodynamically) coupled to engine speed, and their compressors are slower to respond to engine speed and mass-flow changes, a condition known as "turbocharger lag." This is improved by reducing the rotating inertia of the turbocharger, and occasionally by using two (or more) smaller turbochargers in parallel rather than one larger one. (Occasionally two turbochargers, sometimes with intercooling between them, are used in series to further increase intake pressure, particularly in some marine diesel engines.) Winterbone and Jai-In (1991) [2] derived transfer-function models from polynomial fits whose coefficients were evaluated from experimental data, and used them with other engine transfer functions to predict diesel-engine response to transients.

The different mass-flow rates and operating speeds of piston

Contributed by the International Gas Turbine Institute and presented at the 42nd International Gas Turbine and Aeroengine Congress and Exposition, Orlando, FL, June 2–5 1997. Manuscript received November 1, 1996; final revision received February 1, 1997. Paper No. 97-GT-387. Associate Editor: H. A. Kidd.

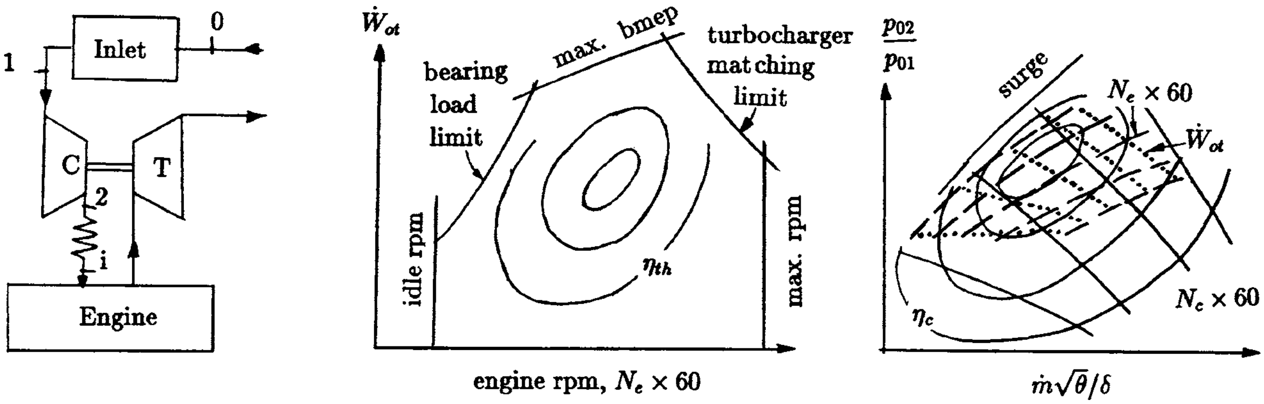

Fig. 1 Engine thermodynamic flow stations (left); and matching of engine fuel map (middle) and compressor map (right)

engines and turbomachines are not naturally well matched, and the combination of any piston engine with a turbocharger must be carefully planned. The turbocharger geometry must be carefully chosen so that the range of speeds and mass flows of good turbocharger performance coincide with those of the piston engine while it is operating with the compressor-outlet and turbine-inlet conditions, with intake and exhaust manifolds [3,4] and with the operating cycle (or mission profile) of the engine [5]. Clearly, for piston engines that operate at a narrow speed and power range the turbocharger will be chosen so that its mass-flow rate and pressure-ratio range of high efficiency coincides with that of the engine and the duty. Compromises must be made in engines operating at a wide range of speeds and powers. Automotive engines, for example, are sometimes fitted with a waste gate, so that at high engine speeds and mass flows, where the engine seldom operates, some of the exhaust flow by-passes the turbine; and the turbocharger is better matched at lower speeds and powers, where the engine operates frequently [6].

Turbocharger Matching

The total pressure at compressor inlet, p_1, is lower than atmospheric (passage friction) and the total temperature T_1 is about atmospheric (Fig. 1). The boost pressure p_2 is first estimated for the target power output (it can reach about 1.8 atm for automotive-type engines, and 3 to 4 for slow speed marine diesels) subject to thermal and mechanical stresses. Using a perfect gas model the turbocharger total-to-total efficiency is estimated and used to calculate the temperature at compressor outlet

$$T_2 = T_1\left(\frac{p_2}{p_1}\right)^{R/(C_p \eta_{p,c})}$$

or

$$T_2 = T_1 + \frac{T_1}{\eta_{s,c}}\left[\left(\frac{p_2}{p_1}\right)^{R/C_p} - 1\right] \tag{5}$$

The total pressure of air at intercooler outlet, $p_{a,i}$, is a little lower than p_2. The corresponding total air temperature and density are estimated from intercooler effectiveness

$$T_i = T_2 - \epsilon(T_2 - T_0), \tag{6}$$

$$\rho_i = \frac{p_i}{RT_i}, \tag{7}$$

$$\frac{\rho_i}{\rho_1} \approx \frac{p_2}{p_1}\left\{1 + \frac{1-\epsilon}{\eta_{s,c}}\left[\left(\frac{p_2}{p_1}\right)^{R/C_p} - 1\right]\right\}^{-1} \tag{8}$$

where the approximation in Eq. (8) is for neglecting the pressure drop in the intercooler. The static density at intercooler outlet, $\rho_{a,i}$ is now evaluated from the total conditions and flow area at station i.

The basic size of the turbocharger is now determined by the air required by the engine, given by Eq. (3) (the volumetric efficiency is approximated from previous experience). The above calculations can be repeated for several design-point and off-design-point operating conditions (such as maximum power, optimum speed and power, part load, etc.) by using appropriate starting values of p_1 and T_1.

If the engine is run at constant speed but increasing load, the mass-flow rate will increase almost proportionately with the increasing charge density or pressure ratio (Eqs. (3) and (8)). These engine constant-speed lines N_e on the turbocharger map of Fig. 1 are the dashed lines. Their slope decreases with intercooler effectiveness (Eq. (8)). The lower engine speeds are nearer the surge line, and the higher engine speeds are at higher compressor mass flows. The engine load lines $\dot{W}_{ot}$ are shown dotted in the same figure, and higher-load lines occur at higher compressor pressure rations.

The appropriate turbocharger can now be chosen from compressor characteristic maps (obtained from steady-flow tests) provided by turbocharger manufacturers, and comparing that with the fuel map of the engine (Fig. 1). The turbocharger compressor maps are used to identify minimum airflow, limit for continuous operation and minimum compressor efficiency. Clearly, in the estimate outlined above prior experience with typical engine fuel maps and compressor characteristics is essential.

When the exhaust valve or port of a cylinder first opens, the gas enters the exhaust system with a fast-diminishing pressure pulse [7–9]. In pulse turbocharging these pulses are arranged in groups from two or three cylinders and away from the timing of inlet valve or port openings to avoid exhaust backflow through the intake. The pulses are then directed in the turbine volute. The widely varying conditions at turbine inlet make pulse charging less efficient than constant-pressure charging; however, pulse charging is advantageous at low-load conditions, where the pulses compensate for the low temperature of exhaust gas. In constant-pressure turbocharging the exhaust gases from all cylinders enter a common manifold with limited recovery of the pulse pressure. Turbines supplied with constant pressure operate more efficiently at high outputs, while pulse-charged turbines are more responsive to changes in engine output (less turbocharger lag). Marine engines were pulse charged before the 1970s, but with increasing brake mean effective pressure (*bmep*) the balance has tipped towards constant-pressure turbocharging [8]. Despite the practical

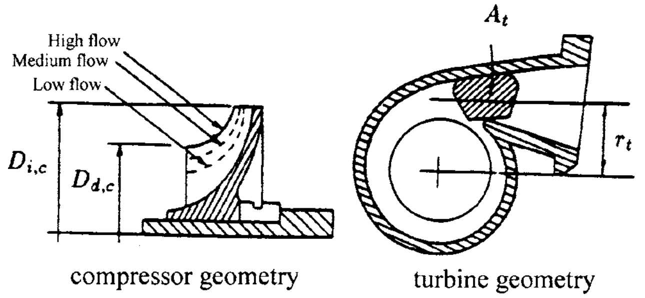

Fig. 2 Compressor and turbine geometries

differences between pulsed and steady-flow operation, performance maps are traditionally obtained from steady-flow tests, and they are used to match turbochargers to engines.

The compressor diffuser will be chosen to allow for sufficient surge margin. Then, the turbine volute can be used to change the effective turbine area, thus changing the energy available from the turbine and therefore the compressor pressure. Although all this can be calculated, final adjustment of the engine and turbocharger is made on the test stand (e.g., engine injection timing and duration, and choice of turbocharger among several options).

Turbocharger Geometries

With analyses similar to the above, Garrett combined several different compressor and turbine impellers, diffusers, and volutes into potential turbochargers for the Mitsubishi 4G63 engine. This is a (1.997) 2 liter in-line four-cylinder turbocharged-intercooled fuel-injected four-stroke gasoline engine with compression ratio of 8.5:1 and dual overhead cam. This engine has been used in the Mitsubishi Eclipse since 1994. The turbocharger compressor and turbine performance and corresponding engine performance were tested with three of these turbochargers, MT-9, MT-13, and MT-15, outlined in Fig. 2. The higher the compressor "trim," $D_{d,c}^2/D_{i,c}^2$ and the higher the A_t/r_t, the higher the speed of the turbocharger. The mass-flow rate through the turbine while it is operating on the engine is limited by a waste gate, in order to optimize turbocharger performance in a midspeed range of the engine.

Turbocharger Tests

In the first set of steady-flow tests the individual compressor and turbine performance were measured in a turbocharger test stand. The turbine (with the waste gate disconnected, i.e., full mass flow) was driven at steady flow conditions by laboratory dehumidified compressed air supplied by a large screw compressor. A valve at turbine inlet was used to control the turbine mass-flow rate. Past this control valve the air enters a large tank (about 2 m^3), a filter, a pressure regulator, and the diffuser to the turbine inlet flange. The turbine outlet exhausts to atmospheric (laboratory) conditions. The compressor inlet receives air from atmospheric (laboratory) conditions. The compressor outlet flows past a set of flow straighteners, past the measurement station, into a cylindrical tank of volume about 4 liters, and out of this tank via a control valve that was used to control the compressor delivery pressure and mass-flow rate. This decoupling of compressor and turbine mass flow rates and pressure ratios resulted in performance maps with wider ranges of operation than could be obtained with the turbochargers coupled to the engine.

The turbochargers were supplied with recirculating lubricating oil from a four-gallon oil tank via an external pump. The alloy nut that secures the compressor impeller on the turbocharger shaft was replaced with a magnetized nut in each turbocharger. The magnetized nut activated an inductive copper coil mounted around the aluminum-alloy compressor inlet, and the frequency of the coil voltage output was used to measure turbocharger speed via an oscilloscope.

After flow straighteners the total pressure, static pressure, and total temperature at compressor outlet, and at turbine inlet and outlet, were measured with static and total pressure transducers and thermocouples (the total conditions at compressor inlet are the ambient laboratory conditions). The thermocouples were ANSI code J type, with ferrous (Fe) positive lead and constantan (Cu-Ni) negative lead, and calibrated at 273 and 373 K. The pressure transducers were of the Kulite ITQ-1000 series, and they were calibrated using a weight gauge tester. In order to obtain area-averaged velocities and mass flows, and therefore total and static properties, the circumferential velocity profiles were measured at each station and at each flow condition, and used to derive the area-averaged velocity from the velocity at midpassage. These properties were used to derive the mass-flow rates, the pressure ratio, and the work of the compressor and turbine. The data were amplified and fed to a PC data acquisition system (Labtech).

At each of about ten settings of turbine-inlet valve positions, measurements were taken at several (about ten) compressor-outlet valve settings, from wide-open valve until the partially closed position where surge occurred, thus varying compressor mass-flow rate and speed. Each measurement point is derived as the statistical average of at least ten measurements within 50 percent of the standard deviation from the mean.

The measured steady-flow compressor and turbine performance maps are shown in Figs. 3, 4, and 5, respectively. The compressor performance figures of pressure ratio versus corrected mass-flow rate show: the surge region (S); lines of turbocharger speed $N_c = N_t$; and lines of total-to-total isentropic (solid lines) and polytropic (dashed and dotted lines) efficiency. The compressor performance figures also show piston-engine rpm regimes N_e and wide-open throttle operation (WOT), measured in the second set of tests with the turbochargers on the engine. The turbine performance maps are presented as specific power versus mass flow rate and they show lines of: turbocharger speed N_t (almost vertical); turbine total-to-total pressure ratio (almost horizontal); and total-to-total isentropic (solid lines) and polytropic (dashed and dotted lines) efficiency.

Gasoline-Engine Tests

In the second set of steady-flow tests each turbocharger was installed on the 4G63 engine. The corresponding engine performance map was measured with a Dynamatic eddy-current dynamometer whose field was used to control engine torque or speed via a Digalog series 1000A controller. The engine coolant fan was eliminated, and the engine was cooled via a water-to-water shell-and-tube heat exchanger that kept the engine coolant temperature between 353 and 368 K. The intercooler was also cooled by water so that its effectiveness remained between 60% and 65% throughout the engine tests. The performance of this fuel-injected engine was measured using the engine's electronic control unit (ECU) and its RAM monitor. The power output of the engine was systematically varied over a range of operating speeds. At each operating condition (engine speed and torque, measured by the dynamometer controller) the fuel consumption was measured as a function of the time during which the injectors were open. In addition to these measurements air flow rate and water temperature were also recorded. The measurements were taken at 100%, 80%, 60%, 40%, and 20% (or more) of the torque at wide-open throttle at every 300–500 rpm from 2000 rpm to 5000 rpm. The data were obtained 15 to 20 times within 5 s at each measuring point. Again, each measurement point is obtained as the statistical average of at least ten measurements within 50 percent of the standard deviation from the mean. The corresponding engine fuel maps with each of the three turbochargers are shown in Fig. 6.

In addition to the engine measurements, the temperature and pressure transducers and thermocouples that were used in the tur-

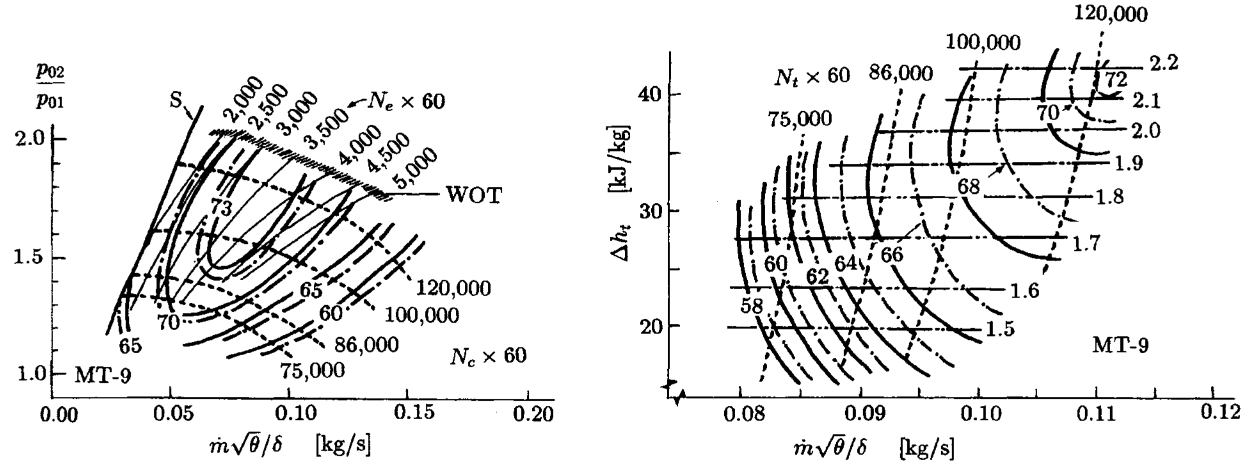

Fig. 3 Measured performance of compressor (left) and turbine (right) of turbocharger MT-9. (Total-to-total efficiency lines: isentropic, solid; and polytropic, dashed and dotted.)

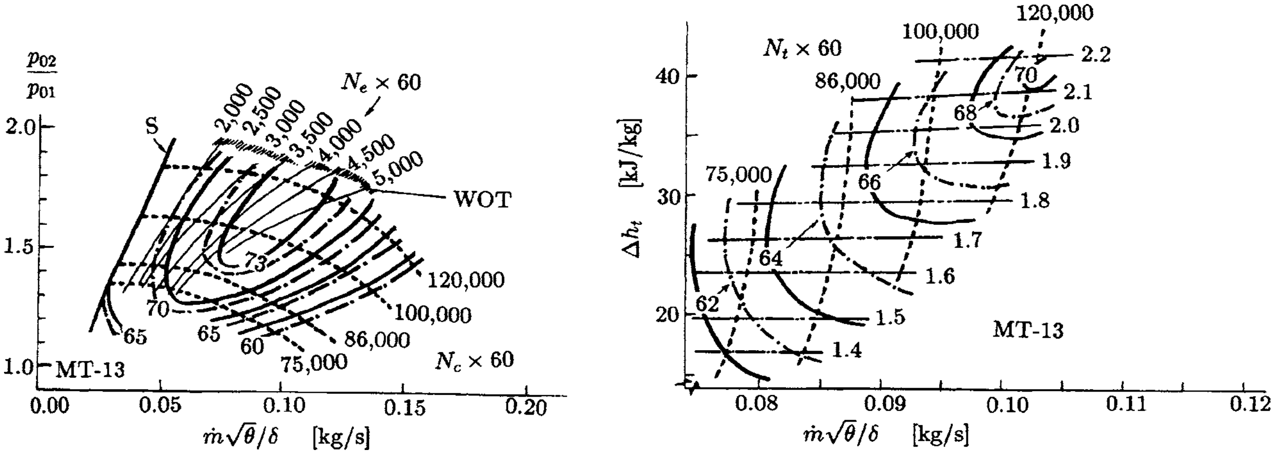

Fig. 4 Measured performance of compressor (left) and turbine (right) of turbocharger MT-13. (Total-to-total efficiency lines: isentropic, solid; and polytropic, dashed and dotted.)

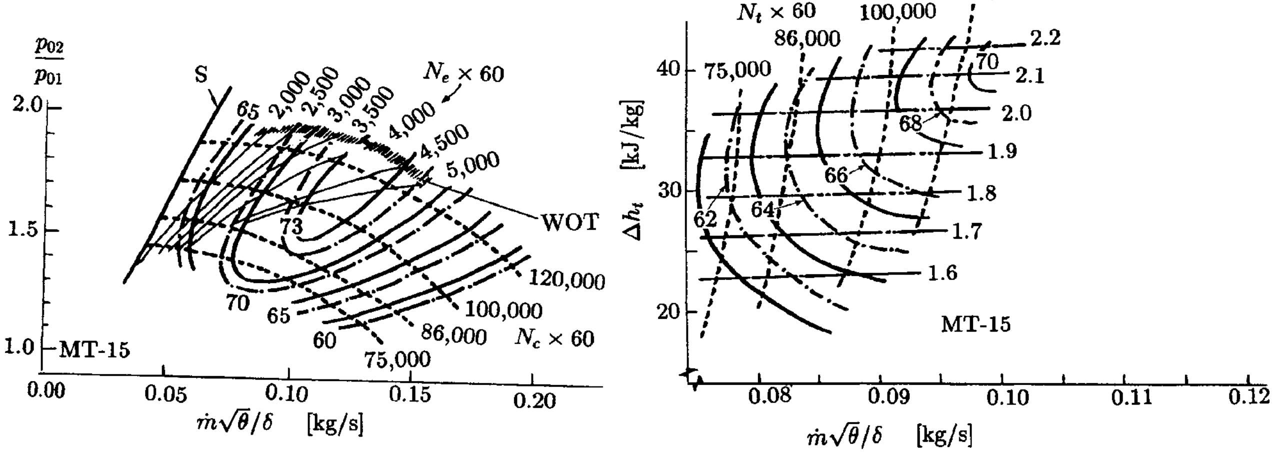

Fig. 5 Measured performance of compressor (left) and turbine (right) of turbocharger MT-15. (Total-to-total efficiency lines: isentropic, solid; and polytropic, dashed and dotted.)

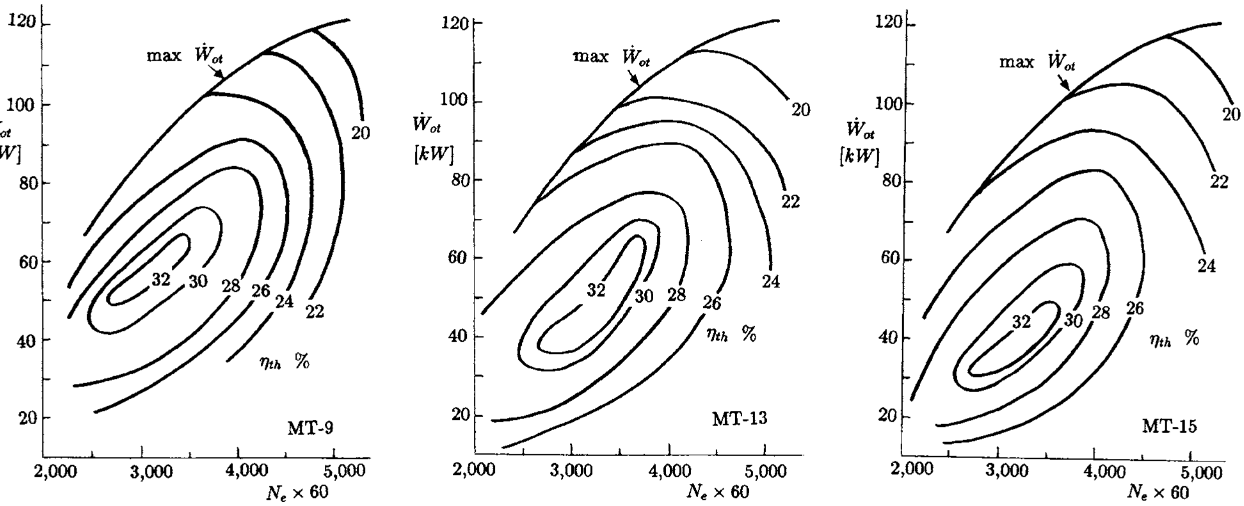

Fig. 6 Measured engine fuel maps: left MT-9; middle MT-13; and right MT-15

bocharger tests were now mounted on the engine compressor ducting, and the mass flow rate, pressure ratio, and efficiency of the compressor were computed. The corresponding engine operating speeds are shown in the compressor maps of Figs. 3, 4, and 5. The turbine waste gate limits the operating range of the compressors near their high-efficiency regimes.

More details on the experiments were presented by Sadoi [10].

Discussion of Results

With the aid of the above test results we can discuss turbocharger-design effects on off-design cycle performance.

The compressor mass-flow rates at the same pressure ratios and turbocharger speeds were MT-9<MT-13<MT-15. For example, at $r_c = 1.6$ and $N_t = 100{,}000$ rpm the mass-flow rates were MT-9 =0.06 kg/s; MT-13=0.075 kg/s; MT-15=0.118 kg/s.

The compressor mass-flow rates at the same turbocharger speeds and the same compressor efficiency were also MT-9<MT-13<MT-15. For example, at $N_t = 100{,}000$ rpm and $\eta_{s,c} = 0.65$ the mass flow rates were MT-9=0.115 kg/s; MT-13=0.123 kg/s; MT-15=0.148 kg/s.

The surge lines of MT-9 and MT-13 are at almost the same position, and that of MT-15 is at a higher mass-flow rate. Therefore, it is harder for MT-15 to give boost at low mass-flow rates (lower engine speeds).

Maximum acceleration at wide-open throttle through the car gears occurs from 2500 to 6000 rpm. Compressor MT-13 has the best efficiency at wide-open throttle in that range. With MT-9 wide-open throttle operation is to the right of the maximum efficiency point (maximum efficiency occurs at lower mass-flow rates). With MT-15 operation at wide-open throttle is to the left of the maximum efficiency point (maximum efficiency occurs at higher mass-flow rates). At 2000 to 2500 rpm (legal highway speeds in the USA) MT-9 operates near compressor surge. Therefore, MT-13 is the best compressor for maximum acceleration. The zones of maximum compressor efficiency are MT-9=0.065–0.100 kg/s; MT-13=0.075–0.11 kg/s; and MT-15=0.10–0.14 kg/s.

The efficiency of compressor MT-9 was the best at low mass-flow rates (best for low-speed engines). The efficiency of compressor MT-15 was the best at high mass-flow rates (best for high-speed engines, spirited or race driving conditions).

The turbine mass flow rates at the same pressure ratios and enthalpy drops were MT-9>MT-13>MT-15. For example at $r_t = 1.8$ and $N_t = 100{,}000$ rpm the mass-flow rates were: MT-9 =0.098 kg/s; MT-13=0.093 kg/s; MT-15=0.089 kg/s. Turbine efficiency is increased as the mass-flow rate is increased.

MT-15 has the smallest turbine, so it can provide a given pressure ratio at the smallest mass flow rate. MT-9 is the best turbine for high-speed engines, and MT-15 is the best turbine for low-speed engines. MT-13 is the best turbine for better overall performance. The turbine is not as critical to engine-turbocharger matching as is the compressor.

The engine performance maps in Figs. 6 and 7 are consistent with the above observations on the location of engine speed lines on the compressor performance maps. The engine with MT-13 gives the widest plateaus of high thermal efficiency (32%) at intermediate speeds and powers, and the best overall maximum power and torque versus speed. Compared with MT-13 engine performance, the best overall thermal efficiency (32%) is at a narrower range and at lower speed and higher power with MT-9; and at a narrower range and at higher speed and lower power with MT-15. The engine with turbocharger MT-13 has the best torque and power curves (Fig. 7), especially in the range of 2500 to 6000 rpm. The torque with MT-9 is good at lower engine speeds (up to 3000 rpm), but at over 3000 rpm the torque decreases, and the

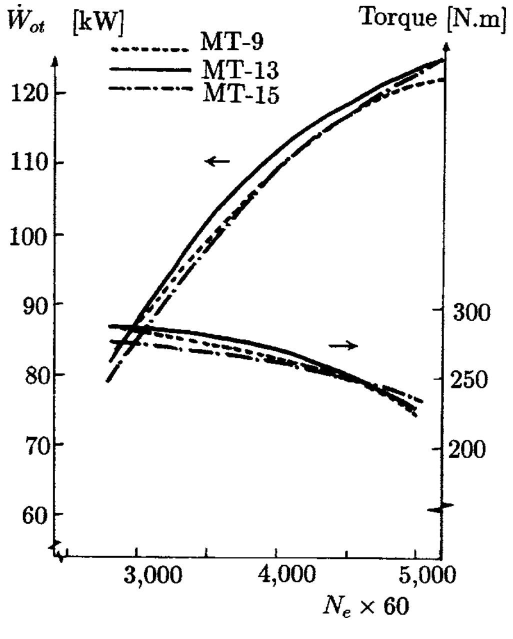

Fig. 7 Engine torque and power curves

power at 5000 rpm is the worst among the three turbochargers. The torque with MT-15 is worst in most of the usual operating range, but it improves at over 4500 rpm.

Operation at 2000 engine rpm is often used for highway speeds in the USA. The turbocharger whose 2000 engine-rpm line is the furthest away from the surge line (MT-13) is the best of the three turbochargers. Also, the engine usually operates at relatively low loads and low speeds, where the fuel map of MT-13 (widest plateaus of thermal efficiency) has thermal efficiencies over 28%.

Conclusions

The tested overall steady-flow design-point and off-design-point thermodynamic cycle (and engine) performance with the three turbochargers (Figs. 6 and 7) are so close that it is unlikely that these differences could be confidently obtained with computations. Theoretical turbocharger matching is useful to approach a range of turbocharger frames, but final testing is essential to investigate the effect of different turbochargers on the overall design-point and off-design-point piston-engine cycle performance.

Different turbochargers are advantageous to an engine for different types of operation.

The performance of a turbocharger is determined by the combination of compressor and turbine specification, and the turbine is not as sensitive to engine matching as the compressor.

Acknowledgments

T. Sadoi completed his SM thesis while supported by the Mitsubishi Motor Corporation, which donated the test engine and three trial turbochargers. We thank Mr. Akira Kijima, General Manager, Engine Design Department, Mitsubishi Motors Corporation, for donating the engine and for useful discussions on the project. We also acknowledge the cooperation of F. Pekar, M. Lee, and K. Chong of Allied Signal, Inc.

Nomenclature

(A/F) = air-fuel ratio
$bmep$ = brake mean effective pressure
C_p = isobaric specific heat capacity
(F/A) = $1/(A/F)$, fuel-air ratio
$LHVF$ = lower heating value of fuel
$m, \dot{m}$ = mass, mass-flow rate
N = shaft speed, rev/sec
$n_c=2, 1$ = four-stroke, two-stroke cycle constant
p = pressure
R = universal gas constant/molecular weight
r = pressure ratio
T = temperature
V_d = engine displaced volume
$W, \dot{W}$ = work, power
δ = corrected pressure, p/p_0
ϵ = intercooler effectiveness
η_{th} = thermal efficiency
η_v = volumetric efficiency
η_p = polytropic total-to-total efficiency
η_s = isentropic total-to-total efficiency
θ = corrected temperature, T/T_0
ρ = density

Subscripts

0 = ambient air
1 = compressor inlet
2 = compressor outlet
a = air
c = compressor
e = (piston) engine
f = fuel
i = intercooler outlet/cylinder inlet
ot = brake power output
t = turbine

References

[1] Heywood, J. B., 1988, *Internal Combustion Engine Fundamentals*, McGraw-Hill, New York.
[2] Winterbone, D. E., and Jai-In, S., 1991, "The Application of Modern Control Theory to a Turbocharged Diesel Engine Power Plant," Proc. Inst. Mech. Eng. Part 1, J. Systems Control Eng., **105**, p. 11.
[3] Horlock, J. H., and Winterbone, D. E., 1982, *The Thermodynamics and Gas Dynamics of Internal Combustion Engines*, Clarendon, Oxford, UK, Vol. 1.
[4] Horlock, J. H., and Winterbone, D. E., 1986, *The Thermodynamics and Gas Dynamics of Internal Combustion Engines*, Clarendon, Oxford, UK, Vol. 2.
[5] Watson, N., and Janota, M. S., 1982, *Turbocharging the Internal Combustion Engine*, MacMillan, New York.
[6] Stone, R., 1992, *Introduction to Internal Combustion Engines*, 2nd Ed., Society of Automotive Engineers, Warrendale, PA.
[7] Henshall, S. H., 1978, *Medium and High Speed Diesel Engines for Marine Use*, The Institute of Marine Engineers, London, UK.
[8] Woodward, J. B., 1981, *Low Speed Marine Diesel*, Wiley, New York (1988 reprint by Krieger).
[9] Rowen, A. L., 1992, "Diesel Engines," Chap. 3 in *Marine Engineering*, edited by R. L. Harrington, Society of Naval Architects and Marine Engineers, New York.
[10] Sadoi, T., 1995, "Turbocharger Effects on Turbocharged-Intercooled Gasoline Engine Performance," SM thesis in Mechanical Engineering, Washington University, St. Louis, MO.

Economic and Scenario Analyses of New Gas Turbine Combined Cycles With No Emissions of Carbon Dioxide

R. Gabbrielli[1]
Dipartimento di Energetica,
Università di Pisa,
Via Diotisalvi, 2,
Pisa 56126, Italy
e-mail: r.gabbrielli@ing.unipi.it

R. Singh
School of Engineering,
Cranfield University,
Cranfield,
Bedfordshire MK43 0AL, UK
e-mail: r.singh@cranfield.ac.uk

In this paper economic and scenario analyses of new gas turbine combined cycles with no emissions of carbon dioxide (CO_2) and nitrogen oxides are described. The cycles, already presented in a recent paper (ASME GT 2002-30117), have water/steam as a working fluid, the compression phase both in liquid and vapor phase, the internal combustion between pure oxygen (O_2) and chemically heated natural gas-based syngas, and the CO_2 capture and sequestration by water condensation from the exhaust gas. The aim of the economic analyses is to estimate the investment per MW and the levelized discounted cost of the electricity (COE) produced by a power plant based on the cycles proposed here in comparison with a standard reference combined cycle power plant (SRCC). To evaluate the equipment costs, several cost functions of the most important operative parameters have been introduced and tuned with the actual data. Using the least square regression technique, explicit functions of the COE have been proposed to highlight the cheapest operative conditions with a derivative approach. Moreover, a wide scenario analysis has been carried out, varying the most important investment parameters, as, for example, the discount rate. In particular, some maps of the COE and break-even carbon tax (BECT) behavior have been constructed to test the importance of the market uncertainty on the economic results obtained. Finally, the possible technological progress effect on the BECT with a cost reduction of some innovative equipment and the O_2 production has been investigated in depth with the 2^k factorial design scenario analysis. The O_2 production has resulted as the most important parameter from an economic point of view.

[DOI: 10.1115/1.1850492]

Introduction

A wide research activity is currently devoted about new technologies for the mitigation of the anthropogenic CO_2 emissions, which derive essentially from the fossil fuel combustion. As recent official data [1], the European Union (EU) CO_2 emissions of 2001 are still largely higher than the Kyoto Protocol commitments, even if their growth is lower than the fossil fuel utilization increment [1].

During the last years in the energy industry sector, whose CO_2 emissions are about 27% of the total amount, the main interventions to mitigate the overall CO_2 emissions concerned the conversion of many old oil fired steam cycle power plants into natural gas (NG) fired gas turbine (GT) combined cycle (CC) power stations. This fact has made it possible to reduce the specific CO_2 emissions per unit of energy obtaining both the thermodynamic efficiency improvement and a wider utilization of a lower carbon content fuel.

To abate more drastically the CO_2 emissions in the fossil fuel fired power generation sector, in the near future it will be necessary to introduce severe changes in the energy conversion processes adopting the CO_2 capture and sequestration. With particular reference to the NG fired GTCC power stations, many new power generation processes have been proposed and analyzed in the literature. Briefly, the proposals include at the same time one or more of the following options: (i) new working fluids to mitigate the flame temperature in the combustion chamber, as CO_2 [2–5] or steam [6–12]; (ii) the adoption of pure oxygen (O_2) as comburent without nitrogen [2–13]; (iii) the introduction of the CO_2 capture from the exhaust gas (end-pipe option) [12,14–16] or from fossil fuel derived syngas to obtain a hydrogen enriched fuel without carbon content [17–20].

The actual future possibility to adopt one of the proposals cited above depends strongly on the overall cost of the electricity (COE) produced, on the availability of safe long-term CO_2 storage options and, finally, on the technological feasibility and reliability of some innovative and expensive equipment required, as, for example, CO_2 GTs, low-nitrogen oxides (NOx) hydrogen fired combustors, H_2 separation membranes, high-temperature steam turbines, O_2 production membranes. From the performance point of view, the most consistent penalization in comparison with standard technologies is due essentially to the CO_2 capture, to the pure O_2 production, and to the CO_2 compression for the long-term storage.

In literature, several economic data concerning the new low/no CO_2 emission GT-based power generation processes are available. Due to the absence of a standard framework for the economic assessments, it is difficult to compare them in a reliable way. Anyhow, concerning the natural gas-fired GTCCs with precombustion CO_2 capture, in comparison with standard power stations, the COE increases by 35%–55% with the relative cost of CO_2 avoided of about 35–45 US\$/t CO_2 [20–22]. When in NGCCs the CO_2 is captured from the exhaust gas, the COE increases by 35%–70%, with a relative CO_2 mitigation cost of \$30–\$50 US\$/t CO_2 [20–22]. For the CO_2 working fluid GT cycles with pure oxygen [5], the COE has been estimated [22] higher by about 90% with a mitigation cost equal to \$40 US\$/t CO_2. For the CES cycle [7], the COE seems to grow by about 20% with a mitigation cost

---

[1] Author to whom correspondence should be addressed.

Contributed by the International Gas Turbine Institute (IGTI) of THE AMERICAN SOCIETY OF MECHANICAL ENGINEERS for publication in the ASME JOURNAL OF ENGINEERING FOR GAS TURBINES AND POWER. Paper presented at the International Gas Turbine and Aeroengine Congress and Exhibition, Vienna, Austria, June 13–17, 2004, Paper No. 2004-GT-54201. Manuscript received by IGTI, October 1, 2003; final revision, March 1, 2004. IGTI Review Chair: A. J. Strazisar.

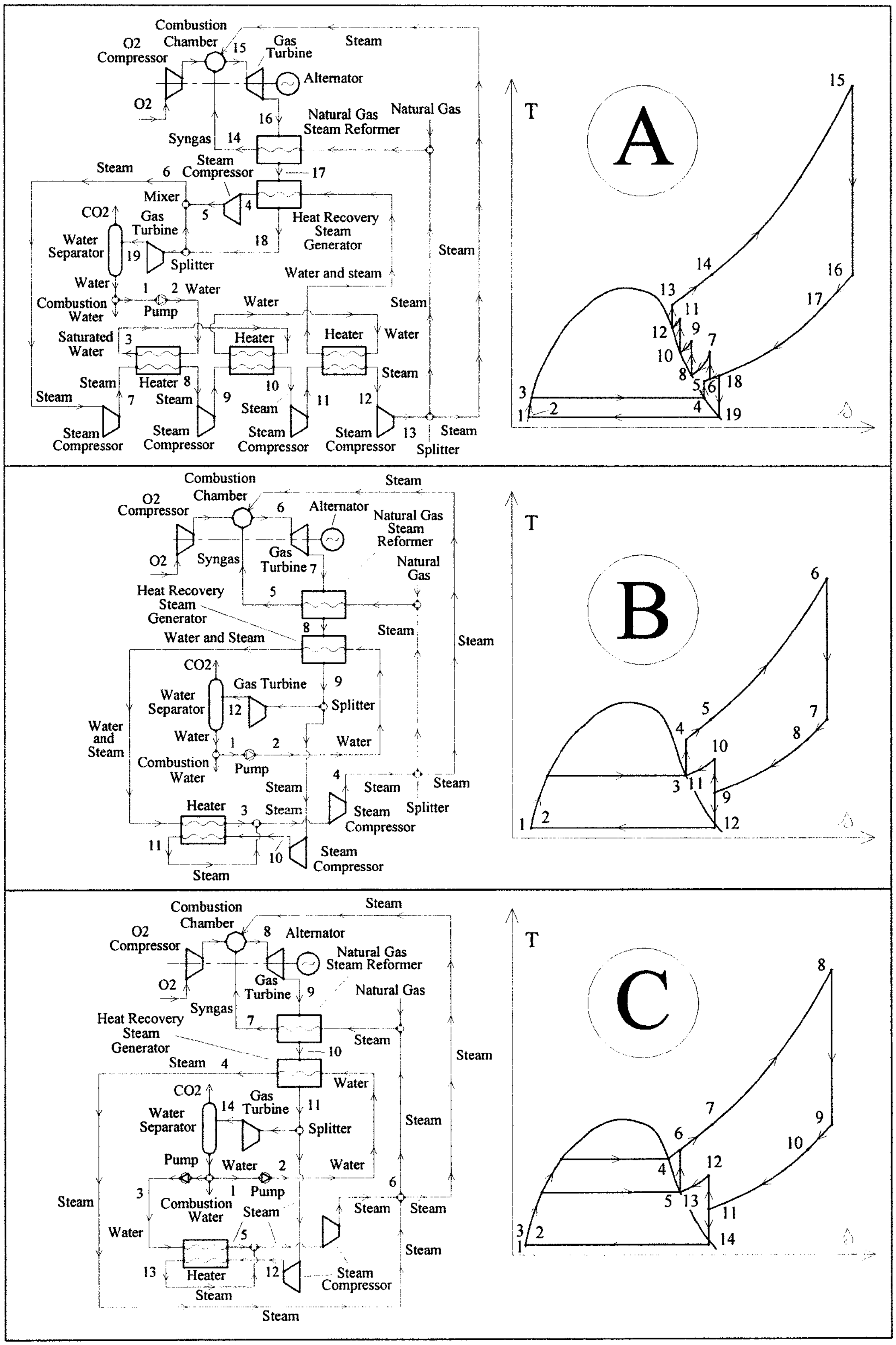

Fig. 1 Process flow diagram and relative qualitative temperature-specific entropy plane of the three cycles analyzed [10]

of 15 US\$/t CO_2 [22]. The CO_2 transportation and storage cost may be estimated equal to about 10–15 US\$/t CO_2 for distances from 100 to 200 km [22]. However, it depends strongly on the storage typology. Indeed, in enhanced oil recovery (EOR), the storage may be cheaper than in direct geological saline water deposits due to the increased productivity of the oil field.

In the present paper, economic and scenario analyses of three new gas turbine combined cycles with no CO_2 emissions [10] are

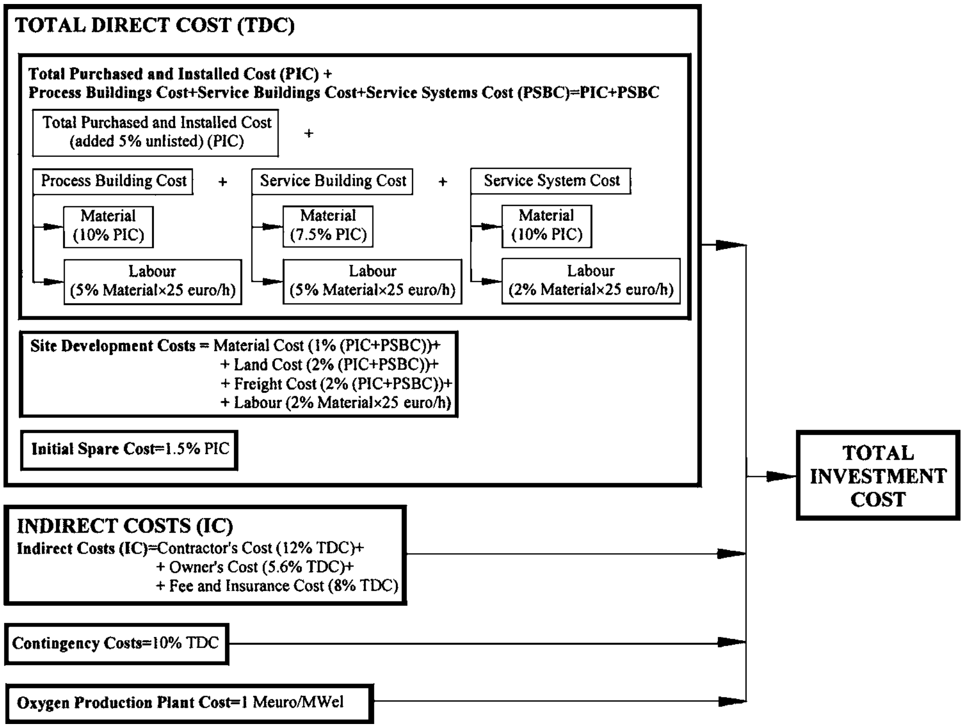

Fig. 2 Factor procedure for the total investment cost evaluation

described. These cycles, which belong to the same typologies of those proposed in [6–8], are characterized by an integration between a top superheated steam Brayton cycle with internal combustion between chemically heated NG-based syngas and pure oxygen and a bottom water/steam Rankine cycle with heat recovery.

So, first the specific investment per MW of net power (SI) and the COE produced by a power plant based on the cycles proposed have been evaluated in comparison with a standard reference combined cycle power plant (SRCC), whose features are described below. With the regression technique, the cheapest operative conditions have been calculated highlighting the relative break-even carbon tax (BECT) with respect to the SRCC. Then, a wide investment scenario analysis has been carried out to provide the investor with an effective investment selection tool. Finally, the possible technological progress effect on the BECT with a cost reduction of some innovative equipment and the O_2 production has been investigated with the 2^k factorial design technique.

Power Plant Configurations

The features and the performance data of the three no CO_2 emission GTCCs analyzed here from the economic point of view have been described in detail in [10]. Briefly (see Fig. 1), the working fluid is compressed in both a liquid and vapor phase, adopting a pump and an intercooled multistage compressor, where the intercoolings are executed down to saturation conditions with steam production; the exhaust gas is partially recirculated and mixed with the working fluid; the fuel is syngas (H_2, CO, CO_2, H_2O, and CH_4), which is produced via steam NG reforming with internal chemical heat recovery from the exhaust gas; the exhaust gas, whose components are steam and CO_2, expand down to subatmospheric pressure and cooled down to nearly ambient temperature with water condensation and consequent separation and capture of the combustion CO_2, which is liquefied at 70 bar.

The cycle A is the combination of a top intercooled steam Brayton cycle and a bottom heat recovery Rankine cycle with one pressure level (SP), which is lower than the exhaust gas pressure. In the cycle B, the single pressure level of the Rankine cycle is higher than the exhaust gas pressure and lower than that of the combustion chamber (HP). Finally, in the cycle C the Rankine cycle has two pressure levels and one reheat.

The thermodynamic efficiency and the net specific work relative to the best operative conditions of the version C, which results in the best one, are equal to 52.3% and 1150 kJ/kg, respectively. The energy expense due to the pure oxygen production (E_O_2) and the HP are the most important factors with respect to the thermodynamic efficiency and the net specific work, respectively.

Economic Analysis

The COE produced by a power plant based on the cycles proposed has been evaluated with the levelized discount cost method [23]. The total investment cost (TIC) has been evaluated adopting the factor procedure [24] reported in Fig. 2. The total purchased and installed cost (PIC) of the equipment has been calculated with suitable cost functions (see the Appendix) [24–32] of the most representative operative features. The right values of the cost function coefficients have been evaluated executing the regression fitting of actual commercial data with the aim of minimizing the mean quadratic error [30]. Due some complex and innovative features, the PIC of the heat recovery steam generator (HRSG), the compressor, the combustor, and the expander has been increased by a factor (MC) equal to 30% [33]. Indeed, for the HRSG, the presence in the hot side of heat exchange sections with different pressures implies the necessity of accurate sealing to avoid gas leakages. In the combustor, the combustion takes place between syngas and pure oxygen with a working fluid that is mainly steam, which is used also in the blade cooling. Consequently, the compression and expansion phases concern essentially a steam–CO_2 mixture with thermodynamic characteristics, as, for example, the specific heat, which are very different from those of the air.

The overall PIC has been increased by a factor equal to 1.05 with the aim of including inside the PIC also the costs of the equipment that could have been eventually neglected in the analysis. The tubular reformer has been considered from the cost point of view as a shell and tube heat exchanger made of special alloys.

Table 1 Results of the economic analysis

		Cycle A			Cycle B			Cycle C		
	HP bar	Power, MW	SI, euro/kW	COE, eurocent/kWh	Power, MW	SI, euro/kW	COE, eurocent/kWh	Power, MW	SI, euro/kW	COE, eurocent/kWh
$T=1225°\text{C}$	10	180	1124	7.48	200	1004	6.61	235	1013.8	6.15
	15	198	1142	7.45	220	1013	6.51	265	1006.7	6.00
	20	208	1179	7.50	231	1038	6.50	282	1019.5	5.95
	25	214	1223	7.58	237	1073	6.54	293	1045.8	5.96
	30	217	1270	7.67	240	1112	6.59	299	1079.2	6.00
	35	220	1321	7.78	242	1155	6.67	304	1116.4	6.05
	40	221	1374	7.91	242	1198	6.76	308	1147.5	6.10
$T=1375°\text{C}$	10	215	1019	6.94	238	917	6.20	275	932.7	5.80
	15	237	1025	6.81	261	920	6.03	309	924.1	5.62
	20	253	1049	6.86	278	934	6.02	335	922.3	5.57
	25	263	1080	6.93	289	956	6.05	353	929.2	5.55
	30	270	1114	7.01	297	981	6.09	365	942.3	5.55
	35	275	1150	7.09	301	1010	6.14	374	959.4	5.56
	40	278	1188	7.18	304	1040	6.19	380	979.5	5.59

So a multiplying factor equal to 5 has been used to increase the cost evaluated with the cost function suitable for standard heat exchangers.

The other cost voices included in the TIC are the following:

- the process buildings are the civil constructions that house the process equipment in the plant;
- the service buildings are used to house, for example, the manpower and the warehouse of the spare parts;
- the service systems distribute auxiliary services to process equipment, as, for example, steam, electricity, and compressed air;
- the site development costs, which consist of material, land, freights, and manpower labor, concern the activities that are necessary to prepare the site where the power plant will be located;
- the initial spare part cost is due to the first purchase of the spare parts at the beginning of the power plant operative life;
- the indirect costs, which can be categorized in contractor's costs, owner's costs, and insurance, include, for example, the engineering activities, the project management and administration, the building yard activities, the inspection, the insurances and legal fees;
- the contingency allowances, as well known, provide for unpredictable events that are statistically likely to occur during a power plant construction;
- the O_2 production plant is supposed to be based on the consolidated technology of the air cryogenic distillation [34]; its cost has been assumed to depend only on the overall power required for the distillation [35].

The period of construction of the power plant has been supposed equal to 5 years as its complexity [36] with the following repartition of the construction investment: 6% in the first year, 25% in the second year, 31% in the third year, 32% in the fourth year, and finally 6% in the last year, during which the operative and productive life has been supposed to start. The interests to pay during the plant construction have been evaluated with a discount rate equal to 8% [20].

The annual operative cost voices, which have been taken into account, are the following:

- the consumption of NG whose price, which has been supposed constant during the plant life, has been established equal to 4.935 euro/GJ;
- the operative and maintenance activities, whose cost has been estimated equal to 3% of the TIC;
- every five operative years the catalyst inside the reforming reactor tubes for the syngas production is supposed to be replaced and renewed with a total price equal to 8025 euro/m^3 [37]; the length and the internal diameter of the tubes have been designed equal to 11 m and 100 mm, respectively.

Finally, the assumptions to perform the economic evaluations have been (1) the equivalent full load operative hours of the plants (H) are 6500; (2) the discount rate for the actualization (i) is equal to 10% [20]; (3) the plant life (N) is equal to 20 years; (4) the thermodynamic efficiency of the power plants is constant during the plant life, and so no plant performance degradation is considered; (5) no costs of CO_2 transportation and storage are considered [22], only the costs due to the CO_2 liquefaction plant are taken into account; indeed, the overall storage costs depend on the length of pipeline and the actual storage option selected; (6) the specific energy consumption for the O_2 production with a purity of 96% is equal to 0.24 kWh/kg [3].

To execute plausible and reliable economic evaluations, the cost assessment procedure described above has been applied to a typical standard reference NGCC power plant (SRCC) whose most important data are (1) the net power is 376 MW; (2) the thermodynamic efficiency is 56%; (3) the GT power is 250 MW; (4) the firing temperature (TIT) is 1225°C; (5) the heat recovery bottom steam cycle has three pressure levels with one reheat; (6) the specific CO_2 emissions are equal to 0.362 kg/kWh. The SI and the COE of the SRCC resulted equal to 651 euro/kW and 4.67 eurocent/kWh, respectively. These data are well aligned with those available in the technical literature, confirming the reliability of the cost assessment procedure proposed.

The economic data of the three cycles have been evaluated for the following operative conditions:

- HP assumes values from 10 bar to 40 bar in steps of 5 bar;
- TIT assumes values from 1225°C to 1375°C in steps of 50°C;
- SP (only for version A) assumes values from 0.55 bar to 0.85 bar in steps of 0.10 bar.

Hence, $7\times4\times4=112$ and $7\times4=28$ operative conditions have been investigated for cycle A and for cycles B and C, respectively. The economic results of each cycle are reported in function of the operative independent variables in Table 1. For simplicity, the results of cycle A are reported only when SP is equal to 0.85, because both SI and COE decrease monotonically with SP. Moreover, the results are reported only when TIT assumes its extreme values, because they decrease monotonically also with TIT for each version.

Once established TIT, the SI has always a monotonous increasing trend with respect to HP only for the cycles A and B. On the contrary, the COE always assumes a convex trend with a minimum value with respect to HP. The cycle A, which has, in general, the worst thermodynamic performances, results also in the most expensive cycle. For each value of TIT, the SI_B is lower than SI_C

Table 2 Regression parameters for COE fitting

Regression parameters	Average quadratic error	Coefficient of determination
COE_A	1.274×10^{-1}	9.994×10^{-1}
COE_B	4.572×10^{-2}	9.997×10^{-1}
COE_C	4.336×10^{-2}	9.996×10^{-1}

when the net power is lower than a specific value. With respect to COE, the cycle C always results markedly the cheapest one thanks to the lower NG consumption due to the higher thermodynamic efficiency.

With the least square method, the regression fitting of the economic results has made it possible to obtain very reliable explicit functions of COE with respect to the independent operative variables. So, once established a value of TIT in terms of technological limit, the cheapest operative condition for each cycle with respect to HP has been calculated with a simple derivative approach. The functions, used to approximate the dependence of COE on the operative variables and listed in the following, have proved to be the best set after detailed statistical comparisons among many functions:

$$\begin{aligned}COE_A(HP,TIT,SP) &= 2.544\times10^{1}+1.136\times10^{-1}\cdot HP-4.637\cdot SP\\ &-2.322\times10^{-2}\cdot TIT-4.412\times10^{-2}\cdot HP\cdot SP\\ &-4.238\times10^{-5}\cdot HP\cdot TIT+3.059\times10^{-3}\\ &\cdot SP\cdot TIT-5.138\times10^{-7}\cdot HP^2+5.795\times10^{-1}\\ &\cdot SP^2+6.682\times10^{-6}\cdot TIT^2+3.389\times10^{1}/HP^2\\ &+1.716\times10^{-1}/SP^2+1.969/TIT^2;\end{aligned}$$

$$\begin{aligned}COE_B(HP,TIT) &= 1.778\times10^{1}+4.411\times10^{-2}\cdot HP-1.558\times10^{-2}\\ &\cdot TIT-2.971\times10^{-5}\cdot HP\cdot TIT+1.301\times10^{-4}\\ &\cdot HP^2+5.017\times10^{-6}\cdot TIT^2+3.005\times10^{1}/HP^2\\ &-9.202\times10^{-3}/TIT^2;\end{aligned}$$

$$\begin{aligned}COE_C(HP,TIT) &= 1.660\times10^{1}+4.139\times10^{-2}\cdot HP-1.484\times10^{-2}\\ &\cdot TIT-3.673\times10^{-5}\cdot HP\cdot TIT+2.123\times10^{-4}\\ &\cdot HP^2+4.972\times10^{-6}\cdot TIT^2+2.781\times10^{1}/HP^2\\ &+2.721\times10^{-1}/TIT^2;\end{aligned}$$

where the unit measures of each coefficient are omitted for simplicity and COE_A (HP,SP,TIT), COE_B (HP,TIT), COE_C (HP,TIT) are the estimated functions of COE for cycles A, B, and C, respectively. The values of the regression parameters reported in Table 2 demonstrate the goodness of the fitting executed.

When TIT is equal to 1375°C, the minimum COE is reached when HP is practically equal to 15 bar (6.81 eurocent/kWh), 20 bar (6.02 eurocent/kWh) and 27.6 bar (5.54 eurocent/kWh) for cycles A, B, and C, respectively. So, the best COE_C is about 19% higher than the COE produced by the SRCC.

For each cycle, in Table 3 the lowest and highest values of the BECT are reported. These values, that for cycles B and C are in the same range of other advanced low/no CO_2 emission GTCCs proposed in the literature [20–22], represent practically the tax to pay for each ton of CO_2 emitted into the atmosphere by the SRCC owner so that the SRCC COE results equal to that produced with the cycles proposed. It is interesting to note that a tax of 1 euro/t CO_2 would correspond to a fictitious increase of the NG price equal to 1.12%.

Table 3 Break-even carbon tax with respect to the reference combined cycle

	SP, bar	HP, bar	TIT, °C	Power, MW	BECT, euro/t CO_2
Cycle A	0.55	40	1225	209	114.8
	0.85	15	1375	237	58.9
Cycle B	⋯	40	1225	242	57.6
	⋯	20	1375	278	37.4
Cycle C	⋯	10	1225	235	40.8
	⋯	27.6	1375	360	23.9

Scenario Analysis

An investment scenario analysis about the COE produced with the cycles proposed and the relative BECT has been carried out to provide the investor with a tool suitable for testing the effects of the market uncertainty on the economic results reported in the previous section. So, for each operative condition, the importance of the main investment parameters, as *i*, *N*, *H*, on the COE and the BECT has been evaluated. For each investment parameter, three values have been considered:

- *i*: 0.08, 0.10, 0.12;
- *H*: 5000 h, 6500 h, 8000 h;
- *N*: 15 yr, 20 yr, 25 yr.

Typically, in an investment analysis, the discount rate value is selected by the decision maker, taking into account the risk of the investment. If the investor wants to reduce the investment risk associated with not standard technologies of power generation, a high *i* value may be used. In less risky conditions, it is possible to adopt a low discount rate. Similar considerations may be executed about the *N* value. In the preliminary phase of an investment, it is necessary to estimate the plant operative life and, consequently, the life of the investment. It is usual to adopt a great value of the plant life (generally 25 years) with standard power generation technologies. If the power plant is innovative, a lower value of the plant life could be more suitable. The *H* value influences largely the levelized cost of the electricity that increases when *H* decreases. A power station may be utilized in peak load conditions with higher COE or base load conditions with lower COE. Indeed, in the future with a free energy market, it is presumable that even large plants could work in peak load conditions. The most meaningful results of the investment scenario analysis are reported in Tables 4 and 5, for the best set of the operative independent variables (the best values of TIT and SP are always equal to 1375°C and 0.85, respectively). In comparison with the standard investment scenario, the BECT of cycle C decreases by about 24% in the best scenario, i.e. when *i*, *H*, and *N* assume the lowest, the highest, and the highest value, respectively.

Finally, a technological and investment scenario analysis has been performed. With the 2^k factorial design analysis [38], the importance of the technological progress and of the investment parameters on the BECT has been tested. The technological

Table 4 Cost of the electricity with different investment scenarios, eurocent/kWh and optimal value of HP

	$H=5000$ h $i=0.12$ $N=15$ yr	$H=6500$ h $i=0.10$ $N=20$ yr	$H=8000$ h $i=0.08$ $N=25$ yr
Cycle A	8.23 (HP=15 bar)	6.81 (HP=15 bar)	5.99 (HP=15 bar)
Cycle B	7.31 (HP=15 bar)	6.02 (HP=20 bar)	5.29 (HP=20 bar)
Cycle C	6.72 (HP=25 bar)	5.55 (HP=30 bar)	4.87 (HP=35 bar)
SRCC	5.49	4.67	4.21

Table 5 Break-even carbon tax with different investment scenarios, euro/t CO_2

	$H=5000$ h $i=0.12$ $N=15$ yr	$H=6500$ h $i=0.10$ $N=20$ yr	$H=8000$ h $i=0.08$ $N=25$ yr
CycleA	75.4	58.9	49.3
CycleB	50.1	37.4	29.8
CycleC	33.9	24.2	18.4

progress could be concretized with a decrease of the cost of the innovative equipment and of the pure oxygen production process. So, the MC and E_O_2 have been considered as technological input variables.

The 2^k factorial design of experiment is a well-known technique that permits us to analyze the average effect of the variation of each input factor on the output variable. Hence, this method provides an answer to the necessity for knowing what independent variables have the most influence on the response of the system. Once established an admissible range of variation for each independent factor, it is necessary, for each combination, to evaluate the output variable value when the input factors assume their minimum and maximum values. Then, the average change of the output variable when a generic input factor changes within its specific range can be calculated in the following way:

$$e_j = \frac{\sum_{i=1}^{2^k} a_{ij} \cdot o_i}{2^{k-1}},$$

where k is the number of input variables, j is the index related to the input variable j, 2^k is the overall number of possible combinations of the k variables, e_j is the main effect of the input variable j on the output variable, o_i is the value of the output variable for the combination i of the input factor, a_{ij} is equal to $+1$ or -1 if the input variable j assumes, respectively, its highest or lowest value in the combination i. If the interaction effect of two input factors has to be found, it is possible to calculate the average of the differences among the effects of each factor when the others assume the extreme values of the range of variation. Hence, the interaction effect between the independent variables j and w on the output of the system (e_{jw}) is evaluated with

$$e_{jw} = \frac{\sum_{i=1}^{2^k} a_{ij} \cdot a_{iw} \cdot o_i}{2^{k-1}},$$

where e_{jw} is obviously equal to e_{wj}.

Referring to the 2^k factorial design analysis described here, the extreme input values of the five variables and the relative values of the BECT are reported in Table 6. For MC and E_O_2, an optimistic value and a pessimistic one have been considered. It is important to note that there are some sets of variables for which the thermodynamic efficiency of cycle C is higher than that of the SRCC and, consequently, the BECT results are slightly negative.

Figure 3 reports the main effects of the variables on the BECT. In the ranges analyzed, E_O_2 always results in the most important variable. Indeed, the decrease of E_O_2 from 0.32 to 0.10 kWh/kg implies a large economic improvement for each version. Also, the reduction of the innovative equipment cost implies a consistent reduction of BECT. For each cycle, the only interaction effect not negligible is that between E_O_2 and H. For cycles A, B, and C, it results equal to -5.59, -4.61, and -4.27 euro/t CO_2, respectively.

Table 6 Input data for the 2^k factorial design scenario analysis of the BECT

H, h	i	N, yr	E_O_2, kWh/kg	MC	Cycle A BECT, euro/t CO_2	Cycle B BECT, euro/t CO_2	Cycle C BECT, euro/t CO_2
5000	0.08	15	0.10	1	30.8	11.5	0.2
5000	0.08	15	0.10	1.6	47.8	30.2	17.5
5000	0.08	15	0.32	1	76.5	48.1	32.5
5000	0.08	25	0.10	1	28.9	10.6	0.1
5000	0.12	15	0.10	1	33.4	12.6	0.3
8000	0.08	15	0.10	1	26.1	9.3	−0.2
5000	0.08	15	0.32	1.6	96.3	70.0	52.3
5000	0.08	25	0.10	1.6	43.1	26.5	14.6
5000	0.12	15	0.10	1.6	53.8	35.1	21.0
8000	0.08	15	0.10	1.6	36.7	21.3	10.8
5000	0.08	25	0.32	1	70.1	43.6	29.0
5000	0.12	15	0.32	1	84.8	54.0	36.9
8000	0.08	15	0.32	1	61.5	37.3	24.1
5000	0.12	25	0.10	1	31.8	11.9	0.2
8000	0.08	25	0.10	1	24.9	8.7	−0.4
8000	0.12	15	0.10	1	27.7	10.0	0.0
5000	0.08	25	0.32	1.6	86.8	62.2	45.8
5000	0.12	15	0.32	1.6	108.7	80.3	60.7
8000	0.08	15	0.32	1.6	73.9	51.2	37.0
5000	0.12	25	0.10	1.6	49.9	32.0	18.8
8000	0.08	25	0.10	1.6	33.8	18.8	9.0
8000	0.12	15	0.10	1.6	40.5	24.4	13.1
5000	0.12	25	0.32	1	79.5	48.0	34.1
8000	0.12	15	0.32	1	66.7	41.1	27.1
8000	0.08	25	0.32	1	57.5	34.4	21.9
8000	0.12	25	0.10	1	26.7	9.5	−0.1
5000	0.12	25	0.32	1.6	100.7	73.7	55.3
8000	0.08	25	0.32	1.6	67.9	46.1	32.8
8000	0.12	15	0.32	1.6	81.6	57.8	42.3
8000	0.12	25	0.10	1.6	38.1	22.4	11.6
8000	0.12	25	0.32	1	63.3	38.7	25.2
8000	0.12	25	0.32	1.6	76.6	53.5	38.9

Conclusions

With a reliable cost assessment framework, the economic aspects of three new gas combined cycles with no CO_2 emissions have been analyzed in depth, taking into account both some investment parameters and technological aspects. The power plant based on cycle C, which has the best thermodynamic performances, is characterized also by the lowest COE and BECT. As the present technological level, with standard operative conditions, the lowest COE results about 19% higher than that relative to the SRCC. A wide investment scenario analysis has made it

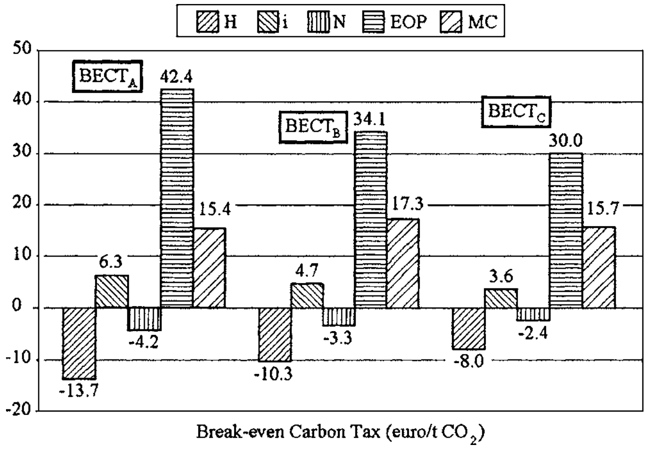

Fig. 3 Main effects of the investment and technological variables on the BECT with the 2^k factorial design scenario analysis

possible to highlight that the difference in terms of COE between cycle C and the SRCC changes only slightly, decreasing to about 16% in the best conditions.

Finally, a technological scenario analysis has pointed out that progress in the technology of oxygen production could imply a large reduction of economic difference between the proposed advanced cycles and the standard reference power plant. So, the present studies about new oxygen production methodologies, as, for example, the ion transport membranes, appear very promising for the success of new power generation processes with low impact in terms of the greenhouse effect.

Moreover, to overcome the economic penalization, the new low/no CO_2 emission power generation processes could be promoted by taxes on the actual CO_2 emissions into the atmosphere from the power plants or by defiscalization on the fuel burned in a greenhouse friendly way.

Obviously, the actual possibility of introduction of these new processes depends strongly on the definition of safe long-term CO_2 storage options. This aspect, which has not been faced in the present paper, is the most critical obstacle on the way toward a no CO_2 emission fossil fuel fired power generation sector.

Acknowledgment

The authors want to thank Franco Donatini (ENEL-Produzione Ricerca, Pisa) for his support provided during the research, a part of which has been described in this paper.

Nomenclature

BECT = break-even carbon tax (euro/t CO_2)
CC = combined cycle
COE = cost of the electricity (eurocent/kWh)
EOR = enhanced oil recovery
E_O_2 = energy consumption to produce 1 kg of pure oxygen (kWh/kg)
EU = European Union
GT = gas turbine
H = equivalent full load operative hours of the plants (h)
HP = combustion pressure (bar)
HRSG = heat recovery steam generator
i = discount rate for the cash flow actualization
MC = multiplying factor of the purchased and installed cost of some innovative and complex equipment
N = duration of the power plant life (yr)
NG = natural gas
NOx = nitrogen oxides
PIC = purchased and installed cost (euro)
SI = specific investment (euro/kW)
SP = low saturation pressure in cycle A (bar)
SRCC = standard reference combined cycle power plant
TIC = total investment cost (euro)
TIT = firing temperature (°C)

Subscripts

A = relative to cycle A
B = relative to cycle B
C = relative to cycle C

Appendix: Cost Functions

The cost functions adopted in the evaluation of the purchased and installed cost of the equipment of the cycles proposed are the following: heat recovery steam generator,

$$\mathrm{Cost}_{\mathrm{HRSG}}=9090\cdot\frac{\mathrm{euro}}{(\mathrm{kW/K})^{0.80}}\cdot\left(\frac{Q}{\Delta\mathrm{TLM}}\right)^{0.80}+23115\cdot\frac{\mathrm{euro}}{\mathrm{kg/s}}\cdot m_{\mathrm{water}}+1286\cdot\frac{\mathrm{euro}}{(\mathrm{kg/s})^{1.20}}\cdot(m_{\mathrm{gas}})^{1.20},$$

where Q (kW) is the heat duty of the HRSG, ΔTLM (K) is the logarithmic mean temperature difference, m_{water} (kg/s) is the mass flow of the steam in the cold side, and m_{gas} (kg/s) is the exhaust gas mass flow in the hot side. In the cost function of the HRSG, a term $Q/\Delta\mathrm{TLM}$ must be considered for each heat exchange section; condensate pump,

$$\mathrm{Cost}_{\mathrm{pump}}=2076\cdot\frac{\mathrm{euro}}{(\mathrm{kW})^{0.71}}\cdot(P)^{0.71}\cdot 1.41\cdot\left[1+\frac{(1-0.80)^3}{(1-\eta_{\mathrm{ex}})^3}\right],$$

where P is the power of the pump (kW), and η_{ex} is the exergetic efficiency; centrifugal compressor,

$$\mathrm{Cost}_{\mathrm{centr.\ compr.}}=431\cdot\frac{\mathrm{euro}}{(\mathrm{kW})^{0.94}}\cdot(P)^{0.94},$$

where P is the power of the compressor (kW); shell and tube heat exchanger,

$$\mathrm{Cost}_{\mathrm{heat\ exchanger}}=2111\cdot\frac{\mathrm{euro}}{(\mathrm{m}^2)^{0.69}(\mathrm{bar})^{0.28}}\cdot(S)^{0.69}\cdot(p)^{0.28},$$

where S is the heat exchange surface (m^2), p is the highest pressure (bar) in the heat exchanger: electrical generator,

$$\mathrm{Cost}_{\mathrm{el.\ gen.}}=70\cdot\frac{\mathrm{euro}}{(\mathrm{kW})^{0.95}}\cdot(P)^{0.95},$$

where P is the power (kW); condenser,

$$\mathrm{Cost}_{\mathrm{condenser}}=168\cdot\frac{\mathrm{euro}}{\mathrm{m}^2}\cdot S+1346\cdot\frac{\mathrm{euro}}{\mathrm{kg/s}}\cdot m_{\mathrm{steam}},$$

where S is the heat exchange surface (m^2) and m_{steam} is the mass flow (kg/s) of the steam to condense; compressor, turbine, and burner,

$$\mathrm{Cost}_{\mathrm{compressor}}=\frac{39}{1-\eta_{\mathrm{is}}}\cdot\frac{\mathrm{euro}}{\mathrm{kg/s}}\cdot m_{\mathrm{air}}\cdot r_c\cdot\ln(r_c),$$

$$\mathrm{Cost}_{\mathrm{turbine}}=\frac{927}{1-\eta_{\mathrm{is}}}\cdot\frac{\mathrm{euro}}{\mathrm{kg/s}}\cdot m_{\mathrm{air}}\cdot\ln(r_{\mathrm{es}})\cdot\left[1+\exp\left(\frac{0.036\cdot\mathrm{TIT}}{\mathrm{K}}-65.66\right)\right]$$

$$\mathrm{Cost}_{\mathrm{burner}}=\frac{453}{1-f_{\mathrm{cc}}}\cdot\frac{\mathrm{euro}}{\mathrm{kg/s}}\cdot m_{\mathrm{air}}\cdot\left[1+\exp\left(\frac{0.018\cdot\mathrm{TIT}}{\mathrm{K}}-31.86\right)\right],$$

where η_{is} is the isoentropic efficiency of the compressor and expander, m_{air} is the air mass flow (kg/s), r_c is the pressure ratio of the compressor, f_{cc} is the pressure drop factor in the burner, TIT is the temperature at the outlet of the burner (K), and r_{es} is the expansion ratio of the expander.

References

[1] Gugele, B., Huttunen, K., and Ritter, M., 2003, "Annual European Community Greenhouse Gas Inventory 1990–2001 and Inventory Report 2003. Submission to the UNFCCC Secretariat," Technical Report, European Environment Agency.

[2] Yantovski, E. I., 1996, "Zero Emission Fuel-Fired Power Plants Concept," Energy Convers. Manage., **37**, pp. 867–877.

[3] Dechamps, P. J., Distelmans, M., Mathieu, P., and Pirard, N., 1994, "Performances of Combined Cycle Power Plants Using CO_2 Gas Turbine," *Proc., Flowers '94 Conference*, Florence, Italy.

[4] Mathieu, P., and Nihart, R., 1999, "Zero-Emission MATIANT Cycle," J. Eng. Gas Turbines Power, **116**, pp. 116–120.

[5] Jackson, A., Neto, A. C., Whellens, M. W., and Audus, H., 2000, "Gas Turbine Performance Using Carbon Dioxide as Working Fluid in Closed Cycle Operation," Proceedings, ASME TURBOEXPO 2000, Munich, Germany, ASME Paper No. 2000-GT-153.

[6] Jericha, H., Sanz, W., Woisetschlager, J., and Fesharaki, M., 1995, " CO_2-Retention Capability of CH_4/O_2-Fired Graz Cycle," *Proceedings, 21st CIMAC World Congress on Combustion Engines*, Interlaken, Switerland.

[7] Anderson, R., Brandt, H., Mueggenburg, H., Taylor, J., and Viteri, F., 1998, ‘‘A Power Plant Concept Which Minimizes the Cost of Carbon Dioxide Sequestration and Eliminates the Emission of Atmospheric Pollutants,’’ *Proceedings, 4th International Conference on Greenhouse Gas Control Technologies*, Interlaken, Switzerland.

[8] Bolland, O., Undrum, H., and Nilsen, M., 2000, ‘‘Natural Gas Fired Power Cycles With Integrated CO_2 Capture,’’ *Proceedings, 5th International Conference on Greenhouse Gas Control Technologies*, Cairns, Australia.

[9] Bannister, R. L., Newby, R. A., and Yang, W. C., 1999, ‘‘Final Report on the Development of a Hydrogen-Fuelled Combustion Turbine Cycle for Power Generation,’’ ASME J. Eng. Gas Turbines Power, **121**, pp. 38–45.

[10] Gabbrielli, R., and Singh, R., 2003, ‘‘Thermodynamic Performance Analysis of New Gas Turbine Combined Cycles With No Emissions of Carbon Dioxide,’’ ASME J. Eng. Gas Turbines Power, **125**, pp. 940–946.

[11] Sugisita, H., Mori, H., and Uematsu, K., 1998, ‘‘A Study of Thermodynamic Cycle and System Configurations of Hydrogen Combustion Turbines,’’ Int. J. Hydrogen Energy, **23**, pp. 705–712.

[12] Bolland, O., Undrum, H., and Nilsen, M., 2000, ‘‘Natural Gas Fired Power Cycles With Integrated CO_2 Capture,’’ *Proceedings, 5th International Conference on Greenhouse Gas Control Technologies*, Cairns, Australia.

[13] Ishida, M., and Jin, H., 1994, ‘‘A New Advanced Power-Generation System Using Chemical-Looping Combustion,’’ Energy, **19**, pp. 415–422.

[14] Freund, P., 1998, ‘‘Abatement and Mitigation of Carbon Dioxide Emissions From Power Generation,’’ *Proceedings, Power-Gen ’98*, Milan, Italy.

[15] Bolland, O., and Undrum, H., 1999, ‘‘Removal of CO_2 From Natural Gas Fired Combined Cycle Plants,’’ *Proceedings, Power-Gen ’99*, Frankfurt, Germany.

[16] Fiaschi, D., and Manfrida, G., 1999, ‘‘A New Semi-Closed Gas Turbine Cycle With CO_2 Separation,’’ Energy Convers. Manage., **40**, pp. 1669–1678.

[17] Hendriks, C. A., and Blok, K., 1992, ‘‘Carbon Dioxide Recovery Using a Dual Gas Turbine IGCC Plant,’’ *Proceedings, 1st International Conference on Carbon Dioxide Removal*, Amsterdam, Netherlands.

[18] Andersen, T., Kvamsdal, M., and Bolland, O., 2000, ‘‘Gas Turbine Combined Cycle With CO_2-Capture Using Auto-Thermal Reforming of Natural Gas,’’ Proceedings, ASME TURBOEXPO 2000, Munich, Germany, ASME Paper No. 2000-GT-162.

[19] Lozza, G., and Chiesa, P., 2000, ‘‘Natural Gas Decarbonization to Reduce CO_2 Emission From Combined Cycles. Part A: Partial Oxidation,’’ Proceedings, ASME TURBOEXPO 2000, Munich, Germany, ASME Paper No. 2000-GT-0163.

[20] Lozza, G., and Chiesa, P., 2000, ‘‘Natural Gas Decarbonization to Reduce CO_2 Emission From Combined Cycles. Part B: Steam-Methane Reforming,’’ Proceedings, ASME TURBOEXPO 2000, Munich, Germany, ASME Paper No. 2000-GT-0164.

[21] IEA Greenhouse Gas R&D Program, 2000, ‘‘Technology Status Report. CO_2 Capture and Storage,’’ Technical Report.

[22] Hustad, C. W., 2000, ‘‘Review Over Recent Norwegian Studies Regarding Cost of Low CO_2-Emission Power Plant Technology,’’ *Proceedings, 5th International Conference on Greenhouse Gas Control Technologies*, Cairns, Australia.

[23] Bejan, A., Tsatsaronis, G., and Moran, M., 1996, *Thermal Design and Optimization*, John Wiley & Sons, New York.

[24] Peters, M. S., and Timmerhaus, K. D., 1991, *Plant Design and Economics for Chemical Engineers*, McGraw-Hill, New York.

[25] Manninen, J., and Zhu, X. X., 1999, ‘‘Optimal Flowsheeting Synthesis for Power Station Design Considering Overall Integration,’’ Energy, **24**, pp. 451–478.

[26] Lazzaretto, A., and Macor, A., 1995, ‘‘Direct Calculation of Average and Marginal Costs From the Productive Structure of an Energy System,’’ J. Energy Resour. Technol., **117**, pp. 171–178.

[27] Foster-Pegg, R. W., 1986, ‘‘Capital Cost of Gas-Turbine Heat-Recovery Boilers,’’ Chem. Eng. **93**, pp. 73–78.

[28] Valero, A., Lozano, M. A., Serra, L., Tsatsaronis, G., Pisa, J., Frangopoulos, C., and Von Spakovsky, M. R., 1994, ‘‘CGAM Problem: Definition and Conventional Solution,’’ Energy, **19**, pp. 279–286.

[29] Araujo da Gama Cerqueira, S. A., and Nebra, S. A., 1999, ‘‘Cost Attribution Methodologies in Cogeneration Systems,’’ Energy Convers. Manage., **40**, pp. 1587–1597.

[30] Agazzani, A., and Massardo, A., 1997, ‘‘A Tool for Thermoeconomic Analysis and Optimization of Gas, Steam, and Combined Plants,’’ ASME J. Eng. Gas Turbines Power, **119**, pp. 885–892.

[31] Lozano, M. A., and Valero, A., 1993, ‘‘Thermoeconomic Analysis of Gas Turbine Cogeneration Systems,’’ *AES-Vol. 30 Thermodynamic and the Design, Analysis, and Improvement of Energy Systems*, Richter, Book No. H00874-1993.

[32] Frangopoulos, C. A., 1994, ‘‘Application of the Thermoeconomic Functional Approach to the CGAM Problem,’’ Energy, **19**, pp. 323–342.

[33] Gambini, M., and Vellini, M., 2000, ‘‘CO_2 Emission Abatement From Fossil Fuel Power Plants by Exhaust Gas Treatment,’’ *Proceedings, 2000 International Joint Power Generation Conference*, Miami Beach, FL.

[34] Smith, A. R., and Klosek, J., 2001, ‘‘A Review of Air Separation Technologies and Their Integration With Energy Conversion Processes,’’ Fuel Process. Technol., **70**, pp. 115–134.

[35] McMullan, J. T., 1995, ‘‘Techno-Economic Assessment Studies of Fossil Fuel and Fuel Wood Power Generation Technologies,’’ Joule II-Program R&D in Clean Coal Technology, Report to the European Commission.

[36] Chiesa, P., and Consonni, S., 2000, ‘‘Natural Gas Fired Combined Cycles With Low CO_2 Emissions,’’ ASME J. Eng. Gas Turbines Power, **122**, pp. 429–436.

[37] Strait, M., Allum, G., and Gidwani, N., 1997, ‘‘Synthesis Gas Reformers,’’ http://www.owlnet.rice.edu/~ceng403/nh3ref97.html, last visit in November 2003.

[38] Montgomery, D. C., 1991, *Introduction to Statistical Quality Control*, John Wiley & Sons, New York.

Preliminary Study of a Novel R718 Compression Refrigeration Cycle Using a Three-Port Condensing Wave Rotor

Amir A. Kharazi
e-mail: kharazia@egr.msu.edu

Pezhman Akbari
e-mail: akbari@egr.msu.edu

Norbert Müller
e-mail: mueller@egr.msu.edu

Department of Mechanical Engineering
Michigan State University,
East Lansing, MI 48824-1226

Using a novel 3-port condensing wave rotor enhancing the turbocompression in a R718 refrigeration cycle, which uses only water as a refrigerant, has been introduced. The wave-rotor implementation can increase efficiency and reduce size and cost of R718 units. The condensing wave rotor employs pressurized water to pressurize, desuperheat, and condense the refrigerant vapor—all in one dynamic process. The underlying phenomena of flash evaporation, shock wave compression, desuperheating, and condensation inside the wave rotor channels are described in a wave and phase-change diagram. The thermodynamic process is shown in pressure–enthalpy and temperature–entropy diagrams. A computer program based on a thermodynamic model was generated to evaluate the performance of R718 baseline and wave-rotor-enhanced cycles. The effect of some key parameters on the performance enhancement is demonstrated as an aid for optimization. A performance map summarizes the findings. It shows optimum wave rotor pressure ratio and maximum relative performance improvement of R718 cycles by using the 3-port condensing wave rotor. [DOI: 10.1115/1.1850503]

Introduction

The potential for using wave devices in thermodynamic cycles for power generation, propulsion, and refrigeration has attracted the attention of researchers since the early twentieth century. Shock tubes, shock tunnels, pressure exchangers, pulse combustors, pulse detonation engines, and wave rotors are among the best-known wave devices developed so far. These devices represent applications of classical nonsteady one-dimensional compressible flow theory. It is well known, but not yet widely employed, that time-dependent flow devices can generate much greater pressure rises than those obtained in steady-state flow devices [1–3]. By generating shock waves in appropriate geometries, unsteady wave machines can transfer the energy of a high-pressure fluid directly to another low-pressure fluid without using mechanical components such as pistons or vaned impellers.

Within the family of wave devices, wave rotors have demonstrated an attractive potential for reaching the ultrahigh performance targets of power systems and for lowering their cost. Considerable amount of research has been devoted to the progress and development of wave rotor technology, especially in the past few decades. Most of the work in the U.S. expands from the early efforts of the General Electric Company (GE), General Power Corporation (GPC), and Rolls Royce [4,5] to the recent activities of the wave rotor team at NASA Glenn Research Center (GRC) collaborated by the U.S. Army Research Laboratory (ARL) and Rolls-Royce Allison [6–14].

In a gas turbine, a wave rotor provides a pressure gain additional to that provided by the compressor. It also enables a higher cycle peak temperature without raising the turbine inlet temperature. This is because a part of the energy of the burned gas leaving the combustion chamber is used in a shock compression process to increase the pressure and temperature of the fresh air before it enters the combustion chamber. Therefore, a wave rotor enhances significantly the performance of a gas turbine engine by increasing both the output work and overall thermal efficiency, hence reducing the specific fuel consumption considerably [15–17]. Detailed descriptions of wave rotor operations and configurations are provided in the references cited above and are not repeated here.

The application of wave rotors is not limited to gas turbine engines. Brown Boveri Company (BBC) in Switzerland, later known as Asea Brown Boveri (ABB), has a long history of using wave rotors as superchargers in passenger car and heavy diesel engines [18–26]. ABB's pressure wave supercharger termed as the Comprex® has been used commercially in several passenger car engines in the past three decades.

Wave rotors also have been used for air-cycle refrigeration systems [27–29]. Power Jets Ltd in the U.K. utilized wave rotor technology in the design and development of two prototype air-cycle refrigerators used for environmental cooling purposes. The prototypes were installed and employed in gold mines in India and South Africa and performed the same duty as equivalent vapor-cycle machines, but with lower weight and bulk.

The present study demonstrates the performance improvement of a turbo-compression refrigeration cycle that uses water as refrigerant (R718) by utilizing a novel 3-port condensing wave rotor. The phase change of the fluid inside the wave rotor channels in a R718 refrigeration application is a major difference when compare to the operation of a wave rotor in a gas turbine cycle or an air refrigeration cycle. Furthermore, the high-pressure fluid used to compress the low-pressure fluid is at lower temperature [3]. Adding a wave rotor to a R718 cycle enables a greater temperature lift or reduces the compressor pressure ratio which is crucial for the R718 chiller technology, where the stage pressure ratio is very much limited by the thermodynamic properties of water vapor. Some structural and economic advantages of integrating both 4-port and 3-port wave rotors in a R718 cycle have been discussed in a previous study [3]. Utilizing a 3-port wave rotor appears more promising because it combines the function of a compressor stage and the condenser in one compact unit. Both pressure rise and condensation occur inside the wave rotor channels.

Contributed by the International Gas Turbine Institute (IGTI) of THE AMERICAN SOCIETY OF MECHANICAL ENGINEERS for publication in the ASME JOURNAL OF ENGINEERING FOR GAS TURBINES AND POWER. Paper presented at the International Gas Turbine and Aeroengine Congress and Exhibition, Vienna, Austria, June 13–17, 2004, Paper No. 2004-GT-53622. Manuscript received by IGTI, October 1, 2003; final revision, March 1, 2004. IGTI Review Chair: A. J. Strazisar.

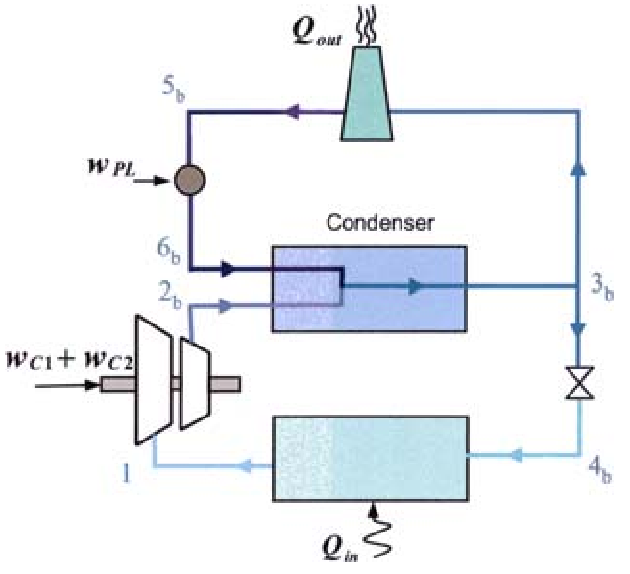

Fig. 1 Schematic of an R718 cycle with direct condensation and evaporation

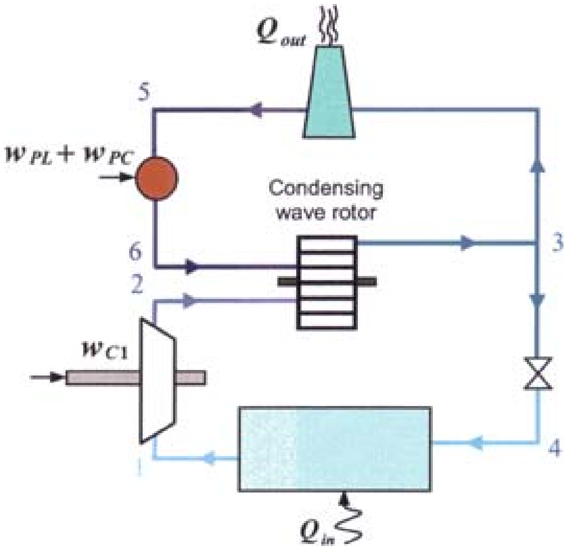

Fig. 2 Schematic of an R718 cycle enhanced by a 3-port condensing wave rotor substituting for the condenser and one compressor stage

Water as a Refrigerant

Water is a natural and clean refrigerant with no Ozone Depletion Potential (ODP=0), no contribution to the global warming (GWP=0), and without any safety risk. It is chemically stable, nontoxic, nonflammable, commonly available, and easily disposable after use. In R718 systems, water serves as both refrigerant and heat transfer fluid. Therefore, direct heat exchangers can be used for evaporator and condenser increasing the energy-saving potential. Moreover, water can function as a working fluid for refrigeration and heat pump cycles in the range of evaporation temperature of 0°C to very high temperatures (e.g., 150°C) [30–33]. Figure 1 depicts schematically a R718 cycle with direct condenser and direct evaporator.

There are a few fundamental differences between water and traditional refrigerants. At the triple point, the vapor pressure of water is only 611 Pa, which is less than 1% of the atmospheric pressure. The low operating pressures of water-vapor refrigeration systems combined with the steep vapor pressure curve of water requires compression systems that can handle large-volume flows and deliver high-pressure ratios [34–36]. This states challenges for the compressor design. While single stage turbocompressors commonly deliver large-volume flows with mostly insufficient pressure ratios, positive displacement compressors can obtain high-pressure ratios but only for relative small-volume flows. A possible compromise is the use of multistage turbocompressors with intercooler. However, this is expensive and bulky. The presented work is part of the ongoing research to improve the compressors, heat exchangers, and to reduce the size of the whole units. Any improvement in compressor and heat exchanger technology has a direct effect on the cost and efficiency of the R718 units.

R-718 Refrigeration Cycle Enhanced With a 3-Port Condensing Wave Rotor

Using a 3-port condensing wave rotor in a water refrigeration cycle appears as a promising technology. It can improve the coefficient of performance (COP) of R718 units while reducing their cost and size. Its successful implementation may substitute three subsystems: the intercooler, one compressor stage, and the condenser.

Figure 2 shows a schematic of a R718 cycle using a 3-port condensing wave rotor. A schematic design of a condensing wave rotor is depicted in Fig. 3. In this innovative design, condensation of vapor happens inside the wave rotor channels as explained below and depicted in Figs. 4 and 5. Figure 4 schematically shows a model for the condensation process inside a channel of a 3-port condensing wave rotor. Figure 5 shows a corresponding schematic wave and phase-change diagram.

Coming from the turbocompressor (2), the superheated vapor flows continuously through a vapor collector (Fig. 3) to the inlet port of the wave rotor located at one of the two stationary end plates. By rotating the wave rotor between the two end plates, the wave rotor channels are opened to the port and filled with the incoming water vapor. The region (*a*) in Figs. 4 and 5 is the state

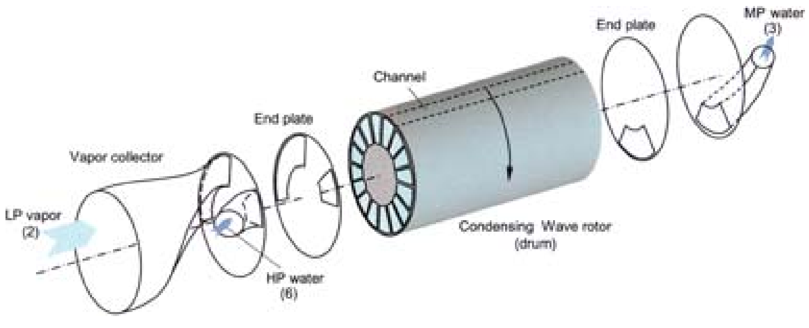

Fig. 3 Schematic of a 3-port condensing wave rotor

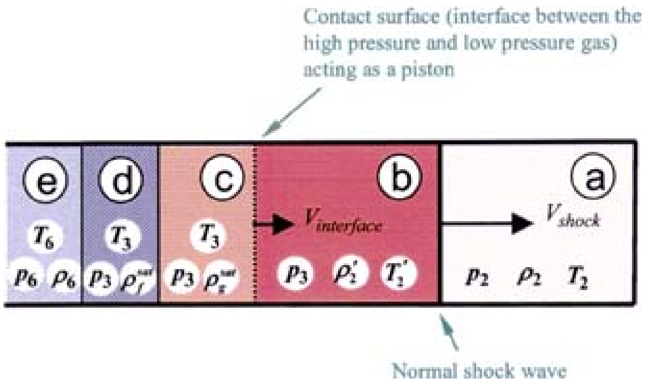

Fig. 4 Regions modeled for each channel during shock compression and condensation

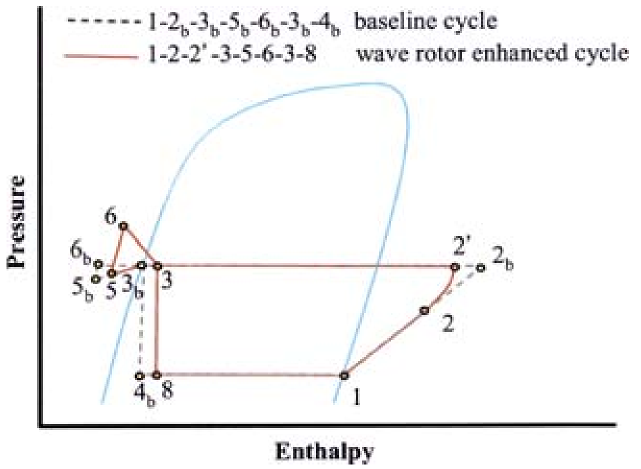

Fig. 6 Schematic $p-h$ diagram of an R718 baseline cycle and enhanced cycle with a 3-port condensing wave rotor

after the filling process is completed. After further rotation, the channels meet the second-inlet port (6) through which the high-pressure low-temperature water (*e*) comes in and is exposed to the low-pressure high-temperature superheated vapor in region (*a*). Due to the sudden pressure drop (from p_6 to p_2), all the heat cannot be contained in the incoming water as sensible heat and the heat surplus is transformed into latent heat of vaporization. It is the so-called flash evaporation or flashing phenomenon [37,38]. Therefore, one portion of the incoming water suddenly vaporizes (*c*) and the remaining part cools down (*d*). The frontal area of the saturated vapor generated by the flash evaporation (*c*) is called *contact interface* and acts like a fast moving piston. It causes a shock wave triggered from the leading edge of the inlet port traveling through the superheated low-pressure vapor which exists inside the channel (*a*). The shock wave travels with supersonic speed (V_{shock}) faster than the contact interface ($V_{\text{interface}}$). Therefore, the trajectory of the shock wave (solid line in Fig. 5) has a smaller slope than the incoming water and the contact interface of the generated vapor (dashed line in Fig. 5). Behind the moving shock wave (*b*) the temperature is increased from T_2 to $T_{2'}$ and the pressure is increased from p_2 to $p_{2'}=p_3$ due to the shock compression. The latter is a design decision similar to a tuning condition. With it, the pressure at the inlet port (p_6) is set to an appropriate value that generates the pressure ratio p_6/p_2 required to trigger the desired shock wave. The shock wave increases the pressure of the superheated vapor from p_2 to p_3 at which the vapor will be condensed. This shows that the fluid in its liquid state serves as a "work capacitor" storing pump work to release it during its expansion in the wave rotor channels for the simultaneous vapor compression. Therefore, in the enhanced system the pump in the cooling water cycle not only has to provide the work necessary to overcome the pressure loss in the heat rejecter cycle (w_{PL}) but also the work necessary for the shock wave compression in the wave rotor channels (w_{PC}). The pressure behind the shock wave (*b*) is imposed on the vapor generated by the flash evaporation (*c*). It is the pressure at the water surface and the equilibrium pressure at which the evaporation decays $p(c)=p(b)=p_3$. Hence, both generated vapor and the cooled water obtain saturation temperature $T_3=T_{\text{sat}}(p_3)$.

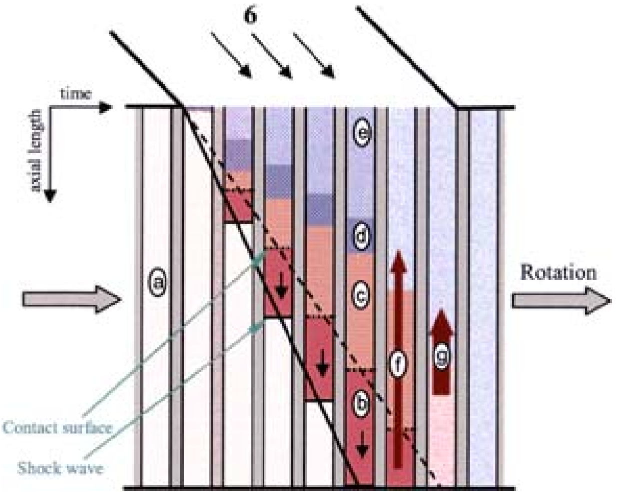

Fig. 5 Schematic wave and phase-change diagram for the 3-port condensing wave rotor (high-pressure part)

Due to the contact of the superheated compressed vapor (*b*) with the cold incoming water, the superheated vapor is desuperheated and its heat is transferred (*f*) to the incoming water. This continues until the equilibrium temperature T_3 is achieved in region (*b*) and the superheated vapor is changed to saturated vapor. Subsequently, the incoming water compresses the saturated vapor further and condenses it, while the latent heat is transferred to the incoming water (*g*). The water, which is nearly a fully condensed two-phase vapor with a typical quality of 0.005, is scavenged through the only outlet of the wave rotor (3). The scavenging process may be supported by gravity and pump power.

The schematic pressure–enthalpy ($p-h$) and temperature–entropy ($T-s$) diagrams of both the baseline and the wave-rotor-enhanced cycle are depicted in Figs. 6 and 7, respectively. Both cycles start at the outlet of the evaporator 1, where the vapor is saturated. Point 2_b represents the compressor outlet of the baseline cycle whereas point 2 is the compressor outlet of the wave-rotor-enhanced cycle that allows using a compressor with a lower pressure ratio. $2'$ is an intermediate point inside the wave rotor channels that corresponds to the flow properties in region (*b*) right after the shock wave. The slope between points 2 and $2'$ is greater than that between points 1 and 2_b because the shock compression typically happens with a higher efficiency [1–3]. Still inside the wave rotor channel, the superheated vapor is desuperheated to the equilibrium temperature $T_3(2'\rightarrow 3)$. State 3 is actually much closer to the liquid region than shown in Figs. 6 and 7 since the mass flow rate of the cooling water cycle is much greater than that of the refrigerant cycle. Knowing about this, it becomes also clear that the distances between points 3, 5, and 6 are exaggerated in both diagrams. The expansion process (6→3) releases the energy consumed by the compression process of the vapor ($2\rightarrow 2'$) all within the wave rotor channels. Coming from the only outlet port of the wave rotor (3), the flow diverges. The small fraction used as refrigerant is directed to the expansion valve and is expanded in a constant enthalpy process (3→4), while the most part of flow out

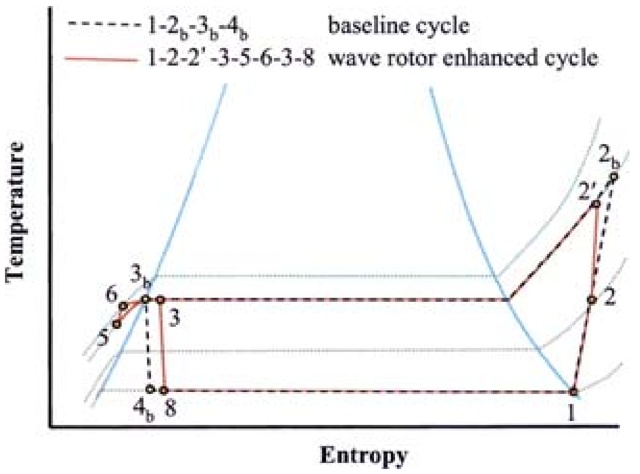

Fig. 7 Schematic *p–h* diagram of an R718 baseline cycle (cooling water cycle not shown) and enhanced cycle with a 3-port condensing wave rotor

of the wave rotor goes to the heat rejecter (cooling tower or similar) where it cools off (3→5). Afterwards the pressure is again increased (5→6) by the pump, providing the energy for the vapor compression in the wave rotor (w_{PC}) and compensating the pressure loss in the heat rejecter and piping (w_{PL}).

Performance Evaluation

A computer code based on the thermodynamic model described above was generated for performance evaluation of R718 refrigeration cycles enhanced with 3-port condensing wave rotors. The evaporator temperature (T_1) and heat rejecter temperature (T_3) are commonly fixed by the application. The objective is to get the highest increase in coefficient of performance ($\mathrm{COP_{gain}}$) compared to the baseline cycle. Independent design parameters are the mass flow ratio ($K=m_6/m_2$) that relates the mass flow of the cooling cycle to the mass flow of the refrigerant cycle, and the pressure ratio of the wave rotor ($PR_W=p_3/p_2$).

Additional assumptions considered in the thermodynamic model are the following:

1. For comparison of baseline and enhanced cycles, the evaporator and condenser inlet temperatures are considered to be the same ($T_1=T_{1b}$ and $T_3=T_{3b}$).
2. Temperature difference across the heat rejecter is kept constant ($T_5-T_3=3$ K).
3. Pressure drop in heat rejecter, evaporator, and pipes is neglected.
4. The condenser and evaporator outlet states are fully saturated.
5. Same polytrophic compressor efficiency is used for baseline and enhanced cycles. Its value of 0.72 is obtained by assuming an isentropic efficiency of 0.7 for a compressor with a pressure ratio of 2.
6. The superheated vapor is considered as an ideal gas ($\gamma=1.33$).
7. One-dimensional gasdynamic shock wave equations are used to calculate the flow properties across the moving normal shock wave. Reflected shock waves are not considered.
8. The hydraulic efficiency of the pump is 0.9.

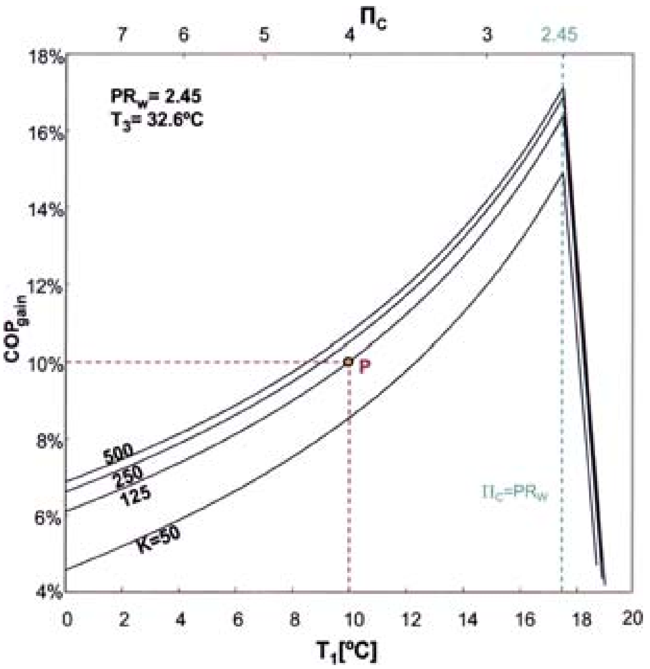

Fig. 8 Relative COP increase versus evaporation temperature for different mass flow ratios

Figure 8 shows the relative $\mathrm{COP_{gain}}$ versus the evaporator temperature (T_1) for different mass flow ratios. By increasing evaporator temperature T_1, the COP of the wave-rotor-enhanced cycle is increased relative to the COP of the baseline cycle. This trend is seen until the compressor pressure ratio in the enhanced cycle ($\Pi_c=p_2/p_1$) is reduced to a value that is equal to the wave rotor pressure ratio ($\Pi_c=PR_W$). After that the relative $\mathrm{COP_{gain}}$ drops dramatically.

Figure 9 represents the relative $\mathrm{COP_{gain}}$ versus mass flow ratio for different evaporator temperatures, like a side view of Fig. 8. It shows only the increasing branches of Fig. 8 up to an evaporation temperature where the pressure ratio of the turbocompressor is reduced to the value of the wave rotor pressure ratio. Increasing the mass flow ratio above 200 appears as ineffective according to Fig. 9.

Figure 10 shows the effect of the wave rotor pressure ratio

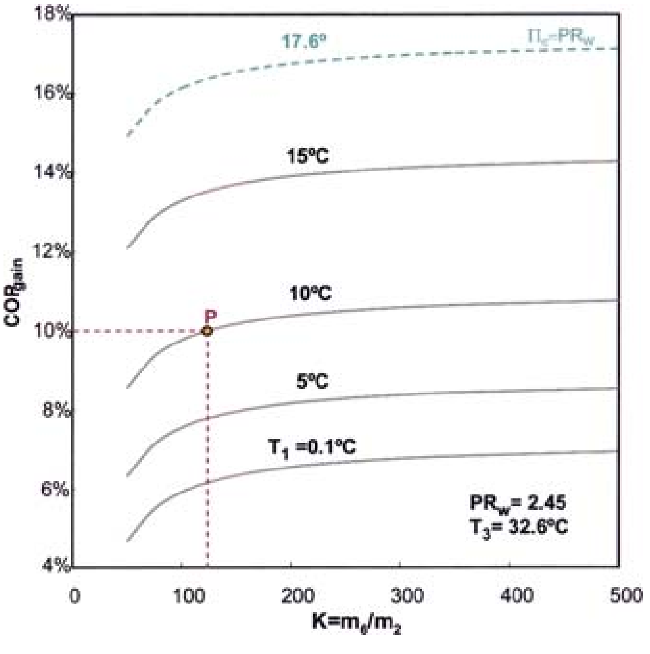

Fig. 9 Relative COP increase versus mass flow ratio for different evaporation temperatures

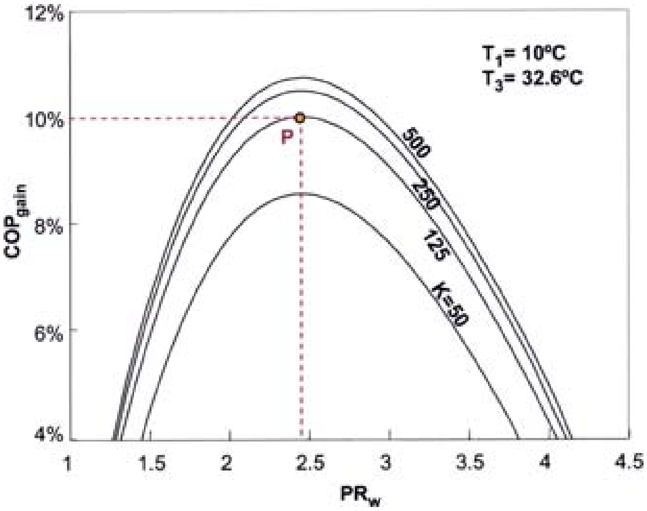

Fig. 10 Relative COP increase versus the wave rotor pressure ratio for different mass flow ratios

(PR_W) on the relative COP$_{gain}$ for different mass flow ratios. Each curve has a maximum point that indicates the best choice of wave rotor pressure ratio for the given system specifications. The location of this point depends on several parameters including the hydraulic efficiency of the pump, compressor polytropic efficiency, evaporator temperature, and temperature lift ($T_3 - T_1$), but not the mass flow ratio. One common characteristic shown in Figs. 8, 9, and 10 is that a continued increase of the independent value does not always increase the COP$_{gain}$. While Fig. 10 shows this effect for the wave rotor pressure ratio, Fig. 8 reveals a growing gradient of COP$_{gain}$ up to the point where further increase of evaporator temperature actually reduces COP$_{gain}$. A similar trend can be seen in Fig. 9 where the curves have an asymptotic behavior for increased mass flow ratio.

Figure 11 shows the heat rejecter temperature (T_3) versus evaporator temperature for different wave rotor pressure ratios and a constant relative COP$_{gain}$ of 10%. The figure indicates that there are several options for the wave rotor pressure ratio to obtain a certain relative COP$_{gain}$. However, only the optimum pressure ratio of 2.45 yields the highest temperature lift.

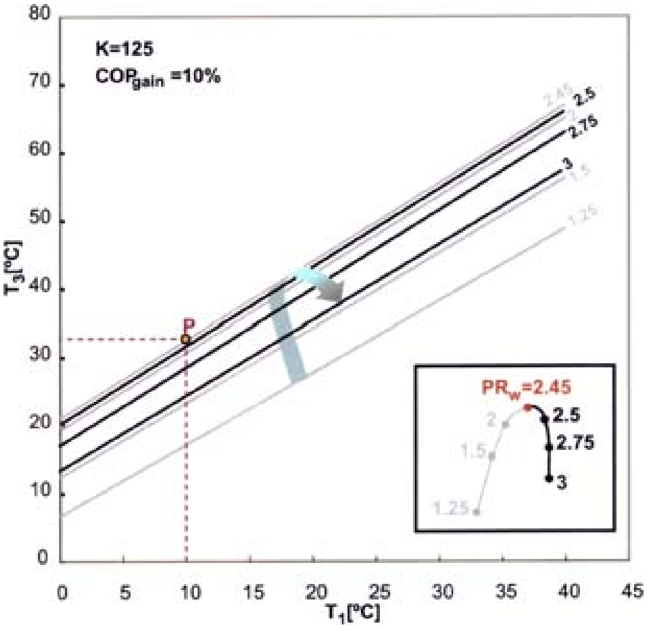

Fig. 11 Heat rejecter temperature versus evaporator temperature for different wave rotor pressure ratios

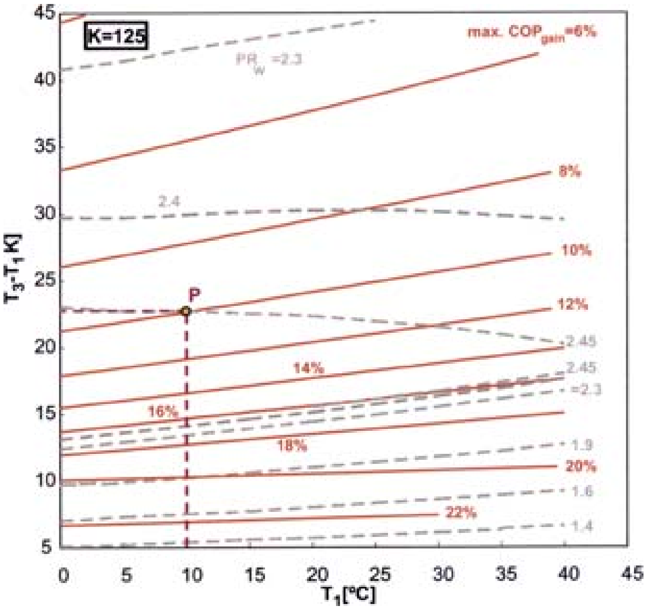

Fig. 12 Performance map: maximum performance increase and optimum wave rotor pressure ratios

Figure 12 is a performance map of the enhanced cycle. Each point on this plot shows the maximum COP$_{gain}$ that can be obtained by the optimum choice of PR_W for a given evaporator temperature and a temperature lift. The constant PR_W lines indicate the optimum PR_W that yields the highest possible COP$_{gain}$ indicated by constant max. COP$_{gain}$ lines.

In this performance plot of optimized points, an arbitrary optimum point P is marked. It is used to show the connection between all the performance graphs. However, it is the only optimum point in the performance plots of Figs. 8–11. All other points of these plots are not found in Fig. 12 because they show a smaller COP$_{gain}$ than the points in Fig. 12.

The trend found in Fig. 8 was that for a given heat rejecter temperature (T_3) and PR_W, an increase of the evaporator temperature results in a higher COP$_{gain}$. Such an effect can also be seen in the performance map of the optimized points (Fig. 12) by moving point P to the right along constant PR_W line of 2.45. However, for smaller temperature lifts below about 15 K (above max. COP$_{gain}$ of about 16%) this effect is reversed such that the max. COP$_{gain}$ decreases with increasing evaporator temperature.

Figure 10 showed that for a given mass flow ratio and a combination of evaporation and heat rejecter temperatures there is a maximum COP$_{gain}$. Since the point P is at the maximum of the dome it also appears in Fig. 12.

The following results can be obtained from the performance map of optimized points:

1. As lower the temperature lift, as higher the relative max. COP$_{gain}$ of the enhanced cycle.
2. The maximum optimum PR_W for a condensing 3-port wave rotor is about 2.51.
3. While below a temperature lift of approximately 18 K the optimum PR_W increases with the temperature lift, decreases slightly for higher temperature lifts. This trend shows a rapidly decreasing gradient with increasing temperature lift.
4. Slope of constant COP$_{gain}$ lines increases as the temperature lift increases, showing that an increase of evaporation tem-

perature is even more beneficial for the enhanced cycle, especially for greater temperature lifts as it is already the case for the R718 baseline cycle.

Summary

The potential of using wave devices in R718 refrigeration cycles is demonstrated. Advantages of cycles working with water as a refrigerant (R718) and challenges involved with designing them are mentioned. To enhance the turbocompression and improve the efficiency of such cycles, the novel concept of using a 3-port condensing wave rotor in a R718 compression refrigeration cycle is investigated. The condensing wave rotor employs pressurized water to pressurize, desuperheat, and condense the superheated vapor coming from the compressor—all in one dynamic process. The $p-h$ and $T-s$ diagrams of the external process and the wave and phase-change diagram of the internal process are discussed. Flash evaporation, shock wave compression, desuperheating, and condensation phenomena inside the wave rotor channels are described. A computer code based on a thermodynamic model was generated to evaluate the performance improvement of R718 cycles enhanced with 3-port condensing wave rotors. The effect of some of the key parameters on the relative increase of the coefficient of performance of the wave-rotor-enhanced cycle is shown. Finally a performance map showing the optimized points of the enhanced cycle is presented. The presented results show an improvement of the COP of up to 22% by using the 3-port condensing wave rotor. Beside this, the condensing wave rotor allows lower compressor pressure ratios for the same temperature lift or increases the temperature lift without changing the compressor. This wave rotor is a simple drum easy to manufacture, rotating at relatively low speed. Since it performs compression, desuperheating, and condensation in one compact device it can reduce the size and cost of modern state-of-the-art R718-chillers that now employ high-tech multistage compressors, intercooler, and relative bulky condensers.

References

[1] Weber, H. E., 1995, *Shock Wave Engine Design*, John Wiley and Sons, New York.
[2] Weber, H. E., 1986, "Shock-Expansion Wave Engines: New Directions for Power Production," ASME Paper 86-GT-62.
[3] Akbari, P., Kharazi, A. A., and Müller, N., 2003, "Utilizing Wave Rotor Technology to Enhance the Turbocompression in Power and Refrigeration Cycles," 2003 International Mechanical Engineering Conference, ASME Paper IMECE2003-44222.
[4] Taussig, R. T., and Hertzberg, A., 1984, "Wave Rotors for Turbomachinery," Winter Annual Meeting of the ASME, edited by Sladky, J. F., Machinery for Direct Fluid-Fluid Energy Exchange, AD-07, pp. 1–7.
[5] Shreeve, R. P., and Mathur, A., 1985, Proceeding ONR/NAVAIR Wave Rotor Research and Technology Workshop, Report NPS-67-85-008, Naval Postgraduate School, Monterey, CA.
[6] Paxson, D. E., 1995, "Comparison Between Numerically Modeled and Experimentally Measured Wave-Rotor Loss Mechanism," J. Propul. Power, **11**, pp. 908–914; see also NASA TM-106279.
[7] Paxson, D. E., 1996, "Numerical Simulation of Dynamic Wave Rotor Performance," J. Propul. Power, **12**, pp. 949–957.
[8] Wilson, J., and Paxson, D. E., 1996, "Wave Rotor Optimization for Gas Turbine Topping Cycles," J. Propul. Power, **12**, No. 4, pp. 778–785; see also SAE Paper 951411, 1995, and NASA TM 106951.
[9] Welch, G. E., Jones, S. M., and Paxson, D. E., 1997, "Wave Rotor-Enhanced Gas Turbine Engines," J. Eng. Gas Turbines Power, **119**, No. 2, pp. 469–477.
[10] Welch, G. E., 1997, "Macroscopic Balance Model for Wave Rotors," J. Propul. Power, **13**, No. 4, pp. 508–516.
[11] Welch, G. E., 1997, "Two-Dimensional Computational Model for Wave Rotor Flow Dynamics," J. Eng. Gas Turbines Power, **119**, No. 4, pp. 978–985.
[12] Wilson, J., 1998, "An Experimental Determination of Loses in a Three-Port Wave Rotor," J. Eng. Gas Turbines Power, **120**, pp. 833–842.
[13] Paxson, D. E., and Nalim, M. R., 1999, "Modified Through-Flow Wave-Rotor Cycle With Combustor Bypass Ducts," J. Propul. Power, **15**, No. 3, pp. 462–467.
[14] Welch, G. E., 2000, "Overview of Wave-Rotor Technology for Gas Turbine Engine Topping Cycles," Novel Aero Propulsion Systems International Symposium, The Institution of Mechanical Engineers, pp. 2–17.
[15] Fatsis, A., and Ribaud, Y., 1999, "Thermodynamic Analysis of Gas Turbines Topped With Wave Rotors," Aerospace Sci. Technol., **3**, No. 5, pp. 293–299.
[16] Jones, S. M., and Welch, G. E., 1996, "Performance Benefits for Wave Rotor-Topped Gas Turbine Engines," ASME Paper 96-GT-075.
[17] Akbari, P., and Müller, N., 2003, "Performance Improvement of Small Gas Turbines Through Use of Wave Rotor Topping Cycles," 2003 International ASME/IGTI Turbo Exposition, ASME Paper GT2003-38772.
[18] Doerfler, P. K., 1975, "Comprex Supercharging of Vehicle Diesel Engines," SAE Paper 750335.
[19] Doerfler, P. K., 1975, "Comprex Supercharging of Vehicle Diesel Engines," SAE Paper 750335.
[20] Eisele, E., Hiereth, H., and Polz, H., 1975, "Experience With Comprex Pressure Wave Supercharger on the High-Speed Passenger Car Diesel Engine," SAE Paper 750334.
[21] Kollbrunner, T. A., 1980, "Comprex® Supercharging for Passenger Diesel Car Engines," SAE Paper 800884.
[22] Gyarmathy, G., 1983, "How Does the Comprex® Pressure-Wave Supercharger Work," SAE Paper 830234.
[23] Schneider, G., 1986, "Comprex® Pressure Wave Supercharger in An Opel Senator With 2.3 Liter Diesel Engine," Brown Boveri Rev., **73**, No. 10, pp. 563–565.
[24] Zehnder, G., Mayer, A., and Mathews, L., 1989, "The Free Running Comprex®," SAE Paper 890452.
[25] Mayer, A., Oda, J., Kato, K., Haase, W., and Fried, R., 1989, "Extruded Ceramic—A New Technology for the Comprex® Rotor," SAE Paper 890453.
[26] Amstutz, A., Pauli, E., and Mayer, A., 1990, "System Optimization With Comprex Supercharging and EGR Control of Diesel Engines," SAE Paper 905097.
[27] Kentfield, J. A. C., 1998, "Wave Rotors and Highlights of Their Development," AIAA Paper 98-3248.
[28] Kentfield, J. A. C., 1993, *Nonsteady, One-Dimensional, Internal, Compressible Flows*, Oxford University Press, Oxford.
[29] Azoury, P. H., 1992, *Engineering Applications of Unsteady Fluid Flow*, Wiley, New York.
[30] Albring, P., 1994, "Water as Refrigerant in Refrigeration Plants With Mechanical Compression," New Applications of Natural Working Fluids in Refrigeration and Air Conditioning, IIR, Hannover, pp. 735–742.
[31] Albring, P., and Heinrich, G., 1996, "R718 Heat Pumps: Applications for Natural Refrigerants," IIR, Aarhus, pp. 553–558.
[32] Albring, P., and Heinrich, G., 1998, "Turbo Chiller With Water as Refrigerant," Natural Working Fluids '98, IIR, Oslo, pp. 93–103.
[33] Heinrich, G., Janik, A., and Albring, P., 1991, "Alternative Kaleprozesse mit R718 (H20)," Luft- und Kaltetechnik, **27**, p. 3.
[34] Albring, P., and Müller, N., 1995, "Turboverdichter für Wasser als Kältemittel" (Turbo-compressors for Water as a Refrigerant) in Faragallah, W., Surek, D., "Beiträge zu Fluidenergiemaschinen," Sulzbach, Band **2**, pp. 16–22.
[35] Müller, N., 2002, "Turbo Chillers Using Water as a Refrigerant," ASME PID Newsletter, p. 3.
[36] Müller, N., 2001, "Design of Compressor Impellers for Water as a Refrigerant," ASHRAE Trans., **107**, pp. 214–222.
[37] Saury, D., Harmand, S., and Siroux, M., 2002, "Experimental Study of Flash Evaporation of Water Film," Int. J. Heat Mass Transfer, **45**, pp. 3447–3457.
[38] Miyatake, O., Murakami, K., and Kawata, Y., 1973, "Fundamental Experiments With Flash Evaporation," Heat Transfer-Jpn. Res., **2**, pp. 89–100.

Analysis of Gas-Steam Combined Cycles With Natural Gas Reforming and CO_2 Capture

Alessandro Corradetti

Umberto Desideri
e-mail: umberto.desideri@unipg.it

Dipartimento di Ingegneria Industriale,
Università di Perugia,
Via G. Duranti 93,
06125 Perugia, Italy

In the last several years greenhouse gas emissions, and, in particular, carbon dioxide emissions, have become a major concern in the power generation industry and a large amount of research work has been dedicated to this subject. Among the possible technologies to reduce CO_2 emissions from power plants, the pretreatment of fossil fuels to separate carbon from hydrogen before the combustion process is one of the least energy-consuming ways to facilitate CO_2 capture and removal from the power plant. In this paper several power plant schemes with reduced CO_2 emissions were simulated. All the configurations were based on the following characteristics: (i) syngas production via natural gas reforming; (ii) two reactors for CO-shift; (iii) "precombustion" decarbonization of the fuel by CO_2 absorption with amine solutions; (iv) combustion of hydrogen-rich fuel in a commercially available gas turbine; and (v) combined cycle with three pressure levels, to achieve a net power output in the range of 400 MW. The base reactor employed for syngas generation is the ATR (auto thermal reformer). The attention was focused on the optimization of the main parameters of this reactor and its interaction with the power section. In particular the simulation evaluated the benefits deriving from the postcombustion of exhaust gas and from the introduction of a gas-gas heat exchanger. All the components of the plants were simulated using ASPEN PLUS software, and fixing a reduction of CO_2 emissions of at least 90%. The best configuration showed a thermal efficiency of approximately 48% and CO_2 specific emissions of 0.04 kg/kWh.

[DOI: 10.1115/1.1850941]

Introduction

Since the second half of eighteenth century anthropogenic emissions have increased atmospheric concentration of greenhouse gases. The radiative forcing (i.e., the increase in the total downward flux of infrared, emitted by the atmosphere, due to the additional amount of gas) is estimated at 2.43 W/m^2. The carbon dioxide alone is responsible for 60% of this radiative forcing because CO_2 has always been the main gas emitted by human activities. As a result CO_2 atmospheric concentration has reached 373 ppm in 2002 [1] while preindustrial value was approximately 280 ppm [2].

The main source of carbon dioxide derives from the combustion of fossil fuels, which generates 90% of globally emitted CO_2. Fossil fuels are used in three fundamental fields: transportation, heating, and power generation. The latter is probably the one in which measures to decrease carbon dioxide emissions could be more effective. In recent years several studies have investigated the performances of innovative power cycles with low CO_2 emissions. These cycles are usually grouped into three different alternatives: (i) postcombustion decarbonization, (ii) oxy-fuel power cycles, (iii) precombustion decarbonization.

Postcombustion decarbonization consists in the removal of carbon dioxide from exhaust gases. This scheme requires minimum modifications to power cycle, as CO_2 separation involves only exhaust gas treatment. Among CO_2 capture technologies (chemical and physical absorption, adsorption, membranes, cryogenic separation), the most promising one for postcombustion decarbonization is chemical absorption because it is the least energy requiring when CO_2 partial pressure is very low, as in exhaust gases [3,4]. Anyway this technology has not been optimized for power generation applications, and further developments in solvent composition is needed to improve the absorption process [5].

The second scheme (oxy-fuel combustion) requires the production of pure oxygen to be used as oxidizer in a close-to-soichiometric combustion, which produces only CO_2 and H_2O. In these plants an air-separation unit is needed for the production of O_2. An example of these cycles can be found in Bolland and Mathieu [6]. They investigated a semi-closed combined cycle, in which the gas turbine uses carbon dioxide as working fluid; therefore, CO_2 capture is accomplished without the need of highly energy-requiring devices. The cycle showed a global efficiency of approximately 47%.

The third option to reduce CO_2 emissions from power plant is known as precombustion decarbonization. In this case fossil fuels are converted to syngas (i.e., a mix of CO and H_2). Syngas is the raw material for several chemical syntheses, such as methanol and ammonia. Both solid and gaseous fuels can be used for this purpose; gasification and reforming are, respectively, the technologies adopted to produce syngas from coal and natural gas. The integration of a gasifier with a combined cycle is nowadays regarded as the most promising way to generate power from coal because integrated gasification combined cycle (IGCC) plants are characterized by higher efficiencies than conventional pulverized coal-fired plant (PCFP). Various IGCC plants are operating worldwide, but CO_2 removal has never been attempted in these cases. However, several studies on the subject have been carried out in the last several years, showing that CO_2 can be easily captured in plants with conventional gas-sweetening processes, based on physical absorption (such as Selexol or Rectisol [7]). One or two "shift" reactors have to be introduced before CO_2 absorber, in order to convert CO to CO_2, so that the gas to be treated contains only hydrogen and carbon dioxide. IGCC net efficiency decreases from 44% to 46% to 37% to 40% if CO_2 is removed following this option [8,9].

For natural gas-fired plants, precombustion decarbonization

Contributed by the International Gas Turbine Institute (IGTI) of THE AMERICAN SOCIETY OF MECHANICAL ENGINEERS for publication in the ASME JOURNAL OF ENGINEERING FOR GAS TURBINES AND POWER. Paper presented at the International Gas Turbine and Aeroengine Congress and Exhibition, Vienna, Austria, June 13–17, 2004, Paper No. 2004-GT-54091. Manuscript received by IGTI, October 1, 2003; final revision, March 1, 2004. IGTI Review Chair: A. J. Strazisar.

[10–13] implies the adoption of either a steam reformer or partial oxidizer. These reactors generate a blend of CO and H_2 (plus nitrogen, if air is used as oxidizer), just as gasifiers do. Of course syngas composition varies with the technology utilized and with operating parameters, but the basic principle is the same. In fact at reformer outlet syngas must be shifted and CO_2 removed in order to feed a gas turbine with a carbon-free fuel. In this case the chemical absorption process is preferred over physical absorption, as the pressure of produced syngas is lower. This option is very interesting because it requires components that have a commercially proven technology and can be operated under the same work conditions as usual. In this paper we have analyzed the thermodynamic performances of a combined cycle, which is fed by the fuel generated by the reforming process and deprived of CO_2. Particular attention was focused on the integration of the power plant with both the syngas production section and CO_2 removal plant. All the components investigated reflect the state of the art.

1 The Reforming Process

The reforming process involves the following reactions:

$$CH_4+H_2O\leftrightarrow CO+3H_2 \quad \text{with} \quad \Delta H=206.11 \ \text{kJ/mol} \tag{1}$$

$$CO+H_2O\leftrightarrow CO_2+H_2 \quad \text{with} \quad \Delta H=-41.17 \ \text{kJ/mol} \tag{2}$$

$$C_nH_m+nH_2O\rightarrow nCO+(m/2+n)H_2 \tag{3}$$

Both (1) and (2) can be considered at equilibrium conditions in commercially available reformers. The first is the methane reforming reaction, which requires steam and must be carried out at 700–950°C, as it is endothermic, and methane conversion is enhanced by the excess of steam and the high temperatures. Reaction (2) is known as the "CO-shift reaction" and also occurs during reforming process, thus determining CO and H_2 concentration at equilibrium. Reaction (3) constitutes the reforming of heavier hydrocarbons, which can be considered irreversible. The reforming process usually takes place in a tubular reactor, called steam methane reformer, where the heat of reaction is supplied externally by a flame fed with methane, too. Auto thermal reformers (ATR) carry out both reforming and combustion in a unique reactor, which supplies itself the energy for reforming reaction and for increasing gas temperature. Air (or pure oxygen) is also introduced into the ATR as oxidizer. In the upper part of the ATR several combustion reactions take place, but in a simplified model the molecular reaction which best represents the whole process is the combustion of methane to carbon monoxide and water [14]:

$$CH_4+1{,}5O_2\leftrightarrow CO+2H_2O \quad \text{with} \quad \Delta H=-519.35 \ \text{kJ/mol} \tag{4}$$

Therefore, a fraction of methane entering the ATR is not reformed because it works as fuel, supplying heat for endothermic reactions.

If air is used as oxidizer, then the gas leaving the ATR contains a large amount of nitrogen. In industrial practice oxygen is more often used instead of air, in order to reduce plant size and costs. Air is preferred over O_2 in ammonia plants, where it feeds a secondary reformer (substantially an ATR placed after SMR), and supplies the nitrogen necessary for ammonia synthesis. Previous studies [7,8] showed that air-blown reactors are perfectly suitable for integration with a combined cycle, for two reasons:

1. Air entering the ATR can be extracted directly from the gas turbine (GT) compressor.
2. Final fuel is diluted with nitrogen, therefore, NO_x emissions are reduced to acceptable values as stoichiometric flame temperature is lower.

In particular, NO_x emission control is a relevant problem when hydrogen is burned in a gas turbine because it is not possible to prevent thermal NO_x formation adopting dry-low-NO_x technologies. In fact hydrogen has a faster flame speed and a shorter autoignition delay time, so premixed combustion is not achievable at present time [15]. Even if more experimental work on this subject is needed, many theoretical studies [15–17] agree that fuel dilution with 50% nitrogen could be sufficient to limit NO_x emissions in the range of 25–50 ppmv.

2 Power Plant Schemes With ATR

Three power plant schemes have been investigated. They differ from each other substantially in the preheating of the streams entering reformer. For this goal, the "Reference Case" is provided with only one heat exchanger, in which GT exhaust gases are used to preheat natural gas and steam. In the supplementary firing (SF) configuration, exhaust gas temperature is increased by supplementary firing, and two heat exchangers are employed. In the GAS-GAS configuration the heat exchangers utilize the hot syngas leaving the reformer, instead of the exhaust gas, for natural gas and steam preheating.

The Reference Case configuration is shown in Fig. 1. Natural gas is mixed with the steam extracted from a medium-pressure level (MP) turbine at 18 bar. The reactants are heated to 480°C by GT exhaust gases in HE-IN-PRE. The mixed streams (2) enter PRE-REF, which provides for the reforming of heavier hydrocarbons. After pre-reforming, the gas (3) goes directly into the ATR, which uses a fraction of the air (Fig. 1(*b*)), leaving the GT compressor as an oxidizer. The pressure of this reactor is therefore imposed by GT pressure ratio. Two different temperatures (850°C and 950°C) have been chosen for ATR operating conditions. In any case the hot syngas leaving the ATR must be cooled down to 400°C, in order to be shifted in high-temperature shift (HTS). A waste heat boiler provides for this cooling, together with the production of high-pressure steam (E), which is sent to the heat recovery steam generator (HRSG) for superheating. CO concentration by volume is reduced from 9% to 3,5% by the shift reaction accomplished in the HTS. The gas (6) is further cooled in two convective heat exchangers (HEs): the first one (HE1) is used to preheat the water that feeds the waste heat boiler (WHB); the second one (fuel regenerator (REG)) is a gas-gas exchanger, which brings GT fuel to 280°C. The syngas (8) enters the low-temperature shift (LTS) at 160°C and exits at temperatures in the range of 200°C.

In order to be appropriately treated in the CO_2 capture plant, the gas leaving the shift reactor is cooled down to 35°C. Successively most of the water is removed, thus decreasing the volumetric flow of the gas to be treated and increasing CO_2 concentration. Carbon dioxide is separated in a typical plant based on chemical absorption. CO_2 is then compressed to 140 bar for liquefaction and transportation. The gas leaving the top of the absorber is poor in carbon and can feed the gas turbine; before entering the combustion chamber, the fuel is compressed to 20 bar and heated in the REG. The exhaust gases (c) from the turbine enter HE-IN-PRE approximately at 590°C, and the HRSG at 557°C. This determines the maximum temperature of the steam, having set the approach point ΔT at 20°C. The HRSG has three pressure levels. Syngas production and decarbonization decrease power produced by the steam turbine because medium pressure steam is extracted from the steam turbine (ST) for the reforming, while low-pressure steam is extracted for solvent regeneration. The interaction between syngas production and the power section has also a positive feature: from syngas cooling it is possible to preheat water and to generate saturated steam, thus increasing the power generated by the ST.

The Reference Case configuration has been slightly modified in order to decrease methane consumption in the ATR. Supplementary firing of the GT exhaust gases has been studied in SF configuration, whose main features are depicted in Fig. 2. Exhaust gas temperature rises to 646°C and the ATR inlet stream (3) can be heated to 600°C in HE-IN-ATR. In GAS-GAS configuration (Fig. 3) two gas-gas heat exchangers have been introduced to recover heat from syngas leaving the ATR. This equipment has to resist

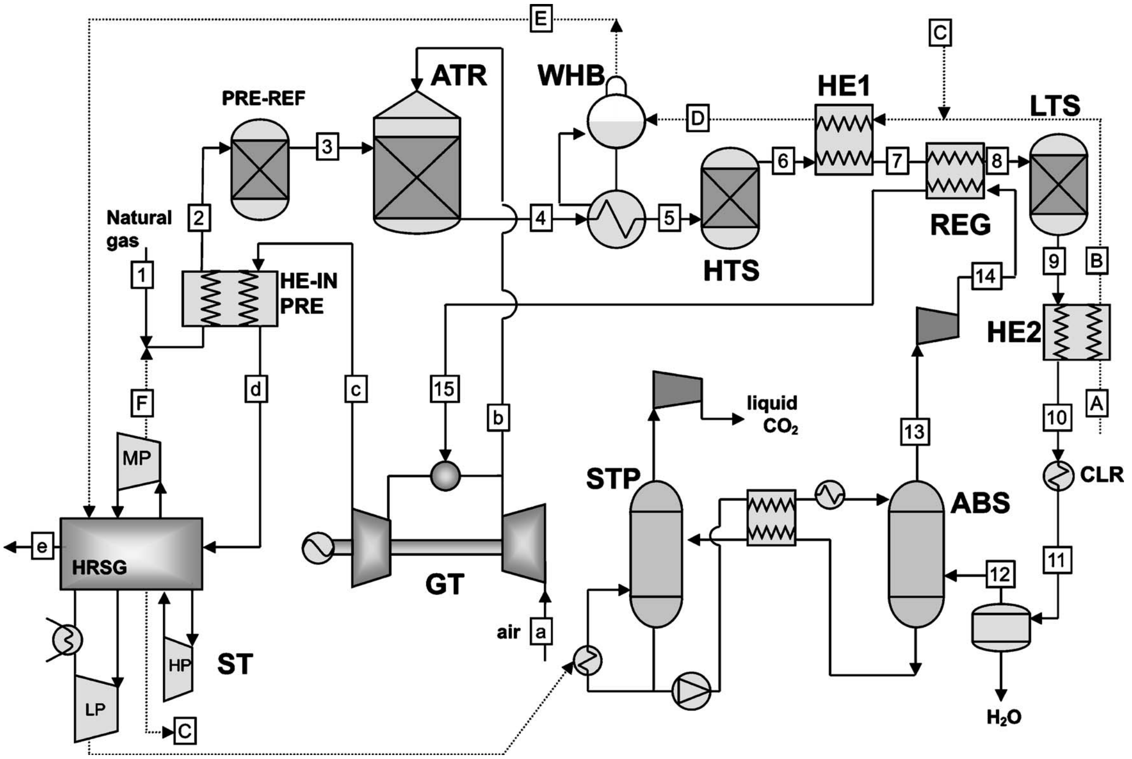

Fig. 1 Reference Case process flowsheet

high temperatures, and it has not been commercially proven. Atthe reformer outlet, syngas is cooled in HE-IN-ATR, which increases ATR inlet streams to 600°C. Syngas is further cooled in HE-IN-PRE, where natural gas and process steam are heated to 500°C. In this configuration the GT exhaust gases go directly into the HRSG.

3 Assumptions and Results

3.1 Syngas Production Section. The whole power plant has been studied with the ASPEN PLUS software [18–20]. The principal reactors (PRE,ATR,HTS,LTS) have been simulated by the Gibbs Reactor, a model available in the ASPEN+ library, which determines equilibrium conditions by minimizing Gibbs energy. The Pre-reformer is an adiabatic reactor, which operates with an inlet stream temperature in the range of 470–550°C, depending on the configuration considered. In the Reference Case, the temperature of stream 2 is the lowest (481°C for T-ATR=850°C, 467°C for T-ATR=950°C), as the parameter fixed in HE-IN-PRE is the outlet temperature of stream *d* (557°C). For the SF configuration this temperature is set at 580°C, so pre-reformer inlet temperature rises to 542°C and 500°C, respectively for T-ATR=850°C and T-ATR=950°C. In GAS-GAS configuration, the pre-reformer inlet temperature is fixed at 500°C. Temperature drop in the pre-reformer is caused by the reforming of heavier hydrocarbons, which is strongly endothermic.

The gas leaving pre-reformer (PRE-REF) contains small amounts of ethane and propane: it enters ATR without preheating in the Reference Case, so ATR inlet temperature (418°C,410°C) is given by temperature drop in the PRE-REF. In the other configurations, syngas is heated to 600°C before entering ATR (the choice

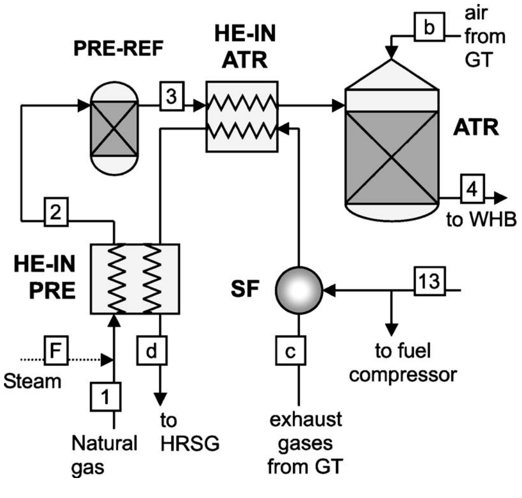

Fig. 2 Variations introduced in SF configuration

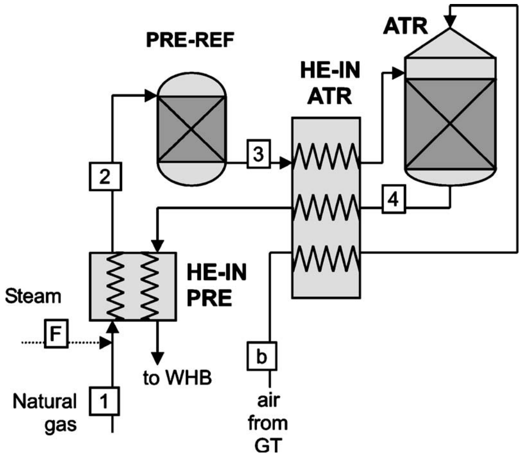

Fig. 3 Variations introduced in GAS-GAS configuration

Table 1 Gas composition in reference case

Stream	1	2	3	4	6	9	12	13
T [°C]	25.0	481.0	417.8	850	459.8	201.2	34.9	281.5
m [kg/s]	17.21	44.94	44.94	125.8	125.8	125.8	111.4	71.96
				composition [% by vol]				
CH_4	91.2	35.9	35.6	0.6	0.6	0.6	0.7	0.8
C_2H_6	4.4	1.7	⋯	⋯	⋯	⋯	⋯	⋯
C_3H_8	0.1	0.04	⋯	⋯	⋯	⋯	⋯	⋯
CO	⋯	⋯	⋯	8.9	3.5	0.2	0.2	0.3
CO_2	⋯	⋯	2.2	5.6	10.9	14.2	16.1	0.9
H_2	⋯	⋯	7.0	30.6	35.9	39.2	44.5	52.4
N_2+AR	4.3	1.7	1.6	33.5	33.5	33.5	37.9	44.7
H_2O	⋯	60.6	53.6	20.9	15.6	12.3	0.4	0.8

of this value derives from the state of the art of heat exchangers preceding the ATR). In the GAS-GAS configuration air stream entering the ATR is heated to 600°C too, while in the other cases, the temperature of air is influenced only by isentropic efficiency of GT compressor (0.89).

The shift reaction, which converts CO to CO_2, is exothermic, so it takes advantage from low temperatures. The HTS inlet temperature is fixed at 400°C by the WHB, while outlet temperature varies in the range of 460–470°C, as also this component is adiabatic and the reaction accomplished is exothermic. Syngas is further cooled in HE1: temperature of stream 7 (290°C) has been determined by imposing a minimum ΔT of 10°C on the hot side of the REG. Syngas goes into the LTS at 160°C and exits at 200–210°C (this reactor is adiabatic, too). Then it is cooled down to 100°C by HE2 and finally to 35°C. Table 1 shows the composition of most significant streams for the Reference Case (with T-ATR =850°C). The pressure of the entire circuit is imposed by GT pressure ratio (β=17) and by pressure losses, which are shown in Table 2.

S/C is the ratio between steam and carbon mole flow at the pre-reformer inlet. Methane conversion and hydrogen production in ATR are enhanced by high values of S/C, but power generation decreases as S/C rises because process steam is extracted from the MP turbine. In this work S/C has been fixed at 1.5, in order to minimize steam extraction. Lower values have not been considered because they have negative effects on carbon deposits formation, which is counteracted by H_2O in excess respect to the stoichiometric minimum. More precisely, since steam extraction is the same for all the cases and natural gas mass flow is variable, S/C is slightly different from a configuration to another. The ATR temperature influences methane conversion too: if T is increased, methane slip is lower. For example in the Reference Case the percentage of unreacted CH_4 decreases from 4.6% to 0.5% if the ATR operating temperature is raised from 850°C to 950°C. This is perfectly in agreement with the chemical equilibrium of reforming reaction, which is endothermic, thus enhanced by higher temperature. Table 3 shows the percentage of unreacted methane in the various configurations.

Methane reacted in the ATR is not completely reformed in accordance with reaction (1) because a fraction of CH_4 is burned to supply the heat of reforming and to increase reactants temperature. The burned fraction increases with higher ATR temperatures and with larger mass flows of reactants because in these cases more energy is required. If the fraction of burned CH_4 is bigger, the low heating valve (LHV) of produced syngas is lower. We have introduced the "Cold syngas efficiency," which represents the ratio between chemical energy of produced syngas and natural gas LHV input. This parameter is used in IGCC performance analysis to express the fraction of coal chemical energy, which is transferred to the produced gas; thus, it does not take into account heat recovery from hot gas, which produces significant amounts of steam, but constitutes the degradation of heat available at high temperature. Cold syngas efficiencies of the studied configurations are shown in Table 4.

The oxygen introduced in ATR is completely consumed by partial and total combustion reactions. Therefore air extraction from the GT compressor is not constant, as it is a function of burned methane fraction. Table 4 shows air mass flow needed by the ATR and the composition of syngas entering CO_2 absorber (stream 12).

H_2/CH_4 is the ratio between the molar flow of hydrogen in stream 12 and CH_4 input molar flow. According to reactions (1) and (2) this ratio has to be 4, if all methane molecules are converted to H_2. Instead H_2/CH_4 is less than 4, thus confirming that a fraction of methane does not take part in reforming, as it is burned. Furthermore, this ratio expresses how much hydrogen can be produced by the same amount of natural gas. By increasing the ATR temperature, H_2/CH_4 increases in SF and GAS-GAS configurations, but it decreases in the Reference Case. This is substantially a consequence of the variation of ATR inlet streams temperature.

3.2 CO_2 Removal Plant.

CO_2 removal is accomplished in an absorption/stripping plant, commonly used for synthesis gas sweetening. Figure 4 illustrates the process flowsheet simulated with ASPEN PLUS. The solvent used in this simulation is a blend of water and two amines: MDEA (30% by weight) and DEA (5%). CO_2 is captured by this solvent in the absorber column (ABS) and it is desorbed in a second column [stripper (STP)] by stripping. The stripping agent is the vapor of the solvent itself, which is produced in a Kettle reboiler. The choice of this mix allows a reduction of reboiler heat duty, as the MDEA requires less heat for regeneration than other amines, like MEA and DEA. Unfortunately the MDEA reaction with CO_2 is very slow and activators

Table 2 Pressure losses in syngas circuit

Component	Outlet pressure [bar]	$\Delta p/p$ [%]
PRE+HE-IN-ATR	17.22	5
ATR	16.36	5
WHB	15.87	3
HTS	15.24	4
HE1+REG	14.78	3
LTS	14.34	3
HE2+cooler	14.06	2

Table 3 S/C and unreacted methane

Configuration	Actual S/C	Unreacted CH_4 [% input]
Ref. case (T-ATR=850°C)	1.53	4.59
Ref. case (T-ATR=950°C)	1.46	0.54
SF (T-ATR=850°C)	1.50	6.17
SF (T-ATR=950°C)	1.43	0.74
Gas-Gas (T-ATR=850°C)	1.63	6.16
Gas-Gas (T-ATR=950°C)	1.56	0.78

Table 4 Main results of syngas production section

	Ref 850°C	Ref 950°C	SF 850°C	SF 950°C	Gas Gas 850°C	Gas Gas 950°C
Air mass flow to ATR [kg/s]	80.8	96.9	73.1	90.1	64.5	78.0
Stream “12” mass flow [kg/s]	111.4	127.3	106.2	123.3	95,9	109.6
Stream “12” composition [% by vol]						
CH_4	0.71	0.08	0.99	0.11	0.99	0.12
CO	0.23	0.22	0.35	0.35	0.28	0.30
CO_2	16.11	15.94	16.26	16.10	16.43	16.30
H_2	44.54	42.19	47.16	44.73	48.35	46.28
N_2+AR	37.97	41.12	34.81	38.26	33.51	36.56
H_2O	0.44	0.44	0.44	0.44	0.44	0.44
H_2/CH_4 input	2.87	2.86	2.95	2.97	3.00	3.05
Cold syngas efficiency [%]	84.3	80.1	88.0	83.7	89.4	85.7

are usually added in order to accelerate the absorption process in proprietary solvents. In this simulation, DEA is used as the activator; this device is often adopted commercially.

Table 5 illustrates the main differences characterizing the CO_2 removal plant, together with fuel mass flow and composition. Both absorber and stripper have been simulated as seven-stage columns, using the RadFrac model, available in the ASPEN PLUS library.

Since the reactions between CO_2 and amines are exothermic, both gas and liquid increase their temperature in the absorber (ABS): the gas exits from top of the absorber at 45–51°C, while the solvent loaded with CO_2 is at 62–63°C at the bottom of the ABS. The absorber works at 13.3 bar, while the stripper at 1.8 bar. Therefore, a flash separator has been put after the ABS, for partially regenerating the solvent by pressure reduction. The rich solvent is preheated to 80°C in H-EX by the lean solution coming from the stripper, which leaves the Kettle reboiler at 101.5°C.

Minimum ΔT between solution and steam condensing in the reboiler is about 10°C. In the stripper, condenser cooling duty is the same (5 MW) for all the configurations. On the contrary, reboiler heat duty changes because the following conditions have been imposed:

1. Same ΔT on H-EX cold side (7.35°C±0.2).
2. Same composition of the solution entering ABS.

The latter has been verified by checking the MDEA+/MDEA ratio of the solution, which represents the percentage of the not-regenerated amine in the stripper. For all the configurations this ratio is in the range 0.210–0.215. CO_2 leaving the top of the stripper is compressed to 140 bar and liquefied for transportation in pipelines. The CO_2 compressor has been modeled by a four-stage intercooled compressor. Isentropic efficiency of the single stage is 0.85, mechanical efficiency is 0.95.

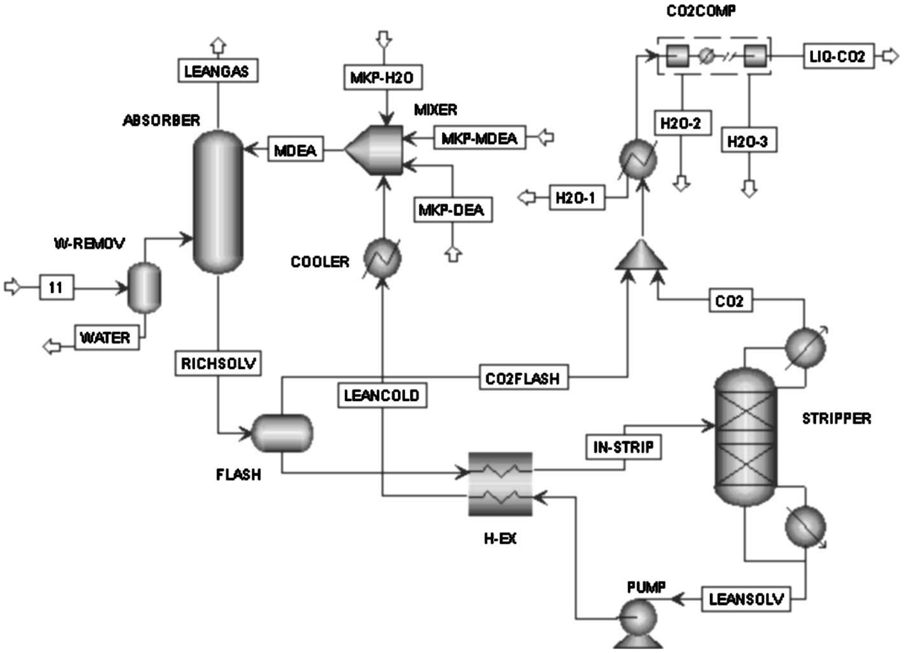

Fig. 4 CO_2 removal and liquefaction plant

Table 5 Main results of CO_2 removal plant and fuel composition

Configuration	REF 850°C	REF 950°C	SF 850°C	SF 950°C	GAS GAS 850°C	GAS GAS 950°C
Solvent mass flow [kg/s]	556.9	582.1	570.9	594.6	526.0	542.7
Q reboiler [MWt]	85.0	89.0	87.0	90.5	80.0	83.3
Steam [kg/s]	36.1	37.8	36.6	38.1	33.7	35.0
CO_2 in ABS [kg/s]	41.72	45.58	41.66	46.09	38.61	42.33
Removed CO_2 [kg/s]	39.74	41.79	40.57	42.67	37.45	39.11
Removed CO_2 [%]	95.3	91.7	97.4	92.6	96.7	92.4
Fuel (stream "13") mass flow [kg/s]	71.96	85.97	65.78	81.0	58.61	70.90
Fuel composition [% by vol]						
CH_4	0.84	0.09	1.17	0.13	1.18	0.14
CO	0.27	0.26	0.41	0.41	0.34	0.35
CO_2	0.90	1.55	0.50	1.40	0.59	1.46
H_2	52.45	49.19	55.92	52.35	57.38	54.25
N_2+AR	44.72	47.95	41.29	44.78	39.78	42.86
H_2O	0.83	0.96	0.70	0.93	0.73	0.94
Fuel LHV [MJ/kg]	9.32	7.80	10.87	8.83	11.44	9.46

The rate of carbon dioxide removal in the ABS is different for the various configurations. In fact a design specification has been created to set at 10% the percentage of all the carbon not removed from syngas. In this way it is possible to take into account CO and CH_4 fractions, which generate CO_2 while burning in GT. Thus, in every configuration CO_2 final emissions are 90% of emissions generated by a gas turbine combined cycle (GTCC) with the same natural gas input. The percentage of removed CO_2 is greater whenever CH_4 and CO conversion is lower; for example, in the Reference Case absorbed CO_2 is 95.3% of the total entering the ABS if T-ATR=850°C. If T-ATR is increased to 950°C, then removed CO_2 decreases to 91.7% because the CH_4 concentration in syngas to be treated is lower (see Table 4). However this variation does not deeply affect power and heat consumption in the CO_2 capture plant, which on the contrary greatly depends on the total mass flow of removed CO_2. In all the configurations if the T-ATR is increased, then the mass flow of carbon dioxide entering the ABS grows, thus increasing the reboiler heat duty needed for solvent regeneration. GAS-GAS (with T-ATR=850°C) is the configuration that requires the least heat duty (80 MW), even though the percentage of absorbed CO_2 is rather high (96.7%). Solvent mass flow has the same behavior of reboiler heat duty, as it depends above all on the total mass flow of CO_2 to be captured. After all GAS-GAS configurations generate less CO_2 than other cases, thus giving the following advantages:

1. Steam extraction from the ST for stripping is lower, as reboiler heat duty decreases.
2. CO_2 to be captured is less, so power consumption for solvent pump and CO_2 compressor is lower.

3.3 Power Generation. Power generation is accomplished by a gas-steam combined cycle. The gas turbine is a heavy-duty machine, corresponding to technology known as FA, characterized by a TIT of approximately 1350°C. The turbine modeled in the simulation matches the main parameters of a real machine, SIEMENS V94.3A (β=17−TIT=1350°C). In particular, air mass flow rate at the compressor inlet is the same as the real machine (634 kg/s); the net efficiency and the net power output are, respectively, 38.2% and 256 MW, TOT is 590°C. The net power output generated by the GT is determined by a calculator block, which uses fuel mass flow and composition and the fixed efficiency as input parameters to calculate the produced power. In any configuration, the natural gas mass flow rate has been changed to match the real machine net power. The HRSG is three pressure levels: 4/35/140 bar, with reheat and condenser at 0.04 bar. Heat recovery has been optimized by setting at 10°C, the minimum pinch point ΔT for all the pressure levels.

In the Reference Case and in the SF configuration, the approach point ΔT has been fixed at 20°C, which corresponds to a superheating (and reheating) steam temperature, respectively, of 537°C and 560°C. In the GAS-GAS configuration, maximum steam temperature is also 560°C, not to exceed the limit connected with corrosion. The ATR requires a significant amount of steam: 27.7 kg/s, needed to achieve a S/C ratio of 1.5, are extracted from MP steam turbine at 18.13 bar. Solvent regeneration also requires steam. A mass flow of 33.7–38.1 kg/s is extracted from the LP steam turbine at 2 bar. The main assumptions made for the power generation section are summarized in Table 6.

Table 6 Assumptions made for power generation section

Gas turbine cycle	
Gas turbine	SIEMENS V94.3A
Pressure ratio	17
TIT [°C]	1350
Inlet air flow rate [kg/s]	634
Thermodynamic efficiency [%]	38.2
Fuel compressor η_{is}	0.9
Steam cycle	
Pressure levels [bar]	140/35/4
Condenser pressure [bar]	0.04
Steam turbine η_{is}	0.9
Steam turbine η_{mec}	0.95
Pump efficiencies	0.9
ΔT pinch point [°C]	10
ΔT approach point [°C]	20
ΔT subcooling [°C]	10

Table 7 Overall performances of the various plants

	Reference 850°C	Reference 950°C	SF 850°C	SF 950°C	Gas Gas 850°C	Gas Gas 950°C
GT net power [MW]	256.27	256.21	256.34	256.30	256.23	256.14
Steam cycle net power [MW]	141.35	158.27	148.79	166.11	122.97	136.97
Fuel compressor [MW]	6.51	7.33	5.90	6.80	5.81	6.61
Solvent pump power [MW]	0.77	0.80	0.78	0.82	0.72	0.75
CO_2 compressor [MW]	12.97	13.64	13.24	13.93	11.84	12.76
Plant net power [MW]	377.37	392.71	385.21	400.87	360.82	372.98
Natural gas LHV input [MW]	797	838	813	855	751	783
Net efficiency [%]	47.37	46.87	47.36	46.88	48.06	47.62
CO_2 emissions [kg/s]	4.38	4.61	4.48	4.70	4.13	4.27
CO_2 specific emissions [g/kWh]	41.8	42.2	41.8	42.2	41.2	41.2
Actual CO_2 reduction [%]	88.3	88.1	88.3	88.2	88.4	88.4

4 Comparison of the Performance

Table 7 shows overall performances of the various plants. For a given configuration, the power generated by the steam cycle increases if the T-ATR is higher, as syngas cooling produces more steam (for example in the Reference Case, waste heat boiler generates 74.1 kg/s of the HP steam if T-ATR=850°C, 94.5 kg/s if T-ATR=950°C). Anyway net efficiency is 47.37% and 46.87% for a reactor temperature, respectively, of 850°C and 950°C. This is a consequence of the decrease in cold syngas efficiency, which forces to burn a greater fraction of natural gas in the ATR and to increase natural gas consumption. Furthermore, CO_2 to remove is 5% higher when T-ATR=950°C, so CO_2 compression work and steam extraction from the ST are greater. For T-ATR=950°C fuel compressor work rises, too, because the fuel flow rate is 19.5% greater than for T-ATR=850°C. This is due to the different fuel composition, which depends above all on air mass flow needed by ATR, as it determines nitrogen concentration in the fuel and its LHV.

For a given ATR temperature, in SF configurations the ST power is higher than in the Reference Case because maximum steam temperature is 560°C versus 537°C. SF configurations require also less power for fuel compression, as the LHV is higher than in the Reference Case. However, net efficiencies are quite similar for the Reference Case and SF configuration. In fact, even if cold syngas efficiencies are higher in SF configuration, a significant fraction of produced fuel is used for supplementary firing (6.2% of the total). This causes an increase by 2% in natural gas consumption. Furthermore, for a given ATR temperature, removed CO_2 is more in SF configurations than in the Reference Case, therefore, compressor work needed is higher.

In the GAS-GAS configuration all the parameters discussed above seem to be better than in other configurations. In particular, Table 7 clearly shows that:

- CO_2 compressor work is much lower, as carbon dioxide to remove decreases (see also Table 5).
- Fuel compressor work decreases, too, because fuel has the highest LHV.
- Cold syngas efficiency is higher. Therefore natural gas consumption is lower; for example for T-ATR=850°C, the Reference Case shows a cold syngas efficiency of 84.3%, while in the GAS-GAS configuration this parameter is 89.4% (see Table 4). This reduces natural gas input from 17.21 kg/s to 16.22 kg/s.
- Stripping requires less steam extracted from the LP for solvent regeneration because CO_2 absorption requires a lower solvent mass flow (see also Table 5).
- The net power is lower because of the reduction of the steam generated by the waste heat boiler, where syngas enters at a lower temperature.
- However, cycle net efficiency is higher. This is due not only to the reduction of auxiliaries consumption, but also to the increase in cold syngas efficiencies. For T-ATR=850°C net efficiency is 48.06%, for T-ATR=950°C net efficiency is 47.62%.

Since carbon removal has been fixed at 90%, both absolute and specific CO_2 emissions are similar for all the configurations. More precisely, specific emissions are lower in GAS-GAS configuration, where the best efficiency implies an increased power generation relative to natural gas input. However, specific emissions are all in the range 41–42 g/kWh.

The last row in Table 7 shows actual CO_2 reduction; this parameter takes into account the decrease in plant thermodynamic efficiency. In fact, if we assume that a conventional GTCC has a global efficiency of 56%, the cycles analyzed in this paper do not reduce CO_2 emissions by 90%, as they need supplementary natural gas to generate same power as GTCC. Therefore actual CO_2 reduction is the ratio between CO_2 specific emissions of the cycle considered and of GTCC characterized by a thermodynamic efficiency of 56% (approximately 356 g/kWh).

Conclusions

In this paper a gas-steam combined cycle with natural gas reforming and CO_2 capture is presented. An Auto Thermal Reformer has been simulated to generate syngas, whose concentration in hydrogen is increased by two CO-shift reactors in series that follow the ATR. Carbon dioxide is removed in an absorption column, using a blend of most common amines (MDEA, 30% by weight, and DEA, 5%). Lean gas leaving the absorber is characterized by a carbon concentration reduced by 90%. It feeds a commercially available gas turbine and the bottoming steam cycle. Power plant and syngas production plant were coupled and investigated in three main configurations. Among them the most promising scheme is the one with a high-temperature gas-gas heat exchanger, which heats the streams entering ATR and cools syngas at ATR outlet. This configuration showed a global thermal efficiency of 48.06% and CO_2 specific emissions of 41.2 g/kWh.

Acknowledgment

The software ASPEN PLUS® Version 11.1 used in this paper is under license of Aspen Technology, Inc.

Nomenclature

ABS = absorber
ASU = air separation unit
ATR = auto thermal reformer
DEA = di-ethanol-amine
GT = gas turbine

GTCC = gas turbine combined cycle
HE = heat exchanger
HP, LP, MP = high, low, medium pressure level
HRSG = heat recovery steam generator
HTS = high-temperature shift
IGCC = integrated gasification combined cycle
LHV = low heating value
LTS = low-temperature shift
MDEA = methyl-di-ethanol-amine
MEA = mono-ethanol-amine
PCFP = pulverized coal-fired plant
PRE-REF = prereformer
REF = reference case
REG = fuel regenerator
SF = supplementary firing
SMR = steam methane reformer
ST = steam turbine
STP = stripper
TIT = turbine inlet temperature
TOT = turbine outlet temperature
WHB = waste heat boiler
β = pressure ratio

References

[1] Keeling, C. D., and Whorf, T. P., 2003, Atmospheric CO_2 Records From Sites in the SIO Air Sampling Network, *Trends: a Compendium of Data on Global Change*, Carbon Dioxide Information Analysis Center, Oak Ridge National Laboratory, U.S. Department of Energy, Oak Ridge, TN.
[2] IPCC Third Assessment Report: "Climate Change 2001: The Scientific Basis—Contribution of Working Group I to the Third Assessment Report of the Intergovernmental Panel on Climate Change (IPCC)," J. T. Houghton, Y. Ding, D. J. Griggs, M. Noguer, P. J. van der Linden, and D. Xiaosu, eds., Cambridge University Press, UK.
[3] Desideri, U., and Paolucci, A., 1999, "Performance Modelling of a Carbon Dioxide Removal System for Power Plants," Energy Convers. Manage., **40**(18), pp. 1899–1915.
[4] Desideri, U., and Proietti, S., 2002, "CO_2 Capture and Removal System for a Gas-Steam Combined Cycle," *Proc. of Int. Mechanical Engineering Congress and Exposition*, November 17–22, New Orleans, LA.
[5] Chapel, D. G., Mariz, C. L., and Ernest, J., 1999, "Recovery of CO_2 From Flue Gases: Commercial Trends," Originally presented at the Canadian Society of Chemical Engineers Annual Meeting. October 4–6, 1999, Saskatoon, Saskatchewan, Canada.
[6] Bolland, O., and Mathieu, P., 1998, "Comparison of Two CO_2 Removal Options in Combined Cycle Power Plants," Energy Convers. Manage., **39**(16–18), pp. 1653–1663.
[7] Korens, N., Simbeck, D. R., and Wilhelm, D. J., 2002, "Process Screening Analysis of Alternative Gas Treating and Sulphur Removal for Gasification," Final Revised Report prepared for US Department of Energy, SFA Pacific, December.
[8] Pruschek, R., Oeljeklaus, G., Brand, V., Haupt, G., and Zimmermann, G., 1994, GUD Power Plant With Integrated Coal Gasification, CO Shift and CO_2 Washing. POWER-GEN EUROPE '94, Conference Papers, **6**, Köln/D, 17–19 May, 1994, pp. 205–225.
[9] Lozza, G., and Chiesa, P., 2002, "CO_2 Sequestration Techniques for IGCC and Natural Gas Power Plants: A Comparative Estimation of Their Thermodynamic and Economic Performance," *Proc. of the Int. Conference on Clean Coal Technologies*, (CCT2002), Chia Laguna, Italy.
[10] Audus, H., Kaarstad, O., and Skinner, G., 1998, "CO_2 Capture by Pre-Combustion Decarbonisation of Natural Gas," *Proc. of 4th Int. Conference on Greenhouse Gas Control Technologies*, Interlaken, Switzerland, Aug. 30–Sep. 2, 1998.
[11] Andersen, T., Kvamsdal, H. M., and Bolland, O., 2000, "Gas Turbine Combined Cycle With CO_2 Capture Using Auto-Thermal Reforming of Natural Gas," ASME Paper 2000-GT-162.
[12] Kvamsdal, H. M., Ertesvåg, I. S., Bolland, O., and Tolstad, T., 2002, "Exergy Analysis of Gas-Turbine Combined Cycle With CO_2 Capture Using Pre-Combustion Decarbonization of Natural Gas," ASME Paper GT-2002-30411.
[13] Lozza, G., and Chiesa, P., 2001, "Low CO_2 Emission Combined Cycles With Natural Gas Reforming, Including NOx Suppression," ASME Paper 2001-GT-0561.
[14] Dybkjær, Ib., 1995, "Tubular Reforming and Autothermal Reforming of Natural Gas-An Overview of Available Processes," Fuel Process. Technol., **42**, pp. 85–107.
[15] Audus, H., and Jackson, A. J. B., 2000, "CO_2 Abatement by the Combustion of H_2-Rich Fuels in Gas Turbines," *Fifth Int. Conference on Greenhouse Gas Control Technologies*, Cairns, Australia, August, 13–16.
[16] Chiesa, P., Lozza, G., and Mazzocchi, L., 2003, "Using Hydrogen as Gas Turbine Fuel," ASME Paper GT-2003-38205.
[17] Todd, D. M., and Battista, R. A., 2000, "Demonstrated Applicability of Hydrogen Fuel for Gas Turbines," *Proc. of IchemE Gasification 4 Conference*, Noordwijk, Netherlands.
[18] Aspen Technology Inc., 2000, "Aspen Plus—User Guide. Version 10.2."
[19] Aspen Technology Inc., 2000, "Aspen Plus—Unit Operation Models. Version 10.2.".
[20] Aspen Technology Inc., 2000, "Aspen Plus—Physical Property Methods and Models. Version 10.2."

H_2/O_2 Cycles: Thermodynamic Potentialities and Limits

M. Gambini
e-mail: gambini@ing.uniroma2.it

G. L. Guizzi

M. Vellini

Department of Industrial Engineering,
University of Rome "Tor Vergata,"
Via del Politecnico n. 1,
00133 Rome, Italy

In this paper, the thermodynamic potentialities and limits of the H_2/O_2 *turbine cycles (afterward named only* H_2/O_2 *cycles) are investigated. Starting from the conventional gas turbine and steam turbine technology, the paper qualitatively tackles problems related to a change of oxidizer and fuel: from these considerations, an internal combustion steam cycle is analyzed where steam, injected into the combustion chamber together with oxygen and hydrogen, is produced in a regenerative way and plays the important role of inert. A proper parametric analysis is then performed in order to evaluate the influence of the main working parameters on the overall performance of* H_2/O_2 *cycles. All the results are carried out by neglecting the energy requirements for* O_2 *and* H_2 *production systems, but taking into account the work required by the* O_2 *and* H_2 *compression. This choice permits a great freedom in the definition of these thermodynamic cycles; moreover, it is possible to come to some general conclusions because the* H_2 *and/or* O_2 *production systems and their integrations with thermodynamic cycles do not have to be specified. Therefore, this paper can be framed in a context of centralized production of oxygen and hydrogen (by nuclear or renewable energy sources, for example) and their distribution as pure gases in the utilization place. By adopting some realistic assumptions, for example, a top temperature of* 1350 °C*, the potentialities of* H_2/O_2 *cycles are very limited: the net efficiency attains a value of about 50%. Instead, by adopting futurist assumptions, for example, a top temperature of* 1700°C*, a different* H_2/O_2 *cycle scheme can be proposed and its performance becomes more interesting (the net efficiency is over 60%). The paper tackles the main thermodynamic and technological subjects of the* H_2/O_2 *cycles: for example, it is underlined how the choice of the working parameters of these cycles strongly influences the attainable performance.* [DOI: 10.1115/1.1924401]

1 Introduction

Fossil fuels are likely to play a major role in global energy supply in the near-medium term future. On the other hand, fossil fuels are the major source of anthropogenic CO_2 emission into the atmosphere. In the future power generation scenario, even though concepts such as efficiency and costs will still be very important, the most significant aspect will be environmental: carbon dioxide emission especially.

In the last years the great attention, addressed to the greenhouse effect, has involved the analysis of potential zero-emission power plants, by using hydrogen as fuel [1–4].

But there are also other potential zero-emission power plants where there is the combustion between oxygen and any gaseous hydrocarbon fuel in order to produce a working fluid, composed of steam and carbon dioxide (CO_2), at high temperature and high pressure, which can power conventional or advanced turbines. With improvements in turbine technology, efficiencies in the range of 50% are possible with nearly 100% carbon capture [5–8].

But hydrogen and electricity may become the favored twin energy carriers in a possible "greenhouse driven" future due to their lack of CO_2 emissions at the point of use [9]. For this reason, in the technical works it is possible to find many examples of cycles based on hydrogen combustion; moreover if oxygen is used as oxidizer, it is possible to obtain semiclosed cycles where the working fluid is H_2O.

These cycles seem to have great thermodynamic potentialities [2], but in these analyses it is very important to adopt some reasonable assumptions. In fact, by choosing very high values for the maximum pressure and temperature and neglecting the energy requirements for the compression and the production of oxygen and hydrogen, these cycles can attain high efficiency (65–70%, depending on the scheme layout), [2,3,10]. But lowering, for example, the maximum temperature, some typologies of thermodynamic cycle do not sustain themselves [10]. Hence, the H_2/O_2 cycles can be studied only from a thermodynamic point of view, but it is very important to assume reasonable hypotheses about the most important working parameters, even if hydrogen and oxygen can be considered available at the ambient condition without any energetic expense.

In this paper we want to point out that the H_2/O_2 *cycles always need an inert fluid. The high energy cost of using oxygen as oxidizer requires very little excess oxygen at the last combustion chamber exit. These cycles commonly suffer from not having an inert fluid; so, they can make up for this lack by providing steam, produced in a regenerative heat exchanger which also limits heat discharged into the environment.*

In this paper we want to discuss the real potentialities of the H_2/O_2 cycles; we will start analyzing conventional steam cycles and combined cycles and, by taking into account the thermodynamic problems related to the use of oxygen and hydrogen, we will propose several cycles, supplied with oxygen instead of air and fed by hydrogen instead of fossil fuel. In these cycles we will point out the technological and thermodynamic limits [for example, the reasonable value of turbine inlet temperature (TIT) and of the final excess oxygen]; then, we will properly modify the thermodynamic cycles and also the plant layouts. In the end *we will demonstrate that, starting both from steam turbine and gas turbine technology, the only practical* H_2/O_2 *cycles are those that use regeneratively formed steam as an inert fluid delivered to the combustion chamber. Such a cycle becomes an Internal Combustion Steam Cycle (ICSC).* These H_2/O_2 cycles can attain a net efficiency of almost 63% only by adopting very high (probably futurist) values for the maximum temperature and pressure.

Contributed by the IGTI Innovations Technology Committee of the American Society of Mechanical Engineers for publication in the ASME JOURNAL OF ENGINEERING FOR GAS TURBINES AND POWER. Manuscript received by IGTI July 29, 2003; final revision received August 10, 2004. Associate Editor: A. Massardo.

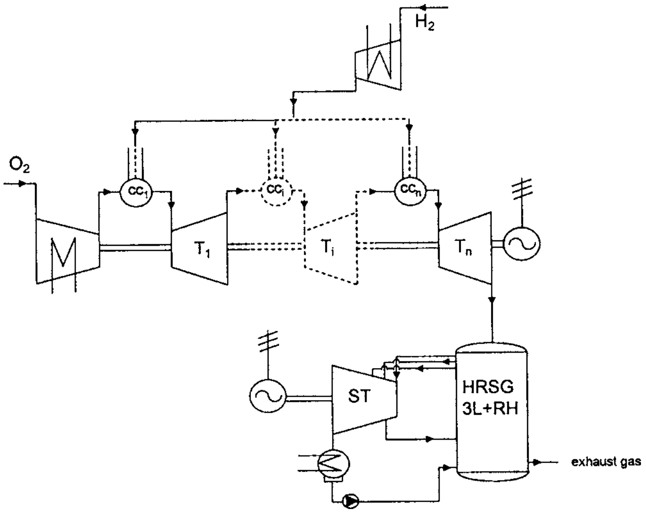

Fig. 1 Combined cycle layout with *n* combustions

2 Conventional Cycles: Effects of Switching Fuel and Oxidizer

The two power plant schemes, which can be considered as a starting point, are the gas turbines and the steam cycle power plants.

2.1 GT Technology. Nowadays, the most important applications of the gas turbine (GT) technology in power production are combined cycle power plants. These solutions, supplied with air as oxidizer and natural gas as fuel, can attain great advantages in terms of high net efficiency and working versatility. From a thermodynamic point of view, in these cycles the overall efficiency must be optimized: in other words, the best integration between the topping cycle (GT)—where the main characteristic is the high temperature at which heat is supplied—and the bottoming cycle [steam cycle (SC)]—where the main characteristic is the low temperature at which heat is discharged—must be investigated, by considering the heat recovery steam generator (HRSG) which joins these two systems. About the total heat discharged into the ambient, we have well known that, in addition to the condenser heat-rejection rate, there is another heat-rejection rate: the gas flow rate exiting from the HRSG; this last heat-rejection rate can be limited, as far as possible, by adopting more pressure levels. In the most up-to-date combined cycle power plants there are very complex boilers [11,12] (with three pressure levels and steam reheat): in this case the final gas temperature is about 85 °C [11].

Using oxygen instead of air and hydrogen instead of natural gas (both produced by any process), the first consequence is a very high (and inadmissible) excess oxygen in the exhaust gases in order to obtain an established value of TIT. By way of example, in a gas turbine with a pressure ratio, β, of 15 and with a maximum temperature, TIT, of 1250 °C, the final oxygen fraction is over 87% (by mass)! The resulting gross efficiency is over 53%, while the net efficiency cannot be quantified because the cycle net work does not satisfy energy requirement for oxygen production ($0.89\ \mathrm{MJ/kg_{O_2}}$). A possible idea for the reduction of the excess oxygen is the subdivision of the total expansion, and the addition of working fluid reheats between two consecutive expansions. In Fig. 1 there is a possible gas turbine scheme with *n* expanders and *n* combustion chambers. In Fig. 2 it is possible to see the results of this simulation, in particular, the oxygen fraction at the power plant discharge for various full compression ratios and various TITs; the results are related to various situations: from 1 to 10 combustions with equal partial expansion ratios, when the total expansion is subdivided. In this graph, only the points, pointed out by means of symbols, are meaningful; the continuous line is drawn in order to show the trend of this working parameter. It is possible to note that, also by adopting futurist temperature (1700 °C), the O_2 fraction is very high: it is always over 70% (by mass), even if the full compression ratio is 30 and there are ten combustions! The result does not change even if we assume a very high maximum pressure: in such a situation it is important to note that both oxidizer and fuel must be compressed until the maximum pressure, and the gas compression requires large energy requirements. In Fig. 2, where a full compression ratio of 90 and a TIT of 1700 °C are chosen, the O_2 fraction is over 65% (by mass) when there are ten combustions!

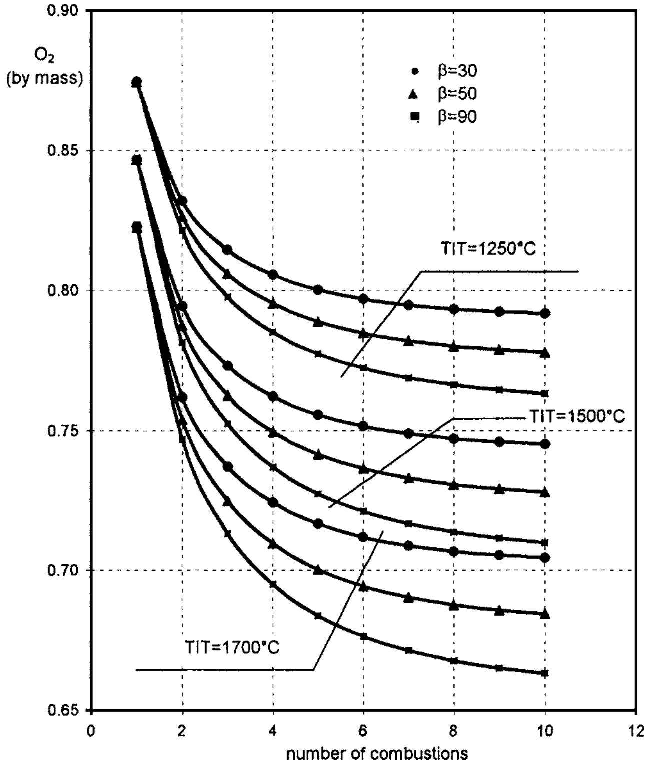

Fig. 2 O_2 fraction as function of the combustion chambers

As stated above, in this graph the partial expansion ratios are equal in all the turbines; in order to obtain optimal performance, the partial expansion ratios could be chosen by means of an optimization calculation. The idea can be the following: in the first turbines the pressure ratios are high so that in the last combustion chambers the working fluid is cooler and thus it requests a higher quantity of fuel in order to reach the maximum temperature. However, in this way, it is not possible to limit properly the oxygen fraction at the power plant discharge and, even if it could happen, there would be another problem. In fact when the oxygen fraction is limited, it means that the working fluid is composed mainly of steam: this steam is discharged into the environment and it involves a great thermal loss because it is steam at ambient pressure.

Because of all the previous reasons, the simple substitution of oxidizer and fuel in a conventional gas-steam combined cycle is not a good proposal: the main problem is the lack of a proper inert in the combustion chamber which can limit the maximum temperature. Therefore the oxygen plays this role and the final result is an inadmissible oxygen excess at the power plant discharge.

When oxygen and hydrogen are used in a gas turbine, the gas cycle and the steam cycle cannot be separated: *the idea is the injection of the steam into the combustion chamber of the topping cycle in order to limit the excess oxygen; the regenerative steam production is performed by the stream, exiting the gas turbine (which becomes a steam turbine); such a cycle becomes an inter-*

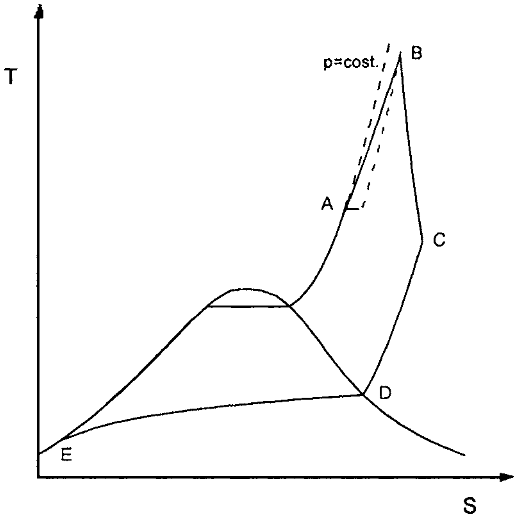

Fig. 3 Qualitative internal combustion steam cycle on the plane T-s

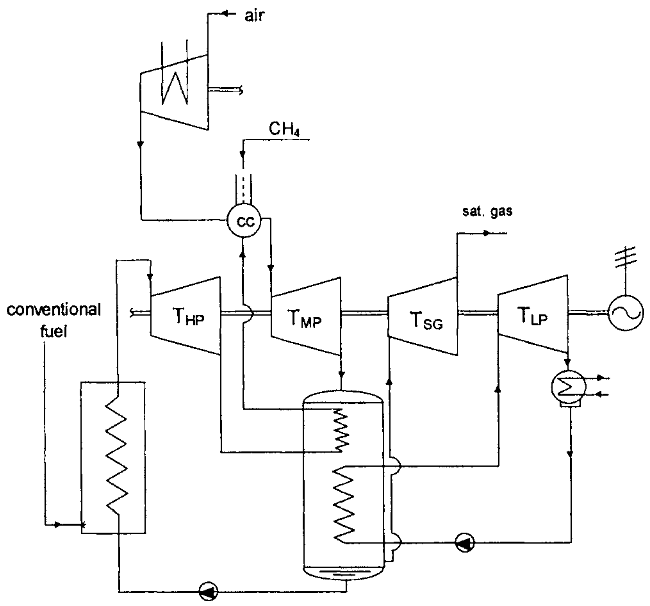

Fig. 4 Hybrid scheme with pressurized separator

nal combustion steam cycle (ICSC). Where the separate steam section is no longer useful, it would be interesting to study expanding working fluid up to pressures typical of the conventional steam cycles because the working fluid is primarily steam. These subjects will be tackled in the next paragraph where a proper parametric analysis will show the great importance in the choice of the maximum pressure and temperature, especially.

2.2 Steam Turbine Technology. Considering that, in the steam cycle the combustion is external, it is not possible to use hydrogen in a conventional steam boiler, because of the thermodynamic penalization related to the low value of the highest temperature of the steam (TIT in the range 540–560°C); this temperature is a consequence of the technological limits of the superheating tube materials in the conventional steam boilers. *In this context, it is necessary to propose an internal combustion steam cycle where a high increase of the TIT can be pursued.*

Some years ago, the authors did a lot of scientific work on this subject (internal combustion steam cycle, but using natural gas and air) and the results were very interesting [13–16]. The authors proposed a new advanced mixed cycle which attains very high performance [13,14]: it was first named gas injection steam cycle (GIST cycle) and then advanced mixed cycle (AMC). In this paragraph it is very interesting to examine the thermodynamic stages which permitted to define this innovative cycle.

An internal combustion cycle—where the steam heating is carried out by combustion of natural gas and compressed air inside the steam flow—was used as starting point for the proposition of a new cycle typology. But, the internal combustion involves some modifications in comparison with a conventional steam cycle. In Fig. 3 the cycle is qualitatively drawn on the T-s thermodynamic plane, with reference to the unitary mass of steam. We can see that the internal combustion produces the following effects:

- mixing between gas and steam: it involves the steam pressure loss (line A-B);
- maximum temperature, TIT, very high: it is much higher than that obtainable in a conventional steam cycle (point A);
- steam final expansion in the superheated field (point C) because of
  - — very high turbine inlet temperature, TIT;
  - — reduction of the maximum pressure of the steam (owing to the mixing between steam and gas and thus the consequent passage from the total to the partial pressure);
  - — increase of the steam final pressure (owing to the final pressure of the gas-steam expansion is limited to the atmospheric pressure)
- need of a proper cooling of the gas-steam mixture; and
- steam condensation (with water separation and recovery) with decreasing temperature (line D-E), owing to the progressive reduction of the steam partial pressure in the mixture during condensation process.

The first cycle proposals were based on hybrid power plants: in other words, the heating until the point B (Fig. 3) was carried out partly by an external combustion (presence of a conventional steam boiler) until the point A, and partly by an internal combustion, until the point B.

In the first plant layouts, a maximum temperature of 900°C was chosen in order to operate with “steam technology” (that is, turbines without cooled blades). The main feature of these cycles was the proper use of the mixture cooling (C-E transformation in Fig. 3) because it is necessary to recover the water, injected in the combustion chamber as steam. For this reason, two paths were taken into account:

(i) use of a pressurized separator, which easily separates water, permits feeding a bottoming cycle (in which unconventional fluids can also be used) by means of the heat released during gas-steam mixture cooling, but interrupts the mixture expansion and thus obliges to introduce a new component, that is a saturated gas turbine, in order to recover the energy pressure of incondensable flow at the separator exit. Unfortunately, these solutions attained very poor performance: the great increase of the maximum temperature of the cycle is made completely useless because of the high final pressure in the expansion of the gas-steam mixture, and the total lack of feed water regenerative heating. In Fig. 4 a plant layout proposal, based on these concepts, is shown.
This power plant solution attains an efficiency of about 38%, by adopting a maximum temperature, TIT, of 900°C, and by using H_2O as working fluid in the bottoming cycle. The ratio between the heat input in the conventional steam boiler and the total heat input is 75%.
(ii) use of an atmospheric separator, which separates water

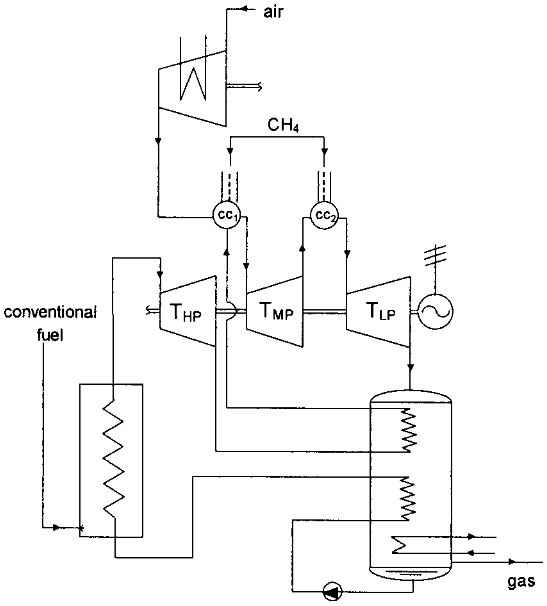

Fig. 5 Hybrid scheme with atmospheric separator

> less easily, eliminates the possibility of feeding a bottoming cycle with heat released during gas-steam mixture cooling but does not interrupt the mixture expansion; moreover, heat released during gas-steam mixture cooling and steam condensation can be profitably used for regenerative heating of the water before the inlet in the conventional steam boiler. These solutions attained interesting performance. In order to increase the mean temperature during the heat adduction, the possible ways, oriented towards an increase of the water regenerative heating, were investigated: the goal was reached by increasing the energetic content of the gas-steam mixture at the separator inlet. For this reason the total expansion was subdivided and another combustion chamber was interposed between the two turbines.

In Fig. 5 a power plant layout proposal, based on these concepts, is drawn. This power plant solution attains an efficiency of about 47%, by adopting a maximum temperature, TIT, of 900°C, and by using two combustion chambers. The ratio between the heat input in the conventional steam boiler and the total heat input is only 32%! The natural evolution of this cycle typology was correlated to the increase of the maximum temperature; for this reason the gas turbine technology was investigated. A proper parametric analysis [13] showed that the TIT increase reduces progressively the heat input in the conventional steam boiler: adopting a TIT=1260°C, it is possible to define a power plant solution, fueled by natural gas fully, where all the steam, injected in the combustion chambers, is regeneratively produced.

This plant layout proposal is not hybrid, but attains very high performance. Following these concepts, the authors proposed the AMC power plant depicted in Fig. 6.

The conversion process is the following: compressed air goes into the first combustion chamber (cc_1) together with the fuel and combustion takes place inside the steam flow. The steam arrives into this combustion chamber after a first expansion in a conventional steam turbine (ST) and after a regenerative partial reheat in the separator, which is now really a heat recovery steam generator (HRSG). The gas-steam mixture expands in a first turbine [high pressure turbine (HPT)]; then it goes into a second combustion chamber where the excess oxygen is combined with fuel nearly stoichiometrically to generate hot exhaust gases. After the medium pressure turbine (MPT) expansion, the stream is cooled in the HRSG where recycled steam, at a single pressure level (supercritical), is produced to expand in the ST. At the HRSG exit the water is pumped into the boiler while the saturated gas is discharged into the environment.

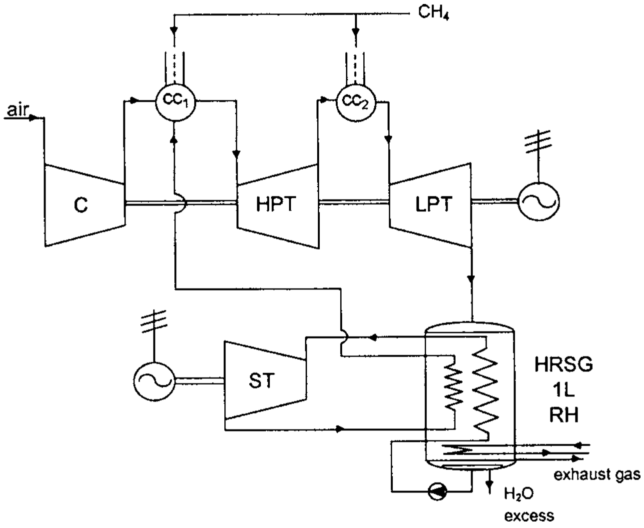

Fig. 6 AMC power plant

The benefits, correlated to the increase of the mean temperature during the heat adduction, are obvious: there is a full regenerative steam generation and a partial regenerative reheating before the steam injection in the first combustion chamber. This power plant solution attains an efficiency of about 57%, very similar to that attainable with combined cycle power plants adopting the same maximum temperature.

We think that this evolution is very important in this paper because, starting from the scheme of Fig. 6, it is possible to understand, qualitatively, the main modifications correlated to a change in the oxidizer and in the fuel in the ST technology. First of all, in this scheme it could be possible to limit the excess oxygen because the steam can play the role of inert fluid in the combustion chamber. The direct consequence would be a working fluid composed mainly of H_2O. Then, if the working fluid is really almost pure steam, also in this case it could be interesting to study the working fluid expansion until pressures, typical of the conventional steam cycle.

From this introduction it is clear that, using hydrogen as fuel and oxygen as oxidizer, both the GT technology and the ST technology suffer the lack and/or the poor availability of a proper inert in the combustion chambers and thus they must become internal combustion steam cycles (ICSC) where H_2O (steam) plays a role of inert in the H_2-O_2 combustion.

3 H_2/O_2 Cycles (Advanced TITs)

From the previous paragraph it is clear that *the only practical H_2/O_2 cycles are those that use regeneratively formed steam as inert fluid delivered to the combustion chamber*. So the reference scheme, here investigated, is depicted in Fig. 7. The evaluation criteria and the main numerical assumptions are reported in the Appendix.

In comparison with the scheme of Fig. 6, in this scheme there are the intercooled compressors for the fuel and the oxidizer. For this scheme, a parametric analysis is performed in order to evaluate H_2/O_2 cycle performance as a function of the most important working parameters.

In Fig. 8 it is possible to see the results of this simulation, in particular, the net efficiency and the oxygen fraction at the power plant discharge as function of the high pressure expansion ratio, for various full compression ratios and for a TIT of 1350°C.

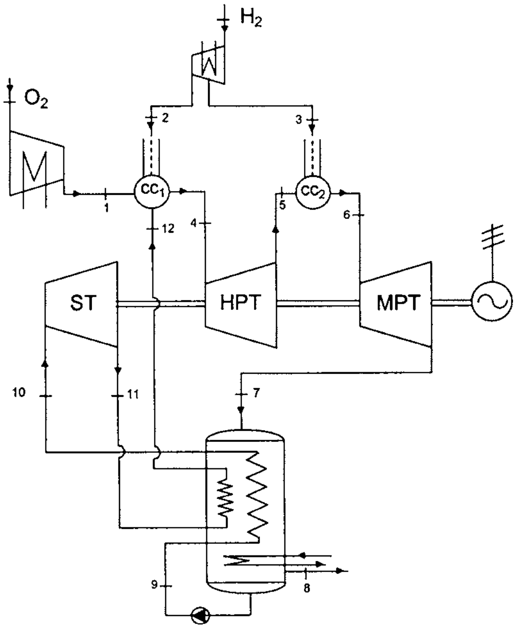

Fig. 7 H_2/O_2 cycle scheme: reference case

In this graph, the discontinuities of the trends are due to the fuel compression: in fact, increasing the β_{HPT} progressively reduces the pressure in the second combustion chamber, cc_2. When the pressure, in the second combustion chamber, is lower than that at the exit of the first fuel compression stage, the fuel, delivered to the cc_2, is separated from the fuel, delivered to the cc_1, because the second compression stage would be useless. The total fuel compression work decreases and the net efficiency increases.

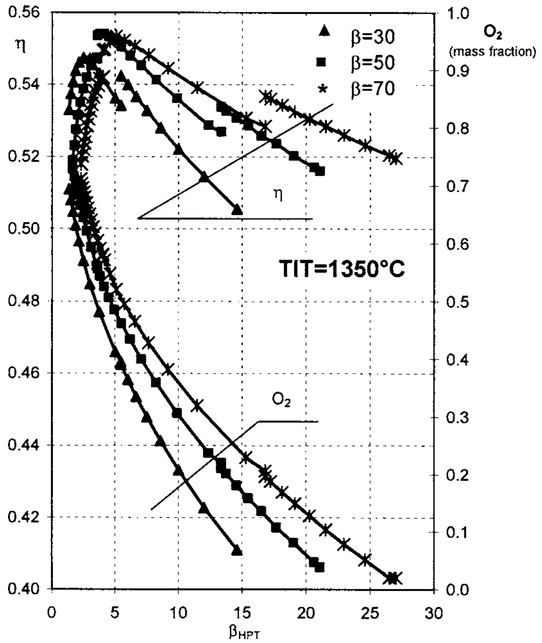

Fig. 8 H_2/O_2 cycle performance (TIT=1350 °C)

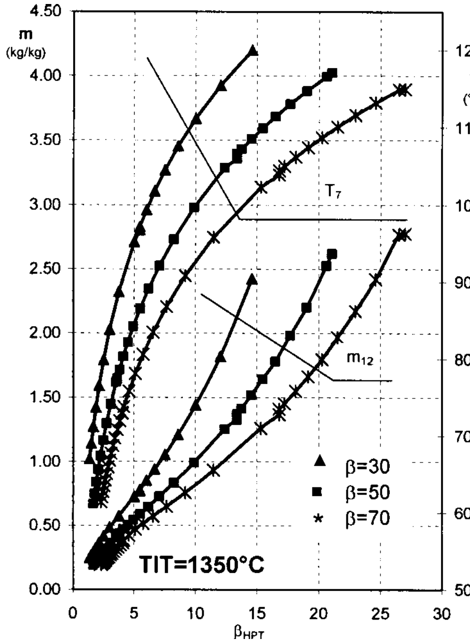

Fig. 9 H_2/O_2 cycle working parameters (TIT=1350 °C)

For each β, the net efficiency attains the maximum value—that depends on the full compression ratio, β. Then, the net efficiency decreases, when β_{HPT} increases. In fact, increasing the β_{HPT} rises the temperature at the MPT exit; because of this, a higher thermal flow can be profitably used in the HRSG by producing a higher quantity of steam at the established pressure and temperature (Fig. 9). But there is another effect correlated to the β_{HPT} increase: the mean temperature during the heat transfer in the second combustion chamber decreases. When the maximum value of the net efficiency is reached, the temperature profiles in the HRSG are perfectly coupled. For higher β_{HPT}, there are greater irreversibilities in the heat exchange and the mean temperature, during the heat transfer in the second combustion chamber, continues decreasing. Moreover, increasing the β_{HPT} reduces the excess oxygen; when the minimum oxygen fraction is attained, the efficiency continues decreasing because the given top temperature cannot be reached in the second combustion chamber.

In these two graphs (Figs. 8 and 9), the results are meaningful only when the minimum excess oxygen is reached: for $\beta=30$ the maximum efficiency attains the value of 50.6% and the quantity of produced steam is 2.42 kg per kg of oxygen at the compressor inlet. Moreover, the energy required for oxygen production involves great energy consumption into the energy balance. In fact, the air separation unit is able to give oxygen at ambient pressure and temperature. The advantage of this method is that it can produce large quantities of high purity oxygen (from 90% to 98%). According to the literature [17], if oxygen is generated at atmospheric pressure and temperature and high purity (over 95%), a specific work of 0.89 MJ/kg of O_2 is required. By considering this energy consumption, the net efficiency becomes only 42.8%. Finally, if hydrogen is produced by coal or natural gas (steam methane reforming) decarbonization the net efficiency becomes very poor: about 24.6 and 19.3%, respectively [18].

Increasing the full compression ratio, the maximum net efficiency increases: 51.6% and 52% when $\beta=50$ and $\beta=70$, respectively. This increase is very limited, while the increase of the maximum pressure of the cycle involves the hydrogen compression until this maximum pressure. Since we do not consider realistic hydrogen compression up to high pressures (for example, up to 70 bars), we assume a maximum full compression ratio of 30: therefore in Fig. 10 there is the cycle scheme with the material and energetic balances, while in Table 1 the most important performance parameters are reported.

Moreover, it is interesting to see Fig. 11 where this cycle representation in the T-s diagram is shown, with reference to the unitary mass of steam. About the heat discharged from the HRSG into environment, it is possible to give the following commentary:

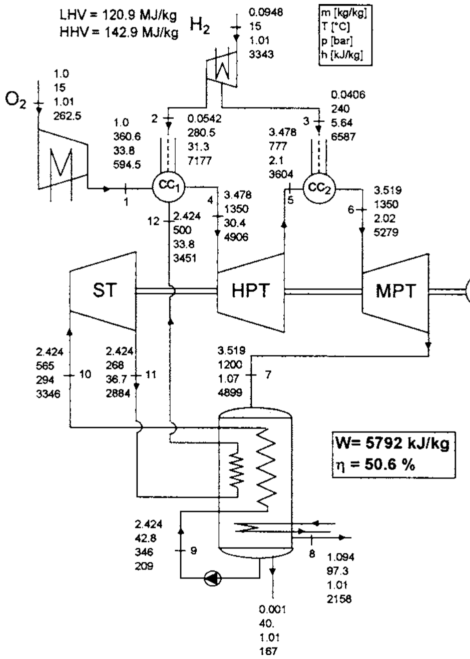

Fig. 10 Reference case: material and energetic balances

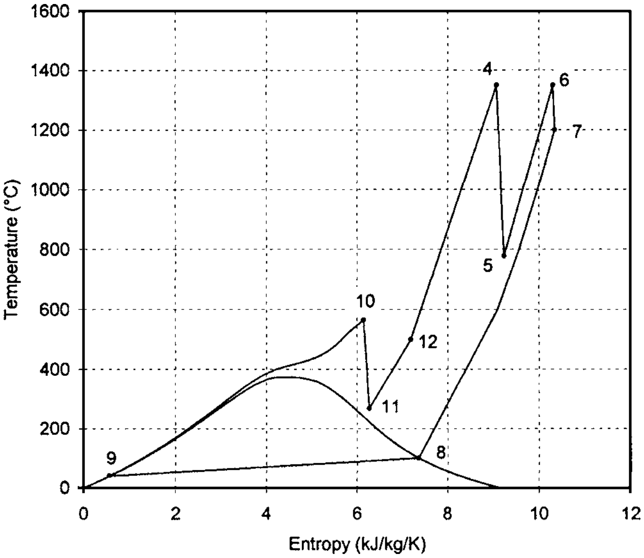

Fig. 11 Reference case: thermodynamic cycle *(referred to the unitary mass of steam)*

this loss includes two contributions, the heat discharged during the condensation of the steam, which is injected in the first combustion chamber [separator (SEP)], and the heat associated with the discharge of the steam, which is produced in the combustion chambers. This loss is very great because it can be considered as the heat associated with the condensation of all steam at the atmospheric pressure. The final conclusion is that, adopting a maximum cycle temperature of 1350°C, the H_2/O_2 cycle performances are rather poor and there are many technological complications which must be taken into account. On the other hand, these power plants have very low ambient impact because they can be considered as zero-emission solutions.

Choosing a maximum temperature of 1350°C, it seems that there are no margins for the performance increase of the H_2/O_2 cycles. But it is interesting to analyze the same working parameters when higher top temperatures are chosen. In Figs. 12 and 13 it is possible to see the net efficiency and the oxygen fraction at the power plant discharge as function of the high pressure expansion ratio, for various full compression ratios and for a TIT of 1500 and 1700°C, respectively.

The first value is, according to some authors [2,3], representative of the conditions of the state-of-the-art cooling and materials for next generation of combustion turbines now in early demonstration phases. The second one is, according to the same authors, a limit which can be reached in a short time because material and coating have been developed for these conditions.

In these two graphs it is possible to note that for high TIT there is a large range of β_{HPT} where the minimum oxygen excess is reached. Over the first β_{HPT}, which permits to reach the minimum oxygen excess, in the second combustion chamber the maximum temperature starts decreasing. For this reason when high TITs are adopted, the proper modifications in the cycle scheme must be investigated in order to increase the H_2/O_2 cycle performance. As stated above, when the oxygen excess is very small, it means that the working fluid is primarily composed of steam: in this case it is possible to study expanding working fluid up to pressures typical of the conventional steam cycles.

Table 1 Reference case: performance parameters

Power plant work balance (kJ/kg)		Power plant heat balance (kJ/kg)	
W_{ST}	1110	$Q_{fuel}+Q_{O2}$	579
W_{HPT}	4482	Q_{fuel} (HHV)	13 547
W_{MPT}	1326	Q_{SEP}	5484
W_{fuel}	505	Q_{HRSG}	2360
W_{O2}	442	$Q_{intercooling}$	267
W_{aux}	91	Q_{losses}	223
Net work output	5792	$Q_{in}-Q_{out}$	5792
Overall performance			
Net work output			5792
Fuel heat (LHV)			11 457
NET EFFICIENCY, %			50.55

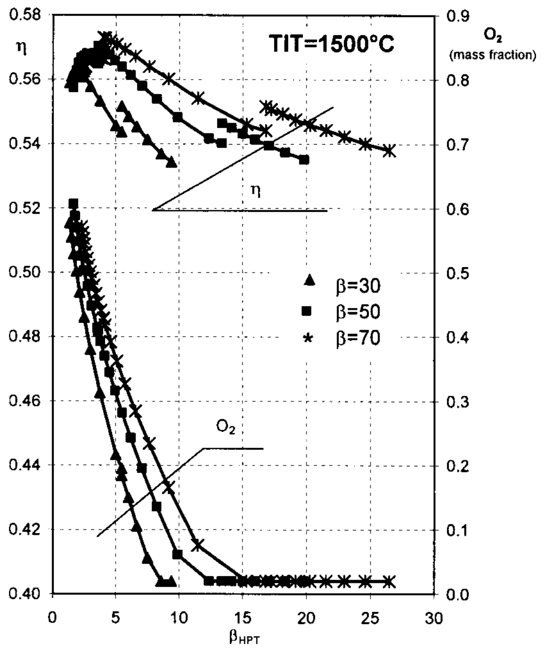

Fig. 12 H_2/O_2 cycle performance (TIT=1500°C)

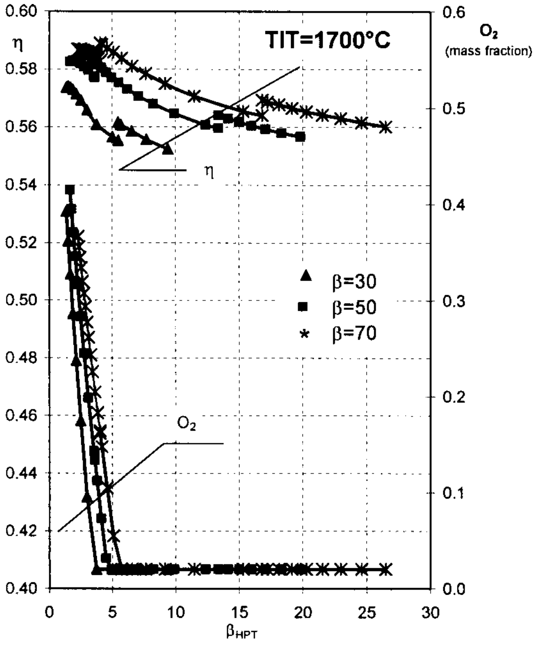

Fig. 13 H_2/O_2 cycle performance (TIT=1700°C)

4 H_2/O_2 Cycles: Further Improvements (Futurist TITs)

From the previous paragraph it is clear that, when we study the H_2/O_2 cycles with very high TITs, the cycle scheme proposals must change in order to take advantage of the strong increase of the maximum cycle temperature.

As stated above, it is necessary to investigate expanding the working fluid up to pressures lower than the atmospheric one. In order to realize such situation, two facts must occur

- the working fluid must be really composed mainly of H_2O (with a minimum excess oxygen);
- at the HRSG exit, the thermodynamic state of the working fluid (pressure and temperature) must guarantee a "good" expansion in the low pressure turbine (LPT).

Obviously, the expansion to a pressure lower than the atmospheric one can be considered only after the regenerative steam production, that is, at the HRSG exit; if we lowered the final pressure in the MPT, there would be many problems: for example, the final point of the expansion in the superheated field and, above all, the impossibility of a regenerative steam production owing to a too low temperature of the working fluid at the MPT discharge.

About the first fact, we must do the following considerations: it is well known that, in a conventional steam cycle power plant, the turbine back pressure limits the net efficiency. The minimum back pressure is dependent on the hotwell temperature which principally depends on condenser cooling water inlet temperature. Excess turbine back pressure is defined as a pressure increase above the temperature dependent hotwell water vapor pressure. This excess back pressure can be provoked by various causes and one of these is air in leak into the condenser. Therefore, adopting a fixed final partial pressure of the steam (depending on the inlet temperature of the condenser cooling water), the final total pressure of the expansion (that is, the turbine back pressure) depends on the incondensable amount in the steam [19]. Hence the incondensable gas fraction is very important: in fact, the total final back pressure greatly increases when there is a large amount of incondensable gas in the steam flow. When the gas fraction is high, a low pressure expansion becomes impossible, especially if the initial pressure of the expansion is the atmospheric pressure (as in this case).

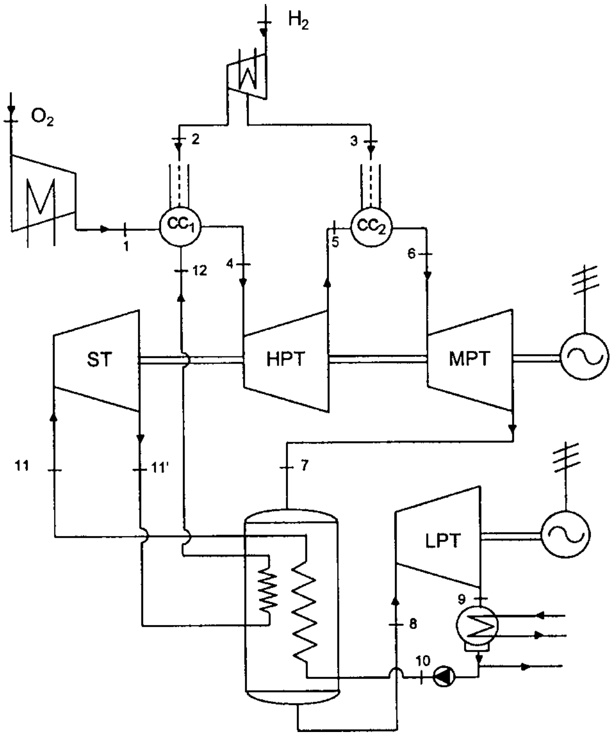

Fig. 14 H_2/O_2 cycle scheme: new reference case

Moreover, the specific work decreases greatly when the incondensable fraction increases because the steam expansion and the steam specific work are fixed, but the steam fraction decreases; simultaneously, even if the gas fraction increases, the specific gas work decreases because of the higher final pressure of the expansion.

About the second fact, instead, it is clear that the working fluid state, at the HRSG exit, must be suitable for a further expansion. Since it is not advantageous to interrupt the MPT expansion, the working fluid pressure will be at one atmosphere pressure. The comment about the temperature is more complex. The steam flow temperature would have to be high but in this case less thermal flow can be profitably used in the HRSG: in other words, in order to have a higher temperature at the HRSG exit, less steam will be produced regeneratively. But this condition must always guarantee achieving the top temperature in the second combustion chamber with a minimum oxygen excess. In this case there will not be water separation in the last HRSG section (SEP); there will be another turbine, low pressure turbine (LPT), and a "conventional" condenser where all the steam will condense. Then, part of the water is sent into the HRSG and part is discharged into environment. So the reference scheme, here investigated, is depicted in Fig. 14.

In Fig. 15, it is possible to see the steam mass flow rate, injected in the first combustion chamber, and the oxygen fraction at the power plant discharge as function of the high pressure expansion ratio, for various full compression ratios and for a TIT of 1350°C when the temperature, at the section 8, is not lower than 200°C. In this graph, it is possible to note that, when the top temperature is 1350°C, the final oxygen fraction is too high in all the range of β_{HPT} and for all three full compression ratios: by adopting a top temperature of 1350°C, these H_2/O_2 cycles cannot sustain themselves. In fact, all the useful thermal flow, at the MPT discharge, would have to be utilized in the regenerative steam production; interrupting the heat exchange limits the steam production and thus more oxygen is necessary in the combustion chamber in order to satisfy the thermal balance.

Moreover, in this case, the high gas fraction in the steam flow prevents the last expansion in the LPT. In conclusion, when TIT

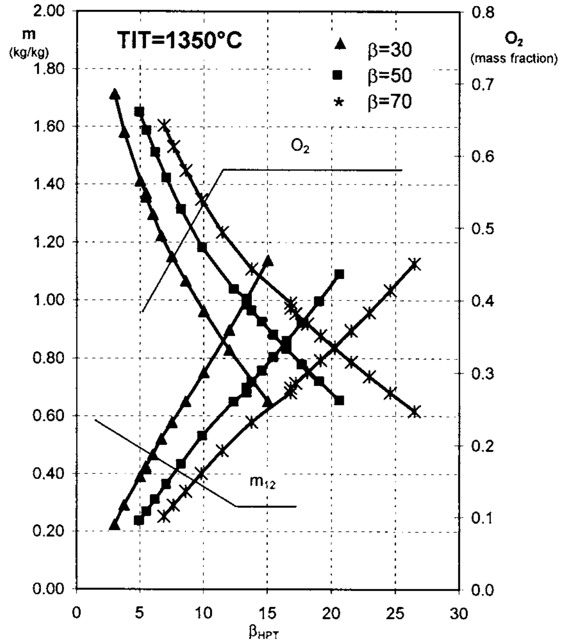

Fig. 15 New H_2/O_2 cycle performance (TIT=1350°C)

=1350°C, the only possible H_2/O_2 cycle scheme is that depicted in Fig. 7. Moreover, by adopting a full compression ratio of 30, the attainable performance is reported in Fig. 10 and listed in Table 1.

But also in this case, it is interesting to analyze the same working parameters, when the top temperatures are higher. In Figs. 16 and 17 it is possible to see the steam flow rate, injected in the first combustion chamber, and the oxygen fraction at the power plant discharge as function of the high pressure expansion ratio, for various full compression ratios and for a TIT of 1500 and 1700°C, respectively.

In these two graphs, there is an important fact which must be taken into consideration: for high TITs, there is a large range of β_{HPT} where the minimum oxygen excess is reached. Over the first β_{HPT}, which permits to reach the minimum oxygen excess, in the second combustion chamber the maximum temperature starts decreasing. For this reason it is clear that the scheme layout of Fig. 13 can be proposed only by adopting top temperatures that are very high.

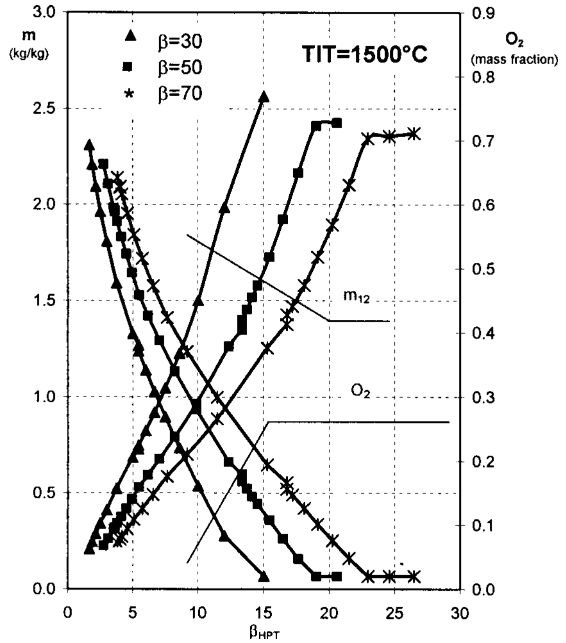

Fig. 16 New H_2/O_2 cycle performance (TIT=1500°C)

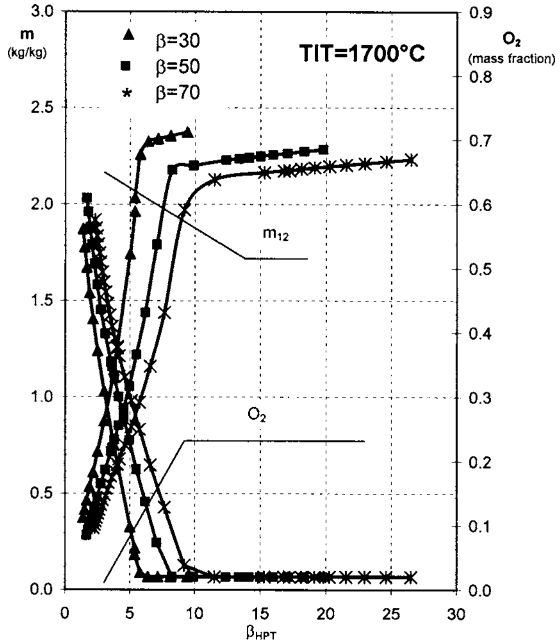

Fig. 17 New H_2/O_2 cycle performance (TIT=1700°C)

In these two graphs (Figs. 16 and 17) the results are meaningful only when the minimum oxygen excess is reached: for a TIT =1500°C, the maximum net efficiency attains the values of 58.1% when β=30, 59.2% when β=50, and finally 59.7% when β=70. These increases are again very limited, while the increase of the maximum pressure of the cycle involves the hydrogen compression until this maximum pressure. By increasing the TIT further, the results are the following: for a TIT=1700°C, the maximum net efficiency attains the values of 61.6% when β=30, about 62.1% when β=50 and finally 62.5% when β=70.

Even if we have great doubts about these numerical assumptions, especially regarding a so high turbine inlet temperature (1700°C), it is possible to analyze the Fig. 18, where there is the cycle scheme with the material and energy balances; in Table 2, the most important performance parameters are listed. In this case futuristic working parameters are adopted: β=70 and TIT =1700°C!

Moreover, also in this case, it is interesting to see Fig. 19 where this cycle representation in the T-s diagram is shown, with reference to the unitary mass of steam. By considering the energy required for oxygen production, the net efficiency becomes only 56.2%. Finally, if hydrogen is produced by coal or natural gas (steam methane reforming) decarbonization, the net efficiency becomes very poor: about 34.8% and 26.1%, respectively [18].

In conclusion, we must admit that, by *adopting realistic assumptions, the potentialities of H_2/O_2 cycle are very limited. With* TIT=1350°C, *the net efficiency attains a value of about 50–52%,* which depends on the full compression ratio. On the other hand, by *adopting futurist assumptions, the* H_2/O_2 *cycles, with a LPT, become more interesting; with* TIT=1700°C, *the net efficiency attains a value of about 61–62.6%,* which depends on the full compression ratio. In this last case the performances are remarkable, but these cycles involve several technological problems which must be taken into account, tackled and properly solved. Finally, it is important to underline that, in all these calculations, oxygen and hydrogen are considered as gases available at the

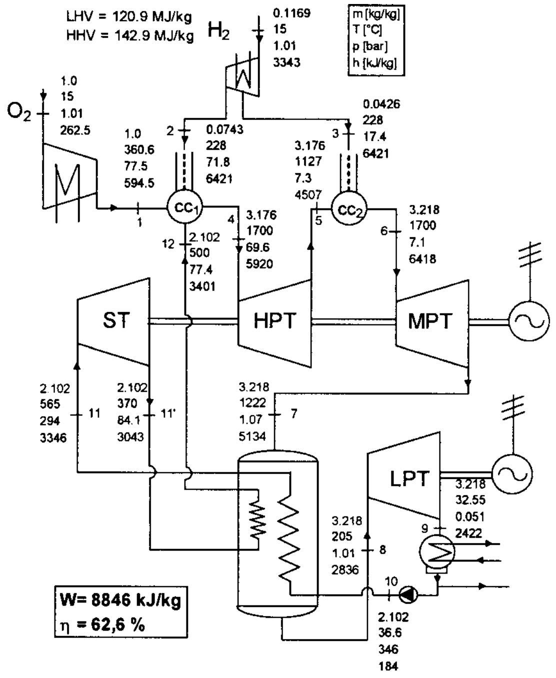

Fig. 18 New reference case: material and energetic balances

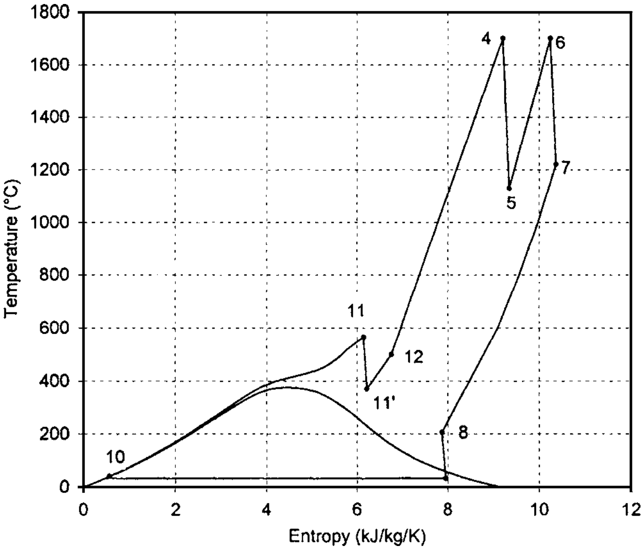

Fig. 19 New reference case: thermodynamic cycle *(referred to the unitary mass of steam)*

ambient conditions, without any energy requirements.

In this context, it is important to remember that hydrogen-fueled combined cycles can attain very high efficiency (over 56%), by neglecting the hydrogen production energy requirements and by adopting the proven and consolidated values for the maximum cycle parameters (for example, a top temperature of about 1350°C). And it is well known that combined cycles are a technological reality compared with these H_2/O_2 cycles. Therefore, this paper has wanted to underline the great limits of the H_2/O_2 cycles: in other words, these cycles would have to be studied deeply, by understanding and solving the numerous technological problems, related to the use of oxygen and hydrogen. But probably, the expected performance, here evaluated, does not justify the enormous R&D investments that this research would have to involve, because other proven technologies, such as combined cycles, can attain similar efficiency levels, by adopting advanced maximum cycle parameters.

A last consideration concerns the economic aspect: authors think that a cost evaluation of the H_2/O_2 cycles can be performed only if the expected performance could really be attained. If the technological levels will allow reaching the cycle parameters, adopted in these calculations, the expected performance will have to be verified and then the economic potentialities of the H_2/O_2 cycle could be investigated.

Table 2 New reference case: performance parameters

Power plant work balance (kJ/kg)		Power plant heat balance (kJ/kg)	
W_{ST}	631	Q_{O2}	263
W_{HPT}	4444	Q_{fuel}	391
W_{IPT}	4089	Q_{fuel} (HHV)	16,718
W_{LPT}	1319	Q_{out}	162
W_{fuel}	841	Q_{COND}	7347
W_{O2}	561	$Q_{intercooling}$	695
W_{aux}	100	Q_{losses}	322
Net work output	8846	$Q_{in}-Q_{out}$	8846
Overall performance			
Net work output			8846
Fuel heat (LHV)			14,140
NET EFFICIENCY, %			62.56

5 Conclusions

In this paper, two possible H_2/O_2 cycle schemes are presented and analyzed. These cycles are the results of the modifications of the conventional thermodynamic cycles (based on steam turbine technology and gas turbine technology) in order to take into account the effects correlated to a change in oxidizer (oxygen instead of air) and fuel (hydrogen instead of fossil fuel).

A parametric analysis is performed in order to evaluate the influence of the main working parameters on the overall performance of these two H_2/O_2 cycle typologies.

The first cycle proposal is substantially a reheat gas turbine with steam injection in the first combustion chamber. The steam is produced regeneratively and the working fluid, composed mainly of H_2O, is discharged into the environment at atmospheric pressure. This cycle sustains itself by adopting a top temperature of 1350°C. In this case, the maximum efficiency attains the value of about 50% and the quantity of produced steam is 2.42 kg per kg of oxygen at the compressor inlet. Increasing the full compression ratio, the maximum net efficiency increases slightly, while the energy requirement for the hydrogen compression becomes very high. The low efficiency depends on the cycle configuration: in fact, the heat associated with the condensation of all steam at the atmospheric pressure, involves a large loss.

The second cycle proposal is an evolution of the previous one; in fact, for high TITs, there is a large range of β_{HPT} where the minimum oxygen excess is reached, for each β. So, it is possible to modify the thermodynamic cycles and the plant layout: since the working fluid is primarily composed of steam, it is possible to perform a further expansion, after the HRSG, up to pressures, typical of the conventional steam cycle power plants. This cycle sustains itself only by adopting a top temperature of 1500°C or over. Even if we have great doubts about these numerical assumptions, especially regarding a so high turbine inlet temperature, a possible scheme is presented and it attains an efficiency value of 62.6% when β=70 and TIT=1700°C!

In conclusion, by adopting realistic assumptions, the potentialities of H_2/O_2 cycle are very limited, while, by adopting futurist assumptions, the H_2/O_2 cycles, with a LPT, become more inter-

Table 3 Numerical assumptions

Oxygen compressor efficiency (polytropic)	88	%
Hydrogen compressor efficiency (polytropic)	85	%
High pressure gas turbine efficiency (polytropic)	86	%
Medium pressure mixed flow turbine efficiency (polytropic)	86	%
High pressure steam turbine efficiency (adiabatic)	87	%
Low pressure steam turbine efficiency (adiabatic)	85	%
Pump efficiency	85	%
Organic-mechanical losses of every single turbomachine	1	%
Combustor heat loss (referred to fuel heat input)	0.4	%
Generator electric-mechanical losses	1.5	%
Combustor pressure loss (air)	3	%
Combustor pressure loss (steam)	10	%
HRSG pressure loss (gas side)	5	%
HRSG pressure loss (RH steam)	8	%
HRSG pressure loss (SH steam, water)	15	%
Pinch point in HRSG	10	°C
Approach point in HRSG	30	°C
Number of hydrogen intercoolers	1-2	
Hydrogen intercooler exit temperatures	35	°C
Number of oxygen intercoolers	1	
Oxygen intercooler exit temperatures	40	°C
Intercooler pressure loss	5	%
Ambient air temperature	15	°C
Low heating value of hydrogen	120.9	MJ/kg

esting. But, in all these considerations we cannot forget that these cycles involve several technological problems which must be taken into account, tackled and properly solved.

Nomenclature

β = pressure ratio
η = efficiency
h = enthalpy (kJ/kg)
m = mass flow rate specific to oxidant flow rate (kg/kg)
p = pressure (bar)
T = temperature (°C)
W = specific work (kJ/kg)

Subscripts

HP = high pressure
LP = low pressure
MP = medium pressure

Acronyms

3L+RH = three pressure levels and reheat
AMC = Advanced mixed cycle
C = compressor
cc = combustion chamber
GT = gas turbine
HHV = high heating value
HPT = high pressure turbine
HRSG = heat recovery steam generator
HRSG = heat recovery steam generator
ICSC = internal combustion steam cycle
LHV = low heating value
LPT = low pressure turbine
MPT = medium pressure turbine
SC = steam cycle
SEP = separator
SGT = saturated gas turbine
ST = steam turbine
TIT = turbine inlet temperature

Appendix: Numerical Assumptions

The results of the performed investigations have been attained by employing a proper numerical model and by numerical assumptions. The numerical model has been developed by the authors and it is based on calculation procedures for conventional components (turbines, compressors, pumps, heat exchangers, etc.) and for an unconventional component.

In this section we like to point out some numerical assumptions, listed in Table 3.

Obviously the main numerical assumptions for the calculations regard the TIT and the polytropic efficiency of the gas turbines.

In our previous works, we assumed an uncooled expansion in the turbine with a reduced value of polytropic efficiency to take into account the losses related to the blade coolings. This was fully in agreement with other calculation models [20] and the results are very close to those related to cooled stage calculations and with manufacturer's data. In particular, with reference to an advanced combined cycle (reheat, three pressure steam cycle) based on GE Frame 9FA, the model has provided results in full agreement with literature [11] and GE data [21]. For example, regarding reheat gas turbines (as GT26 of ABB), the comparison between ABB data (number reference) and the results of the numerical model confirmed the reliability of the above assumptions.

In this work, very high values of the maximum temperature are adopted (until 1700°C). In this case it is not possible to compare our results with any manufacturer's data, because they do not exist! It could also be possible to think about different cooling system options: for example closed-loop steam cooling or the use of advanced materials and coating, developed for these conditions. For this reason in this work, which wants to underline the potentialities as well as the limits of H_2/O_2 cycles, we have adopted our previous numerical assumptions and calculation procedures. If these hypotheses are much too optimistic, the expected performance of such power plants could be lower, and all the technological problems, related to these cycles, will have to be properly solved.

References

[1] Gaudernack, B., and Lynum, S., 1998, "Hydrogen form Natural Gas without Release of CO_2 to the Atmosphere," Int. J. Hydrogen Energy, **23**, pp. 1087–1093.

[2] Bannister, R. L., Newby, R. A., and Yang, W. C., 1998, "Development of a Hydrogen-Fueled Combustion Turbine Cycle for Power Generation," J. Eng. Gas Turbines Power, **120**, pp. 276–283.

[3] Bannister, R. L., Newby, R. A., and Yang, W. C., 1999, "Final Report on the Development of a Hydrogen-Fueled Combustion Turbine Cycle for Power Generation," J. Eng. Gas Turbines Power, **121**, pp. 38–45.

[4] Cau, G., Coco, D., and Montisci, A., 2001, "Performance of Zero Emissions Integrated Gasification Hydrogen Combustion (ZE-IGHC) Power Plants with CO_2 Removal," *Proc. of ASME TURBO EXPO 2001*, New Orleans, LA.

[5] Anderson, R., Brandt, H., Doyle, S., and Viteri, F., "A Demonstrated 20 MWt Gas Generator for a Clean Steam Power Plant," http://www.cleanenergysystem.com/

[6] Anderson, R., Brandt, H., Doyle, S., Pronske, K., and Viteri, F., 2003, "Power Generation with 100% Carbon Capture and Sequestration," Second Annual Conference on Carbon Sequestration, Alexandria, VA, http://www.cleanenergysystem.com/

[7] Marin, O., Bourhis, Y., Perrin, N., Di Zanno, P., Viteri, F., and Anderson, R., 2003, "High Efficiency, Zero Emission Power Generation Based on a High-Temperature Steam Cycle," 28th International Technical Conference on Coal Utilization and Fuel Systems, Clearwater, FL, http://www.cleanenergysystem.com/

[8] Martinez-Frias, J., Aceves, S. M., Smith, J. R., and Brandt, Harry, 2003, "Thermodynamic Analysis of Zero-Atmospheric Emissions Power Plant," Second Annual Conference on Carbon Sequestration, Alexandria, VA, http://www.cleanenergysystem.com/

[9] Kaarstad, O., and Audus, H., 1997, "Hydrogen and Electricity form Decarbonised Fossil Fuels," Energy Convers. Manage., **38**, Suppl. pp. S431–S436.

[10] Gambini, M., Guizzi, G. L., and Vellini, M., 2003, "Critical Analysis of Advanced H_2/O_2 Cycles based on Steam-Methane Reforming," *Proc. of ASME TURBO EXPO 2003*, Atlanta, GA.

[11] Lozza, G., 1993, "Steam Cycles for Large-Size High-Gas-Temperature Combined Cycles," *Proc. the Seventh ASME Cogen Turbo*, Bournemuth, UK.

[12] Dechamps, P. J., 1998, "Advanced Combined Cycle Alternatives with the Latest Gas Turbines," J. Eng. Gas Turbines Power, **120**, pp. 350–357.

[13] Caputo, C., Gambini, M., and Guizzi, G. L., 1997, "Internal Combustion Steam Cycle (G.I.ST. Cycle): Thermodynamical Feasibility and Plant Lay-Out Proposals," Int. Conference ASME ASIA 97, Singapore, ASME Paper 97-AA-134.

[14] Gambini, M., and Guizzi, G. L., 1997, "Parametric Analysis on a New Hybrid Power Plant Based on Internal Combustion Steam Cycle (GIST Cycle)," *Proc. of FLOWERS'97*, Florence World Energy Research Symposium, Firenze, Italy.

[15] Gambini, M., and Guizzi, G. L., 1997, "New Hybrid Power Plant Based on Internal Combustion Steam Cycle (GIST Cycle)" (in Italian), *Proc. of 9th National Conference "Tecnologie e Sistemi Energetici Complessi,"* Milano, Italy.

[16] Gambini, M., Guizzi, G. L., and Vellini, M., 1997, "Calculation Model for Unconventional Components of GIST Cycles" (in Italian), *Proc. of 9th National Conference "Tecnologie e Sistemi Energetici Complessi,"* Milano, Italy.

[17] Bolland, O., and Mathieu, P., 1997, "Comparison of two CO_2 Removal Options in Combined Cycle Power Plants," *Proc. of FLOWERS'97*, Florence, World Energy Research Symposium, Firenze, Italy.

[18] Gambini, M., and Vellini, M., 2003, "Comparative Analysis of H_2/O_2 Cycle Power Plants Based on Different Hydrogen Production Systems from Fossil Fuels," *Proc. of HYPOTHESIS V 2003—HYdrogen POwer THeoretical and Engineering Solutions International Symposium*—Porto Conte, Italy.

[19] Gambini, M., Guizzi, G. L., and Vellini, M., 2002, "The Effects of Incondensable Gases on H_2/O_2 Cycle Performance," *Proc. of ASME TURBO EXPO 2002*, Amsterdam.

[20] Hofstädter, A., Frutschi, H. U., and Haselbacher, H., 1998, "Effects of Steam Reheat in Advanced Steam Injected Gas Turbine Cycles," ASME Paper 98-GT-584.

[21] Gas Turbine World, 1996, "Basic Specifications of Combined Cycles," *Gas Turbine World Handbook*, Pequot Pub., CT.

Modeling and Validation of the Thermal Effects on Gas Turbine Transients

Annette E. Nielsen
Hermann-Eckert-Strasse 20,
D-88634 Herdwangen-Schoenach, Germany
e-mail: annette.nielsen@rolls-royce.com

Christoph W. Moll
Rolls-Royce Deutschland Ltd., & CoKG,
Eschenweg 15,
15827 Dahlewitz, Germany
e-mail: christoph.moll@rolls-royce.com

Stephan Staudacher
Institut für Luftfahrtantriebe,
University Stuttgart,
Pfaffenwaldring 6,
70596 Stuttgart, Germany
e-mail: staudacher@ila.uni-stuttgart.de

Secondary effects, such as heat transfer from fluid to engine structure and the resulting changes in tip and seal clearances affect component performance and stability. A tip clearance model to be used in transient synthesis codes has been developed. The tip clearance model is derived as a state space structure. The model parameters have been identified from thermomechanical finite element models. The model calculates symmetric rotor tip clearance changes in the turbomachinery and symmetric seal clearance changes in the secondary air system for engine transients within the entire flight envelope. The resulting changes in efficiency, capacity, and cooling airflows are fed into the performance program. Corrections for tip clearance changes on the component characteristics are derived from rig tests. The effect of seal clearance changes on the secondary air system is derived using sophisticated air system models. The clearance model is validated against FE thermomechanical models. The modeling method of modifying the component characteristics is verified comparing engine simulation and test data, which show good agreement. Based on a representative transient maneuver typical transient overshoots in fuel flow and turbine gas temperature and changes in component stability margins can be shown. With the use of this model in the performance synthesis the transient engine performance can be predicted more accurate than currently in the engine development program. [DOI: 10.1115/1.1850495]

Introduction

For aircraft certification an engine has to demonstrate that the certified thrust level is achieved at any time without exceeding any operating limits and that power transients are free from dangerous instabilities, such as compressor surge. Based on test experience it can be shown that compressor stability and engine operating limits are strongly affected by thermal dynamic effects in the engine and it requires costly testing to establish the effects of such thermal processes on engine performance.

Modern aeroengines are designed for high overall efficiency to achieve low operating costs at reduced emissions. Improved overall efficiency, however, is reached primarily with increased cycle temperatures and pressure ratios, hence a large amount of heat is exchanged between fluid flows and engine structures. Therefore thermal dynamic processes in the components gain significance and they need to be taken into account to obtain sufficiently high accuracy in performance synthesis calculations. Especially the transient behavior of gas turbine engines, which is known much less exactly compared to the steady-state behavior, could be improved if the transient synthesis models were more precise. Extensive engine testing could be reduced if the detrimental effects of heat soakage and clearance changes are known in the engine development.

This paper presents the method of an extension of a nonlinear aerothermodynamic synthesis model of an advanced technology mixed flow turbofan engine to consider the effects of engine thermal dynamics onto component performance and stability margins. Furthermore the model applicability and validity is shown based on the agreement between simulation and test data for a typical transient engine maneuver.

Performance Synthesis Models

Modern performance modeling tools, such as the Rolls-Royce Aeroengine Performance Program (RRAP) for the BR700 engine family, are modularly structured, with the engine being synthesized component-wise in the computational domain. The gas turbine is split into several components, for example, inlet, compressor, combustor, turbine, bypass duct, and nozzle. The engine performance is synthesized based on the data of its components. The calculation is carried out along the flow path through the engine, applying the laws of conservation of mass and energy. The thermodynamic component behavior is represented with component characteristics as tabulated datasets describing the correlations between the component parameters. Such characteristics allow the inclusion of complex component behavior at acceptable computation times. Data obtained from experiments can be used. The component characteristics are described with similarity parameters; thus they are valid for various engine operating conditions and for structures of similar geometry. To cater to different flight conditions, additional influence parameters, such as Reynolds number corrections, are applied. For transient modeling, the program considers the heat transfer between the gas and the metal, the shaft dynamics, and the gasdynamics. Furthermore, an improvement of engine modeling can be achieved by considering transient tip clearance changes and their effect on the component characteristics. Examples of such approaches are described in [1–3].

Tip Clearance Modeling Methodology

For an enhanced performance program a simulation model is needed, which produces representative results for typical worst engine maneuvers, such as cold stabilization or Bodie transients (reslams) while consuming an acceptable computation time. There are basically two ways for setting up such a tip clearance simulation model:

- use of replacement structure
- use of a state space model

Contributed by the International Gas Turbine Institute (IGTI) of THE AMERICAN SOCIETY OF MECHANICAL ENGINEERS for publication in the ASME JOURNAL OF ENGINEERING FOR GAS TURBINES AND POWER. Paper presented at the International Gas Turbine and Aeroengine Congress and Exhibition, Vienna, Austria, June 13–17, 2004, Paper No. 2004-GT-53344. Manuscript received by IGTI, October 1, 2003; final revision, March 1, 2004. IGTI Review Chair: A. J. Strazisar.

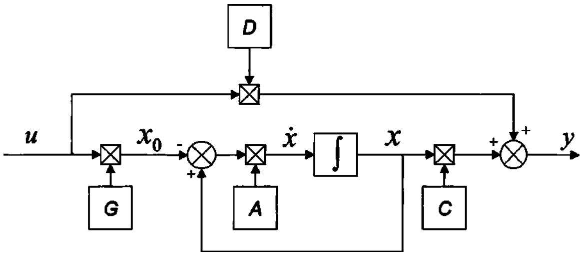

Fig. 1 Graphical representation of a state space system using a *G* matrix

The use of replacement structures serving as substitutes for the real engine structures are up to now a common technique to include tip clearance changes into performance models; examples are given in [2] and [3]. The major disadvantages of this method are the complexity of the models and the need for iterative calculations. Due to the simplification of the structural shape of the components, a calibration of the model to an accurate thermomechanical FE model cannot be avoided.

This paper describes a novel approach using a state space model. The integral approach allows predicting clearance variation without describing the local heat transfer and conduction phenomena in detail while matching the techniques usually applied in aerothermodynamic models. A state space model approach has already been used in [4] for steady state and transient heat flow calculation in performance synthesis models. In [5] such an approach was used successfully as well for the prediction of temperatures and tensions in critical parts of component structures within a gas turbine life monitoring system. The model parameters for the state space model application are derived from the FE models set up with a code developed by Rolls-Royce plc. FE models for each engine component are created using this code. For the calculation of the aeroengine component temperatures, stresses, and displacements, these models are used exclusively. Although the FE models allow calculating accurate data for a large variety of flight and operating conditions, their computation time is high. Therefore, such models are currently not linked directly into the performance synthesis model especially not for transient purposes.

State Space and Derived Model Architecture

Dynamic systems are represented by differential equations. In state space, all differential equations are transformed to a set of first-order differential equations by linearization. A linear state space is represented by two vector equations:

$$\begin{aligned} \dot{x} &= A\cdot x + B\cdot u \\ y &= C\cdot x + D\cdot u \end{aligned} \tag{1}$$

The relationship between the inputs u and the outputs y is defined via the state vector x. The state vector x characterizes independent energy storages. The variables x, y, and u describe offsets to a steady state operation point. For practical reasons Eq. (1) is transformed by introducing the G (Gain) matrix ($G := \cdot A^{-1}\cdot B$):

$$\begin{aligned} \dot{x} &= A\cdot(x - G\cdot u) \\ y &= C\cdot x + D\cdot u \end{aligned} \tag{2}$$

The steady state values of the state vector x can be computed by multiplying the G matrix with the input vector u. Figure 1 shows a graphical representation of Eq. (2). The A, G, C, and D matrices of the linear model consist of the partial derivatives of the nonlinear system at a given operating condition. The linear model represents the nonlinear system in the surrounding of this operation condition. A nonlinear system can be characterized throughout its operating envelope by linearizing the nonlinear model piecewise along its operating lines. For a given operating condition the partial derivatives are interpolated.

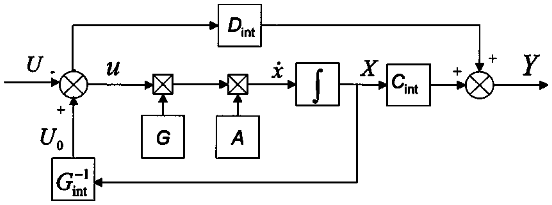

Fig. 2 Quasi-non-linear state space model using integrated *D*, *G*, and *C* matrices

The absolute values of inputs U, states X, and outputs Y of a nonlinear system are typically nonzero at steady state operating conditions. Assuming an unequivocal relationship $X=f(U)$ between inputs U and states X, the steady state operating point $X_0(U)$ of the state is obtained by integrating the partial derivative $G=\delta x/\delta u$ with respect to the input U:

$$X_0(U) = \int_{U_{\mathrm{ref}}}^{U} G\,du = G_{\mathrm{int}}(U) \tag{3}$$

The integration of the partial derivatives $\delta y/\delta x$ and $\delta y/\delta u$ of the C and D matrices, respectively, makes it possible to calculate the absolute value of output Y from absolute value of inputs U and states X:

$$\begin{aligned} C_{\mathrm{int}}(X) &= \int_{X_{\mathrm{ref}}}^{X} C\,dx \\ D_{\mathrm{int}}(U) &= \int_{U_{\mathrm{ref}}}^{U} D\,du \end{aligned} \tag{4}$$

Figure 2 shows a block diagram of the resulting quasi-non-linear model. There are two G matrices in the model. One is the partial derivative matrix used to determine the dynamic behavior for input perturbations. The other one is the integrated G matrix, which is used to determine a steady state value U_0 of the input U from the values of the states X (via a reverse look-up).

System Analysis

An analytical–empirical analysis of the system was carried out. A system schematic is given in Fig. 3, for the example of a HP turbine rotor. The outputs of the system are the radial positions r of points from which the tip clearances of a stage can be calculated, i.e., the rotor tip radius r_r and facing casing position r_c. The inputs of the system are the gas temperature T_g, the temperature of the cooling flows T_{cf}, and the rotational speed ω. The radial displacements result from the thermal growth, and the acting pressure and centrifugal forces.

The thermal growth of the rotor and the casing are depending on the temperature distribution in the structure. The heat transfer finally is a function of the driving temperature difference between the gas and the structure and the acting heat transfer coefficient α. The pressure forces have a relative small influence on the resulting displacements and are therefore disregarded. Displacements due to centrifugal forces result from the design, the choice of material, and the rotational speed ω of the rotor. The magnitude of radial displacements resulting from centrifugal forces is generally smaller than those resulting from thermal growth and displacements. The theoretical knowledge of the physical laws for heat transfer and heat conduction as well as for the displacements resulting from mechanical and thermal stress is now built into the mathematical model defined in Eq. (5) giving the state space model for radial displacements of the HP turbine:

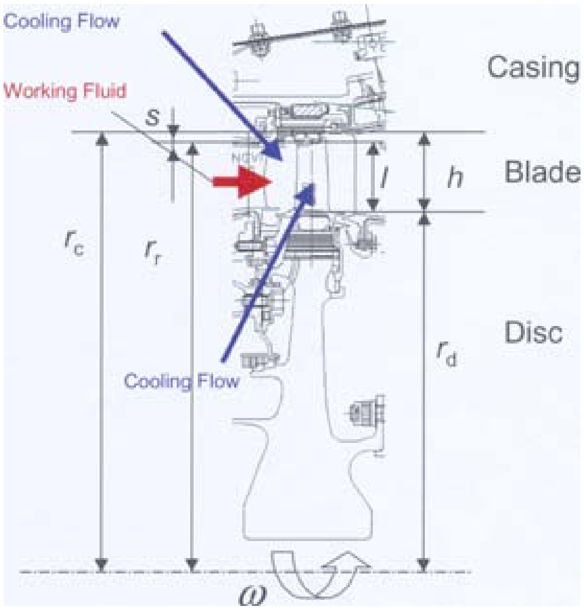

Fig. 3 Geometry and tip clearance definition

$$\dot{T}_m = A(\alpha)\cdot T_m + B\cdot\begin{bmatrix}T_g\\ T_{\mathrm{CF}}\end{bmatrix}$$
$$r = C(T_m)\cdot T_m + D(T_m)\cdot\omega \tag{5}$$

Identification of Model Parameters

The dynamics of the casing, disk, and blading was linearized separately and stagewise for the HPC and HPT. The linearization was carried out at ten points equally distributed between low idle and max power to ensure that the nonlinearities of the system were captured sufficiently accurate. The Matlab system identification toolbox was used to identify the parameters of the model architecture defined in Eq. (5).

For the generation of a quasi-non-linear state space model the following calculations were performed:

- the C_{int} matrix was calculated by integrating the C matrix with respect to the state T_m,
- the D_{int} matrix was calculated by integrating the D matrix with respect to shaft speed ω,
- the G matrix was calculated according to Eq. (3) and scheduled to T_m,
- the G_{int} matrix was calculated by integrating the G matrix with respect to the input T_g (in case of the turbine as well with respect to T_{cf}) and scheduled to T_m,
- the A matrix was scheduled to the heat transfer coefficient α

The inputs to the system are shaft speed and the mean values of the component gas temperature, and in the case of the turbine, additionally the cooling air temperature. The states are representative temperatures of the rotor, blading, and casing corresponding to the stored heat in each part (a positive derivative of time of the representative temperatures stands for heat flux from the gas into the structure). The radial displacements (output) are computed from the thermal growth $C_{\mathrm{int}}(T_m)$ and the effect of the centrifugal forces $D_{\mathrm{int}}(\omega)$. Scheduling the G matrix to the thermal state T_m has advantages in transients and is physically correct for an unequivocal relationship between T_g and T_m. If there is a step in the engine power setting, the G matrix changes along the steady state characteristics. This represents real component behavior, while the G (Gain) matrix may change with the thermal state. Scheduling the A (dynamic) matrix to the acting heat transfer coefficient α accounts for the fact that it is this coefficient that defines the dynamic of the heat exchange between the structure and gas. The acting heat transfer coefficient is calculated within the performance program via a Nusselt correlation from mean values of component gas temperature and gas mass flow.

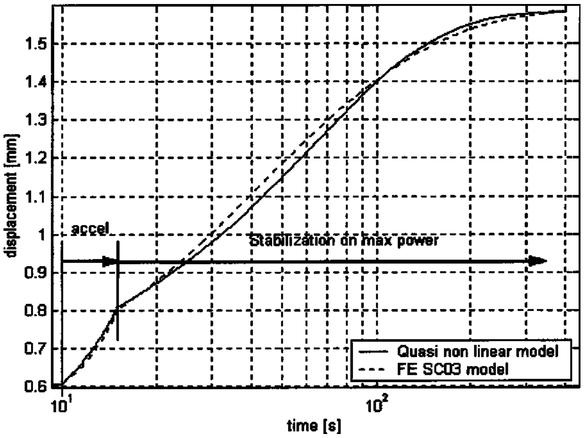

Fig. 4 Predicted HPC rotor 10 displacements and FE model

In Fig. 4 it is shown for slam acceleration from low idle to max power that the prediction of the radial displacements r_d of the quasi-non-linear model is close to the FE model output with a maximum transient error of less than 0.05 mm and no steady state offsets.

Tip Clearance Changes During Transient Maneuvers

The tip clearance variations for the HPC and the HPT are predicted for a cold stabilization maneuver. This is the most serious condition for both the engine and its controller regarding heat transfer and tip clearance changes. A cold soaked engine is fast accelerated to take-off power after a minimum stabilization time at low power conditions with the gas temperatures rising very quickly. The engine is kept at maximum power to provide the thrust for aircraft take-off. During this time the components thermally stabilize. During this stabilization period the tip clearances vary caused by different thermal growth of rotor and casing. The casing of the compressor grows relatively rapidly following the accel; the rotor disks, being more massive, tend to take longer to heat up, and hence a period of increased tip clearance occurs, providing the maximum deterioration of component performance and stability. The time-dependent tip clearances are predicted using the tip clearance model, where the change in tip clearance is given according to Eq. (6)

$$\Delta s = (s_{\mathrm{Tr}} - s_{\mathrm{Nom}})_{\mathrm{NH}} \tag{6}$$

The clearance changes for each stage of the HPT and the HPC are predicted for a cold stabilization maneuver, as illustrated in Fig. 5, exemplified for the turbine rotor stages. The effect of tip clearance variation is translated into a change in efficiency and capacity. For the HP turbine the clearance effect on component characteristics of both stages are evaluated for each stage separately and then added up to single delta in efficiency and a single factor for capacity.

The compressor modeling for the BR700 engines does not allow the accounting of tip clearance changes for all stages separately, thus the compressor tip clearance is defined as a root mean square (rms) of the delta tip clearance of each stage according to Eq. (7).

$$\mathrm{rms}\Delta(s/h) = \sqrt{\frac{\Sigma(s/h)^2}{n}} * 100\% \tag{7}$$

The resulting rms tip clearance change during the cold stabilization maneuver is shown in Fig. 6. Based on this single repre-

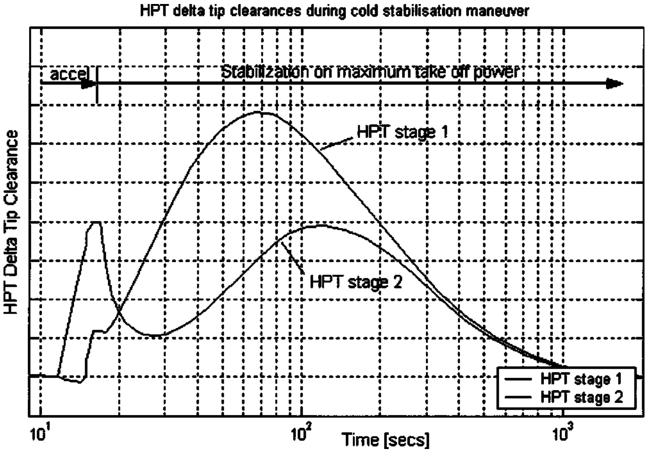

Fig. 5 Stagewise tip clearance changes HPT rotors

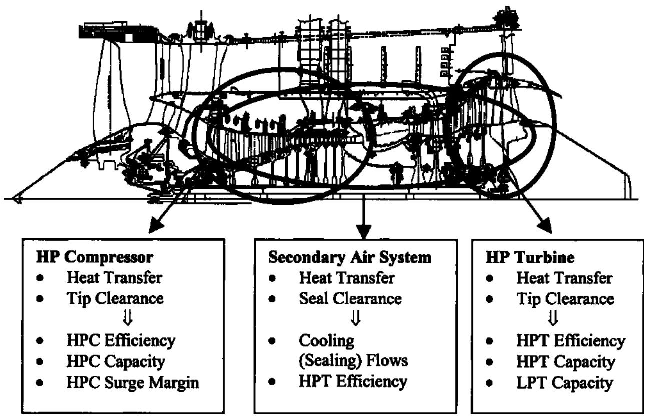

Fig. 7 Secondary processes and their effects in gas turbines

sentative tip clearance change, the effects on HPC efficiency and capacity are derived and implemented into the synthesis model. For the slam acceleration the predicted displacements based on the quasi-non-linear model show a maximum transient error of less than 0.04% in rms$\Delta(s/h)$ that would be equivalent to a maximum error in the performance correction of 0.03% in $\Delta\eta$.

Effects of Clearance Changes on Component Parameters

Secondary effects, such as shaft dynamics, heat transfer, and the resulting changes in tip and seal clearance geometry, cause changes in component performance characteristics and thus influence the thermodynamic cycle. The effect of shaft inertias is important during the acceleration maneuver and will be considered in the transient engine synthesis model. Both the inertia effects combined with thermal effects influence engine performance. However, the latter mentioned effects play the major role during the thermal stabilization period. Extensive testing is required to establish the effects of thermal component dynamics. Figure 7 illustrates the main locations in a modern aeroengine, where such processes occur. Heat flows between gas and structure can adversely affect compressor performance. During fast accelerations heat soakage effects are caused by an axial stage mismatch in the rear stages of a multistage compression system. The compressor characteristic is moved to higher working lines at the front stages and a reduced stability line at the rear stages. Increased tip clearances have strong detrimental effects on component efficiency but will also change capacity. Increased seal clearances cause increased internal airflows, which affect primarily the efficiency of the cooled turbines.

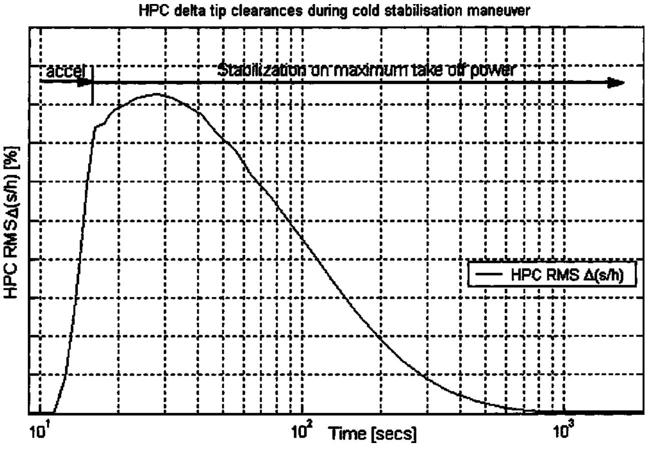

Fig. 6 Averaged tip clearance change HPC rotors

Effect of Tip Clearance Changes. In the region of the blade tips, a certain part of the main fluid flow is expanding within the compressor and turbine tip clearances without participating in the work exchange in the blade rows. These tip leakage flows need to be considered as loss, since they do not contribute to the work exchanged in the turbomachines. Therefore, increased tip clearances result in an overall component efficiency loss. The interference of leakage flow and main fluid flow causes an additional loss when most of the kinetic energy of the leakage flow is dissipated. To account for above-mentioned effects, the component isentropic efficiency of the HP compressor and HP turbine will be corrected.

Leakage flows also affect component capacity. For compressors the capacity will be reduced for increased tip clearances since the direction of the leakage flow at the blade tips is in an opposite direction to the main fluid flow through the blade rows. The situation is different in the turbines, where the direction of the leakage flow and the main fluid flow is the same; thus an increase of turbine capacity can occur. The increase in tip clearance, however, also causes a slightly higher pressure drop across the upstream NGV with a corresponding increase in the NGV throat area and hence an increase in component capacity. There will be a specific turbine work loss if the tip clearances increase, but these changes are already met with the change in efficiency.

For multistage compressors the reduced efficiency at a given flow condition increases the pressure ratio resulting in a rise of the component working line level. The increased turbulences caused by the tip leakage flows affect the aerodynamic entry conditions resulting in flow distortion. Additionally, the mismatch between front and rear stages during transient heat transfer reduces the component stability.

The less efficient HP turbine running at a higher tip clearance does also affect the performance of the downstream LP turbine. Previous investigations on cold stabilization maneuvers suggested a reduction in LP turbine capacity due to the spoiling effects of the less efficient HP turbine. The increased tip clearances in the HP turbine result in a significant drop of efficiency connected with increased tip region flows. The swirl out of the HP turbine will be increased and thus will deteriorate the aerodynamic condition at the LP turbine inlet resulting in a change of effective flow area at the LPT NGV1 and hence affecting the LPT capacity [6].

Effect of Seal Clearance Changes. Seal clearances change during transient maneuvers. Consequently, secondary flows in the HP turbine may change due to an increased flow area through the sealing and different boundary conditions of the airflows. Cooling flow changes have the following effects:

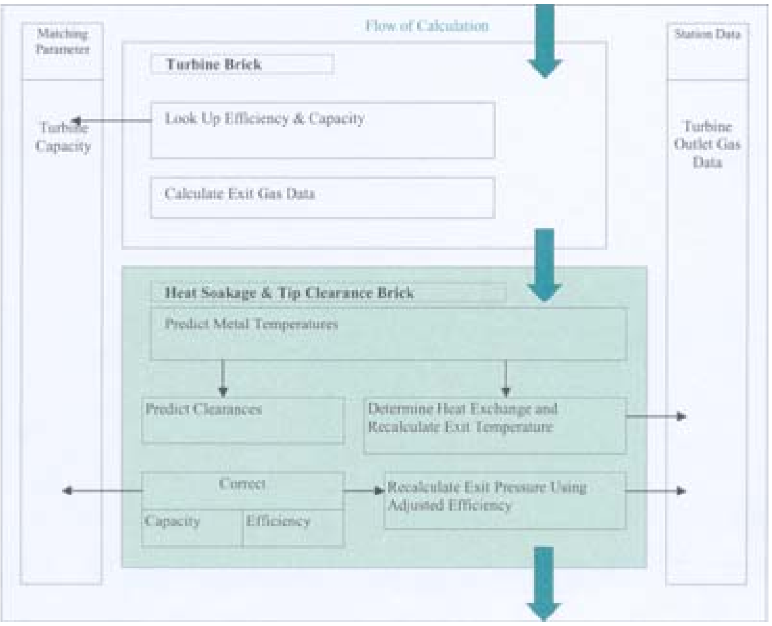

Fig. 8 Flow of nonadiabatic cycle matching

- Direct loss of turbine work due to the reduction in turbine mass flow
- Direct loss of turbine enthalpy due to mixing of cooling flow and main flow at the blade tips
- Loss due to pumping work of turbine blades on the cooling air as it passes radially outwards through cooling passages

The first effect is modeled in the BR700 synthesis deck. Adjusting the cooling flow fraction based on the variations in seal clearances cause a direct loss of turbine work due to a reduction in the turbine mass flow. The latter mentioned losses are not modeled so far. They can be taken into account using a reduced value of turbine efficiency additionally fed into the engine model.

Synthesis Model Correction for Clearance Effects

The BR700 performance model features adaptation factors that allow a correction of flow and efficiency for tip clearance variations. The flow of calculation for a nonadiabatic cycle matching, considering heat soakage and tip clearance changes are illustrated in Fig. 8 as an example for the HP turbine module. Turbine efficiency and capacity are looked up from the characteristics. Exit parameters are calculated using the entry conditions from the upstream components and given heat transfer parameters to calculate the heat flow between the gas and the turbine structure and to adjust the exit gas temperature. With the predicted metal temperatures from the heat soakage brick, tip clearances are obtained from the turbine structure displacements. To correct the effect on component capacity, a factor is used. Efficiency changes are considered calculating the efficiency loss, which is then applied using an efficiency delta. Both correction parameters are derived based on the change in blade tip clearance between the transient clearance and the nominal clearance at the according steady state conditions (Eq. (6)). With the adjusted efficiency the turbine exit pressure can also be adjusted to intercooling/interheating effects. The resultant modified capacity is matched to the capacity calculated for the upstream processes.

The factors and deltas for capacity and efficiency are derived using experimental exchange rates for the HPC and the HPT (see Table 1). An additional exchange rate for the change in the HPC surge pressure ratio is given. Such exchange rates are obtained from rig testing, where different tip clearance standards are tested. For the ten-stage HPC of the BR700 engine efficiency and capacity are corrected via a linear exchange rate given as a single number for all stages based on a representative averaged tip clearance

Table 1 Exchange rates to be used for simulation

Component	Clearance change	Penalty		
		Efficiency	Flow	Surge margin
HPC	$+1\%\Delta\mathrm{RMS}(s/h)$	$-0.8\%\Delta\eta$	$\frac{\mathrm{wrtp}}{\mathrm{wrtp}_{\mathrm{design}}}=f(\Delta\mathrm{rms}(s/h))$	$-6.2\%\Delta\mathrm{SM}$
HPT	$+1$ mm Δs	*Rotor 1*: $-1.75\%\Delta\eta$ *Rotor 2*: $-1.52\%\Delta\eta$	*Rotor 1*: $+0.52\%\Delta\mathrm{wrtp}$ *Rotor 2*: $+0.52\%\Delta\mathrm{wrtp}$	⋯
HPT *cooling flows*	$+1\%\frac{m_{\mathrm{CF}}}{m_{\mathrm{HPTNGV}}}$	*Post throat*: $-0.1045\%\Delta\eta$ *Post rotor*: $-0.149\%\Delta\eta$	⋯	⋯
LPT	$+1$ mm Δs_{HPT}	⋯	$-0.75\%\Delta\mathrm{wrtp}$	⋯

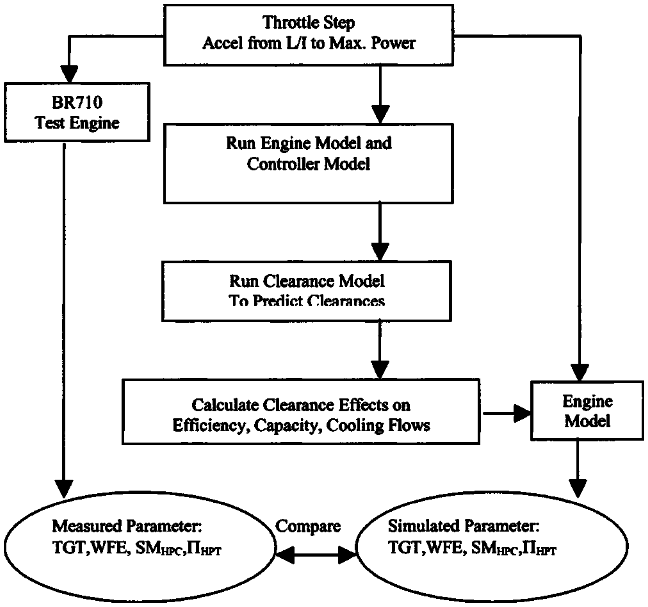

Fig. 9 Validation process

change according to Eq. (7). For the two HPT stages, the exchange rates for each rotor have been given since the HPT stage 1 is designed with a shrouded rotor, whereas the HPT stage 2 blades are unshrouded. The detrimental effect of the changes in the internal air system are incorporated in the engine deck based on a recalculated cooling flow input that is derived with a one-dimensional network model of the internal air system. Changed turbine cooling flows are considered individually in the synthesis model and can be changed during a transient simulation. Indirect losses, such as losses due to mixing and pumping work, are reflected using further correction deltas on the turbine efficiency derived from [7] for the BR710 HP turbine. All experimentally based exchange rates used for the simulation of the cold stabilization maneuver are summarized in Table 1.

Method Validation Based on a BR710 Cold Stabilization Maneuver

Modern aeroengines are controlled via FADEC and are designed to provide a constant certified take-off thrust level. The effects of transient heat transfer and clearance changes therefore are compensated, asking for a higher fuel flow at higher process temperatures and reduced stability margins. Based on the overshoot of, for example, the turbine gas temperature (TGT) and fuel flow, the effects of clearance changes can be identified. The flow chart (Fig. 9) presents the process to be passed for the validation of predicted parameters against measured engine data.

The prediction of clearances and the simulation of their effects have been applied onto the performance models, including the following thermodynamic changes:

- Change of HPC efficiency and capacity due to increased HPC rotor tip clearances
- Change of HPT efficiency and capacity due to change in HPT rotor tip clearances
- Change of HPT cooling flows due to change in HPT seal clearances
- Change of HPT efficiency due to increased cooling flows at increased seal clearances
- Change of LPT capacity due to increased entry swirl at increased HPT rotor tip clearances

Figures 10–13 compare the simulation results to the data measured during a cold stabilization maneuver on a BR710 engine. The calculated TGT overshoot of 2.6% lines up very well with the measured overshoot of 2.4%. The most significant changes are caused by the changes in the characteristics and primarily given by the reduced efficiencies at higher blade tip clearances for both the HPC and the HPT. More than 75% of the overshoot in TGT can be related to the changes in the tip clearances in the turbocomponents. The effects of increased seal clearances are responsible for 12% of the entire overshoot and also the reduction of the LPT capacity, predicted to share 8% in TGT overshoot, play a minor role.

The maximum TGT during the test is achieved after 55 s into the stabilization period, which is slower than for the predicted maximum overshoot at 30 s after power set. Simulating the effects for the single components separately, it is shown that the dynamic

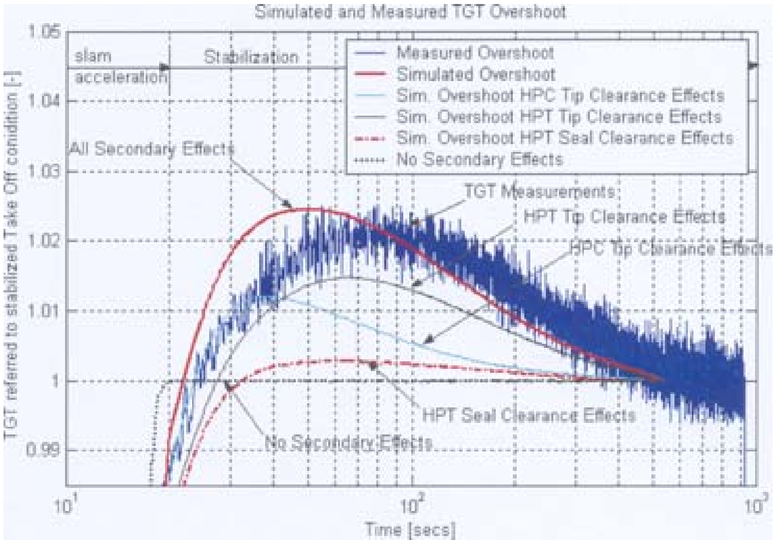

Fig. 10 Simulated and measured TGT overshoot

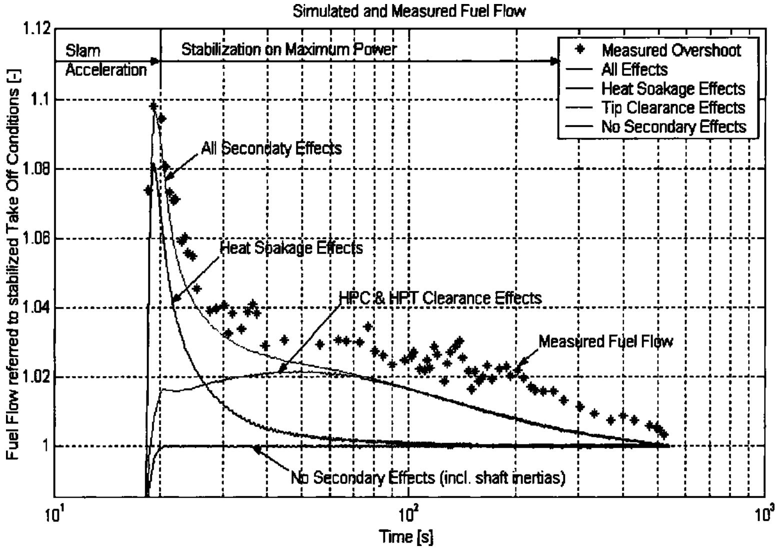

Fig. 11 Simulated and measured fuel flow overshoot

behavior of the HP turbine clearance model agrees with the measured results. However, the HP compressor model predicts the dynamic behavior too fast.

Since the thermal behavior of front and rear stages of the HP compressor is different, the maximum tip clearances for the single stages occur at different times. The front stages of the HPC show a slower time response than the rear stages and interstage rematching effects between these stages cannot be predicted based on an averaged representative component tip clearance.

A comparison of the measured overshoot in fuel flow relative to the simulated overshoot shows good agreement (Fig. 11). The simulation predicts an overfueling of 9.7% at maximum clearance changes, which is close to the measured overshoot of 9.8%. Simulating the heat soakage and tip clearance effects separately allows the quantification of their proportion on the fuel flow overshoot. This analysis shows that most of the overshoot is caused by the heat soakage during the acceleration and the subsequent thermal stabilization period.

The simulated overfueling due to tip clearance effects is much smaller. More than 75% of the demanded fuel flow overshoot is used to heat up the engine parts and it takes several minutes to stabilize on the steady state fuel flow. The total amount of overfueling at top of accel is distributed to the following secondary effects (see Table 2).

The simulated surge margin change during a simulated take-off maneuver is obtained from a calculated surge pressure ratio that includes the detrimental effects of the tip clearance change and related to the nominal steady state surge line given by the model. The deficiencies in the surge pressure ratio are derived using an experimental exchange rate (Table 1). The surge margin is defined according to Eq. (8),

$$SM_{\text{tip clearances}} = \frac{\Pi_{\text{surge, tip clearances}} - \Pi_{\text{working line}}}{\Pi_{\text{working line}}} \cdot 100\% \qquad (8)$$

The measured surge margin is based on fuel spiking tests at maximum take-off power conditions, where the engine is driven into surge after various stabilization times. Figure 12 shows the observed loss of the HP compressor surge margin during the thermal stabilization period compared to the predicted numbers. The data have been referred to the steady state surge margin at maximum power conditions. Although the predicted minimum surge

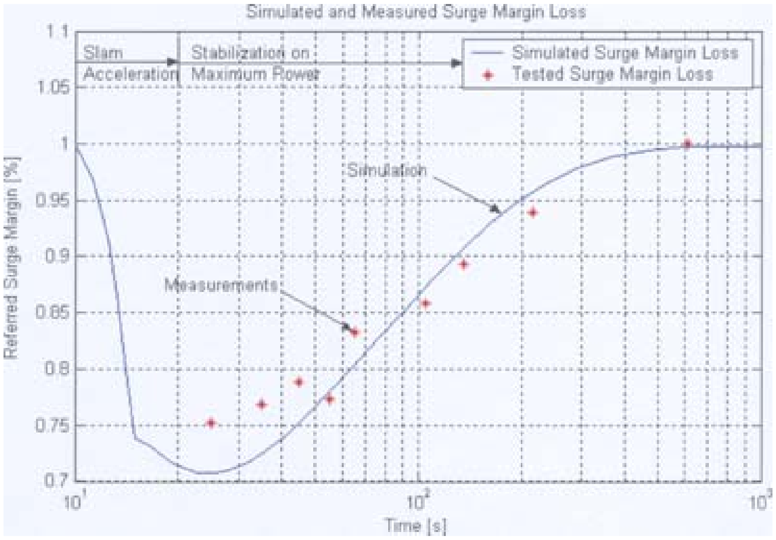

Fig. 12 Predicted and measured surge margin change

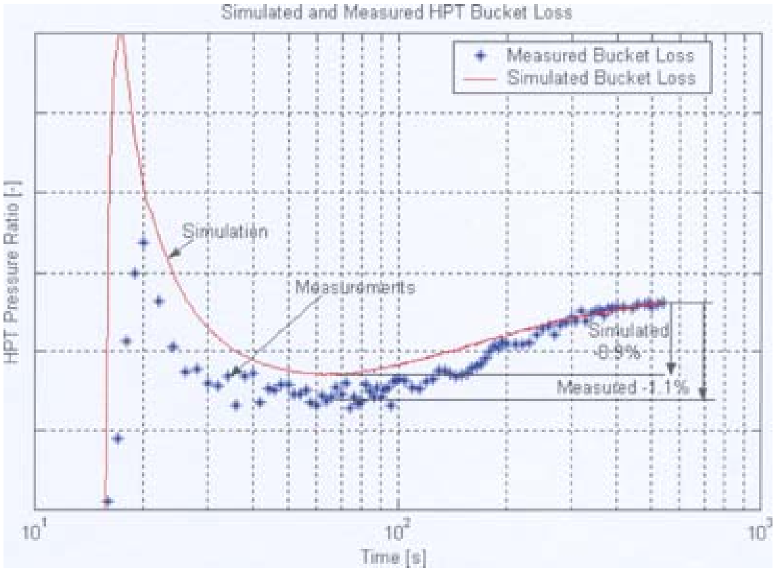

Fig. 13 Predicted and measured HPT pressure ratio

margin is 0.4% lower than the tested minimum, the simulated points match the test results very well. The minimum surge margin is shown at 15 s after maximum power has been set, which agrees with the measured minimum at the same time. This is a unfortunate timing since the critical surge margin occurs close to the time of aircraft rotation. Thus, a sufficient surge margin is to be provided to ensure safe and reliable engine operation.

During the stabilization period on the BR710 engine, the time variation of the HP turbine pressure ratio showed a significant drop on the pressure ratio prior to approaching the steady state level. As a means to validate the assumptions made in the clearance model for the turbine the HPT pressure ratio loss is analyzed for the cold stabilization simulation and compared to the test data. The pressure ratio bucket can be explained by the following aerodynamic changes in the flow path of the turbine blade rows:

- increase in HPT capacity
- reduction of LPT capacity
- increase of HPT cooling flow

Increased blade tip clearances will cause a slightly higher pressure ratio over the upstream NGV with a corresponding increase in throat area giving a higher turbine capacity. The LP turbine capacity is reduced, dominated by the increased exit swirl out of the HP turbine at increased tip region flows. A slight increase in cooling airflows in the HP turbine is assumed based on the thermomechanical prediction for the affected seal clearance changes. Since the turbine pressure ratio is only a weak function of turbine efficiency, such losses will not be primarily indicated in the pressure ratio change. The comparison of HP turbine pressure ratio variation with time is illustrated in Fig. 13. The bucket loss lines up well and the simulated 0.9% is very close to the tested result of 1.1%. The time behavior for the predicted pressure ratio shows good agreement compared to the measured pressure ratio, achieving the minimum at the same time after the engine achieved maximum thrust conditions. The effects taking place in the HP turbine therefore can be predicted adequately.

Table 2 Split of fuel flow overshoot

Secondary effect	Fuel flow overshoot
Heat soakage	7.7%
Tip clearances	1.8%
HP spool inertia	0.2%
All	9.7%

Future Work Potential

The simulations of the secondary effects presented in this paper are derived using averaged tip clearance changes for multistage components. Improvements can be achieved using a split component modeling method, which considers the different thermal response of the single stages [8]. It also allows considering rematching effects taking place within the component as a result of the different thermal behavior of the single stages. The effect of compressor bleeds is not included in the simulations and a split component model yet would allow simulating their effects on the compressor stability margin. A detailed investigation of the changes in the secondary air system caused by the variation of seal clearances in the HPC and the HPT will extend the understanding of matching changes during and after fast transients.

Conclusions

During transient engine maneuver variations in engine component characteristics occur due to the different thermal dynamic behavior of the components. This results in a rematch of the engine cycle parameters and affects the stability margins. The simulation of the transient engine behavior is achieved by modeling the variations in the turbocomponent tip clearances and the seal clearance changes in the secondary air system based on a quasi-nonlinear state space model. The effect of the clearance variations is considered by adjusting the component efficiencies and capacities, the surge margin and the HP turbine cooling flows using experimental exchange rates for the BR700 components. Good agreement between the simulated and the measured performance parameter has been demonstrated. The method of predicting heat transfer and clearance changes via state space models could therefore be validated. The demonstrated model is an effective tool for engine design and the improvements in simulating transient engine behavior reduces expensive test time. The application of the model in gas turbine design processes will help engineers to comprehend the interactions taking place in the engine.

Nomenclature

A, B, C, D, G = system, driving, output, transmission, gain matrix of the state space model
FADEC = full authority digital engine control
FE = finite element
HP = high pressure
HPC = high pressure compressor
HPT = high pressure turbine
h = annulus height
LP = low pressure
LPT = low pressure turbine
l = blade height
NGV = nozzle guide vane
n = number of stages
RMS = poot mean square
r = radius
SM = surge margin
s = absolute tip clearance
s/h = relative tip clearance
Δs = change in tip clearance
T = vector of temperature
TGT = turbine gas temperature
U, X, Y = vector of absolute values of inputs, states, and outputs of the state space model
u, x, y = vector of offsets of inputs, states, and outputs to steady state
wrtp = capacity, corrected mass flow
Π = pressure ratio
η = efficiency

Subscripts

0 = steady-state condition
CF = cooling flow
c = casing
d = disk
g = gas
r = rotor
HPTNGV = HP turbine nozzle guide vane
int = integrated C, D and G matrix
m = metal
Nom = nominal
NH = at HP shaft speed
r = rotor
ref = reference condition
Tr = transient
$\dot{x}$ = derivative of time of x

References

[1] Therkorn, D., 1992, "Fortschrittliches Leistungs-Berechnungsverfahren für luftatmende Turbotriebwerke," Doctor thesis, University of Stuttgart.
[2] Khalid, S. J., and Hearne, R. E., 1980, "Enhancing Dynamic Model Fidelity for Improved Prediction of Turbofan Engine Transient Performance," AIAA 80-1083.
[3] Fiola, R., 1993, "Berechnung des Instationären Betriebsverhaltens unter Besonderer Berücksichtigung von Sekundäreffekten," Doctor thesis, Technical University of Munich.
[4] Riegler, C., 1999, "Correlations to Include Heat Transfer in Gas Turbine Performance Calculations," Aerospace Science and Technology, No. 5, pp. 281–292.
[5] Frank, R., Rist, D., and Kappler, G., 1993, "On-line Überwachung der Ermüdungslebensdauer von Rotierenden Flugtriebwerkskomponenten," DGLR Jahresbuch No. 93-03-048.
[6] Peters, P., Breisig, V., Giboni, A., Lerner, C., and Pfost, H., 2000, "The Influence of the Clearance of Shrouded Rotor Blade on the Development of the Flowfield and Losses in the Subsequent Stator," ASME GT-478.
[7] Staudacher, S., 1995, "Untersuchungen zum sekundären Luftsystem von Luftstrahltriebwerken," Doctor thesis, Technical University of Munich.
[8] Staudacher, S., Berns, W., and Ye, Haiwen, "Modeling Multistage Compressors by Several Split Compressors," Institute for Aircraft Propulsion, University of Stuttgart, ALSTOM, Switzerland, AIAA 2003-1019.

Experiment on Gas Ingestion Through Axial-Flow Turbine Rim Seals

R. P. Roy

J. Feng

D. Narzary

Department of Mechanical and Aerospace Engineering,
Arizona State University,
Tempe, AZ 85287-6106

R. E. Paolillo

Pratt & Whitney,
East Hartford, CT 06108

It has been suggested by researchers that ingestion, through rim seals, of mainstream gas into axial-flow turbine disk cavities is a consequence of the prevailing unsteady three-dimensional flow field. The cause–effect relationship is complex—to help understand it, experiments were performed in a model single-stage turbine rig using two different vane-blade configurations. Selected measurements from one of the configurations were reported earlier (1999–2001). The second configuration is new, featuring smaller numbers of vanes and blades and a larger vane turning angle. Selected measurements are presented and compared to those from the first configuration. The measurements include unsteady and rotor revolution time-average static pressure spatial distributions, and spatial distribution, in the rotor-stator cavity, of time-average ingestion. The parameters in the experiments were the main airflow rate, the purge/seal airflow rate, and the rotor speed. Unsteady three-dimensional CFD simulation may be helpful in identifying the roles of the many intertwined phenomena in the ingestion process. [DOI: 10.1115/1.1850499]

1 Introduction

Gas turbine disk cavities upstream and downstream of high-pressure stage rotors must have a certain level of purge airflow to reduce hot mainstream gas ingestion into the cavities as well as to maintain acceptable under-platform and disk metal temperatures. Cooler, high-pressure purge air bled from the compressor is injected into the cavities, a part or all of this air is ejected back into the main gas path annulus through the gap between disk rim seals. Accomplishing the cavity sealing and metal cooling functions using the smallest possible amount of purge air is a key objective in turbine design since the bleed-off of compressor air and its subsequent mixing with the main gas flow exact penalties on turbine performance.

Gas ingestion into and egress from disk cavities are space and time dependent. It has been pointed out by researchers that they are a consequence of the prevailing unsteady three-dimensional flow field. The main gas flow is unsteady due to several reasons, one being rotor–stator potential interaction in which the pressure field associated with the leading edge of rotor blades travels past the trailing edge of the vanes upstream. Other reasons include vane wakes sweeping downstream and into the rotor blades, and rotor blade wakes. The flow field is unsteady in the disk cavities as well, particularly radially outboard. Numerous factors have an influence—for example, vane/blade geometry and axial spacing, configuration of the rim seals, main and purge airflow rates, and rotor speed.

The state of understanding circa 1988 of the flow and heat transfer processes in rotating-disk systems was presented in a comprehensive monograph by Owen and Rogers [1]. A few works, pre- and post-1988, are briefly discussed in the following because of their relevance to the work reported in this paper.

Dring et al. [2] experimentally studied the aerodynamic interaction between rotor blades and stator vanes in a large-scale turbine stage. The instantaneous and time-mean surface pressures were measured at airfoil mid-span along with time–mean heat transfer. Upstream potential flow influence of the rotor on the stator was observed as was the downstream potential flow and wake influence of the stator on the rotor.

Green and Turner [3] found experimentally that ingestion with both vanes and blades present can be significantly different from that with blades absent. Johnson et al. [4] pointed out that there are several physical mechanisms that affect ingestion—for example, disk pumping, circumferential pressure asymmetry in the main gas path, periodic pressure fluctuation due to vane/blade interaction, and turbulent transport in the fluid.

Bohn et al. [5,6] investigated main gas ingestion through the rim seal of a single-stage turbine experimentally and numerically. The time–mean static pressure distribution was measured, as was the sealing efficiency of the rim seals by the tracer gas method. Three-dimensional steady [5] and unsteady [6] CFD calculations were carried out. A finding from the unsteady calculations was an ingestion zone in the rim seal region that rotated at one-half the rotor speed.

Feiereisen et al. [7] performed experiments to study the ingestion process at the vane-blade rim seal in a single-stage turbine. Unsteady and time-average pressures were measured in both stationary and rotating frames of reference. The tracer gas method was used to measure sealing effectiveness at several locations in the rim seal region and at the vane and blade platforms. To characterize the unsteady flow in the intrastage region downstream of the first vane row, Gallier et al. [8] imaged, by particle image velocimetry, the instantaneous velocity field at ten rotor positions relative to the axial–radial imaging plane. It was found that the purge flow played a strong role in the main gas path secondary flow structure.

Gentilhomme et al. [9] reported measurements in a single-stage axial turbine, steady and unsteady CFD simulations of the same, and an elementary model of ingestion. Time-average pressure distribution and ingestion were measured. Unsteady effects due to rotor blades were found to be key contributors to ingestion. Cao et al. [10] reported a combined CFD and experimental study of the interaction between main gas path and purge flows. The experiments were conducted in a two-stage axial turbine. The CFD model was unsteady and its results exhibited a significant improvement overthe corresponding steady computations. An un-

---

Contributed by the International Gas Turbine Institute (IGTI) of THE AMERICAN SOCIETY OF MECHANICAL ENGINEERS for publication in the ASME JOURNAL OF ENGINEERING FOR GAS TURBINES AND POWER. Paper presented at the International Gas Turbine and Aeroengine Congress and Exhibition, Vienna, Austria, June 13–17, 2004, Paper No. 2004-GT-53394. Manuscript received by IGTI, October 1, 2003; final revision, March 1, 2004. IGTI Review Chair: A. J. Strazisar.

steady flow feature qualitatively similar to Bohn et al. [6] was predicted by the CFD.

In the present paper, we compare measurements in two different model axial turbine stages, the main difference between the models being the vane-blade configuration. The first model (Model 2) results were presented in several papers, Roy et al. [11–13]. The second model (Model 1) is new and its results are reported for the first time.

2 Experimental Apparatus

Main air is drawn through the turbine by a centrifugal blower (Hauck) that is equipped with a variable-frequency motor drive and is capable of providing up to 1.42 m^3/s ($\approx$3000 cfm) airflow rate. This flow rate is measured by a pitot tube rake located in the suction duct of the blower. The rotor–stator section is optically accessible from the radial as well as axial (air inlet) directions. The purge air is supplied through a 38.1 mm i.d. pipe by another centrifugal blower (Hauck), which is also equipped with a variable-frequency motor drive and is capable of providing up to 0.12 m^3/s ($\approx$250 cfm) airflow rate. The purge air flow rate is measured by a turbine flow meter (EG&G Flow Technology).

The vane-blade and the disk cavity configuration for the new turbine stage (Model 1) is based on that of a Pratt & Whitney engine stage, Figs. 1(*a*), 1(*b*). The 0.391 m diameter aluminum rotor disk is equipped with 28 partial-height (compared to the actual engine) blades. A variable-frequency motor drive is used to rotate the disk up to a speed of 5000 rpm. While the main gas flow also drives the rotor, the motor drive is needed for maintaining it at a particular rotational speed during experiments. The Plexiglas stator disk, of the same diameter as the rotor disk, is equipped with 22 partial-height vanes. The vanes turn the incoming main air by 68.6 deg. The partial vane and blade heights allow the axial velocity of the main air in the annulus to be adequately high given the main blower capacity. The rim seal arrangement for the experiments reported here features a static radial clearance of 2 mm and an axial overlap of 2 mm. The running radial clearance at rotor disk speeds of up to 5000 rpm is essentially the same as the static clearance since the radial growth of the disk is less than 0.01 mm.

The vane-blade and disk cavity configuration for the earlier turbine stage (model 2) was based on a Honeywell engine stage, Figs. 2(*a*), 2(*b*). The rotor disk diameter is 0.403 m, the number of blades 52, and the number of vanes 59. The vanes turn the main air by 55 deg. The rim seal arrangement is identical to that of Model 1.

In Figs. 1(*b*) and 2(*b*), the dotted lines at the blade aft indicate the actual blade shape in the engines. To obtain thinner rotor disks in the experiments, the blade chord length was shortened as shown by the solid lines.

Table 1 contains information regarding configuration of the vanes in the two model turbine stages.

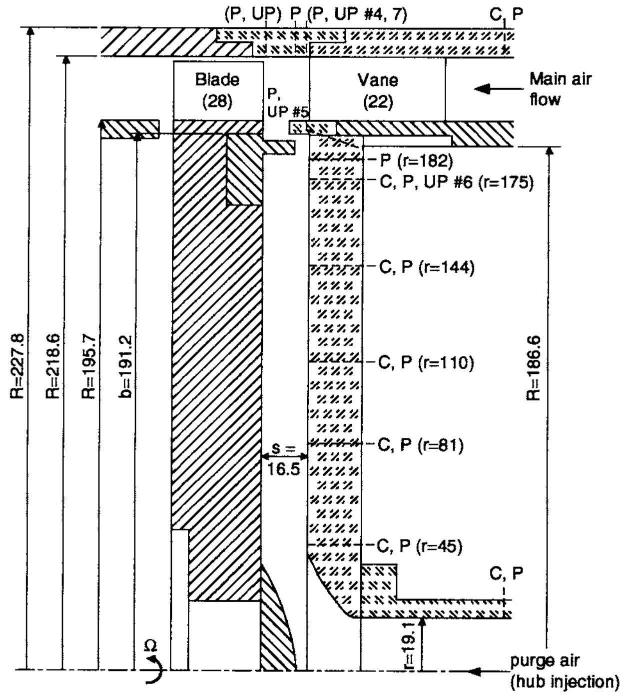

(a) Single-stage turbine

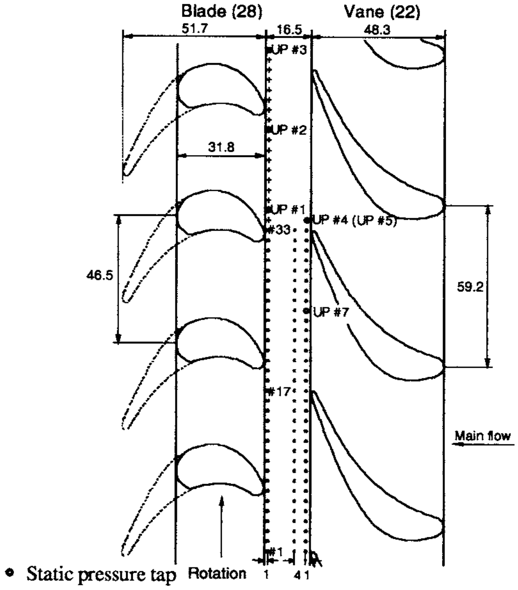

● Static pressure tap

● Unsteady pressure tap

(b) Blades and vanes

Fig. 1 Schematic diagram—Model 1 (C: tracer gas concentration tap, P: time-average static pressure tap, UP: unsteady pressure tap); all dimensions in mm

2.1 Static Pressure Measurement

2.1.1 Time-Average Static Pressure. The time averaging is over an integer number of rotor revolutions. For Model 1, as in the case of the earlier Model 2, a differential pressure transducer (Validyne)—digital manometer (Validyne)—Scanivalve setup was used to measure the time-average static gage pressure distribution in the disk cavity at the stator disk, and in the main gas path at the stator disk rim seal and the outer shroud. All pressure taps are 1 mm i.d. Figure 1(*a*) shows the six radial positions of the taps on the stator disk. At the position $r=175\,\mathrm{mm}\,(r/b=0.91)$, 16 taps were provided circumferentially over one vane pitch. The taps on the outer shroud are shown schematically in Fig. 1(*b*). On the stator disk rim seal, there were 17 taps over one vane pitch on the seal surface facing the main flow at 1 mm downstream from the vane trailing edge (t.e.) plane. The pressure taps for Model 2 are shown in Figs. 2(*a*), 2(*b*).

The uncertainty in the measured time-average static pressure estimated on the basis of the instrument and data acquisition uncertainties is ±2%.

2.1.2 Unsteady Static Pressure. Unsteady static gage pressure was measured at seven locations, all in the stationary frame of reference, Figs. 1(*a*) and 1(*b*): in the main gas path—at two

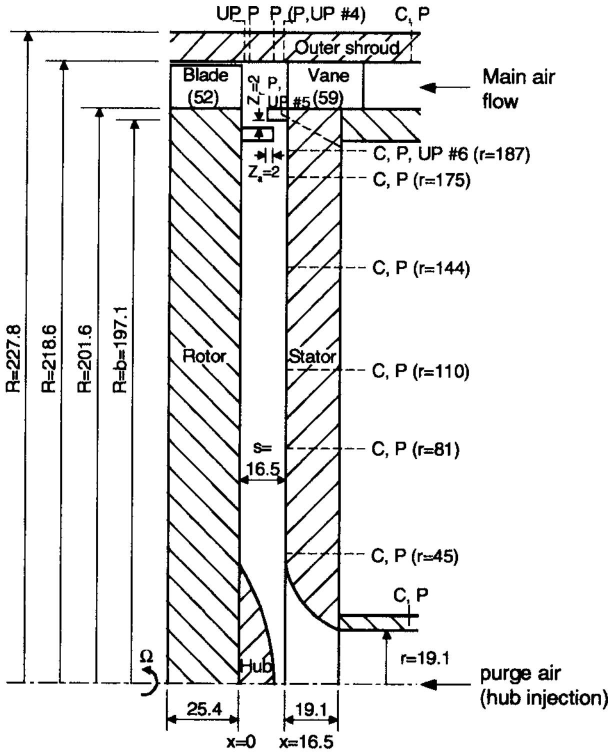

(a) Single-stage turbine

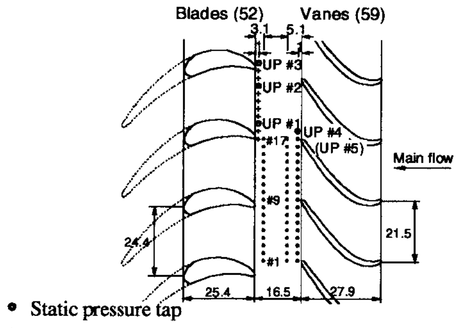

(b) Blades and vanes

Fig. 2 Schematic diagram—Model 2 (C: tracer gas concentration tap, P: time-average static pressure tap, UP: unsteady pressure tap); all dimensions in mm

circumferential locations on the outer shroud 1 mm downstream from the vane t.e. plane, at three circumferential locations on the outer shroud 1 mm upstream from the blade leading edge (l.e.) plane, and at one location on the stator disk rim seal 1 mm downstream from the vane t.e. plane; in the disk cavity—at one location on the stator disk at $r = 175$ mm. The tap on the stator disk (UP #6), one of the two taps on the outer shroud 1 mm downstream from the vane t.e. plane, and the tap on the rim seal are at the same circumferential position. The latter two taps (UP #4 and #5) are in the vane wake. The three taps 1 mm upstream from the blade l.e. plane are distributed circumferentially over one *vane* pitch. The taps for Model 2 are shown in Figs. 2(*a*), 2(*b*).

Kulite pressure transducers (Model XCS-062-5-D) with 1.6 mm tip diameter were used. The transducer signals were amplified, low-pass filtered, and then routed to an eight-channel data acquisition system. Repeated time records, each spanning one complete rotor disk revolution, were acquired for 50 rotor revolutions. Each record was initiated by a once per rotor revolution signal from a laser-based trigger system. Data were acquired at 40 kHz with the low-pass filter set at 20 kHz (Nyquist) frequency to prevent aliasing. The acquired data were subsequently transferred to a computer for post-processing.

Post-processing of the signals followed the procedure suggested by Suryavamshi et al. [14]. In this procedure, the instantaneous pressure is decomposed into an ensemble-average pressure and an unresolved pressure. The ensemble-average pressure correlates with rotor revolution whereas the unresolved pressure represents the random unsteadiness. The ensemble-average pressure is further decomposed into a time-average pressure (this should be the same as the time-average pressure measured by the Validyne transducers), a revolution-periodic pressure, and a revolution-aperiodic pressure. The revolution-periodic pressure is then decomposed into blade-periodic and blade-aperiodic components. The blade-periodic component, which has a zero mean, represents our pressure fluctuation (or oscillation) of interest over one blade passage time period. Auto- and cross-power spectral density (APSD,CPSD) analyses of the blade-periodic time series records were performed using the autoregressive method which provides a better estimation of the APSD and CPSD functions than nonparametric methods when the data length is relatively short, as in our case. The frequency resolution for the obtained spectra is approximately 6.3 Hz.

The uncertainty in the measured unsteady static pressure estimated on the basis of the instrument and data acquisition uncertainties is ±4%.

2.2 Ingestion of Main-Stream Gas. To measure ingestion in the cavity, the purge airflow was seeded with carbon dioxide (tracer) gas. The CO_2 volumetric concentration in the purge air was monitored just upstream of its entrance to the disk cavity and maintained at 4.00 (±0.11)%. The pressure taps at the six radial locations on the stator disk, Fig. 1(*a*), also served as taps for measuring the CO_2 concentration in the cavity at the stator disk surface. To measure the CO_2 concentration distribution in the cavity, sampling tubes (1 mm i.d., 1.6 mm o.d.) were installed at the same radii (except at $r = 182$ mm)[1] and traversed axially one at a time. The CO_2 concentration in the mainstream air was measured during each experiment to serve as a reference. The sampling taps for Model 2 are shown in Figs. 2(*a*), 2(*b*).

The CO_2 concentration in the gas sample was measured by an NDIR gas analyzer (Siemens—Ultramat 23). The uncertainty in the measured CO_2 volumetric concentration is ±0.11% CO_2 concentration.

Because of the nature of the technique, the ingestion measured in the cavity is rotor revolution time averaged but local with respect to the stator vane positions and the radial and axial coordinates.

Table 1 Vane configuration in the two single-stage turbines

	Model 1	Model 2
Vane angle at exit	68.6 deg	55.0 deg
Axial chord length	48.3 mm	27.9 mm
Span	22.9 mm	17.0 mm
Pitch	59.2 mm	21.5 mm
Radius at vane hub	195.7 mm	201.6 mm
Number	22	59

3 Results and Discussion

Selected results of four sets of experiments for Model 1 will be presented and discussed here. Their conditions are shown in Table 2. For these experiments, the ambient pressure and temperature were 97 kPa and 24°C, respectively. The nominal static absolute pressure of the mainstream air at vane inlet was approximately 95

---

[1] A sampling tube could not be installed here because of insufficient space.

Table 2 Experimental conditions for Model 1. *Gas ingestion experiments were not performed for these conditions. However, ingestion experiments have been carried out at c_w values in addition to those shown in this table.

Exp. Set No.	Mainstream flow rate (cfm/$\mathrm{Re}_{\mathrm{vax}}$)	Rotor disk speed (rpm/Re_{ϕ})	β (deg)	Free disk pumping flow rate (cfm/$c_{w,\mathrm{fd}}$)	Purge airflow rate (cfm/c_w)				
					(1)*	(2)	(3)	(4)	(5)
I	1900/9.27×10^4	2200/5.37×10^5	44.0	53.4/8403	0/0	10/1574	20/3148	55/8656	80/12,591
II	1900/9.27×10^4	3000/7.32×10^5	21.3	68.4/10,770	0/0	10/1574	⋯	55/8656	80/12,591
III	2300/1.12×10^5	3000/7.32×10^5	37.4	68.4/10,770	0/0	10/1574	⋯	55/8656	95/14,952
IV	2300/1.12×10^5	3600/8.79×10^5	22.2	79.2/12,461	0/0	10/1574	⋯	55/8656	95/14,952

kPa, and the purge air static absolute pressure just upstream of the disk cavity entry was about 91 kPa. These two pressures changed slightly with the respective airflow rates.

Table 3 shows the Model 2 experiments that were used for comparison. Additional experiments were presented in Roy et al. [11–13].

The estimated uncertainties in the nondimensional parameters Re_{ϕ}, $\mathrm{Re}_{\mathrm{vax}}$, and c_w are, respectively, ±2%, ±3%, and ±5%.

The results are now presented in the following sequence: (1) time-average static pressure distribution; (2) unsteady static pressure distribution; and (3) time-average main air ingestion distribution in the disk cavity.

3.1 Time-Average Static Pressure. The circumferential distribution of time-average static pressure in the main gas path is viewed as one of the key factors in the ingestion process—the vane shape and pitch are of importance here. In Fig. 3, this pressure (gage) distribution is shown for Model 1 at the experimental condition $\mathrm{Re}_{\phi}=7.32\times10^5$, $\mathrm{Re}_{\mathrm{vax}}=1.12\times10^5$, $c_w=1574$. For comparison, Fig. 4 shows the variation for Model 2 at $\mathrm{Re}_{\phi}=7.74\times10^5$, $\mathrm{Re}_{\mathrm{vax}}=8.78\times10^4$, $c_w=1504$. In both cases, the peak-to-peak amplitude is maximum at the outer shroud immediately downstream from the vane trailing edge plane, the highest pressure being at the middle of the wake. The amplitude decreases rapidly downstream. In the cavity, there is no discernible circumferential pressure variation at the stator disk even near its rim ($r/b=0.91$ for model 1, $=0.95$ for model 2). Table 4 shows that the peak-to-peak amplitude is significantly larger in the case of Model 1—the main air mixed-mean axial velocity in the annulus was, respectively, 36.4 m/s for Model 1 and 50.5 for Model 2. The resultant velocities at the vane exit were, respectively, 99.7 m/s for Model 1 and 88.0 m/s for Model 2 (the tangential velocity imparted by the vanes to the air was substantially larger in the case of Model 1). In Fig. 5, the pressure variation amplitude coefficient, $\bar{c}_{p,pk\text{-}pk}$, is plotted versus the axial distance from the vane t.e. plane for the Figs. 3 and 4 data. The coefficient has the same value for Models 1 and 2 at the outer shroud immediately downstream of the vane. At the other locations, the value is higher for Model 1, indicative of a wake whose strength persisted farther downstream.

The circumferential pressure distributions shown in Figs. 3 and 4 are typical of Models 1 and 2, respectively. The differences between the distributions include sharper peaks for Model 1, and a recognizable shift of the peak in the direction of main air tangential motion as the air flows downstream for Model 2.

It should also be noted from Table 4 that the purge airflow rate, c_w, appears to have no significant effect on the time-average circumferential pressure variation in the main gas path (see Roy et al. [13] also).

3.2 Unsteady Static Pressure. Only Model 1 measurements are presented here. Selected plots for Model 2 and related discussion can be found in Roy et al. [13].

In Figs. 6(*a*) and 6(*b*), the *ensemble-average* pressure obtained by averaging the instantaneous unsteady gage pressure (UP) signal over 50 rotor revolutions is shown at the seven locations for the condition $\mathrm{Re}_{\phi}=7.32\times10^5$, $\mathrm{Re}_{\mathrm{vax}}=1.12\times10^5$, $c_w=1574$. Each rotor revolution comprises 28 blade passages—as such, 28 periodic pressure variations exist in each time-series plot.

It is instructive to examine the corresponding *blade-periodic* pressures over three blade passages, Figs. 7(*a*) and 7(*b*). The unsteadiness amplitude, $\Delta\tilde{p}_{pk\text{-}pk}$, is the highest just upstream of the rotor blades—it was suggested by Feiereisen et al. [7] that this is caused by the bow waves created by the blades and their interaction with the vane wakes. The amplitude is attenuated upstream, i.e., toward the vanes, and phase lag occurs, as shown later in Table 8.

Also of significance are the time-average pressure differential

Table 3 Experimental conditions for Model 2.*Gas ingestion experiments were not performed for these conditions. Unsteady static pressure experiments were carried out for the highlighted conditions.

Exp. Set No.	Mainstream flow rate (cfm/$\mathrm{Re}_{\mathrm{vax}}$)	Rotor disk speed (rpm/Re_{ϕ})	β (deg)	Free disk pumping flow rate (cfm/$c_{w,\mathrm{fd}}$)	Purge airflow rate (cfm/c_w)					
					(1)*	(2)	(3)	(4)	(5)	(6)
I	1950/7.08×10^4	2000/5.16×10^5	19.5	54.1/8139	**0/0**	**10/1504**	20/3008	30/4512	**50/7520**	60/9024
II	2400/8.78×10^4	3000/7.74×10^5	7.2	74.9/11,258	**0/0**	**10/1504**	20/3008	30/4512	**50/7520**	75/11280
III	2200/7.98×10^4	2290/5.91×10^5	19.0	60.3/9072	**0/0**	⋯	⋯	⋯	⋯	⋯
IV	2200/7.98×10^4	2750/7.09×10^5	7.2	69.8/10,495	**0/0**	⋯	⋯	⋯	⋯	⋯

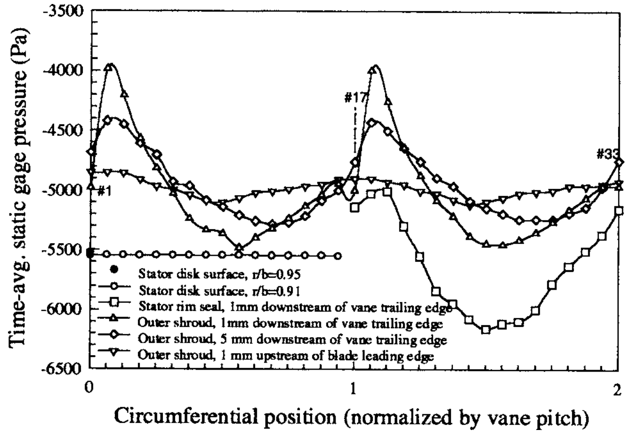

Fig. 3 Circumferential distributions of time-average static pressure at the outer shroud, stator disk rim seal, and stator disk near its rim at $Re_\phi=7.32\times10^5$, $Re_{vax}=1.12\times10^5$, $c_w=1574$—for Model 1

from the stator rim seal outer surface location to the cavity (at stator disk near rim seal), $\bar{p}_5-\bar{p}_6$; the maximum instantaneous pressure differential between the same locations, $(p_5-p_6)_{\max}$; and the minimum instantaneous pressure differential, $(p_5-p_6)_{\min}$. The second quantity may be indicative of one driving force for local ingestion, and the last quantity, if negative, of one driving force for egress locally. Table 5 shows the values for Models 1 and 2. Two remarks: in both Models 1 and 2, the rim seal gap is 6–7 mm downstream from UP5 and UP6; and the tangential component of the main flow motion will influence the circumferential locations of ingestion and egress.

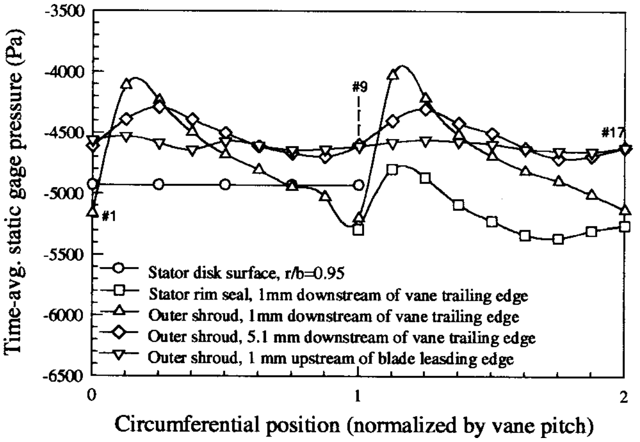

Fig. 4 Circumferential distributions of time-average static pressure at the outer shroud, stator disk rim seal, and stator disk near its rim at $Re_\phi=7.74\times10^5$, $Re_{vax}=8.78\times10^4$, $c_w=1504$—for Model 2

Table 4 Peak-to-peak amplitude of time-average static pressure circumferential variation at the outer shroud 1 mm downstream of the vane trailing edge

Model 1 $Re_{vax}=1.12\times10^5$, $Re_\phi=7.32\times10^5$		Model 2 $Re_{vax}=8.78\times10^4$, $Re_\phi=7.74\times10^5$	
c_w	$\Delta\bar{p}_{pk\text{-}pk}$	c_w	$\Delta\bar{p}_{pk\text{-}pk}$
1574	1495 Pa	1504	1089 Pa
8656	1510 Pa	7520	1055 Pa

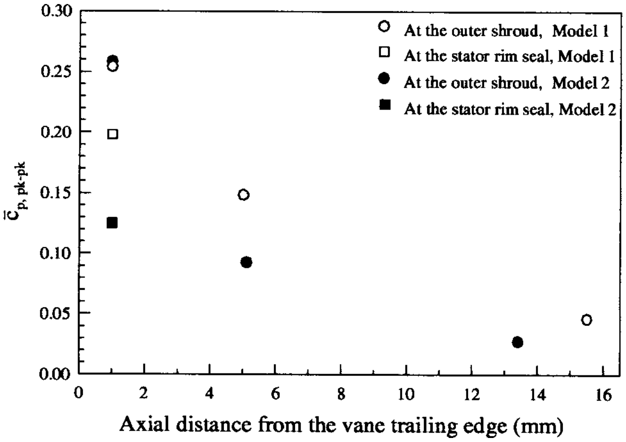

Fig. 5 Time-average static pressure variation amplitude coefficient at the main gas path outer shroud and stator rim seal—$Re_\phi=7.32\times10^5$, $Re_{vax}=1.12\times10^5$, $c_w=1574$—for Model 1; $Re_\phi=7.74\times10^5$, $Re_{vax}=8.78\times10^4$, $c_w=1504$—for Model 2

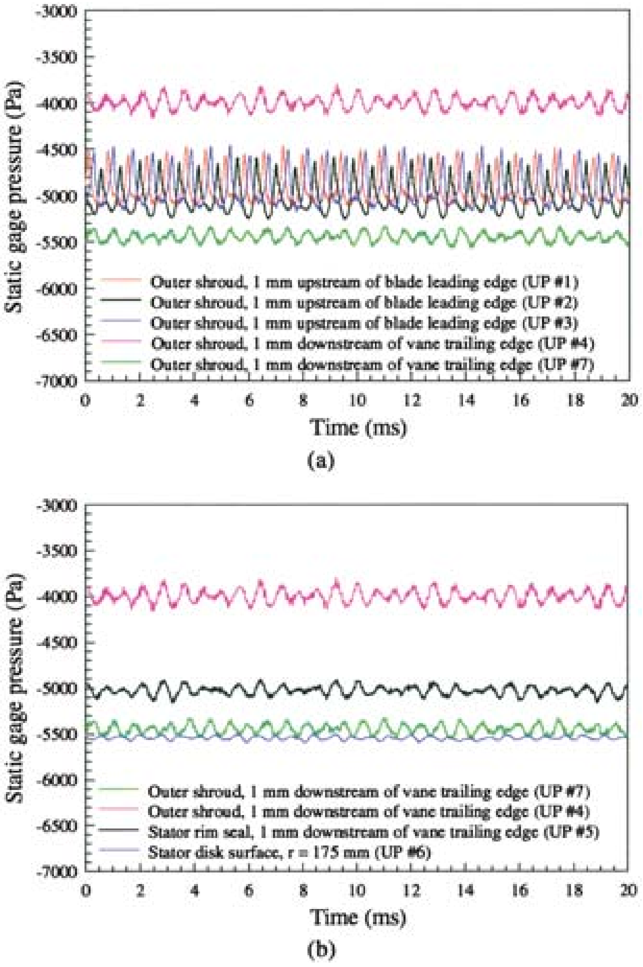

(a)

(b)

Fig. 6 Ensemble-average unsteady static pressure at the outer shroud, stator rim seal, and stator disk near its rim at $Re_\phi=7.32\times10^5$, $Re_{vax}=1.12\times10^5$, $c_w=1574$—one revolution—for Model 1

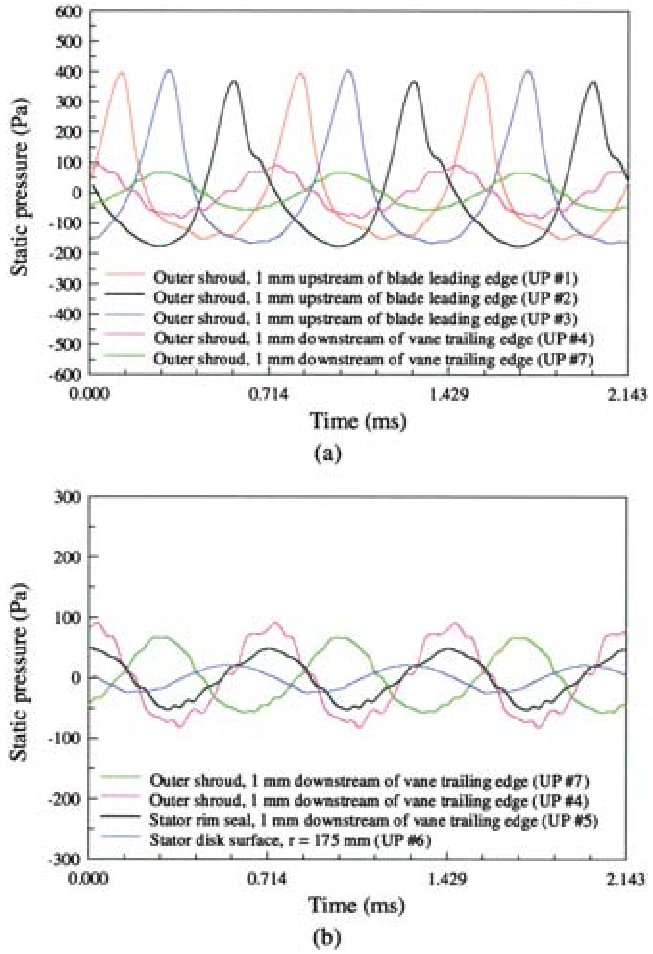

Fig. 7 Blade-periodic static pressure at the outer shroud, stator rim seal, and stator disk near its rim at Re_ϕ=7.32×10^5, Re_{vax}=1.12×10^5, c_w=1574—three blade passages—for Model 1

Table 5 Time-average, instantaneous maximum, and instantaneous minimum static pressure differential from location UP5 to location UP6—for Models 1 and 2

Model 1 $Re_{vax}=1.12\times10^5$, $Re_\phi=7.32\times10^5$				Model 2 $Re_{vax}=8.78\times10^4$, $Re_\phi=7.74\times10^5$			
c_w	$\Delta\bar{p}$ (Pa)	$\Delta p_{\max}$ (Pa)	$\Delta p_{\min}$ (Pa)	c_w	$\Delta\bar{p}$ (Pa)	$\Delta p_{\max}$ (Pa)	$\Delta p_{\min}$ (Pa)
1574	517	566	469	1504	133	196	70
8656	407	545	283	7520	−11	57	−37
14 952	72	315	−155	⋯	⋯	⋯	⋯

Table 6 Effect of blade passage frequency on $\Delta\tilde{p}_{pk\text{-}pk}$ (c_w =1574 for Model 1, =0 for Model 2)

Re_{vax}/Re_ϕ	UP #1 (Pa)	UP #2 (Pa)	UP #3 (Pa)	UP #4 (Pa)	UP #5 (Pa)	UP #7 (Pa)
		Model 1				
$9.27\times10^4/5.37\times10^5$	368	324	355	97	130	80
$9.27\times10^4/6.35\times10^5$	405	397	432	116	115	103
$9.27\times10^4/7.32\times10^5$	629	660	728	220	164	78
		Model2				
$7.98\times10^4/5.91\times10^5$	127	248	115	58	61	⋯
$7.98\times10^4/7.09\times10^5$	265	466	242	21	69	⋯

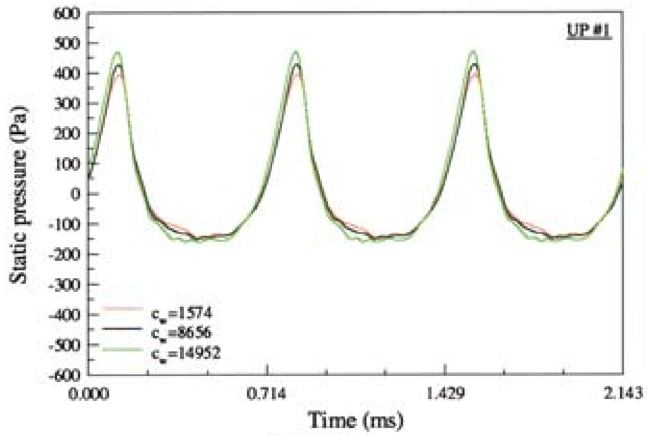

(a) UP #1

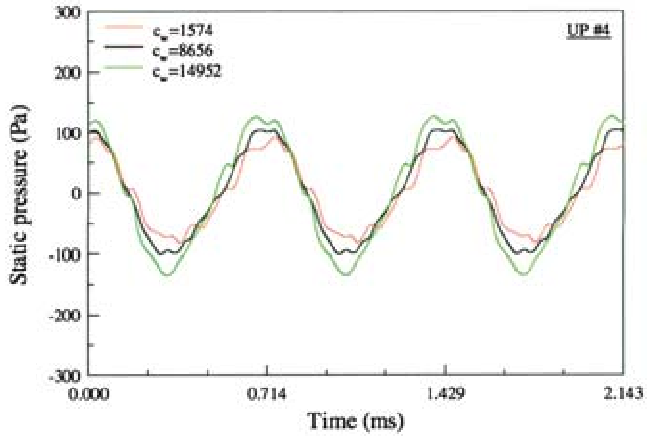

(b) UP #4

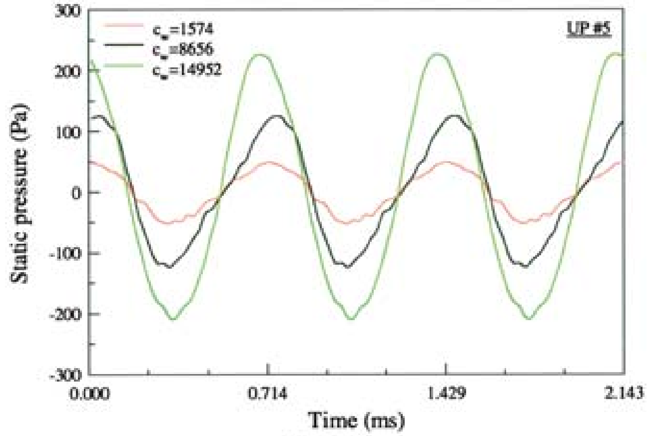

(c) UP #5

Fig. 8 Effect of purge airflow rate on blade-periodic static pressure at the outer shroud (UP #1, UP #4, UP #5) at Re_ϕ =7.32×10^5, Re_{vax}=1.12×10^5—three blade passages—for Model 1

Table 6 indicates that for both models an increase in the blade passage frequency ($\sim Re_\phi$) at the same main and purge airflow rate produces higher unsteadiness in pressure ($\Delta\tilde{p}_{pk\text{-}pk}$) *near the blade row*. It is also seen from Fig. 8(*a*) in the case of Model 1 and from [13] in the case of Model 2 that purge flow has a minimal influence on $\Delta\tilde{p}_{pk\text{-}pk}$ in the blade row proximity. However, in the case of Model 1, purge flow has a small but observable effect

Table 7 Effect of main air flow rate on $\Delta\tilde{p}_{pk\text{-}pk}$ (c_w=1574 for Model 1, =0 for Model 2)

$\mathrm{Re}_{\mathrm{vax}}/\mathrm{Re}_{\phi}$	UP #1 (Pa)	UP #2 (Pa)	UP #3 (Pa)	UP #4 (Pa)	UP #5 (Pa)	UP #7 (Pa)
		Model 1				
$8.29\times10^4/7.32\times10^5$	718	725	808	253	202	55
$9.27\times10^4/7.32\times10^5$	629	660	728	220	164	78
$1.12\times10^5/7.32\times10^5$	547	539	561	174	101	124
		Model2				
$7.98\times10^4/7.09\times10^5$	265	466	242	21	69	⋯
$8.78\times10^4/7.74\times10^5$	207	304	198	20	62	⋯

near the vane at the outer shroud, Fig. 8(*b*), and a strong effect near the vane at the rim seal, Fig. 8(*c*). These effects were less pronounced for Model 2.

It has also been our observation that at higher main airflow rates, the unsteadiness in pressure diminishes in strength near the blade row. Table 7 shows this effect for Model 1 and Model 2, and Fig. 9(*a*) for Model 1. One reason may be that the stronger vane wakes shielded, to a certain extent, from the rotor potential field the region near the blade row where the unsteady pressure taps were. This effect was not as distinct near the vanes, Fig. 9(*b*).

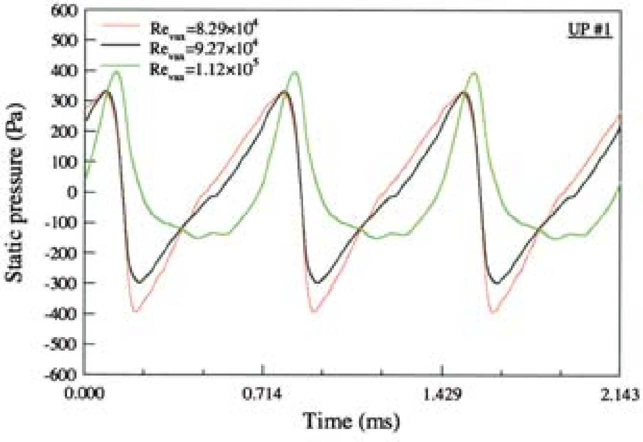

(a) UP #1

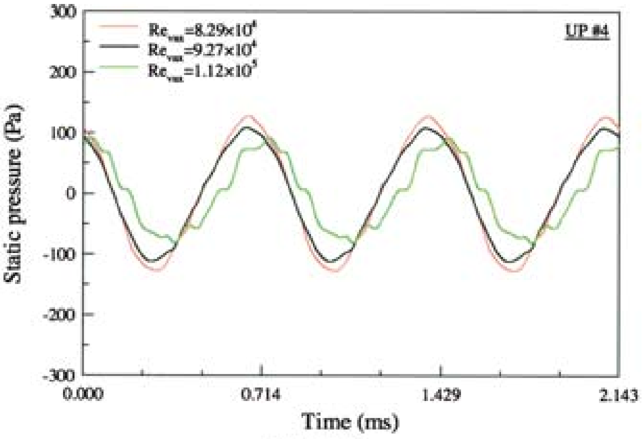

(b) UP #4

Fig. 9 Effect of main airflow rate on blade-periodic static pressure at the outer shroud (UP #1, UP #4) at Re_{ϕ}=7.32×10^5, c_w=1574—three blade passages—for Model 1

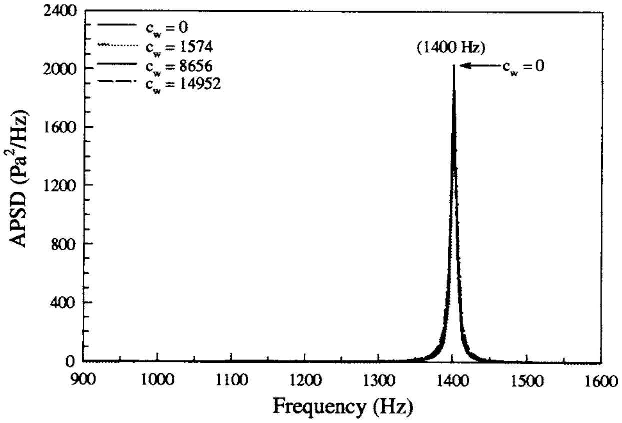

(a) UP #1

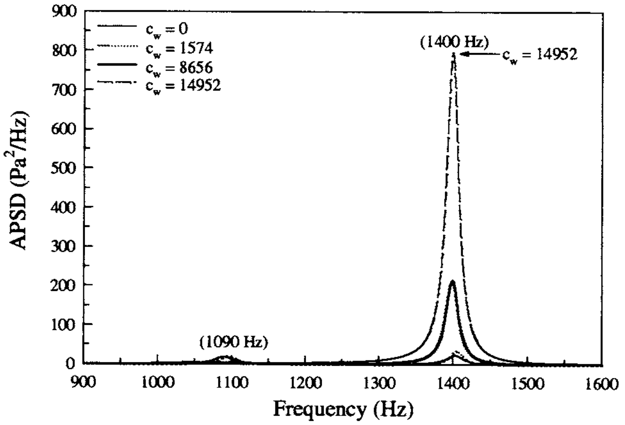

(b) UP #5

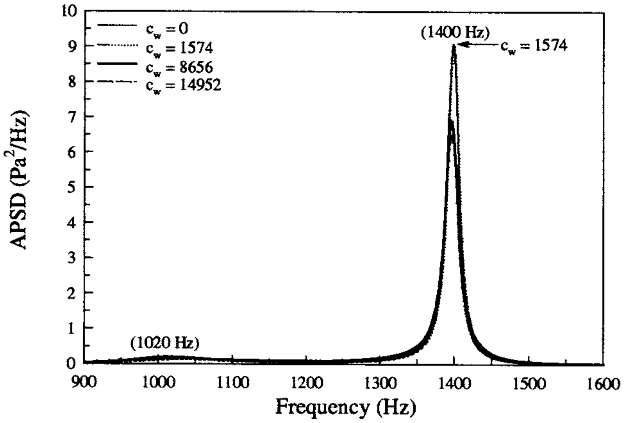

(c) UP #6

Fig. 10 Autopower spectral density function for blade-periodic static pressure at the outer shroud (UP #1), stator rim seal (UP #5) and stator disk near its rim (UP #6) at Re_{ϕ}=7.32×10^5, $\mathrm{Re}_{\mathrm{vax}}$=1.12×10^5, several c_w values—for Model 1

Figures 10(*a*), 10(*b*), 10(*c*) contain autopower spectral density (APSD) functions obtained from the ensemble-average unsteady pressure fluctuation time-series data of Model 1 at locations, respectively, UP #1 (near the blade row), UP #5 (stator rim seal), and UP #6 (stator disk near rim). The experimental conditions were $\mathrm{Re}_{\phi}=7.32\times10^5$, $\mathrm{Re}_{\mathrm{vax}}=1.12\times10^5$, and $c_w=0$, 1574, 8656, 14,952. At UP #1, there is a single dominant frequency at 1400 Hz, which corresponds to the (fundamental) blade passage frequency (the *higher* harmonics are not shown in the figure). As stated earlier, the purge airflow rate does not have much effect here. At UP #5, however, the purge air flow rate exerts a significant influence—also, the APSD energy content is much smaller here compared to that near the blade row. Furthermore, a second, lower-energy, peak appears at 1090 Hz—this has non-negligible

Table 8 Phase differences between unsteady static pressure fluctuations at blade passage frequency—Model 1 at $\mathrm{Re}_{\mathrm{vax}}=1.12\times10^5$, $\mathrm{Re}_\phi=7.32\times10^5$, $c_w=1574$

Locations	Measured (°)	Estimated (°)
UP1→UP2	118.5	131.0
UP1→UP3	−87.5	−98.2
UP1→UP4	−53.3	−57.1
UP1→UP7	−90.2	−73.7

energy at the low c_w's (0 and 1574). This frequency may correspond to the unsteady flow pattern detected in the rim gap region by Cao et al. [10] which rotates at a speed slightly less (90%–97%) than the rotor speed, except that in our case the pattern would be modulated by the 22 vanes around the circumference. Here 90%–97% of the rotor speed corresponds to 45 to 48.5 Hz—multiplying this by 22 yields 990–1067 Hz. Such a second peak is also identifiable at UP #6.

The phase differences between pressure fluctuations at the various UP locations in the main gas annulus were obtained from the respective cross-power spectral density (CPSD) functions. They were also estimated on the basis of pressure waves traveling upstream from the blades toward the vanes. Table 8 contains the results.

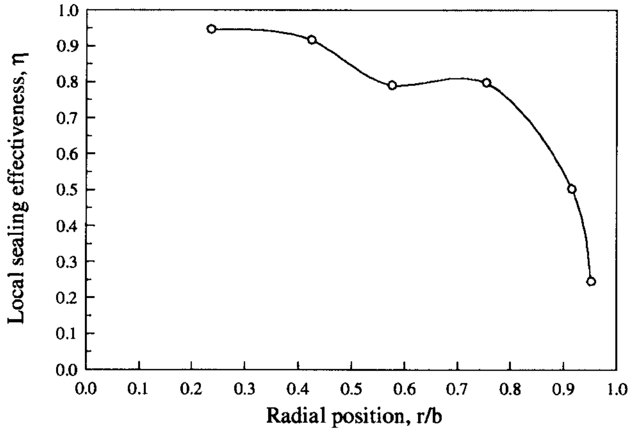

(a) at stator disk

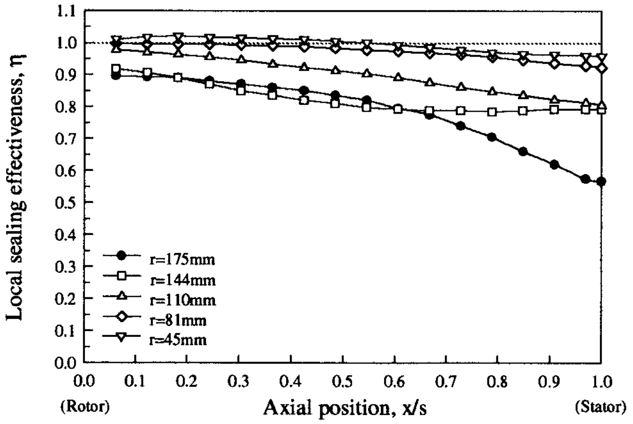

(b) in the cavity

Fig. 11 Sealing effectiveness distributions in the disk cavity at $\mathrm{Re}_\phi=7.32\times10^5$, $\mathrm{Re}_{\mathrm{vax}}=1.12\times10^5$, $c_w=1574$, $\beta=37.4$ deg—for Model 1

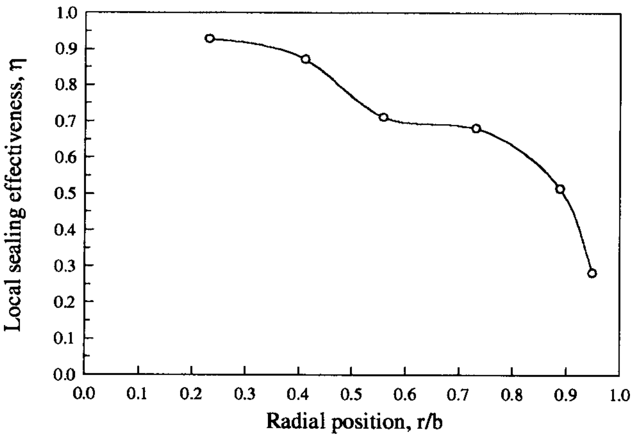

(a) at stator disk

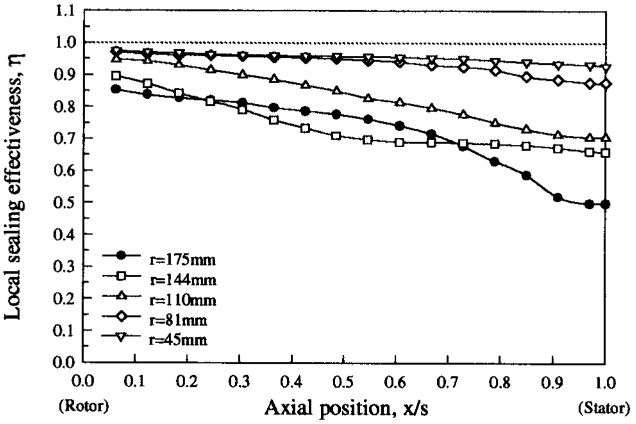

(b) in the cavity

Fig. 12 Sealing effectiveness distributions in the disk cavity at $\mathrm{Re}_\phi=7.74\times10^5$, $\mathrm{Re}_{\mathrm{vax}}=8.78\times10^4$, $c_w=1504$, $\beta=7.2$ deg—for Model 2

3.3 Ingestion of Main-Stream Gas. The magnitude of rotor revolution time-average main air ingestion into the disk cavity is presented in terms of sealing effectiveness. Sealing effectiveness, as the term is used here, represents the combined effects of the rim seals and the purge air in countering ingestion. It is defined as

$$\eta(\underline{r})=\frac{C(\underline{r})-C_{\mathrm{main}}}{C_{\mathrm{purge}}-C_{\mathrm{main}}} \tag{1}$$

The value of η ranges from 0 (no sealing effectiveness) to 1 (perfectly effective seal). It is noteworthy that if the "mass transfer–heat transfer analogy" is invoked, η will represent the *cooling effectiveness* of the purge air as well. This is an important consideration because it is rather difficult to measure the local cooling effectiveness of purge air directly from heat transfer experiments. This is mainly because the purge air temperature changes continuously as it flows through the cavity due to heat exchange between the air and the disks, Roy et al. [15]. As such, the purge air temperature at the cavity inlet cannot be the appropriate temperature in defining local cooling effectiveness.

In Fig. 11(*a*), the radial distribution of sealing effectiveness at the stator disk surface is shown for Model 1 at the condition $\mathrm{Re}_\phi=7.32\times10^5$, $\mathrm{Re}_{\mathrm{vax}}=1.12\times10^5$, $c_w=1574$. The axial distribution within the cavity is shown at five radial positions in Fig. 11(*b*). As is known, ingestion is higher near the stator disk.

In Figs. 12(*a*), 12(*b*), the sealing effectiveness distributions are shown for Model 2 at $\mathrm{Re}_\phi=7.74\times10^5$, $\mathrm{Re}_{\mathrm{vax}}=8.78\times10^4$, $c_w=1504$. The value of β is lower in this case than the preceding Model 1 case.

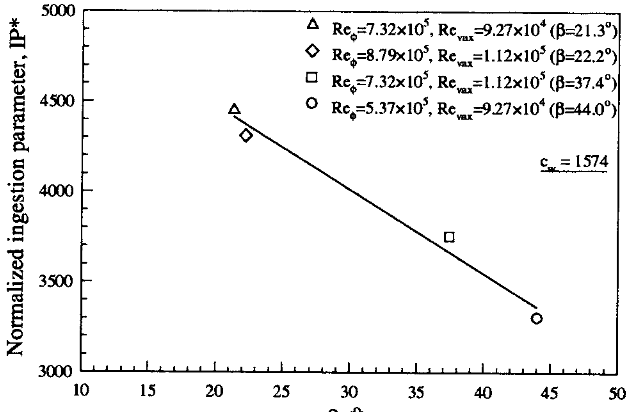

(a) Model 1

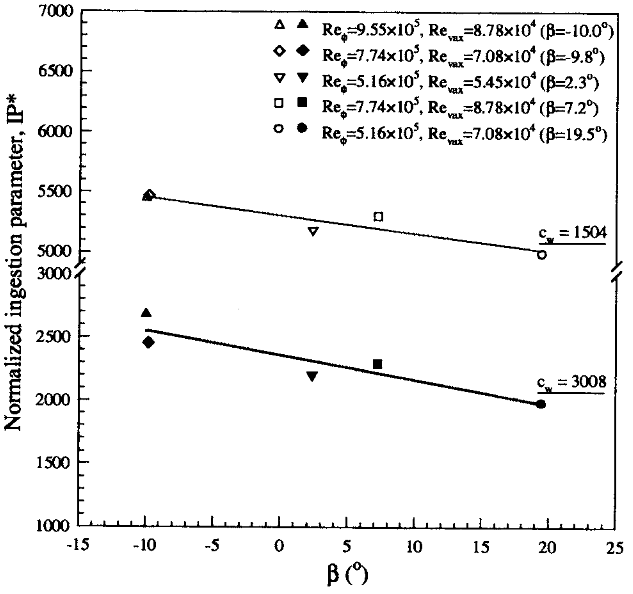

(b) Model 2

Fig. 13 Effect of angle β on the normalized ingestion parameter IP* at stator disk surface for selected conditions—Models 1 and 2

Whether the value of β, or more generally the main gas flow velocity triangle, affects ingestion is a pertinent issue. The extent of ingestion in the cavity may be represented by the integral

$$\text{IP}=\int (1-\eta) r\, dr, \tag{2}$$

the η values being *at the stator disk* (where η usually has the lowest value at any r). Figure 13(*a*) is a Model 1 plot, versus β, of this integral multiplied by (Re_φ at 3000 rpm/Re_ϕ at the actual rotor rpm)$^{0.8}$, dubbed IP*, to normalize the ingestion data at $c_w = 1574$ to a single rotor speed in an attempt to remove the influence of disk pumping. That ingestion decreased as β increased is apparent. The next higher c_w at which ingestion was measured in Model 1 is 4722—while the same trend was found in this case, the data scatter was considerably larger than at $c_w = 1574$.

Figure 13(*b*) contains plots of IP* versus β for Model 2 at $c_w = 1504$ and 3008—a similar decreasing trend is seen. The trend was the same but data scatter was considerably larger for the next higher c_w, 4512, at which ingestion was measured.

Whether the aforementioned trend will be found in other rotor–stator–rim seal configurations remains to be demonstrated, however.

A nondimensional plot, η at stator disk versus $c_w/\text{Re}_{\text{vax}}$, was constructed for all ingestion data—separately for Model 1 and Model 2. The data collapse in the plot was not sufficient to warrant its presentation.

4 Concluding Remarks

We have described experimental measurements of the rotor revolution time-average and unsteady static pressure fields, and time-average ingestion of main air into the rotor–stator disk cavity in a single-stage axial-flow turbine. Two different vane-blade configurations were investigated—an important difference between the configurations was the inlet vane turning angle.

Scrutiny of the measurements suggests that the instantaneous pressure field, which contains an unsteady blade-periodic component as well as circumferential variation following the vane pitch, is one key to ingestion. The flow field in the region is three-dimensional and unsteady. In addition to the configuration of the stage, this field is influenced by the main gas flow rate, rotor speed, and purge airflow rate.

A spectral analysis of the unsteady pressure signal identified, along with the high-energy peak at the blade passage frequency (fundamental) and weaker higher harmonics, a low-energy peak in the rim seal region at a frequency lower than the fundamental.

It may be impossible to experimentally isolate the many intertwined mechanisms at play that lead to ingestion. Three-dimensional, unsteady CFD simulations may hold the most promise in this regard—steps in this direction have already been taken by at least two research teams. The simulations must also have sufficient spatial resolution to capture the rather complex flow structure in the main gas path—see, for example, Pasinato et al. [16]. This structure can be expected to influence ingestion.

Acknowledgment

This research was partially supported by a grant from Pratt & Whitney, CT, whose help is gratefully acknowledged.

Nomenclature

b = outer radius of disk cavity—Figs. 1(*a*), 2(*a*)
C = CO_2 gas concentration
C_{vax} = vane axial chord length
$\bar{c}_{p,pk\text{-}pk}$ = circumferential time-average pressure variation coefficient, $\Delta\bar{p}_{pk\text{-}pk}/Q$
c_w = nondimensional mass flow rate of purge/seal air, $=\dot{m}_{\text{purge}}/\mu b$
$c_{w,\text{fd}}$ = nondimensional free disk pumping mass flow rate, $=0.219\,\text{Re}_\phi^{0.8}$
$\dot{m}$ = mass flow rate of air
p = instantaneous static gage pressure
$\bar{p}$ = rotor revolution time-average static gage pressure
$\tilde{p}$ = blade-periodic static pressure fluctuation
p_{amb} = ambient pressure
$\Delta\bar{p}_{pk\text{-}pk}$ = peak-to-peak amplitude of time-average static pressure circumferential variation
$\Delta\tilde{p}_{pk\text{-}pk}$ = peak-to-peak amplitude of blade-periodic static pressure fluctuation
Q = main air flow dynamic head at the vane exit (based on resultant velocity)
r = radial coordinate
$\underline{r}$ = position vector
Re_{vax} = main air flow Reynolds number, $=\rho V_{\text{ax}} C_{\text{vax}}/\mu$
Re_ϕ = disk rotational Reynolds number, $=\rho\Omega b^2/\mu$
s = axial gap between rotor and stator disks
V_{ax} = mixed-mean axial velocity of main air in annulus
x = axial coordinate measured from rotor disk surface into the cavity

β = angle, to axial direction, of the main air velocity relative to blade—at vane exit
η = sealing effectiveness
μ = dynamic viscosity of air
ρ = density of air
Ω = rotor disk speed

Subscripts

main = main air
purge = purge/seal air

References

[1] Owen, J. M., and Rogers, R. H., 1989, *Flow and Heat Transfer in Rotating-Disc Systems. Volume 1—Rotor–Stator Systems*, Research Studies Press Ltd, Taunton, Somerset, England.
[2] Dring, R. P., Joslyn, H. D., Hardin, L. W., and Wagner, J. H., 1982, "Turbine Rotor–Stator Interaction," ASME J. Eng. Power, **104**, pp. 729–742.
[3] Green, T., and Turner, A. B., 1994, "Ingestion Into the Upstream Wheelspace of an Axial Turbine Stage," ASME J. Turbomach., **116**, pp. 327–332.
[4] Johnson, B. V., Mack, G. J., Paolillo, R. E., and Daniels, W. A., 1994, "Turbine Rim Seal Gas Path Flow Ingestion Mechanisms," AIAA Paper 94-2703.
[5] Bohn, D., Rudzinski, B., Surken, N., and Gartner, W., 1999, "Influence of Rim Seal Geometry on Hot Gas Ingestion Into the Upstream Cavity of an Axial Turbine Stage," ASME Paper 99-GT-248.
[6] Bohn, D., Rüdzinski, B., Sürken, N., and Gärtner, W., 2000, "Experimental and Numerical Investigation of the Influence of Rotor Blades on Hot Gas Ingestion Into the Upstream Cavity of an Axial Turbine Stage," ASME Paper 2000-GT-284.
[7] Feiereisen, J. M., Paolillo, R. E., and Wagner, J., 2000, "UTRC Turbine Rim Seal Ingestion and Platform Cooling Experiments," AIAA Paper 2000-3371.
[8] Gallier, K. D., Lawless, P. B., and Fleeter, S., 2000, "Investigation of Seal Purge Flow Effects on the Hub Flow Field in a Turbine Stage Using Particle Image Velocimetry," AIAA Paper 2000-3370.
[9] Gentilhomme, O., Hills, N. J., Chew, J. W., and Turner, A. B., 2002, "Measurement and Analysis of Ingestion Through a Turbine Rim Seal," ASME Paper GT-2002-30481.
[10] Cao, C., Chew, J. W., Millington, P. R., and Hogg, S. I., 2003, "Interaction of Rim Seal and Annulus Flows in an Axial Flow Turbine," ASME Paper GT-2003-38368.
[11] Roy, R. P., Devasenathipathy, S., Xu, G., and Zhao, Y., 1999, "A Study of the Flow Field in a Model Rotor–Stator Disk Cavity," ASME Paper 99-GT-246.
[12] Roy, R. P., Xu, G., and Feng, J., 2000, "Study of Main-Stream Gas Ingestion in a Rotor–Stator Disk Cavity," AIAA Paper 2000-3372.
[13] Roy, R. P., Xu, G., Feng, J., and Kang, S., 2001, "Pressure Field and Main Stream Gas Ingestion in Rotor Stator Disk Cavity," ASME Paper 2001-GT-564.
[14] Suryavamshi, N., Lakshminarayana, B., Prato, J., and Fagan, J. R., 1997, "Unsteady Total Pressure Field Downstream of an Embedded Stator in a Multistage Axial Flow Compressor," ASME J. Fluids Eng., **119**, pp. 985–994.
[15] Roy, R. P., Xu, G., and Feng, J., 2001, "A Study of Convective Heat Transfer in a Model Rotor–Stator Disk Cavity," ASME J. Turbomach., **123**, pp. 621–632.
[16] Pasinato, H., Squires, K. D., and Roy, R. P., 2004, "Assessment of Reynolds-Averaged Turbulence Models for Prediction of the Flow and Heat Transfer in an Inlet Vane-Endwall Passage," ASME J. Fluids Eng., **126**, pp. 305–315.

Numerical Simulation of Three-Dimensional Bristle Bending in Brush Seals

Cesare Guardino
CD-adapco Group,
London Office,
200 Shepherd Bush Road,
London W6 7NY, UK
e-mail: cesare@uk.cd-adapco.com

John W. Chew
School of Engineering,
University of Surrey,
Guildford,
Surrey GU2 7XH, UK
e-mail: j.chew@surrey.ac.uk

This paper presents a new method for predicting the three-dimensional (3D) bending behavior of bristles in brush seals. The model builds on and addresses shortcomings in an earlier two-dimensional bending model. The work was motivated by the need to develop a general 3D solid mechanical model that can ultimately be incorporated into CFD models of flow and heat transfer through brush seals. The iterative method considered here, which is based on linear beam-bending theory, allows relatively large numbers of bristles to be considered with arbitrary imposed aerodynamic forces. Bristle-to-bristle contacts and deflections are considered, as well as shaft and backing ring contacts. The method also allows arbitrary initial bristle packs and lay-angles to be considered, as well as periodic conditions so that the model represents a sector of a brush seal. Other physically important features, such as the so-called 3D-splay and inclined prop effects, are also taken into account. The method described here has been incorporated into a new computer code called SUBSIS (Surrey University Brush Seal Iterative Simulator). Example results from this code are presented that show the bending behavior of initially hexagonally packed brush seals under model imposed pressure loads acting on the bristle tips. The effects of rotor incursions into the bristle pack, increase of the pressure load, and changes in the lay-angle and Young's modulus are also shown. The results illustrate the expected bending behavior observed in real brush seals. Procedures for coupling SUBSIS with CFD models are also currently under investigation. [DOI: 10.1115/1.1850943]

Introduction

Conventional brush seals comprise of a dense pack of bristles held between a narrow front plate and a backing ring, as shown in Fig. 1. Over the past 20 years, these advanced seals have emerged to be a very promising technology for gas-path sealing applications in turbo-engines. However, despite much experimentation and the fact that brush seals have successfully operated in jet engines, their behavior is far from being fully understood, and advances are still required if brush seals are to be more generally used. Wear, which occurs as bristle tips contact the rotating parts, is a particular problem. There are, therefore, considerable potential benefits in better understanding and possibly controlling the factors that influence wear. This study is aimed at improving the modeling of brush seals and, hence, giving further insight and predictive capability for their behavior.

Previous investigations have established that brush seals offer improved sealing performance as compared to existing labyrinth seals. Useful data, including leakage rates, pressure distributions, forces on the rotor, and stiffness measurements, have been obtained from both CFD and experimental studies (see, for example, Refs. [1–3]). Prediction of the effects of bristle bending has also been carried out by Hendricks [4] using a "bulk flow model." These results suggest that abrupt flow and pressure changes occur as the rotor clearance changes, but they do not take bristle-to-bristle contacts into account. These latter effects have been considered in the two-dimensional (2D) bending model of Chew et al. [5]. Friction due to the backing ring was later included into this model by Turner et al. [3]. This model was later coupled with a porous CFD brush model by Chen et al. [6], and the model was calibrated using experimental data. Aksit and Tichy [7] used a commercially available FEM package in attempting to build a three-dimensional (3D) model of a brush seal. Results show hysteresis effects when rotor interference is relieved during pressure load, leaving the bristles "hung-up" due to frictional forces. However, no results showing bristle-to-bristle contacts are shown. A commercial FEM code was also used more recently by Crudgington and Bowsher [8,9]. Their results, which included bristle-bristle contacts and friction, showed that hysteresis and blow-down effects are important in determining the brush seal characteristics.

This paper describes an alternative efficient 3D bristle-bending model incorporating bristle-to-bristle, backing ring, and rotor contacts. The method and algorithm, which are specifically designed for brush seal applications, have been coded into a new computer program, which can be run stand-alone or as a "plug-in" for a CFD code. Circumferential periodicity conditions are imposed in order for the model to represent a sector of a brush seal, and arbitrary initial packing arrangements can be considered. Rotor incursions into a perfectly packed periodic brush seal (i.e., hexagonal packing with no initial spacing between bristles and the backing ring) would cause displacements in the axial direction, as the volume of the pack cannot be reduced further. This *3D-splay effect* is also included in the model. At present the model neglects the effects of static and kinetic friction due to the backing ring and/or rotor surface, although these effects are important and should be addressed in later versions. Bristle bending predictions are presented here for a typical brush seal geometry, and qualitative comparisons with previous results are discussed. Note that, although the brush seal is modeled here as a linear bristle pack, rather than a circumferential one, lengths in the width (X) and height (Z) directions are referred to as the circumferential and radial directions, respectively, as shown in Fig. 1.

Basic Theory and Notation

Bristles are identified with the coordinates $(X_{i,j,k}, Y_{i,j,k}, Z_{i,j,k})$ of points along their centerline, and each bristle is subdivided into

---

Contributed by the International Gas Turbine Institute (IGTI) of THE AMERICAN SOCIETY OF MECHANICAL ENGINEERS for publication in the ASME JOURNAL OF ENGINEERING FOR GAS TURBINES AND POWER. Paper presented at the International Gas Turbine and Aeroengine Congress and Exhibition, Vienna, Austria, June 13–17, 2004, Paper No. 2004-GT-53176. Manuscript received by IGTI, October 1, 2003; final revision, March 1, 2004. IGTI Review Chair: A. J. Strazisar.

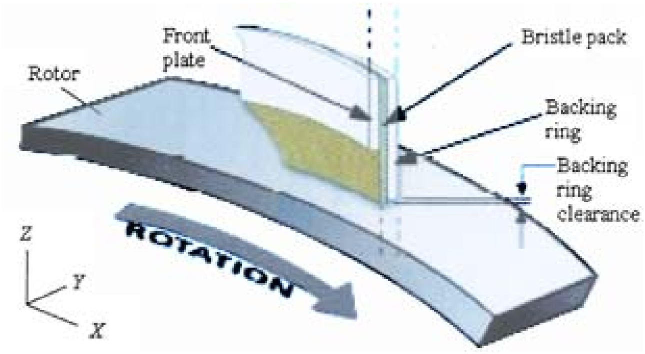

Fig. 1 Schematic of a brush seal

$K-1$ elements, each of length $\Delta\xi = L/(K-1)$. The distance from the fixed bristle root is denoted by $\xi_k = (k-1)\Delta\xi$. A bristle-oriented coordinate system (x, y, z) is also considered, and $b_{i,j,k}$ denotes the point ξ_k along the centerline of the bristle with fixed root at position $(x_{i,j}, y_{i,j})$. This coordinate system is related to the global Cartesian coordinate system (X, Y, Z) using the transformation matrix (see Fig. 2)

$$\begin{pmatrix} X_{i,j,k} \\ Z_{i,j,k} \end{pmatrix} = \begin{pmatrix} \cos\phi & -\sin\phi \\ \sin\phi & \cos\phi \end{pmatrix} \begin{pmatrix} x_{i,j,k} \\ z_{i,j,k} \end{pmatrix} \tag{1}$$

(note that $Y = y$). Here, z is related to the local variable ξ by

$$z_{i,j,k} = L - \xi_k - x_{i,j,k}^{\text{init}} \tan\phi \tag{2}$$

The total force $\mathbf{F}_{i,j,k}$ acting *normal* to a bristle at the point $b_{i,j,k}$ is given by summing the contributions from the aerodynamic pressure force $\mathbf{Q}_{i,j,k}$ and the total reaction force $\mathbf{R}_{i,j,k}$, i.e.,

$$\mathbf{F}_{i,j,k} = \mathbf{Q}_{i,j,k} + \mathbf{R}_{i,j,k}^{\text{bristles}} + \mathbf{R}_{i,j,k}^{\text{rotor}} + \mathbf{R}_{i,j,k}^{\text{br}} \tag{3}$$

Using linear beam-bending theory (see, for example, Ref. [10]) and the Principle of Superposition, it can be shown that the deflection $\Delta\mathbf{s}_{i,j,k}$ of a point is given by

$$\Delta\mathbf{s}_{i,j,k} = \eta_{i,j,k}\mathbf{i} + \zeta_{i,j,k}\mathbf{j} \tag{4}$$

where (see Fig. 3 and Chew et al. [5])

$$\eta_{i,j,k} = \frac{1}{\mathcal{B}} \sum_{m=1}^{K} \tau_{k,m}\mathbf{F}_{i,j,m}\cdot\mathbf{i}, \quad \zeta_{i,j,k} = \frac{1}{\mathcal{B}} \sum_{m=1}^{K} \tau_{k,m}\mathbf{F}_{i,j,m}\cdot\mathbf{j} \tag{5}$$

Here, the *bending stiffness* $\mathcal{B} = E\mathcal{M}$, where E is the modulus of elasticity and $\mathcal{M}$ is the second moment of area, which for a beam of circular cross section of radius R is equal to $\pi R^4/4$. The *beam deformation tensor* $\tau_{k,m}$ is defined here by

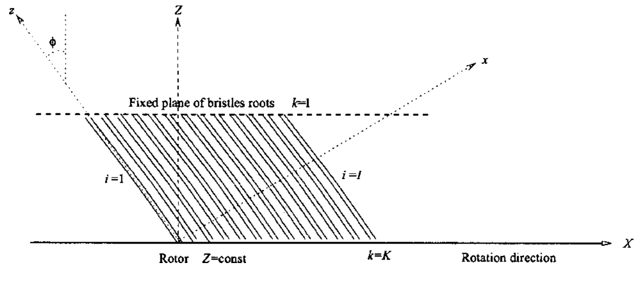

Fig. 2 Global and bristle-oriented coordinates (Y=const plane)

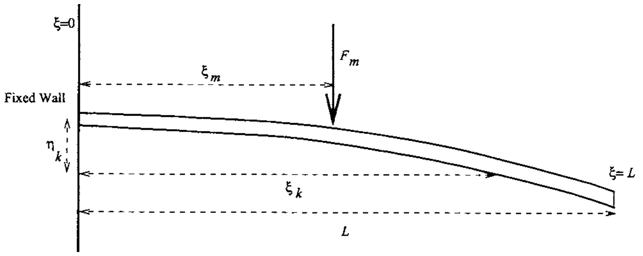

Fig. 3 Bristle deflections and notation

$$\tau_{k,m} = \begin{cases} \dfrac{\xi_k^2 \xi_m}{2} - \dfrac{\xi_k^3}{6} & \text{for} \quad 0 \leqslant \xi_k < \xi_m, \\[2ex] \dfrac{\xi_k \xi_m^2}{2} - \dfrac{\xi_m^3}{6} & \text{for} \quad \xi_m \leqslant \xi_k \leqslant L \end{cases} \tag{6}$$

It can also be shown that in order to move a point $b_{i,j,k}$ by an amount $s_{i,j,k}$, a force of magnitude $r_{i,j,k}$ acting at this point suffices, where

$$r_{i,j,k} = \frac{\mathcal{B}s_{i,j,k}}{\tau_{k,k}} \tag{7}$$

The deflection angles $\alpha_{i,j,k}$ and $\beta_{i,j,k}$ are defined as

$$\tan\alpha_{i,j,k} = \left(\frac{d\eta}{d\xi}\right)_{i,j,k}, \quad \tan\beta_{i,j,k} = \left(\frac{d\zeta}{d\xi}\right)_{i,j,k} \tag{8}$$

Using these definitions, the vector $\mathbf{U}_{i,j,k}$ aligned with the bristle centerline at the point $b_{i,j,k}$ is given by (see Fig. 4)

$$\mathbf{U}_{i,j,k} = -\tan(\alpha_{i,j,k} + \phi)\mathbf{I} - \tan\beta_{i,j,k}\mathbf{J} + \mathbf{K} \tag{9}$$

By taking the dot product of $\mathbf{U}_{i,j,k}$ with $\mathbf{K}$, the deformed lay-angle $\mu_{i,j,k}$ between the Z-axis and the bristle centerline can be shown to be

$$\tan^2\mu_{i,j,k} = \tan^2(\alpha_{i,j,k} + \phi) + \tan^2\beta_{i,j,k} \tag{10}$$

Moreover, the orientation angle $\theta_{i,j,k}$ (relative to the X-axis) of the elliptical cross-sectional geometry of a bristle intersecting a radial (i.e., Z=const) plane is given by

$$\cos\theta_{i,j,k} = \frac{\tan(\alpha_{i,j,k} + \phi)}{\tan\mu_{i,j,k}} \tag{11}$$

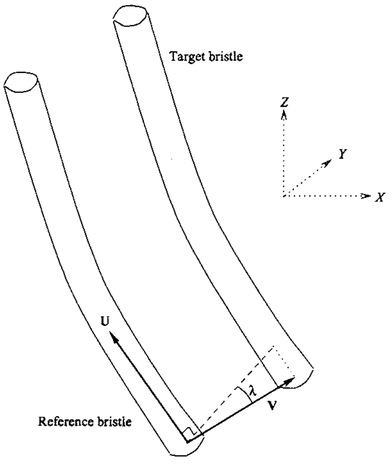

Fig. 4 3D bristle-to-bristle interactions

Method

General Description. A full description of the method and its derivation can be found in Ref. [11], and only a simplified version is presented here. The main idea is to search for points where bristles overlap or where bristles do not contact, but have nonzero reaction forces. The reaction forces $\mathbf{R}_{i,j,k}$ at all points are subsequently corrected in an iterative manner by setting

$$\mathbf{R}_{i,j,k}^{\text{new}}=\mathbf{R}_{i,j,k}^{\text{old}}+\mathbf{r}_{i,j,k} \tag{12}$$

Throughout this report, reaction force vectors in *uppercase* letters denote the actual value of the force, while those in *lowercase* letters represent *corrections* to the force. This results in a consistent set of deflections and reactions when the solution has converged. Bristle points are displaced in an iterative fashion due to either:

1. Movements to enable overlapping points to move "out of" each other (e.g., moving bristle points out of the backing ring)
2. Movements of noncontacting points due to nonzero reaction forces (e.g., a bristle point which is not in contact with the rotor but which has a nonzero reaction force due to the rotor). This will displace a point such that:

a. it just contacts the backing ring, rotor, or another bristle, or
b. it moves until the reaction force at the point has been reduced to zero.

The algorithm can be summarized into the following basic steps, some of which will be decribed further in the proceeding sections. The complete algorithm and the procedures for determining which reaction forces to correct are presented in more detail in Ref. [11].

1. Compute the total forces (i.e., aerodynamic plus reaction forces) on all the bristles and determine their deflections.
2. Calculate resulting deflection, orientation and deformed lay-angles. Apply periodicity conditions.
3. Determine the required corrections to all bristle-bristle, rotor and backing ring reaction forces for all bristles.
4. Compute residuals and determine which reaction forces to adjust by comparing all the computed reactions forces throughout the brush seal.
5. Scan for and adjust the bristle pair with the greatest reaction force surface-angle error (i.e., bristles for which the reaction forces do not point exactly normal to the corresponding bristle surfaces).
6. Apply Newton's Third Law via Eq. (19).
7. Go back to Step 1 and repeat until either the maximum of all the residuals is smaller than a given tolerance or until the calculated reaction forces and displacements have converged.

Bristle-Bristle Interactions. SUBSIS scans bristle pairs by setting the current bristle as a *reference* bristle (i.e., $i=i_{\text{ref}}$ and $j=j_{\text{ref}}$) and identifying *target* bristles by setting

$$i_{\text{tar}}=i_{\text{ref}}+m, \quad j_{\text{tar}}=j_{\text{ref}}+n \tag{13}$$

where the integers m and n range from $-\Lambda$ to Λ. Assigning $\Lambda=1$ means only immediate bristle neighbors are scanned. For $\Lambda>1$, interference of non-neighboring bristles can be considered, but with an increase in computing time. In order to allow all bristles to interact with each other, we can set $\Lambda=\max(I,J)-1$. We also apply periodicity conditions in the circumferential directions if i_{tar} is out of range, i.e.,

$$i_{\text{tar}}=\begin{cases} i_{\text{ref}}+m+I & \text{if} \quad i_{\text{tar}}<1 \\ i_{\text{ref}}+m-I & \text{if} \quad i_{\text{tar}}>I \end{cases} \tag{14}$$

It is convenient to define the vector $\mathbf{V}_{i,j,k,m,n}$ joining two points on neighboring bristles as

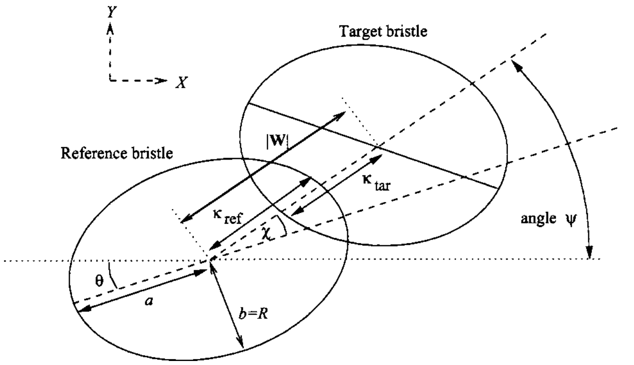

Fig. 5 Bristle interactions in a Z=const plane

$$\mathbf{V}_{i,j,k,m,n}=(X_{i_{\text{tar}},j_{\text{tar}},k}-X_{i,j,k}+\Upsilon C)\mathbf{I}+(Y_{i_{\text{tar}},j_{\text{tar}},k}-Y_{i,j,k})\mathbf{J} + (Z_{i_{\text{tar}},j_{\text{tar}},k}-Z_{i,j,k})\mathbf{K} \tag{15}$$

In order to apply periodicity, the parameter Υ is given by

$$\Upsilon=\begin{cases} 1 & \text{if} \quad i+m>I \\ -1 & \text{if} \quad i+m<I \\ 0 & \text{otherwise} \end{cases} \tag{16}$$

The angle $\lambda_{i,j,k,m,n}$ shown in Fig. 4 can now be found using the following equation:

$$\mathbf{U}_{i,j,k}\cdot\mathbf{V}_{i,j,k,m,n}=|\mathbf{U}_{i,j,k}||\mathbf{V}_{i,j,k,m,n}|\cos(\lambda_{i,j,k,m,n}+\pi/2) \tag{17}$$

It is also useful to define $\mathbf{s}_{i,j,k,m,n}$ as the vector *from* the reference *to* a target bristle *in local bristle coordinates*, i.e.,

$$\mathbf{s}_{i,j,k,m,n}=(x_{i_{\text{tar}},j_{\text{tar}},k}-x_{i,j,k}+\Upsilon C\cos\phi)\mathbf{i}+(y_{i_{\text{tar}},j_{\text{tar}},k}-y_{i,j,k})\mathbf{j} \tag{18}$$

We now define $\mathbf{C}_{i,j,k,m,n}$ to be the reaction force acting *on* a reference bristle centerline point $b_{i,j,k}$ *from* a target point $b_{i_{\text{tar}},j_{\text{tar}},k}$. According to Newton's third law, an equal and opposite reaction force must also be imposed on the target bristle $b_{i_{\text{tar}},j_{\text{tar}},k}$ by setting

$$\mathbf{C}_{i_{\text{tar}},j_{\text{tar}},k,-m,-n}=-\mathbf{C}_{i,j,k,m,n} \tag{19}$$

If contact occurs with a target bristle point $b_{i_{\text{tar}},j_{\text{tar}},k}$ (i.e., if $\iota_{i,j,k,m,n}>0$), then it can be shown that the *corrective* reaction force $\mathbf{c}_{i,j,k,m,n}$ required to just separate the bristles is given by

$$\mathbf{c}_{i,j,k,m,n}=-\frac{\mathcal{B}\iota_{i,j,k,m,n}}{2\tau_{k,k}}\hat{\mathbf{s}}_{i,j,k,m,n} \tag{20}$$

Without the 3D-splay effect, the interference $\iota_{i,j,k,m,n}$ is calculated using

$$\iota_{i,j,k,m,n}=2R-|\mathbf{s}_{i,j,k,m,n}| \tag{21}$$

With 3D-splay effects taken into account, it can be shown using geometric considerations that

$$\iota_{i,j,k,m,n}=(\kappa_{i,j,k,m,n}^{\text{ref}}+\kappa_{i_{\text{tar}},j_{\text{tar}},k,i,j}^{\text{tar}}-|\mathbf{W}_{i,j,k,m,n}|)\cos\lambda_{i,j,k,m,n} \tag{22}$$

where (see Fig. 5)

$$\kappa=\frac{a_{i,j,k}b_{i,j,k}}{\sqrt{a_{i,j,k}^2+(b_{i,j,k}^2-a_{i,j,k}^2)\cos^2\chi_{i,j,k,m,n}}} \tag{23}$$

$$a_{i,j,k}=R/\cos\mu_{i,j,k}, \quad b_{i,j,k}=R \tag{24}$$

$$\chi_{i,j,k,m,n}=\psi_{i,j,k,m,n}-\theta_{i,j,k} \tag{25}$$

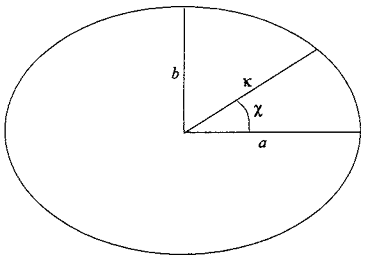

Fig. 6 Ellipse geometry and notation

$$\mathbf{W}_{i,j,k,m,n}=(X_{i_{\mathrm{tar}},j_{\mathrm{tar}},k}-X_{i,j,k}+\Upsilon C)\mathbf{I}+(Y_{i_{\mathrm{tar}},j_{\mathrm{tar}},k}-Y_{i,j,k})\mathbf{J} \tag{26}$$

Here, κ represents the length of a straight line from the center of an ellipse (with semi-major and minor axes denoted by a and b, respectively) to a point on its surface located at an angle χ measured from the major axis, as shown in Fig. 6. The reference-to-target angle $\psi_{i,j,k,m,n}$ shown in Fig. 5 in a radial plane is computed using the relationship

$$\cos \psi_{i,j,k,m,n}=\frac{\mathbf{W}_{i,j,k,m,n}\cdot \mathbf{I}}{|\mathbf{W}_{i,j,k,m,n}|} \tag{27}$$

If contact does not occur for points with nonzero reaction forces (i.e., if $\iota_{i,j,k,m,n}<0$), then it can be shown using geometrical considerations that the displacement, which would cause this point to just contact a neighboring bristle, is given by (see Fig. 7)

$$s_{i,j,k,m,n}=\tfrac{1}{2}\{d \cos \sigma-\sqrt{4R^2-d^2 \sin^2 \sigma}\}_{i,j,k,m,n} \tag{28}$$

It follows that the corrective reaction force at this point is calculated using

$$\mathbf{c}_{i,j,k,m,n}=-\frac{\mathcal{B}}{\tau_{k,k}}\min\left(s_{i,j,k,m,n},\frac{|\mathbf{C}^{\mathrm{old}}_{i,j,k,m,n}|\tau_{k,k}}{\mathcal{B}}\right)\hat{\mathbf{R}}^{\mathrm{old}}_{i,j,k,m,n} \tag{29}$$

where the negative sign indicates the correction force acts in the direction to reduce the magnitude of the reaction force. Finally, the total reaction force at $b_{i,j,k}$ is computed by summing the contributions due to all the scanned target bristles

$$\mathbf{R}^{\mathrm{bristles}}_{i,j,k}=\sum_{m=-\Lambda}^{\Lambda}\sum_{n=-\Lambda}^{\Lambda}\mathbf{c}_{i,j,k,m,n} \tag{30}$$

It should be noted that the computed reaction force may not lie normal to the bristle surfaces (due to other 3D bristle deflections occuring within the bristle pack). In order to reduce this error, the reaction force must be realigned normal to the bristle surface, but with its magnitude kept constant as shown in Fig. 8. The net effect of this rotation is to displace the point $b_{i,j,k}$ by an amount $|\Delta \mathbf{c}_{i,j,k,m,n}|$, where

$$|\Delta \mathbf{C}_{i,j,k,m,n}|=|\mathbf{C}^{\mathrm{new}}_{i,j,k,m,n}-\mathbf{C}^{\mathrm{old}}_{i,j,k,m,n}|\le 2|\mathbf{C}^{\mathrm{old}}_{i,j,k,m,n}| \tag{31}$$

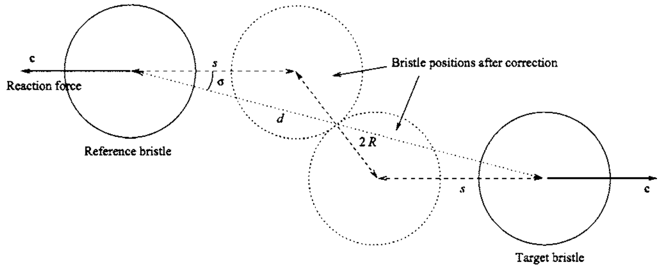

Fig. 7 Free bristle-point movement in a ξ=const plane

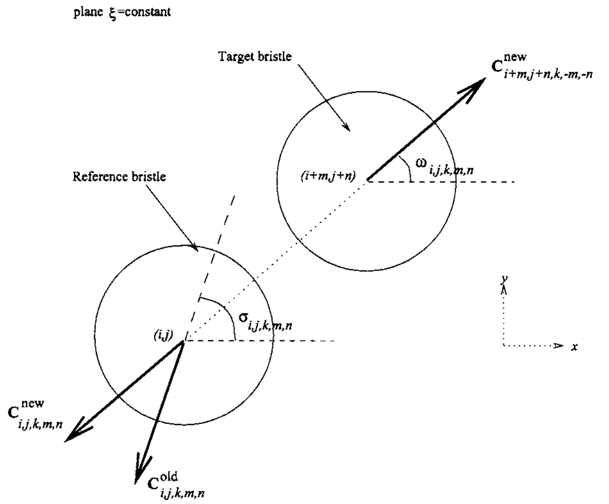

Fig. 8 Rotation of reaction forces

Since this quantity can be quite large, the rotation is relaxed by setting

$$\mathbf{C}^{\mathrm{new}}_{i,j,k,m,n}=\mathbf{C}^{\mathrm{old}}_{i,j,k,m,n}+\Omega_{\mathrm{rotate}}(\mathbf{C}^{\mathrm{new}}_{i,j,k,m,n}-\mathbf{C}^{\mathrm{old}}_{i,j,k,m,n}) \tag{32}$$

In this way, the reaction force is "nudged" in the right direction, and the overall stability of the iterations is conserved.

Bristle-Rotor Interactions. The amount of rotor interference $\iota_{i,j,K}$ is given by (cf. Fig. 9)

$$\iota_{i,j,K}=Z_{\mathrm{rotor}}-Z_{i,j,K} \tag{33}$$

Using 3D vector analysis, it can be shown that the corrective reaction force on the bristles due to interactions with the rotor is given by (see Fig. 9)

$$\mathbf{r}^{\mathrm{rotor}}_{i,j,K}=\frac{r_{i,j,K}}{\sin \mu_{i,j,K}}\{\sin(\alpha_{i,j,K}+\phi)\mathbf{i}+\sin \beta_{i,j,K}\mathbf{j}\} \tag{34}$$

where

$$r_{i,j,K}=\frac{\mathcal{B}}{\tau_{K,K}}\min\left(|\iota_{i,j,K}|,\frac{R^{\mathrm{radial}}_{i,j,K}\tau_{K,K}\sin^2 \mu}{\mathcal{B}}\right) \tag{35}$$

Assuming frictionless contact, the corrective reaction force $\mathbf{n}_{i,j,K}$ on the rotor points entirely in the radial direction and can be computed using

$$\mathbf{n}_{i,j,K}=\frac{|\mathbf{r}^{\mathrm{rotor}}_{i,j,K}|}{\sin \mu_{i,j,K}}\mathbf{K} \tag{36}$$

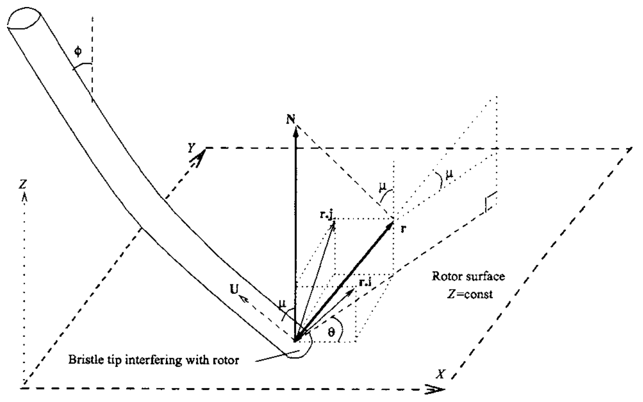

Fig. 9 Rotor interference, 3D global view

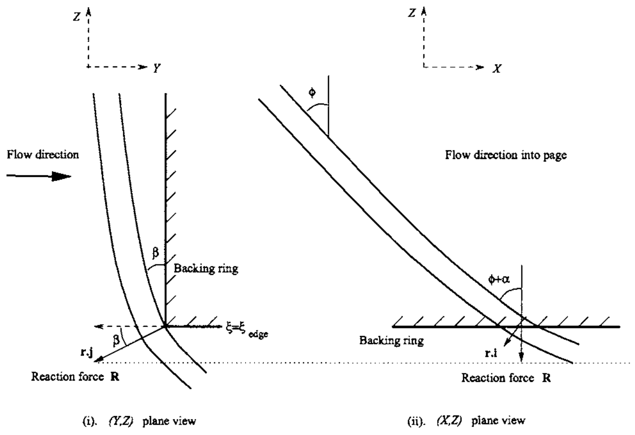

Fig. 10 Bristle-backing ring reactions

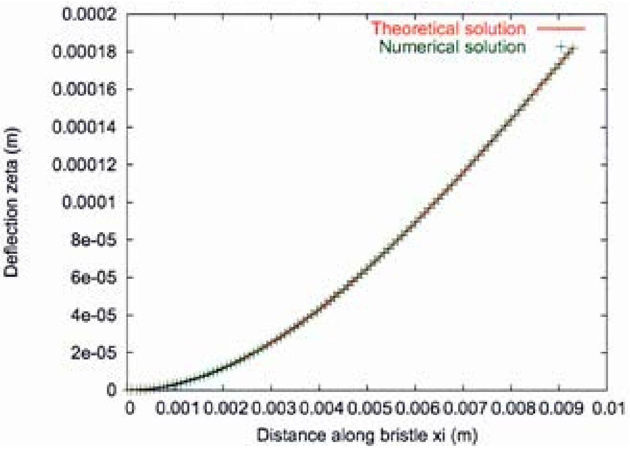

Fig. 11 Bending of a row of bristles

Bristle-Backing Ring Interactions. The amount of interference $\boldsymbol{\iota}_{i,j,k}$ into the backing ring is given by (cf. Fig. 10)

$$\boldsymbol{\iota}_{i,j,k}=Y_{i,j,k}+R-Y_{\mathrm{br}} \tag{37}$$

It can be shown that the corrective reaction force on the bristles due to interactions with the backing ring is given by (see Fig. 10)

$$\mathbf{r}^{\mathrm{br}}_{i,j,k}=-r_{i,j,k}\{\sin\beta_{i,j,k}\sin(\phi+\alpha_{i,j,k})\mathbf{i}+\mathbf{j},\} \tag{38}$$

where

$$r_{i,j,k}=\frac{\mathcal{B}}{\tau_{k,k}}\min\left(|\boldsymbol{\iota}_{i,j,K}|,\frac{|\mathbf{R}^{\mathrm{br}}_{i,j,K}|\tau_{k,k}}{\mathcal{B}}\right) \tag{39}$$

Notice that the **i** component, which is much smaller than the **j** component, is due to the so-called inclined 3D-prop effect. This occurs only if the reaction force is located at (or very close to) the backing ring edge (i.e., if $\xi_k\approx\xi_{\mathrm{edge}}$) and implies that the bristles are bent downward toward the rotor and in the circumferential direction. Otherwise, the reaction force is directed entirely in the axial direction.

SUBSIS (Surrey University Brush Seal Iterative Simulator). The 3D method described here has been implemented into a new FORTRAN 90 code called SUBSIS (Ref. [12]). This code is capable of handling arbitrary initial brush seal geometries, operating conditions, and imposed forces. These forces can either be obtained from CFD calculations, experimental results or simple theoretical models (the latter has been employed here). All target bristles, the backing ring and rotor are considered as generic "objects" with which a reference bristle can interact. This allowed the code to be written in a modular fashion, which can later be expanded to allow additional features to be included. SUBSIS has also been developed with the ultimate aim of being coupled with CFD or other CAD packages. In order to allow this, a generic method of importing/exporting aerodynamic forces and current bristle coordinates to/from SUBSIS was included in the design specification.

A quantitave comparison of the SUBSIS results with experimental data was not possible at this stage due to the idealized conditions, although the results do show the expected behavior. However, comparison with theoretical results have been obtained for a single bristle in contact with the backing ring or rotor. In all cases the comparison with the theoretical solutions was accurate to within the round-off error. The code has also been tested on Windows®, Linux, SGI (IRIX 64-bit), and SUN operating systems.

The main bristle-to-bristle contact routines have also been validated for the case of a single row of four bristles with no initial gap between them (see Fig. 11). The length L and bristle diameter $2R$ were taken as 9.30 mm and 0.0760 mm, respectively. The first bristle is subjected to a concentrated force F of 10^{-3} N at its tip in the plane of the bristle row. This results in a uniform deflection of all the bristles, and the linear beam bending theory provides a simple theoretical solution for the deflection profile ζ of each bristle

$$N\mathcal{B}\zeta_{\mathrm{theory}}=-\frac{F\xi^3}{6}+\frac{FL\xi^2}{2} \tag{40}$$

where the number of bristles $N=4$ in this case.

Figure 12 shows a 3D view of a hexagonally packed brush model with no lay-angle, backing ring, or rotor (the geometrical parameters are the same as those in Table 1, but with $\phi=0$ deg and no periodicity conditions). One of the corner bristles is subjected to a concentrated external force $\mathbf{F}_{1,1,K}=2\times10^{-3}\mathbf{I}+2\times10^{-3}\mathbf{J}$ applied at the tip, causing it to bend and split the brush into two parts. For this simulation, the bristle search parameter Λ was set as 7 in order to allow all bristles to interact with each other. Although no comparsion with analytical solutions was possible, due to the highly nonlinear solution, this case demonstrates the capability of the main bristle-to-bristle contact routines to deal with complicated cases.

Results

Example results using SUBSIS are shown here for brush seals with parameters that are representative of those used in Refs. [2,3,5] (see Table 1). The value of the Young's modulus is representative of a cobalt-based alloy known as Haynes-25 (see Ref. [14]). Table 2 presents a summary of the assumed boundary and operating conditions. Only converged solutions are shown in this paper for which all the displacement residuals are much smaller (typically by a factor of 10^{-3}) than the local point deflections.

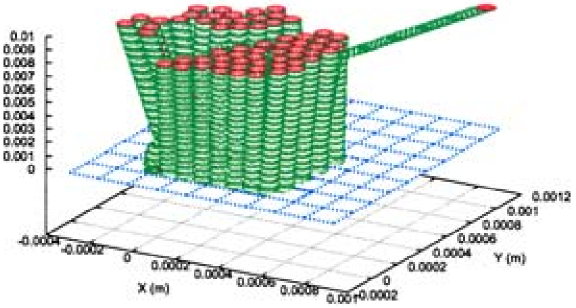

Fig. 12 Incursion of a single bristle into a hexagonally-packed brush

Table 1 "Standard" brush seal parameters

Initial packing type		Hexagonal
Initial minimum spacing	δ	0.000760 mm
Total number of bristles	$I\times J$	64
Lay-angle	ϕ	45 deg
Radial length	$L/\cos\phi$	9.30 mm
Overhang height	H	1.40 mm
Circumferential length	C	0.836 mm
Axial length	W	0.541 mm
Bristle diameter	$2R$	0.0760 mm
Young's modulus	E	2.25×10^{11} N/m^2
Relaxation parameter	Ω	0.01
Number of elements per bristle	K	20

Note also that the results appear to be grid independent provided the number of elements per bristle K is not too small. All results were obtained using double precision accuracy.

In general, the aerodynamic force $\mathbf{Q}_{i,j,k}$ must be supplied from an external CFD program or experimental data. SUBSIS accepts arbitrary force vectors at all bristle points in both the circumferential and axial directions. For the results shown here, the following simple linear distribution in $Y_{i,j,k}$ was employed:

$$\mathbf{Q}_{i,j,k}=\begin{cases}\left\{(1-\gamma)+\dfrac{2\gamma}{W}Y_{i,j,k}\right\}Q^{\text{axial}}_{\text{average}}\mathbf{J} & \text{if} \quad k=K\\ \mathbf{0} \quad \text{otherwise} & \end{cases} \tag{41}$$

In the above equation, $Q^{\text{axial}}_{\text{average}}$ represents the averaged axial force per bristle. This was determined using the following simple relationship based on the pressure gradient Δp across the seal and the cross-sectional area CH between the backing ring and rotor for the segment of the brush seal under consideration:

$$Q^{\text{axial}}_{\text{average}}=\frac{CH\Delta p}{IJ} \tag{42}$$

The parameter γ can be specified by the user, and for all of the solutions shown here, this was taken as 0.2. Although not shown, the numerical results were found to be almost insensitive to this parameter. No external circumferential forces are considered in the results shown here.

Figure 13 shows the tip positions for a converged solution in which there is no pressure load, but in which the rotor position was gradually moved into the pack (in 10,000 iterations) from no initial interference, up to a final incursion of 0.20 mm. For this case, the minimum initial spacing δ between the bristles was taken as 0.0 mm (i.e., the brush was perfectly packed). It is evident that the displacements of the bristles in the axial upstream direction are entirely due to the 3D-splay effect. Figure 14 shows a 3D view of the bristle deflections.

Figures 15–17 show the solution for the case of a brush seal in which both the pressure load and rotor interference were gradually increased from zero up to their final values of 1.0 bar and 0.20 mm in 50,000 iterations. The numerical results show the expected bending behavior of the bristles. Figure 18 shows that the radial force on the rotor is not uniform (which may be partly responsible for the uneven wear typically observed on rotors). These results also suggest a "mechanical transmission" of reaction forces toward the upstream bristles, which help to "hold up" the downstream bristles. Further work is suggested to study this effect. This typical SUBSIS calculation took approximately 50 min to complete using a 1.0 GHz processor with the Red Hat Linux operating system. (For comparison, Ref. [9] report typical computing times of 6–20 h on a Pentium 4 PC for a 9×5 bristle pack simulation obtained using commercial finite-element software.)

Table 2 Summary of operating conditions and assumptions

Circumeferential direction	X	Periodic conditions
Axial direction	Y	Applied force Eq. (41)
Radial direction	Z	Fixed bristle roots at $k=1$
Initial rotor interference	Z_{rotor}	0.0–0.4 mm
Applied pressure load	Δp	0.0–8.0 bar
Bristle-bristle contacts		Yes, with 3D-splay effects
Backing ring contacts		Yes, with 3D-prop effects
Rotor contacts		Yes
Friction		No

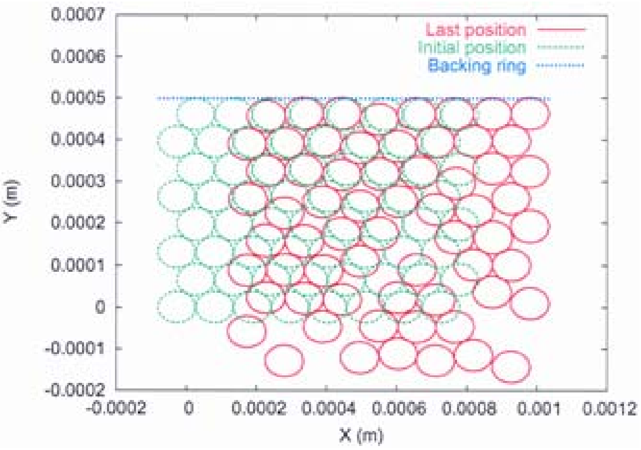

Fig. 13 Bristle tip positions ($\Delta p=0.0$ bar, $Z_{\text{rotor}}=0.20$ mm, $\phi=45$ deg, $\delta=0.0$ mm)

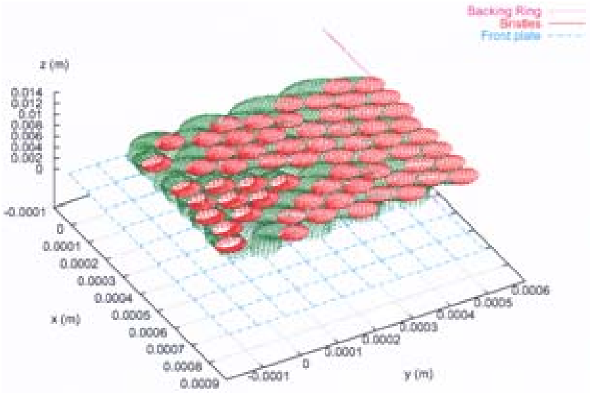

Fig. 14 3D bristle deflections ($\Delta p=0.0$ bar, $Z_{\text{rotor}}=0.20$ mm, $\phi=45$ deg, $\delta=0.0$ mm)

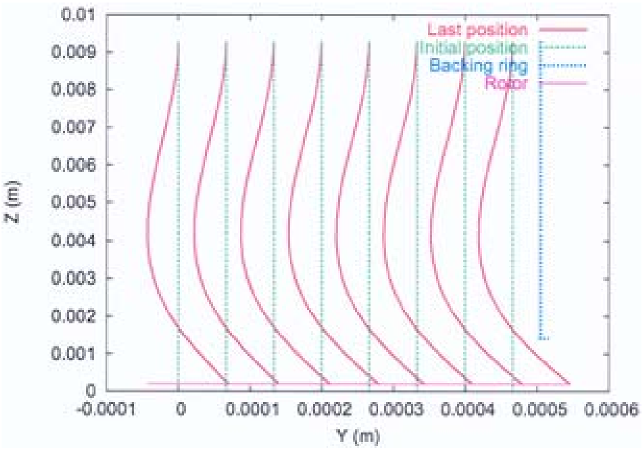

Fig. 15 Deflections of first bristle column ($\Delta p=1.0$ bar, $Z_{\text{rotor}}=0.20$ mm, $\phi=45$ deg)

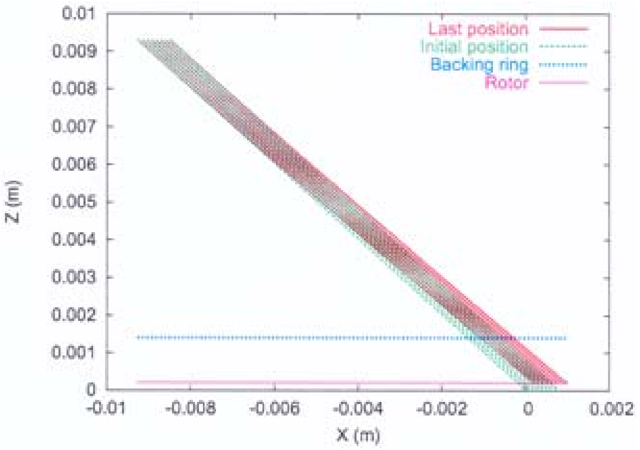

Fig. 16 Deflections of downstream bristle row ($\Delta p = 1.0$ bar, $Z_{\text{rotor}} = 0.20$ mm, $\phi = 45$ deg)

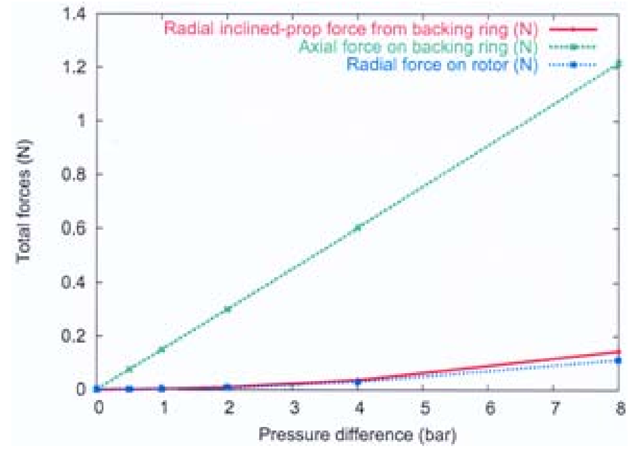

Fig. 19 Effect of increasing the pressure load Δp ($Z_{\text{rotor}} = 0.20$ mm, $\phi = 45$ deg)

Figure 19 presents results for various imposed pressure differences. The rotor was kept fixed throughout the calculation at $Z_{\text{rotor}} = 0$ mm (i.e., no initial rotor interference). As expected, the results show an almost linear increase in the computed value of the axial force $F^{\text{axial}}_{\text{br}}$ on the backing ring. The radial force $F^{\text{radial}}_{\text{rotor}}$ on the rotor is due to bristle-bristle contacts forcing some bristles to come into contact with the rotor, and also due to the radially downward force due to the inclined-prop effect. Moreover, the radial forces $F^{\text{radial}}_{\text{rotor}}$ and $F^{\text{radial}}_{\text{br}}$ on the rotor and backing ring increase approximately as the square of the applied pressure load Δp [this is due to Eq. (38)]. Thus, the inclined-prop effect becomes more significant as the pressure difference increases, with possible consequences for increased wear on the rotor and bristle tips.

Figure 20 presents results for increasing rotor interference Z_{rotor}, but this time with a more severe fixed imposed pressure load of 4.0 bar. Also shown is the theoretical value of the radial force $F^{\text{radial}}_{\text{rotor}}$ on the rotor due to a single bristle (multiplied by the total number of bristles). This is given by

$$R^{\text{radial}}_{\text{theory}} = \frac{3\mathcal{B}Z_{\text{rotor}}}{L^3 \sin^2 \phi} \times I \times J \qquad (43)$$

It is evident from the solutions that Eq. (43) is not a good approximation for the computed value of $F^{\text{radial}}_{\text{rotor}}$. Moreover, there is a significant reaction force on the rotor, mainly due to the inclined prop-effect, even when there is no initial rotor interference. These results highlight the importance of the 3D-splay and inclined-prop effects in order to calculate the forces in a brush seal.

Figures 21 and 22 present additional results for brush seals with parameters as shown in Table 1, but with varying lay-angles and Young's modulus, respectively. In both cases, Eq. (43) gives the same trend as the numerical results, but discrepancies do appear for seals with relatively small lay angles or Young's modulus.

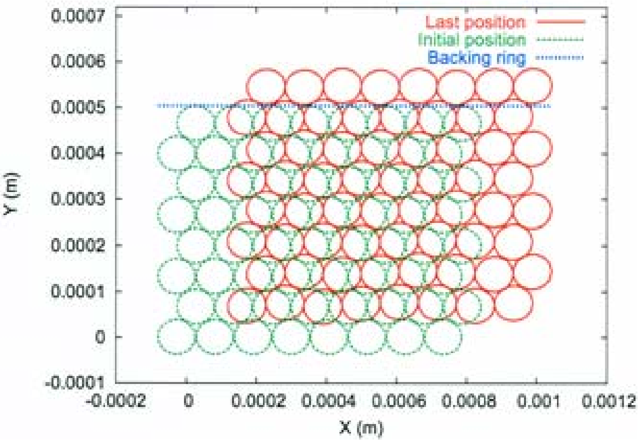

Fig. 17 Bristle tip positions ($\Delta p = 1.0$ bar, $Z_{\text{rotor}} = 0.20$ mm, $\phi = 45$ deg)

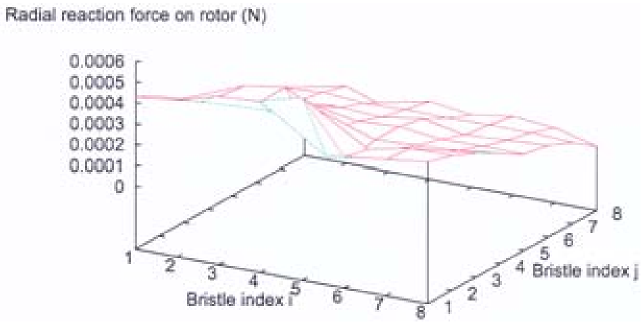

Fig. 18 Radial force on rotor ($\Delta p = 1.0$ bar, $Z_{\text{rotor}} = 0.20$ mm, $\phi = 45$ deg)

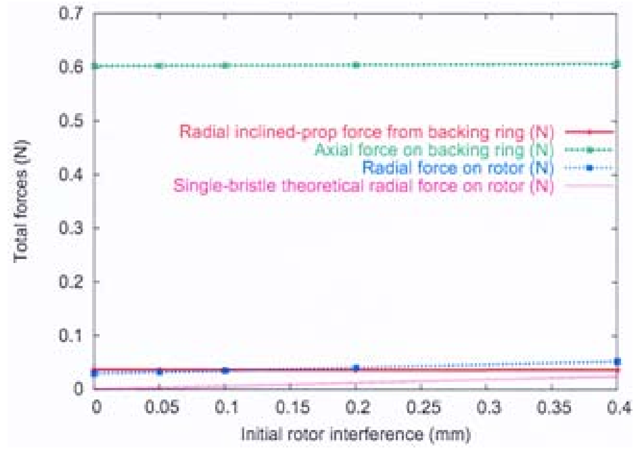

Fig. 20 Effect of increasing rotor interference Z_{rotor} ($\Delta p = 4.0$ bar, $\phi = 45$ deg)

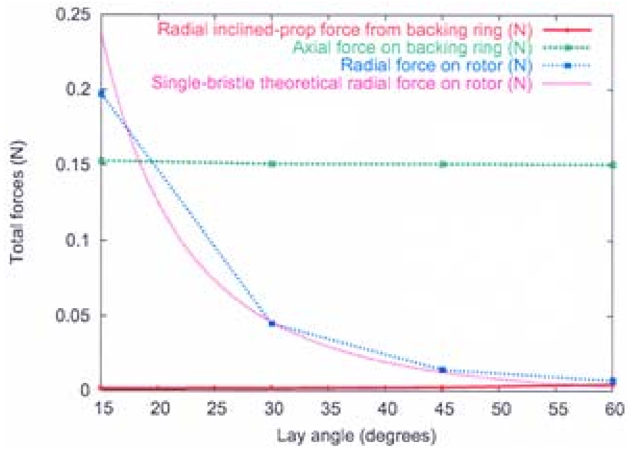

Fig. 21 Effect of increasing the lay-angle ϕ (Δp=1.0 bar, Z_{rotor}=0.20 mm)

Conclusion

A new predictive capability for the 3D bending of bristles in brush seals has been developed and tested. Results using this model have been obtained that are qualitatively consistent with the expected 3D bending behavior of brush seals. Calculated values for the reaction forces on the rotor and backing ring are obtained and compared for different pressure loads and rotor incursions into the bristle pack. The 3D-splay effect is also highlighted in the results as an important effect that must be taken into account. The results show that the classical approximation to the radial force on the rotor due to bristle interactions (see Eq. (43)) may not yield reliable estimates for brush seals operating at high pressure loads or for seals with relatively small lay-angles or Young's modulus. Possible hysteresis due to the deformation history of the bristles has been observed but not reported in the current results, requiring further analysis.

Further work could involve incorporating frictional effects between the bristles and the backing ring or shaft surfaces. As shown by Crudgington and Bowsher [8,9], these effects are important and should be addressed. Additional geometrical effects due to brush seals of small rotor radii may also need to be considered. Conservation of bristle length, which is not satisfied using standard linear beam-bending theory, may also need to be considered for cases with relatively large bristle deflections. The ultimate goal is to couple the current 3D method with a CFD brush seal model similar to that used by Guardino and Chew [13] (see Ref. [6] for details of a 2D coupled model).

Although the new model developed here does not capture the full complexity of brush seal behavior, it can aid in the design stage of new brush seals by parametrically varying the geometrical and operating parameters.

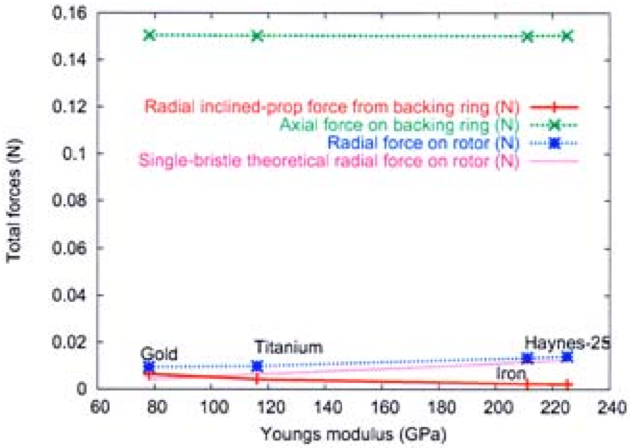

Fig. 22 Effect of varying the Young's modulus E (Δp =1.0 bar, Z_{rotor}=0.20 mm, ϕ=45 deg)

Nomenclature

a, b = elliptical semi-major and minor axes
$\mathcal{B}$ = bending stiffness ($=E\mathcal{M}$)
$\mathbf{c}$ = bristle-bristle corrective reaction force
$\mathbf{C}$ = bristle-bristle actual reaction force
C = circumferential length of brush seal model
E = modulus of elasticity
$F_{\text{br}}^{\text{axial}}$ = axial reaction force on backing ring
$F_{\text{br}}^{\text{radial}}$ = radial reaction force on backing ring
$F_{\text{rotor}}^{\text{radial}}$ = radial reaction force on rotor
$\mathbf{F}$ = total force
H = backing ring overhang height
$\mathbf{i}, \mathbf{j}, \mathbf{k}$ = unit vectors in the x, y and z directions
$\mathbf{I}, \mathbf{J}, \mathbf{K}$ = unit vectors in the X, Y and Z directions
i, j, k = grid point indices in (X,Y,Z) coordinates
I, J, K = maximum value of indices in i, j, k, respectively
L = actual length of bristles
$\mathcal{M}$ = second moment of area
$\mathbf{n}$ = corrective radial force on rotor
$\mathbf{Q}$ = aerodynamic force
$Q_{\text{average}}^{\text{axial}}$ = averaged model axial aerodynamic force
$\mathbf{r}$ = correction force
$\mathbf{s}$ = reference-to-target vector in a ξ=const plane
$\mathbf{R}$ = total reaction force
R = radius of bristles
$\mathbf{U}$ = vector aligned with bristle center-line
$\mathbf{V}$ = reference-to-target vector in a Z=const plane
$\mathbf{W}$ = reference-to-target vector in Z=const plane
W = axial length of brush seal model
x, y, z = bristle-oriented coordinates
X, Y, Z = circumferential, axial and radial coordinates
α, β = deflection angles in x and y-directions
γ = ratio used in Eq. (41)
δ = initial gap clearance between bristles and backing ring
Δp = pressure difference across seal
η, ζ = bristle deflections in the x and y-directions
θ = bristle orientation angle (see Eq. (11))
ι = local interference
κ = ellipse center-to-surface length
λ = 3D bristle interaction angle
Λ = target bristle search parameter (integer$\geqslant$1)
μ = deformed lay-angle (see Eq. (10))
ξ = coordinate along bristle length (=0 at fixed bristle end)
σ = angle between reaction force and target point
τ = beam deformation tensor
ϕ = lay angle (=0 deg for radially aligned bristles)
χ = ellipse center-to-surface angle
Υ = periodicity parameter (see Eq. (16))
ψ = reference-to-target angle in a Z=const plane
ω = reference-to-target angle in a ξ=const plane
Ω = relaxation parameter
$b_{i,j,k}$ = center-line point on bristle (i,j) at position ξ_k.
br = backing ring
edge = edge (overhanging) part of backing ring
init = initial (unperturbed) value
old = value at previous iteration
ref = reference bristle
rotor = rotor surface

tar = target bristle
tip = bristle tip
$\hat{\mathbf{v}}$ = unit vector in the direction of the vector $\mathbf{v}$

References

[1] Chupp, R. E., and Holle, G. F., 1992, "Simple Leakage Model for Brush Seals," *Proc. of 27th AIAA/SAE/ASME Joint Propulsion Conference*, AIAA, Washington, DC, Paper No. 91-1913.
[2] Bayley, F. J., and Long, C. A., 1992, "A Combined Experimental and Theoretical Study of Flow and Pressure Distributions in a Brush Seal," ASME, New York, ASME Paper No. ASME 92-GT-355.
[3] Turner, M. T., Chew, J. W., and Long, C. A., 1997, "Experimental Investigation and Mathematical Modelling of Clearance Brush Seals," ASME Paper No. 97-GT-282.
[4] Hendricks, R. C., Schlumbergeer, S., Braun, M. J., Choy, F., and Mullen, R. L., 1991, "A Bulk Flow Model of a Brush Seal System," ASME Paper No. 91-GT-235.
[5] Chew, J. W., Lapworth, B. L., and Millener, P. J., 1995, "Mathematical Modelling of Brush Seals," Int. J. Heat Fluid Flow, **16**, 493–500.
[6] Chen, L. H., Wood, P. E., Jones, T. V., and Chew, J. W., 1998, "An Iterative CFD and Mechanical Brush Seal Model and Comparison With Experimental Results," ASME Paper No. 98-GT-372.
[7] Aksit, M. F., and Tichy, J. A., 1996, "A Computational Model of Brush Seal Bristle Deflection," *Proc. of 32nd AIAA/ASME/SAE/ASEE Joint Propulsion Conference*, AIAA, Washington, DC, Paper No. 96-2909.
[8] Crudgington, P. F., and Bowsher, A., 2002, "Brush Seal Pack Hysteresis," *38th AIAA/ASME/SAE/ASEE Joint Propulsion Conference and Exhibit*, AIAA, Washington, DC, Paper No. 2002–3794.
[9] Crudgington, P. F., and Bowsher, A., 2003, "Brush Seal Blow Down," *39th AIAA/ASME/SAE/ASEE Joint Propulsion Conference and Exhibit*, AIAA, Washington, DC, Paper No. 2003–4697.
[10] Fenner, R. T., 1989, *Mechanics of Solids*, Blackwell Scientific Publications.
[11] Guardino, C., 2003, "Numerical Simulation of 3D Bristle Bending in Brush Seals," University of Surrey Research Report, FRC/2002.13.
[12] Guardino, C., 2003, SUBSIS (*Surrey University Brush Seal Iterative Simulator*), Version 3.01—User Guide, University of Surrey Research Report.
[13] Guardino, C., and Chew, J. W., 2002, "Simulation of Flow and Heat Transfer in the Tip Region of a Brush Seal," University of Surrey Research Report, FRC/2002.03.
[14] http://www.alloywire.com/haynes25.htm

Cogenerative Below Ambient Gas Turbine (BAGT) Performance With Variable Thermal Power

M. Bianchi
e-mail: Michele.bianchi@mail.ing.unibo.it

G. Negri di Montenegro

A. Peretto

Universitá di Bologna,
Viale Risorgimento, 2,
40136 Bologna, Italia

The use of gas turbine and combined cycle power plants for thermal and electric power generation is, nowadays, a consolidated technology. Moreover, the employment of combined heat and power production, especially for low power requirements, is constantly increasing. In this scenario, below ambient pressure discharge gas turbine (BAGT) is an innovative and interesting application; the hot gases discharged from a gas turbine may be expanded below ambient pressure to obtain an increase in electric power generation. The gases are then cooled to supply heat to the thermal utility and finally recompressed to the ambient pressure. The power plant cogenerative performance depends on the heat and electric demand that usually varies during the year (for residential heating the heat to electric power ratio may range from 0.3 to 9). In this paper, the thermal load variation influence on the BAGT performance will be investigated and compared with those of gas turbine and combined cycle power plants. [DOI: 10.1115/1.1707032]

Introduction

The widespread of cogenerative applications with low temperature levels (district heating, etc.), especially for small-size applications (less than $15\,\mathrm{MW_{el}}$), enhances the interest around advanced gas turbine cycles with higher electric efficiencies and, consequently, lower discharge gas temperatures.

The displacement, at the gas turbine discharge, of an inverted Brayton cycle may represent a way to increase the power plant electric efficiency, [1,2]; in fact, the inverted Brayton cycle reduces the hot gas temperature, producing additional power. The cogenerative application of an inverted Brayton cycle was investigated in an Authors previous work, [3].

The obtained results have encouraged the study of a new gas turbine plant, called below ambient pressure discharge gas turbine (BAGT), [4]. In this power plant the gas expansion continues below the ambient pressure and before stack discharge the gas must be cooled by the thermal utility and recompressed by an additional compressor.

Moreover, in order to enhance BAGT electric performance, before recompression, the exhaust gas may be further cooled employing a cooler, fed with cooling water and disposed after the thermal utility, that reduces the work of second compressor, [5].

The previous papers of the authors highlight that, with respect to gas turbine, when BAGT is employed, in design working conditions, a relevant convenience occurs, in terms of electric and cogenerative performance.

It should be highlighted that the thermal power request often varies, during the day and/or the year, according with the industrial process connected with the cogenerative power plant. As a consequence, the study of the thermal part load of the cogenerative power plants is necessary.

In particular, in the BAGT, the employment of a cooler may help to maintain high electric efficiency also with variable thermal load. In this paper, the BAGT thermal load cogenerative performance is investigated by searching the best cooler design that permits to maximize the electric efficiency minimizing the BAGT investment cost. The obtained results are compared to those regarding a gas turbine and a combined cycle cogenerative power plants within the electric power range from 5 to $15\,\mathrm{MW_{el}}$.

Thermal Part-Load Analysis

The BAGT Configuration and Design Performance. The configuration of the below ambient pressure discharge gas turbine (BAGT) here assumed for the thermal part load analysis is shown in Fig. 1. In particular, the first compressor C1 compresses and sends the air to a combustor where the fuel oxidation provides the temperature increase. The hot gas is then expanded in the turbine T below the ambient pressure and later cooled in the first heat exchanger HX1 and in the cooler CL. Finally, the exhaust gas is recompressed to the ambient pressure in a second compressor C2 and, before its discharge, cooled in the second heat exchanger HX2.

The cold side of the two heat exchanger HX1 and HX2 is fed with water coming from the thermal utilities at 60°C and the temperature of the water sent to the thermal utilities is here assumed equal to 90°C (typical values for residential heating). In both heat exchangers, the minimum temperature difference between the hot gas outlet and the cold water inlet is assumed equal to 15°C. Thanks to this, the cooler employment is necessary when a second compressor inlet temperature lower than 75°C is required.

It should be noted that, the BAGT power plant may be built adding, to an existing gas turbine, an expander stage (from ambient pressure to p_4) and a second compressor; this permits to not redesign all the gas turbine, but only the additional stages strongly reducing the investment costs.

With regard to the cooler, the temperature of the cooling water coming in is assumed equal to 15°C (ambient temperature in temperate climate) and its maximum temperature rise equal to 10°C (typical value compatible with environmental impact); moreover, the hot gas outlet temperature T_5 is imposed equal to 50°C (to avoid water condensing).

In Table 1, the key parameters assumed for the design performance evaluation and for the BAGT power plant dimensioning are reported. In particular, the first compressor pressure ratio and the pressure at the turbine outlet are imposed equal to 22 and 0.5 bar, respectively; these values are chosen to maximize the electric efficiency of the BAGT as shown in [5]. It should be noted that the values assumed are typical for small size gas turbine ranging from 5 to $15\,\mathrm{MW_{el}}$.

Contributed by the International Gas Turbine Institute (IGTI) of THE AMERICAN SOCIETY OF MECHANICAL ENGINEERS for publication in the ASME JOURNAL OF ENGINEERING FOR GAS TURBINES AND POWER. Paper presented at the International Gas Turbine and Aeroengine Congress and Exhibition, Amsterdam, The Netherlands, June 3–6, 2002; Paper No. 2002-GT-30557. Manuscript received by IGTI, Dec. 2001, final revision, Mar. 2002. Associate Editor: E. Benvenuti.

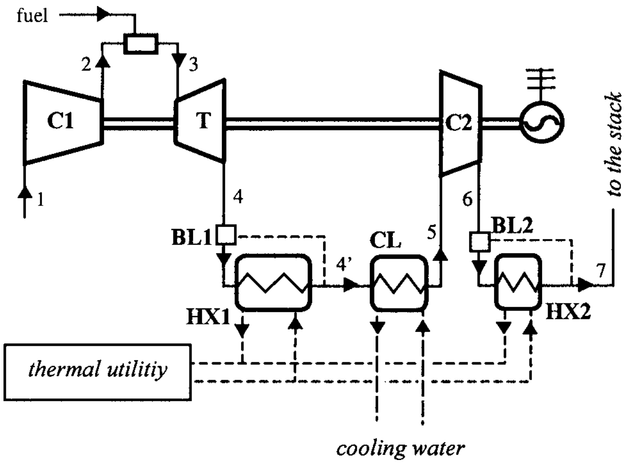

Fig. 1 Schematic layout of a below ambient pressure discharge gas turbine (BAGT) in cogenerative application

Utilizing the above presented data, the BAGT cogenerative performance and main dimensions have been evaluated and summarized in Table 2. Some of these results are reported per first compressor inlet air mass flow rate $\dot{m}_1$. They have been checked for a $\dot{m}_1$ range from 15 to 50 kg/s (corresponding to an electric power ranging from 5 to 15 $\mathrm{MW_{el}}$ being $P_{el}/\dot{m}_1 = 304$ kJ/kg as shown in Table 2).

In Table 2, the utilization factor (η_u) and the Energy Saving Index (ESI) are also reported: η_u is the sum of the electric and the thermal efficiencies and ESI is evaluated utilizing the following expression:

$$\mathrm{ESI} = 1 - \frac{1}{\left(\dfrac{\eta_{\mathrm{el}}}{\eta_{\mathrm{el}}^*} + \dfrac{\eta_{\mathrm{th}}}{\eta_{\mathrm{th}}^*}\right)} = 1 - \frac{1}{\eta_{el}\left(\dfrac{1}{\eta_{\mathrm{el}}^*} + \dfrac{Q_{\mathrm{th}}}{P_{\mathrm{el}}}\dfrac{1}{\eta_{\mathrm{th}}^*}\right)} \qquad (1)$$

where η_{el}^* and η_{th}^* (electric and thermal reference efficiencies) are assumed equal to 0.37 and 0.85, [3].

The energy saving index is a direct measure of savings in fuel consumption and it is an important thermodynamic parameter of interest; in fact, the amount of fuel saving has major impact on the economics of a cogeneration plant, since 80% of the operating cost can be attributed to the cost of fuel in a gas turbine based cogeneration plant. ESI expresses the relative variation of the fuel power consumption in two separate plants producing the same electric and thermal power output of the cogeneration plant, and the fuel power consumption in the process plant.

Table 1 Key design parameters

Ambient Conditions	
First compressor inlet temperature	15°C
Ambient pressure	1.013 bar
Relative humidity of inlet air	60%
BAGT Cycle Parameters	
First compressor pressure ratio	22
First compressor polytropic efficiency	0.87
Turbine inlet temperature	1150°C
Expansion polytropic efficiency	0.87
Outlet turbine pressure	0.5 bar
Second compressor inlet temperature	50°C
Second compressor polytropic efficiency	0.87
Thermal Utility Temperature Levels	
Process water cold temperature	60°C
Process water hot temperature	90°C
General Data	
Heat exchanger pressure drop (related to the inlet pressure value)	2%
Overall heat transfer coefficient (typical value for a countercurrent gas/water HX with water inside finned tube)	45 $\mathrm{W/m^2{}^\circ C}$
Mechanical efficiency	0.98
Combustion efficiency	0.99

Table 2 BAGT design performance

Electric power per inlet air mass flow rate, $P_{\mathrm{el}}/\dot{m}_1$	$304\,\dfrac{\mathrm{kW_{el}}}{\mathrm{kg/s}}$
HX1 thermal power per inlet air mass flow rate, $Q_{\mathrm{th,HX1}}/\dot{m}_1$	$277\,\dfrac{\mathrm{kW_{th}}}{\mathrm{kg/s}}$
HX2 thermal power per inlet air mass flow rate, $Q_{\mathrm{th,HX2}}/\dot{m}_1$	$69\,\dfrac{\mathrm{kW_{th}}}{\mathrm{kg/s}}$
Total thermal power per inlet air mass flow rate, $Q_{\mathrm{th}}/\dot{m}_1$	$346\,\dfrac{\mathrm{kW_{th}}}{\mathrm{kg/s}}$
HX1 surface area per inlet air mass flow rate, $S_{\mathrm{HX1}}/\dot{m}_1$	$76\,\dfrac{\mathrm{m^2}}{\mathrm{kg/s}}$
CL surface area per inlet air mass flow rate, $S_{\mathrm{CL}}/\dot{m}_1$	$14\,\dfrac{\mathrm{m^2}}{\mathrm{kg/s}}$
HX2 surface area per inlet air mass flow rate, $S_{\mathrm{HX2}}/\dot{m}_1$	$52\,\dfrac{\mathrm{m^2}}{\mathrm{kg/s}}$
Electric efficiency, η_{el}	40.1%
Thermal efficiency, η_{th}	45.7%
Utilization factor, η_u	85.8%
Energy Saving Index, ESI	39.6%
Heat to power ratio, $Q_{\mathrm{th}}/P_{\mathrm{el}}$	1.14
Expander outlet temperature, T_4	331°C
Second compressor outlet temperature, T_6	140°C
Equivalent cooling water mass flow rate, μ	$20.8\,\dfrac{\mathrm{kg/s}}{\mathrm{MW_{el}}}\,{}^\circ\mathrm{C}$

Finally, in Table 2, the equivalent cooling water mass flow rate μ is also shown.

It should be noted that HX2, because of the low exhaust gas temperatures (varying from 141 to 75°C), exchanges about 1.3 $\mathrm{kW_{th}/m^2}$ whereas HX1 reaches 3.7 $\mathrm{kW_{th}/m^2}$; in this last case, the hot gas inlet and outlet temperatures are equal to 331°C and 75°C, respectively.

Influence of the Thermal Power Variation on the BAGT Performance. As mentioned, the thermal load requested from the thermal utilities may vary during the day and/or the year.

In the BAGT cogenerative power plant it is possible to reduce the thermal load of about 20% (leading the heat to power ratio, $Q_{\mathrm{th}}/P_{\mathrm{el}}$, from 1.14 to 0.90), bypassing the second heat exchanger with the bypass lock BL2, without any variation on the BAGT electric performance.

When a further reduction is required, the first heat exchanger must be progressively bypassed operating on BL1. Bypassing HX1, the cooler inlet temperature T_4 increases and, consequently, T_5 grows. Nevertheless, to not penalize the BAGT electric efficiency, the temperature at the second compressor inlet should be kept at its design value to not increase the second compressor work. To maintain T_5 close to 50°C, the cooler surface area S_{CL} must be over dimensioned (the second compressor inlet temperature depends on the cooler surface area) with respect to the value reported in Table 2.

In the present analysis, three different cooler surface areas are considered:

- Case A: cooler dimensioned to cool the hot gas from 75°C to 50°C (case of Table 2).
- Case B: cooler designed to have a second compressor inlet temperature equal to 140°C when the HX1 is completely bypassed ($Q_{\mathrm{th}}=0$);
- Case C: cooler designed to keep the second compressor inlet temperature equal to 50°C also when the first heat exchanger HX1 is completely bypassed (gas temperature at the cooler inlet equal to 331°C).

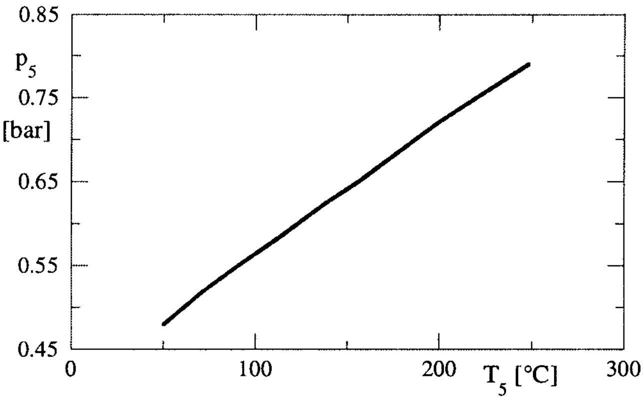

Fig. 2 Second compressor inlet pressure versus second compressor inlet temperature

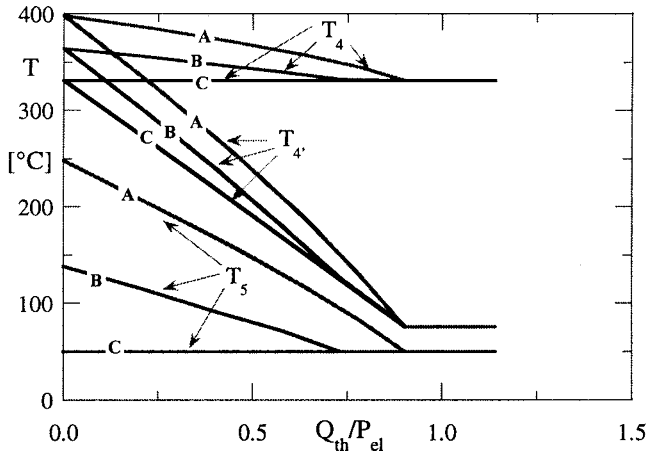

Fig. 3 Expander outlet, cooler and second compressor inlet temperatures (T_4, $T_{4'}$, and T_5) versus heat-to-power ratio

It should be noted that, in every case, the thermal power is regulated with the cooling water mass flow rate variation as shown in the following.

Moving from Case C to Case A, the cooler surface area decreases. In particular, to keep the second compressor temperature equal to 50°C (Case C), a CL surface area (S_{CL}) of about 54 m^2 per mass flow rate of exhaust gas entering in the CL, is needed; this value is reduced at 26 $m^2/(kg/s)$ and 14 $m^2/(kg/s)$ for Case B and A, respectively.

During thermal part load, the first compressor and the combustor are however operated in design condition while, the heat exchangers, the expander, the cooler and the second compressor will be run in off-design mode.

In particular, as regards the second compressor part-load, being the rotational speed constant, the inlet volume flow rate is almost constant and C2 inlet pressure may be evaluated from the following equation (good for ideal gas):

$$p_5 = p_{5,\mathrm{des}} \frac{\dot{m}_5 T_5}{\dot{m}_{5,\mathrm{des}} T_{5,\mathrm{des}}}. \tag{2}$$

It should be noted that C2 inlet mass flow rate is constant because of its dependence on C1 rotational speed. As a consequence, the pressure at the C2 inlet depends on T_5 (p_5 versus T_5 is plotted in Fig. 2).

Moreover, as far as the C2 polytropic efficiency is concerned, even though $p_5/p_{5,\mathrm{des}}$ significantly varies (reaching its highest values at $Q_{th}=0$), the C2 polytropic efficiency variation does not significantly affect the second compressor work because of the low C2 pressure ratio.

As far as the part load of the heat exchangers and the cooler are concerned, the overall heat transfer coefficient is assumed to be variable with the mass flow rates, [6].

Figure 3 shows T_5, T_4 and T_4 trends versus Q_{th}/P_{el} for the three different cases above mentioned: in case C, T_5 and T_4 are constant whereas, for case B, when Q_{th}/P_{el} goes down to 0.73, T_5 and T_4 exceed 50°C and 331°C, respectively. Likewise, for Case A, T_5 and T_4 increase when Q_{th}/P_{el} goes down to 0.90.

It should be noted that, when $Q_{th}=0$, T_4 and $T_{4'}$ coincide because HX1 is completely bypassed.

Figure 4 reports the specific thermal power produced by the first and second heat exchangers ($Q_{th,HX1}/\dot{m}_1$ and $Q_{th,HX2}/\dot{m}_1$) and the one discharged by the cooler ($Q_{th,CL}/\dot{m}_1$) to the ambient, versus Q_{th}/P_{el} and for the three cases considered.

As mentioned, the reduction in heat-to-power ratio from 1.14 to 0.90, is done operating on HX2, while to further decrease Q_{th}, the first heat exchanger must be by-passed increasing the heat discharged by CL.

With regard to the BAGT electric performance, in Fig. 5, the electric efficiency trend versus Q_{th}/P_{el} for the three cases considered, is reported. The dotted lines of Fig. 5 represent the curves at energy saving index (ESI) constant. It should be noted that the bypass of the first and second heat exchangers, reducing the pressure drop at the turbine and at the second compressor discharge, slightly increases the BAGT electric efficiency. On the contrary, the second compressor inlet temperature increase influences negatively the work spent in C2 to re-compress the exhaust gas to the ambient pressure; when T_5 exceeds 50°C, the BAGT electric efficiency strongly decreases. Obviously, Case A is the worst one since T_5 reaches the highest temperature here considered (about 250°C).

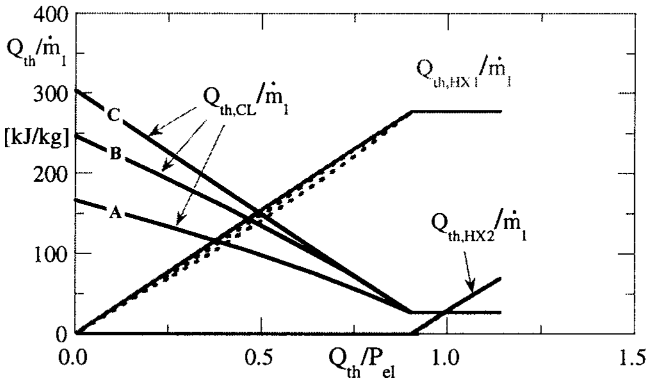

Fig. 4 Specific thermal power exchanged in the heat exchangers and in the cooler versus heat-to-power ratio

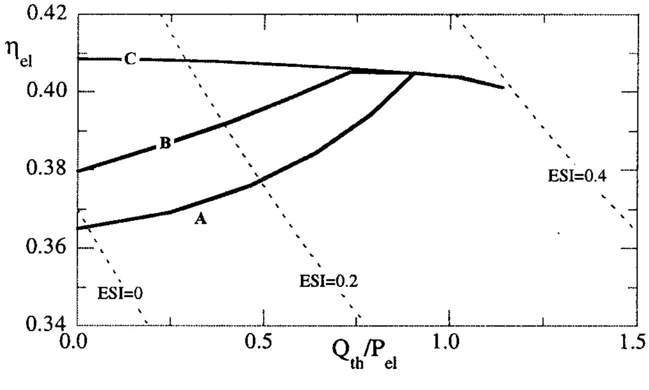

Fig. 5 BAGT electric efficiency versus heat-to-power ratio

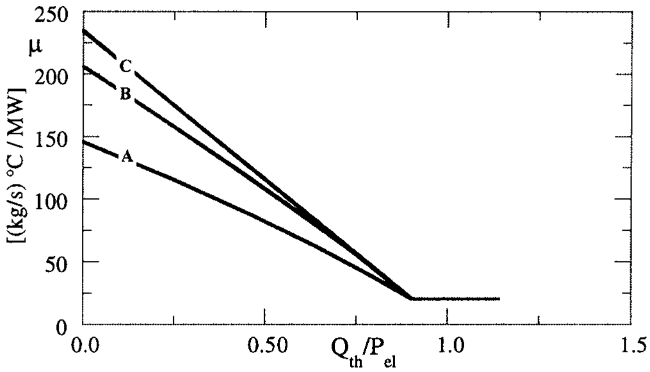

Fig. 6 Equivalent cooling water mass flow rate versus heat-to-power ratio

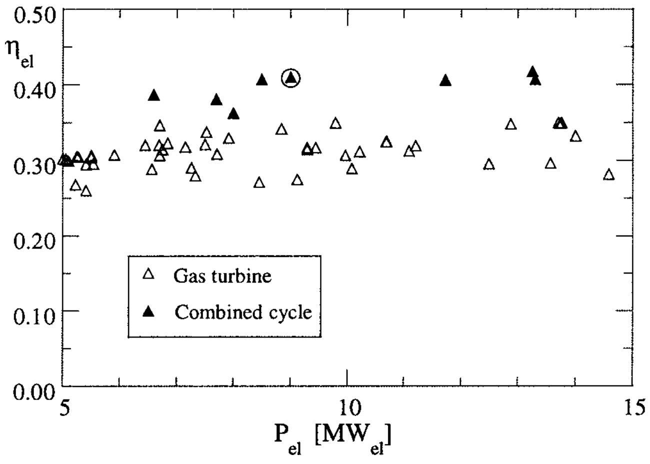

Fig. 7 Gas turbine (GT) and combined cycle electric efficiencies versus electric power

When the BAGT is producing the maximum thermal power, the cooling water mass flow rate through the cooler is the minimum one; this condition lasts till Q_{th}/P_{el} reaches 0.90. Reducing the Q_{th}/P_{el} ratio under 0.90, the thermal power discharged by the cooler ($Q_{th,CL}$) increases reaching its maximum value when Q_{th}/P_{el} is equal to zero (Fig. 4).

As mentioned, the cooler is fed with cooling water to decrease the temperature of the hot gas passing through it. Obviously, the cooling water mass flow rate, $\dot{m}_{cw}$, depends on the Q_{th}/P_{el} ratio and on the cooler design case considered. Figure 6 shows the trend of the equivalent cooling water mass flow rate μ defined as

$$\mu = \frac{\dot{m}_{cw}\Delta T_{cw}}{P_{el}}. \tag{3}$$

The equivalent cooling water mass flow rate represent the cooling water required, per power output, when the cooling water temperature rise is equal to 1°C.

On the basis of the data reported in the figure, it is possible to evaluate the maximum cooling water requirements to operate the BAGT without heat production ($Q_{th}/P_{el}=0$); supposing a maximum water cooling temperature rise of 10°C, the maximum $\dot{m}_{cw}/P_{el}$ varies from about 23.4 to 14.5 (kg/s)/(MW_{el}), depending on the case considered. In particular, moving from Case C to Case B, the cooling water requirements reduce of about 12.0% (from 23.4 to 20.6 (kg/s)/(MW_{el})) and the electric efficiency (Fig. 5) goes down from 0.408 to 0.379 (−7.1%). Moving from Case C to A, the cooling water needs and the electric efficiency reductions are of about 38.0% and 10.5%, respectively.

It should be noted that, besides for the cooling water utilization, the Case A is more convenient, with respect to Case B and C, for the lower cost of the cooler due to the lower surface area (−46.0% respect to Case B and −74.0% to Case C).

To conclude the BAGT thermal part load analysis, it should be highlighted that the choice among the different cooler design cases presented depends on the thermal utility features; for a cogenerative application in which Q_{th}/P_{el} is always over 0.90 the Case A is more convenient since the electric efficiency last around its maximum value and the cooler dimension is the minimum one.

Otherwise, if the thermal load greatly varies and Q_{th}/P_{el} falls below 0.90 or 0.73 for a large part of the year, the choice among the different cases depends on economic cooler cost and on the thermal power requirement trend.

Cogenerative Applications in 5–15 MW Size

As mentioned and known, the cogenerative power plants are often involved to produce variable thermal power to satisfy the thermal utility needs (as happens for example in the residential heating).

Usually, in a gas turbine (GT) cogenerative application, the thermal load does not influence the GT electric efficiency while on the contrary, in a combined cycle (CC) cogenerative application, the CC electric performance depends on the steam bled from the steam turbine.

In this paragraph, the BAGT cogenerative performance above evaluated will be compared with those obtainable with gas turbine and combined cycle cogenerative power plants. This comparison will be carried out considering GT and CC power plants within the same electric range of the BAGT (5 to 15 MW_{el}).

In Fig. 7, the electric efficiency of existing gas turbines (△) and combined cycles (▲) are plotted versus the plant electric power, [7]. In this electric power range, the gas turbine electric efficiency ranges from 0.27 to 0.35, while the combined cycle one varies from 0.36 to 0.42.

The Gas Turbine Cogenerative Application. As known, the cogenerative application of a gas turbine consists in the employment of a heat recovery (HR) fed with the exhaust gas discharged from the GT. The thermal power that may be recovered depends on the gas turbine outlet temperature, on the exhaust gas mass flow rate and on the thermal utility temperature levels. Supposing, as assumed in the BAGT cogenerative application, a thermal utility hot temperature equal to 90°C, a cold temperature equal to 60°C and a minimum temperature rise in the heat recovery equal to 15°C (it means that the heat recovery discharge temperature, $T_{HR,o}$, is imposed equal to 75°C), the maximum thermal power produced from a GT may be evaluated as

$$Q_{th,max} = \dot{m}_{GT,o}[h(T_{GT,o}) - h(T_{HR,o})]. \tag{4}$$

The electric efficiencies of existing gas turbines, [7], are reported in Fig. 8 versus the ratio between the value evaluated from Eq. (4) and the electric power; in the same figure the BAGT cogenerative performance are also shown (dotted lines).

As it is possible to note from Fig. 8, for the gas turbine cogenerative applications, the maximum Q_{th}/P_{el} values decrease with the electric efficiency increase: for the highest η_{el} values, Q_{th}/P_{el} is equal to 1.5 while, for the lowest ones, Q_{th}/P_{el} reaches 2.2. Thanks to this, all the gas turbine cogenerative applications present ESI values included within 0.30–0.35; these values are lower than the maximum obtainable with the BAGT (circle point).

It should be noted that, the triangles in Fig. 8 represent the GT working conditions at maximum heat production; reducing Q_{th} the electric efficiency maintains quite constant (bypassing the HR the GT back pressure lightly decreases).

Moreover, it should be noted that the heat recovery surface area S_{HR}, per exhaust gas mass flow rate $\dot{m}_{GT,o}$, is linked to the gas turbine outlet temperature $T_{GT,o}$ as expressed by the following equation (neglecting the gas composition on the specific heat evaluation):

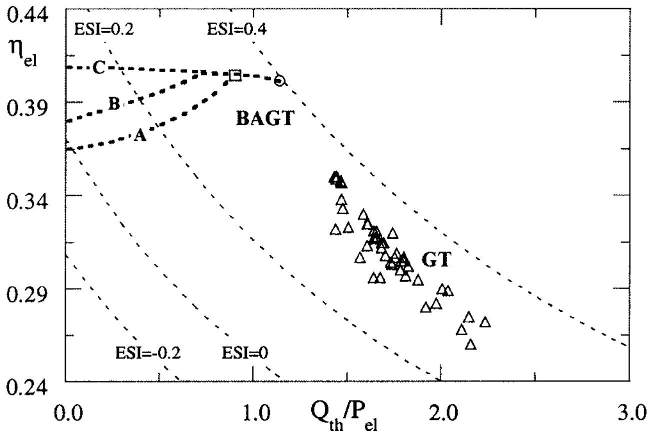

Fig. 8 Gas turbine electric efficiency versus heat-to-power ratio

$$\frac{S_{\mathrm{HR}}}{\dot{m}_{\mathrm{GT},o}} \approx \frac{c_{pm(T_{\mathrm{GT},o}-75)}}{U}\,\frac{T_{\mathrm{GT},o}-75}{T_{\mathrm{GT},o}-105}\ln\frac{T_{\mathrm{GT},o}-90}{15}. \tag{5}$$

For the gas turbines here considered, being $T_{\mathrm{GT},o}$, within 450 and 550°C, the average $S_{\mathrm{HR}}/\dot{m}_{\mathrm{GT},o}$ value, evaluated assuming $T_{\mathrm{GT},o}=500°\mathrm{C}$, is equal to 88 $\mathrm{m}^2/(\mathrm{kg/s})$. In Table 3 the BAGT surface areas, referred to the one of a HR with inlet temperature equal to 500°C, are reported. The results shown in the last row highlight that the total BAGT surface area is higher than that required from the heat recovery disposed at the GT outlet. Nevertheless, as is possible to evaluate from the third-last row, removing the second heat exchanger and designing the cooler as suggested in Case A, the total BAGT surface area is greater than S_{HR} of about 2%. In this case, for the BAGT, the maximum $Q_{\mathrm{th}}/P_{\mathrm{el}}$ is limited to 0.90 (square point in Fig. 8), the electric efficiency lasts considerably higher than the GT one and the ESI is quite the same.

When a reduction in thermal power production is required, the BAGT-C can operate without significant variation in the electric performance as happened for the GT cogenerative application.

On the contrary, for BAGT-A, an electric efficiency decrease occurs when Q_{th} decreases. Nevertheless, the minimum η_{el} value (reached at $Q_{\mathrm{th}}=0$) is greater than the maximum obtained with a GT.

It should be noted that BAGT needs cooling water for its thermal part load operation, whereas the GT can operate without make-up water.

The Cogenerative Combined Cycle Application. Generally, in the power size here considered ($5-15\,\mathrm{MW_{el}}$), the existing combined cycle power plants present a one pressure level bottomer and steam turbine inlet temperature around 450°C. In these plants, an extraction steam turbine may be employed to produce thermal power. The choice of the pressure at which the steam is bled from the steam turbine is linked to the thermal utility temperature levels and affects the CC thermal and electric performance; increasing the bleed pressure, the thermal power that may be produced grows, but consequently the electric efficiency reduces.

Table 3 Comparison between BAGT and GT exchanger surface areas

	Case A	Case B	Case C
$S_{\mathrm{HX1}}/S_{\mathrm{HR}}$	0.86	0.86	0.86
$S_{\mathrm{CL}}/S_{\mathrm{HR}}$	0.16	0.29	0.61
$(S_{\mathrm{HX1}}+S_{\mathrm{CL}})/S_{\mathrm{HR}}$	1.02	1.15	1.47
$S_{\mathrm{HX2}}/S_{\mathrm{HR}}$	0.59	0.59	0.59
$(S_{\mathrm{HX1}}+S_{\mathrm{HX2}}+S_{\mathrm{CL}})/S_{\mathrm{HR}}$	1.61	1.75	2.07

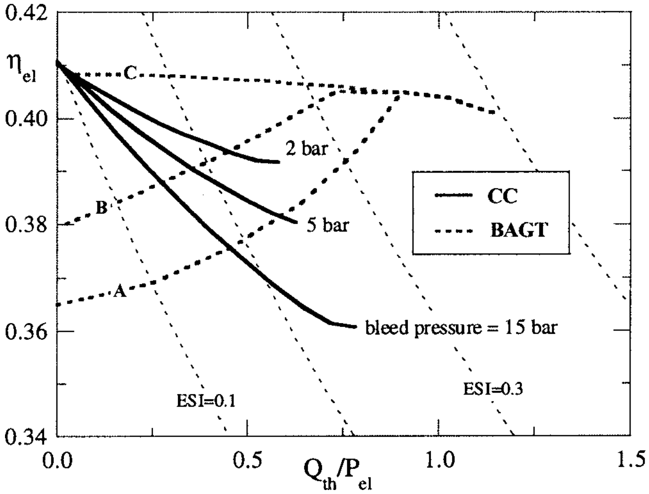

Fig. 9 Combined cycle (CC) electric efficiency versus heat-to-power ratio for different bleed pressure

For the comparison with the BAGT, a combined cycle, with the features above described and with an electric power equal to 9 MW (circled one in Fig. 7), has been chosen. The CC is designed at the maximum electric power production. In Fig. 9, the three continuous lines show the CC electric efficiency trends, versus $Q_{\mathrm{th}}/P_{\mathrm{el}}$, evaluated assuming the same thermal utility temperature levels considered for BAGT and GT cogenerative applications and imposing three different bleed pressures equal to 2, 5, and 15 bar, respectively (all these values are compatible with the thermal utility temperature levels). The dotted lines represent the BAGT electric efficiencies above evaluated for the three different cooler design cases. As the figure shown, in the combined cycle cogenerative applications, the maximum $Q_{\mathrm{th}}/P_{\mathrm{el}}$ increases with the bleed pressure, whereas the electric efficiency decreases. Comparing the CC results with the BAGT ones is possible to highlight that, BAGT-C always presents electric efficiency higher or equal (when $Q_{\mathrm{th}}=0$) than the CC one. As far as BAGT-A and BAGT-B are concerned, their electric efficiencies are greater than the CC one for the highest $Q_{\mathrm{th}}/P_{\mathrm{el}}$ values and less for the lowest ones.

Water Consumption and Cooling System. The results presented in Fig. 9 are evaluated considering a condenser pressure equal to 0.070 bar. This value is typical for a once through open-loop water cooling system. Supposing, a cold cooling water temperature equal to 15°C, the equivalent cooling water mass flow rate trend, versus $Q_{\mathrm{th}}/P_{\mathrm{el}}$, is shown in Fig. 10 (continuous lines).

As happened for the CC cogenerative application, also in the BAGT a cooling system must be present: in the BAGT the cooling water feeds the cooler to decrease the exhaust gas temperature before its recompression, whereas in the CC it is utilized to condense the steam discharged from the steam turbine. In Fig. 10, the BAGT equivalent cooling water consumption is also reported (dotted lines).

Figure 10 shows that, for both power plants, reducing $Q_{\mathrm{th}}/P_{\mathrm{el}}$ the equivalent cooling water consumption increases reaching its maximum value for $Q_{\mathrm{th}}=0$. Moreover, in the CC case, increasing the bleed pressure, the CC equivalent water consumption increases.

It should be noted that, BAGT-C and BAGT-B present equivalent cooling water consumption always greater than that one of a combined cycle. On the contrary, the equivalent cooling water consumption of BAGT-A is quite the same of the combined cycle one for $Q_{\mathrm{th}}/P_{\mathrm{el}}>0.38$, but lower when $Q_{\mathrm{th}}/P_{\mathrm{el}}<0.38$.

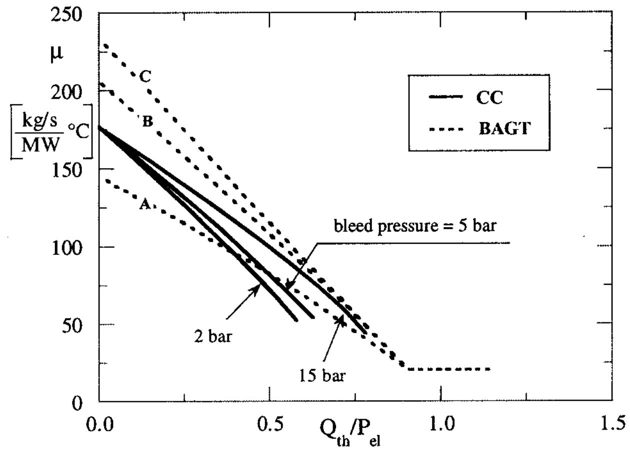

Fig. 10 Equivalent cooling water mass flow rate versus heat-to-power ratio: comparison BAGT versus CC

The water consumption may represent a big problem for the CC and BAGT installation. To reduce the water consumption, both for BAGT and CC, a mechanical draft cooling tower may be employed, whereas to annul the water consumption, a dry cooling tower should be installed.

In the sequel, the results obtained examining these different cooling systems are presented and compared. These results, in terms of cogenerative performance and main cooling system dimensions, refer to a CC and to a BAGT both producing an electric power of about 9 $\mathrm{MW_{el}}$.

In Tables 4, 5, and 6, the main cooling system dimensions and the electric performance of a CC and a BAGT, are shown. In particular, for the BAGT, only two of the three cooler design cases above presented are now considered (Case A and Case C).

In Table 4, the maximum cooling water consumption, the maximum electric efficiency and the condenser and cooler surface areas are reported considering a once through open loop system with the cooling water features already presented. It must be remembered that, the CC and the BAGT-C have their maximum electric efficiency when $Q_{\mathrm{th}}/P_{\mathrm{el}}=0$, whereas the BAGT-A when $Q_{\mathrm{th}}/P_{\mathrm{el}}=0.90$. Moreover, for all the power plants, the maximum cooling water mass flow rate is evaluated at $Q_{\mathrm{th}}=0$.

Table 4 Comparison between CC and BAGT cooling systems: case of an open loop water cooling system

		BAGT	
	CC	(Case A)	(Case C)
Maximum cooling water consumption (kg/s)	155	129	202
Maximum electric efficiency	0.410	0.405	0.408
Condenser surface area (m^2)	110	⋯	⋯
Cooler surface area (m^2)	⋯	410	1580

Table 5 Comparison between CC and BAGT cooling systems: case of wet cooling towers

		BAGT	
	CC	(Case A)	(Case C)
Maximum cooling water consumption(kg/s)	2.53	2.93	3.32
Maximum electric efficiency	0.408	0.405	0.408
Condenser surface area (m^2)	275	⋯	⋯
Cooler surface area (m^2)	⋯	516	1711
Number of cooling towers$^{(1)}$	3	1	4

(1)single cooling tower volume: 17.6 m^3

Table 6 Comparison between CC and BAGT cooling systems: case of dry cooling towers

		BAGT	
	CC	(Case A)	(Case C)
Maximum electric efficiency	0.399	0.403	0.401
Condenser surface area (m^2)	283	⋯	⋯
Cooler surface area (m^2)	⋯	730	2062
Number of cooling towers$^{(1)}$	4	1	5

(1)single cooling tower volume: 405 m^3

It should be highlighted that the lower condenser dimension, with respect to cooler, depends on different overall heat transfer coefficient. Nevertheless, the condenser cost per surface area is about 2–3 times the cooler one, [6], and then the ratio between the costs is lower than the ratio between the cooler and condenser surface areas.

Table 5 refers to the case of a cooling system with mechanical draft cooling tower. In this case, it was assumed a cold cooling water temperature equal to 21°C and a temperature rise $\Delta T_{cw}=17°\mathrm{C}$. As a consequence, the condenser pressure increases to 0.077 bar (reducing the CC electric performance of about 0.5%) as well as the cooler and condenser surface areas (without however any reduction in the BAGT electric efficiency).

How it is possible to note comparing Table 5 with Table 4, the maximum water consumption reduces, in all the cases, of about 60 times. On the contrary, the condenser surface area increases of about 150%, while the cooler one grows of about 26% and 8% for Case A and C, respectively.

Moreover, in Table 5, the number of cooling towers required in the three power plants is reported considering, in all cases, the same cooling tower dimension (with a volume equal to 17.6 m^3).

Finally, Table 6 refers to the case of a cooling system with dry cooling towers. In this case, assuming a cold cooling water temperature equal to 33°C and a temperature rise $\Delta T_{cw}=12°\mathrm{C}$, the condenser pressure may be assumed equal to 0.11 bar. As a consequence, the CC electric performance decreases and S_{CL} increases. Moreover, a BAGT electric efficiency reduction, due to the electric power absorbed by the cooling tower fans, occurs.

It should be noted that, in all the cases, no make up water is now required. With respect to the case of Table 4, the condenser surface area increase of about 157% whereas, S_{CL} grows of about 78% and 30% for BAGT-A and BAGT-C, respectively. As far as the cooling towers are concerned, these are bigger than the wet ones and, for CC and BAGT-C, their number increase to 4 and 5, respectively.

Conclusions

In the present paper, an analysis of a cogenerative application of a Below Ambient pressure discharge Gas Turbine (BAGT), operating with variable thermal power production, has been presented. Moreover a comparison among BAGT, gas turbine and combined cycle cogenerative applications has been carried out within a power range varying from 5 to 15 $\mathrm{MW_{el}}$.

The main results may be summarized as follows:

- The maximum $Q_{\mathrm{th}}/P_{\mathrm{el}}$ value for a BAGT, designed at maximum electric efficiency (that is equivalent at ESI maximum condition as reported in [5]), is around 1.14 or, removing the second heat exchanger, around 0.90. These values are intermediate between those of a combined cycle (ranging from 0.50 to 0.80) and those a gas turbine (that reach 2.2).
- The maximum BAGT electric efficiency (0.408) is strongly higher than those of a GT (0.27–0.35) and comparable with the combined cycle maximum ones (0.36–0.42).

Comparing BAGT with gas turbine, it should be highlighted that

- when the thermal power is varying, the electric efficiency of the BAGT-C (biggest cooler surface area) lasts around its maximum value as happens for the gas turbine cogenerative applications. Nevertheless, the BAGT total surface area (HX1 +CL+HX2) is about twice of the GT heat recovery. It should be observed that, assuming an electric power size around 10 $\mathrm{MW_{el}}$, being the average specific cost of a gas/water heat exchanger (in the size range 500–2500 $\mathrm{m^2}$) equal to 180 $/$\mathrm{m^2}$ [6], the additional cost of the cooler, with respect to HR cost, represents only the 4% of the gas turbine total cost (around 400 $/kW). This cost may be then considered not remarkable and does not alter the economic results obtained in [4]. For its thermal part load operation, the BAGT-C needs significant cooling water not requested by the GT. Nevertheless, this water consumption may be annul employing dry cooling towers that increase the BAGT-C cost of about 650 k$ (tolerable cost considering the fuel saving due to the higher electric efficiency with respect to a GT).
- designing the cooler with the minimum surface area (BAGT-A), the cooler and the dry cooling tower costs reduce, with respect to BAGT-C, of about 3 and 5 times, respectively. Moreover, the BAGT-A electric efficiency is higher than the maximum obtainable with a GT even if is lower than the BAGT-C one.

Comparing BAGT with combined cycle, it should be observed that

- the BAGT presents, as above mentioned, comparable electric efficiency and lower costs being absent expensive devices as the steam turbine, the super heaters, etc. Moreover, the BAGT is more convenient for cogenerative applications with respect to combined cycle since reaches higher ESI value (around 0.40).
- in the BAGT-C, the maximum cooling water consumption is higher than the combined cycle one of about 30%. Moreover, if wet or dry cooling towers are employed, the number of towers requested by BAGT-C is greater than that requested by a combined cycle.
- on the contrary, with BAGT-A, the water consumption is quite the same and the cooling tower number decisively lower than the CC one. Nevertheless BAGT-A results convenient with respect to combined cycle only if, for the most part of the time, the thermal load lasts at relevant values.

It should be highlighted that, the BAGT power plant may result more attractive if it is built modifying an existing gas turbine (adding a further expander stage and the second compressor); this may permit to not redesign the whole plant reducing the investment costs.

The problems connected to the transformation of a gas turbine into a BAGT are now under study and will be presented in a next paper.

Nomenclature

c_{pm} = average specific heat
F = LHV fuel power supplied
h = specific enthalpy
$\dot{m}$ = mass flow rate
P_{el} = electric power output
p = pressure
Q_{th} = thermal power
S = exchange surface area
T = temperature
U = overall heat transfer coefficient
η_{el} = P_{el}/F, lower heating value electric efficiency
η_{th} = Q_{th}/F, lower heating value thermal efficiency
η_u = $\eta_{\mathrm{el}}+\eta_{\mathrm{th}}$, LHV fuel utilization coefficient
μ = $\dot{m}_{cw}\Delta T_{cw}/P_{\mathrm{el}}$, equivalent cooling water mass flow rate: $\dot{m}_{cw}$ required, when the cooling water temperature rise is equal to 1°C, per power output

Subscripts and Superscripts

cw = cooling water
CL = cooler
C = compressor
des = design condition
GT = gas turbine
HR = heat recovery
HX = heat exchanger
max = maximum
o = outlet
* = reference value

Acronyms

BAGT = below ambient pressure discharge gas turbine
BL = bypass Lock
C = compressor
CC = combined cycle
CL = cooler
ESI = energy saving index
GT = gas turbine
HR = heat recovery
HX = heat exchanger
T = turbine

References

[1] Wilson, G. D., 1984, *The Design of High-Efficiency Turbomachinery and Gas Turbine*, M.I.T. Press, Cambridge, MA.
[2] Tsujikawa, Y., Ohtani, K., Kaneko, K., Watanabe, T., and Fujii, S., 1999, "Conceptual Recovery of Exhaust Heat From a Conventional Gas Turbine by an Inter-Cooled Inverted Brayton Cycle," ASME Paper No. 99-GT-0378.
[3] Bianchi, M., Negri di Montenegro, G., and Peretto, A., 2000, "Inverted Brayton Cycle Employment for Low Temperature Cogenerative Applications," ASME Paper No. 2000-GT-0315.
[4] Bianchi, M., Negri di Montenegro, G., and Peretto, A., 2001, "Thermo-Economic Optimization of a Cogeneration Plant With Below Ambient Pressure Discharge Gas Turbine," ASME Paper No. 2001-GT-209.
[5] Bianchi, M., 2001, "Thermal Utility Influence on the Cogenerative Performance of a Below Ambient Pressure Discharge Gas Turbine (BAGT)," ASME International Mechanical Engineering Congress and Exposition, New York, November.
[6] Thermoflex 6 Release 2, 2001, Thermoflow, Inc., Sudbury, MA.
[7] "Gas Turbine World 1999–2000 Handbook," 2000, Pequot Publishing, Inc., Fairfield, CT, Vol. 20.

A Feasibility Study of Inverted Brayton Cycle for Gas Turbine Repowering

M. Bianchi
G. Negri di Montenegro
A. Peretto
P. R. Spina

DIEM-University of Bologna,
Viale del Risorgimento, 2,
40136 Bologna, Italy

In the paper a feasibility study of inverted Brayton cycle (IBC) engines, for the repowering of existing gas turbines, is presented. The following main phases have been carried out: (i) identification of the more suitable gas turbines to be repowered by means of an IBC engine; (ii) designing of the IBC components. Once the IBC engines for the candidate gas turbines were designed, an analysis has been developed to check the possibility to match these engines with other gas turbines, similar to those for which the IBC engines have been designed. In all the analyzed cases the evaluated performance result only slightly worse than that obtainable by repowering the same gas turbine with IBC engines ad hoc designed. [DOI: 10.1115/1.1765121]

Introduction

Disposing of a hot gas at ambient pressure (like the gas turbine exhaust gas), a net positive specific work can be obtained first by expanding the gas below ambient pressure, then by cooling it and, finally, by recompressing it up to the ambient pressure. All these thermodynamic transformations may be performed by an expander, an heat exchanger and a compressor, and this "cycle" is commonly named inverted Brayton cycle (IBC), [1].

In a previous authors' paper, the performance of IBC engines working with the gas exhausted by existing gas turbines has been evaluated, [2].

In the present paper a feasibility study of the IBC engines, for the repowering of existing gas turbines, is presented. The following main phases have been carried out:

(i) identification of the gas turbines more suitable to be repowered by means of an IBC engine. This phase requires the evaluation of the performance which can be obtained by applying IBC engines to the gas turbines available on the market, and the selection, as candidate machines, of the most widespread gas turbines on the market which allow the highest performance gain;
(ii) designing of the IBC components. This phase mainly involves the design of the IBC compressor and expander.

Once the IBC engines for the candidate gas turbines were designed, an analysis has been developed to check the possibility to match these engines with other gas turbines, similar to the ones for which the IBC engines have been designed. This phase of the study involves the performance evaluation of these last gas turbines repowered by using IBC engines not designed for them, considering that these systems (gas turbine and IBC engine) work in off-design conditions, due to the gas temperature and mass flow rate at the IBC entry different from design.

IBC Overview

The IBC is an engine thermodynamic cycle in which a gas is expanded from high temperature and ambient pressure to subatmospheric pressure, cooled, recompressed to ambient pressure and, finally, discharged, [1]. In Fig. 1 the schematic layout of an IBC engine is shown.

The employment of an IBC engine may result convenient when a free flow of hot gas at ambient pressure is available and when the heat exchanged, to cool the gas, can be exploitable for cogenerative applications. A typical IBC employment is as bottomer of an existing engine, such as a reciprocating internal combustion engine (diesel, gas or gasoline fueled) or a gas turbine. A detailed analysis of IBC employment in cogenerative applications and, in particular, when the topper is a gas turbine, is reported in [2].

The results obtained in [2] show that, for each combination of expander inlet temperature (T_{IE}), compressor inlet temperature (T_{IC}) and compressor and expander efficiencies, a value of the expander outlet pressure (p_{OE}), that maximize the IBC specific work, can be determined. These results are summarized in Figs. 2 and 3, which report the curves of the expander outlet pressure (p_{OE}), versus expander inlet temperature, at maximum IBC specific work, for two couples of compressor and expander polytropic efficiency values, 0.86 and 0.90, respectively. Moreover, the curves relative to 95% of maximum specific work are also shown. All the curves are obtained for a compressor inlet temperature $T_{IC}=50°\mathrm{C}$. All the calculations have been performed using commercial software packages, [3,4], assuming the values reported in Table 1.

From Figs. 2 and 3 it can be noted that, for $p_{OE} \cong 0.35$ bar and for all the expander inlet temperature (T_{IE}) considered, the obtained IBC specific work is always higher than 95% of its maximum value.

IBC for Gas Turbine Repowering

In order to evaluate the performance obtainable by repowering existing gas turbines with IBC engines, a preliminary analysis of gas turbines available on the market has been performed to highlight the existing gas turbines that permit the highest improvement in efficiency and specific work with the IBC repowering.

In Figs. 4–6 the values of gas turbine outlet temperature (T_{OGT} that is T_{IE}, when the GT is matched with the IBC), LHV electric efficiency and specific work versus gas turbine power size are reported, respectively, for gas turbines available on the market with a power size lower than 50 MW, [4–7].

Performances Obtainable by Repowering Existing Gas Turbine With IBC Engines. The performance obtainable by repowering the considered existing gas turbines with IBC engines have been evaluated by using commercial software packages, [3,4].

For the calculations, the gas turbines have been grouped in four power size classes ($0.5 \div 2.5$ MW, $2.5 \div 15$ MW, $15 \div 35$ MW and $35 \div 50$ MW) and, for each class, the IBC compressor and ex-

---

Contributed by the International Gas Turbine Institute (IGTI) of THE AMERICAN SOCIETY OF MECHANICAL ENGINEERS for publication in the ASME JOURNAL OF ENGINEERING FOR GAS TURBINES AND POWER. Paper presented at the International Gas Turbine and Aeroengine Congress and Exhibition, Atlanta, GA, June 16–19, 2003, Paper No. 2003-GT-38186. Manuscript received by IGTI, October 2002, final revision, March 2003. Associate Editor: H. R. Simmons.

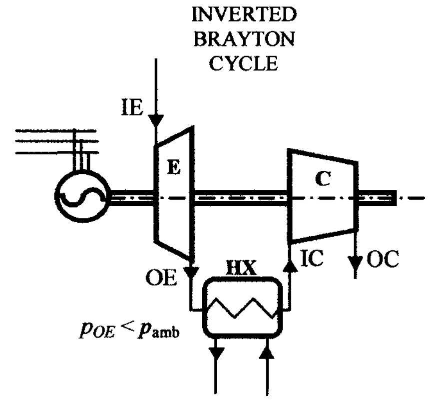

Fig. 1 Inverted Brayton cycle (IBC) schematic layout

Table 1 Key parameters

Heat exchanger pressure drop	2%
Mechanical efficiency	0.98
Working fluid composition	[vol. fraction]
O_2	0.1502
CO_2	0.0276
N_2	0.7602
Ar	0.0091
H_2O	0.0529

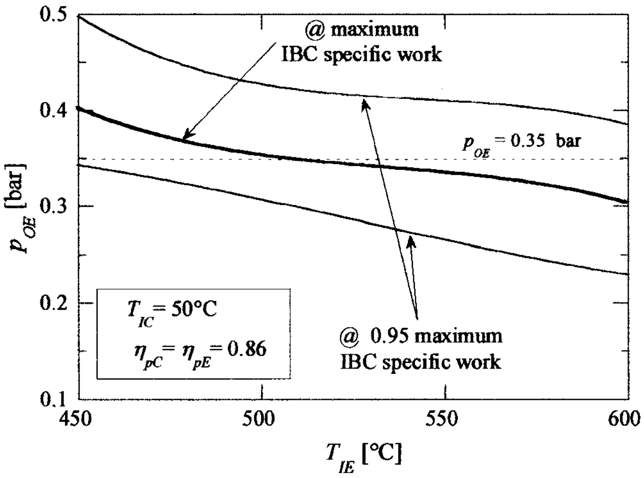

Fig. 2 Expander outlet pressure (p_{OE}) versus expander inlet temperature (T_{iE}) for $\eta_{pC} = \eta_{pE} = 0.86$

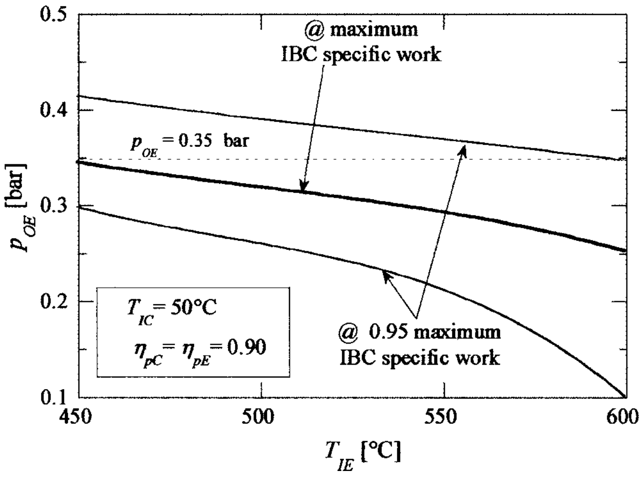

Fig. 3 Expander outlet pressure (p_{OE}) versus expander inlet temperature (T_{iE}) for $\eta_{pC} = \eta_{pE} = 0.90$

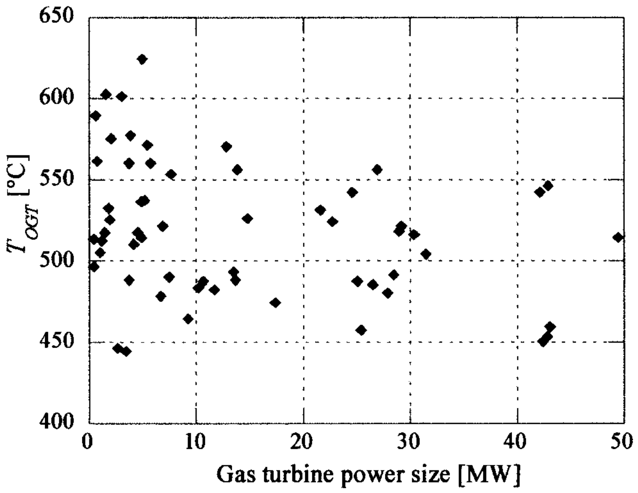

Fig. 4 Gas turbine outlet temperature (T_{OGT}) versus gas turbine power size

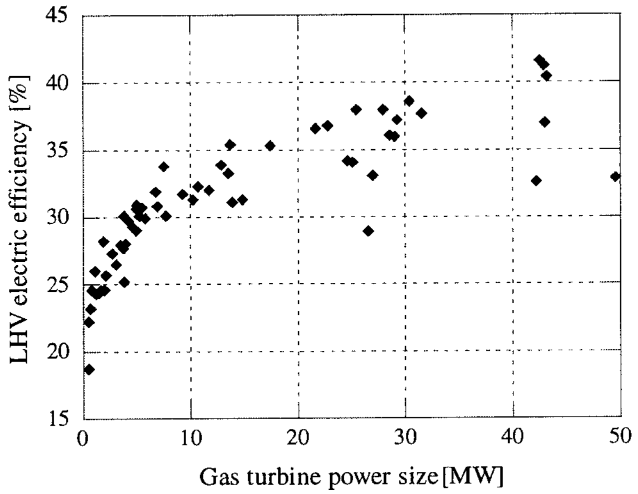

Fig. 5 LHV electric efficiency versus gas turbine power size

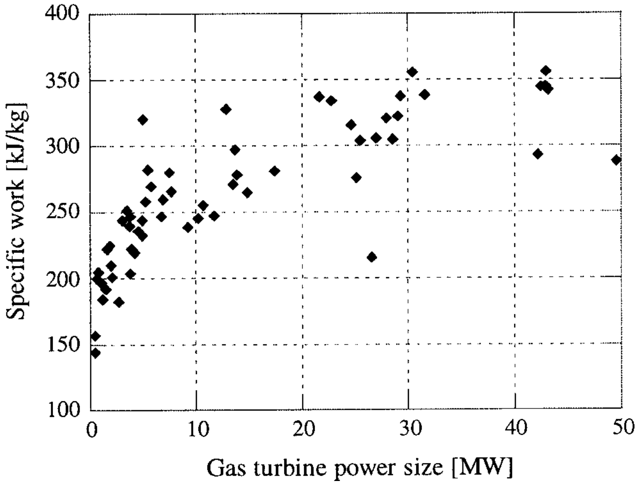

Fig. 6 Gas turbine specific work versus gas turbine power size

Table 2 IBC compressor and expander polytropic efficiencies for the four gas turbine power size classes

Gas turbine power class [MW]	η_{pC} and η_{pE}
0.5–2.5	0.86
2.5–15	0.87
15–35	0.88
35–50	0.89

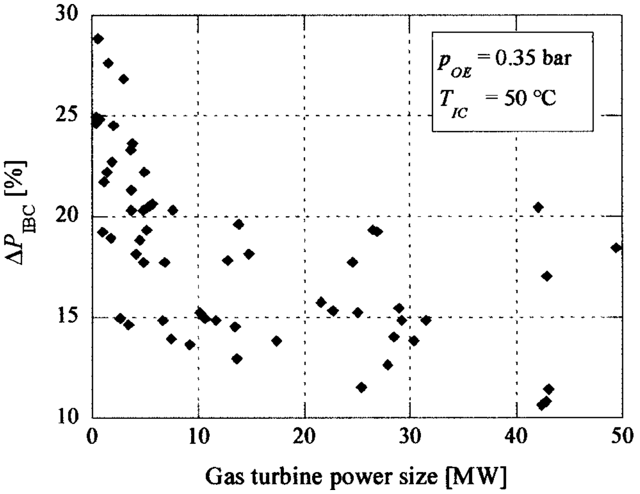

Fig. 7 Percentage electrical power increase due to the IBC employment versus gas turbine power size

pander polytropic efficiencies have been assumed equal among them, according to the values reported in Table 2.

The calculations have been performed considering a compressor inlet temperature $T_{IC}=50°\text{C}$ and an expander outlet pressure $p_{OE}=0.35$ bar. The temperature $T_{IC}=50°\text{C}$ is obtainable by using an intercooler fed with ambient cooling water. Moreover, as shown in Figs. 2 and 3, if p_{OE} is assumed equal to 0.35 bar, the IBC specific work is always higher than 95% of its maximum value for expander inlet temperature (i.e., gas turbine outlet temperature) ranging from 450 to 600°C and IBC compressor and expander polytropic efficiencies ranging from 0.86 to 0.90.

The results of the calculations are reported in Fig. 7, in terms of percentage electrical power increase due to the IBC employment (ΔP_{IBC}) versus gas turbine power size. Obviously, the percentage electrical power increase coincides with the increase in electric efficiency. It can be noted how the percentage increase in electrical power reduces by augmenting gas turbine power size, since the gas turbine specific work increase with size is higher than the IBC specific work variation.

IBC Preliminary Design

In order to evaluate the feasibility of IBC engines for gas turbine repowering, an IBC preliminary design has been carried out with reference to gas turbine models opportunely selected.

The criteria adopted for GT selection have been:

(i) the GT model widespread, [5–7];
(ii) the possibility to adopt the IBC designed for one GT model for the repowering of other GT models (indicated in the follow as OGTMs, other gas turbine models).

As far as this last point is concerned, the main problem for the employment of an IBC as bottomer of OGTMs is that both IBC and OGTM work in off-design conditions. In fact, the IBC expander usually works near to choking conditions and so, the corrected mass flow rate at the expander inlet (μ) can be assumed constant. As a consequence, if an IBC is matched with an OGTM with different exhaust gas mass flow rate and/or temperature than those used for the IBC design, the pressure at the expander inlet (i.e., the pressure at the OGTM outlet) varies to maintain constant the corrected mass flow rate. Nevertheless, the OGTM outlet pressure variation must be limited to assure acceptable gas turbine operating conditions. Therefore, the following range for the OGTM outlet pressure has been assumed as admissible:

$$0.933 \leqslant p_{OGT}[\text{bar}] \leqslant 1.063.$$

This means that the maximum backpressure admitted at the OGTM outlet is equal to 5000 Pa while the maximum depression is equal to 8000 Pa.

In order to evaluate the gas turbines which may be matched with a same IBC, the corrected mass flows at the gas turbine outlet for all the GTs considered have been calculated and compared each other. In particular, the corrected mass flow at the gas turbine outlet has been evaluated by using the following equation:

$$\mu = \dot{m}\frac{\sqrt{\vartheta}}{\delta}$$

where

- $\delta = p_{OGT}/p_{\text{ref}} = 1$, since it has been assumed $p_{OGT} = p_{\text{ref}} = 1.013$ bar,
- $\vartheta = T_{OGT}/T_{\text{ref}}$, with $T_{\text{ref}} = 790$ K (517°C) that is the average T_{OGT} value for all the GT considered.

Figures 8–11 show the corrected mass flow for the four GT power size classes considered. In each figure the GTs chosen for IBC design are written with bold characters. The OGTMs with which the IBC can be matched (i.e., the OGTMs for which the outlet pressure in the off-design conditions is contained within the range above mentioned) are instead written with plain characters. The bars without labels refer to gas turbines which cannot be matched with the designed IBC, since for these engines the p_{OGT} is out of the above mentioned range.

As shown in Figs. 8–11, six GT models have been selected for IBC design which allows to match the designed IBC engines to 23 OGTMs.

The design of the six IBC engines has been performed by using a computational code developed by the authors, which procedure is described in detail in [8].

Compressor Design. For the compressor design, the first rotor blade tip speed and the compressor inlet axial velocity have been assumed equal to 450 m/s and 150 m/s, respectively, in order to obtain the first rotor hub to tip ratio higher than 0.4 and five compressor stages. Moreover, it has been assumed a constant mean diameter (*D*) for all the compressor stages and the polytropic efficiency values reported in Table 2. Finally, the values of the degree of reactions (*R*) reported in Table 3 have been assumed.

In the calculations the work reduction due to non-uniform distribution of axial flow velocity along radial direction has been accounted by using the parameter called "work-done-factor," [9], and the maximum allowable diffusion in each stage cascade has been assessed by using the "de Haller" criteria, which has been considered suitable for a preliminary design, [8]. This last criteria imposes that, for each cascade, the ratio between outlet and inlet flow velocity (relative and absolute for rotor and stator, respectively) must be higher than 0.72.

The main results of compressor design, for the six IBC engines considered, are reported in the Appendix (see Table A1).

Expander Design. A single stage expander has been designed by choosing the stage loading factor (ψ) and the flow factor (ϕ) to obtain the highest total-to-total efficiency with the constraint that the value of the tip blade speed is limited to 450 m/s. The degree of reaction has been set to obtain an axial absolute flow velocity at the stage discharge by using the following equation:

$$R = 1 - \frac{\psi}{2}.$$

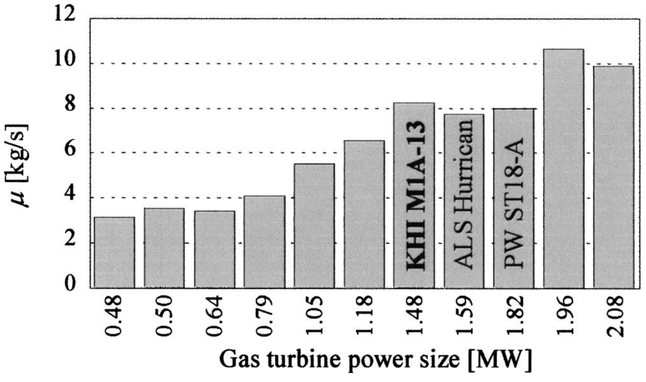

Fig. 8 Corrected mass flow (GT chosen for IBC design: bold; OGTMs to which the IBC can be matched: plain)

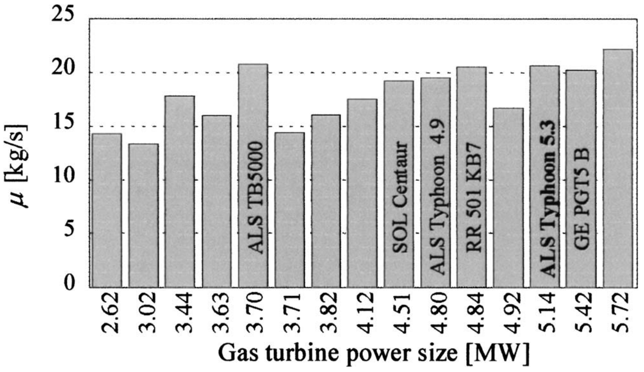

Fig. 9 Corrected mass flow (GT chosen for IBC design: bold; OGTMs to which the IBC can be matched: plain)

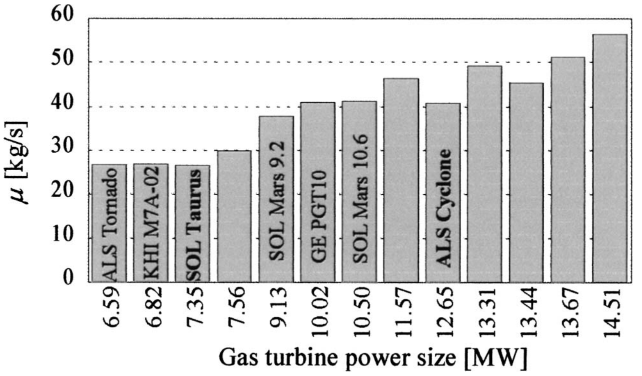

Fig. 10 Corrected mass flow (GTs chosen for IBC design: bold; OGTMs to which the IBC can be matched: plain)

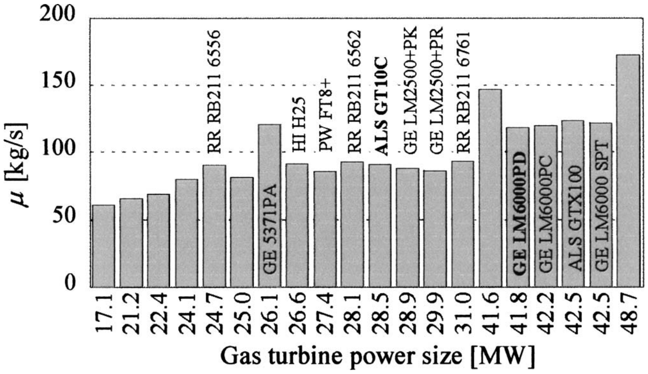

Fig. 11 Corrected mass flow (GTs chosen for IBC design: bold; OGTMs to which the IBC can be matched: plain)

Table 3 Assumed degree of reactions for compressor design

Stage	Degree of Reaction
1	0.87÷0.89
2	0.70
⩾3	0.50

Figure 12 shows the points representative of the IBC expanders in the Smith diagram, [10]. The stage efficiency determined by using the Smith diagram has been corrected to account for the blade tip clearance losses, [8,11], by considering a clearance to blade height ratio (ε/h) equal to 0.030 for all the IBC considered except for the one designed for the smallest GT (KHI M1A-13). For this IBC expander ε/h has been assumed equal to 0.043 in order to account for the expander size. The obtained polytropic efficiency values are close to the ones reported in Table 2.

The main results of expander design, for the six IBC engine considered, are reported in the Appendix (see Table A2).

Performance Obtainable by Repowering Gas Turbines With IBC

Once the six IBC engines for the selected gas turbines were designed, the performance obtainable by matching these IBC with the selected GT models and with the 23 OGTMs have been evaluated. For the IBC off-design calculation the performance of IBC compressors and expanders have been evaluated by using nondimensional performance maps, predicted by means of scaling techniques from performance maps of similar machines, [3,4,12]. In particular, it has been assumed that the IBC expanders work in choking conditions, and, so, with a constant inlet corrected mass flow rate μ.

The obtained performances, in terms of percentage electrical power increase due to the IBC employment with respect to the design GT electrical power are reported for all the 29 GTs considered in Figs. 13 and 14. The six GTs written with bold characters are the selected gas turbines for which the six IBC engines have been designed, while the 23 OGTMs are indicated with plain characters. In these figures the gray bars refer to the electrical power increase obtainable by repowering the 23 OGTMs with the six designed IBC engines, while the black bars refer to the electrical power increase obtainable by repowering the 29 GTs with IBC engines ad hoc designed. It can be noted how the improve-

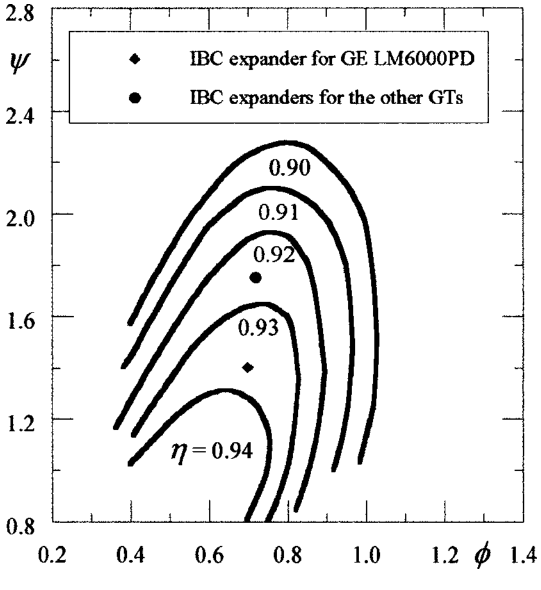

Fig. 12 Smith diagram [10] with points representative of IBC expanders

ments obtainable by using IBC ad hoc designed are negligible and how the percentage power increase (and so the electrical efficiency increase) ranges from 10 to 30%.

Finally, in Table 4, the values of pressure and temperatures at the IBC expander inlet and outlet are reported. It can be noted that all these values refer to off-design condition except those of GTs written in bold characters for which the IBC engines have been designed.

Conclusions

In this paper, an analysis of the performance enhancement obtainable by repowering existing gas turbines with inverted Brayton cycle engines, has been developed.

This analysis has permitted the selection of some of the most widespread gas turbines on the market, which allow the highest performance gain. For these gas turbines, a preliminary design of the main IBC components has been performed showing the feasibility of this type of engines.

In particular, six gas turbines have been selected, in four different power size classes, and six IBC engines have been ad hoc designed.

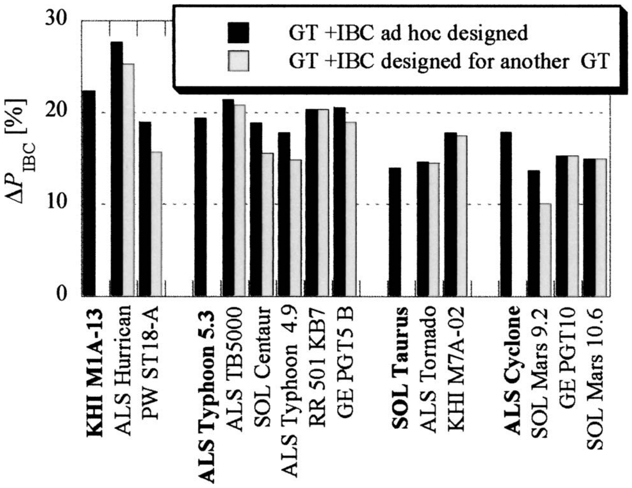

Fig. 13 Percentage electrical power increase due to the employment of an IBC ad hoc designed (black bar) and of an IBC designed for another GT (gray bar). Gas turbine power range up to 15 MW.

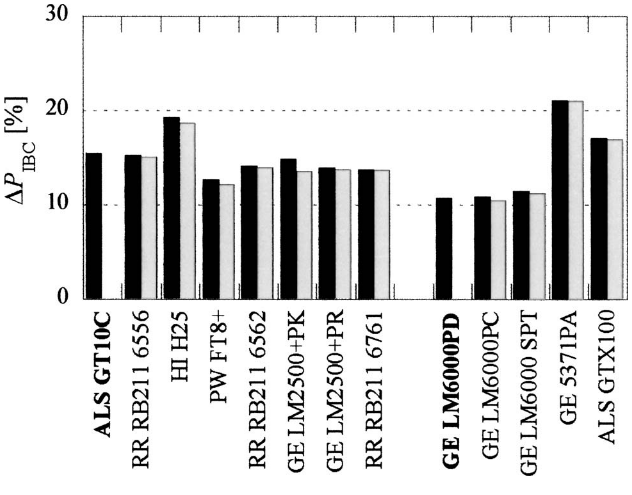

Fig. 14 Percentage electrical power increase due to the employment of an IBC ad hoc designed (black bar) and of an IBC designed for another GT (gray bar). Gas turbine power range over 15 MW.

Table 4 Pressure and temperature off design values

	p_{IE} [bar]	T_{IE} [°C]	p_{OE} [bar]	T_{OE} [°C]
KHI M1A-13	1.013	519	0.350	352
ALS Hurrican	0.978	527	0.336	359
PW ST18-A	0.938	591	0.312	409
ALS Typhoon 5.3	1.013	539	0.350	367
ALS TB5000	1.029	494	0.363	332
SOL Centaur	0.945	511	0.330	346
ALS Typhoon 4.9	0.958	507	0.336	343
RR 501 KB7	1.009	537	0.349	365
GE PGT5 B	0.988	569	0.336	391
SOL Taurus	1.013	493	0.350	329
ALS Tornado	1.023	482	0.356	320
KHI M7A-02	1.024	524	0.348	352
ALS Cyclone	1.013	572	0.350	329
SOL Mars 9.2	0.952	457	0.346	306
GE PGT10	1.034	491	0.371	332
SOL Mars 10.6	1.041	496	0.373	336
ALS GT10C	1.013	520	0.350	349
RR RB211 6556	1.010	489	0.354	326
HI H25	1.012	558	0.343	379
PW FT8+	0.958	473	0.338	315
RR RB211 6562	1.039	496	0.363	331
GE LM2500+PK	0.973	516	0.337	347
GE LM2500+PR	0.960	510	0.332	342
RR RB211 6761	1.044	511	0.362	343
GE LM6000PD	1.013	452	0.350	292
GE LM6000PC	1.024	457	0.353	296
GE LM6000 SPT	1.049	556	0.343	371
GE 5371PA	1.049	466	0.365	305
ALS GTX100	1.038	492	0.349	321

Moreover, the possibility to match these IBC engines with other gas turbines has been analyzed. The study has permitted to identify 23 gas turbines which can employ the designed IBC engines for their repowering. The performance obtainable, in terms of percentage electrical power increase (and so of electrical efficiency increase), range from 10 to 30% and result only slightly worse than that obtainable by repowering the same gas turbines with IBC engines ad hoc designed.

This last result highlights how the design and built of IBC engines may be convenient, also for third manufacturers, since a single IBC engine can be employed for the repowering of more gas turbine models.

Nomenclature

D = mean diameter
h = enthalpy, blade height
$\dot{m}$ = mass flow rate
N = IBC engine rotational speed
p = total pressure
R = radius, degrees of reaction
T = total temperature
U = blade speed at the mean radius
V_a = axial component of absolute flow velocity
V = absolute flow velocity
W = relative flow velocity
α = absolute flow angle
β = relative flow angle
δ = $= p_{OGT}/p_{\mathrm{ref}}$
Δh = stage total enthalpy variation
ΔP_{IBC} = percentage electrical power increase due to the IBC employment
ε = clearance
ϕ = V_a/U flow factor
η = efficiency
ϑ = T_{OGT}/T_{ref}
μ = $\dot{m}\sqrt{\vartheta}/\delta$, corrected mass flow rate
ψ = $\Delta h/U^2$ stage loading factor

Subscripts and Superscripts

amb = ambient
C = compressor

E = expander
GT = gas turbine
h = hub
I = inlet section
O = outlet section
p = polytropic
ref = reference
t = tip

Acronyms

C = compressor
E = expander
GT = gas turbine
HX = heat exchanger
IBC = inverted Brayton cycle
OGTM = other gas turbine model

Appendix

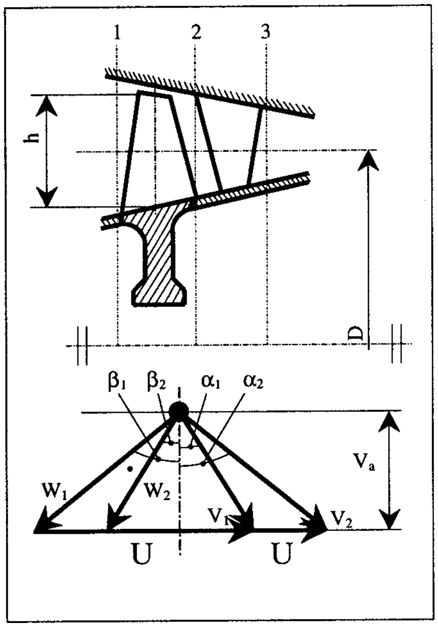

Fig. A1 Compressor stage schematic layout and corresponding velocity triangles

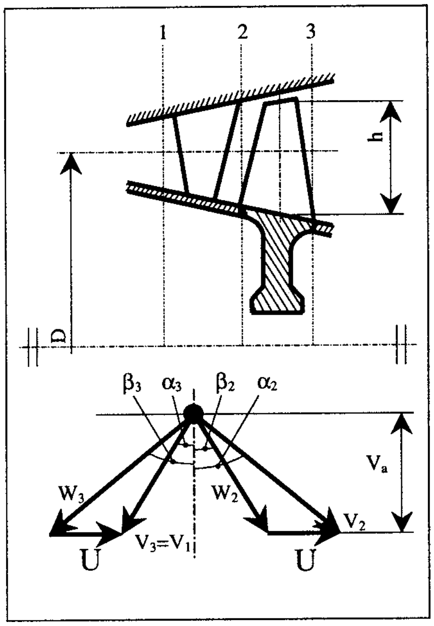

Fig. A2 Expander stage schematic layout and corresponding velocity triangles

Table A1 IBC compressor design

	N [rpm]	U [m/s]	D [m]	Stage	R_{h1} [m]	R_{t1} [m]	R_{h3} [m]	R_{t3} [m]	ψ	ϕ	T_1 [°C]	p_1 [bar]	T_3 [°C]	p_3 [bar]
KHI M1A-13	14950	353	0.451	1 5	0.164 0.193	0.287 0.258	0.174 0.197	0.277 0.254	0.248	0.424	50 158	0.343 0.853	77 186	0.442 1.033
ALS Typhoon 5.3	9525	353	0.708	1 5	0.257 0.303	0.451 0.405	0.273 0.309	0.435 0.398	0.245	0.425	50 157	0.343 0.853	77 184	0.442 1.033
SOL Taurus	8250	354	0.820	1 5	0.299 0.352	0.521 0.469	0.317 0.359	0.502 0.461	0.244	0.424	50 157	0.343 0.853	77 184	0.442 1.033
ALS Cyclone	6800	355	0.997	1 5	0.365 0.428	0.632 0.568	0.387 0.437	0.610 0.559	0.243	0.423	50 157	0.343 0.853	77 184	0.442 1.033
ALS GT10C	4500	354	1.502	1 5	0.548 0.645	0.954 0.858	0.582 0.659	0.921 0.845	0.240	0.423	50 156	0.343 0.852	77 182	0.442 1.033
GE LM6000PD	3600	370	1.961	1 5	0.768 0.869	1.194 1.092	0.803 0.884	1.158 1.078	0.218	0.406	50 154	0.343 0.852	76 180	0.442 1.033

Table A2 IBC expander design

	N [rpm]	U [m/s]	D [m]	R_{h1} [m]	R_{t1} [m]	R_{h3} [m]	R_{t3} [m]	T_1 [°C]	T_3 [°C]
KHI M1A-13	14950	327	0.418	0.176	0.242	0.132	0.287	579	352
ALS Typhoon 5.3	9525	334	0.670	0.283	0.386	0.215	0.455	539	366
SOL Taurus	8250	324	0.750	0.316	0.434	0.238	0.513	493	329
ALS Cyclone	6800	341	0.958	0.408	0.550	0.313	0.645	572	393
ALS GT10C	4500	332	1.408	0.597	0.811	0.455	0.953	520	349
GE LM6000PD	3600	355	1.884	0.844	1.039	0.714	1.169	452	293

References

[1] Wilson, G. D., 1984, *The Design of High-Efficiency Turbomachinery and Gas Turbine*, The MIT Press, Cambridge, MA.

[2] Bianchi, M., Negri di Montenegro, G., and Peretto, A., 2002, ‘‘Inverted Brayton Cycle Employment for Low-Temperature Cogenerative Applications,’’ ASME J. Eng. Gas Turbines Power, **124**, pp. 561–565.

[3] *Gate Cycle, Computational Code–Release 5.22*, Enter Software, Menlo Park, CA.

[4] *Thermoflex 5.2*, Thermoflow 8, Release 1, Thermoflow, Sudbury, MA.

[5] *Gas Turbine World 2001–2002 Handbook*, 2002, published in addition to *Handbook and Performance Specifications* annual, **22**, Pequot, Fairfield, CT.

[6] *Handbook 2002–2003*, 2002, Turbomachinery International, **43**, Business Journal Inc., Norwalk, CT.

[7] *Diesel & Gas Turbine Worldwide Catalog*, 2002, **67**, Diesel & Gas Turbine Pubblications, Waukesha, WI.

[8] Bhargava, R., Bianchi, M., Peretto, A., and Spina, P. R., 2004, ‘‘A Feasibility Study of Existing Gas Turbines for Recuperated, Intercooled and Reheat Cycle,’’ ASME J. Eng. Gas Turbines Power, **126**, pp. 531–544.

[9] Howell, A. R., and Bonham, R. P., 1950, ‘‘Overall and Stage Characteristics of Axial Flow Compressors,’’ Proc. Inst. Mech. Eng., **163**, pp. 235–248.

[10] Smith, S. F., 1965, ‘‘A Simple Correlation of Turbine Efficiency,’’ Journal Roy. Aero. Soc., **69**, pp. 467–470.

[11] Ainley, D. G., and Mathieson, G. C. R., 1951, ‘‘A Method of Performance Estimation for Axial Flow Turbines,’’ Aeronautical Research Council, R&M 2974.

[12] Kurzke, J., and Riegler, C., 2000, ‘‘A New Map Scaling Procedure for Preliminary Conceptional Design of Gas Turbines,’’ ASME Paper 2000-GT-0006.

Optimal Operational Planning of Cogeneration Systems With Microturbine and Desiccant Air Conditioning Units

Satoshi Gamou
e-mail: gamou@ese.energy.osakafu-u.ac.jp

Koichi Ito

Ryohei Yokoyama

Department of Mechanical Engineering,
Osaka Prefecture University,
1-1 Gakuen-cho,
Sakai, Osaka 599-8531, Japan

Economic and energy-saving characteristics of cogeneration systems with microturbine and desiccant air-conditioning units are investigated on system operational planning. An optimization approach is adopted to rationally evaluate these characteristics. In this approach, on/off and rated/part load status of operation of equipment and energy flow rates are determined so as to minimize the hourly energy charge subject to satisfaction of energy demand requirements. In this optimization problem, performance characteristics of the microturbine and desiccant air-conditioning units are modeled in consideration of the influence due to ambient air temperature. Moreover, the influence due to ambient air humidity is also considered in the desiccant air-conditioning unit using the psychrometric diagram. The implementation of the numerical analysis method, discussed in this paper, to two cogeneration systems, clearly shows economic and operational benefits of using desiccant air-conditioning. [DOI: 10.1115/1.1850509]

Introduction

Microturbine generator units with capacities under 100 kW have recently been paid attention to as distributed power sources [1]. This is because the microturbine generator units are expected to have the advantages of low initial capital cost, high electrical generating efficiency for their small capacities, high reliability, low NO*x* emission and so on. Moreover, they can be used as main equipment of cogeneration systems for commercial and public purposes [2]. In using them as cogeneration units, there are some means of utilizing flue gas generated from them. One is for desiccant air-conditioning [3,4]. Desiccant air-conditioning units can supply space cooling and heating energy directly by utilizing flue gas, and they have the advantage of high energy-saving because of dehumidification by the desiccant without subcooling energy. Some field tests for combined microturbine and desiccant air-conditioning units are performed in Japan [5]. However, economic and energy-saving characteristics of the cogeneration systems with the combined microturbine and desiccant air-conditioning units have not sufficiently been investigated.

The purpose of this paper is to construct a model in order to evaluate the economic and energy-saving characteristics on the operation of the aforementioned cogeneration systems as the first stage, and is also to investigate their characteristics through numerical studies. An optimization approach is adopted to evaluate the characteristics rationally. In the following, the configurations of microturbine cogeneration systems investigated here are first described. Second, the evaluation method based on the optimization is described. Finally, the numerical studies are carried out on systems installed in office buildings and hospitals.

System Configurations

Figure 1 shows a schematic diagram and energy flow of a microturbine cogeneration system investigated here. The system has the microturbine cogeneration unit (MT), a flue gas absorption refrigerator (RX), a gas-fired absorption refrigerator (RG), a gas-fired boiler (BG), an air handling unit (AHU), a desiccant air-conditioning unit (DCU), and a device for purchasing electricity (EP). Solid, dotted–dashed, dotted–dotted–dashed, dotted, broken, thick solid, and thick broken lines show flows of hot water, electricity, cold air, cold water, natural gas, flue gas, and hot air, respectively. Moreover, symbols for energy flow rates are listed in the Nomenclature.

In the system, electricity is supplied to users by purchasing electricity through EP from an outside electric power company and by operating MT. Electricity is also used to drive cooling towers and other auxiliary machinery. Flue gas generated from MT is used as heat sources for RX and DCU. Surplus exhaust heat is disposed of to the atmosphere. Cold air for space cooling is supplied by AHU using cold water from RX and RG as heat sinks and by DCU. Hot air for space heating is supplied by AHU using hot water from RX, RG and BG as heat sources and by DCU. Hot water for miscellaneous purposes is supplied by BG.

Optimal Operational Planning Problem

To evaluate the economic benefit of combining the microturbine and desiccant air-conditioning units on the operation, the optimization approach is adopted. In this approach, on/off and rated/part load status of operation of equipment and energy flow rates at each junction for each energy flow are determined so as to minimize the hourly energy charge subject to satisfaction of energy demand requirements. This optimal operational planning problem is described briefly below.

Mathematical Formulation

Performance Characteristics of Equipment. First, performance characteristics of pieces of equipment are considered as constraints in the optimization problem, and are formulated as relationships between input and output energy flow rates. These relationships are expressed by the following piecewise linear approximations [6]:

$$\left.\begin{array}{l} y = pu + q\delta \\ \underline{u}\,\delta \leqslant u \leqslant \bar{u}\,\delta \end{array}\right\}, \tag{1}$$

where u and y denote input and output energy flow rates, respectively; δ denotes a binary variable expressing the on/off status of operation of equipment; p and q denote performance characteristic

---

Contributed by the International Gas Turbine Institute (IGTI) of THE AMERICAN SOCIETY OF MECHANICAL ENGINEERS for publication in the ASME JOURNAL OF ENGINEERING FOR GAS TURBINES AND POWER. Paper presented at the International Gas Turbine and Aeroengine Congress and Exhibition, Vienna, Austria, June 13–17, 2004, Paper No. 2004-GT-53683. Manuscript received by IGTI, October 1, 2003; final revision, March 1, 2004. IGTI Review Chair: A. J. Strazisar.

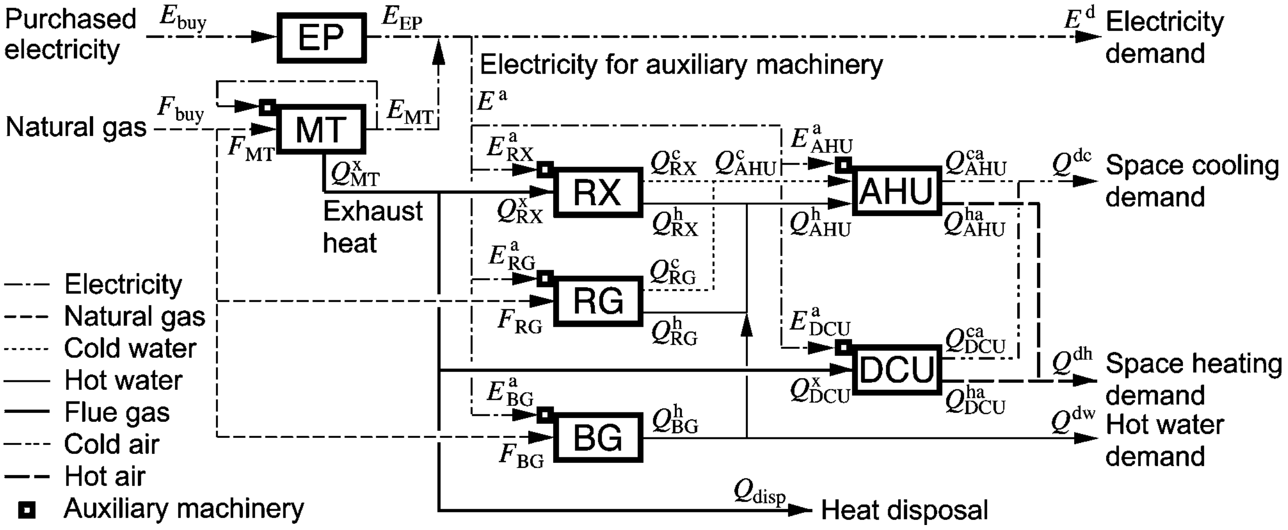

Fig. 1 Schematic diagram and energy flow of a microturbine cogeneration system

values; and $\underline{u}$ and $\bar{u}$ denote lower and upper limits of the input energy flow rate, respectively. In Eq. (1), if $\delta=0$, then $u=y=0$, which expresses off status of operation. On the other hand, if $\delta=1$, then $y=pu+q$ and $\underline{u}\leqslant u\leqslant\bar{u}$, which expresses on status of operation.

It is supposed that coefficients p, q, $\underline{u}$, and $\bar{u}$ in Eq. (1) for RX, RG, and BG are constants, and that those for MT, DCU, and AHU are functions of temperature and absolute humidity of ambient air. This is because the performance characteristics of MT, DCU, and AHU are influenced more greatly than those of other pieces of equipment. As examples, the performance characteristics of MT, DCU, and AHU are described briefly below.

(a) Microturbine cogeneration unit (MT). The relationships between the natural gas consumption F_{MT} and the generated electricity E_{MT} or the amount of generated flue gas Q^{x}_{MT} are expressed by the following equations:

$$\left.\begin{aligned} E_{\mathrm{MT}}&=p_{\mathrm{MT}}(t_i)F_{\mathrm{MT}}+q_{\mathrm{MT}}(t_i)\,\delta_{\mathrm{MT}}\\ Q^{x}_{\mathrm{MT}}&=p^{x}_{\mathrm{MT}}(t_i)F_{\mathrm{MT}}+q^{x}_{\mathrm{MT}}(t_i)\,\delta_{\mathrm{MT}}\\ \underline{F}_{\mathrm{MT}}(t_i)\,\delta_{\mathrm{MT}}&\leqslant F_{\mathrm{MT}}\leqslant\bar{F}_{\mathrm{MT}}(t_i)\,\delta_{\mathrm{MT}} \end{aligned}\right\}, \tag{2}$$

where δ_{MT} denotes a binary variable expressing the on/off status of operation of MT; coefficients p_{MT}, q_{MT}, p^{x}_{MT}, and q^{x}_{MT} are the performance characteristic values; $\bar{F}_{\mathrm{MT}}$ and $\underline{F}_{\mathrm{MT}}$ are the upper and lower limits on the natural gas consumption, respectively; and t_i denotes intake air temperature. These performance characteristic values together with the upper and lower limits are considered as functions of intake air temperature t_i.

(b) Desiccant air-conditioning unit (DCU). The relationships between the input energy flow rate Q^{x}_{DCU} and the heat flow rate for space cooling air $Q^{\mathrm{ca}}_{\mathrm{DCU}}$ or the heat flow rate for space heating air $Q^{\mathrm{ha}}_{\mathrm{DCU}}$ are influenced by temperature and absolute humidity of ambient air, because DCU dehumidifies and cools or heats ambient air directly. To consider these influences, the relationships are formulated according to psychrometric processes in space cooling or heating modes of DCU. The relationship in space cooling mode is first described below, and is followed by the relationship in space heating mode.

Figure 2 shows component configuration and air flows in space cooling mode of DCU, and Fig. 3 shows the corresponding psychrometric process [3]. In Fig. 2, DCU has a desiccant wheel (DW), a sensible heat wheel (SHW), a heat exchanger (HE) and evaporative coolers (EC1 and EC2). The air stream of DCU consists mainly of a process air one expressing States ① to ④ and of a regeneration air one expressing States ⑤ to ⑩. In the process air stream, warm and wet ambient air at State ① is introduced as a process air, passes through DW, and results in hot and dry air at State ②. This temperature increase is due to the release of condensation heat of the water vapor when moisture is removed by the desiccant. This hot and dry air at State ② is cooled sensibly as it passes through SHW. The cool and dry air at State ③ is further evaporatively cooled and humidified by EC1 to air at State ④, and is then introduced to the conditioned space. On the other hand, in the regeneration air stream, the warm and humid regeneration air at State ⑤ from the conditioned space is evaporatively cooled by EC2 to air at State ⑥. The air at State ⑥ is heated sensibly as it passes through SHW. One part of the hot and humid air at State ⑦ is further heated up to the required regeneration temperature of the

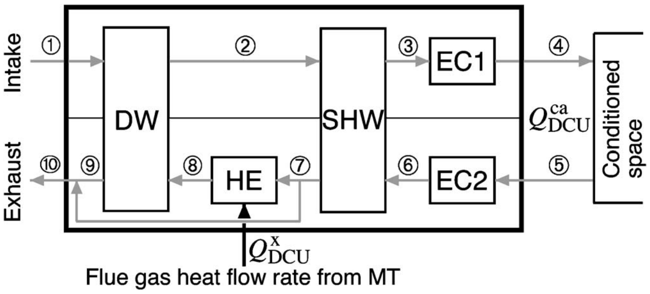

Fig. 2 Schematic diagram and air flow in space cooling mode of DCU

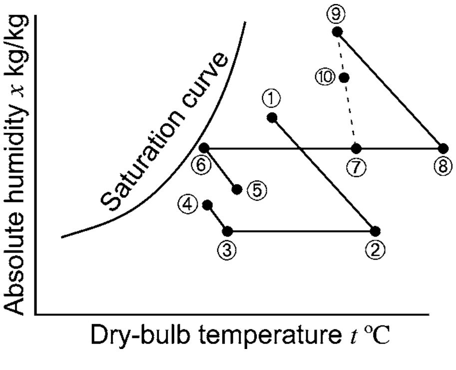

Fig. 3 Psychrometric diagram in space cooling mode of DCU

desiccant by the heat from the flue gas of MT through HE, and the other part bypasses HE and DW. This is because the regeneration air mass flow rate of DW is less than the process air mass flow rate if the regeneration temperature is sufficiently high. The hot and humid air at State ⑧ passes through DW in order to regenerate the desiccant. Even though this air is humid, it is sufficiently hot to remove the moisture from the desiccant. Finally, the warm and very humid air at State ⑨ is mixed with the bypass air at State ⑦, and the mixed air at State ⑩ is exhausted to the surroundings. In the aforementioned process, the input energy flow rate Q_{DCU}^{x} and the output energy flow rate $Q_{\mathrm{DCU}}^{\mathrm{ca}}$ are expressed by the following equations:

$$\left.\begin{aligned} Q_{\mathrm{DCU}}^{x}&=Am_e(h_8-h_7) \\ Q_{\mathrm{DCU}}^{\mathrm{ca}}&=Am(h_5-h_4) \end{aligned}\right\}, \tag{3}$$

where m and m_e denote the air mass flow rates of each stream and the regeneration stream passing through HE/DW, respectively; h denotes specific enthalpy; A denotes a coefficient for unit conversion from J to Wh, i.e., 1/3600 Wh/J; and subscript numbers correspond to air states in Figs. 2 and 3. At this point, let t and x be, respectively, temperature and absolute humidity, and the specific enthalpy h is expressed as follows:

$$h(t,x)=ax+bt+cxt, \tag{4}$$

where coefficients a, b, and c denote latent heat of vaporization, specific heat at constant pressure of air and that of water, respectively. Therefore, Eq. (3) is rewritten by the following equations:

$$\left.\begin{aligned} Q_{\mathrm{DCU}}^{x}&=Am_e[h(t_8,x_8)-h(t_7,x_7)] \\ Q_{\mathrm{DCU}}^{\mathrm{ca}}&=Am[h(t_5,x_5)-h(t_4,x_4)] \end{aligned}\right\}. \tag{5}$$

The temperature and absolute humidity in Eq. (5) are calculated according to the psychrometric process shown in Fig. 3, and each process is formulated below.

Processes ① to ② and ⑧ to ⑨: It is supposed that the air with the required regeneration temperature t_8 is sufficiently supplied to DW, and that DW rotates at the speed most suitable for dehumidification and regeneration. Under this supposition, only process ① to ② is formulated here. Then, it can be assumed from Ref. [4] that temperature t_2 and absolute humidity x_2 at State ② after dehumidification are in proportion to temperature t_1 and absolute humidity x_1 at State ①, and are in inverse proportion to process air velocity v. Therefore, t_2 and x_2 are expressed by the following equations:

$$\left.\begin{aligned} t_2&=\frac{p_tx_1+q_tt_1+r_t}{v}+p_t'x_1+q_t't_1+r_t' \\ x_2&=\frac{p_xx_1+q_xt_1+r_x}{v}+p_x'x_1+q_x't_1+r_x' \end{aligned}\right\}, \tag{6}$$

where coefficients p_t, q_t, r_t, p_t', q_t', r_t', p_x, q_x, r_x, p_x', q_x', and r_x' are dehumidification performance characteristic values. Moreover, the air mass flow rates on the process and regeneration stream sides of DW, i.e., respectively m and m_e, are assumed to be in proportion to the velocity v as follows:

$$\left.\begin{aligned} m&=Bv \\ m_e&=Cv \end{aligned}\right\}, \tag{7}$$

where B and C denote coefficients of proportion.

Processes ② to ③ and ⑥ to ⑦: Let η_s and η_e be the effectiveness on process and regeneration air sides of SHW, respectively, and the relationships among temperature t_2, t_3, t_6, and t_7 are expressed by the following equations:

$$\left.\begin{aligned} \frac{t_2-t_3}{t_2-t_6}&=\eta_s \\ \frac{t_7-t_6}{t_2-t_6}&=\eta_e \end{aligned}\right\}. \tag{8}$$

Moreover, the relationships among absolute humidity x_2, x_3, x_6, and x_7 are expressed by the following equations:

$$\left.\begin{aligned} x_3&=x_2 \\ x_7&=x_6 \end{aligned}\right\}. \tag{9}$$

Processes ③ to ④ and ⑤ to ⑥: These processes are with constant enthalpies. Therefore, the relationships among specific enthalpies are expressed by the following equations:

$$\left.\begin{aligned} h(t_4,x_4)&=h(t_3,x_3) \\ h(t_6,x_6)&=h(t_5,x_5) \end{aligned}\right\}. \tag{10}$$

Moreover, let s and η_c be, respectively, the sensible heat factor and the evaporative effectiveness of EC2, and the following equations hold:

$$\left.\begin{aligned} \frac{h(t_5,x_4)-h(t_4,x_4)}{h(t_5,x_5)-h(t_4,x_4)}&=s \\ \frac{t_5-t_6}{t_5-t_{5,\mathrm{wb}}}&=\eta_c \end{aligned}\right\}, \tag{11}$$

where subscript wb denotes wet-bulb temperature.

Process ⑦ to ⑧: The relationship in this process is expressed by the following equation:

$$x_8=x_7. \tag{12}$$

Substituting Eqs. (4), (6)–(12) into Eq. (5) and arranging them, Q_{DCU}^{x} and $Q_{\mathrm{DCU}}^{\mathrm{ca}}$ become functions of v, t_1, x_1, t_5, x_5, and t_8 as follows:

$$\left.\begin{aligned} Q_{\mathrm{DCU}}^{x}&=p^{\mathrm{in}}(t_1,x_1,t_5,x_5,t_8)v+q^{\mathrm{in}}(t_1,x_1,t_5,x_5,t_8)+r^{\mathrm{in}}(t_1,x_1,t_5,x_5,t_8)\frac{1}{v} \\ Q_{\mathrm{DCU}}^{\mathrm{ca}}&=p^{\mathrm{out}}(t_1,x_1,t_5,x_5,t_8)v+q^{\mathrm{out}}(t_1,x_1,t_5,x_5,t_8)+r^{\mathrm{out}}(t_1,x_1,t_5,x_5,t_8)\frac{1}{v} \end{aligned}\right\}, \tag{13}$$

where p^{in}, q^{in}, r^{in}, p^{out}, q^{out}, and r^{out} are performance characteristic values, which are functions of t_1, x_1, t_5, x_5, and t_8. At this point, the values of r^{in} and r^{out} are very small within the ranges of t and x considered here. Therefore, neglecting the terms with them, both Q_{DCU}^{x} and $Q_{\mathrm{DCU}}^{\mathrm{ca}}$ become linear functions with respect to v. Then, since v can be eliminated from both functions, the relationship between Q_{DCU}^{x} and $Q_{\mathrm{DCU}}^{\mathrm{ca}}$ is finally expressed by the following equations:

$$\left.\begin{aligned} Q_{\mathrm{DCU}}^{\mathrm{ca}}&=p_{\mathrm{DCU}}^{\mathrm{ca}}(t_1,x_1,t_5,x_5,t_8)Q_{\mathrm{DCU}}^{x}+q_{\mathrm{DCU}}^{\mathrm{ca}}(t_1,x_1,t_5,x_5,t_8)\,\delta_{\mathrm{DCU}}^{\mathrm{ca}} \\ Q_{\mathrm{DCU}}^{x}&\geqslant\underline{Q}_{\mathrm{DCU}}^{\mathrm{xc}}(t_1,x_1,t_5,x_5,t_8,\underline{v})\,\delta_{\mathrm{DCU}}^{\mathrm{ca}} \\ Q_{\mathrm{DCU}}^{x}&\leqslant\bar{Q}_{\mathrm{DCU}}^{\mathrm{xc}}(t_1,x_1,t_5,x_5,t_8,\bar{v})\,\delta_{\mathrm{DCU}}^{\mathrm{ca}} \end{aligned}\right\}, \tag{14}$$

where $\delta_{\mathrm{DCU}}^{\mathrm{ca}}$ denotes a binary variable expressing the on/off status of operation in space cooling mode of DCU; coefficients $p_{\mathrm{DCU}}^{\mathrm{ca}}$ and $q_{\mathrm{DCU}}^{\mathrm{ca}}$ are the performance characteristic values, which are functions of t_1, x_1, t_5, x_5, and t_8; $\bar{v}$ and $\underline{v}$ are the upper and lower limits of velocity v; and $\bar{Q}_{\mathrm{DCU}}^{\mathrm{xc}}$ and $\underline{Q}_{\mathrm{DCU}}^{\mathrm{xc}}$ are the upper and lower limits on the input energy flow rate, respectively, which are functions of t_1, x_1, t_5, x_5, t_8 and $\bar{v}$ or $\underline{v}$. If t_1, x_1, t_5, x_5, t_8, $\bar{v}$ and $\underline{v}$, i.e., ambient temperature and absolute humidity, conditioned space temperature and humidity, regeneration temperature of the desiccant, and upper and lower bounds of process air velocity, are given, $p_{\mathrm{DCU}}^{\mathrm{ca}}$, $q_{\mathrm{DCU}}^{\mathrm{ca}}$, $\bar{Q}_{\mathrm{DCU}}^{\mathrm{xc}}$, and $\underline{Q}_{\mathrm{DCU}}^{\mathrm{xc}}$ become constants. Moreover, electricity for auxiliary machinery of DCU, i.e., $E_{\mathrm{DCU}}^{\mathrm{ac}}$, is expressed as follows:

$$E_{\mathrm{DCU}}^{\mathrm{ac}}=p_{\mathrm{DCU}}^{\mathrm{ac}}Q_{\mathrm{DCU}}^{x}+q_{\mathrm{DCU}}^{\mathrm{ac}}\delta_{\mathrm{DCU}}^{\mathrm{ca}}, \tag{15}$$

where $p_{\mathrm{DCU}}^{\mathrm{ac}}$ and $q_{\mathrm{DCU}}^{\mathrm{ac}}$ are performance characteristic values.

On the other hand, Fig. 4 shows component configuration in space heating mode of DCU, and Fig. 5 shows the corresponding psychrometric process. In the similar way to space cooling mode, the performance characteristics in space heating mode are formulated according to the psychrometric process shown in Fig. 5. The relationships between Q_{DCU}^{x} and $Q_{\mathrm{DCU}}^{\mathrm{ha}}$ or $E_{\mathrm{DCU}}^{\mathrm{ah}}$ are finally expressed by the following equations:

$$\left.\begin{array}{r}Q_{\mathrm{DCU}}^{\mathrm{ha}}=p_{\mathrm{DCU}}^{\mathrm{ha}}(t_1,x_1,t_4,t_5,x_5)Q_{\mathrm{DCU}}^{x}+q_{\mathrm{DCU}}^{\mathrm{ha}}(t_1,x_1,t_4,t_5,x_5)\,\delta_{\mathrm{DCU}}^{\mathrm{ha}}\\ E_{\mathrm{DCU}}^{\mathrm{ah}}=p_{\mathrm{DCU}}^{\mathrm{ah}}Q_{\mathrm{DCU}}^{x}+q_{\mathrm{DCU}}^{\mathrm{ah}}\delta_{\mathrm{DCU}}^{\mathrm{ha}}\\ Q_{\mathrm{DCU}}^{x}\geqslant\underline{Q}_{\mathrm{DCU}}^{\mathrm{xh}}(t_1,x_1,t_4,t_5,x_5,\underline{v})\,\delta_{\mathrm{DCU}}^{\mathrm{ha}}\\ Q_{\mathrm{DCU}}^{x}\leqslant\bar{Q}_{\mathrm{DCU}}^{\mathrm{xh}}(t_1,x_1,t_4,t_5,x_5,\bar{v})\,\delta_{\mathrm{DCU}}^{\mathrm{ha}}\end{array}\right\} \tag{16}$$

where $\delta_{\mathrm{DCU}}^{\mathrm{ha}}$ denotes a binary variable expressing the on/off status of operation in space heating mode of DCU; $p_{\mathrm{DCU}}^{\mathrm{ha}}$, $q_{\mathrm{DCU}}^{\mathrm{ha}}$, $p_{\mathrm{DCU}}^{\mathrm{ah}}$, and $q_{\mathrm{DCU}}^{\mathrm{ah}}$ are the performance characteristic values, and the former two are functions of t_1, x_1, t_4, t_5, and x_5; and $\bar{Q}_{\mathrm{DCU}}^{\mathrm{xh}}$ and $\underline{Q}_{\mathrm{DCU}}^{\mathrm{xh}}$ are the upper and lower bounds on the input energy flow rate, respectively, which are functions of t_1, x_1, t_4, t_5, x_5 and $\bar{v}$ or $\underline{v}$.

(c) Air handling unit (AHU). AHU is modeled as a variable air volume system. In the similar way to DCU, the performance characteristics are formulated according to the psychrometric process. The relationships between the cold water heat flow rate Q_{AHU}^{c} and the heat flow rate for space cooling air $Q_{\mathrm{AHU}}^{\mathrm{ca}}$ or the electricity for auxiliary machinery $E_{\mathrm{AHU}}^{\mathrm{ca}}$ and those between the hot water heat flow rate Q_{AHU}^{h} and the heat flow rate for space heating air $Q_{\mathrm{AHU}}^{\mathrm{ha}}$ or the electricity for auxiliary machinery $E_{\mathrm{AHU}}^{\mathrm{ha}}$ are expressed by the following equations:

$$\left.\begin{array}{l}Q_{\mathrm{AHU}}^{\mathrm{ca}}=p_{\mathrm{AHU}}^{\mathrm{ca}}(t_1,x_1,t_{4,\mathrm{AHU}},t_5,x_5)Q_{\mathrm{AHU}}^{c}\\ E_{\mathrm{AHU}}^{\mathrm{ac}}=p_{\mathrm{AHU}}^{\mathrm{ac}}Q_{\mathrm{AHU}}^{c}\\ Q_{\mathrm{AHU}}^{\mathrm{ha}}=p_{\mathrm{AHU}}^{\mathrm{ha}}(t_1,x_1,t_{4,\mathrm{AHU}},t_5,x_5)Q_{\mathrm{AHU}}^{h}\\ E_{\mathrm{AHU}}^{\mathrm{ah}}=p_{\mathrm{AHU}}^{\mathrm{ah}}Q_{\mathrm{AHU}}^{h}\end{array}\right\}, \tag{17}$$

where $p_{\mathrm{AHU}}^{\mathrm{ca}}$, $p_{\mathrm{AHU}}^{\mathrm{ha}}$, $p_{\mathrm{AHU}}^{\mathrm{ac}}$, and $p_{\mathrm{AHU}}^{\mathrm{ah}}$ are the performance characteristic values, and the former two are functions of t_1, x_1, $t_{4,\mathrm{AHU}}$, t_5, and x_5; and $t_{4,\mathrm{AHU}}$ denotes air temperature introduced from AHU to the conditioned space, and is given as input data.

Energy Balance and Supply-Demand Relationships. Next, energy balance and supply-demand relationships are considered as constraints in the optimization problem, and are formulated by linear equations with energy flow rates at each junction for each energy flow illustrated in Fig. 1. For example, the following equations are obtained for the electricity flow:

$$\left.\begin{array}{l}E_{\mathrm{EP}}+E_{\mathrm{MT}}=E^{d}+E^{a}\\ E^{a}=E_{\mathrm{RX}}^{a}+E_{\mathrm{RG}}^{a}+E_{\mathrm{BG}}^{a}+E_{\mathrm{AHU}}^{a}+E_{\mathrm{DCU}}^{a}\end{array}\right\}. \tag{18}$$

Objective Function. The hourly energy charge is adopted as the objective function to be minimized from an economic viewpoint. The hourly energy charge J is expressed by the following equation:

$$J=\varphi_E E_{\mathrm{buy}}+\varphi_G F_{\mathrm{buy}}, \tag{19}$$

where φ_E and φ_G denote the unit costs of electricity and natural gas charges, respectively.

As a result, in this optimization problem, on/off and rated/part load status of operation of equipment and energy flow rates at each junction for each energy flow are determined so as to minimize the objective function (19) under constraints of the equipment performance characteristics such as Eqs. (1), (2) and (14)–(17) and the energy balance/supply-demand relationships such as Eq. (18).

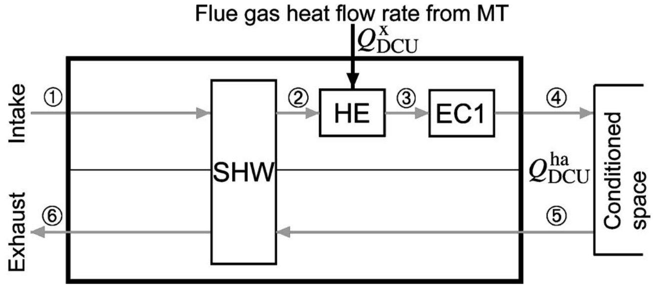

Fig. 4 Schematic diagram and air flow in space heating mode of DCU

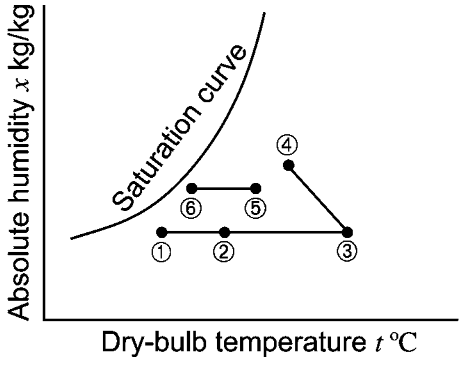

Fig. 5 Psychrometric diagram in space heating mode of DCU

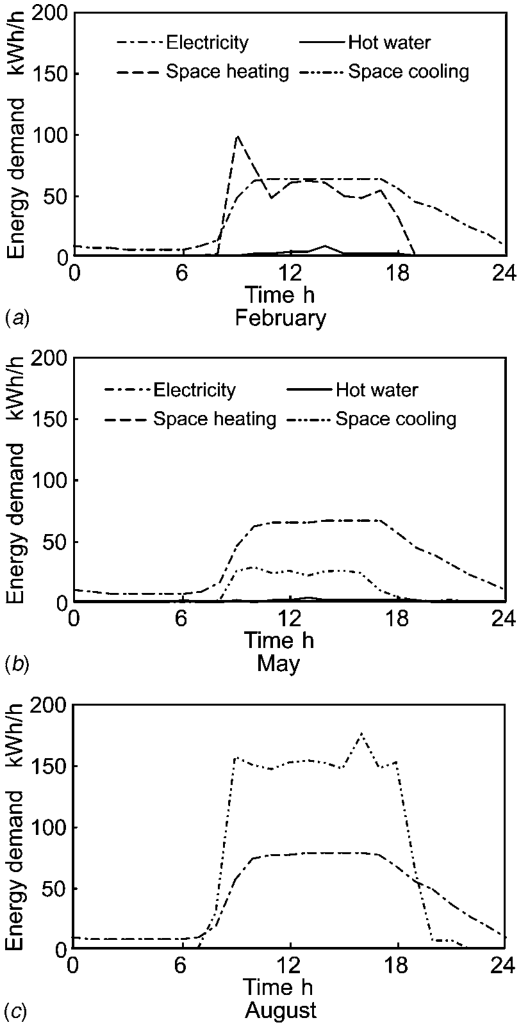

Fig. 6 Hourly energy demands (office building, 2000 m^2)

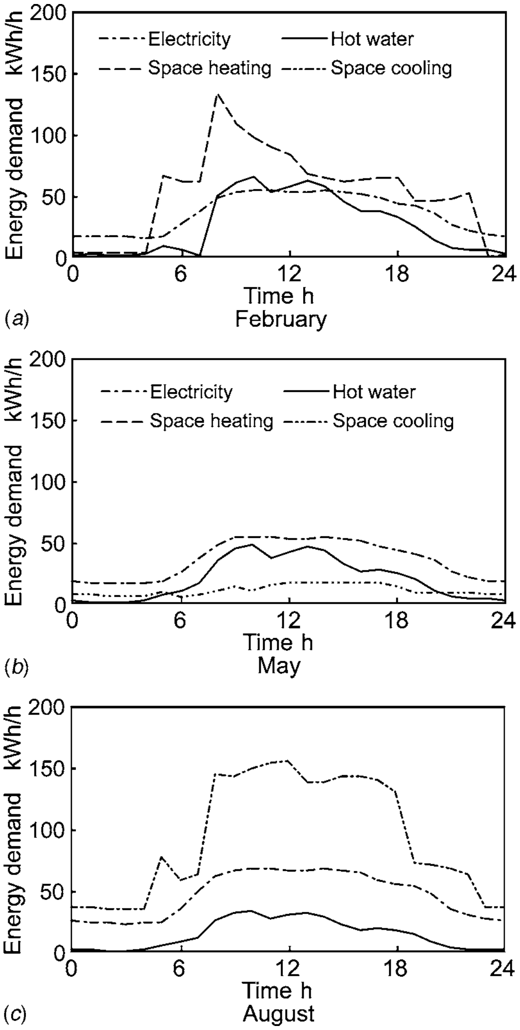

Fig. 7 Hourly energy demands (hospital, 2000 m^2)

Solution Method. The problem formulated and described in the previous section results in a mixed-integer linear programming one, and is solved by the GAMS(General Algebraic Modeling System)/Cplex solver [7], which is a commercial one combining the branch and bound method with the simplex method.

Numerical Study

Input Data. Energy demands of office buildings and hospitals with total floor areas of 1000, 1500, and 2000 m^2 are estimated at 24 sampling times on each month of 12 representative days in a year in order to investigate the annual economic and operational benefits of using desiccant air-conditioning. The maximum electricity demands for unit area of the office buildings and hospitals are 39.6 and 33.4 W/m^2, respectively. As examples, Figs. 6 and 7 show hourly energy demands on February, May and August representative days for total floor area of 2000 m^2 of the office building and hospital, respectively. Moreover, Fig. 8 shows temperature t_1 and absolute humidity x_1 of the ambient air on February, May and August representative days as examples. The ambient air temperature is also adopted as the intake air temperature of MT. Besides, temperature t_5, relative humidity and absolute humidity x_5 in the conditioned space are set to 26°C, 50% and 0.0105 kg/kg for space cooling, respectively, and those are set to 22°C, 40% and 0.0067 kg/kg for space heating, respectively.

Representative values of performance characteristics and capacities of equipment are summarized in Table 1. The maximum output power and the electrical generating efficiency at the rated load status of MT are dependent greatly on the intake air temperature. Figure 9 shows the relationships between the intake air temperature and the maximum output power or the electrical generating efficiency at the rated load status. In assessing the performance characteristics of DCU shown in Table 1, coefficients p_t, q_t, r_t, p'_t, q'_t, r'_t, p_x, q_x, r_x, p'_x, q'_x, and r'_x are determined by regression analysis based on the dehumidifier performance in catalogs. The other parameters such as η_s, η_e, etc. are set based on references and catalog data. Moreover, as examples of the performance characteristic of DCU, the relationship between Q^x_{DCU} and $Q^{\mathrm{ca}}_{\mathrm{DCU}}$ for temperature and absolute humidity are shown in Fig. 10. In this figure, the upper and lower limits of Q^x_{DCU} correspond to those limits of the air velocity of DCU, respectively, as shown in Eq. (14). According to this figure, the efficiency of DCU becomes low with the increase in temperature and absolute humidity, and the efficiency at part-load status is higher than that at rated load status. The latter is reflected in the fact that the more moisture per unit air is removed by the desiccant when the air flows slowly and stays in the desiccant for a long time.

The rates for purchased electricity and natural gas adopted in this study are given in Table 2.

Under the aforementioned conditions, the influence of introducing DCU on the economic and energy-saving characteristics is investigated for the office buildings and hospitals. The economic

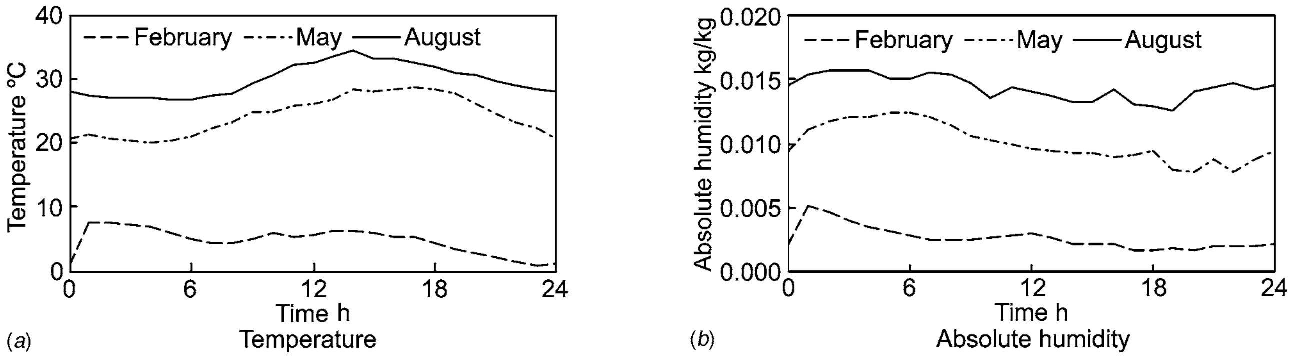

Fig. 8 Temperature and absolute humidity of ambient air

Table 1 Performance characteristic values and capacities of equipment

Equipment	Performance characteristic value (rated load)		Capacity
Microturbine cogeneration unit	Electrical generating efficiency	$0.25^{*1,*2}$	28 kW
	Flue gas recovery efficiency	$0.72^{*1,*2}$	
Flue gas absorption refrigerator	Coefficient of performance	0.56 (space cooling)	56 kW
	Thermal efficiency	0.76 (space heating)	
Gas-fired absorption refrigerator	Coefficient of performance	1.12^{*1} (space cooling)	250 kW
	Thermal efficiency	0.93^{*1} (space heating)	
Gas-fired boiler	Thermal efficiency	0.91^{*1}	125 kW
Receiving device for purchased electricity			70 kW
Desiccant air conditioning unit	Coefficient of performance	0.73^{*3} (space cooling)	62kW^{*3}
	Efficiency	0.90^{*4} (space heating)	62kW^{*4}
Air handling unit	Efficiency	0.75^{*3} (space cooling)	180kW^{*3}
	Efficiency	0.89^{*4} (space heating)	180kW^{*4}

^{*1}The net thermal efficiency is calculated under the assumption that the lower heating value of natural gas is 11.55 kWh/m^3.
^{*2}When intake air temperature is 15°C.
^{*3}When ambient air temperature and absolute humidity are 30°C and 0.012 kg/kg, respectively.
^{*4}When ambient air temperature and absolute humidity are 7°C and 0.005 kg/kg, respectively.

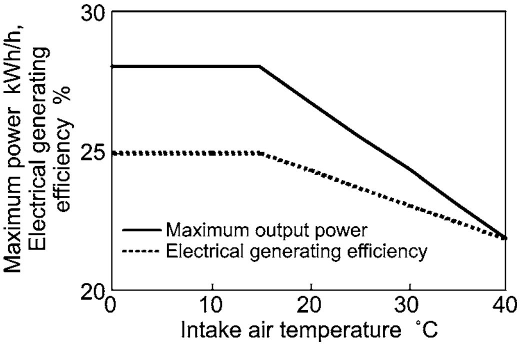

Fig. 9 Relationships between intake air temperature and maximum output power or electrical generating efficiency

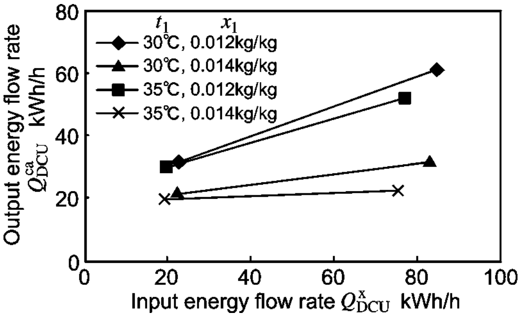

Fig. 10 Performance characteristics of DCU

Table 2 Rates for purchased electricity and natural gas

Utility	Unit cost of energy charge
Purchased electricity	14.15 (Jul.–Sep.) yen/kWh 12.86 (Other months) yen/kWh
Natural gas	43.13 yen/m^3

and energy-saving characteristics are evaluated as the annual operational cost, which is the sum of hourly energy charges through a year, and the annual primary energy consumption, respectively. In evaluating the annual primary energy consumption, it is assumed that the lower heating value of natural gas is 11.55 kWh/m^3, and that the thermal efficiency of purchased electricity is 0.388.

Results and Discussion. Tables 3 and 4 show respectively the annual operational cost and the annual primary energy consumption for all the cases. According to Table 3, the annual operational cost for the system with DCU is smaller than that for the system without DCU for all the cases. The reduction rates of the annual operational cost for the system with DCU to that for the system without DCU are 3%–5% and 6%–10% for the office buildings and the hospitals, respectively. It is found from this result that the reduction rate of the annual operational cost for the hospital is larger than that for the office building. Moreover, for the hospital, the reduction rate of the annual operational cost becomes large with the increase in total floor area. The ranges in the output ratio of DCU to the maximum space cooling demand are 0.26–0.8, 0.2–0.6, and 0.13–0.4 for the hospitals with the total floor areas of 1000, 1500, and 2000 m^2, respectively. It is found

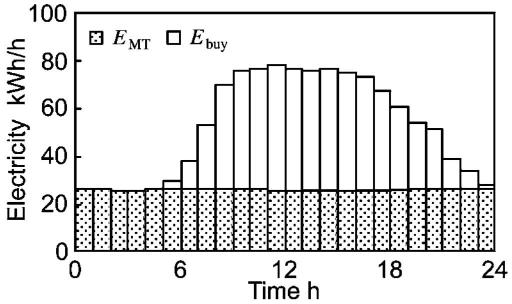

(*a*) Electricity supply

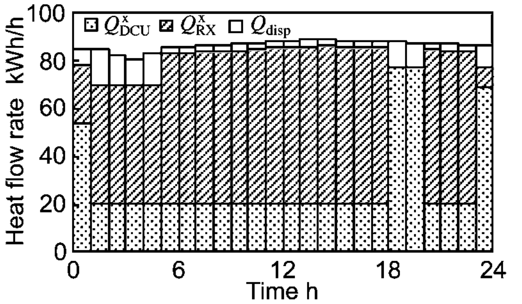

(*b*) Recovered heat

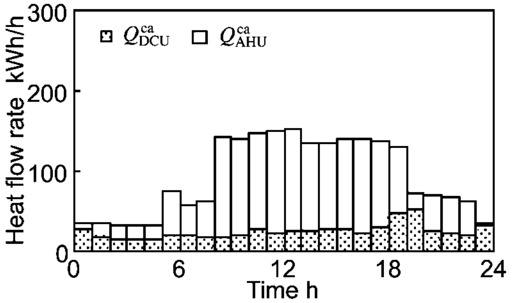

(*c*) Cold air supply

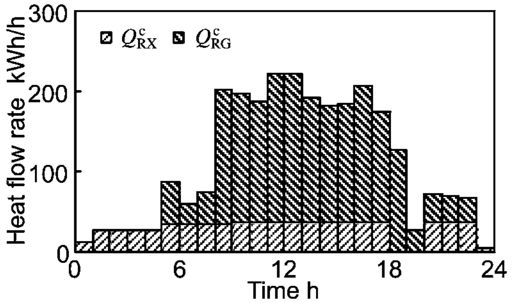

(*d*) Cold water supply

Fig. 11 Example of operational strategies for system with DCU (hospital, 2000 m^2)

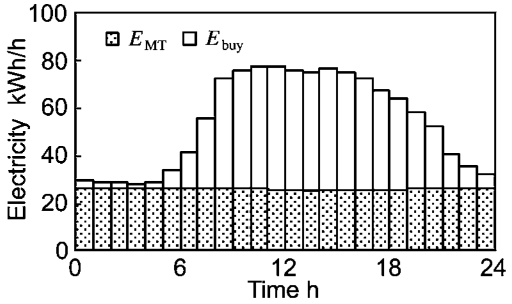

(*a*) Electricity supply

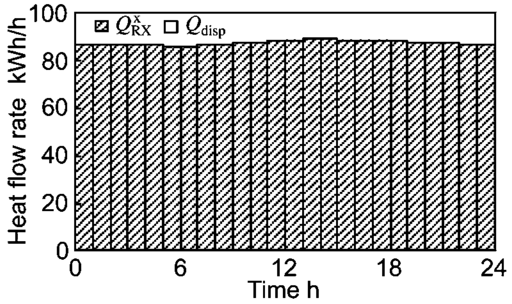

(*b*) Recovered heat

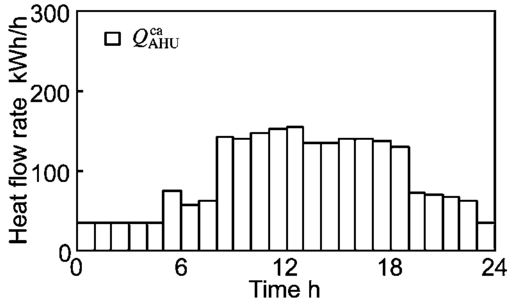

(*c*) Cold air supply

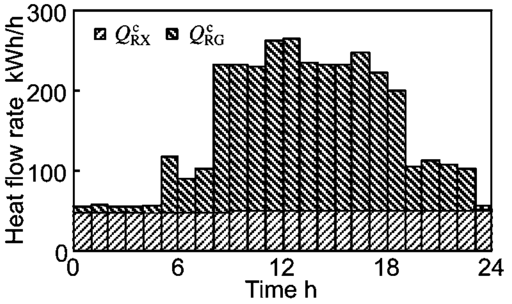

(*d*) Cold water supply

Fig. 12 Example of operational strategies for system without DCU (hospital, 2000 m^2)

Table 3 Annual operational cost and its reduction rates

	Total floor area m^2	Annual operation cost $\times 10^6$ yen/y System with DCU	System without DCU	Reduction rate due to DCU %
Office building	1000	2.47	2.59	4.7
	1500	3.69	3.88	5.0
	2000	4.95	5.15	3.9
Hospital	1000	3.16	3.40	6.7
	1500	4.62	5.07	8.8
	2000	6.14	6.80	9.7

Table 4 Annual primary energy consumption and its reduction rates

	Total floor area m^2	Annual primary energy consumption GWh/y System with DCU	System without DCU	Reduction rate due to DCU %
Office building	1000	0.61	0.63	4.4
	1500	0.89	0.94	4.8
	2000	1.19	1.23	3.8
Hospital	1000	0.80	0.86	6.6
	1500	1.16	1.28	8.9
	2000	1.53	1.69	9.9

from these results that the economic benefit of introducing DCU on the operation is high when the ratio of the capacity of DCU to maximum space cooling demand is less than 0.4 for the hospital with much thermal energy demand. Similar discussion is made for the annual primary energy consumption shown in Table 4. Therefore, it is found that the energy-saving benefit of introducing DCU is also high for the hospital with much thermal energy demand.

As examples, Figs. 11 and 12 show the operational strategies on August representative day in the system with and without DCU for the hospital with the total floor area of 2000 m^2, respectively. Comparing Fig. 11(a) with Fig. 12(a), electricity supply during night in the system with DCU is smaller than that in the system without DCU. This is because the electricity for auxiliary machinery becomes small by using DCU for space cooling supply. Moreover, it is found from (b) of these figures that the flue gas utilized to DCU is small. This is because the efficiency of DCU is high at part-load status as shown in Fig. 10. Besides, it is found from (d) of these figures that the cold water supply in the system with DCU is smaller than that in the system without DCU. By this result, the electricity for auxiliary machinery in the system with DCU becomes smaller than that in the system without DCU, and the electricity supply becomes small as mentioned previously.

The aforementioned results show that the economic and energy-saving benefits of the installation of DCU are high.

Conclusions

In this paper, the economic and energy-saving characteristics of the cogeneration system with the microturbine and desiccant air conditioning units have been investigated on the operation based on the optimization method. Through the numerical studies carried out on the systems installed in office buildings and hospitals, the following results have been obtained:

a. The reduction rates of the annual operational cost for the system with DCU to that for the system without DCU are 3%–5% and 6%–10% for the office buildings and the hospitals, respectively.
b. The reduction rates of the annual primary energy consumption for the system with DCU to that for the system without DCU are 3%–5% and 6%–10% for the office buildings and the hospitals, respectively.
c. The economic and energy-saving benefits of introducing DCU for hospital are larger than those for office building.
d. By the installation of DCU, the cold water supply by RX and RG reduces. Moreover, the DCU is mainly operated at part-load status because the efficiency at part-load status is higher than that at rated load status.

In this paper, the capital costs of pieces of equipment are not taken into account because we have focused on the operational benefit of the aforementioned system as the first stage. However, it is also important to evaluate that system from the economic viewpoint including the capital costs. As the next stage, we will investigate it by extending the aforementioned method to that case.

Acknowledgment

This work was supported by MEXT Grant-in-Aid for Young Scientists (B) 14780400.

Nomenclature

A = coefficient for unit conversion from J to Wh, Wh/J
a = latent heat of vaporization of water, kJ/kg
B, C = coefficients of proportion, kg/m
b = specific heat at constant pressure of air, kJ/(kg °C)
c = specific heat of water, kJ/(kg °C)
E = electricity, kWh/h
F = natural gas consumption, m^3/h
h = specific enthalpy, kJ/kg
J = hourly energy charge, yen/h
m = mass flow rate, kg/h
p, q, r, p', q', r' = performance characteristic values of equipment
Q = heat flow rate, kWh/h
s = sensible heat factor
t = temperature, °C
u = input energy flow rate of equipment, m^3/h, kWh/h
v = velocity of process air, m/h
x = absolute humidity, kg/kg
y = output energy flow rate of equipment, kWh/h
δ = binary variable expressing on/off status of operation
η_c = evaporative effectiveness of EC2
η_e = effectiveness on regeneration air side of SHW
η_s = effectiveness on process air side of SHW
φ = unit cost of energy charge, yen/m^3, yen/kWh
$\underline{(\ )}, \overline{(\ )}$ = lower and upper limits

Equipment symbols (subscripts)

AHU = air handling unit
BG = gas-fired boiler
DCU = desiccant air-conditioning unit
DW = desiccant wheel
EC1, EC2 = evaporative coolers
EP = device for purchasing electricity
HE = heat exchanger
MT = microturbine cogeneration unit
RG = gas-fired absorption refrigerator
RX = flue gas absorption refrigerator
SHW = sensible heat wheel

Superscripts

a = auxiliary machinery
ac = auxiliary machinery in space cooling mode
ah = auxiliary machinery in space heating mode
c = cold water
ca = cold air
d = demand
dc = space cooling demand
dh = space heating demand
dw = hot water demand
h = hot water
ha = hot air
in = input
out = output
x = flue gas
xc = flue gas in space cooling mode
xh = flue gas in space heating mode

Subscripts

1–10 = air state points
buy = purchase
disp = heat disposal
E = electricity
e = regeneration air
G = natural gas
i = intake air
t = temperature
wb = wet-bulb
x = absolute humidity

References

[1] Scott, W. G., 1998, "Micro-Turbine Generator for Distribution Systems," IEEE Ind. Appl. Mag., **4**(3), pp. 57–62.
[2] Carnö, J., Cavani, A., and Liinanki, L., 1998, "Microturbine for Combined Heat and Power in Distributed Generation," ASME Paper No. 98-GT-309.
[3] Davanagere, B. S., Sherif, S. A., and Goswami, D. Y., 1999, "A Feasibility

Study of a Solar Desiccant Air-Conditioning System—Part I: Psychrometrics and Analysis of the Conditioned Zone,'' Int. J. Energy Res., **23**, pp. 7–21.

[4] Kodama, A., 2001, ''Adsorptive Desiccant Cooling Process Equipped With a Honeycomb Rotary Dehumidifier,'' Adsorption News, **15**(1), pp. 6–11 (in Japanese).

[5] Fujita, T., 2003, ''The Desiccant Air-Conditioning System Which Combined the Micro Gas Turbine System in a FURESUTA Yokogawa Store,'' The Cogeneration in Japan, **18**(1), pp. 66–71 (in Japanese).

[6] Ito, K. et al., 1990, ''Influence of Fuel Cost on the Operation of a Gas Turbine-Waste Heat Boiler Cogeneration Plant,'' ASME J. Eng. Gas Turbines Power, **112**, pp. 122–128.

[7] Brooke, A., Kendrick, D., and Meeraus, A., 1996, *GAMS Release 2.25 A User's Guide*, GAMS Development Corp., Washington.

Irebert R. Delgado
Vehicle Technology Directorate,
U.S. Army Research Laboratory,
NASA Glenn Research Center,
Cleveland, OH 44135

Gary R. Halford

Bruce M. Steinetz

NASA Glenn Research Center,
Cleveland, OH 44135

Clare M. Rimnac
Case Western Research University,
Cleveland, OH 44106

Strain-Life Assessment of Grainex Mar-M 247 for NASA's Turbine Seal Test Facility

NASA's turbine seal facility tests air-to-air seals for advanced jet engines. High temperature, speed, and pressure combinations limit test disk life, due to crack initiation in the Grainex Mar-M 247 disk bolt holes. An inspection interval is determined to ensure safe operation. Fatigue strain-life data is presented for test specimens from a test disk. Strain-life models (Manson-Hirschberg method of universal slopes, Halford-Nachtigall mean stress method, and modified Morrow method) were compared to experiment. Using experimental data at −99.95% prediction levels, accounting for six bolt holes at 0.5% total strain and 649°C, the test disk should be inspected after 665 cycles.

[DOI: 10.1115/1.1852563]

Introduction

The high-temperature high-speed turbine seal test facility (Fig. 1), located at NASA's Glenn Research Center in Cleveland, Ohio provides critical testing of air seals for aircraft engines at conditions of high air temperatures, high seal pressures, and surface speeds greater than 305 m/s.

The test facility uses a disk made of Grainex Mar-M 247, a cast nickel-based superalloy. Analysis has shown that, in the vicinity of the disk bolt holes, the material slightly enters the plastic region of the stress-strain curve [1]. Due to these demanding test conditions, the possibility exists that fatigue cracks will develop with cycling at the six bolt hole locations, which fasten the test disk to the main shaft of the test stand. If allowed to grow to a critical size, the cracks could cause the disk to catastrophically burst during use.

Preliminary analyses by Tong and Steinetz [1] have placed a strain-life fatigue limit L_{sys} of 6000 cycles based upon an equivalent -3σ reduction factor and a probabilistic approach [2] accounting for $n=6$ bolt holes:

$$L_{sys}=\frac{L}{n^{1/e}} \tag{1}$$

Equation (1) is based on the Lundberg-Palmgren [3] analysis for rolling element-bearing system lives. L is the predicted life for a disk with a single bolt hole. The predicted life L and Weibull slope parameter e are assumed to be identical for all six disk bolt holes. One cycle is defined as a ramp up and down in speed.

In this study, strain-life tests were conducted over various strain ranges at a temperature of 649°C to determine the cycles to crack initiation. These data were compared with previous analyses as well as with literature data and strain-life model estimates based upon tensile data.

Materials and Methods: Tensile Behavior

Experiment. Tensile tests were performed at Mar-Test Inc. in Cincinnati, Ohio per ASTM E-8, ASTM E-21, and ASTM E-83 Class B-2 standards. The tensile test specimen geometry was 3.56 mm in diameter by 50.8 mm in length per ASTM E-8 small-sized specimens. Four tensile specimens were taken from a Grainex Mar-M 247 sacrificial disk and tested. Tensile testing was conducted on a hydraulic servo controlled test system with a box furnace for specimen heating. Thermocouples were positioned at the gage radius to monitor temperature. The tensile tests were conducted at 649°C at a strain rate of 0.00028 s^{-1}.

Materials and Methods: Fatigue Strain-Life Behavior

Experiment. Fatigue strain-life testing was also performed at Mar-Test, using a closed loop, servohydraulic test system complying with ASTM E-4, ASTM E-606, and ASTM E-83 Class B-2 standards. Induction heating was utilized for specimen heating. Test temperature was controlled to within 1%.

The specimen geometry was 3.18 mm in diameter and 50.8 mm in length per ASTM E-606 standards. A total of 15 strain-life specimens were obtained from the sacrificial disk. The tests were conducted in air at 649°C at a strain ratio of $R=0$, cycled at 0.33 Hz using a triangular wave form. Five strain ranges were tested (0.50%, 0.58%, 0.67%, 0.78%, and 0.90%) with three repeats at each strain range. The cycles to crack initiation (N_i) and cycles to failure (N_f) were recorded for each test. N_i was defined as a rapid change in the load versus time history plot (Fig. 2) while N_f was defined as complete specimen separation.

Data Analysis. The fatigue strain-life results were evaluated following a simple linear model in log-log coordinates:

$$N_f=A(\%\Delta\varepsilon)^{\alpha} \tag{2}$$

where the constant A and exponent α were determined. Linear regression analysis of the log-log transformed fatigue strain-life behavior was conducted to determine the coefficient A and the exponent α for the $R=0$ data. Thus,

$$\log(N_f)=\log A+\alpha\log(\%\Delta\varepsilon) \tag{3}$$

Standard statistical analyses were also performed to check for significance of the regression (R^2), test for normal distribution, outliers, lack-of-fit, and also to calculate the −99.95% prediction interval [4].

Method of Universal Slopes. The Manson-Hirschberg method of universal slopes (MUS) was used to estimate strain life with zero mean stress based only upon tensile data [5]:

$$\Delta\varepsilon=\Delta\varepsilon_{el}+\Delta\varepsilon_{pl} \tag{4}$$

$$\Delta\varepsilon=BN_f^b+CN_f^c \tag{5}$$

Contributed by the International Gas Turbine Institute (IGTI) of THE AMERICAN SOCIETY OF MECHANICAL ENGINEERS for publication in the ASME JOURNAL OF ENGINEERING FOR GAS TURBINES AND POWER. Paper presented at the International Gas Turbine and Aeroengine Congress and Exhibition, Vienna, Austria, June 13–17, 2004, Paper No. 2004-GT-53939. Manuscript received by IGTI, October 1, 2003; final revision, March 1, 2004. IGTI Review Chair: A. J. Strazisar.

Fig. 1 NASA Glenn Research Center turbine seal test facility

$$\Delta\varepsilon = 3.5\frac{\sigma_{uts}}{E}(N_{f0})^{-0.12} + \varepsilon_f^{0.6}(N_{f0})^{-0.6} \tag{6}$$

Thus, the total strain range is the sum of the elastic strain range (first term) and the plastic strain range (second term).

Mean Stress Effects. To estimate the effect of mean stress on cyclic life the Halford-Nachtigall method was used with the MUS [6]:

$$N_{fm}^{-b} = N_{f0}^{-b} - V_\sigma \tag{7}$$

The relationship is derived from [7]:

$$\Delta\sigma = 2(\sigma_f' - \sigma_m)N_{fm}^{-b} \tag{8}$$

This is Morrow's original equation [8], except that N_{fm} is used instead of $2N_{fm}$.

The value for b was -0.12 from the MUS. N_{f0} was calculated using the ratio of the inelastic strain range and the elastic strain range from the MUS at ratios of 0.3, 0.2, 0.1, 0.08, 0.05, and 0.02. V_{eff} was substituted for V_σ [6]:

where

$$V_{\text{eff}} = k\frac{\sigma_m}{\sigma_a} = kV_\sigma \tag{9}$$

and

$$k = \exp\left[-70\left(\frac{\Delta\varepsilon_{in}}{\Delta\varepsilon_{el}}\right)^2\right] \tag{10}$$

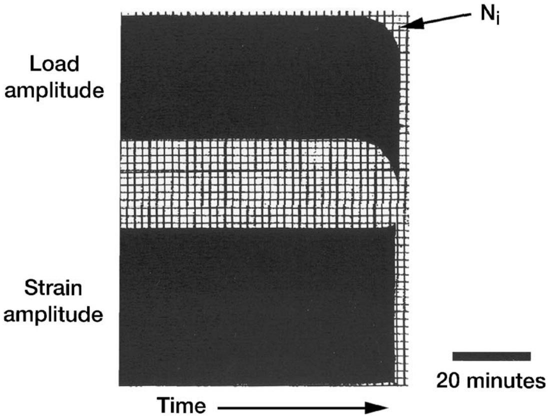

Fig. 2 Sample load- and strain-time history indicating N_i

Table 1 Mean tensile test results for Grainex Mar-M 247 at 649°C

	E [GPa]	σ_{uts} [MPa]	$\sigma_{y\ 0.2\%}$ [MPa]	$\%RA$	$\%EL$	σ_f [MPa]	ε_{fs}
Avg	194.3	1064	821.0	16	6.9	1268	0.177
Std. dev.	12.6	20	18.3	1	1.0	31	0.015

At the beginning of each test, note that for zero to maximum loading it is assumed that $\sigma_m/\sigma_a = 1$. This could be true if the cycle is elastic, but as plasticity is encountered the mean stress ratio begins to relax according to Eq. (9) and Eq. (10).

Modified Morrow With Mean Stress Effects. The modified Morrow equation was used to account for mean stress (σ_m) effects resulting from the $R=0$ tests [7]:

$$\varepsilon_a = \frac{\sigma_f'}{E}\left(1 - \frac{\sigma_m}{\sigma_f'}\right)(2N_f)^b + \varepsilon_f'\left(1 - \frac{\sigma_m}{\sigma_f'}\right)^{c/b}(2N_f)^c \tag{11}$$

The coefficients and exponents were calculated using the $R=0$ strain-life test data and E from the tensile tests. Constraints were placed on exponents b and c based upon previous observations on engineering metal behavior [7]:

$$-0.12 \leqslant b \leqslant -0.05 \tag{12}$$

and

$$-0.9 \leqslant c \leqslant -0.5 \tag{13}$$

In using Eq. (11), various values of σ_m were assumed as needed.

Fractographic Examination. The fracture surfaces of fatigued specimens were cleaned in acetone, alcohol rinsed, and air dried to facilitate fractographic examination. Surfaces were examined using light stereomicroscopy and a JEOL JSM-840A scanning electron microscope (SEM) using secondary-electron and backscattered-electron (BE) modes to determine crack initiation sites.

Results: Tensile Properties

Mean tensile properties of the four tensile tests for the Grainex Mar-M 247 material were determined at 649°C and are shown in Table 1. The ultimate tensile strength and 0.2% offset yield stress were found to be 1064 MPa and 821 MPa, respectively.

Results: Fatigue Strain Life

$R=0$. The cycles to crack initiation (N_i) and cycles to failure (N_f) were determined for each of the $R=0$ fatigue strain-life tests at 649°C (Table 2). Due to cycle recorder malfunctions in the data acquisition system, some results were unavailable.

Linear regression analysis of the $R=0$ total strain range versus cycles to crack initiation (N_i) cyclic strain-life tests (Table 2) resulted in an exponent α of -6.48 and a coefficient A of 162.18 with $R^2=0.86$ using Eq. (2) (Fig. 3, 99.95% prediction interval shown).

Linear regression analysis of the $R=0$ total strain range versus cycles to failure (N_f) cyclic strain life tests (Table 2) resulted in an exponent α of -5.62 and a coefficient A of 316.23 with $R^2=0.87$ using Eq. (2) (Fig. 4, 99.95% prediction interval shown).

Table 3 summarizes the mean and -99.95% prediction cyclic life for the $R=0$ data at both cycles to crack initiation and cycles to failure at the 0.5% design strain range of the Grainex Mar-M 247 disk (see also Figs. 3 and 4). The -99.95% prediction intervals give a failure rate of 1 in 2000 parts.

Method of Universal Slopes. The estimated cycles to failure (N_{f0}) was plotted against the total strain range ($\Delta\varepsilon$) for the

Table 2 Grainex Mar-M 247 strain-life test results at 649°C, $R=0$

%$\Delta\varepsilon$	N_i	N_f
0.50	25,917	26,939
0.50	9557	10,697
0.58	12,266	12,566
0.58	2450	2842
0.58	5910	7970
0.67	2056	3056
0.67	3114	3842
0.67	1322	2234
0.78	585	723
0.78	792	1352
0.78	680	1254
0.90	513	889
0.90	*	554

*N_i occurred between 295 and 500 cycles.

Grainex Mar-M 247 material using tensile data (Table 1) as input for the MUS (Fig. 5). The plastic and elastic strain lines were also plotted. The transition life (N_{t0}), wherein the elastic and plastic strain ranges are equal, was found to be 400 cycles to failure.

Table 3 Grainex Mar-M 247 mean and −99.95% cyclic strain-life predictions at 649°C at the 0.5% design strain range, $R=0$

Number of cycles	Statistic	
	Mean	−99.95%
N_i	14,500	1100
N_f	15,500	1600

Mean Stress Effect. A comparison was made between the MUS, the MUS with mean stress effects (Eq. (7)), and $R=0$ data for the Grainex Mar-M 247 material (Fig. 6). The 0.5% design strain is also shown in Fig. 6 and compared with the data and both estimation methods.

Modified Morrow With Mean Stress Effects. Calculated coefficients and exponents for the modified Morrow equation (Eq. (11)), resulted in an R^2 value of 0.93. The coefficients and exponents (Table 4) were then used in the modified Morrow equation and compared to experimental Grainex Mar-M 247 strain-amplitude data (Fig. 7). The design strain of the Grainex Mar-M 247 disk is also shown at 0.5% strain range.

Assuming the ratio of mean to alternating stress was equal to 1 at the start of the strain-life tests, V_σ was calculated at the approximate half-life for each test (Table 5).

The variation of mean stress and range of stress was also compared with increasing strain amplitude (Fig. 8). Point P1 through point P2 is the elastic line. Point P2 defines where the mean stress and range of stress are equal. Point P3 defines the point of zero mean stress. Finally, point P3 to P4 is the region of zero mean stress.

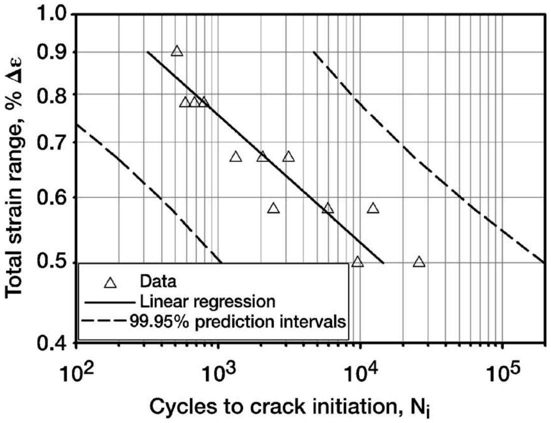

Fig. 3 Crack initiation strain-life results for Grainex Mar-M 247: $R=0$, 649°C, triangular wave form, 0.33 Hz. N_i was plotted on the abscissa, while %$\Delta\varepsilon$ was plotted on the ordinate.

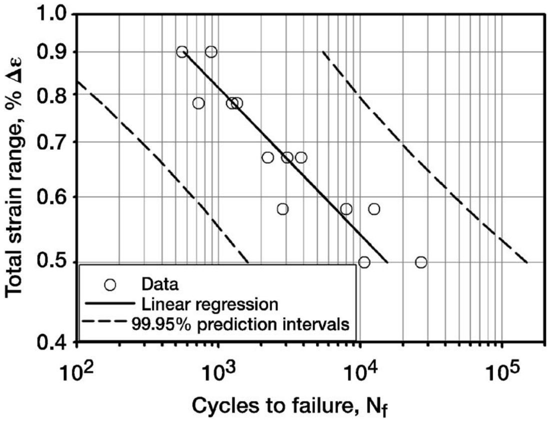

Fig. 4 Cycles to failure strain-life results for Grainex Mar-M 247: $R=0$, 649°C, triangular wave form, 0.33 Hz. N_f is plotted on the abscissa, while %$\Delta\varepsilon$ is plotted on the ordinate.

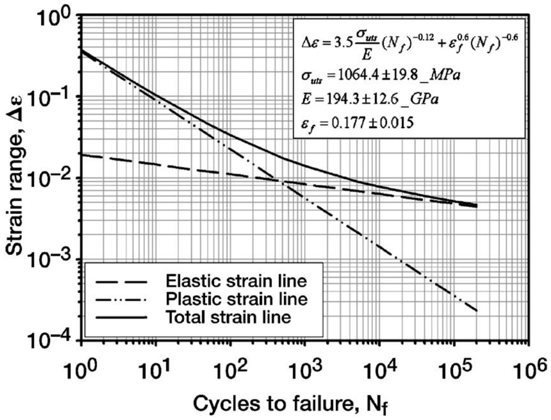

Fig. 5 Strain-life prediction using the method of universal slopes equation and Grainex Mar-M 247 tensile data at 649°C

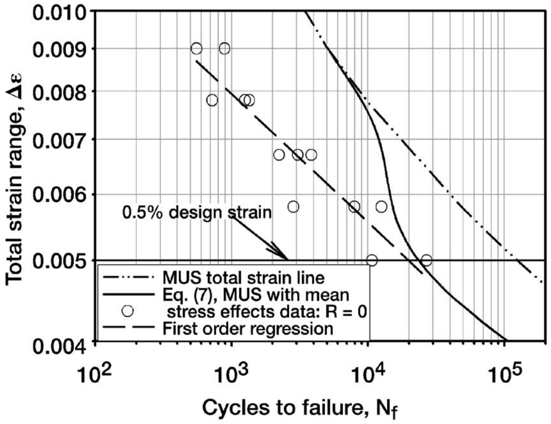

Fig. 6 Comparison of MUS, MUS with mean stress effects, and data for Grainex Mar-M 247 at 649°C

Table 4 Calculated coefficient and exponent values for the modified Morrow equation for Grainex Mar-M 247 at 649°C

Coefficients	Value
σ_f' (MPa)	1507
ε_f'	0.027
Exponents	Value
b	−0.090
c	−0.627

Fractographic Examination. The majority of the crack initiation sites were observed at the gage cross-section perimeter and initiated at carbides. As expected, the fracture surfaces exhibited 3 areas or stages of cracking: crack initiation, propagation, and failure or overload (Fig. 9).

Discussion: Tensile Behavior

The NASA Grainex Mar-M 247 tensile properties were within 5% to 10% of values reported in the literature data (Table 6) [10,11]. The exception was in the *%RA* data, where the NASA values were 30 to 40% higher than that reported in the literature. The higher values were most likely due to a slight amount of necking observed in the gage sections of the tensile test specimens.

Discussion: Fatigue Strain Life

***R*=0.** Testing at $R=0$ and 649°C addressed the actual localized conditions the Grainex Mar-M 247 disk bolt holes encounter in the turbine seal test facility. Specifically, the disk is strained from a zero to maximum strain when the surface speed increases from zero to maximum during testing. The −99.95% prediction interval (1 failure in 2000 samples) on cyclic life was chosen since it was more conservative than the mean cyclic life by a factor of approximately 10. As expected, more data scatter was observed at the lower strain ranges. Overall, the cyclic life to crack initiation of the bolt holes of the Grainex Mar-M 247 disk at the 0.5% design strain with $R=0$ and the lower bound of the 99.95% prediction interval was found to be 1100 cycles. This was nearly 6 times less than the cyclic life predicted from previous analyses [1].

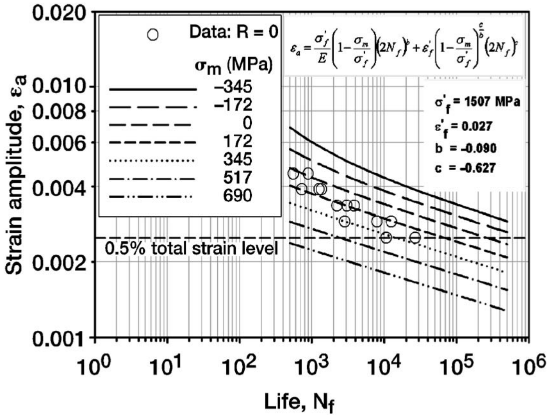

Fig. 7 Comparison of NASA Grainex Mar-M 247, *R*=0 data with the modified Morrow equation at 649°C

Table 5 Comparison of V_σ at $N_f=1$ and $N_f/2$ for Grainex Mar-M 247 at 649°C, *R*=0

Strain range	$N=1$ V_σ	$N_f/2$ σ_m [MPa]	 σ_a [MPa]	$N_f/2$ V_σ
0.50	1	344.1	463.3	0.74
0.50	1	281.0	472.7	0.59
0.58	1	295.1	513.7	0.57
0.58	1	247.9	562.3	0.44
0.58	1	265.8	556.1	0.48
0.67	1	227.5	598.5	0.38
0.67	1	206.9	600.6	0.34
0.67	1	180.6	608.1	0.30
0.78	1	100.3	745.0	0.13
0.78	1	153.8	669.5	0.23
0.78	1	106.9	706.7	0.15
0.90	1	88.6	734.7	0.12
0.90	1	60.0	781.2	0.08

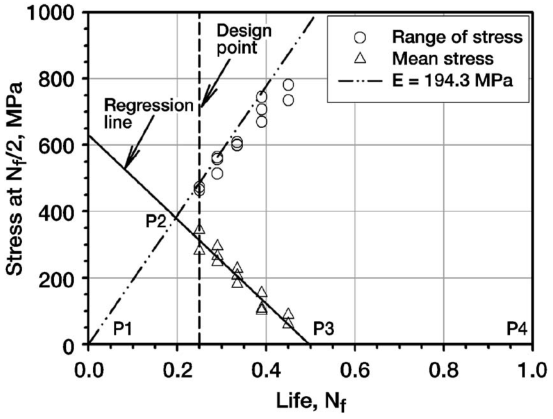

Fig. 8 Variation of mean stress and range of stress with strain amplitude at $N_f/2$ for Grainex Mar-M 247 at 649°C [9]

Comparison to Literature. Comparison of the NASA Grainex Mar-M 247 $R=0$ strain-life data with data reported by Kaufman showed good agreement (Fig. 10) [10]. The NASA data

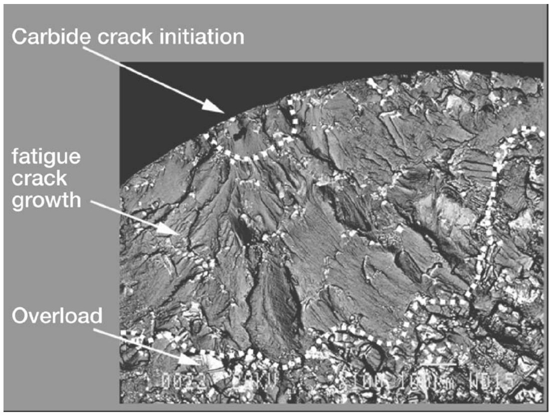

Fig. 9 Typical fatigue crack growth stages for Grainex Mar-M 247 strain-life specimen at 649°C. SEM—BE mode at 100×.

Table 6 Comparison of average Grainex Mar-M 247 tensile properties at 649°C with literature

	NASA*	Kaufman* [10]	Howmet [11]
No. Samples	4	2	N/A
E [GPa]	194.3	N/A	179.3
σ_{uts} [MPa]	1064.4	1011.5	1027.3
$\sigma_{y(0.2\%)}$ [MPa]	821.0	799.1	827.4
%RA	16	9.7	10.7
%EL	6.9	7.1	7.0

*Average data.

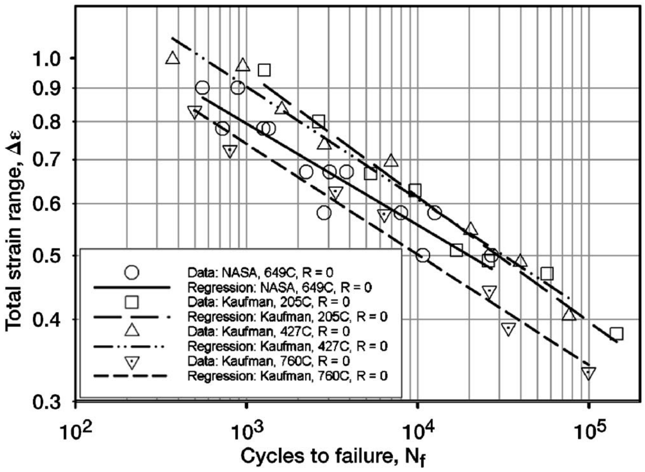

Fig. 10 Comparison of NASA Grainex Mar-M 247, $R=0$ strain-life data with literature [10]

at 649°C fell in between the 427°C and 760°C data reported by Kaufman [10]. As expected, cyclic lives decreased with increasing temperature for a constant strain range.

Comparison With MUS, Mean Stress Effects, and Data. Both the MUS and Eq. (7) provide a means to predict fatigue strain life by use of only tensile data. It was expected that the MUS would overpredict the $R=0$ data (Fig. 6) since it was generally used in comparing $R=-1$ data. At the design point of 0.5% total strain, the MUS predicted N_{f0} at 100,000 cycles. This is five times greater than the average $R=0$ data of approximately 20,000 cycles. In comparison, Eq. (7) predicted a life of approximately 23,500 cycles (Fig. 6). Thus, a more accurate prediction of life at the 0.5% total strain design point was found using only tensile data and modifying the MUS to account for mean stress effects.

Comparison to Modified Morrow Equation. Parametric curves of constant mean stress were compared to the experimental results on a strain-amplitude versus cycles to failure plot using results of the modified Morrow strain-life analysis (Fig. 7). As expected, higher mean stresses were observed at lower strain levels while lower mean stresses were observed at higher strain levels (Fig. 8) [9]. This is because the larger the strain range, the greater the degree of relaxation of the initial mean stress imposed by the $R=0$ strain condition. The effect of mean stress on cyclic life was more pronounced at lower strain levels (Table 5). For example, at the design strain level of 0.5% total strain, the average mean stress was 313 MPa, while at 0.9% total strain, the average mean stress was 74 MPa.

As expected, cyclic life decreased as mean stress increased for constant strain amplitude (Fig. 7). For example, at the design point of $\Delta\varepsilon=0.5\%$ ($\varepsilon_a=0.0025$), the difference in cyclic life between the $\sigma_m=0$ MPa line and the $\sigma_m=172$ MPa line was a factor of nearly 4. The $R=0$ data were observed to trend towards a zero mean stress at the highest strain range ($\varepsilon_a=0.0045$). Finally, as expected, compressive mean stresses predict an increase in cyclic life.

Summary

Tensile properties for the Grainex Mar-M 247 disk at 649°C were presented and compared with literature data. Fatigue strain-life data for the same material were also presented at 649°C at strain ranges of 0.50%, 0.58%, 0.67%, 0.78%, and 0.90%. Both the tensile and $R=0$ strain-life data were comparable with literature.

Evaluation of mean stress effects showed a large effect on cyclic life. The Halford-Nachtigall method used with the MUS was practical for predicting $R=0$ life using only tensile data at 649°C. A difference of only 18% in cyclic life was observed between predicted and experimental lives at the design point of 0.5% strain range. The 10,000 cycle limit suggested by the modified Morrow analysis at the 0.5% design strain range can be reduced accordingly to 1500 cycles using an equivalent -3σ reduction factor and probabilistic accounting for the six bolt holes using Eq. (1).

During operation, the turbine disk is generally cycled at zero to maximum strain conditions ($R=0$). At the design strain of $\Delta\varepsilon=0.5\%$, the $R=0$ results lead to, at the -99.95% prediction level, a cyclic crack initiation life of 1100 cycles, which is nearly six times less than the initial predicted cycles to failure obtained previously by Tong and Steinetz [1]. Probabilistic accounting for the six bolt holes using Eq. (1) gives the most conservative result of 665 cycles with six bolt holes.

Thus, using the experimental data at a -99.95% prediction level and the presence of six bolt holes, it was found that the disk should be inspected for surface cracks after 665 cycles based on a total strain range of 0.50% at 649°C.

Acknowledgments

The authors wish to acknowledge NASA Glenn Research Center, the Army Research Laboratory, and Case Western Reserve University for their support.

Nomenclature

3σ = 3 standard deviations
A = constant coefficient
B = constant coefficient
C = constant coefficient
E = Young's modulus
L = calculated disk life
L_{sys} = overall system life
N_f = cycles to failure
N_{fm} = cycles to failure in presence of mean stress
N_{f0} = cycles to failure under zero mean stress
N_i = cycles to crack initiation
N_{t0} = transition life under zero mean stress
R = strain ratio$=\varepsilon_{\min}/\varepsilon_{\max}$
R^2 = coefficient of determination
V_{eff} = effective ratio of mean stress to stress amplitude
V_σ = ratio of mean stress to stress amplitude
b = fatigue strength exponent
c = fatigue ductility exponent
e = Weibull slope parameter=3.57 (Gaussian)
k = transfer function
n = number of bolt holes=6
α = constant exponent
$\delta\sigma_m$ = change in mean stress (MPa)
$\Delta\varepsilon$ = total strain range
$\Delta\varepsilon_{el}$ = elastic strain range
$\Delta\varepsilon_{in}$ = inelastic strain range
$\Delta\sigma$ = stress range (MPa)
ε_a = strain amplitude
ε_f = true fracture ductility
ε_f = true fracture strain
$\varepsilon_{\max}$ = maximum strain
$\varepsilon_{\min}$ = minimum strain
ε_f' = fatigue ductility coefficient
σ_a = stress amplitude (MPa)
σ_f = true fracture strength (MPa)
σ_m = mean stress (MPa)
σ_{uts} = ultimate tensile strength (MPa)
$\sigma_{y\ 0.2\%}$ = 0.2% yield strength (MPa)
σ_f' = fatigue strength coefficient (MPa)
$\%EL$ = percent elongation
$\%RA$ = percent reduction in area
$\%\Delta\varepsilon$ = percent total strain range

References

[1] Tong, M., and Steinetz, B., 1997, "Grainex Mar-M 247 Disk FEA Thermal and Stress Analysis," *NASA High Speed Seal Test Rig Engineering Manual*, NASA Glenn Research Center, Cleveland, Chapter 7.

[2] Melis, M. E., Zaretsky, E. V., and August, R., 1999, "Probabilistic Analysis of Aircraft Gas Turbine Disk Life and Reliability," AIAA Journal of Propulsion and Power, **15**, pp. 658–666.

[3] Lundberg, G., and Palmgren, A., 1947, "Dynamic Capacity of Rolling Bearings," Acta Polytech. Scand., Mech. Eng. Ser., **1**, pp. 1–49.

[4] Keller, D. J., 1992, *Introduction to Regression*, RealWorld Quality Systems, Inc., Fairview Park.

[5] Manson, S. S., 1965, "Fatigue—A Complex Subject," Exp. Mech., **5**, pp. 193–226.

[6] Halford, G. R., and Nachtigall, A. J., 1980, "Strainrange Partitioning Behavior of an Advanced Gas Turbine Disk Alloy AF2-1DA," J. Aircr., **17**, pp. 598–604.

[7] Dowling, N. E., 1999, *Mechanical Behavior of Materials: Engineering Methods for Deformation, Fracture and Fatigue*, Prentice-Hall, Englewood Cliffs, NJ.

[8] Morrow, J., 1968, *Fatigue Design Handbook*, SAE, New York.

[9] Conway, J. B., and Sjodahl, L. H., 1991, *Analysis and Representation of Fatigue Data*, ASM International, Materials Park.

[10] Kaufman, M., 1984, "Properties of Cast Mar-M 247 for Turbine Blisk Applications," *Superalloys 1984*, M. Gell et al., eds., Metallurgical Society of AIME, Warrendale, PA, pp. 43–52.

[11] Howmet Turbine Components Corporation, "TB 3000: Grainex Cast Mar-M 247 Alloy," Howmet Turbine Components Corporation, Greenwich, CT.

E. Capiez-Lernout
e-mail: capiez@univ-mlv.fr

C. Soize
Professor
e-mail: soize@univ.mlv.fr

Laboratory of Engineering Mechanics,
University of Marne La Vallée,
5, Bd Descartes,
77454 Marne-la-Vallée Cedex, 02, France

J.-P. Lombard
e-mail: jean-pierre.lombard@snecma.fr

C. Dupont
e-mail: christian.dupont@snecma.fr

Snecma Moteurs,
Site de Villaroche,
77550 Moissy Cramayel, France

E. Seinturier
Turbomeca—Snecma Group,
Site de Bordes,
64511 Bordes Cedex, France
e-mail: eric.seinturier@turbomeca.fr

Blade Manufacturing Tolerances Definition for a Mistuned Industrial Bladed Disk

This paper deals with the characterization of the blade manufacturing geometric tolerances in order to get a given level of amplification in the forced response of a mistuned bladed-disk. The theory is based on the use of a nonparametric probabilistic model of blade random uncertainties. The dispersion parameters controlling the nonparametric model are estimated as a function of the geometric tolerances. The industrial application is devoted to the mistuning analysis of a 22 blades wide chord fan stage. Centrifugal stiffening due to rotational effects is also included. The results obtained validate the efficiency and the reliability of the method on three-dimensional bladed disks.

[DOI: 10.1115/1.1850497]

Introduction

It is well known that the description of a bladed disk using its cyclic symmetry properties [1,2] is not sufficient to predict accurately its dynamic forced response. In such a mechanical system, there are random uncertainties on the geometrical parameters, on the mechanical parameters related to the constitutive equations, on the boundary conditions, which are due to the manufacturing process of the blade. The blade mistuning terminology is then introduced because the blades of a bladed disk are slightly different from one to another one. Such a mistuning is not without consequence when analyzing the forced response of the bladed disk. Indeed, it is observed that the vibratory energy of the mistuned bladed disk is localized inducing large dynamic amplification factor [3–5]. Various researches have been carried out (see for instance [6–9] for lumped parameters models [10–14] for reduced order models) in order to understand and to control this phenomenon. This paper concerns a method that could be used for defining the specification of the blade manufacturing tolerances in order to have a given amplification factor due to the mistuning in a probabilistic context.

An exact parametric probabilistic approach should consist in setting up experimental means in order to construct a complete probabilistic model of all the parameters related to the random geometry of the blade. Then functions mapping the domain of uncertain parameters into the mass, damping, and stiffness finite element matrices should be constructed. Then, efficient reduced order models [12,14] should be used in order to analyze the forced response statistics of the bladed disk. It should be noted that such a parametric probabilistic approach would require a large number of uncertain parameters to be experimentally identified, in particular, for modeling the stochastic fields representing the geometrical random uncertainties.

In this paper, an alternative approach based on the use of the nonparametric probabilistic model of random uncertainties developed for linear and nonlinear elastodynamics [15–17] is proposed. The theory concerning this inverse problem related to the definition of the blade manufacturing tolerances has been previously developed and validated for a simple numerical case [18]. Let us recall that the main steps of such an approach are based on (1) the construction of a mean reduced matrix model for each blade because the probability model related to the nonparametric approach is implemented from reduced matrices; (2) the construction of the probability model by using the maximum entropy principle under constraints defined by the available information; three scalar parameters allowing the dispersion of the random mass, damping, and stiffness matrices to be controlled constitute the data input of the nonparametric approach; (3) the identification procedure of these dispersion parameters with respect to the physical parameters that describe the random geometry of the blades. The objective of this paper is the application of the theory previously developed to a realistic case consisting of an industrial bladed disk.

It should be noted that the mistuning is completely controlled by the probabilistic nonparametric model of the blade uncertainties. This nonparametric model is itself completely controlled by two scalar dispersion parameters, δ_M and δ_K, related to the mass and the stiffness operators of the blades. The proposed estimator of these dispersion parameters with respect to the blade geometry uncertainties is weakly sensitive to the choice of the probability

---

Contributed by the International Gas Turbine Institute (IGTI) of THE AMERICAN SOCIETY OF MECHANICAL ENGINEERS for publication in the ASME JOURNAL OF ENGINEERING FOR GAS TURBINES AND POWER. Paper presented at the International Gas Turbine and Aeroengine Congress and Exhibition, Vienna, Austria, June 13–17, 2004, Paper No. 2004-GT-53356. Manuscript received by IGTI, October 1, 2003; final revision, March 1, 2004. IGTI Review Chair: A. J. Strazisar.

model used for generating the blade random geometry. Consequently, it is important to note that the probabilistic model of the blade random geometry is not directly used for predicting the mistuning but only for estimating the dispersion parameters δ_M and δ_K.

In a first part, a mean reduced matrix model both adapted to the nonparametric approach and to industrial numerical computations is briefly recalled. The theoretical results concerning the inverse problem are then adapted to the industrial bladed disk. Finally, the last section is devoted to a large finite element model of an industrial fan stage. A convergence analysis is performed in order to verify the choice of the reduced model dimension required for the stochastic analysis. Furthermore, a random geometry of the blade is defined in order to carry out the identification process of the dispersion parameters. Then the probability distribution of the random dynamic magnification factor is calculated as a function of the tolerance parameters.

Mean Reduced Matrix Model

The structure considered is a three-dimensional rotating fan stage modeled by a bladed disk with N blades. The bladed disk is rotating around a fixed axis with the constant velocity Ω and is submitted to external forces. The vibration analysis is carried out in the rotating frame related to the reference configuration in the low-frequency band $\mathbb{B}$. The centrifugal terms are taken into account in the stiffness terms. Gyroscopic coupling due to rotating motion is not taken into account. All the blades are different from one to another due to manufacturing tolerances. Although the level of uncertainty is homogeneous for the blades, the random uncertainties are statistically independent from one to another blade. The construction of a mean reduced matrix model for each blade is thus required in order to model the random uncertainties with the nonparametric probabilistic approach. In this paper, the mean model of the structure is reduced by the substructuring method introduced by Benfield and Hruda [19]. The efficiency of this method has been proved for mistuned industrial bladed disks [14,20], where each blade constitutes a branch component of the disk substructure. Each blade is reduced by using the Craig and Bampton method [21]. A reduced model of the disk with loaded coupling interface is constructed by modal analysis. In order to connect the substructures, the displacement of each blade on the coupling interface is projected on the disk modes by using the continuity of displacements at the coupling interface. The matrix equation related to the mean finite element model of the bladed disk is written as

$$(-\omega^2[\underline{\mathbb{M}}]+i\omega[\underline{\mathbb{D}}]+[\underline{\mathbb{K}}])\underline{\mathbf{u}}(\omega)=\underline{\mathbf{f}}(\omega), \tag{1}$$

in which $\underline{\mathbf{u}}(\omega)$ and $\underline{\mathbf{f}}(\omega)$ are the $\mathbb{C}^n$ vectors of the degrees of freedom and of the external loads and where $[\underline{\mathbb{M}}]$, $[\underline{\mathbb{D}}]$, and $[\underline{\mathbb{K}}]$ are the mean finite element mass, damping, and stiffness matrices of the bladed-disk that are positive-definite matrices. The projection basis resulting from the substructuring method is written with the following block decomposition as

$$\begin{bmatrix} \underline{\mathbf{u}}_i^d(\omega) \\ \underline{\mathbf{u}}_\Sigma(\omega) \\ \underline{\mathbf{u}}_i^b(\omega) \end{bmatrix} = [\underline{H}] \begin{bmatrix} \underline{\mathbf{q}}^d(\omega) \\ \underline{\mathbf{q}}^b(\omega) \end{bmatrix}, \quad [\underline{H}] = \begin{bmatrix} [\underline{\Phi}_i^{d,c}] & [\mathbb{0}] \\ [\underline{\Phi}_\Sigma^{d,c}] & [\mathbb{0}] \\ [\underline{S}^b][\underline{\Phi}_\Sigma^{d,c}] & [\underline{\Phi}^b] \end{bmatrix}. \tag{2}$$

In Eq. (2), $\underline{\mathbf{u}}_i^d$, $\underline{\mathbf{u}}_\Sigma$, and $\underline{\mathbf{u}}_i^b$ are the $\mathbb{C}^{n_i^d}$, $\mathbb{C}^{Nn_\Sigma}$, and $\mathbb{C}^{Nn_i}$ vectors of the n_i^d internal degrees of freedom of the disk, of the Nn_Σ coupling interface degrees of freedom and of the Nn_i internal degrees of freedom of the blades. The vectors $\underline{\mathbf{q}}^d$ and $\underline{\mathbf{q}}^b$ are the $\mathbb{C}^{N_d}$ and the $\mathbb{C}^{N_b}$ vectors of the generalized coordinates of the disk and of the blades. The block decompositions of matrices $[\underline{S}^b]$ and $[\underline{\Phi}^b]$ with respect to the blades are constituted of matrices $[\underline{S}_{jk}^b]=[\underline{S}^j]\delta_{jk}$ and $[\underline{\Phi}_{jk}^b]=[\underline{\Phi}^j]\delta_{jk}$, where subscript jk is related to blade j and blade k. Matrix $[\underline{\Phi}^j]$ is a matrix in $\mathbb{M}_{n_i,n_b}(\mathbb{R})$ whose columns are the eigenvectors related to the n_b first eigenvalues of each blade with fixed coupling interface. The matrix $[\underline{S}^j]$ is a matrix in $\mathbb{M}_{n_i,n_\Sigma}(\mathbb{R})$ representing the static boundary functions. The matrices $[\underline{\Phi}_i^{d,c}]$ and $[\underline{\Phi}_\Sigma^{d,c}]$ correspond to the block decomposition of matrix $[\underline{\Phi}^{d,c}]$ with respect to the internal degrees of freedom and the coupling interface degrees of freedom of the disk. This matrix $[\underline{\Phi}^{d,c}]$ is the matrix in $\mathbb{M}_{Nn_\Sigma+n_i^d,N_d}(\mathbb{R})$ whose columns are the eigenvectors of the disk loaded at its coupling interface with mass and stiffness terms issued from the static condensation of the blades. The integer N_d is such that $N_d=Nn_d$, in which n_d is the number of loaded disk modes related to the n_d first eigenvalues of the disk for a given circumferential wave number. It should be noted that such a load allows the disk modes to constitute a good approximation of the global modes of the structure. Such modes can be calculated by using the cyclic properties of the disk [1,2]. Using (1) and (2) yields the mean reduced matrix equation

$$[\underline{\mathbb{A}}_{\mathrm{red}}(\omega)] \begin{bmatrix} \underline{\mathbf{q}}^d(\omega) \\ \underline{\mathbf{q}}^b(\omega) \end{bmatrix} = [\underline{H}]^T \underline{\mathbf{f}}(\omega), \tag{3}$$

in which $[\underline{\mathbb{A}}_{\mathrm{red}}(\omega)]=-\omega^2[\underline{\mathbb{M}}_{\mathrm{red}}]+i\omega[\underline{\mathbb{D}}_{\mathrm{red}}]+[\underline{\mathbb{K}}_{\mathrm{red}}]$ is the mean reduced dynamic stiffness matrix of the bladed disk such that, for $\mathbb{E}$ representing $\mathbb{M}$, $\mathbb{D}$, or $\mathbb{K}$,

$$[\underline{\mathbb{E}}_{\mathrm{red}}]=[\underline{H}]^T[\underline{\mathbb{E}}][\underline{H}], \quad [\underline{\mathbb{E}}_{\mathrm{red}}]\in\mathbb{M}_{N_b+N_d}^{+}(\mathbb{R}). \tag{4}$$

Introducing the block decomposition associated with Eq. (3) yields

$$[\underline{\mathbb{A}}_{\mathrm{red}}(\omega)] = \begin{bmatrix} [\underline{\mathcal{A}}^d(\omega)] & [\underline{A}_c(\omega)] \\ [\underline{A}_c(\omega)]^T & [\underline{\mathcal{A}}^b(\omega)] \end{bmatrix}, \tag{5}$$

in which $[\underline{\mathcal{A}}^d(\omega)]$ is the generalized dynamic stiffness matrix of the disk constructed with eigenvectors matrix $[\underline{\Phi}^{d,c}]$ and where the block jk of $[\underline{\mathcal{A}}^b(\omega)]$ is such that $[\underline{\mathcal{A}}^b(\omega)_{jk}]=[\underline{\mathcal{A}}^j(\omega)]\delta_{jk}$ in which $[\underline{\mathcal{A}}^j(\omega)]=-\omega^2[\underline{\mathcal{M}}^j]+i\omega[\underline{\mathcal{D}}^j]+[\underline{\mathcal{K}}^j]$ defines the generalized dynamic stiffness matrix of each blade with fixed coupling interface and constructed with eigenvector matrix $[\underline{\Phi}^j]$.

Mistuning Analysis of the Bladed Disk With Random Uncertainties

A nonparametric probabilistic approach is used for modeling random uncertainties in each blade. Such a probabilistic approach consists in constructing a probability model on the reduced matrices of each blade. This probability model is derived from the maximization of the statistical entropy under constraints defined by the available information. The basis of this theory has been completely developed in linear elastodynamics for the low-frequency range [15,16] and for the medium-frequency range [22]. Furthermore, it has been extended and validated for modeling nonhomogeneous random uncertainties [23] and for modeling homogeneous statistical independent random uncertainties for blade mistuning problematics [24,25].

Nonparametric Probabilistic Model of Random Uncertainties. Below, bold letters are related to deterministic vectors and bold capital letters are related to random vectors. Capital letters between brackets mean deterministic matrices and bold capital letters between brackets mean random matrices. Since the blade is reduced by using the Craig and Bampton method, it can be shown that the reduced matrix equation of tuned blade j with free coupling interface is written as

$$\begin{bmatrix} [\underline{\mathcal{A}}^j(\omega)] & [\underline{A}_s^j(\omega)] \\ [\underline{A}_s^j(\omega)]^T & [\underline{A}_\Sigma^j(\omega)] \end{bmatrix} \begin{bmatrix} \underline{\mathbf{q}}^j(\omega) \\ \underline{\mathbf{u}}_\Sigma^j(\omega) \end{bmatrix} = \underline{\mathcal{F}}^{\,j}(\omega), \tag{6}$$

in which for blade j, $\underline{\mathbf{u}}_\Sigma^j$, and $\underline{\mathbf{q}}^j$ are the vectors of the coupling interface degrees of freedom and of the generalized coordinates. Matrix block $[\underline{\mathcal{A}}^j(\omega)]$ corresponds to the dynamic part of the mean reduced matrix model for blade j with a fixed coupling interface. For each blade, it is assumed that random uncertainties mainly affect the dynamics of the blade with a fixed coupling interface [18]. Consequently, the nonparametric probabilistic approach is implemented with respect to the matrix $[\underline{\mathcal{A}}^j(\omega)]$. The nonparametric model of random uncertainties is then written as

$$\mathbf{U}(\omega)=[\underline{H}]\begin{bmatrix}\mathbf{Q}^d(\omega)\\ \mathbf{Q}^b(\omega)\end{bmatrix}, \tag{7}$$

in which $\mathbf{Q}^d$ is the $\mathbb{C}^{N_d}$-valued vector of the random generalized coordinates of the disk and where $\mathbf{Q}^b=(\mathbf{Q}^0,\ldots,\mathbf{Q}^{N-1})$ is the $\mathbb{C}^{N_b}$-valued vector of the random generalized coordinates of the blades. Random vector $(\mathbf{Q}^d,\mathbf{Q}^b)$ is the solution of the random reduced matrix equation

$$\begin{bmatrix}[\underline{\mathcal{A}}^d(\omega)] & [\underline{A}_c(\omega)]\\ [\underline{A}_c(\omega)]^T & [\boldsymbol{\mathcal{A}}^b(\omega)]\end{bmatrix}\begin{bmatrix}\mathbf{Q}^d(\omega)\\ \mathbf{Q}^b(\omega)\end{bmatrix}=[\underline{H}]^T\underline{\mathbf{f}}(\omega), \tag{8}$$

in which the block jk of $[\boldsymbol{\mathcal{A}}^b(\omega)]$ is such that $[\boldsymbol{\mathcal{A}}^b(\omega)_{jk}]=[\boldsymbol{\mathcal{A}}^j(\omega)]\delta_{jk}$ and where $[\boldsymbol{\mathcal{A}}^j(\omega)]$ is the random reduced dynamic stiffness matrix of blade j defined by $[\boldsymbol{\mathcal{A}}^j(\omega)]=-\omega^2[\boldsymbol{\mathcal{M}}^j]+i\omega[\boldsymbol{\mathcal{D}}^j]+[\boldsymbol{\mathcal{K}}^j]$. The available information for random matrices $[\boldsymbol{\mathcal{M}}^j]$, $[\boldsymbol{\mathcal{D}}^j]$, and $[\boldsymbol{\mathcal{K}}^j]$ is

$$\mathcal{E}\{[\boldsymbol{\mathcal{M}}^j]\}=[\underline{\mathcal{M}}^j],\quad \mathcal{E}\{[\boldsymbol{\mathcal{D}}^j]\}=[\underline{\mathcal{D}}^j],\quad \mathcal{E}\{[\boldsymbol{\mathcal{K}}^j]\}=[\underline{\mathcal{K}}^j], \tag{9}$$

$$[\boldsymbol{\mathcal{M}}^j],\quad [\boldsymbol{\mathcal{D}}^j],\quad [\boldsymbol{\mathcal{K}}^j]\ \text{are}\ \mathbb{M}^+_{n_h}(\mathbb{R})\text{-valued random matrices}, \tag{10}$$

$$\mathcal{E}\{\|[\boldsymbol{\mathcal{M}}^j]^{-1}\|^2_{\mathrm{F}}\}<+\infty,\quad \mathcal{E}\{\|[\boldsymbol{\mathcal{D}}^j]^{-1}\|^2_{\mathrm{F}}\}<+\infty,$$
$$\mathcal{E}\{\|[\boldsymbol{\mathcal{K}}^j]^{-1}\|^2_{\mathrm{F}}\}<+\infty, \tag{11}$$

in which $\mathcal{E}$ is the mathematical expectation and where $\|[A]\|_{\mathrm{F}}$ denotes the Frobenius norm of matrix $[A]$. The use of the maximum entropy principle with the constraints defined by this available information allows the probability distribution of each random matrix to be constructed and it can be proved that $[\boldsymbol{\mathcal{M}}^j]$, $[\boldsymbol{\mathcal{D}}^j]$, $[\boldsymbol{\mathcal{K}}^j]$, $j\in\{0,\ldots,N-1\}$ are independent random variables. It should be noted that these constraints allow the random response $\mathbf{U}(\omega)$ to be a second-order random vector. All the details concerning the construction of this probability model can be found in [15,16].

Identification of the Dispersion Parameters of the Nonparametric Approach With Respect to the Tolerance. For each blade j, the probability distribution of each random matrix depends only on dimension n_b and on a positive parameter δ^j called the dispersion parameter. Consequently, for a given blade j, there are three positive numbers δ^j_M, δ^j_D, and δ^j_K that are the dispersion parameters controlling the dispersion level of the three independent random matrices $[\boldsymbol{\mathcal{M}}^j]$, $[\boldsymbol{\mathcal{D}}^j]$, and $[\boldsymbol{\mathcal{K}}^j]$. The use of these dispersion parameters as parameters of the probability distribution of the random matrices is explained in [16]. It should be noted that the probability distribution of each random matrix is a strongly nonlinear function of its dispersion parameter. Since we are interested in studying the effects of mistuning due to blade manufacturing tolerances, the dispersion parameters have to be quantified with respect to the tolerances specifications. Such an identification is achieved in constructing a random geometry of the blade which respects the tolerances specifications. The random geometry model allows the random mass matrix $[\mathbf{M}^{\mathrm{para},j}]$ and the random stiffness matrix $[\mathbf{K}^{\mathrm{para},j}]$ to be constructed for blade j. It can be shown [18] that dispersion parameters δ^j_M and δ^j_K can be identified by the equation

$$\delta^j_M=\sqrt{\frac{W^{\mathrm{tol},j}_M(n_b+1)}{\mathrm{tr}([\underline{\mathcal{M}}^j]^2)+\mathrm{tr}([\underline{\mathcal{M}}^j])^2}}, \tag{12}$$

$$\delta^j_K=\sqrt{\frac{W^{\mathrm{tol},j}_K(n_b+1)}{\mathrm{tr}([\underline{\mathcal{K}}^j]^2)+\mathrm{tr}([\underline{\mathcal{K}}^j])^2}}, \tag{13}$$

in which tr denotes the trace and where $W^{\mathrm{tol},j}_M$ and $W^{\mathrm{tol},j}_K$ are defined by

$$W^{\mathrm{tol},j}_M=\mathcal{E}\{\|[\underline{\Phi}^j]^T[\mathbf{M}^{\mathrm{para},j}][\underline{\Phi}^j]-[\underline{\mathcal{M}}^j]\|^2_{\mathrm{F}}\}, \tag{14}$$

$$W^{\mathrm{tol},j}_K=\mathcal{E}\{\|[\underline{\Phi}^j]^T[\mathbf{K}^{\mathrm{para},j}][\underline{\Phi}^j]-[\underline{\mathcal{K}}^j]\|^2_{\mathrm{F}}\}. \tag{15}$$

It should be noted that Eqs. (12) and (14) (or Eqs. (13) and (15)) do not assume that the mean value of random mass matrix $[\mathbf{M}^{\mathrm{para},j}]$ (or random stiffness matrix $[\mathbf{K}^{\mathrm{para},j}]$) is equal to the corresponding matrix of the nominal model. Consequently, the calculation of the dispersion parameters includes the bias between the mean value and the nominal value. This assumption corresponds to the following reality: there are no reasons for which the mean value over a set of several blades manufactured with a given specification of tolerances coincides with the nominal blade used for the mean model and used for the manufacturing (mainly because the stiffness and the mass matrix do not linearly depend on the geometry). The Monte Carlo numerical simulation is used for computing δ^j_M and δ^j_K. Once the dispersion parameters are identified, the stochastic equation defined by Eq. (8) is solved with the Monte Carlo numerical simulation.

Random Dynamic Magnification Factor. Let $[\underline{K}^j]$ be the mean finite element stiffness matrix of blade j. The elastic energy of blade j related to the mean dynamical system is written as $\underline{e}^j(\omega)=1/2\underline{\mathbf{u}}^j(\omega)^*[\underline{K}^j]\underline{\mathbf{u}}^j(\omega)$, in which $\underline{\mathbf{u}}^j$ is the vector of the degrees of freedom related to tuned blade j. Due to the cyclic symmetry, we have $\underline{e}^0(\omega)=\cdots=\underline{e}^{N-1}(\omega)$ denoted as $\underline{e}(\omega)$. The similar quantity related to the stochastic dynamic system is defined as $\mathbf{E}^j(\omega)=1/2\mathbf{U}^j(\omega)^*[\underline{K}^j]\mathbf{U}^j(\omega)$, in which $\mathbf{U}^j$ is the random vector of the degrees of freedom related to mistuned blade j. For ω fixed in $\mathbb{B}$, the random dynamic analysis is carried out by introducing the random dynamic magnification factor $\mathbf{B}(\omega)$ defined with respect to the elastic energy by

$$\mathbf{B}(\omega)=\max_{j=0,\ldots,N-1}\sqrt{\frac{\mathbf{E}^j(\omega)}{\underline{e}_\infty}},\quad \underline{e}_\infty=\max_{\omega\in\mathbb{B}}\underline{e}(\omega). \tag{16}$$

Moreover, the random dynamic magnification factor over frequency band $\mathbb{B}$ is defined by

$$B_\infty=\max_{\omega\in\mathbb{B}}\mathbf{B}(\omega). \tag{17}$$

We are interested in estimating the probability density function $b\mapsto p_{B_\infty}(b)$ and the probability $\mathcal{P}(B_\infty>b_\infty)$, in which b_∞ is a given amplification level. A convergence analysis with respect to parameters n_d and n_b allowing the reduction of the model to be controlled is then carried out. The stochastic convergence analysis is limited to the second-order convergence of B_∞ because it implies the convergence in law. We then introduce the mapping $(n_d,n_b)\mapsto|||B_\infty|||$ with $|||B_\infty|||^2=\mathcal{E}\{B^2_\infty\}$. This function $|||B_\infty|||$ is estimated by $\mathrm{Conv}(n_s,n_d,n_b)$, such that

$$\mathrm{Conv}^2(n_s,n_d,n_b)=\frac{1}{n_s}\sum_{i=1}^{n_s}B^2_\infty(\theta_i), \tag{18}$$

in which $\theta_1,\ldots,\theta_{n_s}$ denote the n_s realizations of the Monte Carlo numerical simulation.

Application to an Industrial Fan Stage

Description of the Structure. The structure under consideration is a wide chord supersonic fan geometry called SGC1. The fan has 22 blades. The finite element model of the bladed disk is shown in Fig. 1. It is constructed with 31,812 solid elements and is constituted of $n=473{,}814$ degrees of freedom. Each sector con-

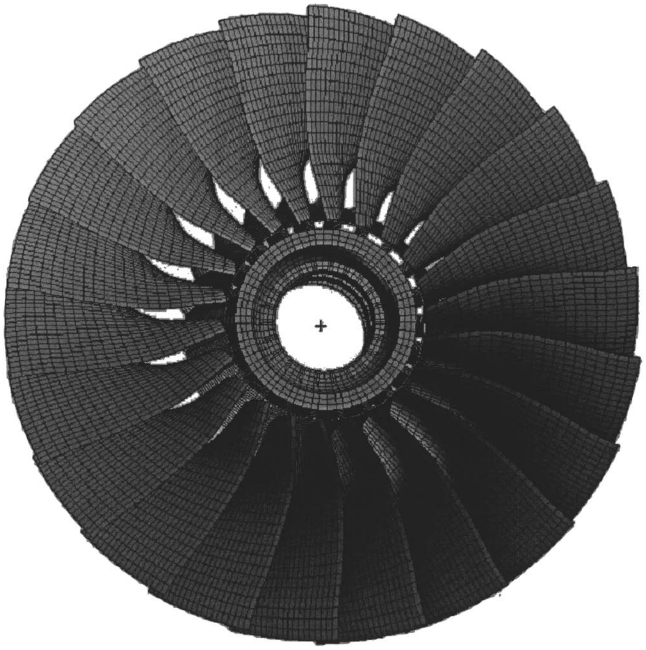

Fig. 1 Finite element mesh for the 22 blades fan stage

tains 8133 nodes, which corresponds to 22,947 degrees of freedom. The structure is also characterized by the following parameters: $n_i = 16{,}197$, $n_\Sigma = 414$, and $n_i^d = 6036$. The structure is in rotation around its revolution axis with a constant velocity $\Omega = 4500$ rpm. Since the dynamic analysis is carried out in the rotating frame of the structure, the rigid-body motion due to the rotation of the structure corresponds to a fixed boundary condition at the inner radius of the structure. The bladed disk is made of titanium. The finite element matrices that include the prestresses due to the rotational motion are generated for one sector. The cyclic symmetry is used in order to construct the mean reduced matrices described in Eq. (5) and allows the generalized eigenvalue problem related to the tuned bladed disk to be solved. Figure 2 displays the eigenfrequencies of the tuned bladed disk with respect to the circumferential wave number. In this work, we are interested in studying the mistuned forced response in a low-frequency band of analysis defined by $\mathbb{B} = [495{,}555]$ Hz with a third engine order excitation. A damping model is added to the bladed disk, which corresponds to a hysteretic model with a mean loss factor $\eta = 0.002$.

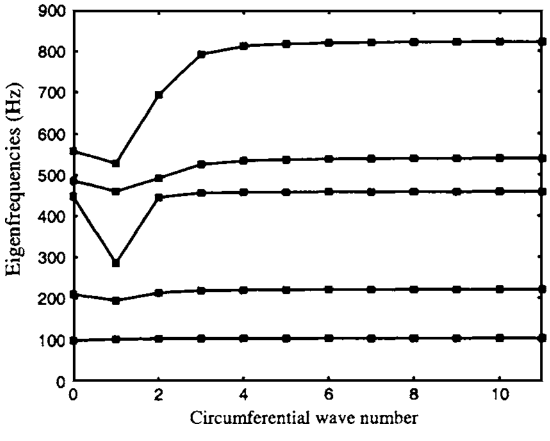

Fig. 2 Graph of the eigenfrequencies with respect to the circumferential wave number for the tuned structure

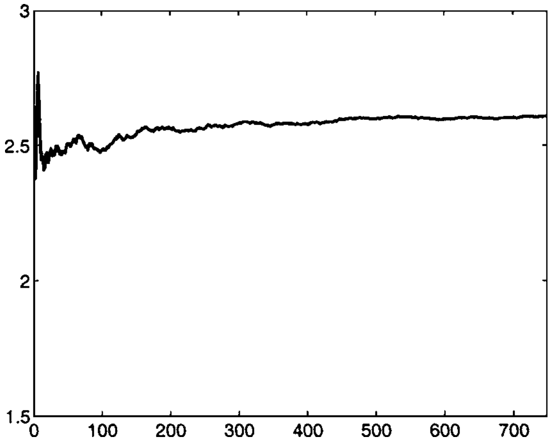

Fig. 3 Graph of function $n_s \mapsto \mathrm{Conv}^2(n_s, n_d, n_b)$ related to the stochastic dynamic equation with $\delta_M^j = \delta_D^j = 0$ and $\delta_K^j = 0.05$ and for $n_d = 10$ and $n_b = 20$

Stochastic Convergence Analysis for the Random Reduced Model. For $\delta_M^j = \delta_D^j = 0$ and $\delta_K^j = 0.05$, Figs. 3 and 4 are relative to the convergence analysis of $|||B_\infty|||$ with respect to parameters n_d and n_a, allowing the dimension of the random reduced matrix model to be controlled and with respect to the number n_s of realizations of the Monte Carlo numerical simulation. Figure 3 displays the graph $n_s \mapsto \mathrm{Conv}^2(n_s, n_d, n_b)$ for $n_d = 10$ and $n_b = 20$. A reasonable convergence is obtained for $n_s = 300$. For $n_s = 300$, Fig. 4 shows the graph $n_b \mapsto \mathrm{Conv}^2(300, n_d, n_b)$ for $n_d = 10$ (black solid line), for $n_d = 7$ (gray solid line), for $n_d = 5$ (black dashed–dotted line), for $n_d = 4$ (gray dashed–dotted line), for $n_d = 3$ (black dotted line), and for $n_d = 2$ (gray dotted line). It can be deduced that $n_d = 7$ and $n_b = 7$ constitute the optimal values of the n_d and of the n_b parameters for the mistuning analysis of this industrial fan. It should be noted that such a reduction allows the dimension of the stochastic finite element model to be reduced of a factor of around 1500.

Identification of the Dispersion Parameters. It results from the manufacturing process of a blade that all manufactured blades are different from one to another one and from the nominal blade. The tolerances that characterize the authorized fluctuations of the

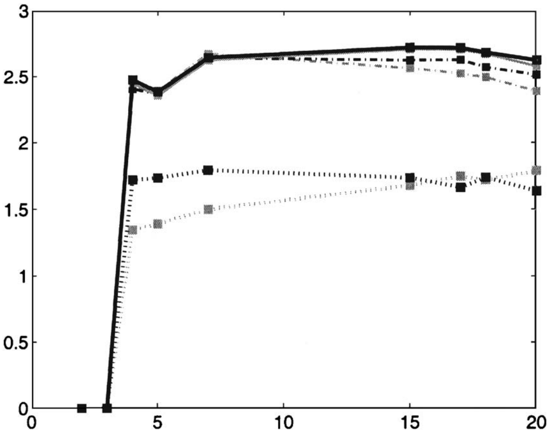

Fig. 4 Graph of function $n_b \mapsto \mathrm{Conv}^2(300, n_d, n_b)$ for $n_d = 10$ (black solid line), for $n_d = 7$ (gray solid line), for $n_d = 5$ (black dashed–dotted line), for $n_d = 4$ (gray dashed–dotted line), for $n_d = 3$ (black dotted line), and for $n_d = 2$ (gray dotted line), related to the stochastic dynamic equation with $\delta_M^j = \delta_D^j = 0$ and $\delta_K^j = 0.05$

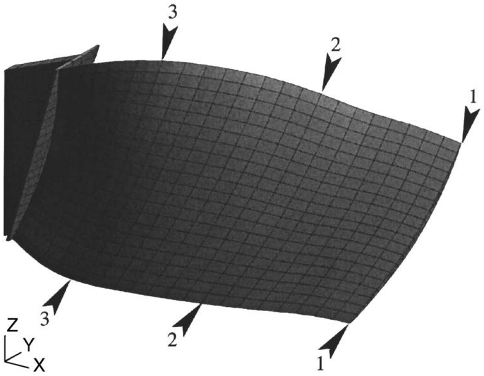

Fig. 5 Mesh of the nominal blade and definition of three section profiles

blade geometry are defined from its nominal geometry. In the context of the blade manufacturing, the tolerances are specified for different sections at a given height from the base of the blade. Let S_1, S_2 and S_3 be three section profiles defined in Fig. 5. For $k=1, 2, 3$, the parameters considered in this paper are the length L_k of the chord and an angular torsion α_k, which allows the shape of the trailing edge to be controlled (see Fig. 6). A random blade geometry has to be constructed in order to identify the dispersion parameters of the nonparametric model of random uncertainties. Such a random geometry has to be representative of a manufactured blade. It means that the random geometry has to respect the constraints due to tolerances specifications and has to have a certain regularity of shape from one section to another one. Let $\underline{\mathbf{x}}$ be the vector in $\mathbb{R}^{3(n_i+n_\Sigma)}$ related to the coordinates of the nodes belonging to the nominal mesh of the blade. Then let $\mathbf{x}$ be the vector in $\mathbb{R}^{3(n_i+n_\Sigma)}$ related to the coordinates of the nodes belonging to the mesh of the manufactured blade. In the probabilistic context of tolerancing, we then model $\mathbf{x}$ by the $\mathbb{R}^{3(n_i+n_\Sigma)}$-valued random variable $\mathbf{X}$. The random fluctuation of the geometry is generated by the following model:

$$\mathbf{X}-\underline{\mathbf{x}}=\sum_{i\in\mathcal{I}} T_i\boldsymbol{\varphi}_i\,, \tag{19}$$

in which $\{\boldsymbol{\varphi}_i, i\in\mathcal{I}\}$ is a vector basis chosen as a subset $\mathcal{I}$ of the set of the eigenmodes of the nominal blade with a fixed coupling interface and where T_i, $i\in\mathcal{I}$ are independent random variables with a uniform distribution. Figure 7 shows several section profiles for one realization of the random blade geometry with an amplification coefficient equal to 20 (gray filled thin line) and for the nominal blade (thick line). It should be noted that the construction of such a probabilistic model of the geometry remains arbitrary and does not constitute a model corresponding to a given manufacturing process. Nevertheless, this model is not directly used to carry out a direct mistuning analysis. It is important to note that the random dynamic magnification factor is strongly sensitive to the choice of the probability model that is constructed with the nonparametric approach and consequently does not directly depend on the probabilistic model of the geometry: this nonparametric model depends only on the dispersion parameters. The probabilistic model of the geometry allows these dispersion parameters to be constructed as a function of the tolerances. An error on this function induces an error on the value of the dispersion parameters for a given tolerance but does not yield an error on the mistuning analysis for a given value of the dispersion parameters.

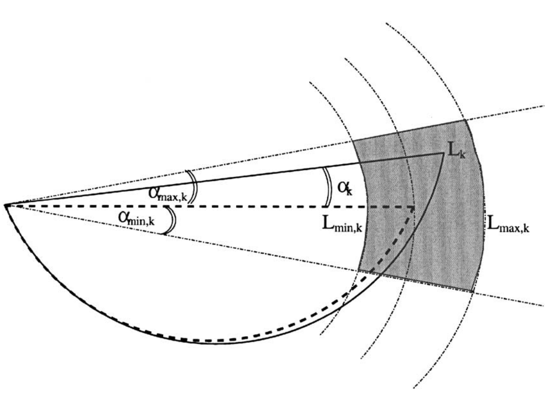

Fig. 6 Geometrical parameters of the tolerances: section S_k of the nominal blade (thick dashed-line) and of the manufactured blade (thick solid line). Location of the trailing edge (gray filled zone) with respect to the tolerances specifications.

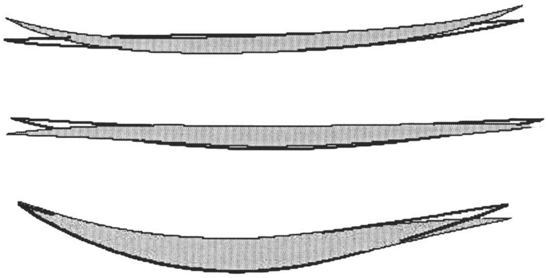

Fig. 7 Section profiles for a realization of the manufactured blade with a zoom 20× (gray filled thin line) and for the nominal blade (thick line)

Let $p\in\{1,\ldots,n_i+n_\Sigma\}$ be a node of the mesh of the blade. The block decomposition of vectors $\underline{\mathbf{x}}$ and $\mathbf{x}$ with respect to a node p of the mesh is denoted as $\underline{\mathbf{x}}_p$ and $\mathbf{x}_p$, which are vectors in $\mathbb{R}^3$. Let n_k be the node related to the trailing edge of S_k, $k\in\{1,2,3\}$. The tolerance specifications allows parameter L_k (or parameter α_k) to be bounded between $L_{\min,k}$ and $L_{\max,k}$ (or between $\alpha_{\min,k}$ and $\alpha_{\max,k}$). The coordinates of node n_k are then bounded such that

$$|\mathbf{x}_{n_k}-\underline{\mathbf{x}}_{n_k}|\leqslant\Delta\underline{\mathbf{c}}_k\,,\quad \forall k\in\{1,2,3\}, \tag{20}$$

in which $\Delta\underline{\mathbf{c}}_k$ is the vector in $\mathbb{R}^3$ related to the bounds of $\mathbf{x}_{n_k}$ induced by the tolerance specifications characterized by $L_{\min,k}$, $\alpha_{\min,k}$, $L_{\max,k}$ and $\alpha_{\max,k}$. The random mesh of the blade is modeled by assuming that all the nodes of the mesh are allowed to fluctuate with respect to the nominal mesh. The probability distributions $p_{T_i}(t_i)$ of uniform random variables T_i, $i\in\mathcal{I}$ are then estimated by the Monte Carlo numerical simulation with an optimization procedure. Let $\theta_1,\ldots,\theta_{n_s}$ be the n_s realizations used by the Monte Carlo numerical simulation. We have then to find $\forall i\in\mathcal{I}$, the probability distribution $p_{T_i}(t_i)$ of uniform random variable T_i such that $\forall p\in\{1,\ldots,n_i+n_\Sigma\}$ and $\forall j\in\{1,\ldots,n_s\}$,

$$\left|\sum_{i\in\mathcal{I}} T_i(\theta_j)\boldsymbol{\varphi}_{i,p}\right|\leqslant \min_{k\in\{1,2,3\}}(\Delta\mathbf{c}_k), \tag{21}$$

in which $\boldsymbol{\varphi}_{i,p}$ is the restriction of vector $\boldsymbol{\varphi}_i$ on the degrees of freedom of node p and where $T_i(\theta_j)$ is the realization number j of random variable T_i. It follows that this random geometry model is in agreement with the tolerance specifications described in Eq. (20). The implementation of this strategy is carried out by using the Monte Carlo numerical simulation with an heterodyne strategy for computing the random variables in order to accelerate the stochastic convergence.

Let us introduce $dL_{\min,k}$ and $dL_{\max,k}$ such that $dL_{\min,k}=L_{k,0}-L_{\min,k}$ and $dL_{\max,k}=L_{\max,k}-L_{k,0}$ in which, for section S_k, the parameter $L_{k,0}$ is the length of the chord related to the nominal blade. In the numerical application, we have $dL_{\min,1}=\cdots$

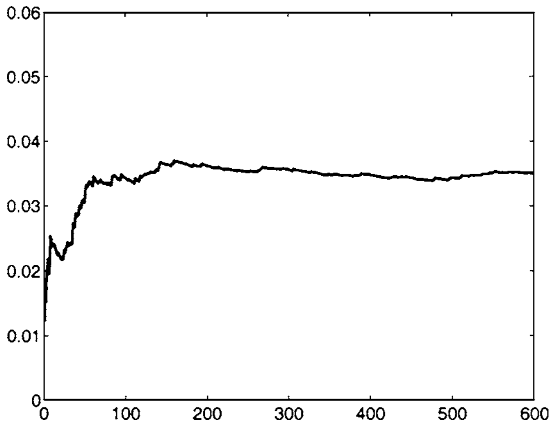

Fig. 8 Convergence with respect to the number n_s of realizations: graph of function $n_s \mapsto \tilde{\delta}_K(n_s)$ for $dL_{\min}=-0.55$ mm, $dL_{\max}=0.75$ mm, $\alpha_{\max}=-\alpha_{\min}=0.55$ deg

$=dL_{\min,3}$, denoted as $dL_{\min}$, $dL_{\max,1}=\cdots=dL_{\max,3}$ denoted as $dL_{\max}$, $\alpha_{\min,1}=\cdots=\alpha_{\min,3}$ denoted as $\alpha_{\min}$ and $\alpha_{\max,1}=\cdots=\alpha_{\max,3}$ denoted as $\alpha_{\max}$. We then introduce that Figs. 8 and 9 are related to the convergence with respect to the number n_s of realizations and display the graphs $n_s \mapsto \tilde{\delta}_K(n_s)$ and $n_s \mapsto \tilde{\delta}_M(n_s)$ in which $\tilde{\delta}_K(n_s)$ and $\tilde{\delta}_M(n_s)$ are the statistical estimators of Eqs. (12), (13) for $dL_{\min}=-0.55$ mm, $dL_{\max}=0.75$ mm, $\alpha_{\max}=-\alpha_{\min}=0.55$ deg. A reasonable convergence is obtained for $n_s=250$. It is then deduced that the dispersion parameters corresponding to the values of the tolerances parameters are such that $\delta_K=0.035$ and $\delta_M=3\times10^{-5}$.

Probabilistic Analysis of the Blade Mistuning Due to Geometric Uncertainties. In this section, the random mistuning analysis is carried out for the complete bladed disk. In this application, it is assumed that the random uncertainties are homogeneous from one blade to another one, yielding $\delta_M^j=\delta_M$, $\delta_D^j=\delta_D$ and $\delta_K^j=\delta_K$, for all $j\in\{0,\ldots,N-1\}$. The mass and the stiffness dispersion parameters induced by the random geometry of the blade are then deduced from the identification procedure above. Such an identification methodology does not include damping uncertainty. Therein, it will be assumed that the damping dispersion parameter δ_D is 0. The Monte Carlo numerical simulation is performed with $n_s=1500$ realizations.

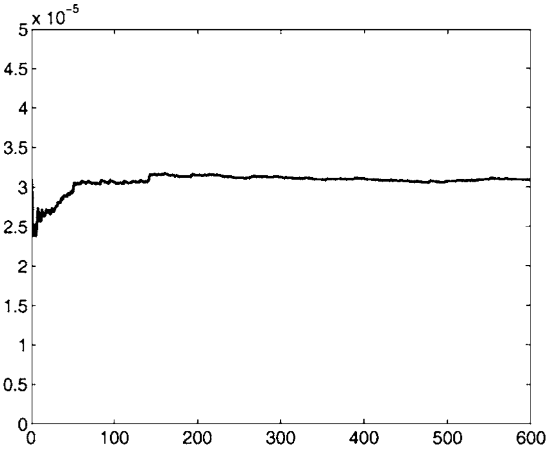

Fig. 9 Convergence with respect to the number n_s of realizations: graph of function $n_s \mapsto \tilde{\delta}_M(n_s)$ for $dL_{\min}=-0.55$ mm, $dL_{\max}=0.75$ mm, $\alpha_{\max}=-\alpha_{\min}=0.55$ deg

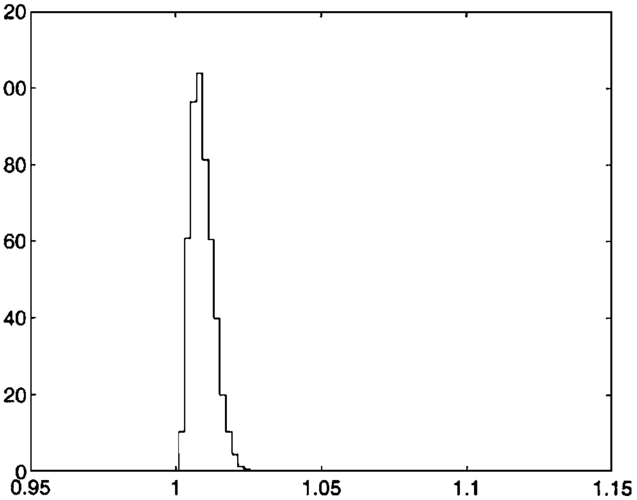

Fig. 10 Graph of the probability density function $b \mapsto p_{B_\infty}(b)$ for $dL_{\min}=-0.55$ mm and $dL_{\max}=0.75$ mm, $\alpha_{\max}=-\alpha_{\min}=0$ deg

Figure 10 shows the probability density function $b \mapsto p_{B_\infty}(b)$ in the case of the blade mistuning is only due to the variation of the chord length related to each blade profile. With $dL_{\min}=-0.55$ mm and $dL_{\max}=0.75$ mm and $\alpha_{\max}=\alpha_{\min}=0$, it is found that the corresponding dispersion parameters are very close to 0 and do not yield significant amplification with respect to the tuned case.

A sensitivity analysis with respect to the tolerances related to the blade torsion angle is then considered. The level of uncertainty related to the blade chord uncertainty is given by $dL_{\min}=-0.55$ mm and $dL_{\max}=0.75$ mm. Figure 11 and Fig. 12 display the probability density function $b \mapsto p_{B_\infty}(b)$ for $\alpha_{\max}=-\alpha_{\min}=0.35$ and $\alpha_{\max}=-\alpha_{\min}=0.55$, which correspond with the following dispersion parameters $\delta_M=2\times10^{-5}$, $\delta_K=0.015$, and $\delta_M=3\times10^{-5}$, $\delta_K=0.035$, respectively.

It shows that there exist configurations of the random geometry that yield amplification factors higher than 1.6. Furthermore, the probability distribution of the amplification factor is very sensitive with respect to $\alpha_{\max}$, which allows the variability related to the twist of the blade to be controlled. It should be noted that due to random tolerances, the amount of uncertainty is mainly distributed on the stiffness because the value of the mass dispersion parameter is less than 1000 times the stiffness dispersion parameter.

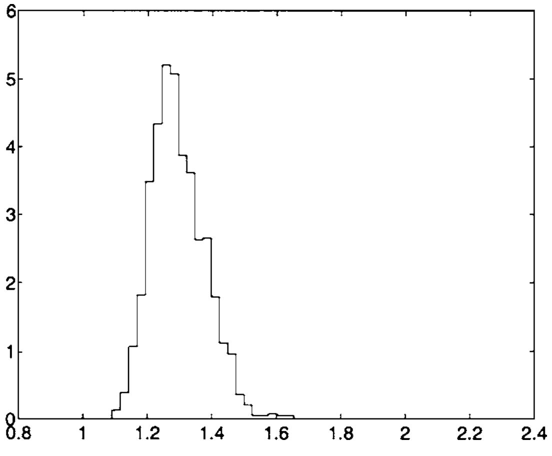

Fig. 11 Graph of the probability density function $b \mapsto p_{B_\infty}(b)$ for $dL_{\min}=-0.55$ mm and $dL_{\max}=0.75$ mm, $\alpha_{\max}=-\alpha_{\min}=0.35$ deg

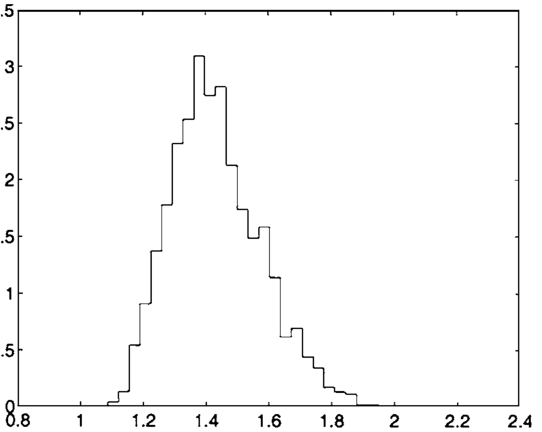

Fig. 12 Graph of the probability density function $b \mapsto p_{B_\infty}(b)$ for $dL_{\min}=-0.55$ mm and $dL_{\max}=0.75$ mm, $\alpha_{\max}=-\alpha_{\min}=0.55$ deg

Figure 13 displays the graphs $\alpha_{\max} \mapsto \mathcal{P}(B_\infty > b_\infty)$ for several values of $b_\infty = 1.2$ (a black solid line), $b_\infty = 1.3$ (a gray solid line), $b_\infty = 1.4$ (a black dashed–dotted line), $b_\infty = 1.5$ (a gray dashed–dotted line), $b_\infty = 1.6$ (a black dotted line), and $b_\infty = 1.7$ (a gray dotted line). As it was seen on a simple numerical example [18], this kind of graph has a maximum that allows two types of specifications to be considered. One specification consists in defining tolerances of the blade with high precision, whereas the other one consists in intentionally mistuning the blade. For $\alpha_{\max}=0.55$ deg, it can be seen that $\mathcal{P}(B_\infty > 1.6) = 0.1593$, $\mathcal{P}(B_\infty > 1.5) = 0.3273$, and $\mathcal{P}(B_\infty > 1.4) = 0.5933$. In addition, the confidence region defined by $\mathcal{P}(B_\infty > 1.7) \leq 0.1$ is obtained for parameter $\alpha_{\max} < 0.48$ deg or $\alpha_{\max} > 1.04$ deg.

Conclusions

This paper deals with the specification of the blade geometrical tolerances for mistuned bladed disks by using a nonparametric probabilistic approach. The theory that has been previously developed for a simple numerical example is applied to an industrial bladed disk. First, a mean reduced model of the bladed disk is constructed with a "branch mode" substructuring method. This model is adapted for implementing the nonparametric methodology for each uncertain substructure. Mistuning is then introduced by using a nonparametric probabilistic approach. It should be noted that such a probabilistic model allows the random matrices to be positive definite that is coherent with the linear structural dynamic theory. Furthermore, the nonparametric approach allows both blade eigenfrequencies and blade eigenvectors to be represented with coherence. For each blade, the quantification of these uncertainties is described by three scalar parameters that allow the global dispersion of mass, damping, and stiffness random matrices to be controlled. In this paper, we are interested by solving the inverse problem, which consists in characterizing the geometrical tolerances for a given confidence region of the random dynamic magnification factor over a narrow-frequency band of analysis. Such a method requires us to relate the dispersion parameters of the nonparametric probabilistic approach to the tolerance parameters of the blades. It should be noted that if the random dynamic magnification factor of the mistuned bladed disk is strongly sensitive to the nonparametric probability model of random uncertainties, then it is weakly sensitive to the probability model for the random geometry, which is only used to estimate the dispersion parameters of the nonparametric model as a function of the tolerance parameters. This is the reason why an arbitrary coherent probability model of the blade random geometry can be chosen. Once the dispersion parameters are quantified, the probability levels concerning the random dynamic magnification factor are then characterized with respect to the specified tolerances. This paper proposes a methodology allowing the dynamic amplification induced by mistuning to be fixed. Finally, the proposed method based on the use of the nonparametric approach could be extended to the case of correlated random uncertainties between blades.

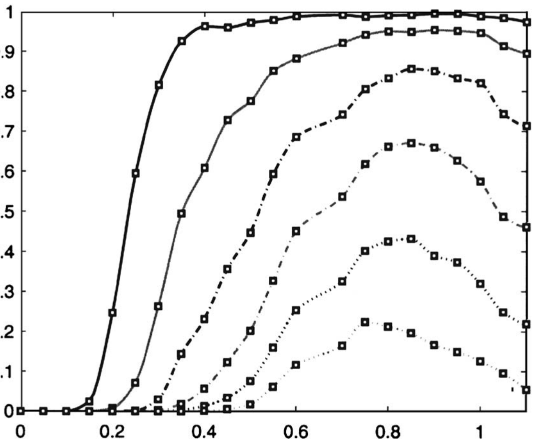

Fig. 13 Graph of $\alpha_{\max} \mapsto \mathcal{P}(B_\infty > b_\infty)$ for several values of $b_\infty = 1.2$ (black solid line), $b_\infty = 1.3$ (gray solid line), $b_\infty = 1.4$ (black dashed–dotted line), $b_\infty = 1.5$ (gray dashed–dotted line), $b_\infty = 1.6$ (black dotted line), and $b_\infty = 1.7$ (gray dotted line)

Nomenclature

n = number of degrees of freedom of the bladed disk
N = number of blades
n_b = number of generalized coordinates for a blade
n_d = number of disk modes per circumferential wave number
n_i^d = number of internal degrees of freedom of the disk
n_i = number of internal degrees of freedom of a blade
n_Σ = number of degrees of freedom on the coupling interface of the blade
N_b = number of generalized coordinates for the blades equal to $n_b \times N$
N_d = number of generalized coordinates for the disk equal to $n_d \times N$
$[A]^T$ = transpose of matrix $[A]$
$[A]^*$ = transconjuguate of matrix $[A]$
$\mathrm{tr}[A]$ = trace of matrix $[A]$
$\|[A]\|_{\mathrm{F}}$ = Frobenius norm of matrix $[A]$ such that $\|[A]\|_{\mathrm{F}} = \mathrm{tr}([A][A]^T)^{1/2}$
$\mathcal{E}$ = mathematical expectation
$\mathcal{P}(X > x)$ = probability that random variable X be greater than a given level x
$\mathbb{M}_{n,p}(\mathbb{R})$ = set of all the $n \times p$ real matrices
$\mathbb{M}_n(\mathbb{R})$ = set of all the $n \times n$ real matrices
$\mathbb{M}_n^+(\mathbb{R})$ = set of all the positive-definite symmetric $n \times n$ real matrices
δ_{ij} = Kronecker symbol such that $\delta_{ij}=1$ if $i=j$ and $\delta_{ij}=0$ if $i \neq j$
$\mathbb{B}$ = frequency band of analysis
Ω = rotation velocity

References

[1] Thomas, D., 1979, "Dynamics of Rotationally Periodic Structures," Int. J. Numer. Methods Eng., **14**, pp. 81–102.
[2] Ohayon, R., and Soize, C., 1998, *Structural Acoustics and Vibration*, Academic Press, San Diego, CA.
[3] Whitehead, D., 1966, "Effects of Mistuning on the Vibration of Turbomachine Blades Induced by Wakes," J. Mech. Eng. Sci., **8**, pp. 15–21.
[4] Ewins, D., 1969, "The Effects of Detuning Upon the Forced Vibrations of Bladed Disks," J. Sound Vib., **9**, pp. 65–69.
[5] Dye, R., and Henry, T., 1969, "Vibration Amplitudes of Compressor Blades

Resulting From Scatter in Blade Natural Frequencies," ASME J. Eng. Power, **91**, pp. 182–187.

[6] Lin, C.-C., and Mignolet, M., 1997, "An Adaptative Perturbation Scheme for the Analysis of Mistuned Bladed Disks," ASME J. Eng. Gas Turbines Power, **119**, pp. 153–160.

[7] Mignolet, M., Lin, C.-C., and LaBorde, B., 2001, "A Novel Limit Distribution for the Analysis of Randomly Mistuned Bladed Disks," ASME J. Eng. Gas Turbines Power, **123**, pp. 388–394.

[8] Griffin, J., and Hoosac, T., 1984, "Model Development and Statistical Investigation of Turbine Blade Mistuning," ASME J. Vib., Acoust., Stress, Reliab. Des., **106**, pp. 204–210.

[9] Sinha, A., and Chen, S., 1989, "A Higher Order to Compute the Statistics of Forced Response of a Mistuned Bladed Disk Assembly," J. Sound Vib., **2**, pp. 207–221.

[10] Yang, M.-T., and Griffin, J., 2001, "A Reduced-Order Model of Mistuning Using a Subset of Nominal System Modes," ASME J. Eng. Gas Turbines Power, **123**, pp. 893–900.

[11] Castanier, M., Ottarson, G., and Pierre, C., 1997, "A Reduced Order Modeling Technique for Mistuned Bladed Disks," ASME J. Vibr. Acoust., **119**, pp. 439–447.

[12] Bladh, R., Castanier, M., and Pierre, C., 2001, "Component-Mode-Based Reduced Order Modeling Techniques for Mistuned Bladed Disks-Part 1: Theoretical Models," ASME J. Eng. Gas Turbines Power, **123**, pp. 89–99.

[13] Petrov, E., Sanliturk, K., and Ewins, D., 2002, "A New Method for Dynamic Analysis of Mistuned Bladed Disks Based on the Exact Relationship Between Tuned and Mistuned Systems," ASME J. Eng. Gas Turbines Power, **124**, pp. 586–597.

[14] Seinturier, E., Dupont, C., Berthillier, M., and Dumas, M., 2002, "A New Aeroelastic Model for Mistuned Bladed Disks," AIAA Paper No. 2002-1533.

[15] Soize, C., 2000, "A Nonparametric Model of Random Uncertainties for Reduced Matrix Models in Structural Dynamics," Probab. Eng. Mech., **15**, pp. 277–294.

[16] Soize, C., 2001, "Maximum Entropy Approach for Modeling Random Uncertainties in Transient Elastodynamics," J. Acoust. Soc. Am., **109**, pp. 1979–1996.

[17] Soize, C., 2001, "Nonlinear Dynamical Systems With Nonparametric Model of Random Uncertainties," E-journal from Resonance Publication (http://www.resonancepub.com), Vol. 1, pp. 1–38.

[18] Capiez-Lernout, E., and Soize, C., 2003, "Specifying Manufacturing Tolerances for a Given Amplification Factor: A Nonparametric Probabilistic Methodology," in American Society of Mechanical Engineers, International Gas Turbine Institute, Turbo Expo (Publication) IGTI, Vol. 4, pp. 183–194.

[19] Benfield, W., and Hruda, R., 1971, "Vibration Analysis of Structures by Component Mode Substitution," AIAA J., **9**, pp. 1255–1261.

[20] Seinturier, E., Lombard, J.-P., Berthillier, M., and Sgarzi, O., 2002, "Turbine Mistuned Forced Response Prediction Comparison With Experimental Results," in American Society of Mechanical Engineers, International Gas Turbine Institute, Turbo Expo (Publication) IGTI, Vol. 4, pp. 943–952.

[21] Craig, R., and Bampton, M., 1968, "Coupling of Substructures for Dynamic Analyses," AIAA J., **6**, pp. 1313–1319.

[22] Soize, C., 2003, "Uncertain Dynamical Systems in the Medium-Frequency Range," ASCE J. Eng. Mech., **129**, pp. 1017–1027.

[23] Soize, C., and Chebli, H., 2003, "Random Uncertainties Model in Dynamic Substructuring Using a Nonparametric Probabilistic Model," ASCE J. Eng. Mech., **129**, pp. 449–457.

[24] Capiez-Lernout, E., and Soize, C., 2004, "Nonparametric Modeling of Random Uncertainties of Mistuned Bladed Disks," ASME J. Eng. Gas Turbines Power, **126**, pp. 610–618.

[25] Capiez-Lernout, E., and Soize, C., 2003, "Probabilistic Model of Random Uncertainties in Structural Dynamics for Mistuned Bladed-Disks," Méc. Ind., **4**, pp. 585–594.

Nagaraj K. Arakere
Associate Professor

Shadab Siddiqui
Graduate Student

Mechanical and Aerospace Engineering,
University of Florida,
Gainesville, FL 32611-6300

Shannon Magnan
Lieutenant Junior Grade,
U.S. Navy Reserve

Fereshteh Ebrahimi
Professor

Luis E. Forero
Graduate Student

Materials Science and Engineering,
University of Florida,
Gainesville, FL 32611-6300

Investigation of Three-Dimensional Stress Fields and Slip Systems for fcc Single-Crystal Superalloy Notched Specimens

Metals and their alloys, except for a few intermetallics, are inherently ductile, i.e., plastic deformation precedes fracture in these materials. Therefore, resistance to fracture is directly related to the development of the plastic zone at the crack tip. Recent studies indicate that the fracture toughness of single crystals depends on the crystallographic orientation of the notch as well as the loading direction. In general, the dependence of crack propagation resistance on crystallographic orientation arises from the anisotropy of (i) elastic constants, (ii) plastic deformation (or slip), and (iii) the weakest fracture planes (e.g., cleavage planes). Because of the triaxial stress state at the notch tips, many slip systems that otherwise would not be activated during uniaxial testing become operational. The plastic zone formation in single crystals has been tackled theoretically by Rice and his co-workers [Rice, J. R., 1987, Mech. Mater. **6***, pp. 317–335; Rice, J. R., and Saeedvafa, M., 1987, J. Mech. Phys. Solids* **36***, pp. 189–214; Saeedvafa, M., and Rice, J. R., 1988; ibid.,* **37***, pp. 673–691; Rice, J. R., Hawk, D. E., Asaro, R. J., 1990, Int. J. Fract.* **42***, pp. 301–321; Saeedvafa, M., and Rice, J. R., 1992, Modell. Simul. Mater. Sci. Eng.* **1***, pp. 53–71] and only limited experimental work has been conducted in this area. The study of the stresses and strains in the vicinity of a fcc single-crystal notch tip is of relatively recent origin. We present experimental and numerical investigation of three-dimensional (3D) stress fields and evolution of slip sector boundaries near notches in fcc single-crystal PWA1480 tension test specimens and demonstrate that a 3D linear elastic finite element model, which includes the effect of material anisotropy, is shown to predict active slip planes and sectors accurately. The slip sector boundaries are shown to have complex curved shapes with several slip systems active simultaneously near the notch. Results are presented for surface and mid-plane of the specimens. The results demonstrate that accounting for 3D elastic anisotropy is very important for accurate prediction of slip activation near fcc single-crystal notches loaded in tension. Results from the study will help establish guidelines for fatigue damage near single-crystal notches.*
[DOI: 10.1115/1.1850939]

Introduction

Turbine blades and vanes in high-performance aircraft and rocket engines are increasingly being made of single-crystal nickel superalloys. Single-crystal nickel-base superalloys were developed to provide superior creep, stress rupture, melt resistance, and thermomechanical fatigue capabilities over polycrystalline alloys previously used in the production of turbine blades and vanes. Currently these single-crystal nickel-base turbine blade superalloys are widely used in aircraft and rocket engine applications and are also being used in the NASA SSME alternate fuel turbopump. These alloys play an important role in commercial, military, and space propulsion systems. Single-crystal materials differ significantly from polycrystalline alloys in that they have highly orthotropic properties, making the position of the crystal lattice relative to the part geometry a significant factor in the overall analysis. Turbine blades and vanes, used in aircraft and rocket engines, are typically the most demanding structural applications for high-temperature materials due to the combination of high operating temperature, corrosive environment, high monotonic and cyclic stresses, long expected component lifetimes, and the enormous consequence of structural failure. Hence failures of blade components account for 40% of all turbine engine component failures attributable to HCF. Estimation of blade fatigue life, therefore, represents a very important aspect of durability assessment.

Metals and their alloys, except for a few intermetallics, are inherently ductile, i.e., plastic deformation precedes fracture in these materials. Therefore, resistance to fracture is directly related to the development of the plastic zone at the crack tip. Recent studies indicate that the fracture toughness of single crystals depends on the crystallographic orientation of the notch (here referred to as the secondary orientation) as well as the loading direction (here referred to as primary orientation) [1–9]. In general, the dependence of crack propagation resistance on crystallographic orientation arises from the anisotropy of (i) elastic constants, (ii) plastic deformation (or slip), and (iii) the weakest fracture planes (e.g., cleavage planes). As far as crack initiation and propagation in metallic alloys are concerned, the effect of crystallographic orientation on the development of the plastic zone in the vicinity of a crack tip is of significant importance. In polycrystal-

---

Contributed by the International Gas Turbine Institute (IGTI) of THE AMERICAN SOCIETY OF MECHANICAL ENGINEERS for publication in the ASME JOURNAL OF ENGINEERING FOR GAS TURBINES AND POWER. Paper presented at the International Gas Turbine and Aeroengine Congress and Exhibition, Vienna, Austria, June 13–17, 2004, Paper No. 2004-GT-53938. Manuscript received by IGTI, October 1, 2003; final revision, March 1, 2004. IGTI Review Chair: A. J. Strazisar.

line metals, although the far field stresses are controlled by their isotropic properties, the behavior at the crack tip is partially governed by the crystal anisotropy.

Many groups have used dislocation theory to study the initiation of plasticity at crack tips and notches, in semi-brittle materials [10–15], however, only limited work has been reported on the development of plastic zones at meso- and macroscopic levels in notched ductile single crystals. Because of the triaxial stress state at the notch tips, many slip systems that otherwise would not be activated during uniaxial testing become operational. The plastic zone formation in single crystals has been tackled theoretically by Rice and his co-workers [16–20], and only limited experimental work has been conducted in this area [21–25].

The study of the stresses and strains in the vicinity of a fcc single-crystal notch tip is of relatively recent origin; despite the analytical and experimental investigations by researchers [16,21–25], a single-crystal model that incorporates 3D elastic anisotropy and near-notch plasticity effects, necessary to accurately predict evolution of slip sectors in 3D stress fields, is far from complete. This paper presents an experimental and numerical investigation of 3D stress fields and evolution of slip sector boundaries near notches in fcc single-crystal tension test specimens and demonstrates that a 3D linear elastic finite element model, which includes the effect of material anisotropy, is shown to predict active slip planes and sectors accurately. This is a first step toward a comprehensive analysis of the evolution of the plastic zone in notches with triaxial stress fields in single-crystal superalloys. We are developing constitutive relations for modeling crystal plasticity in 3D stress fields, to evaluate both monotonic and cyclic plastic stresses and strains, toward evaluating fatigue life in single-crystal superalloy turbine blades. A rate-dependent constitutive model is being developed [26] that is capable of modeling large deformation and large strains. This model enables unique determination of slip rates on each slip system even when many potential slip systems are included in the model, thus, enabling simulation of multiple slip.

Review of Two-Dimensional Plastic Analysis of Notched Single Crystals

Rice [16] provided the foundation for much recent and current work in the area of crack/notch tip stress and strain analysis by examining the mechanics of both fcc and bcc notched specimens loaded in tension. Rice constructs the plastic field at the crack tip based on plane strain [two-dimensional (2D)] isotropic assumptions, and the results represent a continuous solution in terms of the radial and angular displacement from the tip, where the state of stress is constant within each sector. A perfectly plastic stress field is assumed, and therefore the boundaries are defined as the radial lines where a discontinuity occurs at specific angles where the slip shifts from one system to another. The solution does not distinguish between the two orientations' sector boundaries or between fcc or bcc crystal structure. Both crystal orientations and structures predict boundaries at 55, 90, and 125 deg. Rice notes the weakness of this attribute, based on contradictory experimental studies, which is tied to the rotation of the crystal lattice. He acknowledges the simplification of the plane strain assumption and encourages incorporating anisotropy, strain hardening, and 3D effects into future models.

Shield [21] conducted several tests of notched four-point bending single-crystal copper specimens to correlate Rice's analytical models with his experimental observations. Moiré interferometry analysis was used to determine the strain fields and sectors. Shield's results from the low load levels show similarities to Rice's model, but do not correlate to Rice's model at high plastic strains. The strains do not maintain the same order in their relative level of activity in different sectors. This changing slip activity (with load level) contradicts the constant sector boundaries predicted using 2D isotropic assumptions. Shield's experimental results, and their dissimilarity to Rice's analysis, again highlight the need for a more accurate predictive model.

Crone and Shield [23] continued experimental studies of notch tip deformation in two different orientations of single-crystal copper and copper-beryllium tensile specimens. Slip sector boundaries are determined experimentally, again using Moiré interferometry. The visible slip patterns determine slip activity, but as the authors note, a lack of visible slip does not rule out any activity. Slip systems may be activated internally, rather than at the surface, or may show varying patterns on the surface as deformation continues. They compared their experimental results to Rice's analytical solution, as well as numerical finite element analysis (FEA) solutions by Mohan et al. [27] and Cuitino and Ortiz [28]. Both numerical models are based on the plane strain assumption, although Cuitino and Ortiz later conclude the problem cannot truly be plane strain due to large strain differences internally and at the surface. Even with the plane strain assumption, the numerical and analytical models do not match; all three differ from the experimental results. The experimental results are somewhat ambiguous due to the "annulus of validity," where Crone and Shield take their measurements. This annulus, following Shield and Kim [25] corresponds to the radial area from 350 to 750 μm from the notch tip. The notch width is between 100 and 200 μm, making the notch radius between 50 and 100 μm. Therefore the annulus and the region where the sectors are measured is anywhere from 3.5 to 7.0 and 7.5 to 15.0 times the notch radius from the tip. These distances would place the sectors well out of the range of any elastic deformation and clearly can only be used where extreme plastic deformation exists. However, Crone and Shield preserve this annulus to avoid material too close to the notch tip. They note that observed slip activity begins in a single sector; as deformation proceeds, more slip lines become visible in the same sector at further radial distances from the notch. They also clearly observe horizontal slip traces directly ahead of the notch, however, they discount their observations and label the slip as "elastic" in order to compare their solution to other perfectly plastic sharp crack solutions. Citing Saeedvafa and Rice [18] they further explain these traces as a function of hardening and not plastic deformation, but they do not make such accounts for the other sectors. Contrary to the equivalent sectors predicted by Rice, Crone and Shield's observed sectors show a marked difference with orientation, varying in both specific boundary angles and in the number of sectors. The plane strain FEA results on a central plane of the model appeared to correspond more closely to the experimental results. Crone and Shield assert this agreement to the central plane FEA results, which suggests that plane strain is accurate for specific locations.

Schulson and Xu [22] examined the state of stress at a notch tip for single crystal Ni_3Al, the γ' component of single-crystal superalloys, using three-point bending specimens. An analytical model based on elastic isotropic assumptions was used and calculated stress field around the notch based on the equations for a sharp notch. Two solutions based on plane stress and plane strain assumptions were evaluated. They note, however, that since the notch causes a triaxial state of stress, both these assumptions and ignoring anisotropy are approximations. Experimental results after significant plastic deformation reveal results that deviate from those predicted by either plane stress or plane strain, but are closer to the plane stress assumption.

Elastic Anisotropy in fcc Single Crystals

The generalized Hooke's law for a homogeneous anisotropic body in Cartesian coordinates (x, y, z with origin at point O) is given by Eq. (1) [29]

$$\{\boldsymbol{\varepsilon}\}=\lfloor \mathbf{a}_{ij} \rfloor \{\boldsymbol{\sigma}\} \tag{1}$$

$[\mathbf{a}_{ij}]$ is the matrix of 36 elastic coefficients, of which only 21 are independent, since $[\mathbf{a}_{ij}]=[\mathbf{a}_{ji}]$. The elastic properties of FCC

Table 1 Slip plane and slip direction for the 12 primary octahedral slip systems [30]

Slip system	Slip plane $\langle 110\rangle\{111\}$	Slip direction
1	(111)	$[10\bar{1}]$
2	(111)	$[0\bar{1}1]$
3	(111)	$[1\bar{1}0]$
4	$(\bar{1}1\bar{1})$	$[10\bar{1}]$
5	$(\bar{1}1\bar{1})$	$[110]$
6	$(\bar{1}1\bar{1})$	$[011]$
7	$(1\bar{1}\bar{1})$	$[110]$
8	$(1\bar{1}\bar{1})$	$[0\bar{1}1]$
9	$(1\bar{1}\bar{1})$	$[101]$
10	$(\bar{1}\bar{1}1)$	$[011]$
11	$(\bar{1}\bar{1}1)$	$[101]$
12	$(\bar{1}\bar{1}1)$	$[1\bar{1}0]$

crystals exhibit cubic symmetry, also described as cubic syngony. The elastic properties of materials with cubic symmetry can be described with three independent constants designated as the elastic modulus, shear modulus, and Poisson ratio [29], and hence $[\mathbf{a}_{ij}]$ can be expressed as shown in Eq. (2), in the material coordinate system (fcc crystal axes are parallel to x, y, and z coordinate axes). In contrast to the fcc single-crystal material, an isotropic material can only have two independent elastic constants

$$[\mathbf{a}_{ij}]=\begin{bmatrix} a_{11} & a_{12} & a_{12} & 0 & 0 & 0 \\ a_{12} & a_{11} & a_{12} & 0 & 0 & 0 \\ a_{12} & a_{12} & a_{11} & 0 & 0 & 0 \\ 0 & 0 & 0 & a_{44} & 0 & 0 \\ 0 & 0 & 0 & 0 & a_{44} & 0 \\ 0 & 0 & 0 & 0 & 0 & a_{44} \end{bmatrix} \tag{2}$$

$$a_{11}=\frac{1}{E_{xx}}, \quad a_{44}=\frac{1}{G_{yz}}, \quad a_{12}=-\frac{\nu_{yx}}{E_{xx}}=-\frac{\nu_{xy}}{E_{yy}}$$

The elastic constants in the generalized Hooke's law of an anisotropic body $[\mathbf{a}_{ij}]$ vary with the direction of the coordinate axes. For orientations other than the (x,y,z) axes, the $[\mathbf{a}_{ij}]$ matrix varies with the crystal orientation. In the case of an isotropic body the constants are *invariant* in any orthogonal coordinate system. Consider a Cartesian coordinate system (x',y',z') that has rotated about the origin O of (x,y,z). The elastic constant matrix $[\mathbf{a}'_{ij}]$ in the (x',y',z') coordinate system that relates $\{\boldsymbol{\varepsilon}'\}$ and $\{\boldsymbol{\sigma}'\}$ $[\{\boldsymbol{\varepsilon}'\}=[\mathbf{a}'_{ij}]\{\boldsymbol{\sigma}'\}]$ is given by the following transformation [29]:

$$[\mathbf{a}'_{ij}]=[\mathbf{Q}]^T[\mathbf{a}_{ij}][\mathbf{Q}]=\sum_{m=1}^{6}\sum_{n=1}^{6} a_{mn}Q_{mi}Q_{nj}, \quad (i,j=1,2,\ldots,6) \tag{3}$$

The transformation matrix $[Q]$ is a 6×6 matrix that is a function of the direction cosines between the (x,y,z) and (x',y',z') coordinate axes. Knowing the state of stress at a given location, in the material coordinate system (x,y,z), the resolved shear stresses (RSS) on the 12 primary octahedral slip systems, denoted by τ^1, $\tau^2,\ldots,\tau^{12}$, can be readily obtained using the transformation given by Eq. (4) [30]. The slip plane and slip direction of the 12 primary octahedral slip systems are given in Table 1 [30]

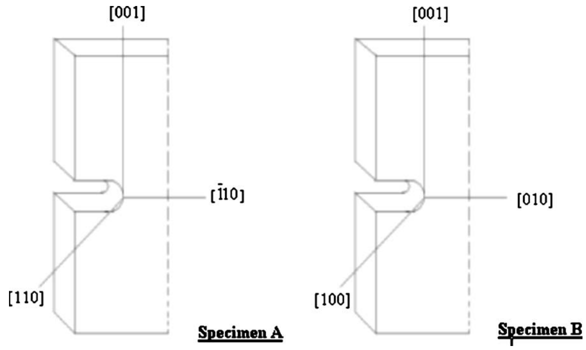

Fig. 1 Finite element analysis, specimens, and orientations [32]

$$\begin{Bmatrix} \tau^1 \\ \tau^2 \\ \tau^3 \\ \tau^4 \\ \tau^5 \\ \tau^6 \\ \tau^7 \\ \tau^8 \\ \tau^9 \\ \tau^{10} \\ \tau^{11} \\ \tau^{12} \end{Bmatrix}=\frac{1}{\sqrt{6}}\begin{bmatrix} 1 & 0 & -1 & 1 & 0 & -1 \\ 0 & -1 & 1 & -1 & 1 & 0 \\ 1 & -1 & 0 & 0 & 1 & -1 \\ -1 & 0 & 1 & 1 & 0 & -1 \\ -1 & 1 & 0 & 0 & -1 & -1 \\ 0 & 1 & -1 & -1 & -1 & 0 \\ 1 & -1 & 0 & 0 & -1 & -1 \\ 0 & 1 & -1 & -1 & 1 & 0 \\ 1 & 0 & -1 & -1 & 0 & -1 \\ 0 & -1 & 1 & -1 & -1 & 0 \\ -1 & 0 & 1 & -1 & 0 & -1 \\ -1 & 1 & 0 & 0 & 1 & -1 \end{bmatrix}\begin{Bmatrix} \sigma_{xx} \\ \sigma_{yy} \\ \sigma_{zz} \\ \sigma_{xy} \\ \sigma_{zx} \\ \sigma_{yz} \end{Bmatrix} \tag{4}$$

Three-Dimensional Elastic Anisotropic FEA of Notched Single Crystal Specimens and Prediction of Slip Sectors

An ideal test would incorporate parameters for specimen size, type of test, plasticity, hardening, lattice rotation, etc., and eventually a fatigue crack rather than a notch. However, before incorporating such complexity the basic model must be better understood. We present a numerical and experimental investigation of 3D stress fields and evolution of slip sector boundaries near notches, using double-notched tensile specimens of a single-crystal superalloy, which has a fcc crystal structure. A 3D linear elastic finite element model that includes the effect of material anisotropy is shown to predict active slip planes and sectors at the specimen surface accurately.

Three-dimensional FEA incorporating elastic anisotropy was used to model test specimens with a fixed [001] primary crystallographic orientation and two different secondary orientations (as shown in Fig. 1) to predict slip activity and sectors around the notch. The two specimens examined have the load direction along the [001] primary orientation, while the notch directions are $[\bar{1}10]$ for specimen A and [010] for specimen B. Three-dimensional FEA of notched single-crystal specimens was accomplished using ANSYS finite element software (Version 5.7). Figure 2 defines the specimen dimensions whose values are given in Table 2. The FEA component stresses were taken from the material coordinate system, around the notch, and then used in the transformation equations to calculate the individual resolved shear stresses. Data were analyzed over a wide range of radial and angular distances to create a complete stress field, and later used to draw conclusions on sectors and slip activation.

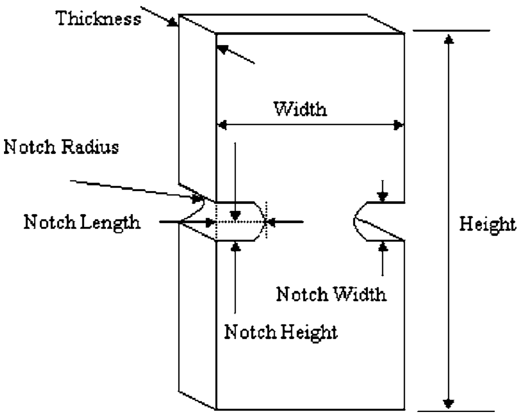

Fig. 2 **Dimensions of specimen A** [31]

ANSYS aligns material properties with the element coordinate system; therefore, the element coordinate system is aligned with the material coordinate system so that the directional material properties are suitably applied. The ANSYS elements chosen for the FEM are PLANE2 (2D six-node triangular element with quadratic displacement functions) and SOLID95 (3D structural solid with 20 nodes) capable of incorporating anisotropic properties. Figure 3 shows the 3D FE model of specimen A and a close-up view of the notch mesh. After the three-dimensional solid model is created, the front face is meshed with the PLANE2 (two-dimensional) elements. This front face has precise element sizing along the defined radial lines around the notch tip at 5 deg intervals [Fig. 4(*a*)]. Once the front face is meshed, three-dimensional elements are swept through the volume to complete the meshing of the model and the two-dimensional mesh is deleted.

Table 2 **Actual and finite element specimen dimensions in mm** [31]

	Specimen A		Specimen B	
Dimensions	Actual	FEM	Actual	FEM
Width	5.100	5.100	5.04	5.04
Height	19.000	19.000	17.594	17.594
Thickness	1.800	1.800	1.82	1.82
Right notch length	1.300	1.550	1.399	1.399
Left notch length	1.550	1.550	1.36	1.399
Right notch height	0.113	0.113	0.084	0.084
Left notch height	0.111	0.113	0.0845	0.084

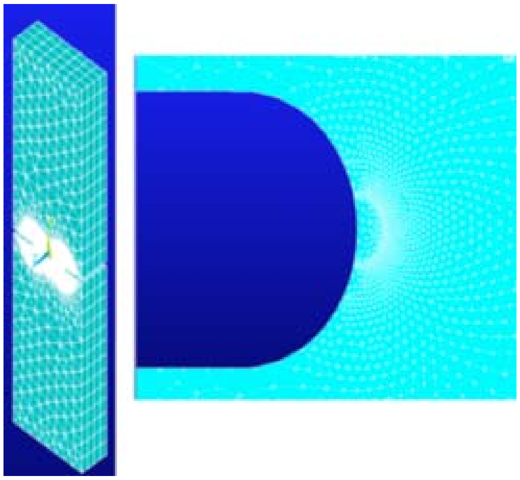

Fig. 3 **3D Finite element model of specimen A with a close-up view of the notch** [31]

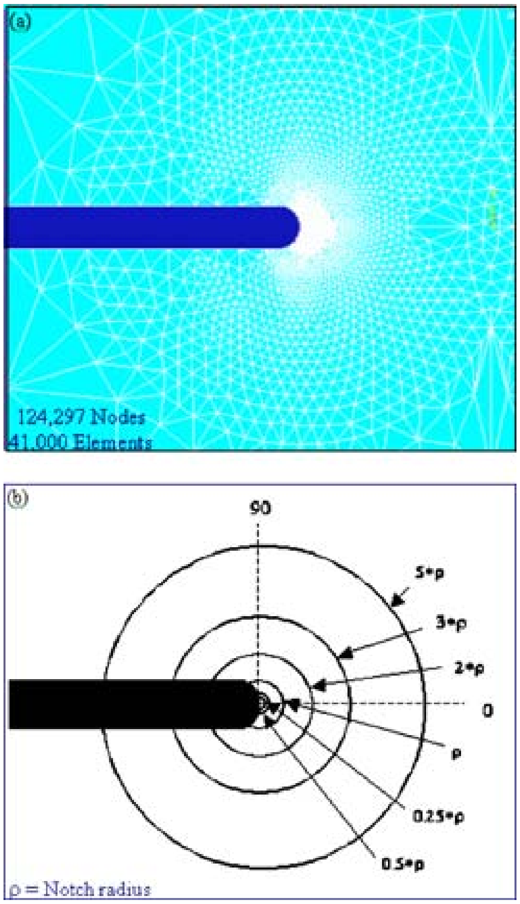

Fig. 4 **(*a*) Close-up view of element sizing on the specimen front face near the notch and (*b*) Radial and angular coordinates used for producing slip sector plots** [32]

To observe both the near-field and far-field state of stress in the vicinity of the notch (radial and angular), six concentric arcs were created at the following radii from the notch tip: $0.25^*\rho$, $0.50^*\rho$, $1.00^*\rho$, $2.00^*\rho$, $3.00^*\rho$, and $5.00^*\rho$; where ρ is the notch radius [Fig. 4(*b*)]. The element sizing of the FEM allows data to be collected on any of five separate x-y planes, including the front, middle, and back planes.

Results From Finite Element Analysis

Results were plotted for the 12 primary RSS values from $r = 0.25^*\rho$ to $5^*\rho$ and from 0 deg to the top of the notch (100 deg for $0.25^*\rho$ up to 170 deg for $5^*\rho$). Figure 5(a) shows a representative plot of RSS values of 12 primary slip systems, on the surface of specimen A, as a function of theta, at $r = 5\rho$. As a stress-based process, slip deformation can be predicted by the numerical model's highest individual resolved shear stresses. The slip systems that are represented by the highest resolved shear stresses, which exceed the experimentally measured critical resolved shear stress (CRSS) value, should then be observable as slip lines in the experimental test samples. The experimentally determined CRSS value of 47 ksi for the primary slip systems is shown as a dark horizontal line in Fig. 5. The dominant slip systems shown in Fig. 5(*a*) (τ^1 from 0 to 54 deg, τ^2 from 54 to 68 deg, τ^6 from 68 to 86 deg, τ^2 from 86 to 122 deg, and τ^3

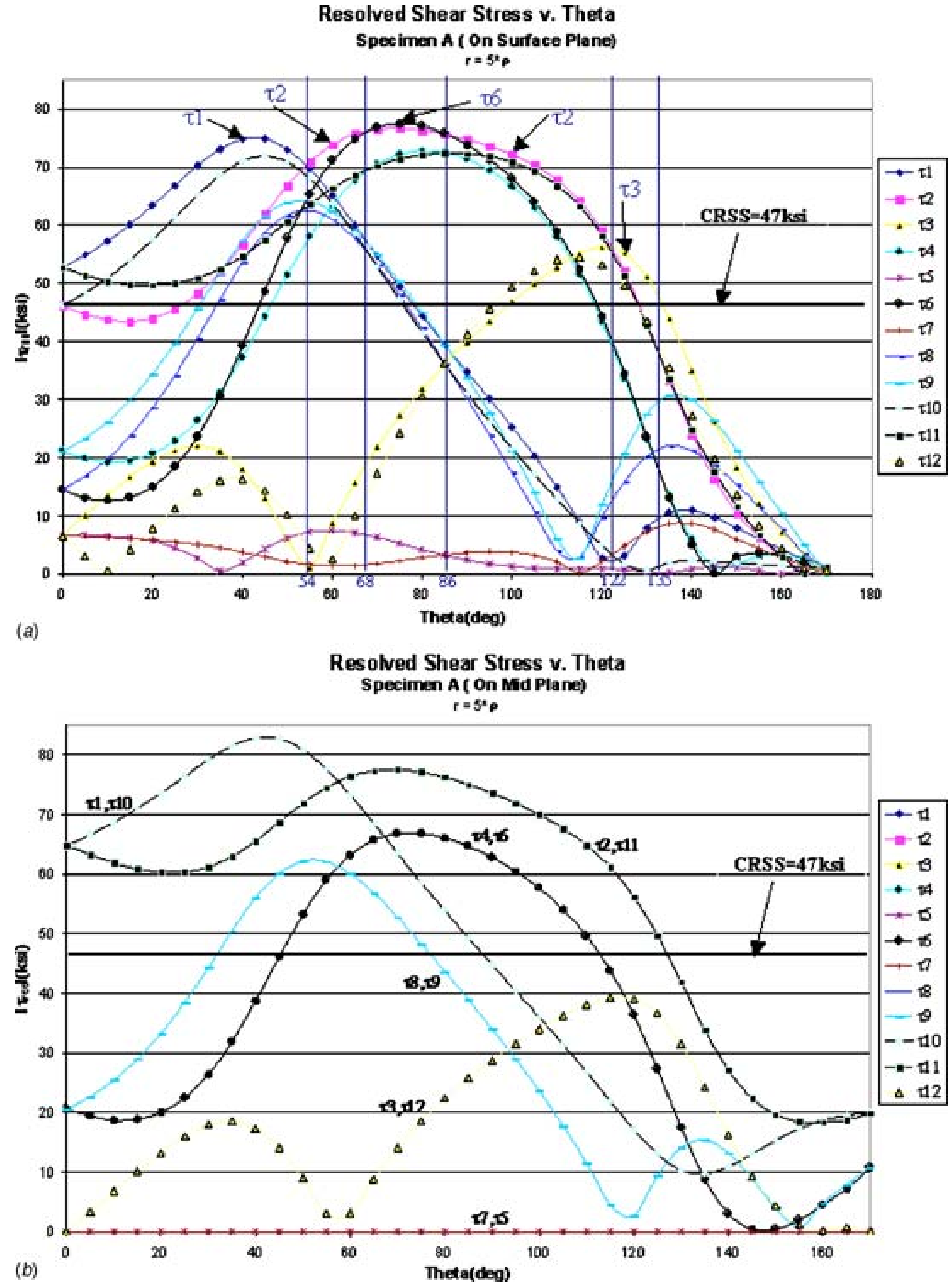

Fig. 5 (*a*) RSS values (specimen A) for the 12 slip systems, as a function of theta, at $r=5*\rho$ on surface [32]; and (*b*) RSS values (specimen A) for the 12 slip systems, as a function of theta, at $r=5*\rho$ on midplane [32]

from 122 to 135 deg), with RSS values above 47 ksi will be activated at that radial and angular location. Although there are other slip systems with RSS values above the CRSS value, the only observed slip systems are the dominant ones.

The slip system with the maximum RSS varies with radial and angular position; sectors were determined for each radius by the overall maximum RSS or the dominant slip system. By carefully studying the RSS plots from $r=0.25*\rho$ to $5*\rho$ a comprehensive picture of activated slip systems emerges. Figure 6 shows activated regions with different colors indicating activated slip systems, around the notch, for specimens A, at the surface. For example, at $r=0.25*\rho$, τ^{11} is activated from 0 to 17 deg, and at $r=5*\rho$, τ^{1} is activated from 0 to 54 deg, and so on. Table 4 also summarizes the dominant slip systems at the surface of specimen A, as a function of θ and r.

The RSS values at the midplane were consistently higher than those at the surface, as shown in Fig. 5(*b*). This indicates that slip is likely to initiate at the midplane and progress to the surface. Crone and Shield [23] also note that slip systems may be activated

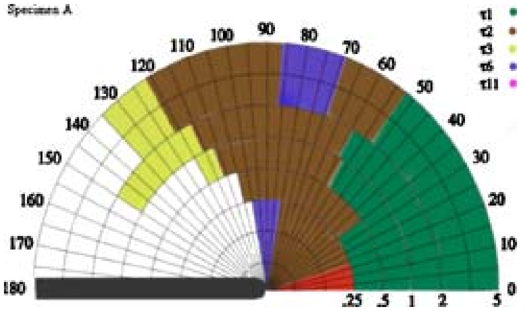

Fig. 6 Dominant and active slip systems at the surface of specimen A as a function of θ and r [32]

internally, rather than at the surface. It is also observed in Fig. 5(*b*) that dominant slip systems occur in pairs (τ^1 and τ^{10}, τ^2 and τ^{11}). The RSS values for other nondominant slip systems also occur in pairs (τ^5 and τ^7, τ^4 and τ^6, τ^3 and τ^{12}, τ^8 and τ^9).

The radial variation produced lobed sectors, rather than straight sectors with constant boundaries (Fig. 6). Note that the boundaries are shaped more like lobes than the constant pie-slice radial boundaries depicted by Rice [16] and Crone and Shield [23].

Comparison of Experimental Results With Finite Element Analysis

Experimental slip field results produced from tensile testing of specimens A and B were compared to FEA predictions. We will discuss the comparison of numerical and experimental results at $r=5^*\rho$, as shown in Fig. 7 and summarized in Table 3. The FEA results predict slip activation from 0 to 135 deg; however, in the experimental test, slip activation is only visible at the given radius up to 110 deg.

The exact slip system cannot be determined by the slip trace analysis alone; nonetheless, correlating the known slip plane to the numerical prediction is still a good measure of the model's accuracy. The single dominant slip system plane predicted for each sector by the FEA and those indicated by the experimental specimen match well (Table 3). The crystal orientation of the tested single-crystal specimen A deviated 8 deg from the $\langle 001\rangle$ load direction. This deviation may result in the apparent asymmetry in certain sectors between the positive and negative half

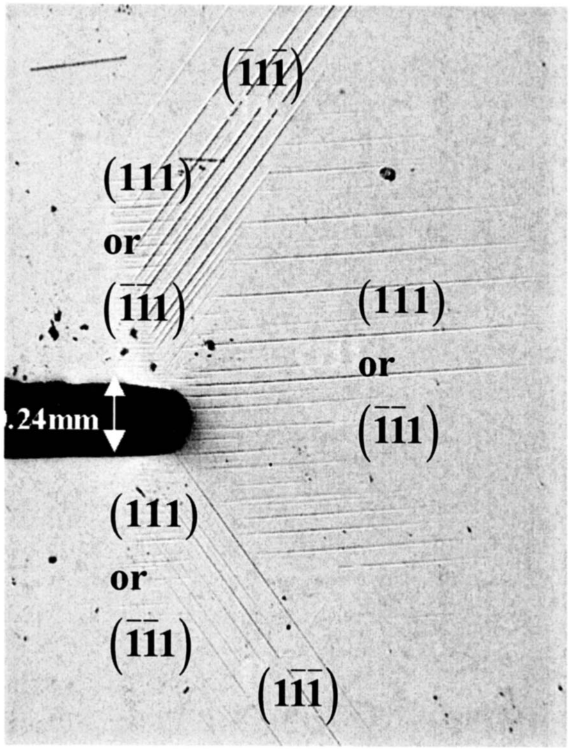

Fig. 7 Experimental slip field results on the surface for specimen A

Table 3 Summary of numerical and experimental results for specimen A at $r=5^*\rho$ [31,32]

Dominant Slip System Sectors
Specimen A
$r=5^*\rho$

	Numerical solution			Experimental results		Isotropic solution		Rice solution	
Sector	θ	τmax	Slip system	θ	Slip plane	θ	Slip plane	θ	Slip plane
I	0–54	τ_1	(111) $[10\bar{1}]$	0–68	(111) or $(\bar{1}\bar{1}1)$	0–56	(111)	0–55	$(\bar{1}11)$ and $(1\bar{1}1)$
II	54–68	τ_2	(111) $[0\bar{1}1]$			56–115	(111)	55–90	$(\bar{1}11)$ and $(11\bar{1})$ or (111)
III	68–86	τ_6	$(\bar{1}1\bar{1})$ $[011]$	68–90	$(\bar{1}1\bar{1})$	—	—	90–125	$(1\bar{1}1)$ and $(11\bar{1})$ or (111)
IV	86–122	τ_2	(111) $[0\bar{1}1]$	85–115	(111) or $(\bar{1}\bar{1}1)$	—	—	125–180	$(\bar{1}11)$ and $(1\bar{1}1)$
V	122–135	τ_3	(111) $[1\bar{1}0]$	—	—	—	—	—	—

Table 4 Numerical prediction of dominant slip systems on the surface of specimen A, for varying radii *r* from the notch [31,32]

Dominant Slip System Sectors Specimen A									
	r=0.25*ρ			r=0.5*ρ			r=1*ρ		
Sector	θ	τmax	Slip system	θ	τmax	Slip system	θ	τmax	Slip system
I	0–17	τ_{11}	$(\bar{1}\bar{1}1)$ $[101]$	0–35	τ_1	(111) $[10\bar{1}]$	0–57	τ_1	(111) $[10\bar{1}]$
II	17–82	τ_2	(111) $[0\bar{1}1]$	35–105	τ_2	(111) $[0\bar{1}1]$	57–113	τ_2	(111) $[0\bar{1}1]$
III	82–100	τ_6	$(\bar{1}1\bar{1})$ $[011]$	⋯	⋯	⋯	113–120	τ_3	(111) $[1\bar{1}0]$

	r=2.0*ρ			r=5.0*ρ		
Sector	θ	τmax	Slip system	θ	τmax	Slip system
I	0–59	τ_1	$(111)[10\bar{1}]$	0–54	τ_1	$(111)[10\bar{1}]$
II	59–116	τ_2	$(111)[0\bar{1}1]$	54–68	τ_2	$(111)[0\bar{1}1]$
III	116–150	τ_3	$(111)[1\bar{1}0]$	68–86	τ_6	$(\bar{1}1\bar{1})[011]$
IV	⋯	⋯	⋯	86–122	τ_2	$(111)[0\bar{1}1]$
V	⋯	⋯	⋯	122–135	τ_3	$(111)[1\bar{1}0]$

planes, as well as any sector boundary differences. Furthermore, the specific irregularities in the notch cutouts may have a different effect from the simplifications of symmetry made in the FEM. The discrepancies seen between the numerical and analytical models may be due to the elastic simplifications of the model, but may also be attributed in part to the 8° deviation from [001] for the experimental load axis.

Specimen B was also analyzed using similar techniques. Figure

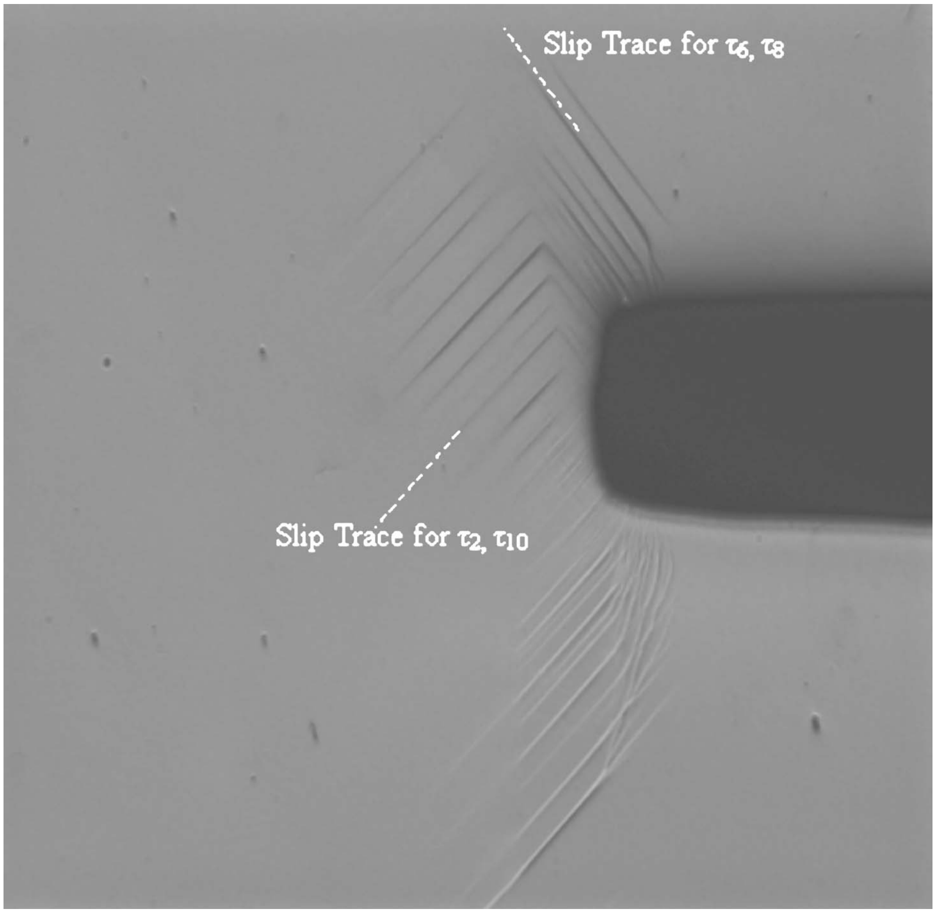

Fig. 8 Experimental slip field results on the surface for specimen B

Table 5 Numerical prediction of dominant slip systems on the surface of specimen B, for varying radii *r* from the notch [32]

Dominant Slip System Sectors Specimen B									
	r=0.25*ρ			r=0.5*ρ			r=1*ρ		
Sector	θ	τmax	Slip system	θ	τmax	Slip system	θ	τmax	Slip system
I	0–41	τ_8	$(1\bar{1}\bar{1})[0\bar{1}1]$	0–56	τ_8	$(1\bar{1}\bar{1})$ $[0\bar{1}1]$	0–52	τ_{10}	$(\bar{1}\bar{1}1)$ $[011]$
II	41–100	τ_6	$(\bar{1}1\bar{1})[011]$	56–105	τ_6	$(\bar{1}1\bar{1})$ $[011]$	52–56	τ_2	(111) $[0\bar{1}1]$
III	⋯	⋯	⋯	⋯	⋯	⋯	56–116	τ_6	$(\bar{1}1\bar{1})$ $[011]$
IV	⋯	⋯	⋯	⋯	⋯	⋯	116–120	τ_4	$(\bar{1}1\bar{1})$ $[10\bar{1}]$

	r=2.0*ρ			r=5.0*ρ		
Sector	θ	τmax	Slip system	θ	τmax	Slip system
I	0–50	τ_{10}	$(\bar{1}\bar{1}1)[011]$	0–46	τ_{10}	$(\bar{1}\bar{1}1)[011]$
II	50–60	τ_2	$(111)[0\bar{1}1]$	46–56	τ_2	$(111)[0\bar{1}1]$
III	60–68	τ_3	$(111)[1\bar{1}0]$	56–64	τ_3	$(111)[1\bar{1}0]$
IV	68–150	τ_6	$(\bar{1}1\bar{1})[011]$	64–131	τ_6	$(\bar{1}1\bar{1})[011]$

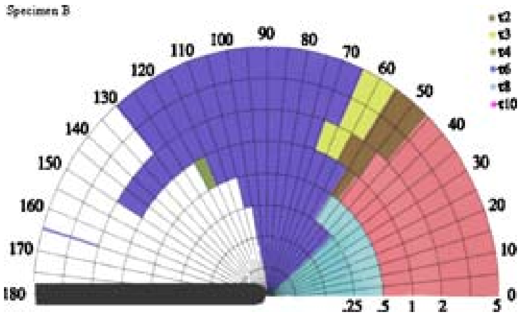

Fig. 9 Dominant and active slip systems at the surface of specimen B as a function of θ and r [32]

8 shows the experimentally predicted slip field results, while Table 5 summarizes the numerical results. Numerically predicted slip systems for specimen B agree extremely well with experimental results, as in specimen A. Experimentally observed slip field results are seen to be very different from those of specimen A, highlighting the importance of crystal orientation in activating specific slip systems. Figure 9 shows the dominant slip sector boundaries at the surface of specimen B, as a function of θ and r. Comparison of the results between Figs. 6 and 9 show that the activated slip systems for the two specimen orientations are very different, as is also evidenced by the experimental slip fields. The RSS values at the specimen midplane were also higher for specimen B, and occurred in pairs, indicating again that slip is likely initiated at the midplane first.

Conclusions

A detailed experimental and numerical investigation of 3D stress fields and evolution of slip sector boundaries near notches in fcc single-crystal tension test specimens is presented, as a function of crystallographic orientation. Results demonstrate that a 3D linear elastic finite element model that includes the effect of material anisotropy predicts active slip planes and sectors accurately. The slip sector boundaries are shown to have complex curved shapes with several slip systems active simultaneously near the notch. Slip sectors determined by the stress field are not constant for a given material, as generally indicated by the literature [16,21–23], but are determined by the applied load. Slip sector boundaries on the surface showed excellent agreement with experimental results. Slip systems activated are shown to be a strong function of crystallographic orientation. Results are presented for the surface and midplane of the specimens. The RSS values at the midplane were consistently higher than at the surface, for both orientations examined, indicating that slip might indeed initiate at the midplane and progress to the surface. The results presented demonstrates that accounting for 3D elastic anisotropy is very important for accurate prediction of slip activation near fcc single-crystal notches under a triaxial state of stress. A linear elastic model can be used to predict the initial slip, based on the CRSS value for the slip system, but cannot predict subsequent behavior due to plasticity around the notch tip. Some other modeling assumptions include low temperature deformation, no account of microstructural (i.e., dislocation) mechanisms, and no crystal lattice rotation. However, for this analysis, we have used the FEA results to only predict the onset of yield on slip systems and not the subsequent effects of plasticity. These advanced effects will be included in subsequent modeling efforts currently underway.

Acknowledgments

This work was partially supported by the NASA Marshall Space Flight Center, Huntsville, AL, and Pratt & Whitney, West Palm Beach, FL. The authors would like to thank Dr. Gregory R. Swanson at NASA MSFC, and William Mitchell and Fred Haake at Pratt & Whitney, FL, for the support. The authors would also like to thank Dan Deluca at Pratt & Whitney, East Hartford, CT, for supplying the single-crystal casting from which the tension test specimens were machined.

References

[1] Shrivastava, S., and Ebrahimi, F., 1997, "Effect of Crystallographic Orientation on the Fracture Toughness of NiAl Single Crystals," Mater. Res. Soc. Symp. Proc., **460**, pp. 393–398.
[2] Gumbsch, P., Riedle, J., Hartmaier, A., and Fischmeister, H. F., 1998, "Controlling Factor for the Brittle-to-Ductil Transition in Single Crystals," Science, **282**, pp. 1293–1295.
[3] Ebrahimi, F., and Kalwani, K., 1999, "Fracture Anisotropy in Silicon Single Crystal," Mater. Sci. Eng., A, **268**, pp. 116–126.

[4] Arakere, N. K., and Swanson, G., 2002, "Effect of Crystal Orientation on Fatigue Failure of Single Crystal Nickel Base Turbine Blade Superalloys," ASME J. Eng. Gas Turbines Power, **124**, pp. 161–176.

[5] Swanson, G., and Arakere, N. K., "Fatigue Failure of Single Crystal Nickel Base Turbine Blade Superalloys," NASA/TP-2000-210074.

[6] Arakere, N. K., [YEAR], "High Temperature Fatigue Properties of Single Crystal Superalloys in Air and Hydrogen," *Proc. of ASME Turbo Expo 2000*, June 4–7, New Orleans, ASME, New York, ASME Paper No. 01-GT-585.

[7] Moroso, J., 1999, "Effect of Secondary Orientation on Fatigue Crack Growth in Single Crystal Turbine Blades," M.S. thesis, Mechanical Engineering Department, University of Florida, Gainesville, FL.

[8] Arakere, N. K., and Moroso, J., 2001, "Fatigue Failure in High Temperature Single Crystal Superalloy Turbine Blades," High Temp. Mater. Process., **20**(2), pp. 117–135.

[9] Arakere, N. K., and Swanson, G., 2001, "Analysis of Fretting Stresses in Single Crystal Ni-Base Turbine Blade Attachment Regions," ASME J. Tribol., **123**, pp. 413–423.

[10] Bilby, B. A., Cottrell, A. H., and Swinden, K. H., 1962, "The Spread of Plastic Yield From a Notch," Proc. R. Soc. London, Ser. A, **272**, pp. 304–314.

[11] Rice, J. R., and Thomson, R., 1974, "Ductile Versus Brittle Behavior of Crystals," Philos. Mag., **29**, pp. 73–97.

[12] Kobayashi, S., and Ohr, S. M., 1980, "In-Situ Fracture Experiments in BCC Metals," Prog. Met. Phys., **42**, pp. 763–772.

[13] Majumdar, B. S., and Burns, S. J., 1981, "Crack Tip Shielding—Anelastic Theory of Dislocation and Dislocation Arrays Near a Sharp Crack," Acta Metall., **29**, pp. 579–588.

[14] Weertman, J., Lin, I.-H., and Thomson, R., 1983, "Double Slip Plane Crack Model," Acta Metall., **31**, pp. 473–482.

[15] Gerberich, W. W., Oriani, R. A., Lii, J.-J., Chen, X., and Foecke, T., 1991, "Necessity of Both Plasticity and Brittleness in the Fracture Thresholds of Iron," Philos. Mag., **63**, pp. 363–376.

[16] Rice, J. R., 1987, "Tensile Crack Tip Fields in Elastic-Ideally Plastic Crystals," Mech. Mater., **6**, pp. 317–335.

[17] Rice, J. R., and Saeedvafa, M., 1987, "Crack Tip Singular Fields in Ductile Crystals With Taylor Power-Law Hardening," J. Mech. Phys. Solids, **36**, pp. 189–214.

[18] Saeedvafa, M., and Rice, J. R., 1988, "Crack Tip Singular Fields in Ductile Crystals With Taylor Power-Law Hardening, II: Plane-Strain," J. Mech. Phys. Solids, **37**, pp. 673–691.

[19] Rice, J. R., Hawk, D. E., and Asaro, R. J., 1990, "Crack Tip Fields in Ductile Crystals," Int. J. Fract., **42**, pp. 301–321.

[20] Saeedvafa, M., and Rice, J. R., 1992, "Crack Tip Fields in a Material With Three Independent Slip Systems: NiAl Single Crystal," Modell. Simul. Mater. Sci. Eng., **1**, pp. 53–71.

[21] Shield, T. W., 1996, "Experimental Study of the Plastic Strain Fields Near a Notch Tip in a Copper Single Crystal During Loading," Acta Mater., **44**, pp. 1547–1561.

[22] Schulson, E. M., and Xu, Y., 1997, "Notch-Tip Deformation of Ni_3Al Single Crystals," Mater. Res. Soc. Symp. Proc., **460**, pp. 555–560.

[23] Crone, W., and Shield, T., 2001, "Experimental Study of the Deformation Near a Notch Tip in Copper and Copper-Beryllium Single Crystals," J. Mech. Phys. Solids, **49**, pp. 2819–2838.

[24] Li, X. M., Chiang, F. P., Wu, J., and Dudley, M., 1992, "Experimental Measurement of the Crack Tip Strain Field in a Single Crystals," Eng. Fract. Mech., **43**, 171–184.

[25] Shield, T. W., and Kim, K.-S., 1994, "Experimental Measurement of the Near Tip Strain Field in an Iron-Silicon Single Crystal," J. Mech. Phys. Solids, **42**, 845–873.

[26] Pierce, D., Asaro, R. J., and Needleman, A., 1983, "Material Rate Dependence and Localized Plastic Deformation in Crystalline Solids," Acta Mater., **31**, pp. 1951–1976.

[27] Mohan, R., Ortiz, M., and Shih, C., 1992, "An Analysis of Cracks in Ductile Single Crystals—II. Mode I Loading," J. Mech. Phys. Solids, **40**(2), pp. 315–337.

[28] Cuitino, A., and Ortiz, M., 1996, "Three-Dimensional Crack Tip Fields in Four-Point Bending Copper Single-Crystal Specimens," J. Mech. Phys. Solids, **44**(6), pp. 863–904.

[29] Lekhnitskii, S. G., 1993, *Theory of Elasticity of an Anisotropic Elastic Body*, Holden-Day, San Francisco, pp. 1–40.

[30] Stouffer, D., and Dame, L., 1996, *Inelastic Deformation of Metals: Models, Mechanical Properties, and Metallurgy*, Wiley, New York, pp. 387–417.

[31] Magnan, S., 2002, "Three-Dimensional Stress Fields and Slip Systems in Single Crystal Superalloy Notched Specimens," M.S. thesis, Dept. of Mech. and Aerospace Eng., University of Florida, Gainesville, FL.

[32] Siddiqui, S. A., 2002, "Finite Element Analysis of Single Crystal Superalloy Notched Tensile Specimens," M.S. thesis, Dept. of Mech. and Aerospace Eng., University of Florida, Gainesville, FL.

Frequency Response Analysis of an Actively Lubricated Rotor/Tilting-Pad Bearing System

Rodrigo Nicoletti
Ford Motor Co.,
Complexo Industrial Ford Nordeste,
Camacari 42810-900, Brazil
e-mail: rnicolle@ford.com

Ilmar Ferreira Santos
Department of Mechanical Engineering,
Technical University of Denmark,
Lyngby 2800, Denmark
e-mail: ifs@mek.dtu.dk

In the present paper, the dynamic response of a rotor supported by an active lubricated tilting-pad bearing is investigated in the frequency domain. The theoretical part of the investigation is based on a mathematical model obtained by means of rigid body dynamics. The oil film forces are inserted into the model by using two different approaches: (a) linearized active oil film forces and the assumption that the hydrodynamic forces and the active hydraulic forces can be decoupled, and (b) equivalent dynamic coefficients of the active oil film and the solution of the modified Reynolds equation for the active lubrication. The second approach, based on the equivalent dynamic coefficients, leads to more accurate results because it includes the frequency dependence of the active hydraulic forces. Theoretical and experimental results reveal the feasibility of reducing resonance peaks by using the active lubricated tilting-pad bearing. By applying a simple proportional controller, it is possible to reach 30% reduction of the resonance peak associated with the first rigid body mode shape of the system. One of the most important consequences of such a vibration reduction in rotating machines is the feasibility of increasing their operational range by attenuating resonance peaks and reducing vibration problems. [DOI: 10.1115/1.1850940]

1 Introduction

Rotating machines as turbo generators, compressors, turbines, and pumps, are often vital elements in the production process. Therefore, these machines must have not only high performance, but also high availability, in order not to jeopardize the production flow. In many situations, this availability depends on the adaptation capacity of the machine to quickly changing demands. In other words, the operational range of the machine must be adjustable.

The dynamic characteristics of a rotating machine strongly depend on the bearings. Once the bearings are designed, the machine has dynamic properties limiting and establishing its operational range. As a result, the operational range of the machine is not adjustable because the bearings have fixed geometry and, consequently, fixed operational properties. Due to variations of production demand, such properties may no longer be suited, and the rotating machine may operate below its expected efficiency.

A possible solution toward modifying the operational properties of journal bearings in situ and increasing the flexibility of the machine operational range may be the use of *active lubrication*. When the hydrostatic and the hydrodynamic lubrication are simultaneously combined in a journal bearing, with the aim of reducing wear between machine elements, one refers to the hybrid lubrication, which offers the advantages of both lubrication mechanisms. When part of the hydrostatic pressure is also dynamically modified by means of hydraulic control systems, one refers to the *active lubrication*. By the combination of electronics, control design and hydraulics, the active lubrication simultaneously allows the reduction of wear between rotating and nonrotating parts of the machinery and the attenuation of rotor vibrations. Such an attenuation of vibration levels leads to machinery with wider operational ranges, since the bearings' properties can be modified according to the imposed operational conditions. Therefore, by taking advantages of the active lubrication an increase in the operational range flexibility can be achieved.

Active lubrication can also be used in the case of machinery failure (unbalance, rubbing, blade loss, instability, etc.). By controlling and keeping the shaft vibrations below acceptable limits, it is possible to keep the machine working until a repair stop, in a suitable moment, can be programmed. Therefore, sudden stops can be avoided and the machine availability can be increased.

The first ideas of active lubrication, applied to a tilting-pad bearing, appeared in the work of Santos [1]. Since then, large developments in the modeling of such bearings have been achieved regarding oil film pressure estimation [2], oil film temperature estimation [3], static and dynamic property analyses [4], and unbalance response control [5]. Some experimental results with tilting-pad bearings show that vibration amplitudes can be reduced up to 50% [6] using active lubrication controlled by simple PD controllers. Such results refer to an unbalance response in the time domain obtained at a fixed angular velocity. The application of active lubrication to other kinds of bearings has also been investigated by other authors. Wu and Pfeiffer [7] proposed a method for theoretically estimating the oil film pressure distribution of an actively lubricated plain journal bearing. Bently et al. [8] experimentally investigated the dynamic behavior of an actively lubricated hydrostatic bearing in the frequency domain. Santos and Watanabe [9,10] explored the advantages of using control techniques to change the dynamic coefficients of a multirecess journal bearing via active lubrication toward compensating bearing cross-coupling effects. By adopting a proper control feedback strategy and control gains the authors concluded that the stability margin of rotor-bearing systems can be significantly enlarged.

The aim of the present work and its main contribution is related to the experimental analysis of an active lubricated tilting-pad bearing in the frequency domain. With focus on the active lubrication's practical applications to industrial compressors, monitored by means of eddy-current probes, the structure of the control loop is intentionally kept as simple as possible. A mathematical model is derived using two different approaches, aiming at including the effect of oil film active forces. Frequency response functions (FRFs) of the rotating system operating passively (under

---

Contributed by the International Gas Turbine Institute (IGTI) of THE AMERICAN SOCIETY OF MECHANICAL ENGINEERS for publication in the ASME JOURNAL OF ENGINEERING FOR GAS TURBINES AND POWER. Paper presented at the International Gas Turbine and Aeroengine Congress and Exhibition, Vienna, Austria, June 13–17, 2004, Paper No. 2004-GT-54034. Manuscript received by IGTI, October 1, 2003; final revision, March 1, 2004. IGTI Review Chair: A. J. Strazisar.

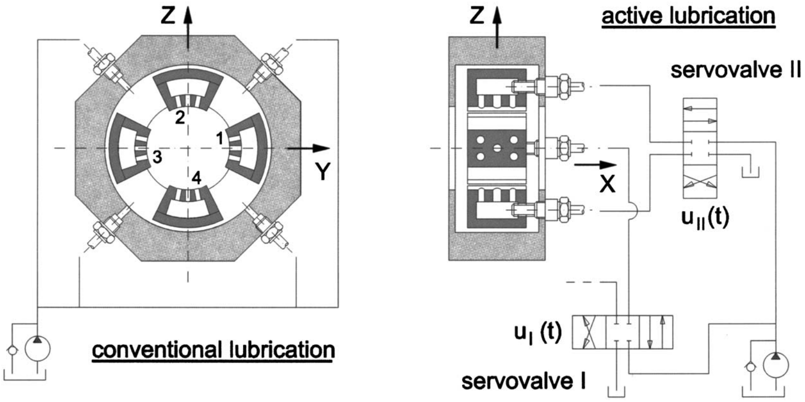

Fig. 1 Actively lubricated tilting-pad bearing and oil injection system

conventional hydrodynamic lubrication) and actively (under active lubrication) are theoretically and experimentally obtained, compared, and discussed.

2 Test Facilities

The actively lubricated bearing under investigation is built by four tilting-pads, in a load-on-pad configuration (Fig. 1). The active control forces acting on the rotating shaft are produced by injecting oil into the bearing gap through orifices machined in the pad sliding surfaces (Fig. 2). By coupling two hydraulic servo valves to the pair of pads arranged in the vertical and horizontal directions (Fig. 1), the pressure of the injected oil can be dynamically controlled. Thus, the hydrodynamic pressure, i.e., the main mechanism of bearing load capacity, can be altered among the different pads, and shaft vibrations can be attenuated aided by properly designing feedback control loops.

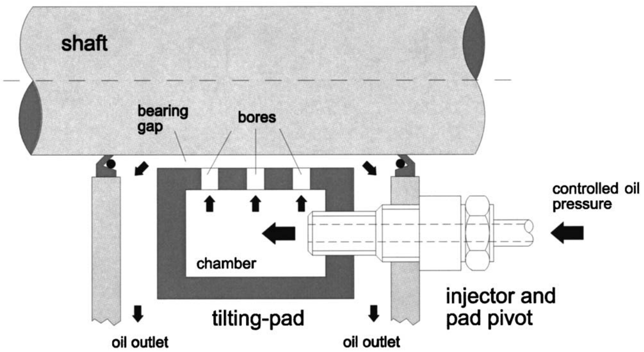

Fig. 2 Schematic view of the injection system connected to one of the bearing pads

It is important to emphasize that conventional lubrication is still the main source of load capacity in this hybrid bearing. In addition, the use of active lubrication in tilting-pad journal bearings has the strong advantage of its negligible cross-coupling effects between orthogonal directions. A secondary advantage of this kind of lubrication is the possibility of cooling the oil film flow by the oil injection through the orifices distributed on the pad surfaces [3,4].

Figure 3 illustrates the test facilities located in the Department of Mechanical Engineering at the State University of Campinas (Brazil), used for the experimental validation and tests of the active tilting-pad bearing. It is composed of a 3 hp electric motor (Fig. 3, element 1) connected to a rigid shaft by means of a flexible universal joint. The motor rotation is controlled by a frequency converter. The rigid shaft is supported by a self-aligning ball bearing (Fig. 3, element 2) and the active bearing (Fig. 3, element 6), which is connected to the servo valves (Fig. 3, element 7) by means of pipelines. Steel discs (Fig. 3, element 3) are mounted on the shaft, which results in a total mass of 80.9 kg. Eddy current probes (Fig. 3, element 5) are used to measure shaft displacements in both orthogonal directions, whereas a load cell is used to measure the excitation force applied by an electromagnetic shaker. It is worth mentioning that the measured displacement signals from the eddy current probes are the only signals used for building the feedback control loop.

The FRFs of the rotor-active bearing system are obtained by using a chirp signal with a period of 2 s and a cutoff frequency of 100 Hz. This excitation signal is applied to an electromagnetic

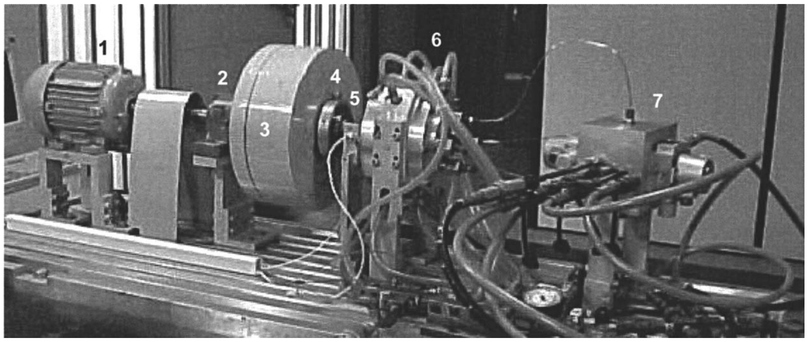

Fig. 3 Active lubricated bearing test rig: (1) electric motor, (2) self-aligning ball bearing, (3) rigid shaft; (4) excitation bearing, (5) eddy current probes, (6) active lubricated tilting-pad bearing and (7) servo valves

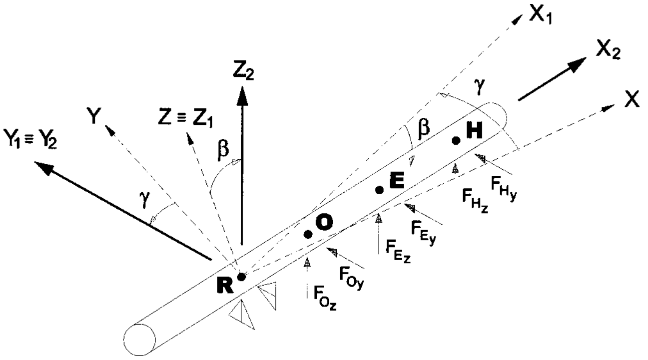

Fig. 4 Points of acting forces (R,O,E,H) and auxiliary reference frames used in the model of the rigid shaft-disk subsystem

shaker attached to the load cell by a wire. The load cell is connected to the shaft via an auxiliary ball bearing (Fig. 3, element 4). Both force and displacement signals are processed by a signal analyzer.

The control signals to the servo valves are on-line computed by a PC, using a parallel signal processing system. The displacement signals are filtered, multiplied by the feedback gain (proportional gain) and sent to the servo valves.

3 Mathematical Modeling

The rotating subsystem consists of a shaft and a disk (Fig. 3). This subsystem is considered as a rigid body in the frequency range of investigation (0–100 Hz). The passive and active forces act on four reference points, highlighted in Fig. 4: point **R**, ball bearing position (reaction force); point **O**, rotor-disk center of gravity (gravity force); point **E**, electromagnetic shaker attachment point (excitation force); and point **H**, active tilting-pad bearing position (control forces).

With help of moving reference frames, the shaft angular displacements (ϕ, β, and γ) around point **R** can be described, following the consecutive Kardan's rotations: first, around Z (inertial reference frame); second, around Y_1 (auxiliary reference frame $B1$); and finally, around X_2 (auxiliary reference frame $B2$, attached to the shaft as illustrated in Fig. 4). By using Euler's equation, considering that the point **R** does not move, a set of nonlinear equations of motion of the rigid rotor-disk is achieved. By the assumption of small angular displacements, constant rotor angular velocity, and low vibration frequencies, such a set of nonlinear equations of motion can be linearized, resulting in the following system of equations:

$$\begin{aligned} I^R_{yy}\ddot{\beta}+I^R_{xx}\dot{\phi}\dot{\gamma}&=-r_{RO}F_{O_z}-r_{RE}F_{E_z}-r_{RH}F_{H_z} \\ I^R_{zz}\ddot{\gamma}-I^R_{xx}\dot{\phi}\dot{\beta}&=r_{RO}F_{O_y}+r_{RE}F_{E_y}+r_{RH}F_{H_y} \end{aligned} \tag{1}$$

The oil film forces are described by using two different approaches in the present work. It is important to point out that such approaches are carefully analyzed with the aim of facilitating the design of the control loop gains.

3.1 First Approach: Linearization of the Active Forces by Means of Quasi-Static Experimental Tests.

The force acting on point **H** comes from the oil film between the shaft and the pad surfaces. Such a force can be split into two basic components: the hydrodynamic force originated from the conventional lubrication and the active force resulting from the oil injection system. The hydrodynamic forces can be represented by equivalent dynamic coefficients

$$\begin{aligned} F_{H_y}&=f_{static_y}-K_{yy}y_H-D_{yy}\dot{y}_H+F_{A_y} \\ F_{H_z}&=f_{static_z}-K_{zz}z_H-D_{zz}\dot{z}_H+F_{A_z} \end{aligned} \tag{2}$$

In the case of tilting-pad journal bearings, the cross-coupling coefficients ($K_{yz}, K_{zy}, D_{yz}, D_{zy}$) can be neglected when compared to the direct coefficients ($K_{yy}, K_{zz}, K_{yy}, D_{zz}$). Thus, only the direct coefficients are considered in Eq. (2).

Considering that $y_H=r_{RH}\gamma$ and $z_H=-r_{RH}\beta$ and inserting Eq. (2) into Eq. (1), the linearized equations of motion for describing the test rig dynamics are achieved

$$\begin{aligned} \text{active case}\quad \mathbf{M}\ddot{\mathbf{x}}+(\mathbf{G}+\mathbf{D})\dot{\mathbf{x}}+\mathbf{K}\mathbf{x}&=\mathbf{f}_E+\mathbf{f}_A \\ \text{passive case}\quad \mathbf{M}\ddot{\mathbf{x}}+(\mathbf{G}+\mathbf{D})\dot{\mathbf{x}}+\mathbf{K}\mathbf{x}&=\mathbf{f}_E \end{aligned} \tag{3}$$

The term $\mathbf{f}_E$ is related to the excitation force applied to the shaft by means of the electromagnetic shaker. The gravity force $\mathbf{f}_O$, not presented in Eq. (3), is canceled by the static part of the hydrodynamic forces, presented in Eq. (2). The force from the active lubrication $\mathbf{f}_A$ is linearized and considered as an external force in the mathematical model. Details about how to experimentally obtain such a force is presented in Section 4.2. The contribution of the conventional hydrodynamic lubrication is inserted into the model by using the matrices **K** and **D** of Eq. (3), which contain the oil film equivalent dynamic coefficients [Eq. (2)]. In the literature, there are several approaches to estimate the equivalent dynamic coefficients of conventionally lubricated bearings, being the works of Lund [11], Lund and Thomsen [12], Springer [13], Someya [14], just a small sample of them. In the present work, specifically in the case of tilting-pad bearings, the perturbation method proposed by Allaire et al. [15] is used to calculate the oil film coefficients of the conventional lubrication, i.e., terms K_{yy}, K_{zz}, D_{yy}, D_{zz} in Eq. (2). It is important to emphasize that the matrices $\mathbf{D}(\text{So},\omega)$ and $\mathbf{K}(\text{So},\omega)$ are dependent on the Sommerfeld number So and the excitation frequency ω.

3.2 Second Approach: Equivalent Dynamic Coefficients Obtained From the Equations of the Active Lubrication.

An alternative way of modeling the test rig is by adopting the global equivalent dynamic coefficients of the active lubrication [16,17]. These coefficients are calculated by simultaneously considering the contributions of conventional (hydrodynamic) and active lubrication. In such a case the Reynolds equation is modified and an additional term is included, in order to consider the controlled radial oil injection into the bearing gap [2]. By also considering the dynamics of the servo valves and the adopted control strategy, it is possible to obtain the equivalent dynamic coefficients of the oil film as function of the control gains. It is important to highlight that the dynamics of the hydraulic system (servo valve parameters, pressure-flow relationship, pipeline and orifice dimensions) play an important role in the oil film global coefficients. The estimation method of these global coefficients is thoroughly deduced in the works of Santos et al. [16,17].

By adopting the global dynamic coefficients, the hydrodynamic forces considering both active and conventional lubrication are given by

$$\begin{aligned} F_{H_y}&=-\bar{K}_{yy}y_H-\bar{D}_{yy}\dot{y}_H \\ F_{H_z}&=-\bar{K}_{zz}z_H-\bar{D}_{zz}\dot{z}_H \end{aligned} \tag{4}$$

Hence, the equations of motion of the shaft-disk subsystem [Eq. (3)] changes to

$$\mathbf{M}\ddot{\mathbf{x}}+(\mathbf{G}+\bar{\mathbf{D}})\dot{\mathbf{x}}+\bar{\mathbf{K}}\mathbf{x}=\mathbf{f}_E \tag{5}$$

where the term $\mathbf{f}_A$ is suppressed and the contribution of the hydrodynamic forces, considering both active and conventional lubrication, is inserted into matrices $\bar{\mathbf{D}}$ and $\bar{\mathbf{K}}$ through the global dynamic coefficients. It is important to emphasize that the matrices $\bar{\mathbf{D}}(\text{So},\omega,G_P,G_D)$ and $\bar{\mathbf{K}}(\text{So},\omega,G_P,G_D)$ are dependent on the Sommerfeld number So, excitation frequency ω, the control loop gains G_P (proportional gain), and G_D (derivative gain). When

Table 1 Rotor/tilting-pad bearing characteristics

Rotor polar momcnt of in ertia (I_{xx}^R)	0.908 kg m^2
Rotor lateral moment of inertia ($I_{yy}^R = I_{zz}^R$)	2.485 kg m^2
Distance from **R** to **O** (r_{RO})	0.146 m
Distance from **R** to **E** (r_{RE})	0.2195 m
Distance from **R** to **H** (r_{RH})	0.376 m
Journal radius	24.96 mm
Pad inner radius	26.0 mm
Pad angle	60.0 deg
Offset	0.5
Pad width	40.0 mm
Pad inertia	2.6×10^{-4} Kg m^2
Number of orifices per pad	5
Assembled bearing gap	170 μm
Oil dynamic viscosity @ 30°	0.043 Pa·s
Supply pressure	8.0×10^6 Pa

such gains are set to null, Eq. (3) in the passive case and Eq. (5) become the same. A typical behavior of the global coefficients as a function of the proportional gain G_P will be presented in Section 4.3.

4 Theoretical and Experimental Results

The test rig parameters are presented in Table 1.

4.1 Passive Case: Theory and Experiment. In the passive case, the active system is turned off and the system is modeled by Eq. (3), setting the term $\mathbf{f_A}$ to zero. In order to investigate the system characteristics in the frequency domain, two constant operational rotating velocities are chosen: 900 rpm (15 Hz) and 1800 rpm (30 Hz). At these two angular velocities, the oil film coefficients are obtained by applying the perturbation method proposed by Allaire et al. [15] and Parsell et al. [18], taking into account the pad inertia. The behavior of such coefficients as a function of the excitation frequency is illustrated in Fig. 5. The cross coupling coefficients (K_{yz}, K_{zy}, D_{yz}, and D_{zy}) are negligible compared to the direct coefficients and not shown in Fig. 5.

The dynamic characteristics of the rotor-bearing system at a constant angular velocity can be analyzed based on the *receptance* curve, which is the ratio between output (rotor displacement) and input (shaker force) expressed as a function of the excitation frequency. Figure 6 presents a comparison between numerical and experimental results of the system receptance (FRFs) in the horizontal direction (y direction) at the rotor angular velocity of 900 rpm (15 Hz). Figure 7 also presents the same comparison, but when the rotor operates at the constant angular velocity of 1800 rpm (30 Hz). As it can be seen, the system has a resonance peak at the frequency of 45 Hz when the angular velocity is 900 rpm (15 Hz) and a resonance peak at 42 Hz when the angular velocity is 1800 rpm (30 Hz).

The predominate spikes in the FRFs (Figs. 6 and 7) are caused by rotor unbalance and misalignment. The signals measured by the displacement probes contain information not only about the system response, but also about unbalance and misalignment. As a result, besides the system frequency response, the FRFs present spikes at harmonics of the rotating frequency exclude, as it can be seen in Figs. 6 and 7 ($1\times\Omega$, $2\times\Omega$, etc.).

Neglecting the harmonic spikes and considering the system response, a good agreement between experiment and theory is achieved, especially in the frequency range between 10 to 50 Hz. Figures 6 and 7 clearly show that, in the passive case, the mathematical model, given by Eq. (3) or (5) considering the linearized oil film coefficients, is able to accurately represent the rotor-bearing dynamics. Moreover, the figures also reveal that the oil film coefficients are very well tuned.

The system FRFs in vertical direction (z direction) are not presented because the system has no resonance in the considered frequency range from 10 to 100 Hz.

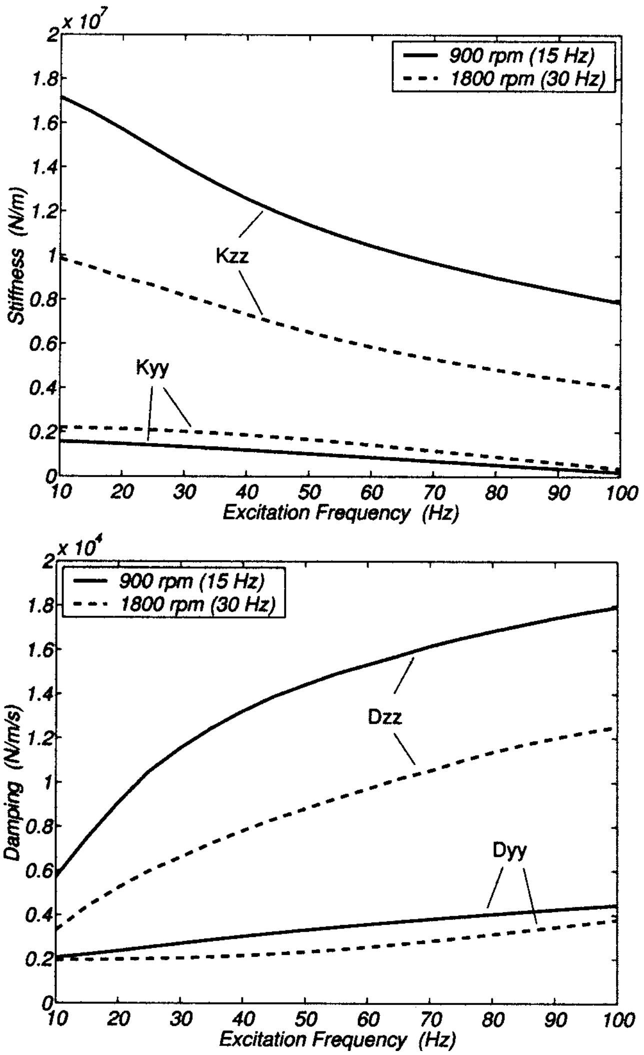

Fig. 5 Oil film coefficients K_{yy}, K_{zz}, D_{yy}, D_{zz} of the TPJB under conventional lubrication condition as a function of the excitation frequency ω and two Sommerfeld numbers So corresponding to the angular velocities of Ω=900 rpm (15 Hz) and Ω=1800 rpm (30 Hz)

4.2 Active Case: Experiment. In the active case, the rotor displacements are measured, and such signals are multiplied by a proportional gain. The resultant signals are sent to the servo valves. Simultaneously, displacement and force signal are on-line acquired and on-line processed with the aim of achieving the new receptance curves for the actively controlled rotor-bearing system.

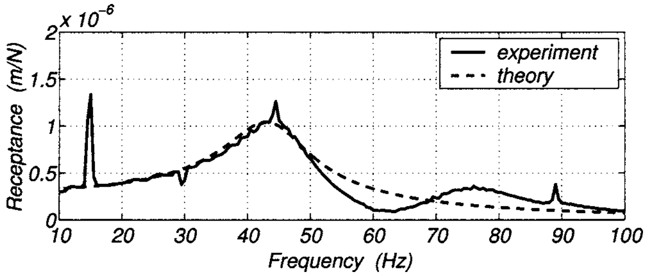

Fig. 6 Frequency response functions of the rotor-bearing system in the passive case for Ω=900 rpm (15 Hz), horizontal direction

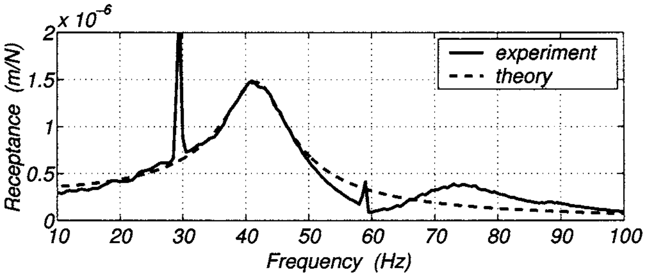

Fig. 7 Frequency response functions of the rotor-bearing system in the Passive case for Ω=1800 rpm (30 Hz), horizontal direction

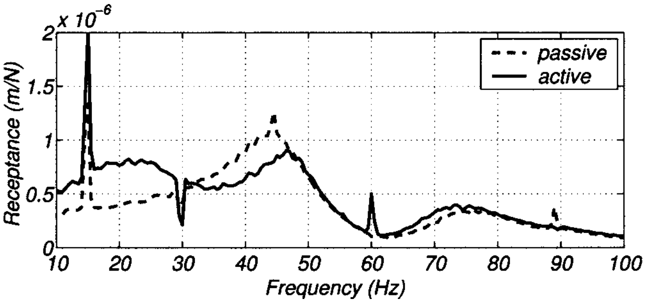

Fig. 9 Experimental FRFs of the rotor-bearing system in the passive and active cases for Ω=900 rpm (15 Hz), horizontal direction

In order to calculate the proportional control gain according to the first approach (Section 3.1), the active oil film force has to be determined based on the input signal sent to the servo valve (Fig. 8). The easiest and most practical assumption is a linear relationship between input signal and active oil film force, represented by a single proportionality coefficient, i.e., λ in N/V. Such a coefficient can be easily obtained by measuring the variation of the oil film force acting on the shaft while the input signal to the servo valve is varied. A force transducer is attached to the test rig (Fig. 3, element 4) and a step function is used as input signal to the servo valve. Such a test is carried out under a quasi-static condition, i.e., using a step function with a low frequency, which in this case was 1Hz. It is worth mentioning that in such a quasi-static test at constant angular velocity, no λ dependency on the excitation frequency ω and Sommerfeld number So can be evaluated, unless the tests are repeated with changing values of excitation frequency in the frequency range until 100 Hz and at different rotor angular velocities inside of the operational range.

Figure 8 illustrates the result of the quasi-static condition test, where the active oil film force is approached in a range of 4 V, from -1 V to $+3$ V, using the linear coefficient λ. Considering that the maximum rotor displacement is 85 μm (bearing gap), a proportional gain of 4.7×10^4 V/m can be estimated. Implementing this gain in the control system, one obtains the results presented in Figs. 9 and 10.

A comparison between the experimental system receptance (FRFs) in the active and passive cases at the angular velocities of 900 rpm (15 Hz) and 1800 rpm (30 Hz) is presented in Figs. 9 and 10. The use of active lubrication with proportional control results in an amplitude reduction of nearly 20% of the resonance peak when the system operates at 900 rpm (15 Hz). Likewise, an amplitude reduction of nearly 30% can be detected at the angular velocity of 1800 rpm (30 Hz). These resonance peaks are related to the first rigid mode shape of the rotor-bearing system. As one can see, it is possible to change the characteristics of the rotating system during operation by adopting the active lubrication with a very simple proportional controller. Further attenuation of vibration levels can be achieved by implementing more sophisticated controllers.

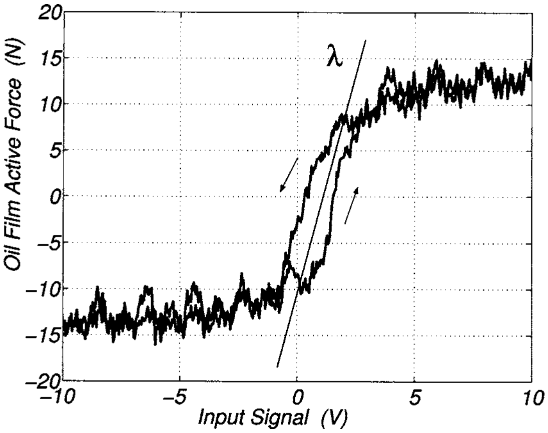

Fig. 8 Active oil film force as a function of the input signal in the servo valve (y direction) in a quasi-static condition test when the rotor operates at the angular velocity of 1200 rpm (20 Hz)

Again, the predominate spikes in the FRFs (Figs. 9 and 10) are caused by rotor unbalance and misalignment, leading the FRFs to present harmonic components of the rotating frequency ($1\times\Omega$, $2\times\Omega$, etc.).

4.3 Active Case: Comparison Between Model Approaches. In this section, the results obtained based on the two different modeling approaches (Sections 3.1 and 3.2) are compared to the experimental results and discussed. In the mathematical model with linearized active forces [first model approach, Eq. (3)], the active forces represented by $\mathbf{f}_A$ can be expressed as a linear function of the input electrical signal of the servo valve, as follows:

$$\mathbf{f}_A=\lambda\cdot\mathbf{u} \tag{6}$$

The coefficient λ is easily obtained from Fig. 8 which is, in the present case, approximately 10 N/V. By adopting the expression (6), and a proportional control law of the form

$$\mathbf{u}=-G_P\cdot y_H \tag{7}$$

with $G_P=4.7\times 10^4$ V/m, the experimental receptance curves (FRFs) are achieved and presented in Figs. 11 and 12 (dash-point lines). Such results (dash-point lines) are obtained adopting Eq. (3) with oil film coefficients illustrated in Fig. 5.

In Figs. 11 and 12 the mathematical model with linearized active forces (first approach) does not properly represent the dynamic behavior of the system with active lubrication. The amplitude of the resonance peak predicted by this approach (dash-point lines) is 40% higher than the peak amplitude obtained experimen-

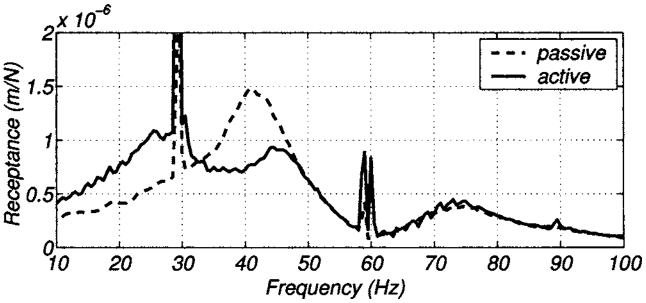

Fig. 10 Experimental FRFs of the rotor-bearing system in the passive and active cases for Ω=1800 rpm (30 Hz), horizontal direction

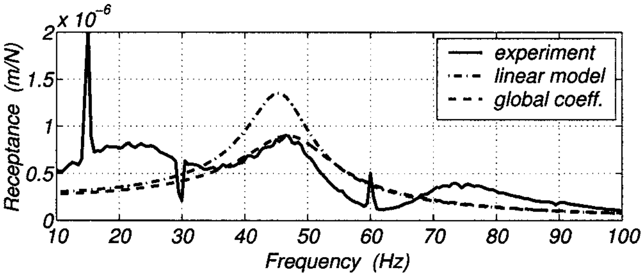

Fig. 11 Comparison between theoretical and experimental FRFs of the rotor-bearing system in the active case for Ω=900 rpm (15 Hz), horizontal direction

tally (continuous lines). Considering that the oil film coefficients of the conventional lubrication are well tuned [left side of Eq. (3)], the cause of such discrepancies must be due to the coefficient λ. The coefficient presented in Fig. 8 was obtained by applying a low-frequency input signal into the servo valves, in a quasi-static condition (1 Hz). Hereby, the dynamics of the servo valve and oil supply system were not encountered. The servo valves work at higher frequencies during operation, hence, based on the obtained results, the coefficient λ is probably not constant but frequency dependent [$\lambda=\lambda(\omega)$]. The coefficient λ obtained from Fig. 8 does not properly represent the dynamics of the hydraulic forces when the vibration frequencies are higher, leading to inaccurate results of the receptance curves.

By adopting the model with equivalent dynamic coefficients of the active lubrication (second approach), one obtains better results concerning the prediction of resonance peak amplitudes (Figs. 11 and 12—dashed lines), with good agreement between theory and experiment. Such an approach takes into account both lubrication mechanisms (conventional and active) simultaneously in order to estimate the global equivalent dynamic coefficients of the oil film. As a result, the stiffness $\bar{\mathbf{K}}(\mathrm{So},\omega,G_P)$ and damping $\bar{\mathbf{D}}(\mathrm{So},\omega,G_P)$ coefficients of the actively lubricated bearing are frequency dependent and strongly influenced by the parameters of the servo valves, their dynamics, and the gains of the control loop [16,17]. Consequently, such an approach leads to more accurate results, as shown in Figs. 11 and 12. The behavior of such coefficients and their dependency on excitation frequency and proportional control gain are illustrated in Figs. 13 and 14.

By setting the control gain G_P to zero and varying the values of the static injection pressure in all pads until 0.8 M Pa the bearing stiffness coefficients are sensitively modified, whereas damping coefficients remain almost constant. It can be seen by comparing the coefficients in Figs. 13 and 14, when $G_P=0$, to the coefficients presented in Fig. 5. By adopting static pressures of 0.8 M Pa in all pads and varying the proportional control gains G_P only in the horizontal direction, a modification of the stiffness and damping coefficients is achieved as illustrated in Figs. 13(*a*) and 13(*c*) and 14(*a*) and 14(*c*). The behavior of the horizontal and vertical oil film coefficients as a function of the proportional gain and excitation frequency very different since only in the horizontal direction are such coefficients altered by the controlled oil injection. In the horizontal direction *Y* the dynamic coefficients of the active lubricated bearing have three different regions, as it is illustrated in Figs. 13(*a*) and 13(*c*) and 14(*a*) and 14(*c*). For a given excitation frequency and varying the control gain, one can easily detect three such different regions: in region (II), the coef-

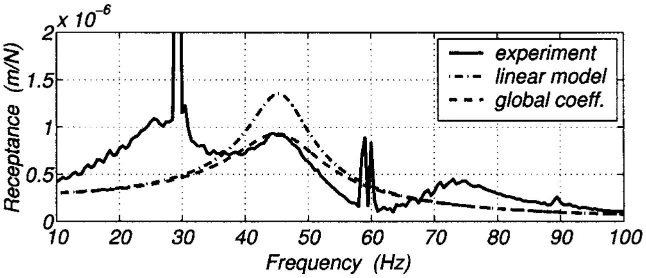

Fig. 12 Comparison between theoretical and experimental FRFs of the rotor-bearing system in the active case for Ω=1800 rpm (30 Hz), horizontal direction

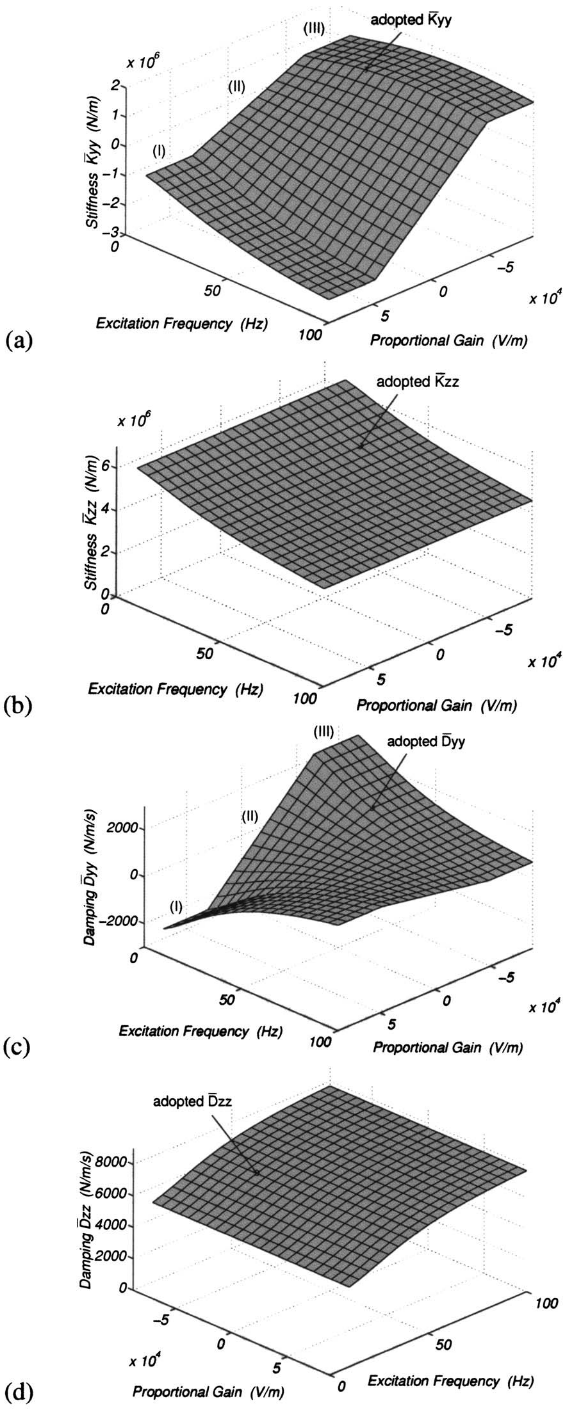

Fig. 13 Oil film coefficients $\bar{K}_{yy}$, $\bar{K}_{zz}$, $\bar{D}_{yy}$, $\bar{D}_{zz}$ of the TPJB under active lubrication condition as a function of the excitation frequency ω, proportional gain G_P, and Sommerfeld number So corresponding to the angular velocity of Ω=900 rpm (15 Hz)

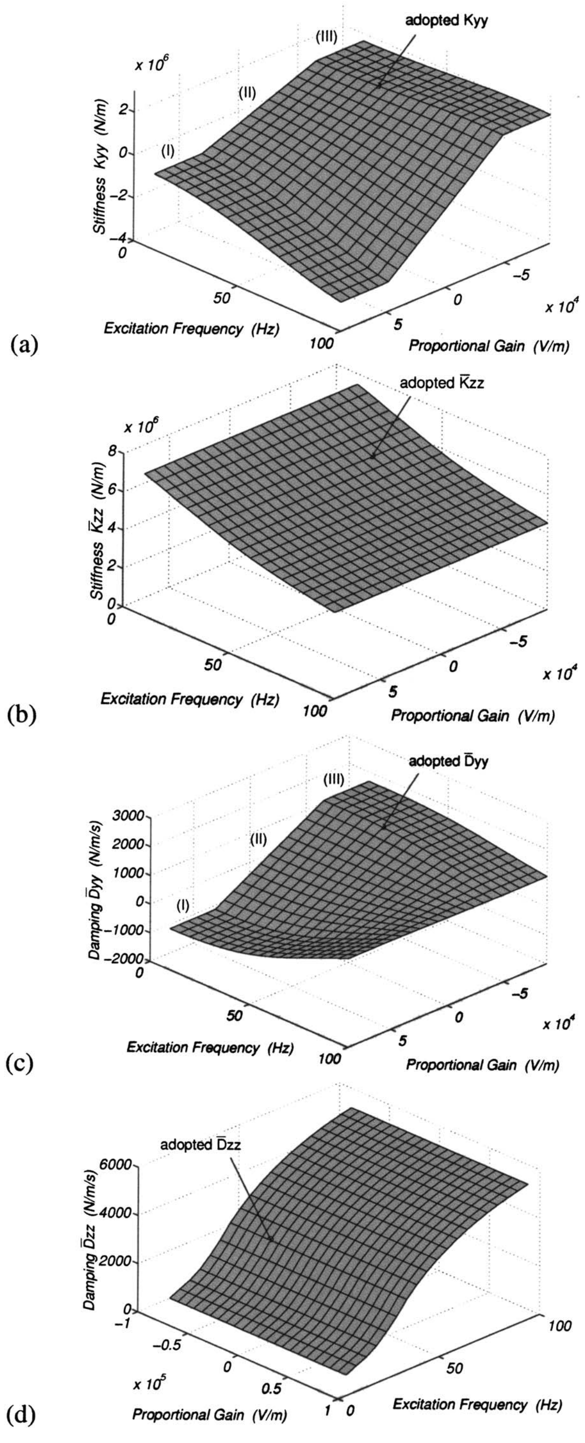

Fig. 14 Oil film coefficients $\bar{K}_{yy}$, $\bar{K}_{zz}$, $\bar{D}_{yy}$, $\bar{D}_{zz}$ of the TPJB under active lubrication condition as a function of the excitation frequency ω, proportional gain G_P and Sommerfeld number So corresponding to the angular velocity of Ω=1800 rpm (30 Hz)

ficient $\bar{K}_{yy}$ varies linearly as function of the control gains. When the control voltage reaches its limit, the coefficients stop varying and remain constant in the so far achieved values, thus forming regions (I) and (III). The damping coefficient $\bar{D}_{yy}$ behaves similarly, presenting also three clear regions. In the vertical direction Z stiffness $\bar{K}_{zz}$ as well as damping $\bar{D}_{zz}$ are not affected by the control gain G_P, as it can be seen in Figs. 13(*b*) and 13(*d*) and 14(*b*) and 14(*d*). In this case, the control gain G_P is set to null in the vertical direction. The cross-coupling coefficients ($\bar{K}_{yz}$, $\bar{K}_{zy}$, $\bar{D}_{yz}$ and $\bar{D}_{zy}$) are not presented because they are negligible compared to the main coefficients, as in the conventional lubrication. The bearing coefficients adopted in case of active lubrication are highlighted in Figs. 13 and 14. Such global oil film coefficients take into account all the parameters of the hydraulic system, the excitation frequency and the control gains.

The use of coefficient λ (first model approach) is a practical tool for designing the controller of the active lubrication because it avoids the modeling of the hydraulic system dynamics (servo valves and flow in the pipelines and orifices). However, some experimental effort is necessary to properly evaluate the dependency of coefficient $\lambda(\omega)$ on the excitation frequency ω. On the other hand, the global oil film coefficients of active lubrication (second model approach) do not require experimental evaluation of force signals of the active system. But, this approach requires a good evaluation of the parameters of the hydraulic system.

5 Conclusion and Future Aspects

A rotor/tilting-pad bearing system with active lubrication is presented, modeled, and a frequency response analysis is carried out, numerically as well as experimentally, for two rotor angular velocities (900 and 1800 rpm). Experimental results in frequency domain show the feasibility of reducing up to 30% of the amplitude resonance peaks of the system, by adopting active lubrication with a very simple proportional controller. The controlled resonance peaks are associated to the first rigid mode shape of the rotating system. A further attenuation of vibration levels can be achieved by implementing more advanced controllers. Focusing on industrial applications of the active lubrication, one can conclude that it may be feasible to adapt rotating machines to different demanding situations by reducing the resonance peaks, attenuating the vibration amplitude levels and avoiding unpredictable stops or shutdowns. Of course, such a conclusion is based on the experimental results obtained with help of a test rig, operating at low rotor angular velocities. Therefore, the influence of the active lubrication at higher rotor angular velocities shall also be investigated.

Good agreement between experimental and numerical results is achieved in the passive case (conventional hydrodynamic lubrication). It was shown that the estimation of oil film coefficients is appropriate and the coefficients themselves are well tuned. In the active case (active lubrication), the first model approach, based on the linearized active forces and the linear coefficient λ, presented resonance peaks with amplitudes 40% higher than those obtained experimentally. Although such an approach is very practical and extremely easy to be implemented, the value of coefficient λ was poorly estimated by the quasi-static test at constant angular velocity. The parameter λ probably is frequency dependent. As a result, the adopted value of λ in the simulations led to inaccurate results. The conventional and active lubrication forces may be accurately decoupled using the coefficient λ, only if such a coefficient also becomes dependent on the frequency and on the Sommerfeld number, i.e., $\lambda=\lambda(\mathrm{So},\omega)$. It means that λ shall be estimated by a series of tests in the operational frequency range, not only by a quasi-static test at low frequency. Such a claim shall be further investigated in the near future.

The second mathematical approach, based on the global equivalent dynamic coefficients of the oil film and obtained from the modified Reynolds equation for the active lubrication, leads to good agreement with the experimental results. Such an approach takes into account both lubrication mechanisms (i.e., conventional and active), the dynamics of the hydraulic system, and the control gains. For this reason, this approach leads to a more accurate mathematical model. The global dynamic coefficients, obtained from the modified Reynolds equation for the active lubrication, represent in an accurate way the rotor-bearing dynamics under active lubrication.

Acknowledgment

The Brazilian research foundation FAPESP (Fundação de Amparo à Pesquisa do Estado de São Paulo) is gratefully acknowledged for the support given to this project.

Nomenclature

A = active lubrication
D_{ii} = oil film damping coefficient
$\mathbf{D}$ = damping matrix
$\mathbf{E}$ = excitation point
$\mathbf{f_i}$ = force vector acting on point i ($i = H, E, O$)
F_{i_j} = force acting on point i, direction j
FRF = frequency response function
$\mathbf{G}$ = gyroscopic matrix
G_P = proportional gain
$\mathbf{H}$ = active bearing point
I_{xx}^R = rotor polar moment of inertia related to point $\mathbf{R}$
I_{yy}^R, I_{zz}^R = rotor lateral moment of inertia related to point $\mathbf{R}$
K_{ii} = oil film stiffness coefficient
$\mathbf{K}$ = stiffness matrix
$\mathbf{M}$ = inertia matrix
$\mathbf{O}$ = rotor center of gravity point
r_{ij} = distance between points i and j
$\mathbf{R}$ = ball bearing point
$\mathbf{x}$ = displacement vector
y_i, z_i = displacements of point i in the inertial reference frame
X, Y, Z = inertial reference frame
X_1, Y_1, Z_1 = auxiliary reference frame $B1$
X_2, Y_2, Z_2 = auxiliary reference frame $B2$
β = angular displacement around Y_1
γ = angular displacement around Z
λ = coefficient of linearization of active force
$\dot{\phi}$ = rotor angular velocity
Ω = operational rotating frequency

References

[1] Santos, I. F., 1994, "Design and Evaluation of Two Types of Active Tilting-Pad Journal Bearings," *IUTAM Symposium on Active Control of Vibration*, Bath, England, "Mechanical Engineering Publications Limited, London," pp. 79–87.

[2] Santos, I. F., and Russo, F. H., 1998, "Tilting-Pad Journal Bearings With Electronic Radial Oil Injection," ASME J. Tribol., **120**(3), pp. 583–594.

[3] Santos, I. F., and Nicoletti, R., 1999, "THD Analysis in Tilting-Pad Journal Bearings Using Multiple Orifice Hybrid Lubrication," ASME J. Tribol., **121**(4), pp. 892–900.

[4] Santos, I. F., and Nicoletti, R., 2001, "Influence of Orifice Distribution on the Thermal and Static Properties of Hybridly Lubricated Bearings," Int. J. Solids Struct., **38**(10–13), pp. 2069–2081.

[5] Nicoletti, R., and Santos, I. F., 2003, "Linear and Non-Linear Control Techniques Applied to Actively Lubricated Journal Bearings," J. Sound Vib., **260**(5), pp. 927–947.

[6] Santos, I. F., and Scalabrin, A., 2003, "Control System Design for Active Lubrication With Theoretical and Experimental Examples," ASME J. Eng. Gas Turbines Power, **125**(1), pp. 75–80.

[7] Wu, W., and Pfeiffer, F., 1998, "Active Vibration Damping for Rotors by a Controllable Oil-Film Bearing," *Proc. of IFToMM International Conference on Rotor Dynamics*, Darmstadt, Germany, "Vieweg-Verlag Braunschweig, Wiesbaden," pp. 431–443.

[8] Bently, D. E., Grant, J. W., and Hanifan, P., 1999, "Active Controlled Hydrostatic Bearings for a New Generation of Machines," ASME Paper No. 2000-GT-354.

[9] Santos, I. F., and Watanabe, F. Y., 2003, "Feasibility of Influencing the Dynamic Fluid Film Coefficients of a Multirecess Journal Bearing by Means of Active Hybrid Lubrication," J. Brazilian Soc. Mech. Sci. Eng., **15**(2), pp. 154–163.

[10] Santos, I. F., and Watanabe, F. Y., 2004, "Compensation of Cross-Coupling Stiffness and Increase of Direct Damping in Multirecess Journal Bearings Using Active Hybrid Lubrication, Part I: Theory," ASME J. Tribol., **126**(1), pp. 146–155.

[11] Lund, J. W., 1964, "Spring and Damping for the Tilting Pad Journal Bearings," ASLE Trans., **7**(4), pp. 342–352.

[12] Lund, J. W., and Thomsen, K. K., 1978, "A Calculation Method and Data for the Dynamic Coefficients of Oil-Lubricated Journal Bearings," *Topics in Fluid Film Bearing and Rotor Bearing System Design and Optimization*, S. M. Rhode, P. E. Allaire, and C. J. Maday (eds.), ASME, New York, pp. 1–28.

[13] Springer, H., 1980, "Dynamische Eigenschaften von Gleitlagern mit beweglischen Segmenten," *VDI-Berichte*, N. 381, pp. 177–184.

[14] Someya, T., 1989, *Journal Bearing Data Book*, Springer-Verlag, Berlin.

[15] Allaire, P. E., Parsell, J. A., and Barret, L. E., 1981, "A Pad Perturbation Method for the Dynamic Coefficients of Tilting Pad Journal Bearings," Wear, **72**, pp. 29–44.

[16] Santos, I. F., Scalabrin, A., and Nicoletti, R., 2001, "Ein Beitrag zur Aktiven Schmierungstheorie," *Schwingungen in rotierenden Machinen VI*, H. Irretier, R. Nordmann, and H. Springer, eds., Vieweg Verlag, Vol. 5, pp. 21–30.

[17] Santos, I. F., Nicoletti, R., and Scalabrin, A., 2004, "Feasibility of Applying Active Lubrication to Reduce Vibration in Industrial Compressors," ASME J. Eng. Gas Turbines Power, **126**(4), pp. 848–854.

[18] Parsell, J. A., Allaire, P. E., and Barret, L. E., 1983, "Frequency Effects in Tilting Pad Journal Bearing Dynamic Coefficients," ASLE Trans., **26**(2), pp. 222–227.

Recent Developments in Turbomachinery Modeling for Improved Balancing and Vibration Response Analysis

Peter Y. P. Chen
Visiting Research Fellow

Ningsheng Feng
Lecturer

Eric J. Hahn
Visiting Professor
e-mail: e.hahn@unsw.edu.au

Wenlong Hu
Research Student

School of Mechanical and Manufacturing Engineering,
The University of New South Wales,
Sydney NSW 2052, Australia

Present day turbogenerator installations are statically indeterminate rotor-bearing-foundation systems utilizing nonlinear hydrodynamic bearings. For optimal balancing and diagnostic purposes it is important to be able to correctly predict the system vibration behavior over the operating speed range. Essential aspects of this involve identifying the unbalance state, identifying appropriate dynamic foundation parameters, and identifying the system configuration state (relative location of the support bearings). This paper shows that, provided the system response is periodic at some speeds over the operating range and appropriate rotor and bearing housing motion measurements are made, it is possible, in principle, to satisfactorily achieve the above identifications without relying on the Reynolds equation for evaluating bearing forces. Preliminary results indicate that the identifications achieved promise to be superior to identification approaches that use the Reynolds equation. [DOI: 10.1115/1.1850942]

Introduction

Turbogenerators used for power generation consist of several rotor stages that are rigidly coupled together to form a single rotor supported on many hydrodynamic bearings, resulting in a statically indeterminate rotor-bearing-foundation system (RBFS). For safe and efficient operation, vibration levels must be kept to a minimum. Even if perfectly balanced at time of installation, balance condition deteriorates with service, and to keep vibration at acceptable levels, it is occasionally necessary to balance the unit in the field (i.e., identify and then modify its unbalance state). At present, such balancing often requires many costly runups and/or rundowns [1] and satisfactory vibration attenuation sometimes necessitates changing the relative transverse alignment of the bearing housings (the so-called configuration state of the system). It is important to minimize the number of these expensive runups and/or rundowns, and this can be achieved if one can predict sufficiently accurately the vibration response of the RBFS when it is subjected to some known unbalance excitation; for this, one requires a sufficiently accurate model of the system [2,3].

Modeling of the system necessitates an appropriate representation of the rotor, bearings, and bearing supports (i.e., the foundation). It is generally accepted that the rotor can be modeled to the desired degree of accuracy. On the other hand, the hydrodynamic bearings create major modeling problems, since their stiffness and damping properties are reaction-load dependent. For statically indeterminate systems, these loads depend (among other parameters) on the configuration state of the system [4,5]. Hence, it is essential to know this configuration state to be able to predict system stability and unbalance response. The problem occurs because the actual configuration state during operation is often different from that at the time of installation due to foundation settlement and thermal effects; its determination (i.e., identification) is still a major challenge [6,7]. Also, one needs to be able to adequately model (i.e., identify) the foundation. Again, this is a major task owing to the difficulty in properly representing the many joints and ground effects [8]. For this reason, one seeks an equivalent foundation that accurately reflects the vibration response of the system over the operating speed range (i.e., one seeks to identify appropriate equivalent foundation parameters). This challenge has involved extensive research investigations over the years [9–12].

Numerical experiments have shown that, in theory, identification of the unbalance state, the configuration state, and the foundation is feasible, provided one can rely on the Reynolds equation for hydrodynamic lubrication to evaluate bearing forces, using, as input, measurable journal and bearing housing motions [3,7,13]. In practice, however, one has incomplete knowledge of the actual bearing clearances and lubricant viscosities due to thermal effects and poor knowledge of the actual extent of the full fluid film due to air entrainment and cavitation. Indeed, laboratory experiments indicate that reliance on the Reynolds equation may result in poor identification of foundation parameters [14] and poor prediction of system stability [15]. Hence, alternative techniques are sought that avoid such reliance altogether. This paper evaluates such alternative identification techniques.

General Theory

The basic theory (which has been developed in varying notations and with varying degrees of generality for foundation, unbalance state, and configuration state identifications using the Reynolds equation [3,7,13] and for the alternative foundation and unbalance state identification approaches [12,16]) is summarized here in a unified format to complement the development of an alternative approach for configuration state identification. Such a summary will also serve to highlight differences between the alternative identification approaches and those using the Reynolds equation.

Equations of Motion of Rotor

A schematic of a general RBFS is shown in Fig. 1. It is assumed that one has an adequate model of the rotor, which is axially symmetric and can be adequately represented by system matrices. The rotor is connected to the foundation via bearings, which may be any type and combination of hydrodynamic and rolling element bearings. If the former, then the bearing reaction forces (which equal the transmitted forces to the foundation) are nonlinear functions of the rotor motion. The equations of motion of the rotor at some constant speed Ω are [12]

Contributed by the International Gas Turbine Institute (IGTI) of THE AMERICAN SOCIETY OF MECHANICAL ENGINEERS for publication in the ASME JOURNAL OF ENGINEERING FOR GAS TURBINES AND POWER. Paper presented at the International Gas Turbine and Aeroengine Congress and Exhibition, Vienna, Austria, June 13–17, 2004, Paper No. 2004-GT-54305. Manuscript received by IGTI, October 1, 2003; final revision, March 1, 2004. IGTI Review Chair: A. J. Strazisar.

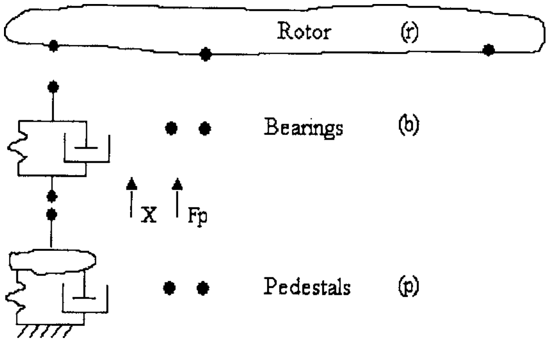

Fig. 1 Schematic of a general RBFS

$$\mathbf{M}_r\ddot{\mathbf{X}}_r+\mathbf{C}_r\dot{\mathbf{X}}_r+\mathbf{K}_r\mathbf{X}_r=\mathbf{F}_b+\mathbf{F}_e+\mathbf{F}_u \tag{1}$$

or

$$\mathbf{M}_r\left\{\begin{matrix}\ddot{\mathbf{X}}_r^f\\ \ddot{\mathbf{X}}_r^c\end{matrix}\right\}+\mathbf{C}_r\left\{\begin{matrix}\dot{\mathbf{X}}_r^f\\ \dot{\mathbf{X}}_r^c\end{matrix}\right\}+\mathbf{K}_r\left\{\begin{matrix}\mathbf{X}_r^f\\ \mathbf{X}_r^c\end{matrix}\right\}=\left\{\begin{matrix}\mathbf{0}\\ \mathbf{F}_b^c\end{matrix}\right\}+\left\{\begin{matrix}\mathbf{F}_e^f\\ \mathbf{F}_e^c\end{matrix}\right\}+\left\{\begin{matrix}\mathbf{F}_u^f\\ \mathbf{F}_u^c\end{matrix}\right\} \tag{2}$$

The unknown bearing forces $\mathbf{F}_b$ are generally motion dependent, and the other external forces $\mathbf{F}_e$ (e.g., gravity forces) are assumed known. The unknown unbalance forces $\mathbf{F}_u$ are synchronous and may exist at any of the rotor degrees of freedom (DOFs). On the other hand, the q DOFs at which rotor responses can be measured, the so-called connection DOFs, are normally quite limited. Usually they are restricted to the DOFs at the bearings, though, in general, they may also include DOFs elsewhere along the rotor. Because the bearing reaction forces are usually nonlinear functions of rotor motion, the equations of motion are usually nonlinear. Restricting analysis to those speeds Ω at which the system response is periodic with fundamental frequency ω, the steady-state solution may be expressed as

$$\mathbf{X}_r=\sum_{k=0}^{n}\mathbf{x}_{rk}e^{jk\omega t} \tag{3}$$

On substitution into Eq. (2), one obtains $(n+1)$ sets of simultaneous equations of the form

$$\mathbf{H}_{rk}\left\{\begin{matrix}\mathbf{x}_{rk}^f\\ \mathbf{x}_{rk}^c\end{matrix}\right\}=\left\{\begin{matrix}\mathbf{0}\\ \mathbf{f}_{bk}^c\end{matrix}\right\}+\left\{\begin{matrix}\mathbf{f}_{ek}^f\\ \mathbf{f}_{ek}^c\end{matrix}\right\}+\left\{\begin{matrix}\mathbf{f}_{uk}^f\\ \mathbf{f}_{uk}^c\end{matrix}\right\}\quad k=0,1\cdots n \tag{4}$$

where

$$\mathbf{H}_{rk}=-k^2\omega^2\mathbf{M}_r+jk\omega\mathbf{C}_r+\mathbf{K}_r \tag{5}$$

$$\mathbf{f}_{ek}=\begin{cases}\mathbf{F}_e & k=0\\ \mathbf{0} & \text{otherwise}\end{cases} \tag{6}$$

and

$$\mathbf{f}_{uk}=\begin{cases}\mathbf{f}_u & k=\Omega/\omega=s\\ \mathbf{0} & \text{otherwise}\end{cases} \tag{7}$$

Equations of Motion of Foundation

It is assumed that the foundation, as the rotor, can also be adequately represented by system matrices with equations of motion given by

$$\mathbf{M}_p\ddot{\mathbf{X}}_p+\mathbf{C}_p\dot{\mathbf{X}}_p+\mathbf{K}_p\mathbf{X}_p=\mathbf{F}_p \tag{8}$$

or

$$\mathbf{M}_p\left\{\begin{matrix}\ddot{\mathbf{X}}_p^f\\ \ddot{\mathbf{X}}_p^c\end{matrix}\right\}+\mathbf{C}_p\left\{\begin{matrix}\dot{\mathbf{X}}_p^f\\ \dot{\mathbf{X}}_p^c\end{matrix}\right\}+\mathbf{K}_p\left\{\begin{matrix}\mathbf{X}_p^f\\ \mathbf{X}_p^c\end{matrix}\right\}=\left\{\begin{matrix}\mathbf{0}\\ \mathbf{F}_p^c\end{matrix}\right\} \tag{9}$$

Again, the connection DOFs refer to those DOFs where measurements are taken. They may be different than q in number, but are assumed to include at least all DOFs that reflect the bearing transmitted forces. The force vector $\mathbf{F}_p$ comprises the reaction forces exerted on the foundation at these measured DOFs. For periodic motions,

$$\mathbf{X}_p=\sum_{k=0}^{n}\mathbf{x}_{pk}e^{jk\omega t} \tag{10}$$

and on substituting into Eq. (9) one obtains $(n+1)$ sets of simultaneous equations of the form

$$\mathbf{H}_{pk}\left\{\begin{matrix}\mathbf{x}_{pk}^f\\ \mathbf{x}_{pk}^c\end{matrix}\right\}=\left\{\begin{matrix}\mathbf{0}\\ \mathbf{f}_{pk}^c\end{matrix}\right\}\quad k=0,1\cdots n \tag{11}$$

where

$$\mathbf{H}_{pk}=-k^2\omega^2\mathbf{M}_p+jk\omega\mathbf{C}_p+\mathbf{K}_p \tag{12}$$

If rotor measurements and foundation measurements are restricted to measurements at the bearings, then one can ensure that

$$\mathbf{f}_{pk}^c=-\mathbf{f}_{bk}^c \tag{13}$$

This will be assumed here for simplicity of further exposition.

The applicability of the above equations to the identification of the foundation, the unbalance state and the configuration state is discussed in turn. Note that both the unbalance state identification and the configuration state identification assume that the foundation is known, whereas foundation identification does not require a knowledge of the unbalance state nor of the configuration state.

Foundation Identification: Theory

For foundation identification, one seeks the elements of the matrices $\mathbf{M}_p$, $\mathbf{C}_p$ and $\mathbf{K}_p$. Considering synchronous motions, where $k=s=\Omega/\omega$, Eq. (4) becomes

$$\mathbf{H}_{rs}\left\{\begin{matrix}\mathbf{x}_{rs}^f\\ \mathbf{x}_{rs}^c\end{matrix}\right\}=\begin{bmatrix}\mathbf{A} & \mathbf{B}\\ \mathbf{D} & \mathbf{E}\end{bmatrix}\left\{\begin{matrix}\mathbf{x}_{rs}^f\\ \mathbf{x}_{rs}^c\end{matrix}\right\}=\left\{\begin{matrix}\mathbf{0}\\ \mathbf{f}_{bs}^c\end{matrix}\right\}+\left\{\begin{matrix}\mathbf{f}_u^f\\ \mathbf{f}_u^c\end{matrix}\right\} \tag{14}$$

and on eliminating the nonconnection rotor displacements

$$\mathbf{f}_{bs}^c=[\mathbf{E}-\mathbf{D}\mathbf{A}^{-1}\mathbf{B}]\mathbf{x}_{rs}^c+\mathbf{D}\mathbf{A}^{-1}\mathbf{f}_u^f-\mathbf{f}_u^c. \tag{15}$$

Similarly, for the foundation, Eq. (11) becomes

$$\mathbf{H}_{ps}\left\{\begin{matrix}\mathbf{x}_{ps}^f\\ \mathbf{x}_{ps}^c\end{matrix}\right\}=\begin{bmatrix}\mathbf{I} & \mathbf{J}\\ \mathbf{L} & \mathbf{N}\end{bmatrix}\left\{\begin{matrix}\mathbf{x}_{ps}^f\\ \mathbf{x}_{ps}^c\end{matrix}\right\}=\left\{\begin{matrix}\mathbf{0}\\ \mathbf{f}_{ps}^c\end{matrix}\right\} \tag{16}$$

and on eliminating the nonconnection pedestal displacements

$$\mathbf{f}_{ps}^c=-\mathbf{f}_{bs}^c=[\mathbf{N}-\mathbf{L}\mathbf{I}^{-1}\mathbf{J}]\mathbf{x}_{ps}^c \tag{17}$$

Equation (17) is true for a general foundation. Such general foundation identification is outside the scope of this paper, which is restricted to simple foundations consisting of pedestal supports to ground at each bearing, with each pedestal represented by a single mass with a single DOF in each lateral direction. Hence, all foundation DOFs become connection DOFs, $\mathbf{L}$ and $\mathbf{J}$ are null matrices, and Eq. (17) simplifies to

$$\mathbf{f}_{ps}^c=-\mathbf{f}_{bs}^c=\mathbf{N}\mathbf{x}_{ps}^c \tag{18}$$

Foundation identification can then be achieved by relating, at some rotor speed Ω, the pedestal response components $\mathbf{x}_{ps}^c$ (measured) to the transmitted force components $\mathbf{f}_{ps}^c$ or $\mathbf{f}_{bs}^c$, which, as shown by Eq. (15), are functions of the elements of the rotor dynamic stiffness $\mathbf{H}_{rs}$ (assumed known), the unbalance force components $\mathbf{f}_u$ (generally not known), and the absolute rotor response components at the bearing supports $\mathbf{x}_{rs}^c$ (measured). The problem of unknown $\mathbf{f}_u$ can be overcome by adding a known unbalance distribution and repeating the response measurements at the same speed. Assuming that steady-state conditions are again reached, all the above equations apply, but the responses will be different, as will $\mathbf{F}_b$ and $\mathbf{F}_u$. On subtracting the corresponding equation sets for the synchronous motion solutions for the rotor and foundation for the respective unbalance distributions, one obtains

$$\mathbf{H}_{rs}\begin{Bmatrix}\Delta\mathbf{x}_{rs}^{f}\\ \Delta\mathbf{x}_{rs}^{c}\end{Bmatrix}=\begin{bmatrix}\mathbf{A} & \mathbf{B}\\ \mathbf{D} & \mathbf{E}\end{bmatrix}\begin{Bmatrix}\Delta\mathbf{x}_{rs}^{f}\\ \Delta\mathbf{x}_{rs}^{c}\end{Bmatrix}=\begin{Bmatrix}\mathbf{0}\\ \Delta\mathbf{f}_{bs}^{c}\end{Bmatrix}+\begin{Bmatrix}\Delta\mathbf{f}_{u}^{f}\\ \Delta\mathbf{f}_{u}^{c}\end{Bmatrix} \tag{19}$$

or

$$\Delta\mathbf{f}_{bs}^{c}=[\mathbf{E}-\mathbf{D}\mathbf{A}^{-1}\mathbf{B}]^{-1}\Delta\mathbf{x}_{rs}^{c}+\mathbf{D}\mathbf{A}^{-1}\Delta\mathbf{f}_{u}^{f}-\Delta\mathbf{f}_{u}^{c} \tag{20}$$

and

$$\mathbf{H}_{ps}\begin{Bmatrix}\Delta\mathbf{x}_{ps}^{f}\\ \Delta\mathbf{x}_{ps}^{c}\end{Bmatrix}=\begin{bmatrix}\mathbf{I} & \mathbf{J}\\ \mathbf{L} & \mathbf{N}\end{bmatrix}\begin{Bmatrix}\Delta\mathbf{x}_{ps}^{f}\\ \Delta\mathbf{x}_{ps}^{c}\end{Bmatrix}=\begin{Bmatrix}\mathbf{0}\\ \Delta\mathbf{f}_{ps}^{c}\end{Bmatrix} \tag{21}$$

or

$$-\Delta\mathbf{f}_{bs}^{c}=\mathbf{N}\Delta\mathbf{x}_{ps}^{c} \tag{22}$$

where $\Delta\mathbf{f}_u$ is the vector of the unbalance force components corresponding to the added known unbalance distribution, $\Delta\mathbf{x}_{rs}^{c}$ is the vector change in the synchronous rotor displacements at the connection coordinates upon addition of the known unbalance, etc.

The only constraint applicable to this approach is that the response subtractions be at the same speeds. Furthermore, because Eq. (20) uses the response differences to calculate the forces, errors in response measurements due to existing mechanical runout on the measuring surface are eliminated automatically. Should the number of equations available to solve for the unknown parameters in $\mathbf{M}_p$, $\mathbf{C}_p$, and $\mathbf{K}_p$ be insufficient, one needs to repeat the process at some other speed(s) until the number of equations exceeds the number of unknowns. Least-squares regression analysis can then be used to find the optimal foundation parameters [17].

In the foundation identification approach using the Reynolds equation, one can evaluate (in theory) the transmitted bearing forces $\mathbf{f}_{bs}^{c}$ from measurements of the rotor motion relative to the pedestal [13]. Hence, Eq. (17) or (18) can be used immediately to identify the foundation parameters (i.e., one does not need to assume a knowledge of the rotor dynamic stiffness nor does one need to know the unbalance state, thereby avoiding the need for a second set of measurements).

Unbalance State Identification: Theory

For unbalance state identification it is assumed that the foundation model is known (i.e., that the foundation system matrices $\mathbf{M}_p$, $\mathbf{C}_p$, and $\mathbf{K}_p$ are available). Again, we are interested in the rotor and foundation equation sets corresponding to synchronous motion (i.e., when $k=\Omega/\omega=s$). The operative equation is Eq. (15) with the transmitted bearing forces $\mathbf{f}_{bs}^{c}$ obtained from Eq. (17), in general, using the known (measured) values $\mathbf{x}_{ps}^{c}$. Since the $\mathbf{x}_{rs}^{c}$ are also known (measured) and the rotor dynamic stiffness $\mathbf{H}_{rs}$ is assumed known, the only unknowns in Eq. (15) are the unbalance force components $\mathbf{f}_u$. Thus, Eq. (15) represents a set of $2q$ linear simultaneous equations (since each rotor response measurement involves magnitude and phase) at the balance speed Ω in the unknown unbalance force components $\mathbf{f}_u$, with each unbalance force component contributing two unknowns, viz. its magnitude and direction. If the number of equations is less than the number of unknowns, then the above measurements need to be repeated at other selected balance speeds until the number of equations exceeds the unchanged number of unknowns. Least-squares regression can then be used to identify the unknown unbalances. Note that the transmitted bearing forces $\mathbf{f}_{bs}^{c}$ are obtained solely from rotor and pedestal motion measurements.

In the unbalance identification approach using the Reynolds equation, the operative equation is also Eq. (15), except now the bearing transmitted forces can (in theory) be evaluated from measurements of the rotor motion relative to the pedestal [3]. In such a case, one does not need to measure pedestal motions nor does one need a foundation model.

Configuration State Identification: Theory

Whereas neither the foundation nor the unbalance state identification approaches necessitated a knowledge of the configuration state, its knowledge is essential for determining the mean bearing reaction forces and, hence, for predicting the vibration response of the RBFS. Again, it is assumed that the foundation system matrices $\mathbf{M}_p$, $\mathbf{C}_p$, and $\mathbf{K}_p$ are known. There is, however, no need to know the unbalance distribution.

Here, we are interested in the equation sets for the rotor and foundation when $k=0$. Equation (4) then simplifies to

$$\mathbf{K}_{r}\begin{Bmatrix}\mathbf{x}_{ro}^{f}\\ \mathbf{x}_{ro}^{c}\end{Bmatrix}=\begin{bmatrix}\mathbf{T} & \mathbf{U}\\ \mathbf{V} & \mathbf{W}\end{bmatrix}\begin{Bmatrix}\mathbf{x}_{ro}^{f}\\ \mathbf{x}_{ro}^{c}\end{Bmatrix}=\begin{Bmatrix}\mathbf{0}\\ \mathbf{f}_{bo}^{c}\end{Bmatrix}+\begin{Bmatrix}\mathbf{f}_{e}^{f}\\ \mathbf{f}_{e}^{c}\end{Bmatrix} \tag{23}$$

and on eliminating the nonconnection rotor displacements

$$[\mathbf{W}-\mathbf{V}\mathbf{T}^{-1}\mathbf{U}]\mathbf{x}_{ro}^{c}=\mathbf{K}_{r}^{c}\mathbf{x}_{ro}^{c}=\mathbf{f}_{bo}^{c}+\mathbf{f}_{e}^{c}-\mathbf{V}\mathbf{T}^{-1}\mathbf{f}_{e}^{f} \tag{24}$$

Similarly, Eq. (11) simplifies to

$$\mathbf{K}_{P}\begin{Bmatrix}\mathbf{x}_{po}^{f}\\ \mathbf{x}_{po}^{c}\end{Bmatrix}=\begin{bmatrix}\mathbf{P} & \mathbf{Q}\\ \mathbf{R} & \mathbf{S}\end{bmatrix}\begin{Bmatrix}\mathbf{x}_{po}^{f}\\ \mathbf{x}_{po}^{c}\end{Bmatrix}=\begin{Bmatrix}\mathbf{0}\\ \mathbf{f}_{po}^{c}\end{Bmatrix} \tag{25}$$

and on eliminating the nonconnection pedestal displacements

$$[\mathbf{S}-\mathbf{R}\mathbf{P}^{-1}\mathbf{Q}]\mathbf{x}_{po}^{c}=\mathbf{K}_{p}^{c}\mathbf{x}_{po}^{c}=\mathbf{K}_{p}^{c}\mathbf{b}=\mathbf{f}_{po}^{c} \tag{26}$$

Also in conformity with Eq. (13)

$$\mathbf{f}_{po}^{c}=-\mathbf{f}_{bo}^{c} \tag{27}$$

The configuration state identification problem is illustrated for a four-bearing system in Fig. 2 where the elements of $\mathbf{x}_{ro}$ corresponding to the lateral displacements of the deformed rotor centerline $\mathbf{r}_i$ can be measured with respect to any arbitrary fixed datum line, here selected to be the line through the centers of the first and last unloaded bearing housings. The locations of the centers of the other unloaded bearing housings relative to this datum line define the configuration state of the system ($\mathbf{c}_2$ and $\mathbf{c}_3$ in Fig. 2). If the mean eccentricities $\mathbf{e}_i$ of the rotor journals define the locations of the centers of the bearing housings relative to the deformed rotor centreline and the mean displacements $\mathbf{b}_i$ define the displacements of the centers of the bearing housings from their original unloaded positions, then one can see from Fig. 2 that at the bearing stations,

$$\mathbf{r}_i=\mathbf{c}_i+\mathbf{b}_i+\mathbf{e}_i \quad i=1,2,3,4 \tag{28}$$

Hence, if we restrict the connection DOFs to the two lateral directions at each bearing, then Eq. (24) involves eight simultaneous equations in the eight unknown bearing force components in $\mathbf{f}_{bo}$ and the four unknown configuration components in $\mathbf{c}_2$ and $\mathbf{c}_3$ [since the $\mathbf{e}_i$ are measured and the $\mathbf{b}_i$ can be expressed in terms of the $\mathbf{f}_{bo}$ by virtue of Eqs. (26) and (27)]. Thus, one has an excess of unknowns. Taking measurements at another speed would yield eight additional equations, but there would also result eight additional unknown values of $\mathbf{f}_{bo}$. This problem may be resolved by evaluating some of the unknown $\mathbf{f}_{bo}$ via the Reynolds equation, and this is the approach adopted for configuration state identification when using the Reynolds equation. However, since reliance on the Reynolds equation is to be avoided, additional measurements are in order. The current identification approach assumes that one can measure with sufficient accuracy the slopes of the deformed rotor centreline in both the XY and XZ planes at any two of the bearings. Hence, if the connection DOFs in Eq. (23) are increased to 12 by including the above-mentioned slopes as measurements (the corresponding transmitted moments will be zero) one has the requisite number of equations. Extension of the concept to more than four bearings is straightforward. Note that this need to also measure slopes is potentially a significant shortcoming of this alternative identification technique, as the instrumentation needed to achieve this (e.g., displacement transducers on both sides of the bearings) may not normally be present in existing

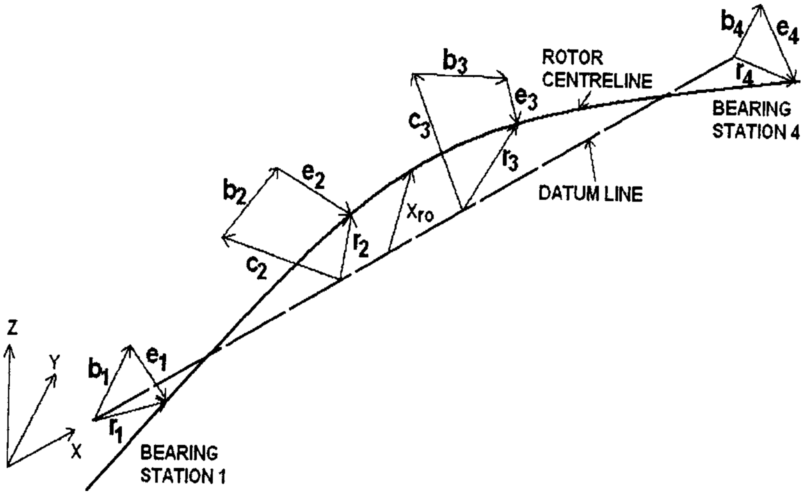

Fig. 2 Location of the bearing centers with respect to the deformed rotor centreline

turbomachinery. Also, to achieve desired accuracy, datum measurements may need to be made at the time of rotor installation [18].

Results and Discussion

Numerical experiments were carried out to illustrate the applicability of these alternative identification techniques. The experiments involved selecting fictitious RBFSs that exhibited the salient problematic features likely to be encountered in practical systems. Short circular bore hydrodynamic journal bearings were used to provide the typical type of nonlinearity common to hydrodynamic bearings. The system response was generated numerically, using harmonic balance software [19]. These responses then served as the "measurements" from which the respective parameters were identified. Such experiments served first to prove in principle the applicability of the proposed identification techniques; in such cases, the measurements retained many more significant digits than one could hope to achieve in actual measurements. Then, by truncating the measurements to one, two, or three significant digits, one could assess the sensitivity of the identification techniques to truncation errors inherent in actual measurements.

Foundation Identification: Results

Figure 3 is a schematic of a fictitious RBFS used for numerical foundation identification experiments. Required is the solution for **N** using Eq. (22). For the pedestal model used (i.e., 1 DOF in each lateral direction), all the mass, damping, and stiffness matrices are diagonal so that the pedestals are decoupled from each other and decoupled in the two lateral directions. Thus, one has for each lateral direction

$$-\Delta f_{bs}^{c}=(-\Omega^{2}M_{p}+j\Omega C_{p}+K_{p})\Delta x_{p}^{c} \tag{29}$$

Since the Δx_{ps}^{c} and Δf_{bs}^{c} involve both magnitude and phase, Eq. (29) embodies two simultaneous equations for the three unknowns K_p, C_p, and M_p. Hence, the minimum number of speeds at which measurements are required is two. Response data were generated at speeds of $\Omega=100$, 200, 300, 400, and 500 rad/s, and the pedestal parameters K_{py}, K_{pz}, C_{py}, C_{pz}, M_{py}, and M_{pz} were identified by least-squares regression analysis using both seven- and two-digit measurement accuracy. The identification results are summarized in Table 1. The perfect identification achieved with seven-digit measurement accuracy proves that the approach is sound in principle. It can be seen that even with two-digit measurement accuracy, excellent accuracy in identified

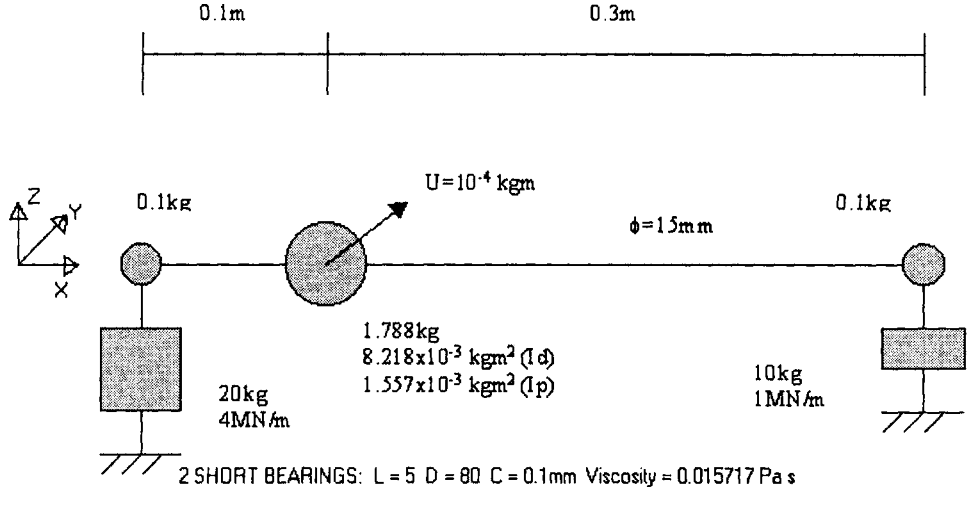

Fig. 3 Schematic of RBFS used for numerical experiments on foundation identification

Table 1 Numerically identified pedestal parameters using current approach (L: left bearing; R: right bearing)

	K_{py}	K_{pz}	C_{py}	C_{pz}	M_{py}	M_{pz}
	(MN/m)		(Ns/m)		(kg)	
(L)	4.0000	4.0000	0.0	0.0	20.000	20.000
Actual						
(R)	1.0000	1.0000	0.0	0.0	10.000	10.000
(L)	3.9985	3.9985	0.8	0.8	19.992	19.992
7 digits						
(R)	0.9994	0.9994	0.9	0.9	9.994	9.994
(L)	3.9910	3.9944	29.1	−0.6	19.945	19.948
2 digits						
(R)	0.9921	0.9949	−7.4	−4.1	9.906	9.962

Table 3 Numerically identified unbalance state with two-digit measurement accuracy

	Actual		Current		Reynolds	
DOF	u [g mm]	θ deg	u [g mm]	θ deg	u [g mm]	θ deg
5	200.0	180.0	199.2	180.0	196.7	178.7
6			199.7	179.1	205.5	178.2
9	400.0	90.0	400.2	90.1	404.6	90.6
10			403.8	90.0	394.2	88.8
13	316.2	18.4	315.7	18.3	318.5	17.7
14			315.3	18.0	309.4	19.5

results is still maintained. Numerical experiments gave similarly good identification results when the Reynolds equation was used to calculate the bearing forces [13]. However, the superior results obtainable with the current approach are clearly demonstrated in Table 2, which summarizes the results obtained using both the current approach and that using the Reynolds equation when identifying the pedestal of the flexibly supported bearing in a simple three-disk experimental rotor rig. Full details are given in Refs. [12] and [14].

Unbalance State Identification: Results

Figure 4 is a schematic of the fictitious RBFS used for numerical unbalance state identification experiments. Required is the determination of the unbalance mass moments at the three disks. Measurements here are assumed to be restricted to the bearing locations and the corresponding pedestal support locations (i.e., $q=4$), so that Eq. (15) yields eight equations per balance speed. Normally, each unknown unbalance results in two unknowns. However, unbalance force input to the in-house harmonic balance software, used to generate the system responses, is achieved as a special case of simultaneous sinusoidal excitation to the two transverse DOFs at a particular unbalance location, with unbalance excitation being achieved by inputting excitations of the same amplitude, but 90 deg out of phase. Since the program still regards the excitations as totally unrelated, they are treated and identified independently, so that at each unbalance location there are four unknowns to be identified, giving a total of 12 unknowns. Hence, data from at least two balance speeds are required. Actually, balance speeds of 4500, 6500, and 8500 rpm were used in conjunction with least-squares regression to determine the unbalance. With nine-digit measurement accuracy, the identified unbalance excitations agreed to within 0.1 g mm in amplitude and to within 0.1 deg in direction for both the current identification approach and the identification approach using the Reynolds equation. Both identification approaches are clearly correct in principle. Table 3 lists the unbalance identification results with two-digit measurement accuracy. The slightly poorer identification results when using the Reynolds equation are probably due to the increased data processing requirements. Full details are given in Ref. [16].

Table 2 Experimentally identified pedestal parameters

	K_{py}	K_{pz}	C_{py}	C_{pz}	M_{py}	M_{pz}	ω_y	ω_z
	(MN/m)		(Ns/m)		(kg)		(Hz)	
Actual	0.2830	0.2714	⋯	⋯	3.047	3.047	48.5	47.5
Current	0.2692	0.2748	225	80	2.810	3.053	49.3	47.8
Reynolds	0.1594	0.3735	−130	−129	1.561	4.651	50.9	45.1

No laboratory experiments have yet been carried out to compare this current unbalance identification approach to that which uses the Reynolds equation. However, it is expected that, provided the foundation motions are large enough to provide noise-free signals to two-digit accuracy, superior unbalance identification will result with the current approach.

Configuration State Identification: Results

Figure 5 is a schematic of the fictitious RBFS used for numerical configuration state identification experiments. It corresponds to the BA combination analyzed in Ref. [4], except the bearings here are flexibly supported. Table 4 summarizes the relevant system dimension and properties used as input data for generating the

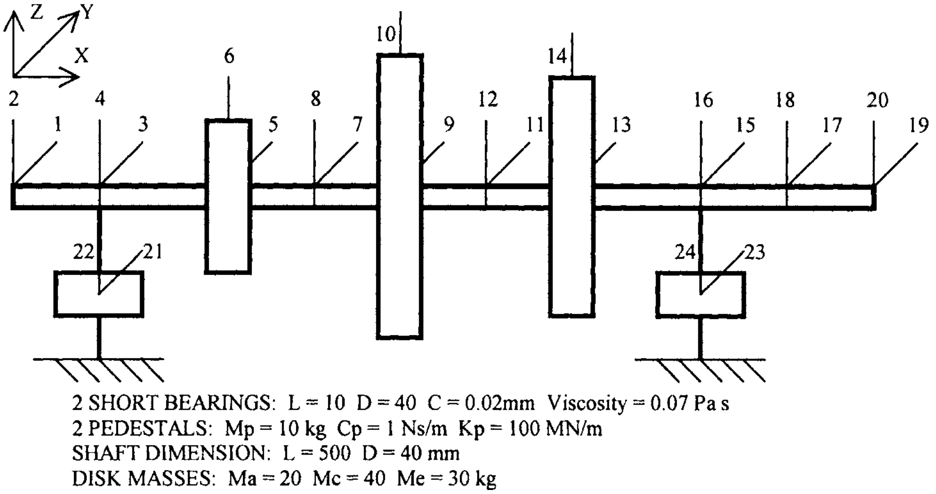

Fig. 4 Schematic of RBFS used for numerical experiments on unbalance state identification (disk masses from left to right are 20, 40, and 30 kg, respectively)

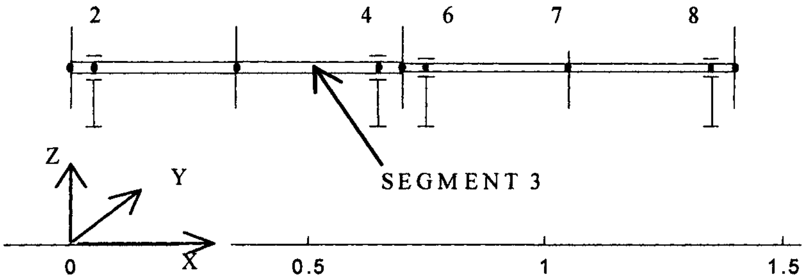

Fig. 5 Schematic of RBFS used for numerical experiments on configuration state identification

measurements. Response data were generated at 80 and 200 rad/s for both balanced and unbalanced rotors. With seven-digit measurement accuracy, the identified parameters agreed with the actual configuration state to within 0.03 μm for both the current approach and that using the Reynolds equation, proving that both identification techniques were sound in principle.

Table 5 lists the identifications obtained with the current approach using three- and one-digit measurement accuracy. Table 6 lists the identifications obtained with the Reynolds equation using three-digit measurement accuracy, as well as no measurement inaccuracy but a 1% error in estimating the running bearing clearance [7]. The three-digit measurement accuracy results indicate superior identification with the current technique over that obtained using the Reynolds equation. It is, however, uncertain whether slopes can be measured in practice to such accuracy, so one-digit measurement accuracy results are also obtained for the current technique. While there results a significant decrease in identification accuracy, the identification is still superior to that obtained using the Reynolds equation when there is no measurement error but a 1% error in estimating the running bearing clearance [7]. The current approach is likely to give superior identification to that using the Reynolds equation, and provided errors in measuring the slope can be kept sufficiently low, the current approach promises to provide believable configuration state identification in practice.

Table 4 Input data for numerical experiments on configuration state identification

Segment	ROTOR Diameter (m)	Length (m)
1, 4	0.02	0.05
2, 3	0.02	0.3
5, 8	0.015	0.05
6, 7	0.015	0.3

Density: 7850 kg/m^3
Young's Modulus: 200 GPa
Unbalance: 0.000 kg m or 0.001 kg m at node 7
BEARING
Diameter: 0.036 m
Length: 0.018 m
Radial Clearance: 90×10^{-6} m
Mean Viscosity: 0.014 Pa·s
PEDESTAL
M_y, M_z: 100 kg
C_y, C_z: 10^5 Ns/m
K_y, K_z: 10^7 N/m
CONFIGURATION STATE (c_y,c_z)
Bearing Station 1: (0,0)
Bearing Station 2: (+0.65,−1451.34) μm
Bearing Station 3: (−90.65,−1601.27) μm
Bearing Station 4: (0,0)

Figure 6 is a three-dimensional view of a four-bearing test rig designed to run up to 3000 rpm. Load cells are attached to the flexible bearing supports to enable the transmitted forces to be measured. Changes in the configuration state can be introduced at the two inboard bearings. The bearing shells of the four circumferentially grooved journal bearings are free to pivot in the bearing housing, minimizing angular misalignment effects, and the flexible bearing supports are fixed to a rigid concrete block that is isolated from floor vibrations by air springs. Full details of this rig are given in Ref. [20]. Preliminary results indicate that errors in configuration state identification using the current approach are of the order of 20 μm, whereas those obtained using the Reynolds

Table 5 Numerically identified configuration state obtained by current approach [(a) three-digit measurement accuracy, (b) one-digit measurement accuracy;* balanced,$^+$unbalanced]

	c_{y2} [μm]		c_{y3} [μm]		c_{z2} [μm]		c_{z3} [μm]	
Speed [rad/s]	(a)	(b)	(a)	(b)	(a)	(b)	(a)	(b)
80*	0.72	−5.26	−90.41	−92.10	−1451.92	−1382.79	−1601.73	−1584.40
200*	0.42	−9.26	−90.70	−92.10	−1452.21	−1372.79	−1601.94	−1584.40
80$^+$	0.53	−5.26	−90.71	−92.10	−1452.08	−1382.79	−1601.87	−1584.40
200$^+$	0.54	−6.26	−90.53	−92.10	−1452.62	−1382.79	−1602.77	−1584.40

Table 6 Numerically identified configuration state using Reynolds equation ((a) three-digit measurement accuracy, (b) 1% error in running clearance; seven-digit measurement accuracy; *balanced,$^+$unbalanced)

	c_{y2} [μm]		c_{y3} [μm]		c_{z2} [μm]		c_{z3} [μm]	
Speed [rad/s]	(a)	(b)	(a)	(b)	(a)	(b)	(a)	(b)
80*	+5.18	+89.68	−85.65	+7.18	−1457.51	−1868.61	−1608.00	−2052.40
200*	−6.04	+70.07	−97.96	−14.21	−1445.81	−1745.74	−1595.35	−1919.63
80$^+$	+1.77	+92.89	−89.44	+10.66	−1453.22	−1873.80	−1603.32	−2058.02
200$^+$	+2.11	+79.24	−89.08	−4.14	−1451.83	−1773.54	−1601.81	−1949.36

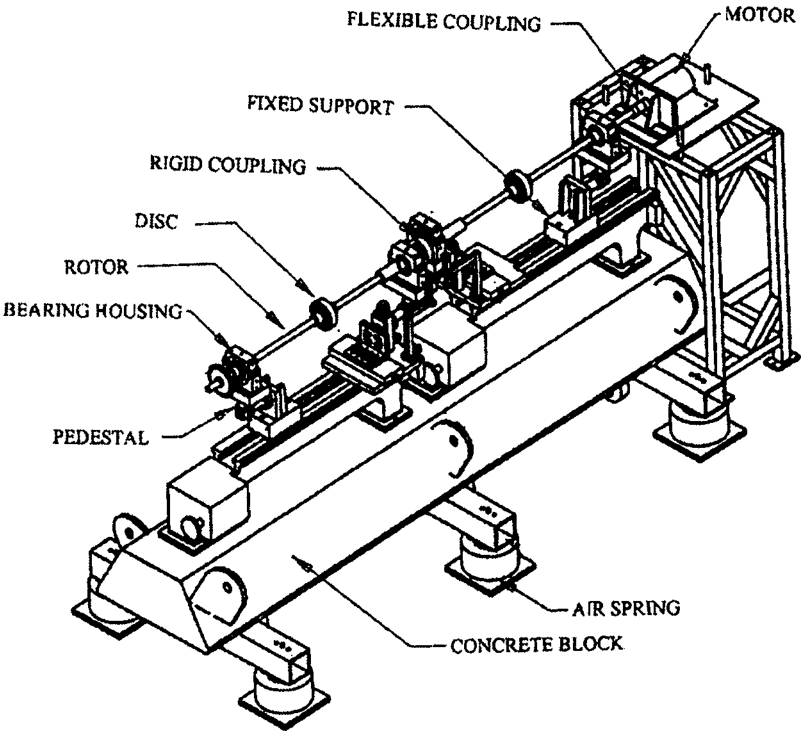

Fig. 6 Experimental RBFS rig for identifying the configuration state

equation appear to be significantly higher. Since the radial clearances of the test rig bearings are approximately 100 μm, these results suggest that the current method for configuration state identification is practically feasible and useful though further investigation is needed to establish the viability of measuring the slope sufficiently accurately. Full details of these tests and of the associated data processing are given in Ref. [18].

Conclusions

Provided the unbalance response of an RBFS is periodic at some speeds and one has a good model of the rotor, it is possible, in theory, to identify the foundation and then the unbalance state and/or the configuration state, provided appropriate journal eccentricities and bearing housing motions are measured over a period at a sufficient number of speeds. Such identification is possible even if the bearing reaction forces are nonlinear functions of the relative motion between the rotor journals and the corresponding bearing housings.

Such identification can use the Reynolds equation to evaluate the bearing reaction forces. Alternatively, reliance on the Reynolds equation can be avoided by the current approaches by adding a known unbalance and repeating measurements at the same speed in the case of foundation identification, utilizing bearing housing motion measurements in the case of unbalance state identification, and utilizing rotor slope measurements in the case of configuration state identification.

Numerical experiments indicate that satisfactory identification of foundation parameters, unbalance state, and configuration state is possible with measurement accuracies attainable in the laboratory, regardless of whether one uses the Reynolds equation or not, though configuration state identification using the Reynolds equation deteriorates significantly if there is error in the assumed running clearance.

Preliminary laboratory experiments indicate that satisfactory foundation and configuration state identification results can be obtained by the current approaches and that these results appear to be superior to those obtained using the Reynolds equation approaches.

Acknowledgments

This research was partly sponsored by the Australian Research Council, Pacific Power International, and Sigma Processing Solutions.

Nomenclature

$\mathbf{A}, \mathbf{B}, \mathbf{D}, \mathbf{E}$ = partition matrices defined by Eq. (14)
$\mathbf{b}$ = vector of the mean displacement of the bearing housings
$\mathbf{b}_i$ = mean displacement of ith bearing housing
$\mathbf{C}, C$ = damping and gyroscopic matrix, element therein
$\mathbf{c}_i$ = location of ith unloaded bearing housing
$\mathbf{e}_i$ = mean journal eccentricity at ith bearing
$\mathbf{F}$ = force vector
$\mathbf{f}, f$ = force frequency component vector, element therein
$\mathbf{H}$ = dynamic stiffness matrix
$\mathbf{I}, \mathbf{J}, \mathbf{L}, \mathbf{N}$ = partition matrices defined by Eq. (16)
$\mathbf{K}, K$ = stiffness matrix, element therein
k = order of harmonic
$\mathbf{M}, M$ = mass matrix, element therein
n = highest order harmonic
$\mathbf{P}, \mathbf{Q}, \mathbf{R}, \mathbf{S}$ = partition matrices defined by Eq. (25)
q = number of rotor connection degrees of freedom
$\mathbf{r}_i$ = location of rotor centreline at ith bearing station as measured from datum line in Fig. 2
s = harmonic order of synchronous component
$\mathbf{T}, \mathbf{U}, \mathbf{V}, \mathbf{W}$ = partition matrices defined by Eq. (23)
t = time
$\mathbf{X}, X$ = displacement vector, element therein
$\mathbf{x}, x$ = displacement frequency component vector, element therein
Ω = rotor speed
ω = fundamental frequency of steady state solution

Superscripts (if not otherwise defined)

$\cdot$ = differentiation with respect to time t
c = connection degree of freedom
f = free (nonconnection) degree of freedom

Subscripts (if not otherwise defined)

b = bearing
e = external
o = zero-order harmonic or mean value
p = foundation or pedestal
r = rotor
u = unbalance
y, z = horizontal and vertical directions, respectively

References

[1] Lund, J. W., and Tonnesen, J., 1972, "Analysis and Experiments on Multi-Plane Balancing of a Flexible Rotor," ASME J. Eng. Ind., **94**, pp. 233–242.
[2] Feng, N. S., and Hahn, E. J., 1996, "Using Vibration Analysis Software to Balance Turbomachinery," Mech. Eng. Trans., IEAust, **21**, pp. 147–155.
[3] Chen, P. Y. P., Feng, N. S., and Hahn, E. J., 2001, "Flexible Rotor Balancing Taking Bearing Non-Linearity Into Account," ASME Paper No. DETC2001/VIB-21380.
[4] Hori, Y., and Uematsu, R., 1980, "Influence of Misalignment of Support Journal Bearings on Stability of a Multi-Rotor System," Tribol. Int., **13**, pp. 249–252.
[5] Feng, N. S., and Hahn, E. J., 1998, "Vibration Analysis of Statically Indeterminate Rotors With Hydrodynamic Bearings," ASME J. Tribol., **120**, pp. 781–788.
[6] Krodkiewski, J. M., and Ding, J., 1993, "Theory and Experiment on a Method for On-Site Identification of Configurations of Multi-Bearing Rotor Systems," J. Sound Vib., **164**, pp. 281–293.
[7] Hu, W., Feng, N. S., and Hahn, E. J., 2004, "A Comparison of Techniques for Identifying the Configuration State of Statically Indeterminate Rotor Bearing Systems," Tribol. Int., **37**, pp. 149–157.
[8] Lees, A. W., Friswell, M. I., Smart, M. G., and Prells, U., 1998, "The Identification of Foundation Vibration Parameters From Running Machine Data," *Proc. of 7th Int. Symposium on Transport Phenomena and Dynamics of Rotating Machinery*, Honolulu, pp. 715–724.
[9] Diana, G., Cheli, F., and Vania, A., 1988, "A Method to Identify the Foundation Modal Parameters Through Measurements of the Rotor Vibrations," *Proc. 4th Int. Conference on Vibrations in Rotating Machinery*, IMechE, Edinburgh, pp. 217–222.
[10] Vazquez, J. A., and Barret, L. V., 1996, "Representing Flexible Support by Polynomial Transfer Functions," ASME Paper No. 96-GT-27.
[11] Smart, M., Friswell, M. I., Lees, A. W., and Prells, U., 1998, "Estimating Turbogenerator Foundation Parameters," Proc. Inst. Mech. Eng., Part C: J. Mech. Eng. Sci., **22**, pp. 653–665.
[12] Feng, N. S., and Hahn, E. J., 2001, "Identification of Pedestal Parameters in Rotor Bearing Systems Using Known Unbalance," ASME Paper No. DETC2001/VIB-21553.
[13] Feng, N. S., and Hahn, E. J., 1998, "On the Use of Linearised Hydrodynamic Bearing Force Coefficients for Foundation Identification Purposes," *Proc. of 5th Int. Tribology Conference*, AUSTRIB '98, Brisbane, pp. 383–387.
[14] Feng, N. S., and Hahn, E. J., 2000, "Experimental Evaluation of Linear and Non-Linear Pedestal Identification," *Proc. of ISMA25, Noise and Vibration Engineering Conference*, Leuven, pp. 877–883.
[15] Pham, D., Feng, N. S., and Hahn, E. J., 2003, "The Effect of the Lubricant Supply Situation on the Vibration Behavior of Rotor Bearing Systems," *Proc. of 10th Int. Congress on Sound and Vibration*, Stockholm, pp. 3597–3604.
[16] Chen, P. Y. P., Feng, N. S., and Hahn, E. J., 2002, "On the Balancing of Non-Linear Rotor Bearing Foundation Systems," *Proc. of 9th Int. Symposium on Transport Phenomena and Dynamics of Rotating Machinery*, Honolulu.
[17] Feng, N. S., and Hahn, E. J., 1995, "Including Foundation Effects on the Vibration Behavior of Rotating Machinery," Mech. Syst. Signal Process., **9**, pp. 243–256.
[18] Hu, W., 2004, "On Identifying the Configuration State of Rotor-Bearing-Pedestal Systems," Ph.D. thesis, UNSW.
[19] Hahn, E. J., and Chen, P. Y. P., 1994, "Harmonic Balance Analysis of General Squeeze Film Damped Multi-Degree-of-Freedom Rotor Bearing Systems," ASME J. Tribol., **116**, pp. 499–507.
[20] Miah, H., 2002, "An Experimental Rig to Study Lateral Misalignment Effects in Rotor Bearing Pedestal Systems," M.E. thesis, UNSW.

Perturbations Methods in Structural Dynamics and Applications to Cyclic Symmetric Domains

Bernard Lalanne
TURBOMECA,
64511 Bordes, France
e-mail: bernard.lalanne@turbomeca.fr

The design of components must take into account the irregularities inherent to the manufacturing process. When the structures have close eigenvalues, small mass and stiffness variations or the damping generate strong variations of the eigenmodes: these structures are then not robust. Here, their dynamics has been analyzed by perturbation method, in the dissipative cases and with coupling within a light fluid. A new perturbation method allows first order developments whatever the spectral density may be. Applications to many different vibration problems are presented: aeroelasticity, mode veering problem, maximum amplitude of forced response in cyclic symmetric domains, with detuning and/or mistuning, i.e., the most important reliability problem in turbomachinery. The results of this study provide a new estimation of the amplification factor and damping due to mistuning and aerodynamic coupling. [DOI: 10.1115/1.1924430]

1 Introduction

In structural dynamics, the formulation and associated developments of the discrete model describing a conservative system take a preponderant place. Multiple eigenvalues may exist in structures exhibiting specific symmetry conditions, such as axisymmetry and cyclic symmetry, or independence/uncoupledness. Such structures are widely encountered in rotating machines, e.g., gears, compressors, and turbines, where they are also often immersed in a fluid.

The definition of the eigenmodes becomes arbitrary when they are associated with multiple eigenvalues. Vibration control requires the prediction of the vibration amplitude but the forced response and stability of the system are very sensitive to any symmetry breaking, as explained in [1]. Such symmetry breaking induced by the manufacturing tolerances will here be referred to as “mistuning” or detuning if it is intentional.

This symmetry breaking induces a unique definition of the eigenmodes at contrary of the multiple eigenvalues case, but leads to insufficiently robust configurations, as they are sensitive to small parameters.

In this study, we start from the conservative system corresponding to a structure in vacuum. The system will be perturbed by small mass and stiffness variations or by the introduction of damping. These perturbations will be of any kind. Since the perturbed matrices will not necessarily be symmetrical, we will be able to deal with any weakly coupled multiphysical problem as encountered for example in aeroelasticity.

In classical perturbation methods [2], eigenvalues and eigenvectors variations are assumed to be small. Obviously, these methods become inappropriate if the eigenvalues are multiple. As a matter of fact, the corresponding natural modes of the perturbed system are obtained as a small variation of a particular combination of the eigenmodes corresponding to the multiple eigenvalues of the tuned conservative system [2]. Thus, the forced response will be strongly dependent on the rupture of symmetry. Wei and Pierre [3] proposed a different approach in the case of structures with cyclic symmetry and composed of N quasi-independent sectors, i.e., exhibiting a weak mechanical coupling. In the tuned and uncoupled case, the multiplicity of the eigenvalues is equal to the number of sectors N. The natural modes of the perturbed system are therefore a small variation of a particular combination in an eigen subspace of dimension N. To avoid this difficulty, Wei and Pierre consider the mistuned coupled structure to be a small perturbation of the uncoupled mistuned structure. The mechanical coupling is then the perturbation. However, the resulting perturbation methods [2,3], which differently deal with the cases of simple and multiple eigenvalues, are not applicable in the general case when the spectral density is high.

In the present approach, the natural modes of the mistuned fluid-structure domain will be obtained through a decomposition in the complete basis of the eigenmodes of the tuned conservative structure. Only the perturbations of the eigenvalues will be considered as small. The resulting system of equations describing these perturbations is nonlinear but a neighborhood condition, related to the spectral density, makes it possible to define what eigenmodes will contribute to each of the mistuned natural modes. The effects of the perturbations on the damping, stability, natural modes, and forced response are analyzed. The difficulty of prediction due to the sensitivity to small parameters is the image of the poor robustness of these structures. It is worth noting that the rupture of symmetry is a current concern in physics, as described by Nobel price winner Cohen Tannoudji [4].

2 Conservative System

The dynamics of the discretized structure is classically described by the following equation:

$$\mathbf{M}\ddot{\mathbf{q}} + \mathbf{K}\mathbf{q} = \mathbf{f} \tag{1}$$

$\mathbf{M},\mathbf{K}$ positive symmetric matrices of dimension $\hat{n}$

The eigenvectors $\mathbf{x}_{(r)}$ and the eigenfrequencies ω_{0r} satisfy the following:

$$\mathbf{x}_{(s)}^T\mathbf{K}\mathbf{x}_{(r)} = \omega_{0r}^2\delta_{rs}\mu_r \tag{2}$$

$$\mathbf{x}_{(s)}^T\mathbf{M}\mathbf{x}_{(r)} = \delta_{rs}\mu_r \tag{3}$$

where μ_r and ω_{0r}^2 are the generalized mass and eigenfrequency associated with the eigenvector $\mathbf{x}_{(r)}$. In the cases of structures with

---

Contributed by the Structures and Dynamics Division of THE AMERICAN SOCIETY OF MECHANICAL ENGINEERS for publication in the ASME JOURNAL OF ENGINEERING FOR GAS TURBINES AND POWER. Manuscript received by the S&D Division August 8, 2002; final revision received December 13, 2004. Editor: M. Mignolet.

symmetry, some eigenfrequencies can be repeated and the corresponding modes will be selected to satisfy the orthogonality condition, Eq. (2). In turbomachinery applications, the components in the flow path are generally designed according to cyclic symmetry. Then, most of their modes appear in pair in the ideal tuned case. According to [5], either the stationary or the rotating wave modal base can be used to analyze the dry structure. With fluid coupling, however, the solution of these periodic equations is, according to Floquet theorem, best described in rotating waves. Therefore, the rotating wave modal base will be adopted here as well for the conservative structure. Aeroelastic forces, damping, and any variation of this perfect model will be considered later as perturbations to the cyclic symmetric conservative structure.

To illustrate this perfect model, consider a bladed disk model with a stiff disk, i.e. with a weak coupling between adjacent sectors. Then, any coupling between adjacent sectors, whatever its origin may be (elastic or aerodynamic), will be considered as a perturbation.

3 Perturbed System

The mass and stiffness matrices are first perturbed in the conservative system, then a "damping" matrix is introduced; these perturbations are assumed to be small, but the symmetry of perturbed matrices is not required. This choice will allow us to obtain solutions for the dissipative system and for the weakly coupled system.

$$[\mathbf{M}+\mathbf{\Delta M}]\ddot{\mathbf{q}}+\mathbf{C}\dot{\mathbf{q}}+[\mathbf{K}+\mathbf{\Delta K}]\mathbf{q}=\mathbf{f}$$

$$\mathbf{M},\mathbf{K}, \quad \text{positive symmetric matrices of dimension } \hat{n} \tag{4}$$

$$\mathbf{C},\mathbf{\Delta M},\mathbf{\Delta K} \quad \text{general matrices of dimension } \hat{n}$$

In the case of a "light fluid" coupling and with low "damping," both aerodynamic and dissipative forces are ignored with respect to the mechanical forces except in the neighborhood of resonance where the latter vanish. The component of the aerodynamic and dissipative forces in phase with the displacement acts as stiffness and the component in quadrature of phase as damping.

4 Perturbation Method

The kth natural mode and its eigenvalue are obtained through a decomposition in the complete modal basis using a first order perturbation method. Specifically, the natural mode of eigenvalue $j\omega_{0k}+\Delta\lambda_k$ will be expressed as

$$\mathbf{z}_{(k)}=\sum_r \eta_k^r\mathbf{x}_{(r)}; \quad \eta_k^k=1 \tag{5}$$

where η_k^r denotes the modal perturbations.

To first order in the perturbation, Eq. (4) becomes

$$(j\omega_{0k}\mathbf{C}+2j\omega_{0k}\Delta\lambda_k\mathbf{M}+\mathbf{K}+\Delta\mathbf{K}-\omega_{0k}^2(\mathbf{M}+\Delta\mathbf{M}))\sum_{r\neq k}\boldsymbol{\eta}_k^r\mathbf{x}_{(r)}$$
$$+(j\omega_{0k}(\mathbf{C}+2\Delta\lambda_k\mathbf{M})+\Delta\mathbf{K}-\omega_{0k}^2\Delta\mathbf{M})\mathbf{x}_{(k)}\approx 0 \tag{6}$$

Multiplying Eq. (6) to the left by $\mathbf{x}_{(k)}^T$ yields the small perturbation of the eigenvalue

$$\Delta\lambda_k\approx\frac{-\sum_r \eta_k^r\gamma_{kr}}{2\mu_k j\omega_{0k}} \text{ with } \gamma_{mn}=k_{mn}-\omega_{0k}^2m_{mn}+j\omega_{0k}\beta_{mn}$$
$$\text{with } \eta_k^k=1;\ m_{lk}=\mathbf{x}_{(l)}^T\mathbf{\Delta M}\mathbf{x}_{(k)};\ \beta_{lk}=\mathbf{x}_{(l)}^T\mathbf{C}\mathbf{x}_{(k)};\ k_{lk}=\mathbf{x}_{(l)}^T\mathbf{\Delta K}\mathbf{x}_{(k)} \tag{7}$$

The above relationship, Eq. (7), is both an approximation and a generalization of the Rayleigh's quotient.

Multiplying Eq. (6) to the left by $\mathbf{x}_{(l)}^T$ yields similarly a system of equations for the modal perturbations, i.e. the coefficients η_k^l of the decomposition of the perturbation of the mode k, see Eq. (5),

$$(\eta_k^l)\left(\frac{\mu_l}{\mu_k}\left(\sum_r \eta_k^r\gamma_{kr}\right)+\mu_l(\omega_{0k}^2-\omega_{0l}^2)\right)-\left(\sum_r \eta_k^r\gamma_{lr}\right)=0$$
$$l\neq k; \quad \text{with } \eta_k^k=1; \quad \gamma_{mn}=k_{mn}-\omega_{0k}^2m_{mn}+j\omega_{0k}\beta_{mn} \tag{8}$$

Note that this system of equations is nonlinear in the coefficients η_k^l. If the perturbation of the eigenmodes is small, the quadratic terms—maybe even the linear ones—can be neglected. The participation of one mode in the decomposition of the perturbation of another depends on the "proximity" of these two modes. The two modes s and k will be said to be distant from each other if

$$(\omega_{0k}\beta_{sk})^2\ll\mu_s^2(\omega_{0k}^2-\omega_{0s}^2)^2-(k_{sk}-\omega_{0k}^2m_{sk})^2 \tag{9}$$

This condition implies a small modal perturbation coefficient η_k^s. Further, it involves the split between the corresponding natural frequencies as well as the mass, stiffness and damping cross terms. Thus, spectral density and cross terms are pertinent factors in the proximity of two modes.

On the basis of Eq. (9), it is possible to determine the ensemble of modes $\{s,k\}$, and the subspace they form, which are neighbor to mode k. The uniqueness of the perturbation does not exist with the nonlinear equation (8), except if the modes are distant according to Eq. (9). Note further that the perturbed modes of conservative systems must satisfy the conditions of orthogonality. However, these conditions can only be satisfied if the perturbed eigenvectors are determined together. It is therefore necessary to return to the determination of the eigenvalues and eigenvectors but restricted to the subspace of the neighbors of mode k, i.e., of the modes $\{s,k\}$.

To this end, note first that Eq. (1) can be written in modal basis as

$$\boldsymbol{\mu}\ddot{\mathbf{r}}+\boldsymbol{\omega}^2\boldsymbol{\mu}\mathbf{r}=\mathbf{0} \tag{10}$$

where $\boldsymbol{\mu}$ and $\boldsymbol{\omega}^2\boldsymbol{\mu}$ are diagonal matrices of elements equal to μ_l and $\omega_{0l}^2\mu_l$, respectively. Further, r_l denotes the generalized coordinate associated with the mode l. In each subspace of the modes $\{s,k\}$ in the neighborhood of k, the perturbed system is governed by

$$(\tilde{\boldsymbol{\mu}}+\tilde{\mathbf{X}}^{\mathrm{T}}\mathbf{\Delta M}\tilde{\mathbf{X}})\ddot{\tilde{\mathbf{r}}}+(\tilde{\mathbf{X}}^{\mathrm{T}}\mathbf{C}\tilde{\mathbf{X}})\dot{\tilde{\mathbf{r}}}+(\boldsymbol{\omega}^2\tilde{\boldsymbol{\mu}}+\tilde{\mathbf{X}}^{\mathrm{T}}\mathbf{\Delta K}\tilde{\mathbf{X}})\tilde{\mathbf{r}}=\mathbf{0} \tag{11}$$

The matrices $\tilde{\boldsymbol{\mu}}$ and $\omega^2\tilde{\boldsymbol{\mu}}$ are the restrictions, according to Eq. (9), of the perturbed system. The matrix $\tilde{\mathbf{X}}$ is similarly the restriction to the subspace $\{s,k\}$ of the eigenvectors matrix $\mathbf{X}=\lfloor\mathbf{x}_{(l)}\rfloor$, $l\in\{s,k\}$. The solution of Eq. (11) which can be expressed in the form $\tilde{\mathbf{r}}_l=\tilde{\boldsymbol{\eta}}_l e^{\lambda t}$ with $\tilde{\boldsymbol{\eta}}_l=\lfloor\tilde{\eta}_l^r\rfloor$ yields the natural modes of the perturbed system in the subspaces composed of neighboring modes as

$$\|\Delta\lambda_k\|=\min_l\|\tilde{\lambda}_l-j\omega_{0k}\|$$
$$\eta_k^r=\frac{\tilde{\eta}_l^r}{\tilde{\eta}_l^k} \tag{12}$$
$$\mathbf{z}_{(k)}=\sum_{r\in\{s,k\}}\eta_k^r\mathbf{x}_{(r)}$$

Note that the orthogonality of these perturbed modes in the subspace with respect to the modes not belonging to the subspaces is ensured by definition.

An approximation of the eigenvalue is then obtained from Eq. (7) and the generalized mass is determined as

$$m_k = \sum_r (\eta_k^r)^2 \mu_r \tag{13}$$

Finally, the forced response is obtained by considering the contributions of the generalized forces on the neighboring modes using the perturbations determined as above.

4.1 Application 1: Mode Veering. Consider first time-dependent structures without "damping," dependent on a slowly varying parameter [6]. For such systems, two neighboring eigenmodes k and l may evolve to the point of having equal eigenfrequencies. However, such a crossing can only occur in structures having exhibiting either uncoupledness/independence or an appropriate symmetry. Except in such cases, the coupling by a cross term γ_{kl} leads to veering. Accordingly, the cross term will be considered as the perturbation. The corresponding perturbation of the mode k by the mode l can then be obtained from Eq. (8) as

$$\eta_k^l\left(\frac{\mu_l}{\mu_k}\left(\sum_r \eta_k^r \gamma_{kr}\right) + \mu_l(\omega_{0k}^2 - \omega_{0l}^2)\right) - \left(\sum_r \eta_k^r \gamma_{lr}\right) = 0$$

$$l \neq k; \quad \text{with } \eta_k^k = 1; \quad \gamma_{mn} = k_{mn} - \omega_{0k}^2 m_{mn};\ r = k \ or \ l \tag{14}$$

The perturbation of the mode l by the mode k is obtained similarly by switching the indices l and k. Without lack of generality, the norm the eigenmodes $\mathbf{x}_{(k)}$ and $\mathbf{x}_{(l)}$ will be selected so that the corresponding generalized masses of the non perturbed system are equal, that is $\mu_l = \mu_k$. Then, the perturbations of the eigenmodes are of opposite sign while satisfying the conditions of orthogonality. From the solutions of the quadratic Eq. (14), one introduces next $\tan(\theta) = \eta_k^l = -\eta_l^k$.

The perturbed eigenmodes, after normalization and multiplication by $\cos\theta$, can then be represented as

$$\hat{\mathbf{z}}_{(k)} = \mathbf{z}_{(k)} \cos\theta = \mathbf{x}_{(k)} \cos\theta + \mathbf{x}_{(l)} \sin\theta$$

$$\hat{\mathbf{z}}_{(l)} = \mathbf{z}_{(k)} \cos\theta = -\mathbf{x}_{(k)} \sin\theta + \mathbf{x}_{(l)} \cos\theta \tag{15}$$

They are therefore obtained by a rotation of the nonperturbed eigenvectors; the rotation angle is linked with the perturbed eigen frequencies ω_k' and ω_l' by

$$\sin^2\theta \approx \frac{1}{2}\left(1 - \sqrt{1 - \frac{4(\gamma_{kl})^2}{((\omega_k')^2 - (\omega_l')^2)^2}}\right) \tag{16}$$

In case of a crossing (i.e., of a double eigenvalue), the combination of modes is achieved in the eigen subspace and the perturbed eigenvalues given by Eq. (7) depend on the perturbation of the eigenvector. The maximum proximity of the eigenvalues provides an estimate of the cross term γ_{kl} as

$$\min\{(\omega_k')^2 - (\omega_l')^2\} \cong 2\gamma_{kl} \tag{17}$$

5 Aeroelasticity

The aeroelasticity of structures having two modes with close natural frequencies is investigated next. These modes can represent the bending and torsion of an aircraft wing, or, for structures with cyclic symmetry, mistuned twin modes or two neighbor rotating waves [5].

With the assumption of light fluids, the aeroelastic forces are negligible, except in the vicinity of any resonance. In the case of neighbor eigen frequencies, we know, according to [5], that this situation is favorable to instability. It is still possible, after a change of basis if necessary, to go back to the following:

$$\ddot{x}_k + \beta_{kk}\dot{x}_k + \beta_{kl}\dot{x}_l + (\omega_{0k})^2 x_k = 0$$

$$\ddot{x}_l + \beta_{ll}\dot{x}_l + \beta_{lk}\dot{x}_k + (\omega_{0l})^2 x_l = 0 \tag{18}$$

The matrix associated with the velocity terms will be referred to as the "damping" matrix, since the system studied is an active system.

5.1 Stability According to Routh's Criterion [5]. Routh's criterion provides a basis to determine the conditions for the stability of the system. Of particular interest here are the stability conditions involving the coupling of both generalized coordinates, i.e.,

$$\left(\frac{\omega_{0l}^2 - \omega_{0k}^2}{2\hat{\omega}}\right)^2 + (\beta_{kk}\beta_{ll} - \beta_{kl}\beta_{lk}) > 0$$

with:

$$(2\hat{\omega})^2 = \frac{\beta_{kk} + \beta_{ll}}{\beta_{kk}\beta_{ll}}(\beta_{kk}\omega_{0l}^2 + \beta_{ll}\omega_{0k}^2) \tag{19}$$

Using the sum of the elastic and kinetic energies as Ljapounov function, it can be shown that the positive definiteness of the "damping" matrix is a sufficient condition for stability. This condition is necessary, according to the inequality of Eq. (19), only if the eigenfrequencies are equal. Note further that the split of the eigenfrequencies increases the stability margin.

5.2 Perturbations Approach. It is now desired to find the perturbations of the eigenvalues and of the eigenvectors corresponding to a small "damping" matrix. When the generalized masses μ_k and μ_l are equal to 1, the perturbation η_k^l of the mode k by the mode l can be evaluated from Eq. (14) as

$$\eta_k^l = \frac{-\beta_{kk} + \beta_{ll} + j\left(\dfrac{\omega_{0k}^2 - \omega_{0l}^2}{\omega_{0k}}\right) - \operatorname{sign}(-\beta_{kk} + \beta_{ll})\sqrt{\left[(-\beta_{kk} + \beta_{ll}) + j\left(\dfrac{\omega_{0k}^2 - \omega_{0l}^2}{\omega_{0k}}\right)\right]^2 + 4\beta_{kl}\beta_{lk}}}{2\beta_{kl}} \tag{20}$$

and the corresponding perturbation of the eigenvalue λ_k can then be found from Eq. (7) as

$$2\Delta\lambda_k = -\beta_{kk} - \eta_k^l \beta_{kl}$$

The conditions for stability in the veering zone are then

$$\Re[\Delta\lambda_k] < 0 \text{ and } \Re[\Delta\lambda_l] < 0$$

where $\Re[\cdot]$ denotes the real part of a complex number. With the above perturbations in eigenvalue, these conditions become

$$\left(\frac{\omega_{0l}^2 - \omega_{0k}^2}{2\omega_{0k}}\right)^2 + (\beta_{kk}\beta_{ll} - \beta_{kl}\beta_{lk}) > 0$$

$$\left(\frac{\omega_{0l}^2 - \omega_{0k}^2}{2\omega_{0l}}\right)^2 + (\beta_{kk}\beta_{ll} - \beta_{kl}\beta_{lk}) > 0 \tag{21}$$

and the exact solution (19) is recovered that the frequencies be close or far from each other. Note again that a small split of the twin modes frequencies improves the stability in a manner similar to that of damping.

5.3 Symmetry Breaking and Passive Flutter Control.

5.3 Symmetry Breaking and Passive Flutter Control. It should be restated that the approximate condition for the stability of the system, Eq. (19), has been equivalently by the perturbation approach. Further, it demonstrates that a split of the conservative system eigenfrequencies, corresponding to symmetry breaking, can give stability to active systems, i.e. those exhibiting a negative definite damping matrix.

On the contrary, eigenfrequencies coming closer to each other or, in the limit, coalescing decreases both the stability and controllability of the system.

When applied to the aeroelasticity of structures with cyclic symmetry, these results imply that: symmetry breaking increases stability when only 1 set of twin modes (one rotating wave) is considered [5]; when two waves (either forward or backward) are considered, minimum stability occurs with veering.

In turbomachinery applications, the passive control of flutter could be achieved by splitting the twin modes of the structure to avoid their combination as an unstable rotating wave. This passive control needs the knowledge of the pattern of the modes, i.e., of their interblade phase angle. This result is not new, see for example [7].

6 Extremum Response in Cyclic Symmetric Domains due to Mistuning

The determination of the extremum response due to mistuning has been investigated for decades but has led to various solutions which are not consistent with respect to each other. Certainly, the solution of this problem depends on the selected model. With the exception of Whitehead [8,9], priority has for many years been given to intensive digital simulations by using either the Monte Carlo methods [10,11] or the statistical approach [12]. The goal here is to resume analytical efforts in a general setting and to rederive previously published results by considering the models used therein.

The tuned system coupled with a light fluid will be considered as the starting point for the analysis. The presence of the light fluid implies aeroelastic terms in phase (additional stiffness) and in quadrature of phase ("damping" terms) with the displacement. These terms are calculated in the neighborhood of the resonances of the conservative system, as their contribution to the dynamics is considerable. The coupling of dual modes at the same frequency, corresponding to a same number of nodal diameters or to a same phase difference index n [5], for which the phase difference between adjacent sectors is $2\pi n/N$. This coupling by nonreciprocal (in the sense of the Betty–Maxwell principle) aeroelastic terms leads to rotating wave or progressive wave solutions, in the forward and backward directions, for each phase difference index. The solutions obtained are real, even with damping, since the modes of the cyclic symmetric structure occur in pairs [5].

Given that the excitation by harmonic rotating forces has a spatial periodicity in backward direction, the resonance of the tuned system implies two separate conditions:

(1) a frequency condition,
(2) a modal appropriation condition, i.e., a non-null generalized force given in Eq. (23).

The analysis of the mistuned system will be carried out by the perturbation approach in the rotating wave basis for a wavelike excitation.

The mode will be perturbed by other waves satisfying the neighborhood condition and separated according to their respective phase difference indices, i.e., the waves with the same phase difference index as the tuned mode at resonance; the waves with different phase difference indices than the tuned mode at resonance.

This separation arises naturally in the determination of the generalized force acting on the mode at resonance. Specifically, the perturbed mode

$$\mathbf{z}_{(k)} = \sum_r \eta_k^r \mathbf{x}_{(r)};\ \eta_k^k = 1;\ \Im[\eta_k^r] \approx 0, \tag{22}$$

where $\Im[\cdot]$ denotes the imaginary part of a complex number, yields the generalized force

$$\mathbf{z}_{(k)}{}^T\mathbf{f} = \sum_r \eta_k^r \mathbf{x}_{(r)}{}^T\mathbf{f};\ \eta_k^k = 1. \tag{23}$$

However, $\mathbf{x}_{(r)}^T\mathbf{f}=0$ if $\mathbf{x}_{(r)}$ and $\mathbf{x}_{(k)}$ have different phase indices, $n(r) \neq n(k)$, with force $\mathbf{f}$ not appropriate with $\mathbf{x}_{(k)}$, so that

$$\sum_r \eta_k^r \mathbf{x}_{(r)}{}^T\mathbf{f} = \mathbf{x}_{(k)}{}^T\mathbf{f} + \sum_s \eta_k^s \mathbf{x}_{(s)}{}^T\mathbf{f};\ n(s) = n(k) \tag{24}$$

The perturbations are real, since there is no coupling by the damping between waves of different phase difference indices.

Furthermore, it will be assumed that the maximum response amplitude is obtained at the resonance of the perturbed system.

The different modes involved in the perturbed response would in general contribute differently to the increase of the relevant norm, e.g. the maximum amplitude at one point in one direction, or the maximum stress on the perturbed mode, denoted here as $\|\cdot\|$. To properly assess the magnitude of the perturbations η_k^r, the tuned modes must be rescaled to have independent, equal contributions to the quantity being maximized. That is, they will be redefined as $\theta_k^l \mathbf{x}_{(l)}$ where the parameters θ_k^l are selected so that all modes have the same norm, i.e.,

$$\|\theta_k^l \mathbf{x}_{(l)}\| = \|\mathbf{x}_{(k)}\| \tag{25}$$

Assuming further that all generalized masses are equal to 1, it is found that the norm of the resonant forced response is

$$\begin{aligned} \|q\| &= \frac{\left\|\mathbf{x}_{(k)} + \sum_{l\neq k} \eta_k^l \theta_k^l \mathbf{x}_{(l)}\right\|}{1 + \sum_{l\neq k} \eta_k^l \eta_k^l \theta_k^l \theta_k^l} \times \frac{\mathbf{z}_{(k)}{}^T\mathbf{f}}{2\omega_k \Re(\lambda_k + \Delta\lambda_k)} \\ &= \frac{\|\mathbf{x}_{(k)}\|\left(1 + \sum_{l\neq k} \eta_k^l\right)}{1 + \sum_{l\neq k} \eta_k^l \eta_k^l \theta_k^l \theta_k^l} \times \frac{\mathbf{z}_{(k)}{}^T\mathbf{f}}{2\omega_k \Re(\lambda_k + \Delta\lambda_k)} \end{aligned} \tag{26}$$

Maximizing the above norm requires first its derivative with respect to each of the perturbation parameters which can be expressed as

$$\frac{\partial}{\partial \eta_k^l}\|q\| = A + B + C \tag{27}$$

$$\begin{aligned} A = &\left[\frac{\|\mathbf{x}_{(k)}\|\mathbf{z}_{(k)}{}^T\mathbf{f}}{2\omega_k} \times \frac{1}{\Re(\lambda_k + \Delta\lambda_k)}\right] \\ &\times \left[\frac{\left(1 + \sum_{h\neq k} \eta_k^h \eta_k^h \theta_k^h \theta_k^h\right) - 2\,\eta_k^l \theta_k^l \theta_k^l \left(1 + \sum_{h\neq k} \eta_k^h\right)}{\left(1 + \sum_{h\neq k} \eta_k^h \eta_k^h \theta_k^h \theta_k^h\right)^2}\right] \end{aligned} \tag{28}$$

$$\begin{aligned} B = &\left[\frac{\|\mathbf{x}_{(k)}\|\mathbf{z}_{(k)}{}^T\mathbf{f}}{2\omega_k} \times \frac{1}{\Re(\lambda_k + \Delta\lambda_k)}\right] \times \left[-\frac{\left(1 + \sum_{h\neq k} \eta_k^h\right)}{1 + \sum_{h\neq k} \eta_k^h \eta_k^h \theta_k^h \theta_k^h}\right. \\ &\left.\times \frac{\frac{\beta_{kl}}{2}}{(\Re(\lambda_k + \Delta\lambda_k))}\right] \end{aligned} \tag{29}$$

$$C = \frac{\|\mathbf{x}_{(k)}\|\left(1 + \sum_{h \neq k} \eta_k^h\right)}{1 + \sum_{h \neq k} \eta_k^h \eta_k^h \theta_k^h \theta_k^h} \times \frac{1}{2\omega_k \Re(\lambda_k + \Delta\lambda_k)} \times \left[\frac{\partial \mathbf{z}_{(k)}{}^T \mathbf{f}}{\partial \eta_k^l} - \frac{\dfrac{\partial \omega_k}{\partial \eta_k^l}}{(\omega_k)} \right] \tag{30}$$

A few comments are in order. First, the nullity of all derivatives, Eq. (27) for $l=1,\ldots,N$, indicates an extremum of the norm. Next, Eq. (27) reflects some of the observations drawn earlier, i.e.,

(a) the positive effect of detuning on damping (term B) for waves exhibiting the same phase difference index, see Eq. (9) or Eq. (19) for the inhibition of the cross damping term by detuning;
(b) the coupling between the optimum values of the different perturbations;
(c) the contribution of the modes having the same phase difference index;
(d) the effect of the variation of the eigenfrequency, which is negligible according first order perturbation method used.

As will confirmed later, the maximum amplitude of response is obtained for small perturbations; therefore, the following linear approximations can be adopted:

$$\eta_k^l(\mu_l(\omega_{0k}^2 - \omega_{0l}^2)) - \left(\sum_r \eta_k^r \gamma_{lr}\right) = 0 l \neq k;$$
$$\text{with } \eta_k^k = 1; \quad \gamma_{mn} = k_{mn} - \omega_{0k}^2 m_{mn} + j\omega_{0k}\beta_{mn} \tag{31}$$

or also

$$\eta_k^l = \frac{\gamma_{lk}}{(\mu_l(\omega_{0k}^2 - \omega_{0l}^2))}$$

We will now compare this optimality result with the published results [13,14].

6.1 McBain and Whaley Model [15]. McBain and Whaley investigated the effects of detuning on two waves of equal frequency in [15]. The solution obtained for the maximum response amplitude matched numerical results [13]. In particular, the maximum amplitude obtained equal the amplitude of the tuned disk multiplied by 1.2. Further, this maximum amplitude was obtained with a detuning of 0.414.

The dynamic model considered in [15] can be simulated within the present formulation by selecting

$$\beta_{kl} = 0; \ \eta_k^l = \eta \ l \neq k; \ \theta_k^l = 1; \ N = 2. \tag{32}$$

Next, consider the optimality condition of Eq. (27), i.e., $A+B+C=0$, and note first that both B and C are zero (zero cross damping and no significant change in eigenfrequency). Further, a zero value of A, Eq. (28), occurs when

$$\eta^2 + 2\eta - 1 = 0 \tag{33}$$

That is,

$$\eta = \frac{1}{1 + \sqrt{2}} = 0.414 \tag{34a}$$

and, from Eq. (26),

$$\|q_{\text{maximum}}\| = \|q_{\text{tuned}}\|^* \frac{1 + \sqrt{2}}{2} = \|q_{\text{tuned}}\|^* 1.207. \tag{34b}$$

Thus, the present formulation has recovered the results of McBain and Whaley. This finding indicates that the other modes must induce a negligible perturbation. Therefore, this result is obtained with a strong coupling but with a low detuning.

6.2 Whitehead Model [8,9]. Whitehead used a heuristic model of a structure with cyclic symmetry and a single degree of freedom to represent the motion of each of the N sectors. In the tuned case, the response is a rotating wave that satisfies the appropriation condition.

Whitehead assumed that the rotating waves can be combined with each wave contributing to the increase in vibration amplitude but also to the dissipation of the work accomplished by the external forces. This work is proportional to the amplitude of the tuned wave, since the other waves do not contribute; but the dissipation is proportional to the square of the amplitude.

Relying on the virtual work principle, Whitehead obtained in 1966 the following results below under the assumption that each wave is equally damped:

(1) The wave corresponding to the tuned case must be equally perturbed by the other $N-1$ waves (forward and backward) by a factor of

$$1/(\sqrt{N} + 1) \tag{35}$$

(2) The amplification with respect to the tuned case is

$$\frac{1 + \sqrt{N}}{2} \tag{36}$$

These results, which were again presented in 1998 [9], relate to a significant maximum amplification factor reached with low probability. They further demonstrate that the maximum amplification increases with the number of sectors.

The model investigated by Whitehead is reconsidered here in connection with the present perturbation formulation, i.e., Eqs. (27) and (31).

In a rotating wave basis, with one degree of freedom in each sector, there are N forward and backward rotating waves which will all be assumed equally damped as in [8,9]. Further, with each generalized mass equal to 1 all waves equally contribute to the vibration amplitude. From the above discussion, it is thus concluded that the Whitehead model can be simulated by the present formulation with

$$\beta_{kl} = 0; \ \eta_k^l = \eta \ \forall \ l \neq k; \ \theta_k^l = 1 \tag{37}$$

As already noted in connection with the McBain and Whaley model, the maximization of the amplitude is achieved by setting A, Eq. (28), to zero. This criterion leads to the following condition

$$\eta^2(N-1) + 2\eta - 1 = 0 \tag{38}$$

That is,

$$\eta = \frac{1}{1 + \sqrt{N}}. \tag{39a}$$

and, from Eq. (26),

$$\|q_{\text{maximum}}\| = \|q_{\text{tuned}}\|^* \frac{1 + \sqrt{N}}{2} \tag{39b}$$

The results of Eq. (39) are identical to those obtained by Whitehead in a very different manner. Note in particular that the maximum amplitude is obtained with a small contribution of each inappropriate wave but with each wave contributing.

Next, it is necessary to find under what conditions the extremum of Eq. (39) is reached. Combining Eqs. (39) and (31), it is found that

$$\eta = \frac{1}{1 + \sqrt{N}} = \eta_k^l = \frac{\gamma_{lk}}{(\omega_{0k}^2 - \omega_{0l}^2)} \tag{40}$$

It is easy to verify that this condition is satisfied if there is a localized perturbation, since the terms γ_{kl} can be interpreted as the decomposition, in Fourier series, of the perturbation. Clearly, the mistuning necessary is a function of the mechanical coupling involved in the frequency difference $(\omega_{0k}^2 - \omega_{0l}^2)$. If the mechanical coupling is weak, the perturbation η is small for the extremum.

On the other hand, if the mechanical coupling is strong, the term $(\omega_{0k}^2-\omega_{0l}^2)$ will be significant, and a strong perturbation γ_{kl} will be necessary to satisfy the condition (40).

This condition is fulfilled with mistuning on adjacent blades giving localization of the natural mode.

6.3 Generalization. The results obtained above show that there is a maximum amplitude for a given number of perturbing modes. The amplification is a function with an extremum.

In the general case, far from the stability limit, it can be assumed that all rotating waves are equally damped. Close to the stability boundary, however, the damping of the different waves is lower and very dependent on the phase difference index. Note however that the detuning will increase the effective damping per Eq. (21).

The knowledge of the spectrum of the cyclic symmetric structure allows to identify the $M-1$ neighbor modes that are likely to contribute to the amplification of the forced response.

The neighbor modes can therefore be classified into three categories:

(1) the very close modes, giving perturbations approximately equal to the tuned wave amplitude, i.e., $\|\eta\|\cong 1$,

(2) the distant neighbor modes, likely to satisfy

$$\frac{1}{1+\sqrt{M}} = \eta_k^l = \frac{\gamma_{lk}}{((\omega_{0k}^2-\omega_{0l}^2))},$$

(3) the distant modes whose (much lower) contributions can be ignored.

The neighborhood condition (9) allows the counting of the neighbor modes.

From the extremality condition obtained [$A+B+C=0$, see Eqs. (27)–(31)], the forward mode corresponding to the appropriate backward mode is a close mode, and therefore it cannot satisfy the condition

$$\frac{1}{1+\sqrt{M}} = \eta_k^l = \frac{\gamma_{lk}}{((\omega_{0k}^2-\omega_{0l}^2))}$$

6.3.1 Improved Assessment. Knowing the coupling and the amplitude of the perturbations, the above classification of the rotating wave modes can be used to estimate the amplification due to the detuning under the equal damping assumption, i.e., far from flutter.

Let $P-1$ be the number of very close modes, i.e., satisfying $\|\eta_k^l\|\cong 1$.

Let $M-P$ be the number of distant neighbor modes with equal but unknown perturbation η

Then, the optimality condition $A=0$ implies that

$$\eta^2(M-P)+2\eta P-P=0; \quad \text{i.e., the peturbation } \eta = \frac{1}{1+\sqrt{\dfrac{M}{P}}} \tag{41a}$$

The corresponding maximum amplification is then from Eq. (26)

$$\|q_{\text{maximum}}\| = \|q_{\text{tuned}}\|^* \frac{1}{2}\left(1+\sqrt{\frac{m}{p}}\right) \tag{41b}$$

It is Whitehead result for $M=N$ and $P=1$ in Eqs. (41).

The spectral density associated with the modes of the conservative system and the perturbations represent the relevant information for the estimation of the maximum amplification. Note further that the maximum amplification factor obtained by Whitehead is largest value than can be obtained from Eq. (41*b*) and is achieved when all modes participate equally. As demonstrated in [10], Whitehead's limit is achieved for a strongly coupled system, with perturbations large enough for all modes to contribute. However, there is still the forward mode, which remains a close neighbor mode.

6.3.2 Minimization of the Amplitude of Vibration. It is possible to find detuning that reduces the amplitude of vibration with respect to the tuned case. Consider for example the amplification corresponding to a perturbation by two modes:

$$\beta_{kl}=0;\ \eta_k^l=\eta_1 \text{ or } \eta_2;\ l\neq k;\ \theta_k^l=1;\ M=3;\ P=1$$

Then, shown in Fig. 1 is the 3D representation of the response amplification which clearly demonstrates the existence of perturbations that reduce the response amplitude with respect to the tuned case.

The results of Fig. 1 are consistent with the maximum amplification of 1.366 for a perturbation $\eta=0.366$ of each of the 2 modes, see Eqs. (26)–(28). Figure 1 also indicates the domains of the perturbations that yield an amplification less than 1.

6.4 Veering Situations. Veering may occur when the modes are functions of a parameter. In turbomachinery, the most sensitive parameters are the rotation speed, the temperature, and the phase difference index of the cyclic symmetric structures. Two examples are next examined that can give rise to a high amplification of the response with a mistuning obtained by a local perturbation.

6.5 Application 2: Bladed Disk Resonance With Mistuning. The modes of bladed discs can be blade modes, i.e. when the disk behaves as if it was rigid. Then, the corresponding eigenfrequencies do not depend on the phase difference index. This situation is often encountered for the first modes of vibration of bladed disks. The modes can also be disk modes. Then, the eigenfrequencies strongly vary with the phase difference index. The veering phenomenon may then be observed between these two sets of modes at a certain phase difference index, see Fig. 2. The situation depicted in Fig. 2 is representative of very thin disks with small blades, i.e. the disk mode frequencies are very dependent on the phase difference index, at the contrary of the blade first flap mode at 380 Hz. If the excitation falls in the veering region, the condition of amplification by the N blade modes with different phase difference indices can be verified by a localized mistuning ($N=17$).

For the example shown (Fig. 2) in the rotating frame, an excitation by a wake with 5 nodes diameter at a frequency of 370 Hz in the veering yields the critical resonance: with $M=18$ and $P=2$, the maximum amplification factor is 2.0. This result should be compared with an excitation by a wake with 3 nodes diameter at 380 Hz: with $M=18$ and $P=16$, the maximum amplification factor is 1.0303.

6.6 Application 3: Bladed Disk Veering With Acoustic Resonance. Consider now a bladed disk in which the disk is rigid. In the rotating frame, the eigenfrequency of a mode varies with both rotation speed (for a rotor) and temperature. Each cavity has acoustic modes, also characterized by their phase difference index. In the rotating reference, the eigenfrequency of each acoustic mode behaves as the rotation frequency multiplied by the phase difference index. If one such mode has the same phase difference index and a very similar eigenfrequency as a bladed disc mode, veering by coupling may occur. Figure 3 shows, in the rotating frame, the frequencies of the cavity modes with 1 nodal diameter and those of the blade modes on the rigid disk. The blade mode and the acoustic mode are defined without coupling. The veering occurs near the 300 Hz rotating frequency. The proposed approach can explain the failure of the blade with the highest frequency observed sometimes in this configuration. The localization occurs in highest frequency blade. Indeed, in this situation too, a localized perturbation on a bladed region can give rise to Whitehead's maximum amplification.

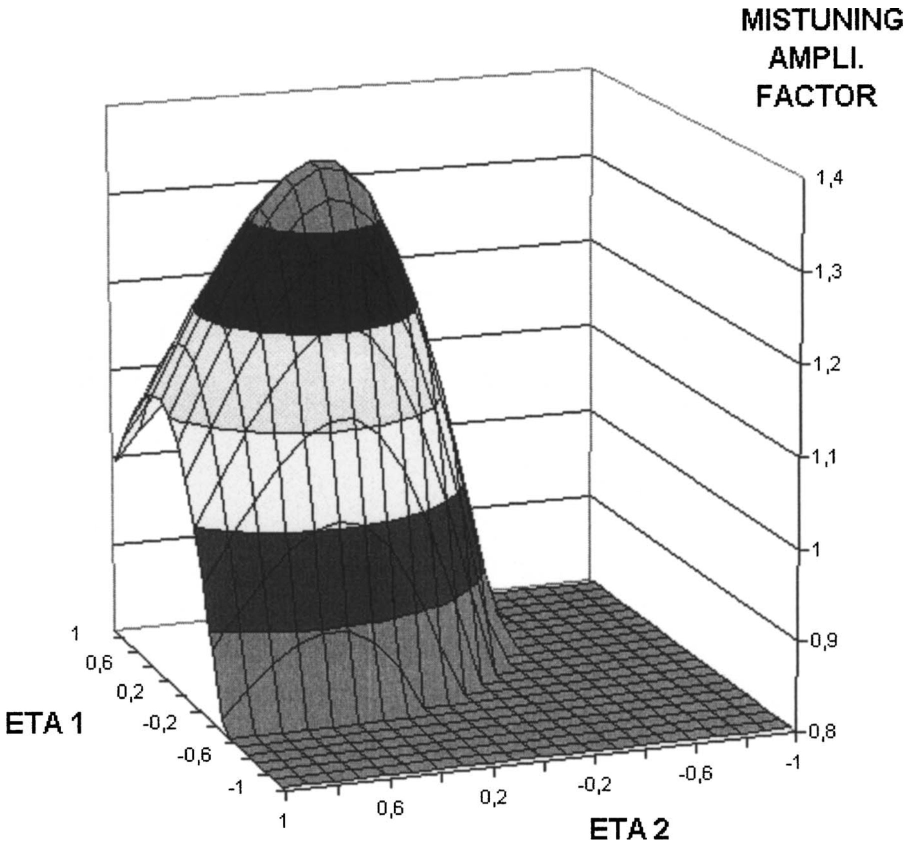

Fig. 1 Amplification factor with two modal perturbations

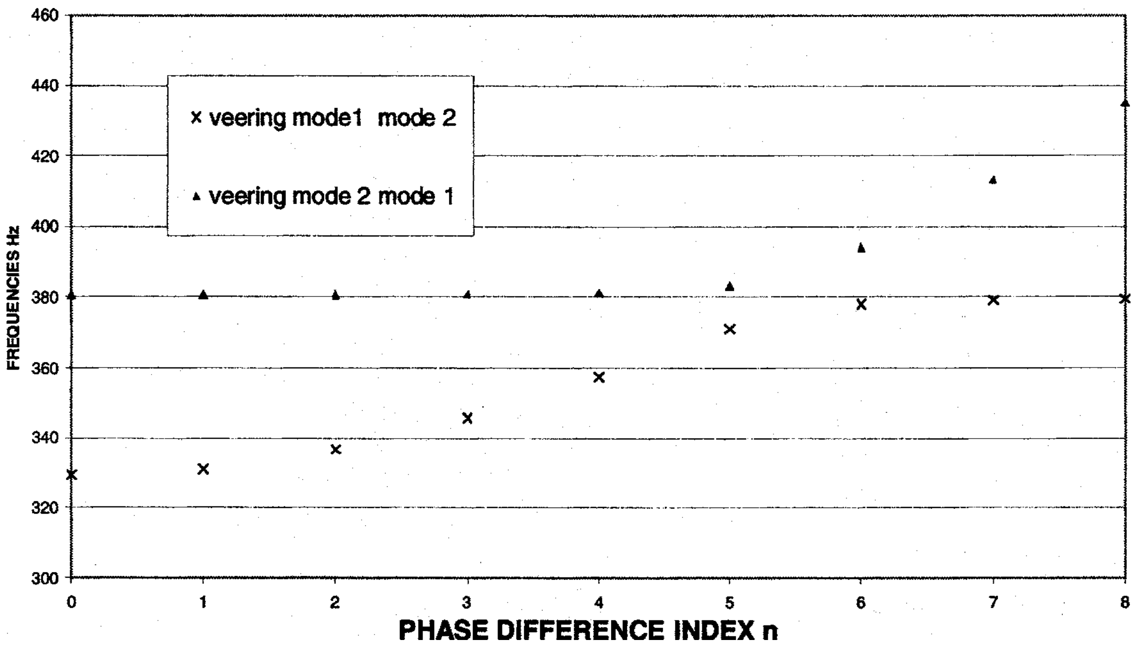

Fig. 2 Bladed disk veering

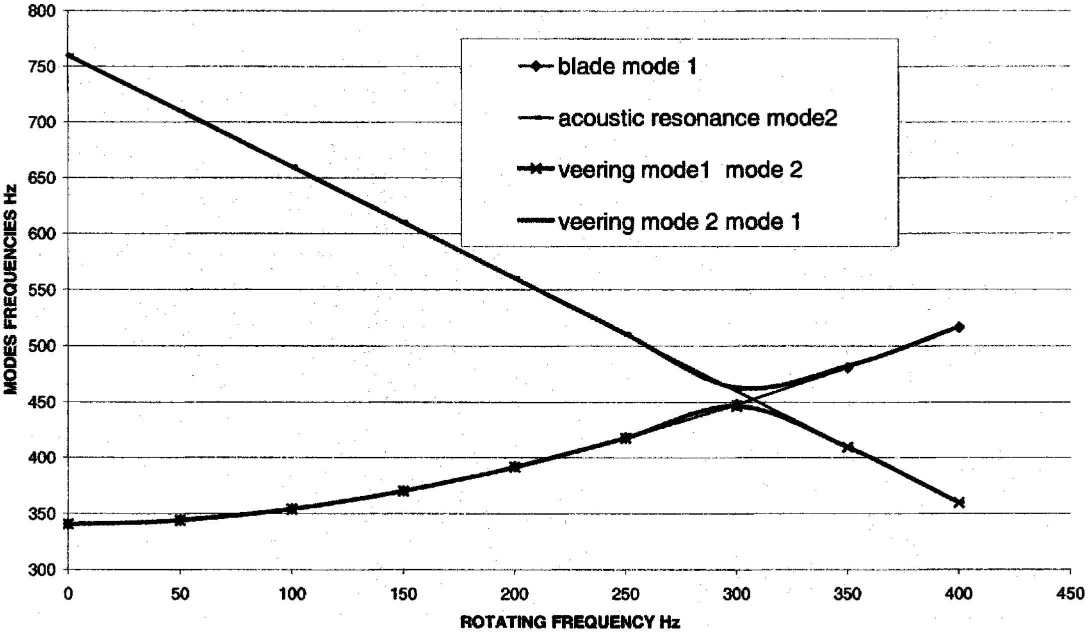

Fig. 3 Veering acoustic resonance-bladed disk mode

6.7 General Spectrum. The knowledge of the modes of the cyclic symmetric structure for all phase difference indices and the perturbations are the required information to estimate the number of close modes and neighbor modes that can contribute to the amplification of the response.

7 Detuning: Good or Bad?

It has been seen that detuning can stabilize a structure and thus be very beneficial. However, it has also been seen that detuning can have negative implications through the amplification off the forced response, especially when this detuning is localized.

Using the results above, and according to [14], it is possible to design structures detuned by a harmonic perturbation. In this case, the damping increases according Eq. (19) and the generalized excitation force can be reduced to a few modes. On the other hand, the number of excitable modes increases. The design procedure must then yield a compromise between these two trends.

8 Conclusions

Structures exhibiting many neighbor modes, as defined by Eq. (9), or equivalently having a strong spectral density, are insufficiently robust: small mass and/or stiffness variations or simply the "damping" may generate important changes of the modes. Their stability thus depends on small parameters, such as the manufacturing tolerances. The applications presented and involving aeroelasticity show that it is often necessary to investigate simultaneously the effects of tolerances and aeroelastic coupling for the prediction of the eigenvalues, the natural modes, and the forced response. For forced response problems, new analytical results were derived that are applicable independently of the model and its spectral density. The amplification factor due to mistuning was shown to depend on the model chosen. Extreme value amplification cases were presented, and more realistic amplification, in line with engineering practices, were obtained in Eq. (41). The maximum amplification factor is obtained from the dynamic properties of the conservative system and the perturbations due to mistuning and aeroelastic coupling. A discussion of the advantages of detuning summarizes this analysis. The statistical methods, such as those developed for reliability, naturally complete the approach presented here.

Acknowledgments

The author is pleased to acknowledge his colleagues in Turbomeca, Ludovic Mezière and Marc Dijoud for their discussions and comments on this subject, and also Marc P. Mignolet, from Arizona State University, for his contribution in this area, for his help in the preparation of this text and his very pleasant exchanges on this problem. Many thanks to Marc. Turbomeca Company is gratefully acknowledged for the permission to publish this work.

Nomenclature

$\mathbf{M}$ = mass matrix
$\mathbf{K}$ = stiffness matrix
$\Delta\mathbf{M}$ = perturbation of mass matrix
$\Delta\mathbf{K}$ = perturbation of stiffness matrix
$\mathbf{f}$ = external force
$\mathbf{q}$ = displacement vector of the discretized continious domain
$\dot{\mathbf{q}}$ = velocity vector of the discretized continious domain
$\ddot{\mathbf{q}}$ = acceleration vector of the discretized continious domain
$\mathbf{C}$ = damping matrix
$\mathbf{x}_{(r)}$ = eigenvector number r
$\mathbf{x}_{(r)}^T$ = transposition of eigenvector r
$\mathbf{z}_{(r)}$ = perturbed eigenvector number r
A,B,C = terms of Eq. (27) defined in Eqs. (28)–(30)
N = number of blades in the bladed disk model
$(M-P)$ = number of distant neighbor modes
$(P-1)$ = number of very close modes
$\|q_{\text{maximum}}\|$ = maximum amplitude of the forced response
$\|q_{\text{tuned}}\|$ = amplitude of the tuned forced response
x_l = generalized coordinates number l
$\dot{x}_l$ = velocity of the generalized coordinates number l
$\ddot{x}_l$ = acceleration of the generalized coordinates number l
n = phase difference index for the cyclic symmetric modes

$n(l)$ = phase difference index for the cyclic symmetric mode l
k_{lp} = projection of stiffness matrix perturbation in modes l and p
m_{lp} = projection of mass matrix perturbation in modes l and p
m_l = generalized mass of the perturbed eigenvector number l
δ_{rs} = Kroneker symbol=1 if $r=s$; =0 if $r \neq s$
μ_r = generalized mass for mode r
ω_{0r} = eigenfrequency for unperturbed mode r
$\Delta\lambda_r$ = variation of eigenfrequency ω_{0r}
η_l^r = modal perturbation of mode l by mode r
$\|\eta_l^r\|$ = norm for modal perturbation of mode l by mode r
η = value of constant modal perturbation whatever mode l and mode r
β_{lp} = projection of damping matrix perturbation in modes l and p
γ_{lp} = generalized projection of perturbation in modes l and p
θ = rotation angle of eigen vector in a plane

References

[1] Srinivasan, A. V., 1997, "Flutter and Resonant Vibration Characteristics of Engine Blades," J. Eng. Gas Turbines Power, **119**(4), pp. 742–775.
[2] Courant, R. and Hilbert, D., 1963, *Methods of Mathematical Physics*, Vol. 1, Interscience Publishers, New York.
[3] Wei, S. T., and Pierre, C., 1988, "Localization Phenomena in Mistuned Assemblies with Cyclic Symmetry—Part 1. Free Vibrations," J. Vibr. Acoust., **10**(4), pp. 429–438.
[4] Cohen Tannoudji, G. and Sacquin, Y., 1999, *Symétrie et Brisure de Symétrie*, EDP Sciences, Paris, France.
[5] Lalanne, B. and Touratier, M., 2000, "Aeroelastic Vibrations and Stability in Cyclic Symmetric Domains," Int. J. Rotating Mach., **6**(6), pp. 445–452.
[6] Morand, H. J. P. and Ohayon, R., 1995, *Fluid-Structure Interaction*, Wiley, New York.
[7] Kielb, R. E. and Kaza, K. R. V., 1983, "Aeroelastic Characteristics of a Cascade of Mistuned Blades in Subsonic and Supersonic Flows," J. Vibr. Acoust., **105**, pp. 425–433.
[8] Whitehead, D. S., 1966, "Effects of Mistuning on the Vibration of Turbomachine Blades Induced by Wakes," Int. J. Mech. Sci., **8**, pp. 15–21.
[9] Whitehead, D. S., 1998, "The Maximum Factor by Which Forced Vibrations of Blades Can Increase Due to Mistuning," J. Eng. Gas Turbines Power, **120**, pp. 115–119.
[10] Rivas-Guerra, A. J. and Mignolet, M. P., 2001, "Local/Global Effects of Mistuning on the Forced Response of Bladed Disk," Turbo Expo 01, New Orleans, LA.
[11] Mignolet, M. P., Hu, W., and Jadic, I., 2000, "On the Forced Response of Harmonically and Partially Mistuned Bladed Disk, Parts I and II," Int. J. Rotating Mach., **6**, pp. 29–56.
[12] Sinha, A. and Chen, S., 1989, "A Higher Order Technique to Compute the Statistics of Forced Response of Mistuned Bladed Disk," J. Sound Vib., **130**, pp. 207–221.
[13] Ewins, D. J., 1969, "The effect of Detuning Upon the Forced Vibration of Bladed Disk," J. Sound Vib., **9**, pp. 65–69.
[14] Choi, B. K., Lentz, J., Rivas-Guerra, A. J., and Mignolet, M. P., 2001, "Optimization of Intentional Mistuning Patterns for the Reduction of the Forced Response Effects of Unintentional Mistuning: Formulation and Assessment," J. Eng. Gas Turbines Power, **125**, pp. 131–140.
[15] McBain, J. C. and Whaley, P. W., 1983, "Maximum Resonant Response of Mistuned Bladed Disks," Vibrations of Bladed Disk Assemblies, ASME, New York, pp. 153–160.

Dieter Bohn
Institute of Steam and Gas Turbines,
Aachen University of Technology,
Templergraben 55,
D-52056 Aachen, Germany
e-mail: post-bohn@idg.rwth-aachen.de

Tom Heuer
Borg Warner Turbo Systems GmbH,
Marnheimer Str. 85/87,
D-67292 Kirchheimbolanden, Germany
e-mail: heu@turbos-bwauto.de

Karsten Kusterer
B&B-AGEMA,
Gesellschaft für Energietechnische Maschinen
und Anlagen GmbH,
Jülicher Str. 338,
D-52070 Aachen, Germany
e-mail: kusterer@bub-agema.de

Conjugate Flow and Heat Transfer Investigation of a Turbo Charger

In this paper a three-dimensional conjugate calculation has been performed for a passenger car turbo charger. The scope of this work is to investigate the heat fluxes in the radial compressor, which can be strongly influenced by the hot turbine. As a result of this, the compressor efficiency may deteriorate. Consequently, the heat fluxes have to be taken into account for the determination of the efficiency. To overcome this problem a complex three-dimensional model has been developed. It contains the compressor, the oil cooled center housing, and the turbine. Twelve operating points have been numerically simulated composed of three different turbine inlet temperatures and four different mass flows. The boundary conditions for the flow and for the outer casing were derived from experimental test data (Bohn et al.). Resulting from these conjugate calculations various one-dimensional calculation specifications have been developed. They describe the heat transfer phenomena inside the compressor with the help of a Nusselt number, which is a function of an artificial Reynolds number and the turbine inlet temperature.

[DOI: 10.1115/1.1839919]

Introduction

In recent years the turbo charging of Diesel engines gained an increased importance. Considering mainly performance perspectives the present research and development efforts also focus on economic and environmental aspects. The specific fuel consumption and the exhaust emissions need to be reduced and the dynamic behavior of the engine needs to be improved.

For these considerations the unsteady behavior of the whole engine is of interest, i.e. the unsteady interactions between the individual engine components (core engine, compressor and turbine of the turbocharger, exhaust gas recycling, control systems). Common design tools are computer programs for unsteady cycle analysis computations, which receive information about the components' operating behavior from maps.

Usually the rotating mass of the turbocharger is modeled as a system neglecting the unsteady aerodynamic behavior of the compressor and the turbine. Therefore, steady compressor and turbine maps are needed which cover an increased range of operating points realizable in the steady operation of the whole engine.

Especially for small mass flows the use of these maps is critical because in this range nonadiabatic effects dominate the behavior of a turbo charger. Besides the heat that is passed away through the surface, the flanges, and the bearing oil, a non-negligible amount of heat flows from the hot turbine into the distinctly colder compressor.

Bulaty [1] published a method for the extrapolation of component maps that is still used in programs for cycle analysis computations. Since the heat fluxes are neglected, the results are inaccurate so that the understanding and the quantification of the heat fluxes becomes crucial.

Thus, the quantification of the occurring heat fluxes is one condition for the adaptation of various component efficiencies. Designers need to distinguish the adiabatic from the diabatic change of state and respective efficiency. Figure 1 shows the compression process illustrating that the end point of the diabatic change of state differs from the adiabatic one by the amount of q_C.

The need of a diabatic approach has already been stated by various researchers [2–4]. Therefore, the scope of this work is a contribution to overcome this deficiency.

Heat Transfer Model

The first step of the analysis is to set up a model that adequately describes the heat fluxes in a turbo charger. Figure 2 shows the developed model, which has been divided into a turbine, center housing, and compressor part. Applying a heat balance to the system clarifies the paths of heat and power.

One part of the enthalpy drop in the turbine results from the power output transferred to the shaft, which drives the compressor wheel. The mechanical efficiency describes the amount of power that is converted into heat and taken away by the lubricating oil, which also has a cooling function. The other part of the enthalpy drop in the turbine is heat. It divides into one amount transferred to the surrounding area due to natural convection and thermal radiation and into one amount flowing into the center housing splitting into several parts. Additional to the portion leaving the system due to natural convection and radiation another portion is transferred to the oil channel. The rest of the heat enters the compressor where the amount that is not delivered to the surrounding area, can heat up the compressor fluid depending on the operating point. This dependency is the main objective of this investigation.

Computational Model

Geometry and Grid. Since the modeling of the complete turbocharger would require approximately 40 Mio grid points a less time-consuming geometric model has been developed (Fig. 3). First, the compressor and the turbine are divided into periodic segments. Second, due to the necessary periodic boundary conditions at the cutting planes, the volutes are substituted by annular rings. The 60 deg compressor segment consists of 2.9 Mio grid points including 2 splitter blades. The 32.7 deg turbine segment is composed of 1.45 Mio grid points and 1 blade. The intermediate center housing is not segmented because of its asymmetry. Thus, the inner oil cooling system is considered in a simplified manner. In total, the three parts of the turbo charger required 4.5 Mio grid points distributed among 151 blocks.

Numerical Procedure. In order to investigate the heat transfer mechanisms in the turbo charger the $\underline{\text{C}}$onjugate $\underline{\text{H}}$eat $\underline{\text{T}}$ransfer and $\underline{\text{Flow}}$ solver CHTflow has been chosen.

Contributed by the International Gas Turbine Institute (IGTI) of THE AMERICAN SOCIETY OF MECHANICAL ENGINEERS for publication in the ASME JOURNAL OF ENGINEERING FOR GAS TURBINES AND POWER. Paper presented at the International Gas Turbine and Aeroengine Congress and Exhibition, Atlanta, GA, June 16–19; 2003, Paper No. 2003-GT-38445. Manuscript received by IGTI, Oct. 2002, final revision, Mar. 2003. Associate Editor: H. R. Simmons.

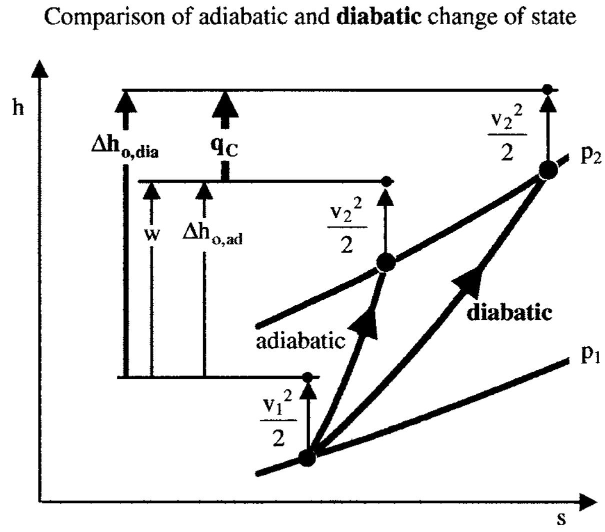

Fig. 1 Compression process in a compressor

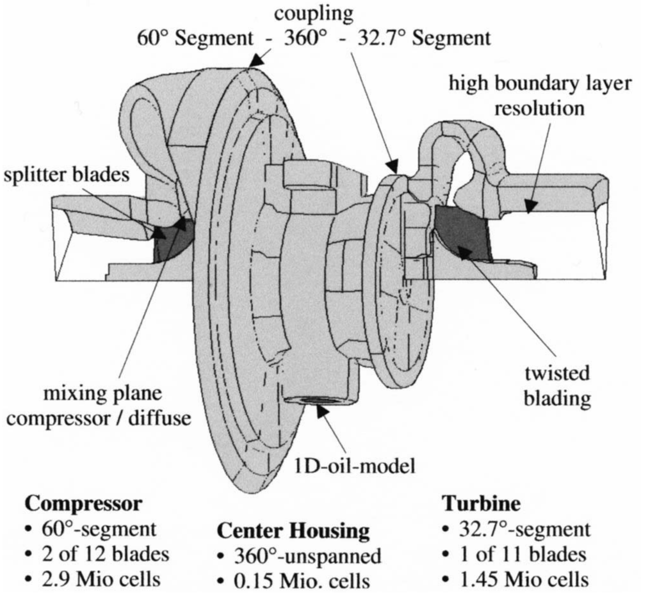

Fig. 3 Geometric model

For this code a unique Conjugate Calculation Technique has been developed which involves the direct coupling of the fluid flow and the solid body using the same discretization and numerical principle for both zones. This allows an interpolation-free transition of the heat fluxes between the neighboring cell faces (Bohn and Bonhoff [5], Bohn et al. [6,7]). Thus, additional information on the boundary conditions at the blade walls, such as the distribution about the heat transfer coefficient, becomes redundant, and the wall temperatures as well as the temperatures in the blade walls are a direct result of the simulation. Due to a high resolution of the boundary layer including the viscous sublayer (the dimensionless wall distance of the first cell is $y^+=1$ or smaller), the local heat fluxes are determined with sufficient accuracy. The calculated wall temperature serves as an internal boundary condition for the coupling procedure. Thus, this procedure is stable even for complex conjugate heat transfer problems.

The numerical scheme works on the basis of an implicit finite volume method combined with a multi-block technique. The physical domain is divided into different blocks for fluid flow and solid body regions. The full, compressible, three-dimensional Navier–Stokes equations are solved in the fluid blocks. The Fourier equation is solved in the solid body blocks.

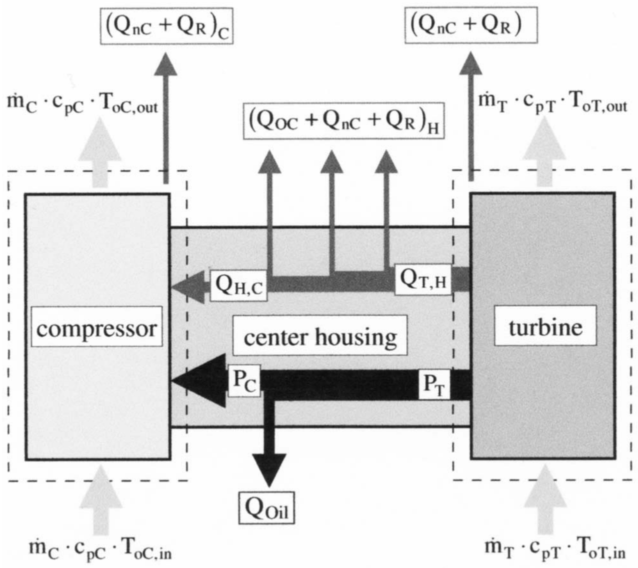

Fig. 2 Heat transfer model

The closure of the Reynolds averaged equations is provided by the Baldwin–Lomax algebraic eddy-viscosity turbulence model (Baldwin and Lomax [8]). The model has been chosen because of its low computation time and the good experiences in other conjugate calculations [9–11]. Different conjugate calculation approaches have been presented by other authors (e.g. Kao and Liou [12], Han et al. [13], Montenay et al. [14], Li and Kassab [15,16]).

Boundary Conditions. Two types of calculations have been conducted. One configuration is the complete model including the compressor, the center housing, and the turbine. The limited project duration required a time saving model for the parametric study. Hence, the single compressor was taken from the full model reducing the computational grid and with that the computation time.

The same car turbocharger has been investigated experimentally (Bohn et al. [17]). From these experiments the boundary conditions for the calculations have been deduced for various operating points. This includes the aerothermal boundary conditions for the fluid at the inlet and at the outlet of the compressor and turbine as well as the thermal boundary conditions on the surface of the casing.

In order to achieve realistic boundary conditions on the surface of the casing, pictures have been taken with a thermography-camera. Combined with information from resistance thermometers a surface temperature distribution has been determined. This procedure implicitly contains the influence of natural convection as well as the influence of thermal radiation.

Since the turbo charger consists of different materials for the casings, blades, and shaft, their different thermal behavior is taken into account by setting the corresponding material properties like density and thermal conductivity.

Complete model. One operating point has been simulated according to Table 1. The number of revolutions must be identical for the turbine and compressor, but also the mass flows have been adjusted to the same value in the experiment and in the calculation.

Compressor model. The single compressor needs further information at the boundary towards the center housing. Here, a radial

Table 1 Passenger car turbocharger: Operating points

		Turbine inlet temperature $\vartheta_{oT,1}/\vartheta_{o,\text{ref.}}$ [-]			
		Complete model	Parametric study compressor		
		1	<1	1	>1
	1	x	x	x	x
mass flow	↓		x	x	x
$\dot{m}_C/\dot{m}_{C,\text{ref}}$			x	x	x
[-]	>1		x	x	x

temperature profile is prescribed which was determined in the calculation of the complete model. Since it was derived from a certain operating point it had to be adjusted to further operating points by the following method:

a. Nondimensionalization of the radial temperature profile with help of the surface temperature of the compressor casing at the plane towards the center housing. This information is dependent on the operating point and results from the experiment.
b. Redimensionalization of the radial temperature profile with help of the corresponding surface temperature of the desired different operating point.

The solid body temperature distribution at the surface of the casing, the blades, and the shaft is shown in Fig. 4. At the outer walls of the casing this temperature distribution is identical with the boundary condition received from the experiment as explained in the preceding paragraph. Furthermore, the visualization of the multiplied and rotated compressor and turbine segments illustrates the shape of the geometric model with the modified volutes.

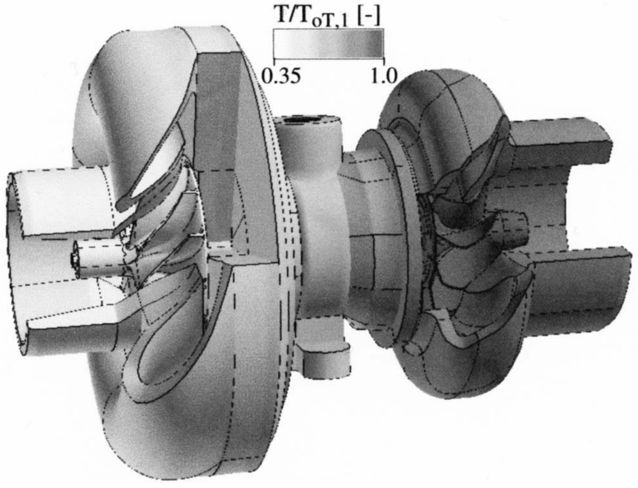

Fig. 4 Surface temperature distribution

Table 1 shows a matrix of the test cases investigated experimentally and numerically. Starting with the operating point corresponding to Fig. 5 three higher mass flows and two further turbine inlet temperatures were combined. Both increasing the mass flow and raising the turbine inlet temperature results in a higher number of revolutions.

Results

Heat Flux Distribution. Figure 5 shows the temperature distribution of the complete model computation in a longitudinal section. It also shows the heat flux from the turbine through the center housing into the compressor. At this operating point, the detail with a finer temperature resolution clearly reveals the temperature difference between the fluid and the solid body of the compressor.

In order to evaluate the heat fluxes between the fluid and the solid body (casing, blades, and shaft) of the compressor, 60 cutting planes have been positioned equidistantly according to Fig. 6. After that, the local heat fluxes have been determined and assigned to the individual cutting planes.

This produces the heat flux distribution shown in Fig. 7. Several peaks indicate either a significant change in the heat transfer area or a change in the local heat transfer coefficient. Positive values mean a heat flux from the solid body to the fluid; negative values describe a heat flux in opposite direction, from the fluid to the solid body.

Figures 8–10 show the summation of the local heat fluxes between fluid and solid body along the planes specified in Fig. 6. The local values were added subsequently, so that a particular value represents the amount of heat transferred from the compressor inlet to the specific position. If the gradient of the curve is positive the heat flux is directed by definition from the solid body into the fluid and vice versa if the gradient is negative.

For all investigated cases the heat flux passes into the fluid in the first half of the compressor. Further downstream, the fluid heats up as a result of the compression process to such a high extent that its temperature exceeds the solid body temperature. Consequently, heat flows from the fluid into the solid body in the rear part of the compressor. This phenomenon is intensified with rising mass flow because on the one hand the compression, and with that, the fluid temperature rise increases. On the other hand, the expansion in the turbine grows, so that less heat is transferred to the compressor. Figure 11 illustrates this interaction. Rising the

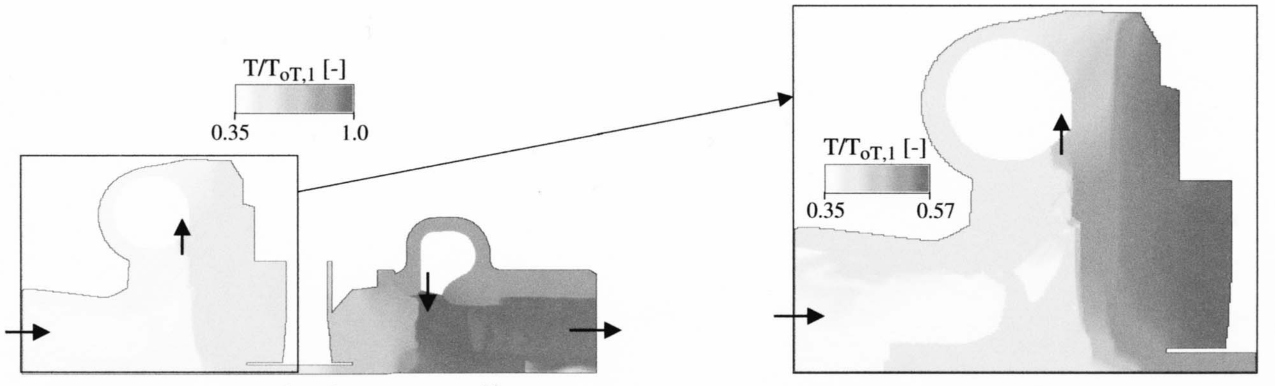

Fig. 5 Temperature distribution—longitudinal section ($\dot{m}_C/\dot{m}_{C,\text{ref}}=1$, $\vartheta_{oT,1}/\vartheta_{o,\text{ref}}=1$, $n/n_{\text{ref}}=1$)

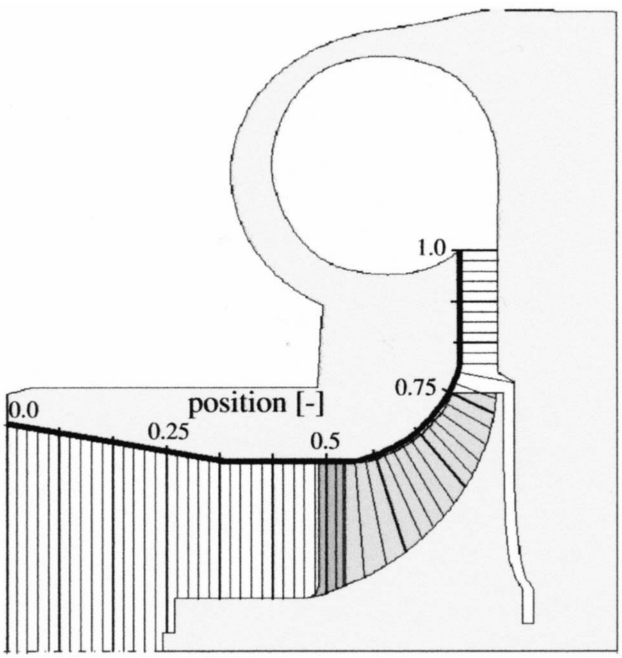

Fig. 6 Compressor geometry and positioning of cutting planes for thermal evaluation (Figs. 7–10)

turbine inlet temperature at constant mass flow also leads to an intensified heat transfer from the fluid to the solid body. This is caused by a sequence of changes. First, the enthalpy drop in the turbine increases and consequently the number of revolutions, too. With the same mass flow as in the turbine, the compressor pressure ratio rises with increased enthalpy rise. Consequently, the higher exit pressure is directly linked to a higher exit temperature.

Heat Transfer Number. Dependent on the operating point the heat transfer inside the compressor may be represented by

$$Q_C=f(\mu_{C,1},\lambda,\dot{m}_C,T_{T,1},D_{C,1},D_{C,2},H_{C,1},H_{C,2}) \tag{1}$$

It is a function of the working fluid, the material, the aerothermodynamics, and the geometry. Further magnitudes of influence are dependent magnitudes and therefore they have to be neglected. In dimensionless notation the equation is

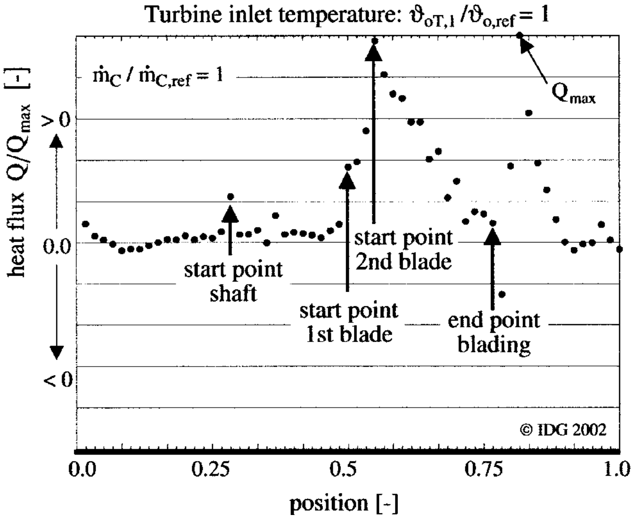

Fig. 7 Compressor heat flux solid body↔fluid $\dot{m}_C/\dot{m}_{C,\mathrm{ref}}=1$, $\vartheta_{oT,1}/\vartheta_{o,\mathrm{ref}}=1$

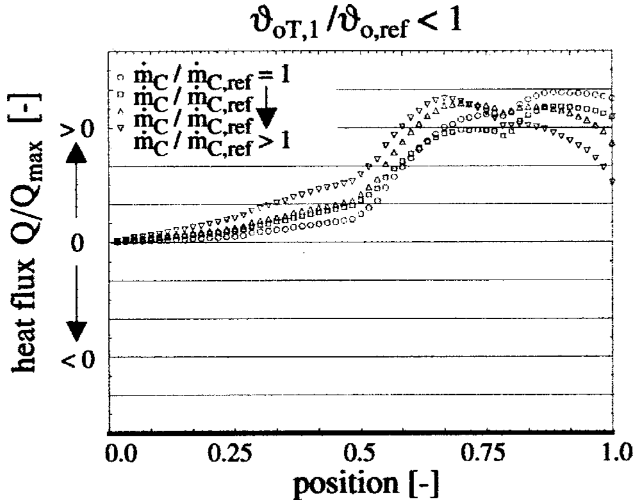

Fig. 8 Compressor heat flux solid body↔fluid $\dot{m}_C/\dot{m}_{C,\mathrm{ref}}=1$, $\vartheta_{oT,1}/\vartheta_{o,\mathrm{ref}}<1$

$$\mathrm{Nu}_C=f(\mathrm{Re}_C,T_{oT,1})f(\mu_{C,1},\dot{m}_{C1},T_{oC,1},D_{C,2},H_{C,1},H_{C,2}) \tag{2}$$

Based on the common definition for the Reynolds number an adjusted artificial Reynolds number has been derived taking into account the compressor mass flow and blading geometry,

$$\mathrm{Re}_C=\frac{\rho_{C,1}\cdot c_{C,1}\cdot l_C}{\mu_{C,1}}=\frac{\dot{m}_C}{\mu_{C,1}}\cdot\frac{D_{C,2}-D_{C,2}+2\cdot H_{C,1}}{4\cdot D_{C,2}\cdot H_{C,2}} \tag{3}$$

The parameters for the geometry are shown in Fig. 12. The CFD code calculates the heat fluxes and subsequently an artificial heat transfer coefficient, which is needed for the Nusselt number:

$$Q_C=\bar{h}_C\cdot\Delta T_o\cdot A_C \tag{4}$$

$$\Delta T_o=T_{oT,1}-T_{oC,1} \tag{5}$$

$$A_C=\frac{\pi}{2}(D_{C,2}-D_{C,1}+2\cdot H_{C,1})^2 \tag{6}$$

$$\mathrm{Nu}_C=\frac{\bar{h}_C\cdot l_C}{\bar{k}} \tag{7}$$

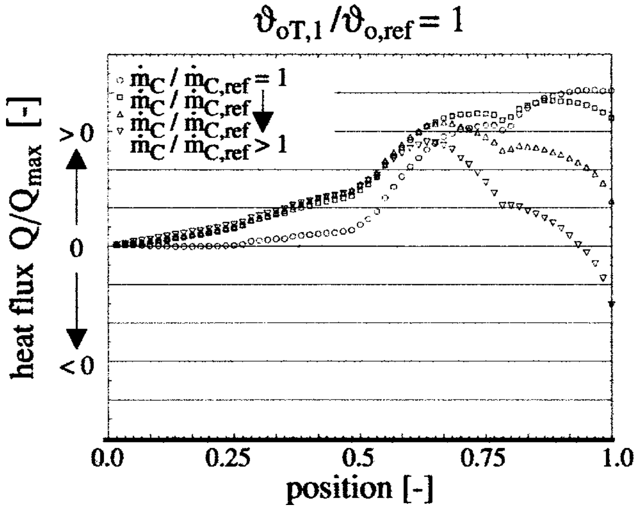

Fig. 9 Compressor heat flux solid body↔fluid $\dot{m}_C/\dot{m}_{C,\mathrm{ref}}=1$, $\vartheta_{oT,1}/\vartheta_{o,\mathrm{ref}}=1$

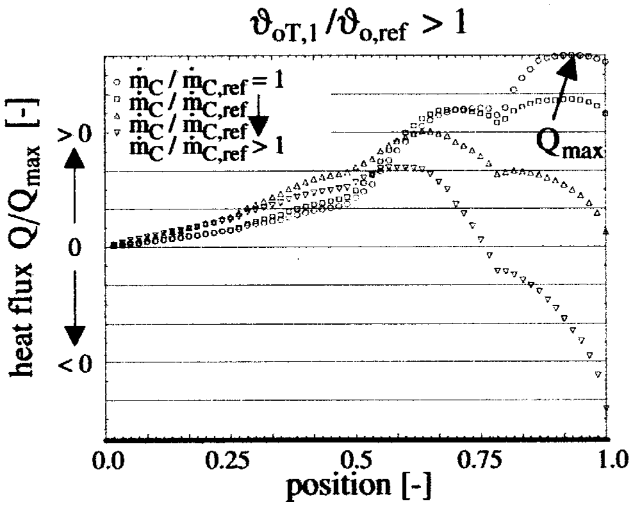

Fig. 10 Compressor heat flux solid body↔fluid $\dot{m}_C/\dot{m}_{C,\mathrm{ref}}=1$, $\vartheta_{oT,1}/\vartheta_{o,\mathrm{ref}}>1$

$$\bar{k}=k(\bar{T}=0.5\cdot(T_{C,1}+T_{T,1})) \tag{8}$$

$$l_C=\frac{\pi}{4}(D_{C2}-D_{C1}+2\cdot H_{C,1}) \tag{9}$$

This compressor Nusselt number has been calculated for each operating point and is plotted versus the compressor Reynolds number as shown in the diagram, Fig. 13. To enable the Nusselt number prediction for additional operating points, the following calculation specification has been developed:

$$\mathrm{Nu}_C=\mathrm{Nu}_0-\sqrt{p^2-\left(\frac{\mathrm{Re}_C^2}{1-\varepsilon^2}\right)}. \tag{10}$$

This function best describes the curve through the points of constant turbine inlet temperature. It is derived from the vertex equation describing the geometry of conical sections. It contains the Re-number and a temperature dependent coefficient, as well as several constants as listed in Table 2. Inserting ε^2 and Eq. (3), the notation for the artificial Nusselt number is:

$$\mathrm{Nu}_C=\mathrm{Nu}_0-\sqrt{p^2-\frac{\left(\frac{\dot{m}_C}{\mu_{C,1}}\cdot\frac{D_{C,2}-D_{C,2}+2\cdot H_{C,1}}{4\cdot D_{C,2}\cdot H_{C,2}}\right)^2}{1-(\varepsilon_0\cdot e^{-T_{oT,1}/\varepsilon_1}+\varepsilon_2\cdot T_{oT,1})}} \tag{11}$$

For all temperatures the curves in the Re_C–Nu_C-diagram start from a common starting point. They drop with rising Reynolds numbers or with rising mass flows, respectively. According to the explanation in the preceding paragraph the drop increases with higher turbine inlet temperatures.

In order to show the relation between the artificial Nusselt number and the heat flux the following function for the nondimensional heat flux was derived from Eqs. (4), (7), and (10). In Fig. 14 it is plotted versus the compressor mass flow:

$$Q_C=\frac{\bar{k}}{l_C}\cdot A_C\cdot\Delta T_o\cdot\left\{\mathrm{Nu}_{0_C}-\sqrt{p^2-\frac{\left(\frac{\dot{m}_C}{\mu_{C,1}}\cdot\frac{D_{C,2}-D_{C,1}+2\cdot h_{C,1}}{4\cdot D_{C,2}\cdot h_{C,2}}\right)^2}{1-(\varepsilon_0\cdot e^{-T_{oT,1}/\varepsilon_1}+\varepsilon_2\cdot T_{oT,1})}}\right\} \tag{12}$$

The artificial Nusselt number inside the curly brackets is multiplied with a factor. This factor only depends on the turbine inlet temperature, so that it is constant for each curve. With a rising turbine inlet temperature different phenomena occur. At operating points with small compressor mass flow the heat flux into the compressor fluid increases, but at high mass flow, the heat flux

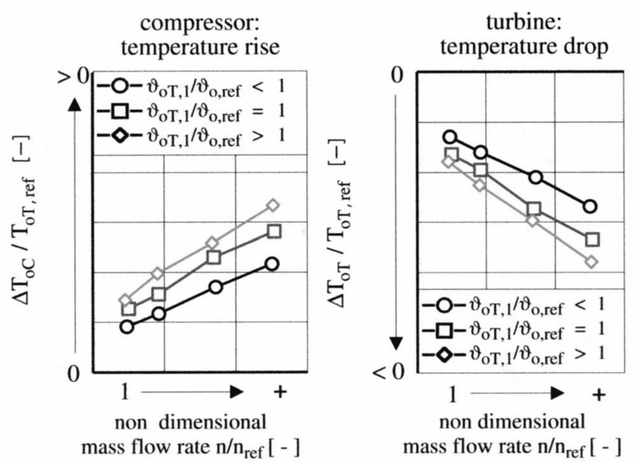

Fig. 11 Temperature differences between inlet and outlet of compressor and turbine

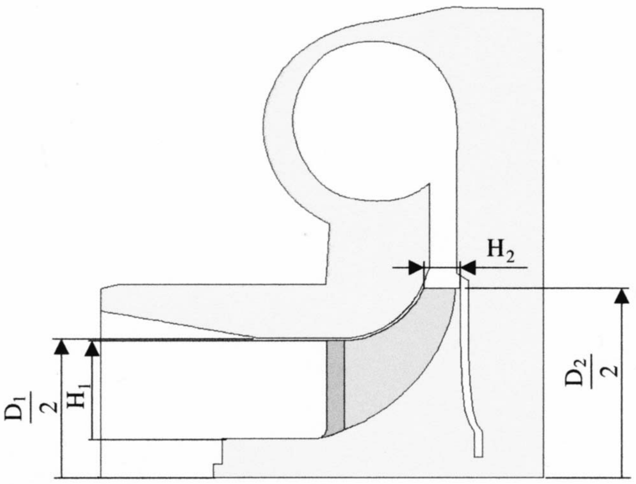

Fig. 12 Compressor: geometry parameters

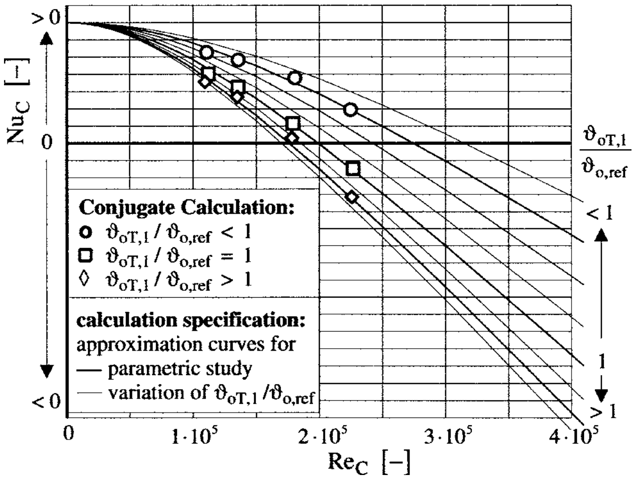

Fig. 13 Compressor: Re_C–Nu_C-diagram

Table 2 Constants and coefficients of Nusselt law

Coefficient	Equation for coefficient	Constant	Value
ε^2	$\varepsilon_0 \cdot e^{-T_{oT,1}/\varepsilon_1} + \varepsilon_e \cdot T_{oT,1}$	ε_0	$5 \cdot 10^8$
		ε_1	143 K
		ε_2	1123 K^{-1}
		Nu_0	170
		p	100

from the compressor fluid into the solid body grows. This results in an operating point with a heat flux independent of the turbine inlet temperature.

Discussing the special case of $Nu_C = 0$, which almost coincides with the simulated operating point $Re_C = 1.78 \cdot 10^5$, $\vartheta_{oT,1}/\vartheta_{o,\text{ref}} > 1$ (◇) in Fig. 13, helps to understand the heat transfer processes in the compressor. Referring to Fig. 1 it does not mean that no heat is transferred and the change of state is identical with the adiabatic case. Instead of that, the correct interpretation is, that the same amount of heat is transferred to the fluid as it is discharged from the fluid. The change of state is not adiabatic because of the diverging isobars as illustrated in Fig. 15. For clarification, the velocities have been neglected in this diagram. Furthermore, Fig. 10 reveals this fact for the same operating point ($\dot{m}_C/\dot{m}_{C,\text{ref}} = 1.0$, $\vartheta_{oT,1}/\vartheta_{o,\text{ref}} > 1$ (◇)). In the front part of the compressor heat is transferred into the fluid and in the rear part heat is transferred into the solid body.

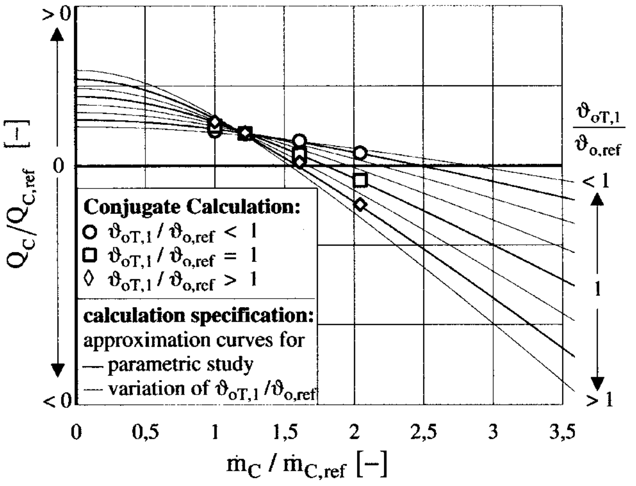

Fig. 14 Compressor: m_C–Q_C-diagram

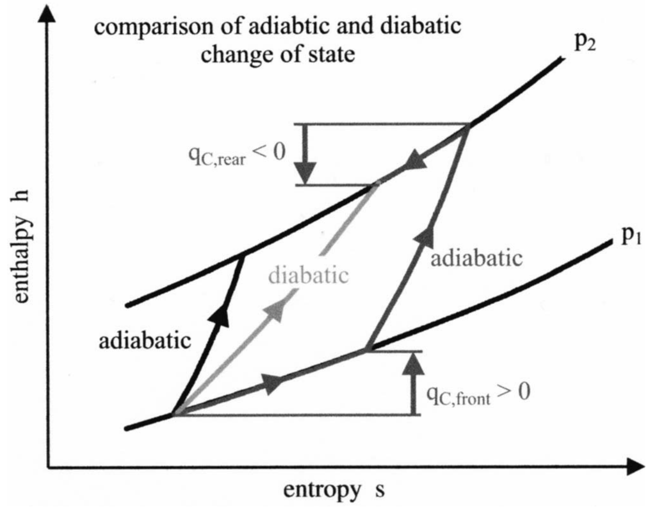

Fig. 15 Refined model of the compression process

Conclusions

A conjugate calculation of a turbo charger including the compressor, the oil cooled center housing, and the turbine has been performed. It is shown that the heat transfer from the hot turbine into the cold compressor significantly influences the change of state during the compression process. A parametric study has been carried out for three-dimensional conjugate calculations with variations of the mass flow and the turbine inlet temperature. From this parametric study a one dimensional Nusselt law has been developed which enables the prediction of the heat transfer even for additional operating points and similar geometries. For small Reynolds numbers the compressor fluid is heated up by the heat flux from the turbine. With increasing Reynolds number the compression heats up the fluid so strong that heat is discharged into the casing and blading. Therefore, the understanding of the diabatic change of state in a compressor is crucial for the successful thermal design of a turbo charger.

Acknowledgments

This report is the scientific result of a research project which was initiated and funded by the Forschungsvereinigung Verbrennungskraftmaschinen e.V. (FVV, Frankfurt, Germany) and carried out at the Institute of Steam and Gas Turbines at the RWTH Aachen headed by Professor Dr.-Ing. D. Bohn and accompanied by a counseling circle headed by Dr. P. Prenninger, AVL List, Graz, Austria. On demand of the financier the results presented in this paper merely contain tendencies.

Nomenclature

c_p = specific heat at constant pressure ($J\,kg^{-1}\,K^{-1}$)
D = diameter (m)
h = enthalpy ($J\,kg^{-1}$)
h = heat transfer coefficient ($W\,m^{-2}\,K^{-1}$)
H = height (m)
k = thermal conductivity ($W\,m^{-1}\,K^{-1}$)
L = length (m)
$\dot{m}$ = mass flow rate ($kg\,s^{-1}$)
Nu = Nusselt number
n = number of revolutions (s^{-1})
p = pressure ($N\,m^{-2}$)
P = power ($N\,m^{-2}$)
q = specific heat ($J\,kg^{-1}$)
Q = heat flux rate (W)
Re = Reynolds number
T = temperature (K)
v = velocity ($m\,s^{-1}$)
w = specific work ($J\,kg^{-1}$)
Δ = difference
ε^2 = coefficient
η = efficiency
μ = dynamic viscosity ($kg\,m^{-1}\,s^{-1}$)
ρ = density ($kg\,m^{-3}$)
ϑ = temperature (°C)

Subscripts/Superscripts

— = averaged quantity
C = compressor
H = center housing
m = mechanical
nC = natural convection
oil = bearing oil
OC = oil channel in center housing
o = stagnation conditions
ref = reference value

R = thermal radiation
T = turbine
1, 2 = inlet and outlet of a blade row

Constants from calculation specifications

Nu_0, p, ε_0, ε_1, ε_2

References

[1] Bulaty, T., 1974, "Spezielle Probleme der schrittweisen Ladungswechselrechnung bei Verbrennungsmotoren mit Abgasturboladern," MTZ 35, 6, pp. 177–185.
[2] Rautenberg, M., Mobarak, A., and Malobabic, M., 1983, "Influence of Heat Transfer Between Turbine and Compressor on the Performance of Small Turbochargers," JSME Paper 83-TOKYO-IGTC-73, Int. Gas Turbine Congress.
[3] Rautenberg, M., and Kämmer, N., 1984, "On the Thermodynamics of Non-Adiabatic Compression and Expansion Process in Turbomachines," ICMPE, Proceedings of the 5th International Conference for Mechanical Power Engineering, Cairo, Egypt.
[4] Malobabic, M., 1989, "Das Betriebsverhalten Leitschaufel- und bypass-geregelter PKW-Abgasturbolader," Ph.D. thesis, University of Hannover, Germany.
[5] Bohn, D., and Bonhoff, B., 1994, "Berechnung der Kühl- und Störwirkung eines filmgekühlten transsonisch durchströmten Turbinengitters mit diabaten Wänden," *VDI-Berichte 1109*, pp. 261–275.
[6] Bohn, D., Bonhoff, B., Schönenborn, H., and Wilhelmi, H., 1995, "Prediction of the Film-Cooling Effectiveness of Gas Turbine Blades Using a Numerical Model for the Coupled Simulation of Fluid Flow and Diabatic Walls," AIAA Paper 95-7105.
[7] Bohn, D., Krüger, U., and Kusterer, K., 2001, "Conjugate Heat Transfer: An Advanced Computational Method for the Cooling Design of Modern Gas Turbine Blades and Vanes," *Heat Transfer in Gas Turbines*, B. Sunden and M. Faghri, eds., WIT Press, Southampton, pp. 58–108.
[8] Baldwin, B. S., and Lomax, H., 1978, "Thin Layer Approximation and Algebraic Model for Separated Turbulent Flows," AIAA Paper 78-257.
[9] Bohn, D., and Schönenborn, H., 1996, "3-D Coupled Aerodynamic and Thermal Analysis of a Turbine Nozzle Guide Vane," *Proceedings of the 19th ICTAM*, Kyoto, Japan.
[10] Bohn, D., Bonhoff, B., and Schönenborn, H., 1995, "Combined Aerodynamic and Thermal Analysis of a Turbine Nozzle Guide Vane," IGTC Paper 108, *Proceedings of the 1995 Yokohama International Gas Turbine Congress*.
[11] Bohn, D., and Heuer, T., 2001, "Conjugate Flow and Heat Transfer Calculation of a High Pressure Turbine Nozzle Guide Vane," AIAA Paper 2001-3304.
[12] Kao, K.-H., and Liou, M.-S., 1996, "On the Application of Chimera/Unstructured Hybrid Grids for the Conjugate Heat Transfer," ASME Paper 96-GT-156.
[13] Han, Z.-X., Dennis, B. H., and Dulikravich, G. S., 2000, "Simultaneous Prediction of External Flow-Field and Temperature in Internally Cooled 3-D Turbine Blade Material," ASME Paper 2000-GT-253.
[14] Montenay, A., Paté, L., and Duboué, J. M., 2000, "Conjugate Heat Transfer Analysis of an Engine Internal Cavity," ASME Paper 2000-GT-282.
[15] Li, H., and Kassab, A. J., 1994, "Numerical Prediction of Fluid Flow and Heat Transfer in Turbine Blades With Internal Cooling," AIAA Paper 94-2933.
[16] Li, H., and Kassab, A. J., 1994, "A Coupled FVM/BEM Solution to Conjugate Heat Transfer in Turbine Blades," AIAA Paper 94-1981.
[17] Bohn, D., 2003, "Conjugate Flow and Heat Transfer Investigation of a Turbo Charger: Part II: Experimental Results," ASME Paper 2003-38449.

Applying Thermodynamics in Search of Superior Engine Efficiency

Charles A. Amann
KAB Engineering,
984 Satterlee Road,
Bloomfield Hills, MI 48304

Historically, a succession of thermodynamic processes has been used to idealize the operating cycles of internal combustion engines. In this study, the 256 possible combinations of four reversible processes—isentropic, isothermal, isochoric, and isobaric—are surveyed in search of cycles promising superior thermal efficiency. Regenerative cycles are excluded. The established concept of the air-standard cycle, which mimics the internal combustion engine as a closed-cycle heat engine, is used to narrow the field systematically. The approach relies primarily on graphical interpretation of approximate temperature-entropy diagrams and is qualitative only. In addition to identifying the cycles offering the greatest efficiency potential, the compromise between thermal efficiency and mean effective pressure is addressed. [DOI: 10.1115/1.1804537]

Introduction

Historically, thermodynamics has been a useful tool for understanding the energy conversion process that occurs in the internal combustion (IC) engine. The actual engine cycle has been approached through a succession of computational approximations of increasing complexity.

In its simplest form, the engine is represented as a series of successive reversible thermodynamic processes. The working medium is assumed to be a perfect diatomic gas having the properties of room-temperature air. In place of combustion, energy is transferred into the cycle from an external source. In place of the exhaust process essential to an IC engine, energy is transferred from the working gas to the surroundings to return the gas to its original state for repetition of the cycle. Aside from these two functions, energy exchange between the working gas and its surroundings is assumed to be zero. This closed-cycle approximation of the actual engine, which treats the IC engine as a heat engine, is known as the air-standard cycle.

The IC engine is not, of course, such a heat engine. Unlike the heat engine, it operates on an open circuit. Unlike the heat engine, its efficiency is not limited by the Carnot efficiency [1]. As a measure of its effectiveness as an energy converter, the output work it delivers ought to be measured against the difference effected in Gibbs free energy between reactants and products. However, common practice in industry is to express the effectiveness of energy conversion in terms of specific fuel consumption (SFC), i.e., mass of fuel consumed per unit of energy delivered. Because SFC depends not only on engine performance, but also on the energy content of the fuel, thermal efficiency is also used. It is inversely proportional to the product of SFC and the heating value of the fuel. For the common hydrocarbon fuels, it happens that the heating value of the fuel has approximately the same value as the associated change in free energy [2].

The next closest approximation to the engine treats it as an open cycle incorporating combustion. Gas exchange is recognized during the intake of a fresh charge and the exhausting of combustion products. As a result, some residual combustion products from the previous cycle are allowed to remain in the cylinder once it has been closed to the surroundings. The gas within the cylinder is assumed to be spatially homogeneous. Changes in the specific heat of the working gas with temperature are recognized. Changes in composition are also recognized during combustion and expansion, with the products assumed always to be in chemical equilibrium (except for freezing of carbon monoxide late during expansion, as has been observed experimentally during engine operation). Again, temperature-differential-driven energy exchange between the working gas and the surroundings is neglected. This approximation is known as the fuel-air cycle.

A series of increasingly accurate approximations to actual IC engine operation follow. First, energy transfer from the working gas to the surroundings, driven by temperature difference, may be allowed. Then equilibrium gas composition may be replaced through consideration of time-dependent chemical kinetics. Spatial differences in gas composition within the cylinder may be considered as a flame front is allowed to progress through the cylinder space. Possible options include the two-zone model (unburned- and burned-gas fractions) and the three-zone model (in which a boundary layer is added to accommodate energy transfer between the cylinder gas and its confining walls). Ultimately, computational fluid dynamics (CFD) models treat the cylinder contents as a three-dimensional mesh of computational cells, each analytically linked to its neighbors but following its own chemical/thermodynamic path.

Approach

In this paper the simplest model—the air-standard cycle—is used to explore qualitatively the thermal efficiency potential of a broad range of thermodynamic cycles. This simplified approach to the engine cycle offers some valuable insights, but is no replacement for more complex models. Important factors not comprehended by the air-standard-cycle approach include the effects of heat transfer on the cycle, and of changing temperature and composition of the working gas on thermodynamic properties. All cycles considered are for nonregenerative, naturally aspirated engines, with a starting pressure of 1 atm and a fixed initial temperature. Energy added to the cycle is held constant. The approach is principally graphical, employing temperature-entropy diagrams. In fact, the objective of this work is to identify cycles promising high thermal efficiency without resorting to a multiplicity of complex equations, irrespective of historical developments that have led to established IC engine practice. Although the thermodynamic concept of availability has been shown to have great utility in analyzing engine performance [3,4], that approach has been purposely avoided in this qualitative assessment.

For the reversible air-standard engine cycle, the First Law of Thermodynamics states that

---

Contributed by the Internal Combustion Engine Division of THE AMERICAN SOCIETY OF MECHANICAL ENGINEERS for publication in the ASME JOURNAL OF ENGINEERING FOR GAS TURBINES AND POWER. Manuscript received by the ICE Division, January 2, 2003; final revision received March 26, 2004. Associate Editor: D. Assanis.

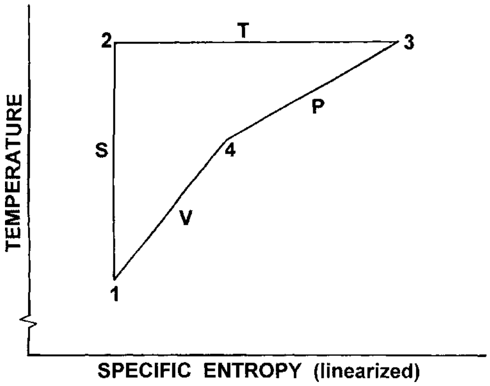

Fig. 1 Temperature-entropy diagram for STPV cycle

$$W=(Q_{add}-Q_{rej})-\Delta U \quad (1)$$

where W=net work output, Q_{add}=energy added to cycle, Q_{rej}=energy rejected from cycle, ΔU=net change in internal energy.

Because the cycle returns the working gas to its original state, $\Delta U=0$ and the net work is equal to the net energy exchanged between the working gas and its surroundings. It further follows that the cycle efficiency (η), which is the ratio of work output to energy added, is given by

$$\eta=1-\frac{Q_{rej}}{Q_{add}} \quad (2)$$

Because Q_{add} is held constant in the following comparisons, it follows that the most efficient cycle is the one rejecting the least energy. It is further known that for a reversible cycle, dQ=T dS, where energy interchange Q is expressed per unit mass, T represents absolute temperature and S represents specific entropy. Consequently, Q_{add} and Q_{rej} for each process in a reversible cycle are represented by the areas under the energy-addition and energy-rejection paths when those process paths are plotted on a temperature-entropy plane. Using T-S diagrams of air-standard cycles to compare the thermal efficiencies of established IC engine cycles has a long tradition [5,6]. In this paper that technique is broadened to include a large number of possible cycles not in common use.

An air-standard cycle is comprised of combinations of three or more of the following reversible thermodynamic processes: isentropic (constant specific entropy, denoted by S), isothermal (constant temperature, denoted by T), isobaric (constant pressure, denoted by P), and isochoric (constant specific volume, denoted by V). Thus, by way of example, STPV designates a possible four-process cycle comprised successively of an isentropic, an isothermal, an isobaric, and an isochoric process, with the last isochoric process returning the working gas to its original state.

The STPV cycle is represented in Fig. 1. Isentropic process 1–2 follows a vertical line because it involves no energy exchange with the surroundings, hence cannot have area beneath it. The isothermal path is a horizontal line, 2–3. The area under 2–3 represents the energy added to the cycle, which is held constant in comparisons to follow. Isobaric energy rejection is represented by the area under 3–4. Energy rejection continues isochorically, proportional to the area under more steeply sloped line 4–1. In Fig. 1 and all subsequent figures in this paper, the isobaric and isochoric paths have been linearized for simplicity. In reality, these paths both have a slight upward concavity, but for the qualitative comparisons of this study, showing them as straight lines does not affect the relative rankings of the cycles. (In the T-S diagrams in this paper, abscissas labeled "linearized" remind the reader that isobars and isochores are shown as straight lines rather than as having their true logarithmic curvatures.)

To limit this study to manageable proportions, only four-process combinations are considered. That yields $4^4=256$ combinations, as listed in Table 1. To comprise an engine cycle, the thermodynamic processes must circumscribe a closed area on temperature-entropy coordinates, generating that area in the clockwise sense. (A T-S diagram generated in the counter-clockwise sense constitutes a refrigeration cycle.)

One- to Three-Process Combinations

Clearly, such one-process combinations as SSSS cannot generate an enclosed area. Neither can such two-process combinations as SSPP, SSSP, or SPPS. In Table 1, such combinations are eliminated by a double strikethrough. However, such two-process combinations as SPSP do comprise legitimate cycles. This elimination of candidates that do not enclose a T-S diagram cuts the count of possibilities from 256 combinations to 180 actual cycles eligible for further consideration.

Combinations generating three-sided T-S diagrams are eliminated by a single strikethrough in Table 1 as having efficiencies noncompetitive with four-process combinations. To illustrate, compare cycle VSPP (three-sided diagram 1–2′–3′) to cycle SVSP (four-sided diagram 1–2–3–4) in Fig. 2. Recalling that the areas under the respective isochoric energy-addition lines (1–2′ and 2–3) represent the quantities of energy added to the cycles and are being held equal, it is clear that SVSP, with its higher average temperature during energy addition, requires a smaller increase in entropy than VSPP. Consequently, the energies rejected from the cycles, which are represented by the areas under the isobaric lines returning the working gas to the original state of the cycle (3′–1 and 4–1), is less for SVSP than for VSPP, and the

Table 1 Possible combinations of four processes (double strikethrough marks noncycles; single strikethrough marks three-process cycles; surviving cycles in bold type)

~~SSSS~~	~~SPSS~~	~~STSS~~	~~SVSS~~	~~TSSS~~	~~TPSS~~	~~TTSS~~	~~TVSS~~
~~SSSP~~	**SPST**	**STSP**	**SVSP**	~~TSSP~~	**TPSP**	~~TTSP~~	**TVSP**
~~SSST~~	**SPSP**	**STST**	**SVST**	~~TSST~~	~~TPST~~	~~TTST~~	~~TVST~~
~~SSSV~~	**SPSV**	**STSV**	**SVSV**	~~TSSV~~	**TPSV**	~~TTSV~~	**TVSV**
~~SSPS~~	~~SPPS~~	~~STPS~~	~~SVPS~~	**TSPS**	~~TPPS~~	~~TTPS~~	**TVPS**
~~SSPP~~	~~SPPT~~	~~STPP~~	~~SVPP~~	~~TSPP~~	~~TPPP~~	~~TTPP~~	~~TVPP~~
~~SSPT~~	~~SPPP~~	**STPT**	**SVPT**	~~TSPT~~	~~TPPT~~	~~TTPT~~	~~TVPT~~
~~SSPV~~	~~SPPV~~	**STPV**	**SVPV**	**TSPV**	~~TPPV~~	~~TTPV~~	**TVPV**
~~SSTS~~	~~SPTS~~	~~STTS~~	~~SVTS~~	**TSTS**	**TPTS**	~~TTTS~~	**TVTS**
~~SSTP~~	~~SPTT~~	~~STTP~~	**SVTP**	**TSTP**	**TPTP**	~~TTTP~~	**TVTP**
~~SSTT~~	**SPTP**	~~STTT~~	~~SVTT~~	~~TSTT~~	~~TPTT~~	~~TTTT~~	~~TVTT~~
~~SSTV~~	**SPTV**	~~STTV~~	**SVTV**	**TSTV**	**TPTV**	~~TTTV~~	**TVTV**
~~SSVS~~	~~SPVS~~	~~STVS~~	~~SVVS~~	**TSVS**	**TPVS**	~~TTVS~~	~~TVVS~~
~~SSVP~~	**SPVT**	**STVP**	~~SVVP~~	**TSVP**	**TPVP**	~~TTVP~~	~~TVVP~~
~~SSVT~~	**SPVP**	**STVT**	~~SVVT~~	~~TSVT~~	~~TPVT~~	~~TTVT~~	~~TVVT~~
~~SSVV~~	~~SPVV~~	~~STVV~~	~~SVVV~~	~~TSVV~~	~~TPVV~~	~~TTVV~~	~~TVVV~~
~~PSSS~~	~~PTSS~~	~~PPSS~~	~~PVSS~~	~~VSSS~~	~~VPSS~~	~~VTSS~~	~~VVSS~~
~~PSSP~~	~~PTSP~~	~~PPSP~~	~~PVSP~~	~~VSSP~~	**VPSP**	**VTSP**	~~VVSP~~
~~PSST~~	**PTST**	~~PPST~~	**PVST**	~~VSST~~	**VPST**	**VTST**	~~VVST~~
~~PSSV~~	**PTSV**	~~PPSV~~	**PVSV**	~~VSSV~~	~~VPSV~~	~~VTSV~~	~~VVSV~~
PSPS	**PTPS**	~~PPPS~~	**PVPS**	**VSPS**	~~VPPS~~	**VTPS**	~~VVPS~~
~~PSPP~~	~~PTPP~~	~~PPPP~~	~~PVPP~~	~~VSPP~~	~~VPPP~~	~~VTPP~~	~~VVPP~~
PSPT	**PTPT**	~~PPPT~~	**PVPT**	**VSPT**	~~VPPT~~	**VTPT**	~~VVPT~~
PSPV	**PTPV**	~~PPPV~~	**PVPV**	~~VSPV~~	~~VPPV~~	~~VTPV~~	~~VVPV~~
PSTS	~~PTTS~~	~~PPTS~~	**PVTS**	**VSTS**	**VPTS**	~~VTTS~~	~~VVTS~~
~~PSTP~~	~~PTTP~~	~~PPTP~~	~~PVTP~~	**VSTP**	**VPTP**	~~VTTP~~	~~VVTP~~
~~PSTT~~	~~PTTT~~	~~PPTT~~	~~PVTT~~	~~VSTT~~	~~VPTT~~	~~VTTT~~	~~VVTT~~
PSTV	~~PTTV~~	~~PPTV~~	**PVTV**	~~VSTV~~	~~VPTV~~	~~VTTV~~	~~VVTV~~
PSVS	**PTVS**	~~PPVS~~	~~PVVS~~	**VSVS**	**VPVS**	**VTVS**	~~VVVS~~
~~PSVP~~	~~PTVP~~	~~PPVP~~	~~PVVP~~	**VSVP**	**VPVP**	**VTVP**	~~VVVP~~
PSVT	**PTVT**	~~PPVT~~	~~PVVT~~	**VSVT**	**VPVT**	**VTVT**	~~VVVT~~
~~PSVV~~	~~PTVV~~	~~PPVV~~	~~PVVV~~	~~VSVV~~	~~VPVV~~	~~VTVV~~	~~VVVV~~

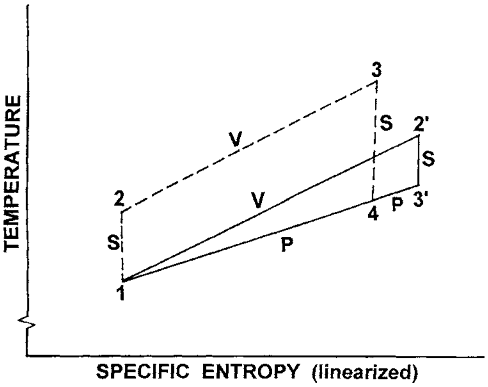

Fig. 2 Comparing three-process VSPP cycle to four-process SVSP cycle

three-sided diagram is unable to match the efficiency of a four-sided diagram. This second cut, eliminating three-sided diagrams, reduces the number of cycles under consideration to 84.

Cycles With Subatmospheric Pressure

Next, consider cycles started isobarically. The initiating isobaric process must be endothermic, i.e., effected by an absorption of energy and an increase in entropy, because an exothermic isobaric process would entail the unreasonable requirement of initially cooling the working medium below its starting temperature.

All such cycles started with an endothermic isobaric process are eliminated because in order to close a clockwise-generated T-S diagram, processes completing the cycle must occur at pressures lower than the atmospheric pressure at which the cycle starts. The result is a negative mep (mean effective pressure, i.e., the average height of the enclosed diagram representing the cycle on a pressure-volume plane). This third cut removes 21 cycles, leaving 63 for further consideration.

Of the remaining cycles, those beginning with pressure-increasing processes that subsequently require cylinder pressure to drop below atmospheric pressure in closing the diagram are eliminated. Such cycles require recompression of the cylinder gas after it has been expanded for the extraction of positive work. From a practical standpoint, such cycles are likely to suffer from low power density. This is true because the required subatmospheric area of the P-V diagram lowers mep. For a specified output, this can be expected to require a large piston displacement.

Recalling from Fig. 1 that the slopes of the processes mapped on a T-S plane decrease from isentropic (infinite slope) to isochoric to isobaric to isothermal (zero slope), it can be reasoned that subatmospheric pressure is encountered in closing the 14 cycles initiated isochorically that are closed with T or S, and the seven cycles initiated isentropically that are closed with T. All of the remaining 21 isothermally initiated cycles survive except TSVP, which, if cooling below the starting temperature is disallowed, can be closed only in the counter-clockwise direction and therefore constitutes a refrigeration cycle. The 41 cycles surviving this fourth cut—20 initiated isothermally, 14 initiated isentropically, and 7 initiated isochorically—are listed in Table 2.

In exploring these 41 candidates, each cycle can be considered as comprised of two phases—an opening and a closing phase. All cycles begin the opening phase at a common thermodynamic state—atmospheric pressure and an arbitrarily selected initial temperature. The opening phase terminates with the end of energy addition. That point on the T-S diagram is marked by maximum cycle temperature. In cycles where the final process of the opening phase is isothermal, the opening phase terminates at the point of maximum temperature and maximum entropy. Then the closing phase is comprised of the one to three processes used to return the working gas to its initial state.

Table 2 Cycles surviving the fourth cut

SPSP	VSTP	TPSP
SPSV	VSVP	TPSV
SPTP	VPSP	TPTS
SPTV	VPTP	TPTP
SPVP	VPVP	TPTV
STSP	VTSP	TPVS
STSV	VTVP	TPVP
STPV		TVSP
STVP	TSPS	TVSV
SVSP	TSPV	TVPS
SVSV	TSTS	TVPV
SVPV	TSTP	TVTS
SVTP	TSTV	TVTP
SVTV	TSVS	TVTV

At this point the 20 cycles initiated isothermally are set aside temporarily for subsequent examination because, unlike the other 21 cycles, they reject energy during the opening phase. Next, the most desirable closing path for those 21 cycles is considered.

Isentropic and Isochoric Initiation

In Fig. 3, the closing phase begins at point *b*, the termination of opening phase $a-b$. The irregular path plotted for the opening phase indicates that the present consideration of the closing phase is independent of the path followed in the opening phase. The only requirement imposed on the opening phase in this study is that when comparing cycles, the area under $a-b$, i.e., the energy added to the cycle, is held constant. Because of this constancy of energy added, the cycle with the least area under the closing path, i.e., rejecting the least energy, is the most efficient.

The lowest line plotted in Fig. 3 represents the atmospheric isobar. As previously discussed, cycles with closing phases going below that isobar have been rejected because of low mean effective pressure. Three possible closing paths are illustrated in Fig. 3: --SV, --SP, and -VSP. It is obvious from inspection that the least energy is rejected with the two-process closing path SP. Discarding, from the 31 cycles being considered, those not closed by SP leaves only five of them, viz., SPSP, STSP, SVSP, VPSP, and VTSP.

In Fig. 4, the opening phases of these five cycles are compared. In each case these opening-phase paths are drawn to have equal areas (equal energy added) beneath them, and are completed with an SP closing, in keeping with the previous finding. Immediately apparent is that for the isochorically initiated cycles, the opening phase must be extended to a much higher entropy, with a consequent greater energy rejection, than is the case for the three cycles beginning isentropically. It is clear from these diagrams that for the prescribed boundary conditions of this figure, a cycle beginning isochorically cannot compete in efficiency with one beginning isentropically. It is further seen that for a specified compres-

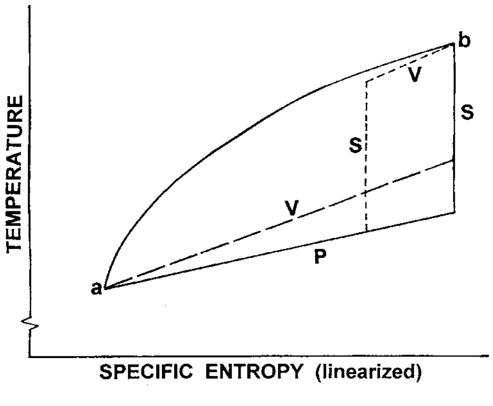

Fig. 3 Comparing cycle closing phases —SP, —SV, and -VSP

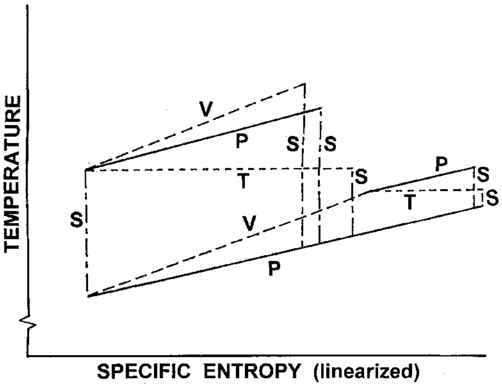

Fig. 4 Comparing isentrope- and isochore-initiated cycles

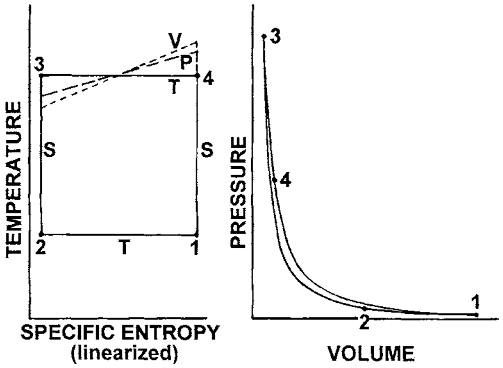

Fig. 5 Comparing Carnot (1–2–3–4) to two other isotherm-initiated cycles

sion ratio, which is set by the shared isentropic process beginning the other three cycles, adding energy isochorically offers the greatest cycle efficiency because it requires the least energy rejection. Cycles adding energy at constant pressure and at constant temperature offer decreasing efficiency, in that order.

This superiority of the SVSP cycle, the Atkinson cycle, stems from the fact that compression ratio was held constant. However, this cycle produces a comparatively high peak pressure. Engine design may be constrained by that pressure, which adversely affects the engine weight/durability/cost tradeoff and typically increases combustion-generated noise. As can be deduced from Fig. 4, if the limiting design parameter is peak pressure rather than compression ratio, the initial temperature rise for the SVSP cycle must be reduced, making the SPSP cycle more efficient than the SVSP cycle. SPSP defines the Brayton, or Joule, cycle.

Isothermal Initiation

Now attention is turned to the remaining 20 isothermally initiated cycles—7 of them ending isentropically, 7 isochorically, and 6 isobarically. A feature distinguishing those ending with an isentrope is that all of the cycle energy rejection occurs during isothermal compression. In contrast, the other 13 isothermally initiated cycles experience energy rejection during two of the four processes comprising the cycle.

Three of the seven ending isentropically follow the initial isotherm with a second isentrope, as superimposed with identical initial isothermal compression paths and equal energy inputs in Fig. 5. TSTS (1–2–3–4) is the Carnot cycle, the efficiency of which, from the Second Law of Thermodynamics, cannot be exceeded by any cycle operating between the same temperature limits. As drawn, the other two cycles in Fig. 5 have the same efficiency as the Carnot cycle illustrated, but both require higher maximum temperatures. They are of interest because on a P-V plane, the isothermal energy addition of the Carnot cycle leads to an unattractively low mep. This is apparent from the limited enclosed area of the Carnot P-V diagram in Fig. 5. TSPS improves slightly on that mep while decreasing peak pressure. TSVS offers a little greater mep, but at the expense of a higher peak pressure than TSPS.

Treating the other isentropically terminated cycles—TPTS, TVTS, TPVS, and TVPS—by the same procedure, it is found that they can be closed on a P-V plane only if V_2, the volume at the end of the initial isothermal compression, is less than V_4, the volume at the beginning of the final isentropic expansion. It can be shown that for this condition to exist, V_1/V_2, the volume ratio of the initial isothermal compression, must be greater than the following function of the ratio of specific heats (γ) and the cycle temperature ratio: $(T_{max}/T_{min})^{1/(\gamma-1)}$. Even at that, none of the T--S cycles is particularly attractive because the convergence of the T and S paths at maximum volume V_1 forces a rather limited enclosed work area on the P-V plane, as previously noted for the Carnot P-V diagram of Fig. 5.

To compare the efficiency of the Carnot cycle to two offering greater work areas, two different Carnot cycles, viz., $1-a-b-2$ and $1-c-d-e$, are compared in Fig. 6 to cycle 1–2–3–4, which may represent either an Otto (SVSV) or a Brayton/Joule (SPSP) cycle. It makes no difference which, for in terms of the volume ratio of the initiating process, each has the same air-standard efficiency. Note that, as in earlier comparisons, the energy additions for all cycles of Fig. 6 are equal. The efficiency of the Otto cycle (η_O) is widely recognized as a function of its compression ratio, V_1/V_2, and is expressed [7] as

$$\eta_O = 1 - \left(\frac{V_2}{V_1}\right)^{\gamma-1} = 1 - \frac{T_1}{T_2} \tag{3}$$

Not only is this equation appropriate for both the Otto and the Brayton cycles, but it also fits the Carnot cycle if T_1 is its minimum temperature and T_2 is its maximum temperature.

With that information in hand, reference to Fig. 6 indicates that Carnot cycle $1-a-b-2$ has the same efficiency as the Otto (or Brayton/Joule) cycle illustrated because its T_{min}/T_{max} is the same as T_1/T_2 for the non-Carnot cycle. Of course, this particular Carnot cycle achieves that efficiency with a much lower peak temperature. At the same time, Carnot cycle $1-c-d-e$, drawn to have the same maximum temperature as cycle 1–2–3–4, has a higher efficiency because of its lesser energy rejection. Thus the efficiency of a Carnot cycle can vary over a wide range, compared to an Otto (or Brayton/Joule) cycle with the same energy input. It can certainly exceed the efficiency of those isentropically initiated cycles, depending on temperature limits chosen for the Carnot cycle.

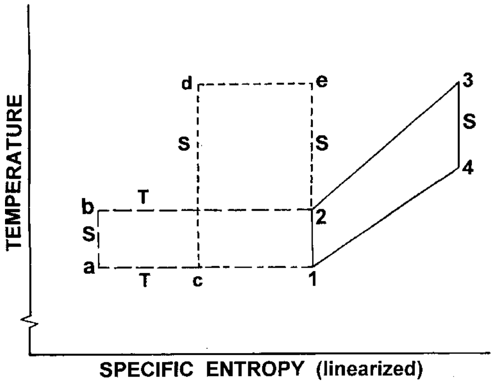

Fig. 6 Comparing Otto (1–2–3–4) to two Carnot cycles

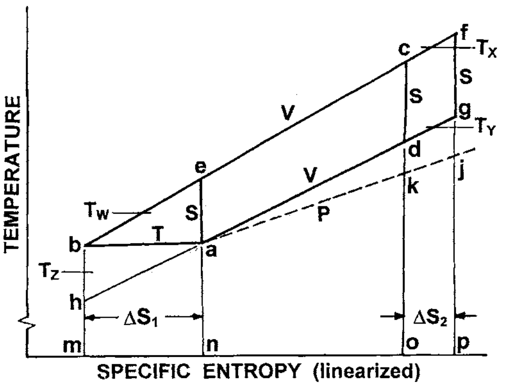

Fig. 7 Comparing isotherm- and isentrope-initiated cycles

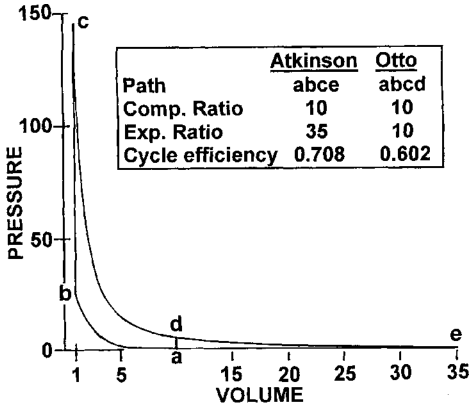

	Atkinson	Otto
Path	abce	abcd
Comp. Ratio	10	10
Exp. Ratio	35	10
Cycle efficiency	0.708	0.602

Fig. 8 Comparing Atkinson (SVSP) and Otto (SVSV) cycles

The remaining 13 isothermally initiated cycles need additional analysis because they incorporate two energy-rejecting processes. The germane question is whether any of them is more efficient than the best equivalent cycle initiated isentropically. To address that question, first SVSV is compared to its isothermally initiated counterpart, TVSV, in Fig. 7. Cycle TVSV is represented by path a–b–c–d. Cycle SVSV is path a–e–f–g. Because the same energy is added to each cycle, it follows that $\boxed{\mathrm{mbco}}$ must equal $\boxed{\mathrm{nefp}}$. (In this text, a path notation enclosed within a rectangle designates the area enclosed by that path.) Because $\boxed{\mathrm{neco}}$ is common to both, $\boxed{\mathrm{mbcn}} = \boxed{\mathrm{ocfp}}$.

Let $(S_n - S_m) = \Delta S_1$ and $(S_p - S_o) = \Delta S_2$. Further, let T_w represent the average of T_a and T_e, T_x represent the average of T_c and T_f, and T_y represent the average of T_g and T_d. Then $\boxed{\mathrm{mben}} = T_w \Delta S_1$, $\boxed{\mathrm{ocfp}} = T_x \Delta S_2$, and $\boxed{\mathrm{odgp}} = T_y \Delta S_2$:

$$\Delta S_1 = \frac{T_x}{T_w}\Delta S_2 \tag{4}$$

Now the closing isochore, g–a, is extended down to point h, and T_z is defined as average of T_b and T_h. Because paths h–b, a–e, d–c and g–f are all isentropes between the same pair of isochores, it follows that

$$\frac{T_x}{T_w} = \frac{T_y}{T_z} \tag{5}$$

With equal energy inputs, the most efficient cycle is the one with the least energy rejected. TVSV rejects energy proportional to $\boxed{\mathrm{mbado}}$. SVSV rejects energy proportional to $\boxed{\mathrm{nagp}}$. Since $\boxed{\mathrm{nado}}$ is common to both, the efficiency question resolves down to the difference between $\boxed{\mathrm{mban}}$ and $\boxed{\mathrm{odgp}}$, which can be expressed as follows:

$$T_a \Delta S_1 - T_y \Delta S_2 = T_a \frac{T_x}{T_w}\Delta S_2 - T_z \frac{T_x}{T_w}\Delta S_2 > 0 \tag{6}$$

Thus cycle TVSV rejects more energy than cycle SVSV, making the isothermally initiated cycle less efficient than the corresponding cycle initiated isentropically.

The dotted line at the bottom of Fig. 7 is the atmospheric isobar. Suppose that both cycles were closed with this isobar rather than isochores g–a and d–a, respectively. This leads to SVSP (path aefj), previously cited for its superior efficiency, and the corresponding TVSP (path abck). Applying the methodology of Eq. (6) to this new pair of cycles, TVSP falls even further behind SVSP in efficiency. This leads to the conclusion that for the boundary conditions imposed, cycle SVSP (Atkinson) is the most efficient of the 256 original combinations, provided isothermally initiated cycles that are closed isentropically (like the Carnot cycle) are rejected on grounds of inadequate work area on the P-V plane, i.e., unacceptably low mep. In line with previous findings, however, if maximum cycle pressure is a limiting factor, cycle SPSP (Brayton, or Joule) has the highest efficiency.

Practical Limitations

Although isothermally initiated cycles are of thermodynamic interest, in practice their implementation is problematic. The energy transfer from the working gas that would be needed to maintain isothermal compression depends on the transfer area, the temperature difference between the gas and its confining walls, and the time available for transfer. During compression in a reciprocating engine, the energy-transfer area is determined by cylinder dimensions, which are normally based on considerations other than energy transfer. Because the confining walls are exposed to combustion gases and are influenced by a coolant temperature above ambient, early during compression, energy is actually transferred into the working gas rather than from it. When a favorable temperature difference for energy rejection can exist late during the compression process, high engine speed limits the time available for energy rejection. Consequently, attention is appropriately directed to cycles initiated isentropically.

If SVSP is the most efficient of those cycles, it is logical to question why it is not now broadly accepted in practice. The reason is illustrated in the pressure-volume diagrams of Fig. 8, where path a–b–c–e traces the Atkinson (SVSP) cycle and path a–b–c–d traces the familiar Otto (SVSV) cycle. For the Atkinson cycle illustrated, the compression ratio (V_a/V_b) is arbitrarily chosen as 10. Then using the cycle analysis methodology of Stone [7], for a stoichiometric mixture of gasoline the expansion ratio (V_e/V_c) required to expand the gas isentropically from its peak pressure at c back down to initial pressure $(p_a = p_e)$ is 35. For the Otto cycle, the compression and expansion ratios are both 10. The large cylinder displacement required for SVSP increases the cycle efficiency by 18%, from 0.602 for the Otto cycle to 0.708 for the Atkinson cycle.

The mep of the cycles depicted in Fig. 8 is given by

$$\bar{p} = \frac{\eta Q_f \rho (R_c - 1)}{(A/F)(R_e - 1)}. \tag{7}$$

where $\bar{p}$=mean effective pressure, Q_f=Fuel heating value, ρ=Intake manifold density, A/F=gravimetric air/fuel ratio, R_c=compression ratio, and R_e=Expansion ratio.

Holding heating value, intake density, and A/F constant, and using values of the other parameters fitting Fig. 8, the 18% improvement in efficiency of the Atkinson cycle over the Otto comes at the expense of a 69% reduction in mep.

For a four-stroke engine, power (P) is given by

$$P = \frac{\bar{p} U_p \pi n B^2}{4} \tag{8}$$

where $\overline{p}$=mean effective pressure, U_p=mean piston speed, n=number of cylinders, and B=cylinder bore.

In practice, consideration of both the pressure loss in the intake system and mechanical friction restrict maximum mean piston speed to a comparatively narrow range. If mean piston speed is held constant, along with bore, the power loss associated with the approximately 2/3 reduction in mean effective pressure in the Atkinson engine can be compensated by tripling the number of same-size cylinders. The consequent effects on engine size, weight, and cost are obvious.

Alternatively, holding mean piston speed and bore/stroke ratio constant, the same number of cylinders can be retained if their bores are increased in this example by about 80%. With the stroke similarly increased to maintain bore/stroke ratio, this calls for an 80% longer stroke. Then to maintain mean piston speed, a slower engine rotational speed is required. Again, the overall size and weight of the engine increase.

For these and other reasons, the Atkinson cycle is not a popular choice, despite its efficiency advantage. A compromise between the Otto and Atkinson cycles is commonly effected in which the expansion ratio exceeds the compression ratio, but not by enough to expand the cylinder contents all the way down to the initial pressure. This is accomplished simply by closing the intake valve late during the compression stroke. The resulting SVSVP cycle, comprised of five processes, falls beyond the bounds of this study. Variable intake-valve timing may be used to combine the respective advantages of the Otto and Atkinson cycles beneficially as load is varied [8].

Summary and Conclusions

Employing air-standard cycle analysis, 256 combinations of reversible thermodynamic processes have been surveyed qualitatively to identify engine cycles with constant energy input per unit mass of working gas that offer the greatest thermal-efficiency potential. Only nonregenerative, naturally aspirated cycles comprised of no more than four reversible processes were considered.

1. For a fixed compression ratio, the SVSP (Atkinson) cycle promises the highest efficiency. However, it suffers from low mean effective pressure.
2. For a fixed peak cycle pressure, the SPSP (Brayton, or Joule) cycle promises the highest efficiency. However, it suffers from low mean effective pressure.
3. If some efficiency is traded off to avoid unreasonably low mean effective pressure, then at fixed compression ratio, the SVSV (Otto) cycle is the appropriate choice.
4. If some efficiency is traded off to avoid unreasonably low mean effective pressure, then at fixed peak cycle pressure, the $SPSV$ (Diesel) cycle is the appropriate choice.
5. Isothermally initiated cycles, of which the Carnot is the most widely recognized example, are thermodynamically interesting but considered unattractive for a reciprocating internal-combustion engine because of the practical problem of effecting isothermal compression, and among the most efficient versions, because of their low mean effective pressures.
6. A cycle comprised of more than four thermodynamic processes offers greater flexibility in trading off cycle efficiency for mean effective pressure. Such cycles are beyond the scope of this study. Variable intake-valve timing may be used to combine the respective advantages of the Otto and Atkinson cycles as load is varied.

References

[1] Lauck, F., Uyehara, O. A., and Myers, P. S., 1963, "An Engineering Evaluation of Energy Conversion Devices," SAE Trans., **71**, Paper 630466.

[2] Heywood, J. B., 1988, *Internal Combustion Engine Fundamentals*, McGraw-Hill, New York.

[3] Flynn, P. F., Hoag, K. L., Kamel, M. M., and Primus, R. J., 1984, "A New Perspective on Diesel Engine Evaluation Based On Second Law Analysis," SAE Paper 840032.

[4] Caton, J. A., 2000, "Operating Characteristics Using the Second Law of Thermodynamics: Effects of Speed and Load," SAE Paper 2000-01-0952.

[5] Lichty, L. C., 1939, *Internal Combustion Engines*, McGraw-Hill Book Company, New York.

[6] Jennings, B. F., and Obert, E. F., 1944, *Internal Combustion Engines: Analysis and Practice*, International Textbook Company, Scranton, PA.

[7] Stone, R., 1999, *Introduction to Internal Combustion Engines*, Society of Automotive Engineers, Warrendale, PA.

[8] Luria, D., Taitel, Y., and Stotter, A., 1982, "The Otto-Atkinson Engine—A New Concept in Automotive Economy," SAE Paper 820362.

Dimitrios N. Tsinoglou

Grigorios C. Koltsakis[1]
e-mail: greg@antiopi.meng.auth.gr

Laboratory of Applied Thermodynamics,
Aristotle University of Thessaloniki,
GR-54124 Thessaloniki, Greece

Influence of Pulsating Flow on Close-Coupled Catalyst Performance

Close coupling of automotive three-way catalytic converters is becoming a common practice in order to reduce pollutant emissions during cold start. In such applications, the exhaust gas mass flow may fluctuate, as a function of crankshaft angle. A simplified one-dimensional channel model is developed, assuming that pollutant conversion in the catalyst is mass transfer limited. This model is applied to evaluate the effect of pulsations in catalyst performance, and assess the accuracy of the "quasi-steady state" approach usually involved in three-way catalytic converter models, when applied to simulate converters under pulsating flow. [DOI: 10.1115/1.1924402]

1 Introduction

Close-coupled catalytic converters, i.e., catalytic converters placed very close to the engine, are becoming a commonly applied solution by the manufacturers, in order to reduce pollutant emissions during the cold start phase. A close-coupled catalytic converter is exposed to higher exhaust gas temperatures, and as a result, may reach light-off temperatures as quickly as 15 s after engine start, even at idle conditions [1]. Due to the very small pipe length between the exhaust ports and the converter inlet, the exhaust gas mass flow entering a close-coupled catalyst is not expected to be constant for a given engine operating point, but it is expected to present fluctuations as a function of the crankshaft angle. The pattern and intensity of these pulsations is not easy to characterize, as they strongly depend on the design and operational characteristics of each engine and exhaust system. Such pulsations are not likely to be encountered in traditional underfloor converters, due to the dampening effect exerted by the long exhaust pipes between the engine and the converter.

The nature of such pulsations has been previously studied in the literature. Zhao et al. [2] conducted an experimental study which demonstrated the pulsating nature of the flow at the inlet of an underfloor converter, and characterized the pulsation patterns at various engine speeds and loads. Computational fluid dynamics (CFD) techniques have also been extensively applied to study the pulsating flow phenomena. Such techniques are often combined with engine modeling methodologies. Berkman and Katari [3] have recently performed CFD simulations of a close coupled converter and have demonstrated that both exhaust gas velocity and flow uniformity at the monolith inlet present significant fluctuations during a full exhaust cycle (720 deg crankshaft angle). Their results imply that the exhaust gas velocity may reach peak values, which are four times higher than the "cycle average" velocity at certain instances and at certain locations of the monolith inlet face. This is also in agreement with the study of Badami et al. [4], who performed CFD simulations to compare the transient with the cycle-averaged flow phenomena in a close-coupled converter. Yoshizawa et al. [5] also performed CFD simulations of a close-coupled catalyst and observed local peaks of inlet velocity about three times higher than the average value during a full cycle (720 deg crankshaft angle). They also demonstrated the existence of pulsations by experimental data (pressure measurement using a piezoelectric sensor and flow visualization). Both the above studies agree that pulsation phenomena are significantly less severe in underfloor converters. Benjamin and Roberts [6] studied the effect of flow pulsation in the warm-up of a catalytic converter under nonreacting conditions using a single channel CFD model. They demonstrated that pulsation frequency plays a very small role in monolith warm-up, while pulsations with amplitude set to 90% of the mean value may result in locally lower monolith temperatures by up to 10 K. The same authors in a more recent study investigated the effect of flow pulsations on local velocity maldistribution using an experimental test rig, and compared their results with CFD simulations [7].

From the technical point of view, it is interesting to assess the impact of such pulsations on pollutant conversion efficiency. The increased mass flow rate during a pulse may result in lower pollutant conversion, due to limitations in the mass transfer from the gas phase to the channel walls. From the catalyst modeling point of view, pulsating flow poses an interesting challenge to transient models employing the quasi-steady state approach [e.g. [8,9]]. The latter approach assumes that the residence time of the exhaust gas inside the converter is much smaller than the rate at which the monolith inlet conditions (exhaust gas temperature, mass flow, and concentration) change. Indeed, the changes in cycle-averaged exhaust gas mass flow rate during transient operating conditions is in the order of a few seconds, while the typical residence time inside the monolith is less than 0.1 s. This approach is sufficient in the case of underfloor catalytic converters, where the flow pulsations are dampened. It is also computationally more efficient, as it allows the use of longer time steps (about 0.1 s) thus resulting in low computational times. However, this assumption may be far from reality in the case of pulsating flow calculations, where the mass flow rate may fluctuate with a time scale ranging from 20 to 150 ms.

The aim of this study is twofold; first, to assess the effect of pulsations on pollutant conversion in a typical close coupled catalyst under a wide range of operating conditions. Second, to assess the accuracy of the quasi-steady state approach, when applied to simulate close coupled converters exposed to pulsating flow. A simplified one-dimensional (1D) model of the mass transfer in the monolith channels is developed and applied to simulate the pulsating flow entering a close-coupled catalyst.

2 Simulation Model

2.1 Model Description Assumptions. The pollutant conversion efficiency of a catalytic converter is controlled by chemical reaction kinetics at low temperatures (below 500 K), by gas diffusion in the catalyst pores at medium temperatures (500–650 K)

---

[1] To whom correspondence should be addressed.

Contributed by the Internal Combustion Engine Division of THE AMERICAN SOCIETY OF MECHANICAL ENGINEERS for publication in the ASME JOURNAL OF ENGINEERING FOR GAS TURBINES AND POWER. Manuscript received by the ICE Division, August 27, 2003; final revision received June 21, 2004. Associate Editor: D. Assanis.

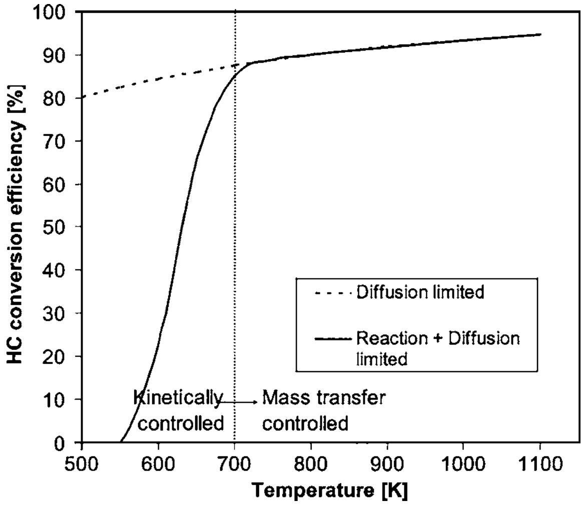

Fig. 1 Comparison between HC conversion predicted by the simplified mass transfer limited model and the one predicted by the full model, including mass diffusion and chemical reactions

and by bulk mass transfer at higher temperatures (above 650 K) [10]. The main difference between treating constant flow problems and pulsating flow problems is that in pulsating flow problems, the increased flow velocity during a pulse may result in decreased pollutant conversion, due to mass transfer limitations, even if the cycle-average velocity is the same as in a constant flow case. Therefore, a model of the mass transfer phenomena inside a monolith channel would allow assessing the possible decline in pollutant conversion due to the increased velocity involved in pulsating flows.

The main tool used to examine the behavior of a catalytic converter is a simplified 1D channel model. This model assumes that pollutant conversion efficiency depends only on the mass transfer phenomena in the gas phase. The main assumptions compared to a quasi-steady state heat and mass transfer and chemical reactions model previously presented [8] are listed below:

- The pollutant concentration at the wall-gas interface is considered to be very small compared to the gas phase concentration. Thus, the conversion depends only on the mass transfer in the gas phase.
- The channel is treated as isothermal, i.e., no heat transfer is considered between the solid and gas phase, and no gas temperature oscillations are assumed at catalyst inlet.
- Partially active converters can be simulated by assuming that they consist of an active (front) part and an inactive (rear) part. In the active part, conversion is given by Eq. (2), while in the inactive part conversion is assumed to be zero.
- The Sherwood number is considered constant along the channel, i.e., no entrance effects are accounted for.
- Only one species is considered, namely hydrocarbons (HCs), which are known to have the lowest diffusivity among the pollutants encountered in gasoline engine exhaust gas.

Taking into account the above assumptions, the simplified diffusion limited model gives realistic results for moderate and high temperatures (above 700 K). Figure 1 presents the comparison between the HC conversion efficiency predicted by the simplified mass transfer limited model, and the one predicted by the model presented in Ref. [8], which accounts for both mass transfer and chemical reactions. The results suggest that the conversion efficiency predicted by the two models is practically the same above 750 K.

2.2 Model Equations. The fundamental differential equation describing the species balance in the channel is [11]

$$\varepsilon \frac{\partial c(x,t)}{\partial t} + v \frac{\partial c(x,t)}{\partial x} = -k \cdot S \cdot (c - c_s). \qquad (1)$$

In this equation, k is the mass transfer coefficient, and S is the specific surface area of the channel $[\mathrm{m}^2/\mathrm{m}^3]$.

Based on the assumption of diffusion limited operation, the term c_s which refers to the pollutant concentration at the gas-solid interface, is equal to zero.

The calculation of the concentrations field along the channel during a fully transient problem is performed by solving Eq. (1) using the one-step Lax–Wendroff method [12]. Each time marching comprises the solution of the concentrations field for each node. Equation (1) can be solved to calculate the pollutant concentration at the node i, in the time step $n+1$

$$c_i^{n+1} = c_{i-1}^n - \frac{dt \cdot v^n}{dx} c_i^n - dt \cdot k \cdot S \cdot c_i^n. \qquad (2)$$

The channel is discretized by approximately 800 axial nodes, depending on the length of the simulated monolith. The relatively high value of the space step was necessary to obtain grid-independent results for all patterns of pulsating flow, due to the highly transient conditions assumed. For a given space step, the duration of each time step satisfies the stability criteria derived by the Von Neumann analysis

$$\left| \frac{\frac{\varepsilon}{dt}\cosh(k \cdot dx) - \frac{v}{dx}\sinh(k \cdot dx)}{\frac{\varepsilon}{dt} + k} \right| \leq 1. \qquad (3)$$

In all previously published models, the first term of the left-hand side of Eq. (1) is neglected, assuming quasi-steady state conditions, in this case, Eq. (1) reduces to

$$v \frac{\partial c(x,t)}{\partial x} = k \cdot S \cdot (c - c_s), \qquad (4)$$

where again the term c_s is equal to zero in the diffusion controlled problem. Equation (4) can be easily solved analytically, and gives

$$c_i^n = c_{i-1}^n \cdot e^{-dx \cdot k \cdot S}. \qquad (5)$$

The main difference between the above fully transient approach, and the commonly applied quasi-steady state approach, is that in the fully transient model, each differential flow element may change its velocity during its travel inside the channel, according to the flow pulsations.

A typical execution time for the fully transient simulation of one cycle (720 deg crank angle) is in the order of 0.5–1 s for a 2.4 GHz PC, depending on the catalytic converter dimensions. On the other hand, with the quasi-steady state approach, grid independent results may be obtained even using much higher space steps in the simulation. Therefore, a similar quasi-steady state simulation would require 3–6 times less computation time. Using the steady state approach, i.e., assuming constant mass flow, equal to the cycle average, further reductions in computation time may be obtained; similar 1D simulations may performed at least one order of magnitude faster.

2.3 Boundary Conditions. In this paper we are dealing with the effects of exhaust gas pulsations in terms of mass flow rate fluctuations during an engine cycle. The oscillating character of temperature and pressure at catalyst inlet are not considered. Therefore, the mass flow rate should be given as function of crank angle as a boundary condition to our problem. This information can be conveniently provided from widely used thermodynamic engine models, which take into account the exhaust system geometry, including the catalytic converter [13].

For the purpose of our exploratory study, we will use as bound-

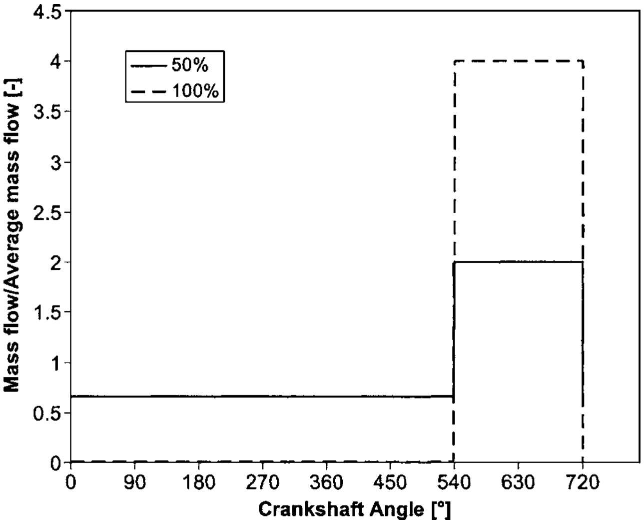

Fig. 2 Mass flow variation during an exhaust cycle for two pulsation patterns examined. The percentage denotes the percentage of exhaust gas mass emitted during the pulse phase. Average mass flow $\dot{m}=0.02$ kg/s, 1000 rpm.

ary condition various artificial mass flow rate patterns, which consist of two phases. These patterns involve a constant mass flow during the 3/4 of the exhaust cycle, and a "pulse phase" which lasts for 1/4 of the exhaust cycle. The amount of exhaust mass emitted in the pulse phase compared to the total exhaust flow during the engine cycle is a parameter for our problem. This artificial flow condition is a simplification for the case of a four-cylinder, four-stroke engine with a close coupled catalyst and a 4 in 1 manifold geometry. Nevertheless, this simplification is useful to better quantify our results as regards pulsating flow effects.

Figure 2 presents the mass flow rate as a function of crank angle for two cases; in the first one (indicated as 50%), half of the exhaust gas mass flows during the pulse phase, and the other half is divided to the rest 3/4 of the cycle. In the second case, (indicated as 100%), the entire mass flows through the catalyst during the pulse phase. The latter case corresponds to a close coupled catalyst with a cone connected to the exhaust ports by four pipes. The cylinders are considered to fire consecutively, and during each firing the flow is directed to an area equal to 1/4 of the monolith frontal area.

The hypothetical engine considered here is a 2 l four-cylinder engine, which operates from 1000 to 6000 rpm, with volumetric efficiencies ranging from 0.2 to 1. The close-coupled converter simulated here has a volume of 0.825 [ℓ], which was selected as approximately half of the engine displacement, which could be considered typical for a preconverter. Since the model results are basically a function of the space velocity, the results can be directly generalized for any other engine displacement, with the corresponding catalyst volume. The monolith considered had a cell density of 400 cpsi (62 cells/cm^2) and an open frontal area equal to 76%. The monolith diameter is 0.1 m.

With the given monolith geometry, and the pulsation pattern presented in Fig. 2, we may easily calculate the peak velocities at the monolith inlet face. For a mass flow rate of 0.02 [kg/s], the cycle averaged velocity at the monolith inlet is 5.78 [m/s]. The peak velocity during the pulse phase varies from 11.67, in the case where half of the exhaust gas mass flows during the pulse phase (indicated as 50%), to 23.34 [m/s], in the case where the entire mass flows through the catalyst during the pulse phase (indicated as 100%).

In real world applications, peak gas velocities may be even higher, because of two reasons: First, due to the local velocity distribution at the monolith inlet face; the shape of the piping and diffuser is known to cause local velocity peaks at the monolith inlet face. Second, due to the temporal velocity profiles which are observed during the exhaust stroke; in reality, the pulses are usually not square shaped, but velocity peaks are observed right after the exhaust valve opening [13]. The nature of these local and temporal velocity peaks depends strongly on the engine operation and the design of the exhaust system, and can be studied using engine modeling techniques. In the framework of this preliminary study, the simplified square pulse pattern serves a more universal quantification of the effect of flow pulsations.

The space velocity inside the catalytic converter is a critical factor when evaluating the effects of pulsating flows, since it has a direct effect on the residence time of the gas inside the catalytic converter. In the present study, different values of space velocity are obtained by modifying the "active length" of the catalytic converter; thus, we assume that only a part of the catalyst volume is working at mass transfer limiting conditions, whereas the rest is totally inactive [14]. This may also be considered as a rough approximation of catalyst operation during the first seconds after cold start, where the first part of the catalyst is warmed up faster compared to its rear part therefore the catalyst is partially active [15]. However, in order to examine the effect of pulsations during the cold start phase in more detail, one should also consider the reaction kinetics, and their effect on pollutant conversion, since a significant part of the monolith is operating at temperatures near the light-off temperature. These effects are examined in more detail in another research work [16].

The boundary condition for the assumed constant species concentration at the channel inlet is

$$c_1^n = c_{\text{in}}. \tag{6}$$

The initial concentration field inside the channel is supposed to correspond to ambient conditions, where pollutant concentrations are considered equal to zero

$$c_i^1 = 0. \tag{7}$$

The temperature used for the gas thermophysical properties is 800 K and the HC concentration in the exhaust gas is 3000 ppm C1.

3 Results and Discussion

3.1 Pulsating Flow Simulation. The previously described scenario is simulated using the quasi-steady and the fully transient approach. The HC emissions as a function of crankshaft angle are examined below. The pulsation pattern used is the one previously designated as "50%." Two different active volumes were examined, in order to clearly illustrate the effect of increased flow velocity (decreased gas residence time in the converter).

Figure 3 presents the simulated HC emissions during three consecutive exhaust cycles. Both the quasi-steady state and the "fully transient" approach results are included. As a result, in case (a), which corresponds to a converter with a small active volume, the HC concentration rises slowly after the pulse begins, and reaches the quasi-steady state value after a short time interval. This time interval is equal to the gas residence time in the active part of the channel, when the gas is moving with the high mass flow rate. The slow rise is due to the fact that each "flow element" which is found inside the channel at the moment the pulse begins has a different residence time, according to its position when the pulse begins. After the pulse ends, again HC concentration drops slowly, to reach the quasi-steady state value which corresponds to the lower mass flow rate, after a time interval which is equal to the residence time of the gas moving at the low velocity.

On the other hand, the changes in quasi-steady state concentration results are exactly synchronized with the changes in mass flow rate. Since the cumulative emissions are calculated based on the instantaneous concentration and mass flow rate, the two simulation methods may give significantly different cumulative emissions. This will be further examined and quantified in the next

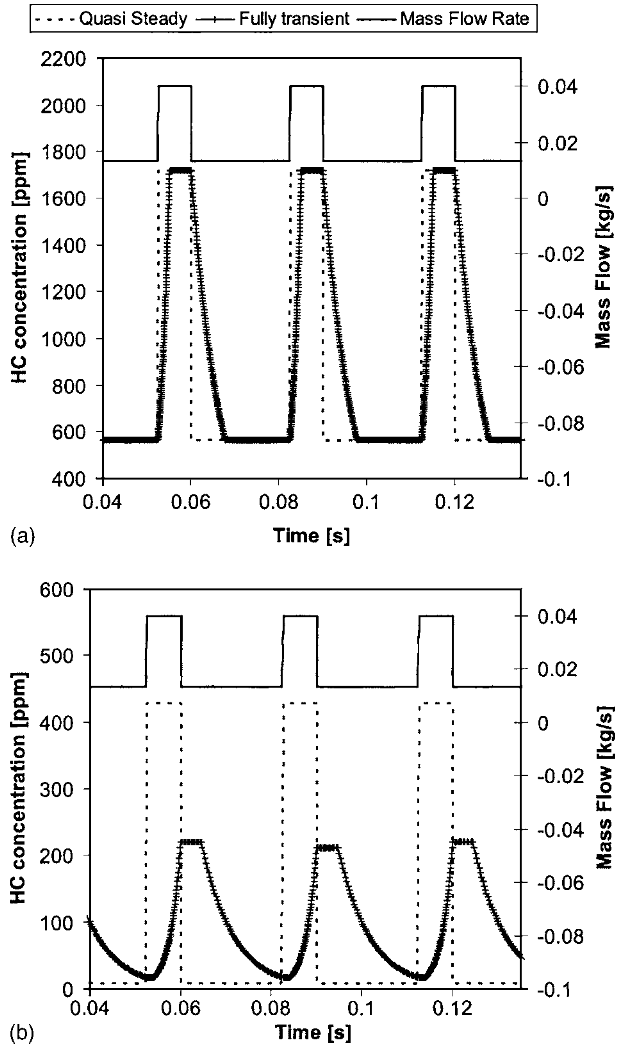

Fig. 3 Simulated HC conversion during a series of three exhaust cycles, assuming quasi-steady state simulation of pulsating flow and transient simulation of pulsating flow. (a) Active volume ratio AV=0.12. (b) AV=0.41. 4000 rpm, η=0.23.

section. Case (b) corresponds to a converter where the entire channel length is active. Therefore the residence times are longer, and the pollutant outlet concentrations are naturally lower. In this case, it is observed that after the pulse begins, the HC concentration rises (as mentioned before) however, the pulse ends before the quasi-steady state concentration is reached. This implies that the duration of the pulse is shorter than the residence time of the gas flowing with the high mass flow rate. After the pulse ends, the concentration remains constant for some time. This concentration corresponds to flow elements which have entered the channel during the low mass flow rate phase, and are exiting the channel during the next low mass flow rate phase, i.e., which have been inside the channel during the entire pulse duration. In this case, the difference between the quasi-steady state modeling approach and the fully transient modeling approach is even more pronounced.

3.2 Effect of Simulation Method. As previously described, the fully transient approach for simulation of the pulsating flow may give significantly different results than the quasi-steady state approach, due to the fact that the mass flow, hence exhaust gas velocity, may change during the travel time of each exhaust gas flow element inside the monolith channel. As a result, each flow element may change its speed while moving inside the channel. An interesting magnitude for quantifying the frequency at which the mass flow changes is the Pulsation Index, defined as the ratio of the gas mean residence time, divided by the pulse duration

$$\mathrm{PI} = \frac{\text{mean residence time}}{\text{pulse duration}} = \frac{\dfrac{L}{v_{\text{average}}}}{\Delta t_{\text{pulse}}}. \tag{8}$$

At very small values of PI ($\mathrm{PI} \ll 1$), the results obtained by the quasi-steady state approach are expected to be similar with those of the fully transient approach. At higher PI values, the quasi-steady state approach will not necessarily be sufficient, since the main assumption of this approach is that the pulse travel time is very small compared to the inlet conditions fluctuation period.

Figure 4 illustrates the range of PI values which can be encountered for the engine and catalyst configuration described in Sec. 2.3. The ratio of the catalyst active volume/engine displacement is modified by modifying the active channel length, in order to simulate catalytic converters in the warm-up phase. The value of the PI is directly proportional to the active channel length, because increasing channel length increases the residence time, and also inversely proportional to the engine volumetric efficiency, because higher volumetric efficiencies are associated with higher gas mass flow, hence higher gas velocity. Engine speed does not affect this diagram, as increasing engine speed decreases both the numerator (gas travel time) and the denominator (pulse duration) of the PI fraction by the same percentage.

The catalytic converter previously described was simulated by varying its active length, in order to simulate different instances during the light-off phase. The simulation was performed at three different engine speeds (1000, 4000, and 6000 rpm). Three different modeling approaches have been examined: a steady state approach, where the mass flow rate is constant and equal to the average mass flow rate, the quasi-steady state approach described previously, and the fully transient approach. Figure 5 presents the total conversion efficiency over a full exhaust cycle for these conditions. The simulations presented in this figure were performed with a volumetric efficiency approximately 0.2. The steady state approach always predicts higher efficiencies than the pulsating approaches. This indicates that pulsations have a detrimental effect on catalyst performance. It is worth mentioning that all the approaches converge in regions of low catalyst efficiency. The efficiency predicted by the quasi-steady state approach is very close to the one predicted by the fully transient approach at 1000 rpm, which is the most interesting engine speed for the catalytic converter warm-up. At higher mass flow rates the efficiency naturally drops, due to the higher gas velocity, which results in increased mass transfer limitations. The fully transient approach presents little deviation from the quasi-steady state approach for low PI values, however this deviation increases for higher PI values, reaching a maximum of about 5–7 percentage units. This could be expected based on the results presented in Sec. 3.1.

Using higher volumetric efficiencies does not affect the shape of the curves but limits the maximum values of PI that the curves would reach, i.e., the simulation results for η_v=0.4 would consist of the left half of the curves presented in Fig. 5. This implies, that for higher volumetric efficiencies, the deviation between the quasi-steady and fully transient approach is less important. The same applies to the effect of pulsating flow, compared to nonpulsating.

3.3 Effect of Pulsation Pattern. As mentioned earlier, the shape of the pulses depends strongly on the engine and exhaust design and operational characteristics. The aim of this section is to examine the effect of the maximum pulse velocity during square shaped pulses, on the conversion efficiency over an exhaust cycle. The simulation is performed at 4000 rpm, using varying active catalyst length, as in the previous simulations, and the results are presented in Fig. 6. The variation of the catalyst length results in variation of the space velocity in the active part of the catalyst.

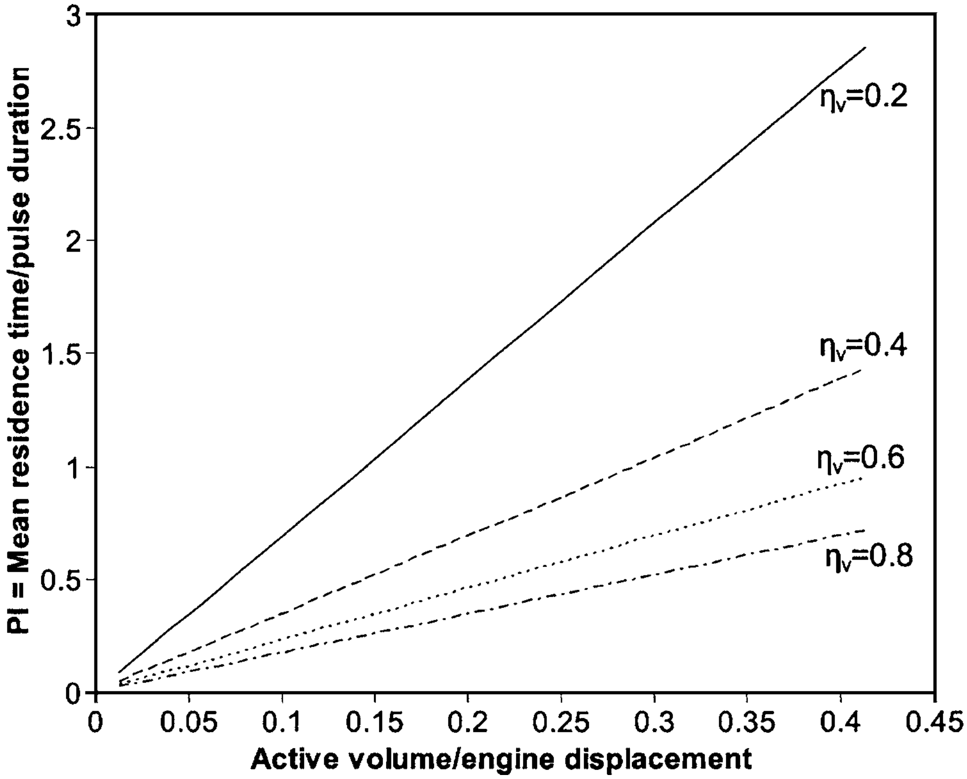

Fig. 4 Pulsation Index (PI) dependence from active catalyst volume and engine volumetric efficiency

The cycle averaged space velocity is included in the plot. Peak space velocities, during the pulse phase, are expected to be 2–4 times higher, depending on the percentage of the exhaust gas mass emitted during the pulse phase. The latter was modified from 50% to 100%. Figure 6(*a*) presents the efficiency predicted by the fully transient approach, compared to the steady state efficiency. The plot indicates that increasing the maximum pulse velocity decreases almost proportionally the conversion efficiency. The deviation between the steady state and fully transient conversion in the case of the most "intense" pulses is in the order of 20 percentage units. On the other hand, Fig. 6(*b*) indicates that the decline predicted by the quasi-steady state approach gradually becomes more severe as the maximum pulse velocity increases. This implies that the quasi-steady state approach tends to somehow over-

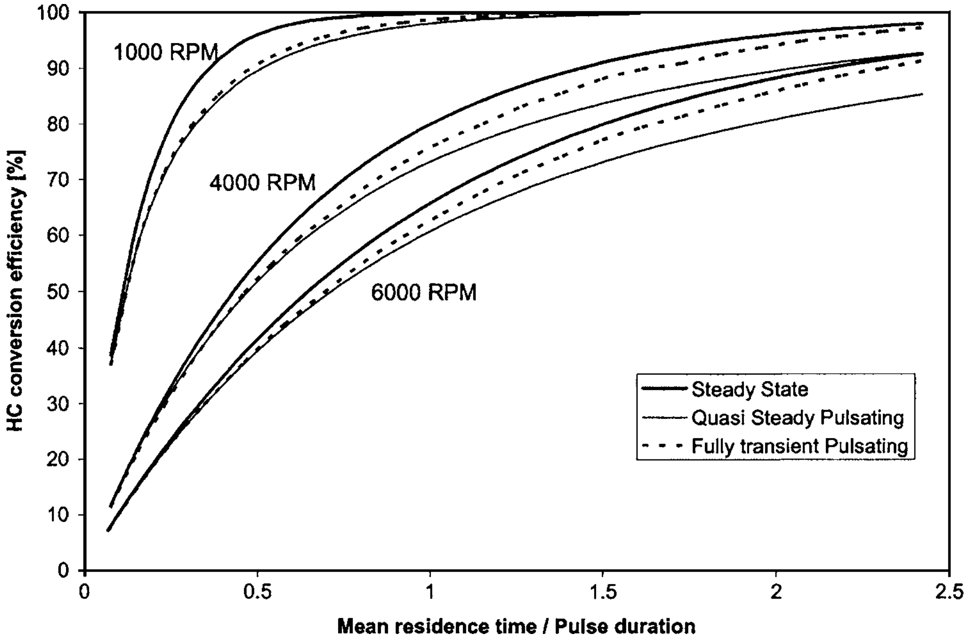

Fig. 5 HC conversion efficiency during an exhaust cycle as a function of Pulsation Index; effect of engine speed and simulation method. Fifty percent of the exhaust gas mass emitted during the pulse phase.

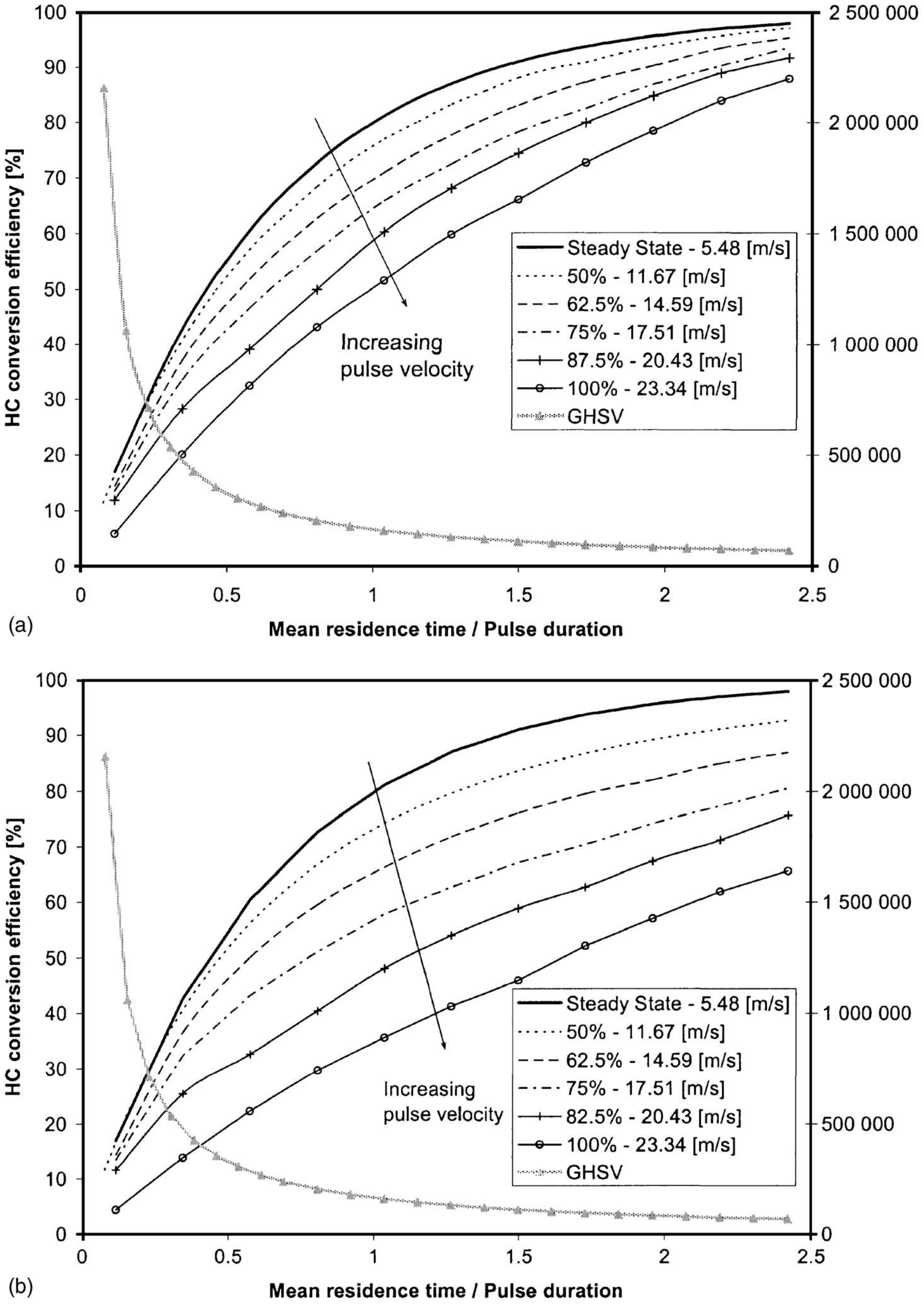

Fig. 6 HC conversion efficiency during an exhaust cycle as a function of Pulsation Index; effect of maximum pulse velocity (a) on fully transient conversion, (b) on quasi-steady state conversion. 4000 rpm. The percentage denotes the percentage of exhaust gas mass emitted during the pulse phase. The peak velocity at the monolith inlet face during the pulsation is also included.

estimate the negative effect of pulsations on conversion efficiency. The comparison between Figs. 6(*a*) and 6(*b*) shows that the deviation between the quasi-steady state approach and the fully transient approach also increases with increasing pulse velocity, reaching a maximum of approximately 20 percentage units in the case of the highest pulse velocity. It also suggests that the deviation between the two approaches increases with increasing gas residence time in the channel. This is justified based on the results presented in Fig. 3.

The above results indicate that the quasi-steady state approach might be applicable in the simulation of pulsating flows, with a penalty in the accuracy of the order of 2–7%, in the case of pulses with moderate intensity (pulse velocity up to twice the average velocity). However, in the case of more intense pulsation, this deviation might exceed 20%, which makes the quasi-steady state approach inappropriate. Moreover, pulsating flows may result in significantly different results than nonpulsating flows, when the maximum pulse velocity is high. Therefore, the applicability of the steady state approach, which is also computationally more time efficient, depends on the ratio of the maximum pulse velocity to average velocity over an exhaust cycle.

4 Conclusions

Flow pulsations are present in many close-coupled catalytic converter applications. The performance of a catalytic converter under pulsating flow can be different from its performance under steady state flow, due to the mass transfer limitation associated with the increased velocity in the pulse phase. In order to assess the impact of pulsations on close-coupled catalyst performance, the fully transient 1D channel problem was solved for some extremely transient operation modes. The main model assumption is that the pollutant conversion depends only on the mass transfer in the gas phase.

The model has been applied to simulate pulsating flows with square shaped pulses of various intensities, at various engine operating points. The instantaneous pollutant emissions of a catalytic converter operating under pulsating flow were shown to depend on the gas residence time inside the channel, and the pulse duration. As a result, the quasi-steady state approach used by many mathematical models of three-way catalytic converters may give different results from the fully transient approach, in the case of extreme transients, which can be met in close-coupled applications.

A parametric analysis has been performed to assess the effect of engine operating point, catalyst active length, and pulsation pattern on close-coupled catalyst performance under pulsating flow. The catalyst active length (which is directly linked to the gas residence time) has an interesting effect on performance under pulsating flow. Both for very low and for very high values of the residence time, the effect of pulsations is negligible. For residence time values found near the middle of the expected range, the pulsating flow conversion presents a deviation from steady state conversion. The magnitude of this deviation depends significantly on pulsation pattern. The latter appears to be a very critical parameter when evaluating the effect of pulsating flow on catalyst performance. In this study, square pulses with various amplitudes (peak velocities) have been examined. The influence of pulsating flow starts to become important when the maximum pulse velocity is more than two times higher than the average velocity. For lower peak velocity values, the influence of pulsations on pollutant conversion is less than 4%, and the accuracy of the steady state approach is expected to be sufficient. At higher peak velocities, flow pulsations have a detrimental effect on pollutant conversion.

This parametric analysis has also served as a means to evaluate the deviation between the catalyst efficiency predicted by the quasi-steady state approach, and that predicted by the fully transient approach, in a wide range of operating conditions. It appears that the quasi-steady state approach tends to overestimate the detrimental effect of pulsations, and predict lower conversion efficiency than the fully transient approach. This deviation becomes more significant as engine speed and maximum pulse velocity increases. The maximum deviation between quasi-steady state and fully transient approach observed in this series of simulations is in the order of 20 percentage units, in terms of conversion efficiency.

As mentioned earlier, the exact shape and intensity of the pulsations depends on the engine and exhaust design and operational characteristics. A more detailed investigation on this topic could involve using mass flow rate data from engine models as input to the simplified channel model. This could be the subject of future work.

Nomenclature

AV = active volume ratio
AV = active catalyst volume/engine displacement
c = molecular concentration
dt = time step (m)
dx = space step (m)
i = Axial node indicator
k = mass transfer coefficient (m/s)
L = channel length (m)
$\dot{m}$ = mass flow rate (kg/s)
η = conversion efficiency
PI = Pulsation Index
S = channel specific surface area $(\mathrm{m}^2/\mathrm{m}^3)$
v = exhaust gas velocity inside the channel (m/s)
ε = monolith void fraction
η_V = engine volumetric efficiency

References

[1] Ogura, H., Koga, M., Momoshima, S., Nishizawa, K., and Yamamoto, S., 2003, "Development of Third Generation of Gasoline P-ZEV Technology." SAE paper 2003-01-0816.

[2] Zhao, F. Q., Bai, L., Liu, Y., Chue, T. H., and Lai, M. C., 1997, "Transient Flow Characteristics Inside the Catalytic Converter of a Firing Gasoline Engine." SAE Paper 971014.

[3] Berkman, M., and Katari, A., 2002, "Transient CFD: How Valuable is it for Catalyst Design?." SAE paper 2002-01-0064.

[4] Badami, M., Millo, F., Zuarini, A., and Gambarotto, M., 2003, "CFD Analysis and experimental Validation of the Inlet Flow Distribution in Close Coupled Catalytic Converters." SAE paper 2003-01-3072.

[5] Yoshizawa, K., Mori, K., and Kimura, S., 2001, "Numerical Analysis of the Exhaust Gas Flow and Heat Transfer in a Close-Coupled Catalytic Converter System During Warm-Up." SAE paper 2001-01-0943.

[6] Benjamin, S. F., and Roberts, C. A., 2000, "Warm-Up Of An Automotive Catalyst Substrate by Pulsating Flow: A Single Channel Modeling Approach." Int. J. Heat Fluid Flow, **21**, pp. 717–726.

[7] Liu, Z., Benjamin, S. F., and Roberts, C. A., 2003, "Pulsating Flow Maldistribution within an Axisymmetric Catalytic Converter—Flow Rig Experiment and Transient CFD Simulation." SAE paper 2003-01-3070.

[8] Koltsakis, G. C., Konstantinidis, P. A., and Stamatelos, A. M., 1997, "Development and Application Range Of Mathematical Models for Three-Way Catalytic Converters." Appl. Catal., B, **12**, pp. 161–191.

[9] Braun, J., Hauber, T., Többen, H., Windmann, J., Zacke, P., Chatterjee, D., Correa, C., Deutschmann, O., Maier, L., Tischer, S., and Warnaz, J., 2002, "Three-Dimensional Simulation of the Transient Behavior of a Three-Way Catalytic Converter." SAE paper 2002-01-0065.

[10] Heck, R. M., and Farrauto, R. J., 1995, *Catalytic Air Pollution Control—Commercial Technology*, Van Nostrand Rheinold, New York, pp. 6–8, Chap. 1.3.

[11] Oh, S. H., and Cavendish, J. C., 1982, "Transients of Monolithic Catalytic Converters: Response to Step Changes in Feedstream Temperature as Related to Controlling Automobile Emissions," Ind. Eng. Chem. Prod. Res. Dev., **21**, pp. 29–37.

[12] Ferziger, J. H., 1981, *Numerical Methods for Engineering Application*, Wiley, New York, pp. 234–240, Chap. 20.

[13] Liu, Z., Benjamin, S. F., Roberts, C. A., Zhao, H., and Arias-Garcia, A., 2003, "Coupled 1D/3D Simulations for the Flow Behavior Inside a Close-Coupled Catalytic Converter." SAE paper 2003-01-1875.

[14] Mondt, J. R., 1987, "Adapting the Heat and Mass Transfer Analogy to Model Performance of Automotive Catalytic Converters." J. Eng. Gas Turbines Power, **109**, pp. 200–206.

[15] Koltsakis, G. C., and Tsinoglou, D. N., 2003, "Thermal Response of Close-Coupled Catalysts During Light-Off." SAE paper 2003-01-1876.

[16] Tsinoglou, D. N., and Koltsakis, G. C., 2004, "Modeling the Effect of Flow Pulsations in Close Coupled Catalytic Converter Light-Off." SAE paper 2004-01-1835.

Modeling of MEMS-Type Rankine Cycle Machines

Ling Cui

J. G. Brisson
e-mail: brisson@mit.edu

Massachusetts Institute of Technology,
77 Massachusetts Avenue,
Cambridge, MA 02139

Preliminary design and performance calculations for a silicon-based micro Rankine machine are discussed. The designs considered draw heat from a high temperature air stream with inlet temperatures between 770 and 1000 K *and reject heat to an ambient air stream at* 300 K. *Most of the designs have a typical footprint of* 6 cm^2. *Water and benzene are considered as working fluids. Effects of the limits of heat exchanger and turbomachinery performance are analyzed and discussed. The designs of two types of heat exchangers (hole type and fin type) are described in detail. Their respective performances are compared. The calculations indicate that a machine with a* 6 cm^2 *footprint area is capable of delivering in excess of* 40 W *of shaft power.*

[DOI: 10.1115/1.1924400]

Introduction

In the past few decades, small-scale battery-powered electronic devices such as computers, handheld global positioning receivers, and mobile phones have been successfully marketed. The length of time that these devices can be operated between battery chargings is an important market feature and has driven the development of commercial high energy density batteries. The use of electronics in the military has also mushroomed in the past decade with a concomitant need for a long-life portable power source. Microscale power generators using a high energy density hydrocarbon-based fuel show promise for fulfilling the need for a long-life portable power source.

Using Microelectromechanical System (MEMS) technologies, the MIT microengine group has been developing centimeter-scale power systems. The emphasis of the efforts has been on two power systems, namely a micro gas turbine engine and a micro rocket engine [1]. Due to the increasing influence of viscous effects, turbomachinery efficiencies are relatively low in the microscale, typically between 30% and 70% [2]. Nevertheless, calculations show that these devices could produce power with a power to weight ratio that is on the order of 100 times that of a conventional gas turbine engine [2].

Another strong candidate cycle for microscale power production is the Rankine cycle. The major advantage of a Rankine cycle over the Brayton cycle used in the gas turbine engine is that it can deliver reasonable cycle efficiencies and useful power output despite low turbomachinery efficiency. This fact alone makes the Rankine cycle attractive for microscale power generation. Unfortunately, because the working fluid of the Rankine cycle is not air, as it is in the gas turbine, heat exchangers are needed to transfer energy into and out of the working fluid. These heat exchangers dictate both the size and the overall performance of the Rankine machine.

There are many discussions of microscale components such as heat exchanger designs [3–6] but there are few discussions of Rankine-based machines on the microscale [7]. Here we analyze potential Rankine machine designs based on the experience of the MIT microengine group. The designs we have chosen to analyze reflect the current capabilities of MEMS fabrication. Our intent here is to establish a realistic base line for what might be the expected performance from a microscale Rankine machine using silicon-based MEMS technology.

The following sections introduce the theoretical approaches in both the design of a stand-alone micro Rankine-based machine and the design of a combined cycle machine (a combined micro Rankine and micro gas turbine engine). The layout and modeling of the Rankine devices are outlined and the performance is optimized based on current turbomachinery designs and fabrication limits of silicon-based MEMS techniques. In most of the calculations in this work, steam (H_2O) is the working fluid. The pros and cons of using other working fluids in a Rankine machine are also discussed.

Overview

A block diagram and a T-s diagram for the proposed micro Rankine power cycle is shown in Fig. 1. The micro Rankine machine absorbs heat from a high temperature air stream that is provided by a combustor or possibly a micro gas turbine topping cycle.[1] The waste heat is discharged to a low temperature ambient air stream. The working fluid, presumably steam, flows through the circuit in Fig. 1(*a*) denoted by the state points 1, 4, 5 and 7. The high temperature heat exchanger (HTHEX) is fed hot gas from a combustor or from the discharge stream of a micro gas turbine engine. The HTHEX plays the role of a boiler and superheater in process 1–2 to 3–4 in Fig. 1(*b*). The turbine extracts work from the fluid in the (irreversible) process 4–5. The low temperature heat exchanger (LTHEX) desuperheats and condenses the working fluid in process 5–6–7. State 7 is assumed to be saturated liquid throughout this work. The feed pump pumps the liquid in state 7 up to high pressure in state 1.

The turbine drives three other devices: the feed pump, the blower, and the generator, as indicated by the dotted line in Fig. 1(*a*). The feed pump is necessary to close the Rankine cycle and the generator converts the mechanical power to useful electricity. The blower is used to force ambient air through the LTHEX to condense the working fluid to state 7 and represents a parasitic load on the cycle. Ideally, the heat transfer to the ambient air flow through the LTHEX could be by natural convection but our preliminary estimates show that a natural convection design results in an unacceptably large LTHEX (which is more than 20 times larger than a forced flow LTHEX of comparable performance).

The air flow through the HTHEX is assumed to be forced by the upstream combustor or gas-turbine engine. The HTHEX designs considered here have low pressure drops and we presume that the upstream devices are capable of driving the appropriate flow through the HTHEX. Consequently, there is no penalty as-

Contributed by the Power Division of THE AMERICAN SOCIETY OF MECHANICAL ENGINEERS for publication in the ASME JOURNAL OF ENGINEERING FOR GAS TURBINES AND POWER. Manuscript received by the Power Division October 23, 2003; final revision received June 25, 2004. Editor: L. S. Langston.

---

[1] We arrived at this somewhat arbitrary upper limit for the HTHEX pressure drop through internal discussions with MIT micro gas turbine engine designers as an acceptable backpressure for a micro gas turbine engine.

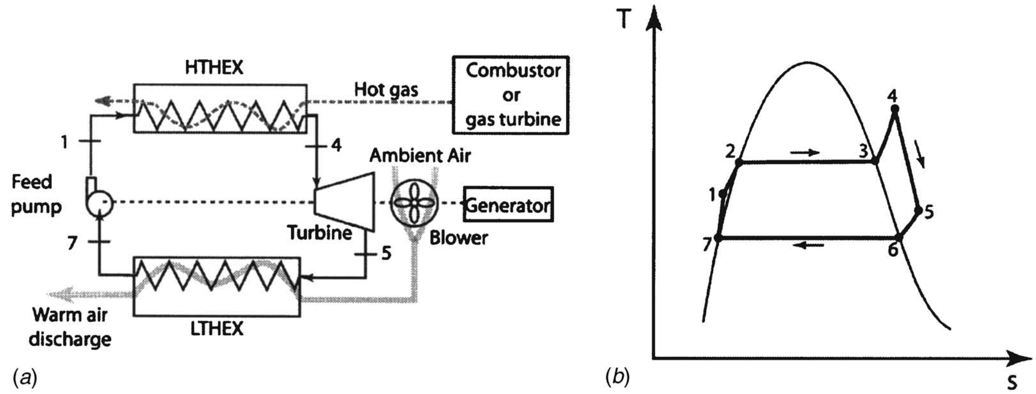

Fig. 1 A block diagram (*a*) and T-s diagram (*b*) for the proposed micro Rankine cycle

sessed against the Rankine engine for this loss other than the requirement that the high temperature heat exchanger design must have a pressure drop less than 5 kPa.

A schematic design for a Rankine-cycle prime mover is shown in Fig. 2. The device consists of four parts. A module that provides hot air to the Rankine machine indicated by a dashed box at the top of the figure. This could be a microcombustor or a micro gas turbine engine. The other three modules consist of the high temperature heat exchanger module (HTHEX), the feedpump/turbine/blower module, and the low temperature heat exchanger module (LTHEX). An exploded view of the engine is shown in Fig. 3.

The feedpump/turbine/blower module contains all the turbomachinery for the Rankine machine. The electric generator, not shown in Figs. 2 and 3, would be incorporated into this turbomachinery module. The blower draws cooling air from the ambient and drives it through the LTHEX air channels as shown in these figures. The turbomachinery module, HTHEX module, and the LTHEX module are connected by connecting tubes that provide thermal isolation as well as allowing the working fluid to be transferred from one module to another. A candidate material for the connecting tubes is Kovar [8].

The modular approach to the design of the micro Rankine engine is driven by fabrication limits. All the parts of the engine are assumed to be made using etched silicon wafers that are bonded into a vertical stack to form the engine (as suggested by the exploded view, Fig. 3). The structures on each of the wafers are extruded two-dimensional structures. There are limits on how many layers can be bonded to form a stack. (Currently, this limit is about six layers. A six-wafer micro gas turbine has been fabricated using direct wafer bonding [9,10].) The modular approach allows several multilayer stacks to be combined to form a complete engine.

The connecting tubes also form thermal breaks between the components. Large areas of contact between thin layers of thermally conductive silicon are not conducive to good thermal isolation. Patterned layers of glass (SiO_2) can also be used to achieve

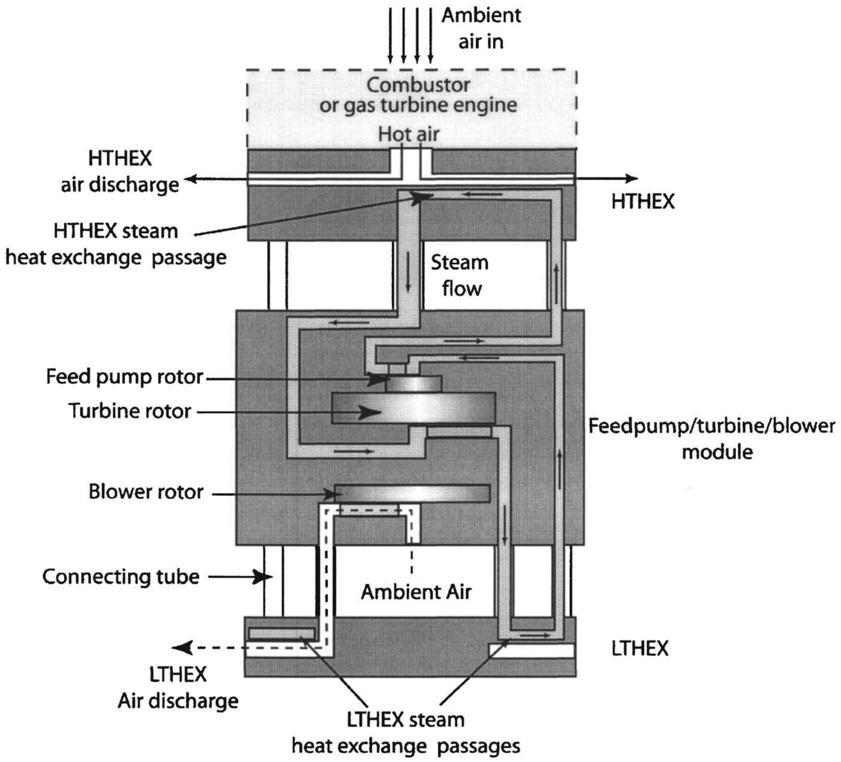

Fig. 2 A cross-sectional view of a first-cut design for a micro Rankine prime mover. Driving mechanism for the blower is not shown.

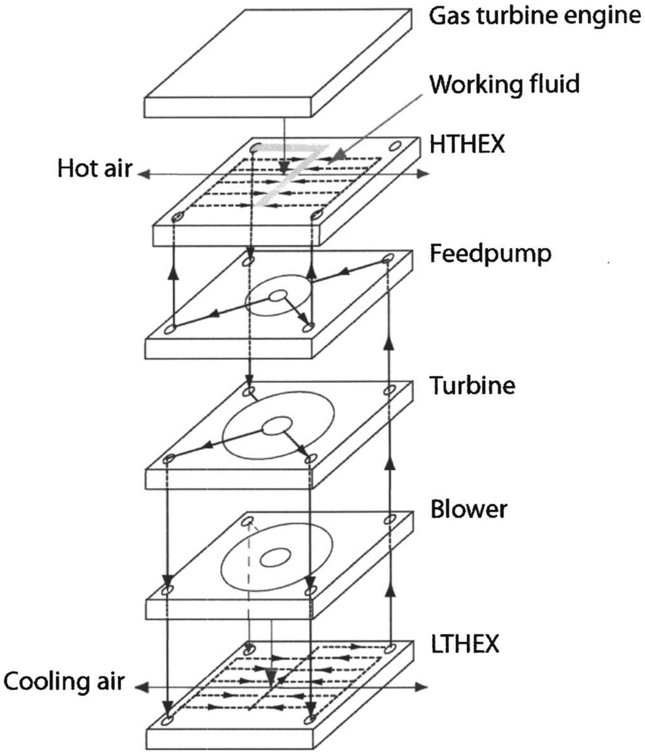

Fig. 3 Exploded schematic view of the micro Rankine engine

thermal isolation; however, due to the difference in thermal expansion coefficients between glass and silicon, large thermally induced strains in the structure could render the engine inoperative.

We have glossed over the fact that the mechanical coupling between the turbine and the blower must be hermetic. This might be achieved by using a magnetic coupling between the turbine and blower rotors through a thin layer of silicon that seals between the steam passages and the air passages. The specifics of this hermetic coupling require further work and will not be discussed here.

Heat Exchangers

The performance of the heat exchangers contributes significantly to the overall performance of a microscale Rankine machine. High performance in the LTHEX is particularly important to achieving a high performance micro Rankine system. Two basic heat exchanger designs will be considered in this work. The first we denote as a "fin-type" heat exchanger and the second as a "hole-type" heat exchanger.

Figure 4 is an exploded view of the fin-type LTHEX design assumed in this work. (The "fins" are the vertical walls of the air heat transfer passages.) The design consists of three etched wafers that are bonded together to form the heat exchanger. The middle wafer (Wafer II) in the heat exchanger carries all the working fluid (steam) heat transfer passages. Wafers I and III carry all the heat transfer passages that are exposed to the air.

The steam vapor discharged by the turbine enters the LTHEX through a hole in Wafer I and is distributed to the heat transfer channels in Wafer II by large distribution channels etched in Wafer II. There are fewer steam-side channels than air-side channels in this heat exchanger. The low mass flow rate of the water (typically a tenth that of the hot air in this machine) allows reasonable pressure drops with fewer passages. In addition, the high heat transfer coefficient for two-phase flow also allows all the heat transfer passages for the steam to be located on one wafer (versus two for the air passages).

The HTHEX, shown in Fig. 5, is designed as a counter-flow heat exchanger. Unlike the LTHEX, the HTHEX is comprised of only two silicon wafers: one for the hot air flow and the other for

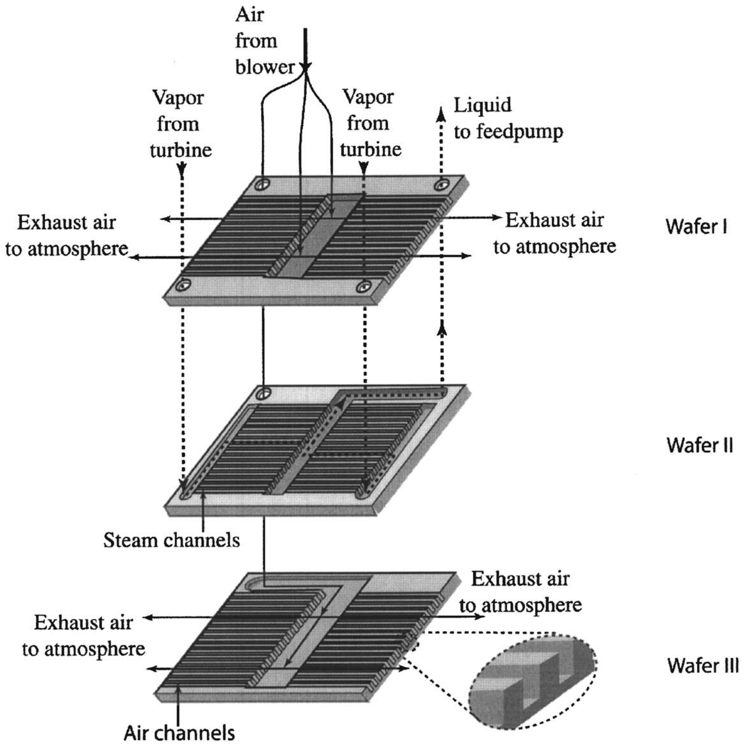

Fig. 4 Exploded view of the LTHEX. Each wafer is individually etched. The wafers are then bonded together to form the heat exchanger. A cover plate that ultimately bonds to and seals the passages of Wafer I is not shown. (Relative dimensions and number of passages do not correspond to the modeled device.)

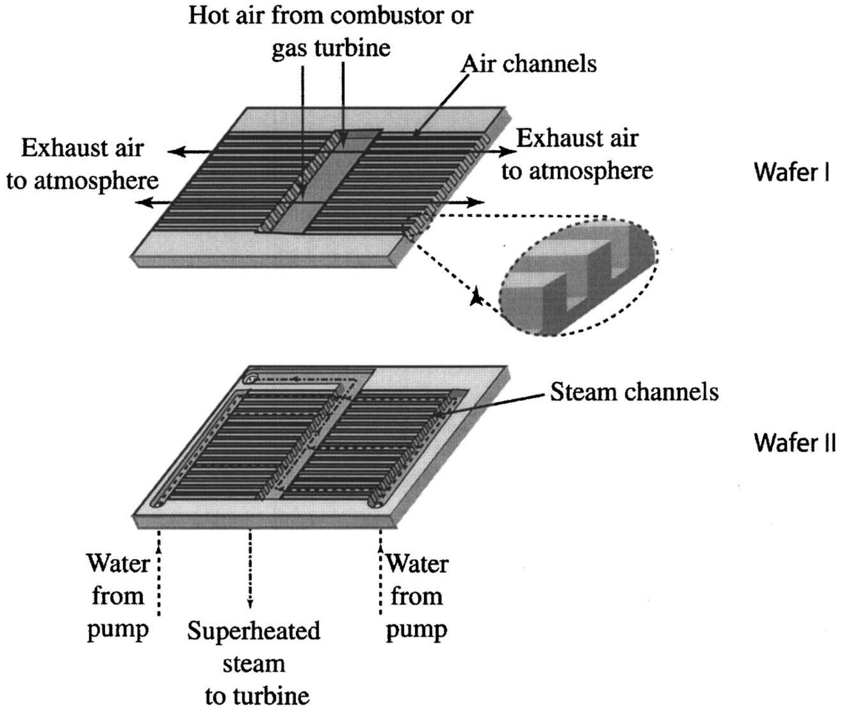

Fig. 5 Exploded view of the HTHEX. Each wafer is individually etched and then bonded together to form the heat exchanger. The air passages in Wafer I are closed by bonding a cover plate (not shown) to Wafer I or by bonding the lowest wafer in the combustor or gas turbine module to Wafer I. (Relative dimensions and number of passages do not correspond to the modeled device.)

the working fluid. In all the designs discussed here, the volumetric flow rates on the air side of the HTHEX are lower than those in the LTHEX which allows a reduction in the required number of air-side wafers in the HTHEX.

The HTHEX is assumed to be both a boiler as well as a superheater. In the boiler part of the HTHEX the temperature is uniform due to the presence of the two phases in the steam stream. In the superheating part of the HTHEX passages there will be large temperature gradients along the length of the passage and the high thermal conductivity of the silicon walls will tend to thermally short the heat exchange process. Consequently, the HTHEX will either have to be constructed with extremely thin walls or as a separate superheat heat exchanger module and boiler module to mitigate this effect.

Figure 6 is an exploded schematic view of a two-wafer hole-type heat exchanger. In this figure, the horizontal working fluid channels pass between the vertical air holes. This heat exchanger is a cross-flow type. The air flow is vertical through etched holes in the silicon plate. The diameter of these holes is between 100 and 300 μm. It can be seen that the air holes are etched through the whole thickness of the silicon wafer, and a heat exchanger could have several bonded stacks with these holes aligned. Thus the length of the holes is equal to the thickness of the wafer times the number of the stacks.

The working fluid channels and air channels occupy separate regions of the wafer. Heat transfer between the channels and the air holes is by conduction through the solid (high thermal conductivity) silicon wafer. In a more ideal design, the air holes and working fluid channels would be interspersed to minimize the distance that the heat must be conducted in the heat exchanger.

The primary advantage of the hole-type heat exchanger over the fin-type heat exchanger is the low air-side pressure drop with similar heat transfer rates and heat exchanger sizes. For example, if the hole-type design were adopted in the bottoming cycle (which will be discussed later), the air-side pressure drop would be in the order of 1 kPa compared to 3 kPa for a fin-type design. The low pressure drop of the hole-type heat exchanger comes from the use of many short air passages that can easily be formed by etching directly through the short dimension of the wafer (its thickness). The fin-type designs with channels in the long direction of the wafer waste a significant amount of available area for

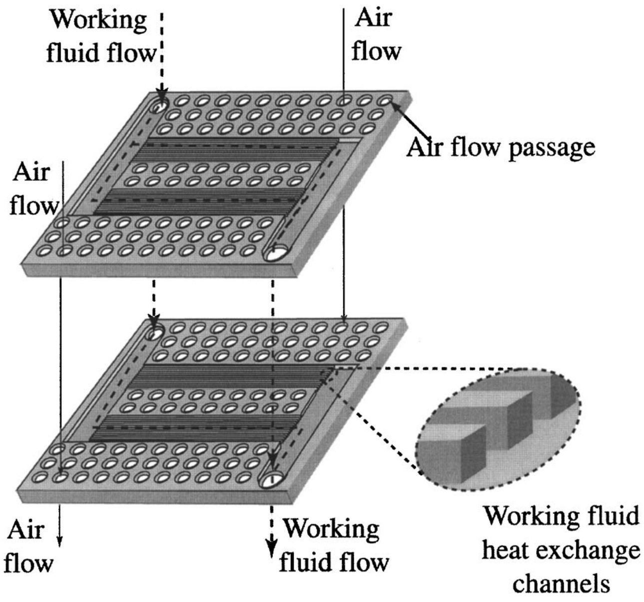

Fig. 6 An exploded diagram of a two-wafer hole-type heat exchanger structure. (Relative dimensions and number of passages do not correspond to the modeled device.)

fluid distribution channels. The net effect is that the hole-type heat exchanger performance is superior to that of the fin type.

On the other hand, there is an advantage of the fin-type heat exchanger designs over the hole-type heat exchanger. In the fin-type heat exchanger, there is only one fluid type that flows in each wafer. If the heat exchanger design were made with the air and steam flow passages interspersed on the same wafer, each flow passage will have a wafer bond in it that could potentially leak working fluid to the atmosphere (which results in an engine failure). The fin-type designs above minimize the length of the wafer/wafer bonds that must be leak tight and, consequently, reduce the (already stringent) requirements for wafer bonding the heat exchanger.

Specific Assumptions and Methods of the Analysis

In analyzing the expected performance of the micro Rankine cycle, it was assumed that the machine is operated in air with an ambient temperature and pressure of 300 K and 10^5 Pa, respectively. The machine absorbs heat from a hot air stream and discharges heat to a cold air stream. Water is chosen as the working fluid because it has suitable thermophysical properties [11], is commonly available, is safe and stable.

The assumed turbomachinery performance (turbine, pump, and blower) in the Rankine cycles is 50%. This is consistent with the current microturbomachinery that is being developed by the MIT microengine group. The interfaces between turbine, blower, and pump are all assumed to be adiabatic.

As discussed earlier, the pressure of the gas entering the HTHEX is assumed to be 5 kPa higher than ambient pressure. The temperature of the steam exiting the HTHEX in the Rankine machine is always assumed to be 20 K lower than the air inlet temperature to the HTHEX.

The performance of the heat exchangers for a given geometry is predicted using a few assumptions. The walls (fins) in the LTHEX are assumed to be isothermal. Most of the area of the LTHEX is devoted to the (isobaric and isothermal) condensation process which has a high thermal conductance to the wall. This combined with the high thermal conductivity of silicon (148 W/m K) and the low thermal conductivity of the air (0.03 W/m K) [12] drives us to conclude (and assume) that the thermal resistance between the two fluid flows is dominated by the air-Si interface in the heat exchanger. The fluid discharged by the LTHEX is assumed to be saturated liquid. In the HTHEX, however, the walls are not assumed to be isothermal, because substantial area in that heat exchanger is devoted to the (single phase and hence not isothermal) superheating of the steam. The pressure losses in the heat exchangers are calculated using standard Darcy friction factor calculations for fully developed flow. Similarly, standard heat transfer correlations for fully developed flow are used to determine the heat transfer coefficients in the heat exchanger [12]. The ε-NTU method is used for LTHEX calculations and the LMTD method is used for HTHEX calculations. The minor losses in the heat exchangers and the pressure losses in connecting passages are neglected.

One of the characteristics of these microscale heat exchangers is that the airflow in all of the passages is laminar. In the calculations in this paper, the Reynolds numbers in the LTHEX and HTHEX are all lower than 500. This is due to the small hydraulic diameter of the passage, the cycle limitations (turbomachinery efficiency and pressure ratio, etc.) and a necessarily low blower power. (Low blower power is necessary to achieve a net positive power output from the cycle.) The air-side heat transfer correlations used in this work are for fully developed laminar flow in circular and rectangular passages assuming a constant axial wall temperature. For a circular passage, the correlation consists of a constant Nusselt number of value 3.657. (Other correlations are available in Table 4.5 in Ref. 13).

Unless otherwise noted, the output power of the Rankine engine quoted here is a shaft power. It is the power delivered by the turbine to the electric generator (the generator is shown in Fig. 1). A more detailed exposition of the calculations is given in the thesis by Cui [13]. As an aside, there are efforts being made to develop microscale generators at MIT but no fully operational systems have been demonstrated. Some of these generator designs are anticipated to have electromechanical conversion efficiencies between 40% and 50% [14].

The goal of the calculations is to determine what the overall performance limitations of a small (6 cm^2 footprint) Rankine-cycle-based machine are. The first set of calculations determines the maximum power that can be generated from a device using a hole-type LTHEX and a fin-type HTHEX with an unlimited 770 K hot air supply, an unlimited turbine pressure ratio and a limited engine footprint. (The 770 K hot air supply temperature is representative of the expected exhaust gas of a MIT micro gas turbine engine.) This is followed by calculations for the maximum power output for a device using a fin-type LTHEX and a fin-type HTHEX. It will be found that these optimum cycles will require very large pressure ratios across the power turbine.

Initial Rankine turbine designs will probably be restricted to a single-stage design with a limited pressure ratio. (Current MIT micro gas turbine turbine designs are limited to values of 2–4 [2].) More complicated multistaged (high pressure ratio) designs are likely to be developed after a single-stage turbine proof-of-principle machine is developed. Since we are interested in estimating the performance of these initial single-stage designs, we continue with an analysis to determine the maximum power output of a Rankine cycle with pressure ratios of 4 across the turbine. We also use higher hot air supply temperatures in these latter calculations to see the effect of higher heat source temperatures (950 and 1000 K).

The air mass flow rates determined in the calculations described in the previous paragraph are much higher than the air mass flow rates associated with the current MIT micro gas turbine engine designs. We are interested in using these Rankine engines as the bottoming cycle for a micro gas turbine engine. To this end, the performance of the Rankine device combined with a MIT micro gas turbine engine design is calculated by restricting the mass flow rate of the hot air supply to 0.1 g/s. Table 1 is a summary of the general assumptions.

Maximum Power Output With a 6 cm^2 Footprint, 770 K Inlet Air

To find an optimal design for the Rankine machine with an unlimited hot air mass flow rate, the calculations start with a three-wafer hole-type low temperature heat exchanger design (LTHEX). The geometry for the LTHEX is fixed with dimensions consistent with current fabrication limits (critical dimensions of the heat exchanger are summarized in Table 2).

Reiterating, the calculations begin with the assumption of a hot air inlet temperature of 770 K. The steam's exit temperature from the HTHEX is assumed to be 20 K cooler than this temperature or 750 K. For the moment, we will assume that a HTHEX can be constructed to provide this thermal performance with less than a 5 kPa air pressure drop across it. The pressure of the steam in the HTHEX is assumed to have a value of 4 MPa. Ambient air conditions are 300 K and 1 atm.

There exists an optimal condenser operating temperature as a result of the trade-off between the thermodynamic cycle efficiency and the blower power consumption. The thermodynamic efficiency improves as the temperature of the low temperature reservoir, essentially the condenser discharge temperature, is reduced. So from purely thermodynamic considerations, the condenser discharge temperature should be as low as possible. However, as the condenser discharge temperature approaches the ambient temperature (300 K) with a low temperature heat exchanger of fixed dimensions, the mass flow rate of the cooling air through the heat exchanger must be increased. This increases the blower's parasitic

Table 1 Summary of the basic assumptions of the micro Rankine machine (unless otherwise stated in the text)

Hot air supply	
Temperature	770–1000 K
Pressure	$\sim 1.05 \times 10^5$ Pa
Mass flow rate	0.1 g/s or unlimited
Ambient air	
Temperature	300 K
Pressure	10^5 Pa
Turbomachinery	
Efficiency	50%
Turbine pressure ratio	4:1 or unrestricted
HTHEX	
Inlet hot air temperature	770–1000 K
Hot air pressure drop	≤5 kPa
Working fluid outlet temperature	20 K less than inlet hot air temperature

load on the power turbine to pump air through the LTHEX, reducing the overall power output of the engine. The result is that there is an optimum in the net work output for a condenser discharge temperature between the hot air inlet temperature and the ambient temperature.

The start of the calculations requires the choosing of the condenser discharge temperature, T_7 in Fig. 1, and the mass flow rate of the steam in the Rankine cycle. With these assumptions, the air mass flow rates through the heat exchangers and the work output of the cycle can be calculated.

For a given condenser discharge temperature, there is a steam mass flow rate which maximizes the net work output of the cycle. This optimum mass flow rate for a given T_7 can be found by plotting the results of the calculation described in the previous paragraph for several different steam mass flow rates at fixed T_7. The results of three sets of these optimum mass flow calculations for different condenser discharge temperatures are shown in the plot of the maximum net work of the cycle versus the condenser discharge temperature in Fig. 7. The maximum power output reaches 41.4 W when T_7 has a value of 420 K. The maximum in the power output shows the trade-off between leveraging cycle thermal efficiency (by lowering T_7) and minimizing the blower power consumption (as a result of increasing T_7).

The performance of the same steam cycle was calculated using a fin-type heat exchanger design for the LTHEX whose dimensions are summarized in Table 3. The fin (wall) heights for this LTHEX are a rather large 2 mm, whereas the wafers in the hole-type LTHEX above are only 1.5 mm thick. This suggests that the hole-type LTHEX is likely to be easier to fabricate than the corresponding fin-type LTHEX.

The maximum power output and thermal efficiency of the Rankine cycle with the fin-type LTHEX as a function of the condenser discharge temperature, T_7, with this LTHEX is shown in Fig. 8. The power curve shows a broad maximum at a temperature of 420 K with a maximum power output of 22.4 W, approximately half of the power delivered by the Rankine cycle with a hole-type LTHEX in Fig. 7. This is due to the better performance of the hole-type heat exchanger. Once again, the air passages in the hole-type heat exchanger are shorter and more numerous than those in the fin-type heat exchanger, resulting in lower pressure drops (and hence less blower power) for similar thermal performance.

The optimum performance of the cycle has been established given an assumed performance for the HTHEX. (More specifically, the HTHEX steam discharge temperature is assumed to be 20 K lower than incoming hot air temperature.) It remains to determine a HTHEX geometry that will deliver that performance. The calculations determine what the heat transfer and mass flow rates are that will be handled by the HTHEX. The HTHEX hot air mass flow rates that result from the calculations used to develop Fig. 8 vary from a value of 0.6–1.6 g/s and the corresponding water/steam circulation rates vary from 0.06 to 0.17 g/s. The steam mass flow rate at $T_7=420$ K equals 0.15 g/s and the hot air mass flow is about 1.4 g/s. The corresponding heat transfer rates in the LTHEX and HTHEX are 372 and 415 W. The dimensions of a heat exchanger design that can handle these mass flow rates and perform as assumed for the optimized cycle above ($T_7=420$ K) are listed in Table 4.

The HTHEX needs only two-thirds of the total surface area of the LTHEX (two wafers versus three wafers), as described in Tables 4 and 3. In general, we have observed that the size of the entire Rankine machine is dominated by LTHEX requirements.

Maximum Power Output With Turbine Pressure Ratio Restricted to 4

The total pressure ratio across the power turbines in a Rankine machine is usually quite high. The cycles considered above are no exception; the pressure ratios vary from values of 5.5–64.3. Currently, microturbines have been designed and built for pressure ratios of 2 to 3 [2]. It is likely that the first Rankine machines built will have a single-stage power turbine that will impose a pressure ratio that is lower than the optimum one. Consequently, it is of interest to see how much the performance of the engine is reduced if the pressure ratio across the power turbine is restricted to a low value.

The deleterious effect of reduced turbine pressure ratio can be mitigated by increasing the turbine inlet temperature from the value of 750 K assumed above to 930 and 980 K. These temperatures should be near the maximum temperature that can be tolerated by a silicon turbine rotor. (Silicon goes through a softening transition between 900 and 1000 K [15].) In this case, the hot air

Table 2 Hole-type LTHEX dimensions (air side) for maximum power calculation

Hole diameter	0.2 mm	Wafer thickness	1.5 mm
Number of rows of holes	57 per stack	Number of wafers	3
Holes per row	75 per stack	Footprint	6 cm^2
Distance between holes	0.1 mm		

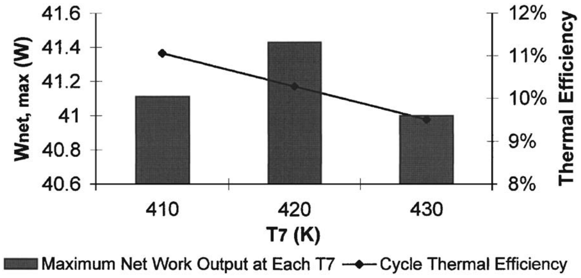

Fig. 7 The net work output and cycle thermal efficiency of a Rankine cycle with the hole-type LTHEX design specified in Table 2. Turbine inlet temperature equals 750 K. LTHEX footprint is about 6 cm^2. Turbine pressure ratios are unrestricted.

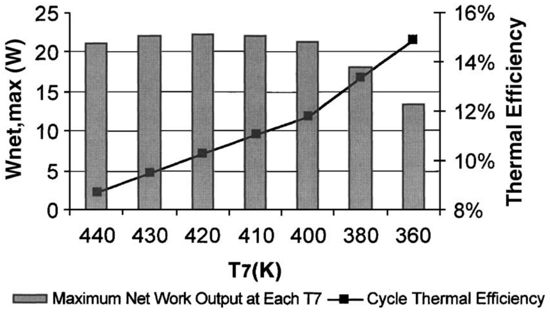

Fig. 8 Net work output and thermal efficiency as a function of LTHEX saturation temperature (T_7) for the fin-type heat exchanger specified in Table 3. Turbine inlet temperature equals 750 K. The turbine pressure ratios are unrestricted.

is likely to be supplied by a microcombustor. A rotor made with silicon carbide should be able to tolerate still higher temperatures [16].

The cycle calculations for the two cases proceed in the same manner as before. The air entering the HTHEX is assumed to be 1000 K (or 950 K). In the HTHEX steam outlet temperature (turbine inlet temperature) is assumed to be 20 K cooler than the inlet air temperature. The LTHEX is assumed to be of the fin type with the dimensions given in Table 3. The pressure ratio of the turbine is fixed at a value of 4. The performance of the cycle is then evaluated as a function of the condenser discharge temperature (the discharged liquid is assumed to be saturated.) Unlike the earlier calculations, the pressure in the HTHEX is not fixed. It is determined by the product of the pressure ratio of the turbine and the saturated pressure of water at the condenser discharge temperature. The results are shown in Fig. 9.

The net power output for this design is between 30.5 and 45.6 W. The highest power outputs of 45.6 and 40.6 W correspond to HTHEX inlet hot air temperatures of 1000 and 950 K, respectively. The optimized condenser discharge temperature is 480 K. The net work output increases monotonically with increasing condenser outlet temperature, T_7. This result initially concerned us since we expected that increasing T_7 would result in a lowering of the power output from the cycle. The cause of this is that for an assumed T_7, a corresponding LTHEX discharge (saturation) pressure is determined, and since the turbine pressure ratio is fixed, the pressure drop across the turbine increases with the increased of T_7. At the same time, with a higher T_7, more heat can be transferred in the LTHEX (under the same external conditions) and the mass flow rate of the steam can be increased. The increased steam mass flow rate combined with the increased pressure drop across the turbine results in a higher net work output.

Ideally, the net work output of the cycle can be increased above the values shown in Fig. 9 by further increasing T_7. There is, however, a practical upper limit to the pressures that can be sustained in the silicon structure. The turbine inlet pressure when T_7 is chosen to be 480 K is about 7 MPa, which we have (somewhat arbitrarily) chosen as a limiting pressure for the cycle.

Some of the assumptions made above are rather ambitious from a fabrication point of view. The uniform width heat exchange channels in the LTHEX have a depth of 2 mm that is beyond the currently achievable etch depths. The first turbines may only have a pressure ratio of 2 instead of the value 4 assumed above. If a similar LTHEX were fabricated with more conservative 1-mm-deep channels and inserted into a Rankine engine with a pressure ratio equal to 2, the optimum power output is about 16 W with a hot air inlet temperature of 1000 K.

Finally, we note that the performance of a Rankine engine could be higher than the performance shown by Fig. 9 if a hole-type LTHEX were used instead of the fin-type LTHEX.

Rankine Engine as a Bottoming Cycle to a Micro Gas Turbine

It is possible to drive a micro Rankine device with the exhaust from a micro gas turbine engine. This improves the overall cycle efficiency over that of either device. The current MIT micro gas turbine engine design has a typical mass flow rate of 0.1 g/s, which is significantly less than the hot air mass flow rates calculated for the optimized cycle. (The air mass flow rates for the results in Fig. 7 are approximately 2.6 g/s for a hole-type LTHEX and the air mass flow rates for the results in Fig. 8 are approximately 1.2 g/s for a fin-type LTHEX.) This low mass flow rate then becomes an added restriction for the bottoming Rankine engine design. The gas turbine exhaust temperature is assumed to be 770 K (hot air supply to the Rankine machine). We also assume, as before, that the pressure of the gas turbine engine exhaust is 5 kPa greater than the ambient pressure. The fin-type LTHEX and fin-type HTHEX dimensions are assumed to be the same as those in Tables 3 and Table 4 with the exception that the channel depths are 1 mm. The pressure ratio across the power turbine is unrestricted.

Figure 10 shows the predicted maximum net work output and thermal efficiency of a bottoming Rankine machine as a function of condenser discharge temperature. The maximum in the power output results from the trade-off between high cycle thermal efficiency (by lowering T_7) and reducing the blower power consumption (as a result of increasing T_7). Comparing the results in Fig. 10 to those shown in Fig. 8, the first observation is that the net power output of this machine is 4.0 versus 22.4 W in the optimized machine. This is a result of the reduced energy available in the hot air stream as well as the reduced size of the LTHEX. The efficiency of the cycle at the maximum work output is substantially

Table 3 Fin-type LTHEX dimensions (air side) for maximum power calculation

Channel depth	2 mm	Total number of air channels	480
Channel length	5 mm	Number of cooling-air wafers	2
Channel width	100 μm	Sets of channels per stack	2
Fin thickness (channel wall thickness)	100 μm	Footprint	~5.3 cm^2

Table 4 High temperature heat exchanger design for results shown in Fig. 8

Channel depth	2 mm	Total number of air channels	220
Channel length	5 mm	Number of wafers for hot air	1
Channel width	100 μm	Sets of channels per stack	2
Fin thickness	100 μm	Footprint	~5 cm^2

better than that for the large mass flow case discussed earlier (15% versus 10%) primarily because the optimum condenser operating temperature is lower than the previous case (360 versus 420 K). With a restricted turbine pressure ratio of 2, the same calculation process produces a net work output of 1.6 W from the cycle.

The disparity of the Rankine engine power output here in comparison to the previous unrestricted mass flow case makes it clear that running a 2.3 cm by 2.3 cm Rankine engine on the exhaust stream of a single gas turbine engine (of the current MIT design) underutilizes the Rankine engine. The Rankine engine is better utilized using the waste heat from a larger gas turbine or from an array of small gas turbines.

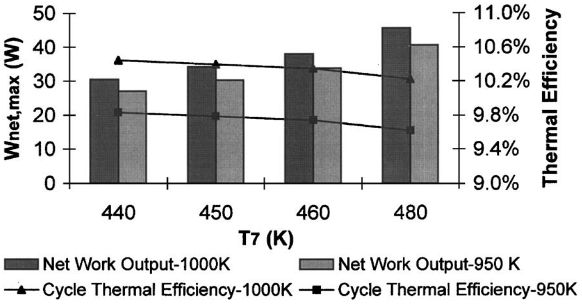

Fig. 9 The net work output and thermal efficiency of a single cycle as a function of LTHEX discharge temperature. The turbine pressure ratio is set to a value of 4. The assumed LTHEX dimensions are listed in Table 3. Two cases are shown, one corresponds to an entering hot air temperature of 950 K, the other corresponds to 1000 K.

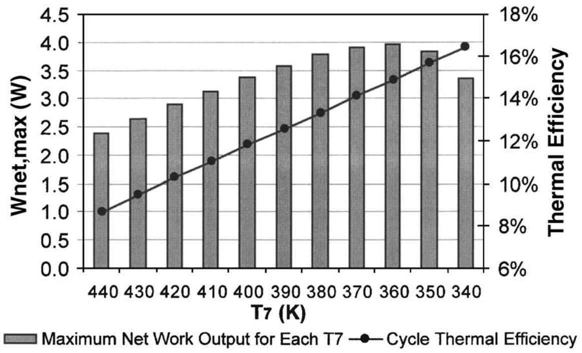

Fig. 10 The net work output and thermal efficiency versus condenser discharge temperature in the LTHEX. The hot air mass flow rate is 0.1 g/s and steam mass flow rate is 0.011 g/s. The turbine inlet temperature is 750 K and turbine pressure ratios are unrestricted. LTHEX and HTHEX dimensions are same in Tables 3 and 4 but with channel depths equal to 1 mm.

Other Fluid Choices for the Micro Rankine Machine

We have assumed that microturbines could be built to handle the small steam mass flow rates required for the bottoming cycle applications discussed earlier. The mass flow rates in the steam are typically ten times smaller than the mass flow rates associated with the hot air flow. This small mass flow rate combined with the relatively high density of high pressure steam results in small volumetric flows through the power turbine. These volumetric flows are outside the range of designs that have been examined as part of the MIT microengine project. For example, in one of the bottoming Rankine machine designs ($T_7=440$ K) in Fig. 7, the mass flow rate of the steam is about 0.17 g/s. However, the scaled steam mass flow rate for a MIT 6 mm turbine design with similar pressures, temperatures, and pressure ratio is about 6 g/s.

There are several approaches to accommodate the small volumetric flow of the working fluid. The first is to reduce the size of the turbine, which will be limited by current manufacturing capabilities. Another is to increase the size of the heat exchanger (allowing larger air mass flow rates and hence increase the working fluid mass flow rate) which will increase the footprint of the device. Still another is increasing the volumetric flow rate through the turbine by choosing a new working fluid.

There are several criteria for choosing a new working fluid to increase the volumetric flow rate. The first requirement would be a fluid with a lower latent heat than water. The large latent heat of water results in a small mass flow for a given heat transfer rate into the HTHEX. The critical pressure of the fluid should not be too high (~4 MPa) to avoid excessively high pressures in the device. The triple point temperature of the fluid must be below 283 K (10°C) to avoid the crystallization of the working fluid within the engine. Preferably, the vapor density of the fluid should be lower than that of water at the turbine inlet which increases the volumetric flow rate for the same mass flow rate. The material must be chemically stable and not react with silicon. And finally, the thermophysical properties must be available.

Benzene (C_6H_6) is a good alternative to water [13]. (The thermophysical properties of benzene are available in Ref. [17].) We have not concerned ourselves with other issues such as toxicity (benzene is a carcinogen) or flammability of the working fluid. The benzene mass flow rates will typically be about 5–6 times larger than the steam mass flow rate for the same heat transfer in the HTHEX. (The latent heat of water is about seven times that of benzene at $T=420$ K). The calculations show that benzene is suitable for the current micro gas turbine turbine designs.

Models for a Rankine cycle using the heat exchangers with dimensions summarized in Tables 5 and 6 were constructed. The number of fin-type LTHEX air channels was varied in order to examine the sensitivity of the net work output versus the size of the low temperature heat exchanger. Several sets of operating conditions were analyzed using the methods described earlier. The hot air mass flow rates were adjusted to match the assumed benzene

Table 5 Dimensions of the fin-type LTHEX in the benzene Rankine cycle

Channel depth	1.5 mm	Total number of channels	800–1200
Channel width	0.1 mm	Number of stacks (air)	2
Channel length	4 mm	Total width	3.8 cm
Wall thickness	0.1 mm	Total length	4–6 cm

Table 6 Dimensions of the fin-type HTHEX in the benzene Rankine cycle

Channel depth	1.5 mm	Wall thickness	0.1 mm
Channel width	0.1 mm	Number of channels	Varies
Channel length	3 mm	Number of stacks (air)	2

mass flow rates through the HTHEX. The results of these calculations are shown in Table 7 for different turbine pressure ratios (π), turbine inlet temperatures ($T_{\text{superheat}}$), and LTHEX geometries (n is the number of air channels in the LTHEX). The pressure inside the HTHEX is assumed to be 3 MPa in all cases. Within a footprint of 24 cm^2 (6 cm × 4 cm), a benzene-based Rankine engine with a turbine pressure ratio equal to 2 could generate 22.5 W work, when the turbine inlet pressure and temperature are 3 MPa and 650 K.

Summary and Conclusions

Microscale Rankine-based power machines with footprints no more than 6 cm^2 were designed and their performance analyzed. These engines are assumed to absorb heat from a hot air stream and reject heat to ambient air. Rankine machines can act as a bottoming cycle to a micro gas turbine engine or as a stand-alone prime mover when supplied with hot air from a microcombustor.

The performance of these Rankine machines depends critically on the specific performance of the components that comprise the engine. To this end, several calculations were performed to simulate physical as well as current constraints on microengine components. Two types of heat exchanger designs, the hole-type heat exchanger and the fin-type heat exchanger, were introduced. The hole-type heat exchanger performance proved to be superior to that of the fin-type in that its air-side pressure drop was one-third that of the fin-type for the same heat transfer rate. The limits on the turbomachinery considered in this work were based on the current MIT gas turbine microengine group designs. We assumed a 50% adiabatic efficiency for all turbomachinery.

The first calculations assumed an unrestricted hot air supply at 770 K. The 6 cm^2 steam-based Rankine engine was optimized for a maximum useful power output using designs with hole-type and fin-type heat exchangers. The optimized power outputs were predicted to be 41.4 and 22.4 W for the hole and fin-type heat exchanger designs, respectively.

The 770 K inlet temperature used in the above calculations is a rather conservative value. Material limits in the silicon may allow operation with inlet air temperatures as high as 950 and perhaps 1000 K. In addition, the first micro-Rankine machines are likely to be built with single-stage turbines that will limit the working fluid pressure ratio to values near 4. In an effort to realistically predict the "short-term" potential for a micro-Rankine machine, designs (using the better hole-type heat exchanger design) were optimized under the restrictions of 950 and 1000 K inlet air temperature and turbine pressure ratios of 4. The maximum power outputs of these devices were 40.6 and 45.6 W for the 950 and 1000 K cases, respectively.

The hot air mass flow rates necessary to drive both the unrestricted and restricted cases above are much larger than the expected air mass flow rates of the discharge of a MIT micro gas turbine. In anticipation that a Rankine cycle could be used as a bottoming cycle to a gas turbine engine, a Rankine engine model was optimized around the discharge characteristics of a MIT micro gas turbine engine. (A hot air mass flow rate of 0.1 g/s and an inlet air temperature of 770 K to the HTHEX.) In this optimization, the Rankine cycle turbine pressure ratio was unrestricted and the heat exchangers were of the fin type. The optimized power was only 1.6 W due to the rather low hot air mass flow rate provided by the MIT gas-turbine design.

Finally, it was found that the volumetric flows of the steam through the Rankine-cycle turbine were very small. If the performance of current micro gas turbine turbines (with a diameter of 6 mm) is scaled to the high pressure steam conditions found in the Rankine cycle, the volumetric flow rate is 35 times higher than that required in the first set of calculations discussed above (770 K, unrestricted hot air mass flow). Turbine designs that are substantially smaller than the current ones are likely to have unacceptably high viscous and clearance losses. Increasing the temperature and/or lowering the pressure of the steam entering the turbine will increase the volumetric flow rate, albeit the temperature will be limited by the material and lowering pressure will decrease the power output. Our calculations show that current micro gas turbines are not compatible with a 6 cm^2-footprint silicon-steam-based Rankine machine. We thus considered using another working fluid with properties that increase the overall volumetric flow rate within the cycle. We found that benzene provided a larger volumetric flow rate for the same heat transfer rate. A benzene-based Rankine cycle was then analyzed under the assumption that the volumetric flow rate through the turbine was the volumetric flow rate that was scaled from current MIT gas-turbine turbine designs. Even with benzene's increased volumetric flow, the size of the heat exchangers had to be increased to provide enough volumetric flow to the 6-mm-diameter turbine. Several designs were considered, the best performing design delivered 22.5 W of useful shaft power.

The analysis of this article did not consider the efficiencies associated with the mechanical to electrical conversion in the generator. There are efforts being made to develop generators at MIT.

Table 7 Maximum net work output for the benzene-based micro Rankine cycle

	LTHEX footprint	Cycle net work output	
		$\pi_{\text{turbine}}=2$	$\pi_{\text{turbine}}=3$ or 3.5
$T_{\text{superheat}}=600$ K	4 cm × 4 cm, $n=800$	11.3 W	⋯
	5 cm × 4 cm, $n=1000$	14.7 W	6.9 W ($\pi_{\text{turbine}}=3$)
	6 cm × 4 cm, $n=1200$	16.7 W	20.7 W ($\pi_{\text{turbine}}=3$) 12.8 W ($\pi_{\text{turbine}}=3.5$)
$T_{\text{superheat}}=650$ K	4 cm × 4 cm, $n=800$	15.4 W	⋯
	5 cm × 4 cm, $n=1000$	19.9 W	⋯
	6 cm × 4 cm, $n=1200$	22.5 W	12.0 W ($\pi_{\text{turbine}}=3.5$)

Note: n is the number of air channel in the LTHEX.

However, no working systems have been fully demonstrated. Some of these generator designs are anticipated to have electromechanical conversion efficiencies between 40% and 50% [15].

In summary, steam-based Rankine machines with a 6 cm^2 footprint will require power turbines that are substantially smaller than those used in current micro gas turbine designs. Assuming such a turbine can be built and that it has an adiabatic efficiency of 50%, a silicon-based micro Rankine engine, with an internal pressure ratio of 4 and a 6 cm^2 footprint, should be able to deliver up to 45 W of shaft power. Alternatively, if a larger footprint is allowed, a small benzene-powered machine can be built using the existing MIT microgas turbine designs. For example, a 4-cm by 6-cm footprint benzene-powered machine could deliver up to 22.5 W of shaft power.

References

[1] Epstein, A. H. et al., 1997, "Micro-Heat Engines, Gas Turbines, and Rocket Engines the MIT Microengine Project," AIAA Paper 97-1773.

[2] Savoulides, N., 2004, "Development of a MEMS Turbocharger and Gas Turbine Engine," Department of Aeronautics and Astronautics, MIT, Cambridge, MA.

[3] Sullivan, 2001, "Development and Testing of Microscale Silicon Heat Exchangers for the MIT Micro Gas-Turbine Engine," Masters thesis, Department of Mechanical Engineering, MIT, Cambridge, MA.

[4] Harris, C., Despa, M., and Kelly, K., 2000, "Design and Fabrication of a Cross Flow Micro Heat Exchanger," J. Microelectromech. Syst., **9**(4), pp. 502–508.

[5] Hijikata, K., Yamamoto, N., and Takagi, S., 1997, "Boiling Heat Transfer from a Micro Heater," Microelectromechanical Systems, ASME, DSC-Volume 62/ HTD-Volume 354.

[6] Choquette, S. F., Faghri, M., Charmchi, M., and Asako, Y., 1996, "Optimum Design of Microchannel Heat Sinks," *Microelectromechanical Systems*, DSC-Vol. 59, ASME, New York.

[7] Muller, N., and Frechette, L.-G., 2002, "Performance Analysis of Brayton and Rankine Cycle Microsystems for Portable Power Generation," ASME IMECE 2002-39628.

[8] Mehra, A., Zhang, X., Ayón, A. A., Waitz, I. A., Schmidt, M. A., and Spadaccini, C. M., 2000, "A Six-Wafer Combustion System for a Silicon Micro Gas Turbine Engine," J. Microelectromech. Syst., **9**(4).

[9] Turner, K. T., and Spearing, S. M., 2002, "Modeling of Direct Wafer Bonding: Effect of Wafer Bow and Etch Patterns," J. Appl. Phys., **92**(12), pp. 7658–7666.

[10] Miki, N., Zhang, X., et al., 2003, "Multi-Stack Silicon-Direct Wafer Bonding for 3D MEMS Manufacturing," Sens. Actuators, A, **103**, pp. 194–201.

[11] Online database of National Institute of Standards and Technology webbook.nist.gov/chemistry/fluid

[12] Mills, A. F., 1999, *Heat Transfer*, 2nd ed., Prentice–Hall, Englewood Cliffs, NJ.

[13] Cui, L., 2003, "Modeling, Design and Analysis of Micro-Scale Rankine-Based Systems," Masters thesis, Department of Aeronautics and Astronautics, MIT, Cambridge, MA.

[14] Livermore, C., Department of Mechanical Engineering, MIT (private communication).

[15] Chen, K.-S., 1998, "Materials Characterization and Structural Design of Ceramic Micro Turbomachinery," Ph.D. thesis, Department of Aeronautics and Astronautics, MIT, Cambridge, MA.

[16] Chen, K.-S., Spearing, S. M., and Nemeth, N. N., 2001, "Structural Design of a Silicon Micro-Turbo-Generator," AIAA J., **39**(4).

[17] Lide, D. R., and Kehiaian, H. V., 1994, *CRC Handbook of Thermal and Thermochemical Data*, CRC, Cleveland, OH.

Journal of Engineering for Gas Turbines and Power

Technical Brief

Hardware-in-the-Loop Simulation Study on the Fuel Control Strategy of a Gas Turbine Engine

Huisheng Zhang, Ming Su, and Shilie Weng
The Key Laboratory of Power Machinery and Engineering of Education Ministry, Shanghai Jiao Tong University,
Shanghai 200030, P.R. China

A hardware-in-the-loop simulation of a three-shaft gas turbine engine for ship propulsion was established. This system is composed of computers, actual hardware, measuring instruments, interfaces between actual hardware and computers, and a network for communication, as well as the relevant software, including mathematical models of the gas turbine engine. "Hardware-in-the-loop" and "volume inertia effects" are the two innovative features of this simulation system. In comparison to traditional methods for gas turbine simulation, the new simulation platform can be implemented in real time and also can test the physical hardware's performance through their integration with the mathematical simulation model. A fuel control strategy for a three-shaft gas turbine engine, which can meet the requirement to the acceleration time and not exceeding surge line, was developed using this platform.

[DOI: 10.1115/1.1805012]

Introduction

"Hardware-in-the-loop simulation" is an effective tool to study the dynamic process of a gas turbine engine. However, many difficulties exist in establishing the simulation system [1]. First, effective communication between the actual hardware and the mathematical model need to be resolved. Second, the mathematical model calculation in the computer must occur in real time. In order to overcome these difficulties, we not only need to construct a hardware-in-the-loop simulation platform to effectively and quickly transfer data; but we also need to develop the mathematical model and corresponding algorithm of the simulation object—the gas turbine engine, and then to synchronize the calculation process with the real processes of the physical parts. A three-shaft gas turbine engine for ship propulsion is taken as an object to establish the hardware-in-the-loop simulation platform, with which the fuel control strategy is investigated.

Simulation Model of Gas Turbine Engine

Establishing the dynamic characteristics of a gas turbine engine is an important task during its development. The thermal inertia, volume inertia, and rotor inertia are three important factors that affect the engine performance. For some engines (especially the aeroderived engine), the thermal and volume inertia are usually omitted in conventional models [2,3]. Only the rotor inertia is considered, making the equation very simple. In order to capture the coupling of the pressure and flow rate between components, the calculation must be iterative. Because the time for the iteration is not known a priori, the real-time simulation, which demands strict time constraints, must not contain the iterative calculation. Here we modeled the volume inertia [4,5], by adding one volume module between the components. Thus the inlet and outlet pressure of the components, such as the compressor and the turbine, can be determined; the flow rate change in the volume module yields the pressure change. The model reflects the real physical process, and the iteration calculation can be eliminated, which is vital to the hardware-in-the-loop simulation.

A three-shaft gas turbine is taken as the object, its modular simulation model is shown in Fig. 1, where LCP and HCP represent low-pressure and high-pressure compressor, respectively; HTB, LTB, and DTB represent high-pressure, low-pressure, and power turbine, respectively; HRD, LRD, and DRD represent high-pressure rotor, low-pressure rotor, and power rotor and gear box; CC is the combustion chamber; LD is the load to the propeller, and V are volume modules. Because of introducing the volume module, we can implement real-time simulation without iterative calculation. SR indicates the speed-regulator module; its input parameter is the rotor speed of the high-pressure rotor (HRD) and its output variable is the fuel flow rate. Here, we will use an actual speed regulator to study the control strategy of fuel flow rate when the gas turbine engine accelerates the ship.

Configuration of Simulation Platform

The system configuration of the hardware-in-the-loop simulation platform is shown in Fig. 2.

Section I of Fig. 2 implements the mathematical model of the gas turbine. The HP rotor speed, which is calculated from the model, is transferred to the control PC through a network switch. In Section II of Fig. 2, the control PC interfaces the actual hardware (speed regulator) and performs data acquisition. The frequency converter drives the motor and speed regulator according to the HP rotor-speed value received from Section I. When the regulator rotates, the rack bar will move with the change of HP rotor speed. The displacement of the rack bar is read into the Control PC via the position displacement sensor and converted to the appropriate fuel flow rate. The fuel flow rate is transmitted to Section I of the figure as a model input and forming a closed-loop simulation. Section III of Fig. 2 is for the dynamic display of system information; it receives and displays, via a network connection, the running status and results of Sections I and II.

Contributed by the Controls, Diagnostics and Instrumentation Committee of THE AMERICAN SOCIETY OF MECHANICAL ENGINEERS for publication in the ASME JOURNAL OF ENGINEERING FOR GAS TURBINES AND POWER. Manuscript received by the CD&I Committee March 24, 2003; final revision received February 12, 2004. Associate Editor: A. J. Volponi.

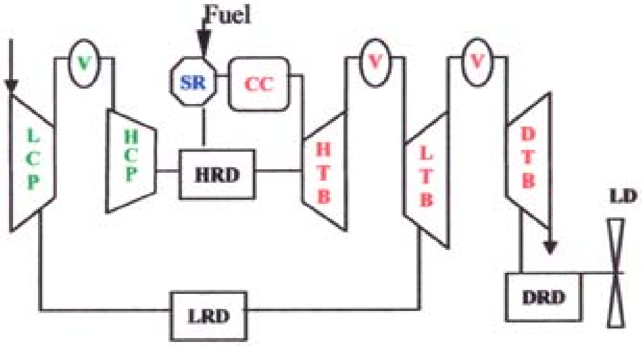

Fig. 1 Modular simulation model of three-shaft gas turbine

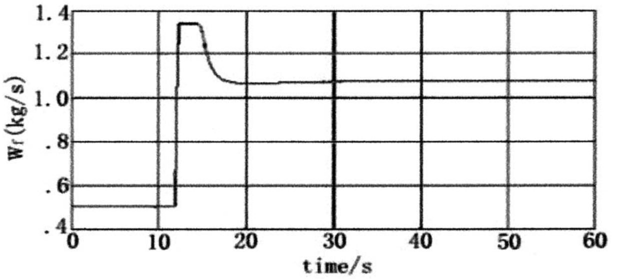

Fig. 3 Fuel flow rate based on the real displacement of rack bar

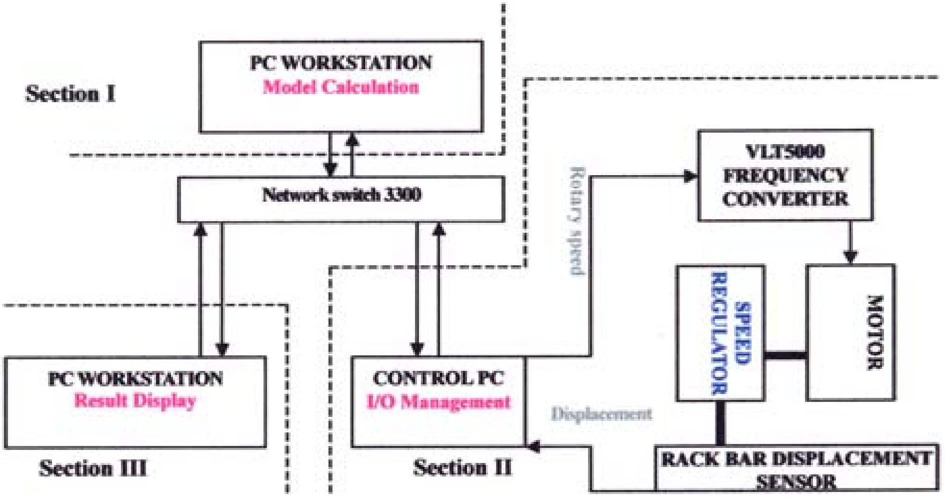

Fig. 2 System configuration of hardware-in-the-loop simulation platform

Simulation Results and Analysis

The speed regulator is considered as the controller for the gas turbine engine. The function of speed regulator handle is analogous to an engine throttle command. When the speed of the speed regulator is disturbed, the displacement of the rack bar will be changed. Because the position of the rack bar corresponds to the fuel flow rate into the combustor, a change in rack bar position will affect the fuel going into the combustion chamber. The fuel flow control must be designed to achieve the desired performance without exceeding operating limits, such as compressor surge lines or maximum rotor speed limits.

Compressor surge, particularly at high speed and pressure ratio, must be avoided under all circumstances. Surge is a condition of repeated flow breakdown so catastrophic that it propagates back through the compressor exit. In addition to causing very high cyclic stresses in the long low-pressure compressor blading, surge will almost certainly extinguish combustion.

In this paper, we will study a fuel flow control strategy to avoid compressor surge. After the engine has been running for 12 s, the handle is pushed from a lower-power to a higher-power setting. If the fuel flow is suddenly increased to the maximum, a compressor surge will occur. Figure 3 shows fuel flow versus time as determined by the displacement of the rack bar. When we adopt this fuel flow, the system will experience a compressor surge, as can be seen from the performance map of low-pressure compressor (Fig. 4, PR_LCP is the pressure ratio). The dashed line indicates

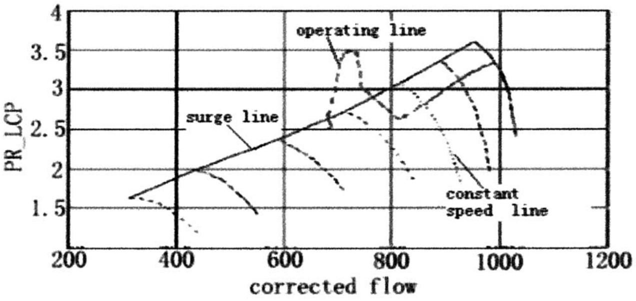

Fig. 4 Performance map of low-pressure compressor

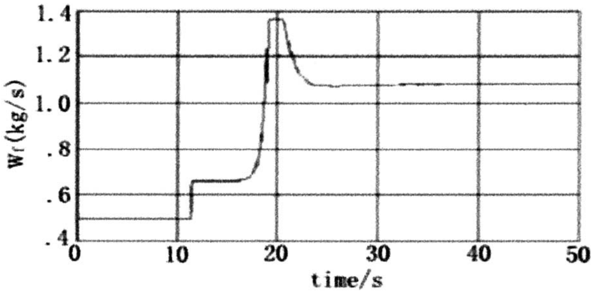

Fig. 5 Fuel flow rate based on the fuel control strategy

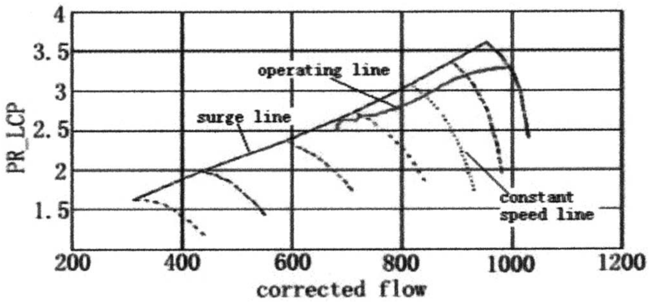

Fig. 6 Performance map of low-pressure compressor

the compressor operating line based on the fuel flow shown in Fig. 3. This line exceeds the surge line, which is not allowed. Thus, a control strategy must be developed that keeps the operating line below the surge line.

When the speed regulator handle is pushed, the rack bar will move suddenly. The sudden increase of fuel will change the system performance. Because of the inertia of the low-pressure compressor, the system tends to run immediately toward the surge line. In order to prevent the compressor working line from crossing the compressor surge line, the fuel flowing into the combustion chamber should be limited at the beginning of the acceleration. After many experimental tests on the gas turbine engine using this hardware-in-the-loop simulation platform, we obtained a successful fuel control strategy for the engine, which is shown in Fig. 5. The corresponding working line on the performance map is indicated in Fig. 6.

Because the fuel is limited at the beginning of the acceleration, the fuel input can be efficiently consumed and compressor surge is avoided. From the result of three rotor speeds associated with this control strategy, we can know that the acceleration process is accomplished in less than 10 s. This also meets the maneuverability requirement for marine shaft-power ships. Additionally, these rotor transients are similar to the optimum acceleration process, according to Refs. [4], [6], [7].

Besides controlling the fuel input, a control system requires, on many engines, other means of affecting the engine characteristics, such as turbine inlet temperature, smoke formation, etc. These additional requirements can also be studied using this hardware in the loop simulation technology.

Concluding Remarks

This paper reports a fuel control simulation implementation of hardware-in-the-loop system for gas turbine. The main conclusions of this work are

i. Based on the volume inertia and modular modeling ideas, the modular simulation models of a three-shaft gas turbine engine have been established. This method is more convenient than conventional modeling concepts because it eliminates the iterative calculation in the coupling of pressure and flow rate.
ii. The hardware-in-the-loop simulation platform is established using a modular framework with independent functions; it is flexible to add or delete a module. This platform implements the hardware-in-the-loop simulation, it is a useful tool for the simulation study of gas turbine engine dynamics.
iii. A fuel control strategy is determined for a three-shaft gas turbine engine system that experiences sudden acceleration. This demonstrates that we can study the transient characteristics of a gas turbine engine using this platform.

Acknowledgments

This work was supported by the State Key Fundamental Research Program under Contract No. G1999022303, and the National Nature Science Foundation of China (NSFC) under the contract No. 59976022.

References

[1] Hanselmann, H., 1993, "Hardware-in-the-Loop Simulation as a Standard Approach for Development, Customization and Production Test," SAE Paper 930207.

[2] Carcasci, C., Facchini, B., and Roccardo, M., 1993, "Modular Approach to Off-Design Gas Turbines Simulation: New Prospect for Reheat Applications," ASME Paper 96-GT-395.

[3] Heyen, G., Murphy, K., Marchio, D. et al., 1994, "Dynamic Simulation and Control of Gas Turbine and Compressor Systems," Comput. Chem. Eng., **18**(11/12), pp. 1071–1082.

[4] Su, M., 1998, "Mathematical Model of Dynamic Real Time Simulation on 3-Shaft Gas Turbine for Ship," J. Shanghai Jiaotong Univ., **3**, pp. 11–13.

[5] Zhang, H., Liu, Y., Su, M. et al., 2002, "Simulation Study on The Speed Regulation of Gas Turbine," Comput. Simul., **1**, pp. 79–81.

[6] Ni, W., and Liu, S., 1992, "The Design of Acceleration Control Strategy Within Minimum Time for Aerospace Engine," J. Aerospace Power, **4**, pp. 45–49.

[7] Weng, S. L., 1996, *Gas Turbine and Steam Turbine*, Publishing House of Shanghai Jiaotong University, Shanghai.